
Fluxional Organometallic and Coordination Compounds

Physical Organometallic Chemistry

Editorial Board

Marcel Gielen, Free University of Brussels, Belgium
Rudolph Willem, Free University of Brussels, Belgium
Bernd Wrackmeyer, Universität Bayreuth, Germany

Books previously published in this Series

Volume 1 Advance Applications of NMR to Organometallic Chemistry

Edited by

Marcel Gielen, Free University of Brussels, Belgium
Rudolph Willem, Free University of Brussels, Belgium
Bernd Wrackmeyer, Universität Bayreuth, Germany
ISBN 0 471 95938 3

Volume 2 Solid State Organometallic Chemistry

Edited by

Marcel Gielen, Free University of Brussels, Belgium
Rudolph Willem, Free University of Brussels, Belgium
Bernd Wrackmeyer, Universität Bayreuth, Germany
ISBN 0 471 97920 1

Volume 3 Unusual Structures and Physical Properties in Organometallic Chemistry

Edited by

Marcel Gielen, Free University of Brussels, Belgium
Rudolph Willem, Free University of Brussels, Belgium
Bernd Wrackmeyer, Universität Bayreuth, Germany
ISBN 0 471 49635 9

PHYSICAL ORGANOMETALLIC
CHEMISTRY VOLUME 4

Fluxional Organometallic
and
Coordination Compounds

Edited by

MARCEL GIELEN

Free University of Brussels, Belgium

RUDOLPH WILLEM

Free University of Brussels, Belgium

BERND WRACKMEYER

Universität Bayreuth, Germany



John Wiley & Sons, Ltd

Copyright © 2004 John Wiley & Sons Ltd, The Atrium, Southern Gate, Chichester,
West Sussex PO19 8SQ, England

Telephone (+44) 1243 779777

Email (for orders and customer service enquiries): cs-books@wiley.co.uk
Visit our Home Page on www.wileyurope.com or www.wiley.com

All Rights Reserved. No part of this publication may be reproduced, stored in a retrieval system or transmitted in any form or by any means, electronic, mechanical, photocopying, recording, scanning or otherwise, except under the terms of the Copyright, Designs and Patents Act 1988 or under the terms of a licence issued by the Copyright Licensing Agency Ltd, 90 Tottenham Court Road, London W1T 4LP, UK, without the permission in writing of the Publisher. Requests to the Publisher should be addressed to the Permissions Department, John Wiley & Sons Ltd, The Atrium, Southern Gate, Chichester, West Sussex PO19 8SQ, England, or emailed to permreq@wiley.co.uk, or faxed to (+44) 1243 770620.

This publication is designed to provide accurate and authoritative information in regard to the subject matter covered. It is sold on the understanding that the Publisher is not engaged in rendering professional services. If professional advice or other expert assistance is required, the services of a competent professional should be sought.

Other Wiley Editorial Offices

John Wiley & Sons Inc., 111 River Street, Hoboken, NJ 07030, USA

Jossey-Bass, 989 Market Street, San Francisco, CA 94103-1741, USA

Wiley-VCH Verlag GmbH, Boschstr. 12, D-69469 Weinheim, Germany

John Wiley & Sons Australia Ltd, 33 Park Road, Milton, Queensland 4064, Australia

John Wiley & Sons (Asia) Pte Ltd, 2 Clementi Loop #02-01, Jin Xing Distripark, Singapore 129809

John Wiley & Sons Canada Ltd, 22 Worcester Road, Etobicoke, Ontario, Canada M9W 1L1

Wiley also publishes its books in a variety of electronic formats. Some content that appears in print may not be available in electronic books.

Library of Congress Cataloging-in-Publication Data

Fluxional organometallic and coordination compounds / edited by Marcel Gielen, Rudolph Willem, Bernd Wrackmeyer.

p. cm. – (Physical organometallic chemistry : v. 4)

Includes bibliographical references and index.

ISBN 0-470-85839-7 (cloth : alk. paper)

1. Coordination compounds. 2. Organometallic chemistry. 3. Molecular dynamics.
4. Nuclear magnetic resonance spectroscopy. I. Gielen, M. (Marcel), 1938- II. Willem, R. (Rudolf) III. Wrackmeyer, Bernd, 1947- IV. Series.

QD411.F58 2004

541'.2242-dc22

2004003666

British Library Cataloguing in Publication Data

A catalogue record for this book is available from the British Library

ISBN 0 470 85839 7

Typeset in 10.5/12pt Times New Roman by TechBooks, New Delhi, India

Printed and bound in Great Britain by MPG, Bodmin, Cornwall

This book is printed on acid-free paper responsibly manufactured from sustainable forestry in which at least two trees are planted for each one used for paper production.

Contents

Contributors	xi
Series Preface	xiii
Preface	xv
1 Polyhedral Dynamics and the Jahn–Teller Effect	
<i>R. Bruce King</i>	
1 Introduction	1
2 Polyhedron Topology	2
3 Polyhedral Isomerizations: Microscopic Models	6
3.1 Diamond–Square–Diamond Processes	6
3.2 Gale Diagrams	11
3.3 Generation of Metallaborane Structures by Diamond–Square–Diamond Transformations in Deltahedra	18
4 Polyhedral Isomerizations: Macroscopic Models	21
4.1 Topological Representations of Polyhedral Isomerizations	21
4.2 Topological Representations of Jahn–Teller Distortions	28
5 Acknowledgement	37
6 References	37
2 NMR Studies of Intramolecular Dynamics in Allylic Type Triorganoboranes	
<i>I. D. Gridnev and O. L. Tok</i>	
1 Introduction	41
2 Discovery Activation Parameters of [1,3]-B Shifts	42
3 Fluxional Linear Polyunsaturated Allylboranes	47
3.1 2,4-Pentadienyl(di- <i>n</i> -propyl)borane	47
3.2 2,4,6-Heptatrienyl(di- <i>n</i> -propyl)borane	50
4 Dynamic Behavior of Cyclic Allylboranes	53
4.1 Dynamic Equilibria Between 2-(Dialkylboryl)methylenecyclobutanes and 1-(Dialkylboryl)cyclobutenes	53
4.2 Dynamic Properties of Cyclopentadienyl and Pentamethylcyclopentadienyl Derivatives of Boron	58
4.3 Synthesis and Dynamic Properties of 1-Indenyl(diethyl)borane	58

4.4	Dynamic Behavior of Cycloheptadienyl(di- <i>n</i> -propyl) borane	60
4.5	Synthesis and Dynamic Properties of Cycloheptatrienyl(di- <i>n</i> -propyl)borane. Equilibrium with 7-(Di- <i>n</i> -propylboryl)norcaradiene	61
4.6	Three Independent Dynamic Processes in the Irontricarbonyl Complex of Cycloheptatrienyl(di- <i>n</i> -propyl)borane	65
4.7	Cyclooctatetraenyl(di- <i>n</i> -propyl)borane	67
4.8	Sigmatropic Migrations and Thermal Rearrangements in Cyclononatetraenyl(di- <i>n</i> -propyl)borane. Comparison with the Dynamic Properties of Cyclononatetraenyl(trimethyl)tin	70
4.9	Borotropic Migrations in Phenalenyl(di- <i>n</i> -propyl)borane 24	75
5	Diverse Chemoselectivity of Cyclic Polyunsaturated Organoboranes	77
5.1	Chemical Behavior of Borane 23	77
5.2	Diverse Chemoselectivity of 9-Cyclopentyl-9-borabarbaralane 54e	79
6	Conclusion	81
7	References	81

3 Dynamic Behavior of Group 5 and 6 Transition Metal Complexes with NMR

S. Sakharov

1	Introduction	85
2	Rotational Isomerism in Amido and Ketimido Complexes	86
2.1	Rotational Isomerism in Oxofluoramido Complexes of Tungsten(VI)	86
2.2	Restricted M–NR ₂ Rotation in the Dinuclear Complexes with M ₂ ⁶⁺ Core (M = W, Mo)	91
2.3	Features of Dynamic Behavior of Amido Cyclopentadienyl Complexes of Group 5 Transition Metals	93
2.4	Internal Hindered Rotation of Ketimido Ligands	95
3	Dynamic Behavior of d ⁰ Transition Metal Complexes with n-Donor Two-Center Ligands	98
3.1	Isomerization of Fluorocomplexes of Group 5–6 with O, N-Two-Center Ligands	98
3.2	Isomerism of Transition Metal Complexes with N, N-Two-center Ligands	110
3.3	Nature of Bonding of n-Donor Two-center Ligands in d ⁰ Transition Metal Complexes	119
3.4	Mechanism of Internal Hindered Rotation of η ² -Bound Ligands	121
4	Conclusion	126
5	References	126

4	Conformational Mobility in Chelated Square-planar Rh, Ir, Pd, and Pt Complexes	
	<i>P. Espinet and J. A. Casares</i>	
1	Introduction	131
2	Conformational Changes in Five-member Metallacycles	132
3	Conformational Changes in Six-member Metallacycles	142
4	Conformational Changes in Five- or Six-member Metallacycles Involving Coordinated Olefins	152
5	Conformational Changes in Seven-member Metallacycles	154
6	Conformational Changes in Higher Metallacycles	156
7	Acknowledgment	158
8	References	158
5	Dynamic and Kinetic Aspects of Metallodrugs by NMR	
	<i>F. Li and H. Sun</i>	
1	Introduction	163
2	Methods of Study by NMR	164
3	Platinum Anticancer Drugs	169
3.1	^{195}Pt , ^{15}N and Inverse [^1H , ^{15}N] NMR Spectroscopy	170
3.2	Activation of Platinum Anticancer Drugs: Kinetics and Equilibria of Aquation	173
3.3	Platination of Nucleotides and DNA	176
3.4	Interaction of Platinum Agents with Amino Acids, Peptides and Proteins	182
4	Titanium and Ruthenium Anticancer Agents	185
5	Gold Antiarthritic Drugs	188
6	Antimony Antiparasitic and Bismuth Antiulcer Drugs	193
7	Vanadium Antidiabetic Mimetics	197
8	MRI Contrast Agents	202
9	Concluding Remarks	209
10	Abbreviations	209
11	Acknowledgements	210
12	References	210
6	Dynamics by EPR: Picosecond to Microsecond Time Scales	
	<i>S. Van Doorslaer and G. Jeschke</i>	
1	Introduction	219
2	Scope of EPR Spectroscopy	221
2.1	Native Paramagnetic Centers	221
2.2	Spin Labels and Spin Probes	222
3	A Brief Primer on EPR Spectroscopy	223
3.1	Interactions of Electron Spins with Their Environment	223
3.2	Relaxation	226
3.3	Measurement Techniques	227

4	Detection of Dynamic Processes by EPR	229
4.1	Slow Tumbling	229
4.2	Exchange Processes	231
4.3	Dynamic Jahn–Teller Effect	231
4.4	Chemically Induced Dynamic Electron Polarization (CIDEP)	234
5	Application Example: How to Combine Different EPR Techniques	236
6	Acknowledgements	240
7	References	240
7	μSR Studies of Molecular Dynamics in Organometallics <i>U. A. Jayasooriya</i>	
1	Introduction	243
2	Muon	243
3	Muon in Matter	244
4	Experiment	246
5	Muon in a Longitudinal Magnetic Field	247
6	Muon–Electron (Muonium Like) System	250
7	Molecular Dynamics	251
8	Studies of Organometallics	252
8.1	Tetraphenyl Metals	252
8.2	Benzene Chromium Tricarbonyl	252
8.3	Cyclopentadienyl Manganese Tricarbonyl	255
8.4	Ruthenocene	256
8.5	Ferrocene	256
8.6	Ferrocene Encapsulated in Zeolite	261
9	Conclusion	263
9	Acknowledgements	264
10	References	264
8	Proton Dynamics in Solids: Vibrational Spectroscopy with Neutrons <i>F. Fillaux</i>	
1	Introduction	267
2	Vibrational Spectroscopy Techniques	269
2.1	Some Definitions	269
2.2	Optical Techniques	270
2.3	Neutron Scattering Techniques	271
2.4	Potassium Hydrogen Bistrifluoroacetate	276
3	Vibrational Dynamics of Protons in Solids	278
3.1	Force-Field Calculations: Normal versus Localized Modes	278
3.2	The Proton Crystal Model	280

CONTENTS

4	Tunnelling	282
4.1	Proton Transfer	282
4.2	Rotational Tunnelling	285
5	Conclusions	301
6	References	302
	Index	305

Contributors

R Bruce King, Department of Chemistry, University of Georgia, Athens, Georgia 30602, USA

Ilya D Gridnev, COE Laboratory, Department of Chemistry, Graduate School of Science, Tohoku University, Sendai 980-8578, Japan

Oleg L Tok, Anorganische Chemie II, University of Bayreuth, D-95440 Bayreuth, Germany

Sergei G Sakharov, Kurnakov Institute of General and Inorganic Chemistry, Russian Academy of Sciences, Leninskii pr. 31, Moscow 119991, Russia

Pablo Espinet, Departamento de Química Inorgánica, Universidad de Valladolid, E- 47005 Valladolid, Spain

Juan A Casares, Departamento de Química Inorgánica, Universidad de Valladolid, E- 47005 Valladolid, Spain

Hongzhe Sun, Department of Chemistry and Open Laboratory of Chemical Biology, University of Hong Kong, Pokfulam Road, Hong Kong

Fei Li, Department of Chemistry and Open Laboratory of Chemical Biology, University of Hong Kong, Pokfulam Road, Hong Kong

Sabine Van Doorslaer, SIBAC Laboratorium, Universiteit Antwerpen – Department Natuurkunde, Universiteitsplein 1, B-2610 Wilrijk, Belgium

Gunnar Jeschke, Max-Planck-Institute for Polymer Research, Postfach 3148, D-55021 Mainz, Germany

Upali Jayasooriya, School of Chemical Sciences, University of East Anglia, Norwich, UK

Françoise Fillaux, Laboratoire de Spectrochimie Infrarouge et Raman, CNRS, 2 rue Henry Dunant, Thiais, France

Series Preface

Physical organic chemistry, the study of the basic physical principles of organic reactions, is not a new field: in 1940, Hammett had already written a book with this title. This area has developed during the last 20 years mainly because of the explosive growth of sophisticated analytical instrumentation and computational techniques, going from the simple Hückel molecular orbital theory to *ab initio* calculations of increasing accuracy enabled by the advent of fast supercomputers.

An analogous genesis characterized physical organometallic chemistry. Understanding the basis of chemical reactivity and the detailed pathways of reactions of organometallic compounds is now one of the major goals of physical organometallic chemists. Correlation of structure with reactivity, increasing in sophistication, contributes powerfully to the understanding of electronic transmission, as well as of steric and conformational properties, including solvent effects. Homogeneous catalysis has reached a development stage making it a wide, complex topic deserving special consideration. Chiral induction is also becoming increasingly important, considering the economic importance of asymmetric syntheses in the design of pharmaceuticals: organometallic compounds play a key role in this area; understanding this role is the key to further progress.

Accordingly, the major developments of physical organometallic chemistry are not only relevant to *ab initio* calculations of metal-based organic compounds or new spectroscopic tools like multidimensional high-resolution NMR. They also involve new ingenious technologies to study reaction mechanisms, group-theoretical approaches to investigate the fluxionality of organometallic molecules, photochemical reactions on organometallic substrates, and, last but not least, experimental highlights like unstable organometallic compounds in matrices, piezochemistry, and sonochemistry.

The main goal of this series 'Physical Organometallic Chemistry' is to offer to post-graduates and researchers leading contributions written by well-known scientists reviewing the state-of-the-art of hot topics animating this wide research area, in order to develop new insights and to promote novel interest and investigations.

Preface

Dynamic processes are of prime importance in all fields of chemistry in order to understand structure and reactivity. With the ever-increasing performance of analytical tools both slow and fast dynamics can be studied and analyzed nowadays to reveal properties of matter which previously have not been fully understood and sometimes not even anticipated. Frequently, we find situations where theory is ahead of experiment, but there are also numerous experimental results which await theoretical explanation. Indeed, fluxional processes taking place in molecules can be determined and explained on various levels of experiment and theory. It is therefore important to be aware of different concepts and techniques, and to look out for the methodologies and research strategies which are most appropriate to tackle dynamic problems. Certainly, this fascinating complex and broad field cannot be covered completely in this book. The topics selected here address some key concepts and methods which may be regarded as useful examples of an interdisciplinary approach. This volume starts off with the dynamic behavior of polyhedral compounds in the light of the Jahn–Teller effect. The first chapter has a general bearing for clusters containing main group elements and/or transition metals. Then, the application of NMR spectroscopy to dynamics is addressed, a field which is very familiar to most people working in organometallic and coordination chemistry. This general topic is treated in many text books and has been reviewed regularly. Therefore, we have picked out examples for a few classes of compounds, and by this we expect that stimulating information is provided to initiate studies in related areas. Allylic boranes open the view into a fascinating world of dynamic behavior of organic compounds when an apparently innocent heteroatom like boron, the neighbor of carbon in the Periodic Table, is present. Transition metal complexes can be regarded as an Eldorado of fluxionality, and representative examples of Groups 5 and 6 and of the platinum metals of Groups 9 and 10 serve to illustrate this point. The origin of dynamics can be sought in the ligands, in the electronic structure of the metal center, or in synergetic effects arising from both ligand and metal. This topic is further elaborated by an excursion to metallo drugs, where the structure–reactivity relationship plays a really vital role. We have left out solid-state NMR in this volume, since dynamic aspects seen by solid-state NMR have been discussed in previous volumes of this series. This is also true for dynamics in single crystals studied by X-ray diffraction analysis. Some people may miss the dynamic behavior of paramagnetic compounds, studied by NMR. Considering the recent monograph (I. Bertini, C. Luchinat,

G. Parigi, *Solution NMR of Paramagnetic Molecules*, Elsevier, Amsterdam, 2001), we decided not to include this subject. Since paramagnetic samples are readily studied by EPR, a relevant chapter provides information on application of EPR to fluxionality. This is not only meant as a report; it also intends to stimulate potential applications in organometallic chemistry. A sufficient muon flux generation requires an appropriate particle accelerator, and therefore, μ -SR spectroscopy (here SR stands for spin relaxation) is rarely applied to investigate fluxionality in organometallic compounds. However, this technique has considerable potential, and it reveals information complementary to other methods, and also shows unexpected new features, where the unpaired electron is playing an active role. The final chapter deals with inelastic neutron scattering (INS) aiming at the study of proton dynamics in solids. The dynamic properties of hydrogen bridges, the behavior of rotors containing hydrogen atoms, starting with the famous dihydrogen ligand in transition metal complexes, followed by the ammonia molecule in various surroundings, and by methyl groups can be analyzed by INS to give a completely new insight into these processes. It can be envisaged that this technique will be applicable to other systems which show pronounced proton fluxionality such as metal hydroborates, metal fluoride complexes, e.g. with M-F...H-F bridges, and to numerous compounds which possess so-called weak hydrogen bridges as in metal hydride complexes with M-H...H-N or M-H...H-C bridges.

1 Polyhedral Dynamics and the Jahn–Teller Effect

R. BRUCE KING

Department of Chemistry, University of Georgia, Athens, GA 30602, USA

1 INTRODUCTION

The role of polyhedra in the static description of chemical structures makes of considerable interest their dynamic properties. In this connection the central concept in the study of polyhedral dynamics is that of a polyhedral isomerization. In this context a polyhedral isomerization is defined as a deformation of a specific polyhedron \mathcal{P}_1 until its vertices define a new polyhedron \mathcal{P}_2 . Of particular interest are sequences of two polyhedral isomerization steps $\mathcal{P}_1 \rightarrow \mathcal{P}_2 \rightarrow \mathcal{P}_3$ in which the final polyhedron \mathcal{P}_3 is combinatorially equivalent to the initial polyhedron \mathcal{P}_1 although with some permutation of the vertices. Such polyhedral isomerization sequences are called degenerate polyhedral isomerizations.

Polyhedral isomerizations may be studied using either a microscopic or macroscopic approach. The microscopic approach uses details of polyhedral topology to elucidate possible single polyhedral isomerization steps, namely which types of isomerization steps are possible. Such isomerization steps consist most commonly of so-called diamond–square–diamond processes or portions thereof. The microscopic approach to polyhedral isomerizations is relevant to understanding fluxional processes in borane and metallaborane polyhedra.

The earliest work on polyhedral isomerizations by Muetterties [1–4], Gielen [5–12], Musher [13,14], Klemperer [15–17] and Brocas [18,19] used a macroscopic approach involving relationships between different permutational isomers. Such relationships may be depicted by reaction graphs called topological representations (or top-reps) in which the vertices correspond to different permutational isomers and the edges correspond to single degenerate polyhedral isomerization steps. The macroscopic point of view is also useful for the classification of Jahn–Teller distortions of polyhedra [20] relating to the instability of a non-linear symmetrical nuclear configuration in an electronic degenerate state [21–24].

Both approaches will be reviewed in this chapter, which expands and updates reviews published by the author in 1988 [25] and 1994 [26] and a book in 1992 [27].

2 POLYHEDRON TOPOLOGY

Before considering polyhedral dynamics it is first necessary to consider the static topology of polyhedra. Of fundamental importance are relationships between possible numbers and types of vertices (v), edges (e), and faces (f) of polyhedra. In this connection the following elementary relationships are particularly significant [28]:

1. Euler's relationship:

$$v - e + f = 2 \quad (1.1)$$

This theorem is illustrated by the five regular polyhedra depicted in Figure 1.1.

2. Relationship between the edges and faces:

$$\sum_{i=3}^{v-1} i f_i = 2e \quad (1.2)$$

In Equation (1.2) f_i is the number of faces with i edges (i.e., f_3 is the number of triangular faces, f_4 is the number of quadrilateral faces, etc.). This relationship arises from the fact that exactly two faces share each edge of the polyhedron. Since no face can have fewer edges than the three of a triangle, the following inequality must hold in all cases:

$$3f \leq 2e \quad (1.3)$$

3. Relationship between the edges and vertices:

$$\sum_{i=3}^{v-1} i v_i = 2e \quad (1.4)$$

In Equation (1.4) v_i is the number of vertices of *degree* i (i.e., having i edges meeting at the vertex in question). This relationship arises from the fact that each edge of the polyhedron connects exactly two vertices. Since no vertex of a polyhedron can have a degree less than three, the following inequality must hold in all cases:

$$3v \leq 2e \quad (1.5)$$

4. Totality of faces:

$$\sum_{i=3}^{v-1} f_i = f \quad (1.6)$$

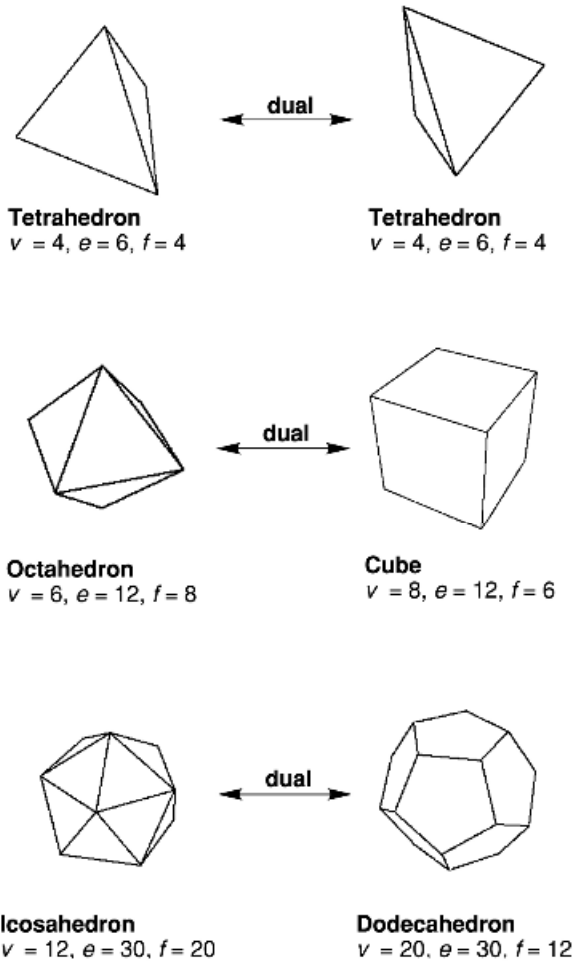


Figure 1.1 The five regular polyhedra depicted as dual pairs.

5. Totality of vertices:

$$\sum_{i=3}^{v-1} v_i = v \tag{1.7}$$

Equation (1.6) relates the f_i s to f and Equation (1.7) relates the v_i s to v .

In generating actual polyhedra, the operations of capping and dualization are often important. *Capping* a polyhedron \mathcal{P}_1 consists of adding a new vertex above the center of one of its faces \mathcal{F}_1 followed by adding edges to connect the new vertex with each vertex of \mathcal{F}_1 . If \mathcal{F}_1 has k edges, then the capping process can be more specifically described as k -capping.

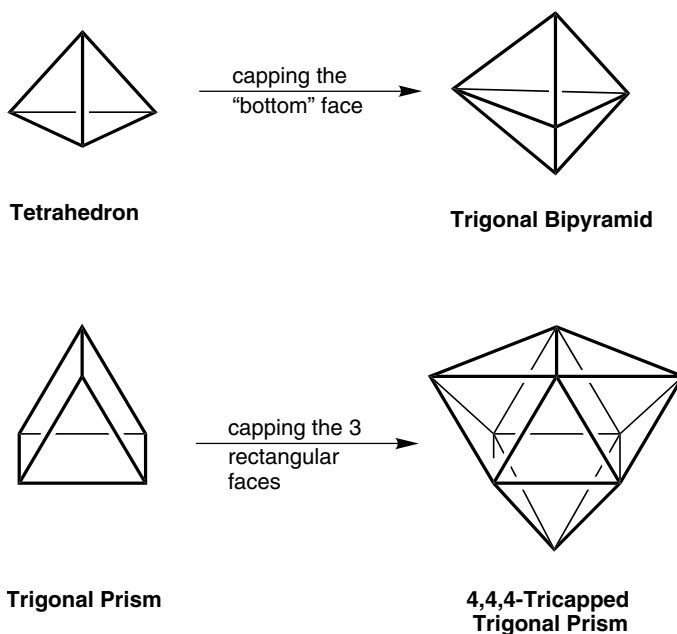


Figure 1.2 (a) Capping a face of the tetrahedron to form a trigonal bipyramid. (b) Capping all three rectangular faces of a trigonal prism to form a D_{3h} tricapped trigonal prism.

The capping process gives a new polyhedron \mathcal{P}_2 having one more vertex than \mathcal{P}_1 . If a triangular face is capped (i.e., 3-capping), the following relationships will be satisfied in which the subscripts 1 and 2 refer to \mathcal{P}_1 and \mathcal{P}_2 , respectively:

$$v_2 = v_1 + 1; \quad e_2 = e_1 + 3; \quad f_2 = f_1 + 2 \quad (1.8)$$

Such a capping of a triangular face is found in the capping of a tetrahedron to form a trigonal bipyramid (Figure 1.2a). In general if a face with f_k edges is capped (i.e., k -capping), the following relationships will be satisfied:

$$v_2 = v_1 + 1; \quad e_2 = e_1 + f_k; \quad f_2 = f_1 + f_k - 1 \quad (1.9)$$

For example, application of such a capping process to each of the three rectangular faces of a trigonal prism generates the 4,4,4-tricapped trigonal prism (Figure 1.2b). This nine-vertex deltahedron appears in both coordination chemistry (e.g., ReH_9^{2-}) and borane chemistry (e.g., $\text{B}_9\text{H}_9^{2-}$).

Another process of interest in polyhedral topology is the *dualization* of polyhedra. A given polyhedron \mathcal{P} can be converted into its dual \mathcal{P}^* by locating the centers of the faces of \mathcal{P}^* at the vertices of \mathcal{P} and the vertices of \mathcal{P}^* above the centers of the faces of \mathcal{P} . Two vertices in the dual \mathcal{P}^* are connected by an edge when the corresponding faces in \mathcal{P} share an edge.

The process of dualization has the following properties:

- (1) The numbers of vertices and edges in a pair of dual polyhedra \mathcal{P} and \mathcal{P}^* satisfy the relationships $v^* = f$, $e^* = e$, $f^* = v$, in which the starred variables refer to the dual polyhedron \mathcal{P}^* . Thus for the octahedron (\mathcal{P})/cube(\mathcal{P}^*) dual pair depicted in Figure 1.1 $v = f^* = 6$, $e^* = e = 12$, $f = v^* = 8$.
- (2) Dual polyhedra have the same symmetry elements and thus belong to the same symmetry point group. Thus in the example above both the octahedron and the cube have the O_h symmetry point group. Also note in general that the dualization of a prism gives the corresponding bipyramid and vice versa.
- (3) Dualization of the dual of the polyhedron leads to the original polyhedron.
- (4) The degrees of the vertices of a polyhedron correspond to the number of edges in the corresponding face polygons in its dual.

The process of dualization can be illustrated by the regular polyhedra (Figure 1.1). Thus the octahedron and cube are dual to each other as are the icosahedron and dodecahedron. The tetrahedron is self-dual.

The problem of the classification and enumeration of polyhedra is a complicated one. Thus there appear to be no formulas, direct or recursive, for which the number of combinatorially distinct polyhedra having a given number of vertices, edges, faces, or any given combination of these elements can be calculated [29,30]. Duijvestijn and Federico have enumerated by computer the polyhedra having up to 22 edges according to the numbers of vertices, edges, and faces and their symmetry groups and present a summary of their methods, results, and literature references to previous work [31]. Their work shows that there are 1, 2, 7, 34, 257, 2606, and 32,300 topologically distinct polyhedra having 4, 5, 6, 7, 8, 9, and 10 faces or vertices, respectively. Tabulations are available for all 301 ($= 1 + 2 + 7 + 34 + 257$) topologically distinct polyhedra having eight or fewer faces [32] or eight or fewer vertices [33]. These two tabulations are essentially equivalent by the dualization relationship discussed above.

In coordination chemistry, the polyhedra of greatest significance in coordination chemistry are those that can be formed by the nine orbitals of the sp^3d^5 valence orbital manifold accessible to d-block transition metals. There are, however, some polyhedra having fewer than nine vertices that cannot be formed by these nine orbitals; such polyhedra are called *forbidden polyhedra* [34,35]. Group theoretical arguments show that polyhedra of the following types are always forbidden polyhedra:

- (1) Polyhedra having eight vertices, a direct product symmetry group $R \times C_s$ or $R \times C_i$ (R contains only *proper* rotations) and the plane in C_s fixing either 0 or 6 vertices.
- (2) Polyhedra having a six-fold or higher C_n rotation axis.

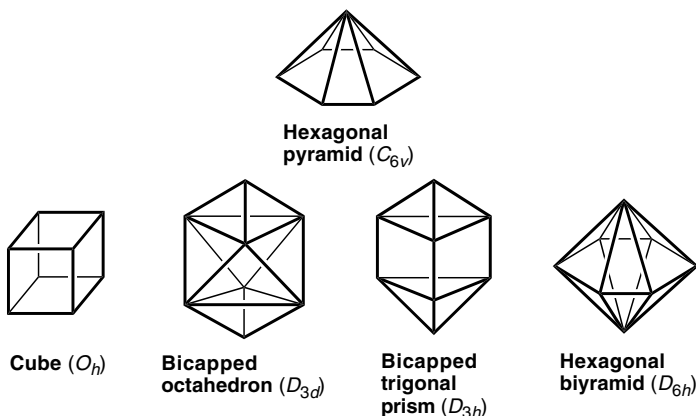


Figure 1.3 Chemically significant forbidden polyhedra: (a) the hexagonal pyramid; (b) examples of eight-vertex polyhedra (all with inversion centers) which cannot be formed from a nine-orbital sp^3d^5 manifold.

Chemically significant forbidden polyhedra include the seven-vertex hexagonal bipyramid and the eight-vertex cube, D_{3d} bicapped octahedron, D_{3h} 3,3-bicapped trigonal prism, and hexagonal bipyramid (Figure 1.3).

In the chemistry of polyhedral boranes and related compounds including their organometallic derivatives, the polyhedra of greatest importance are deltahedra, i.e., polyhedra in which all faces are triangles. Among the large number of such possible deltahedra, the most important deltahedra are the so-called ‘most spherical’ deltahedra, i.e., those where the vertex degrees are as similar as possible to each other. In terms of the structures of the deltahedral boranes $B_nH_n^{2-}$, this means deltahedra having from six to 12 vertices in which all of the vertices are of degree 4 or degree 5 (Figure 1.4).

3 POLYHEDRAL ISOMERIZATIONS: MICROSCOPIC MODELS

3.1 DIAMOND–SQUARE–DIAMOND PROCESSES

A polyhedral isomerization can be defined as a deformation of a specific polyhedron \mathcal{P}_1 until its vertices define a new polyhedron \mathcal{P}_2 . Of particular interest are sequences of two polyhedral isomerization steps $\mathcal{P}_1 \rightarrow \mathcal{P}_2 \rightarrow \mathcal{P}_3$ in which the final polyhedron \mathcal{P}_3 is combinatorially (i.e., topologically) equivalent to the initial polyhedron \mathcal{P}_1 although with some permutation of its vertices, generally not the identity permutation. In this sense two polyhedra \mathcal{P}_1 and \mathcal{P}_3 may be considered to be combinatorially equivalent [36] when there are three one-to-one mappings \mathcal{V} , \mathcal{E} , and \mathcal{F} from the vertex, edge, and face sets, respectively, of \mathcal{P}_1 to

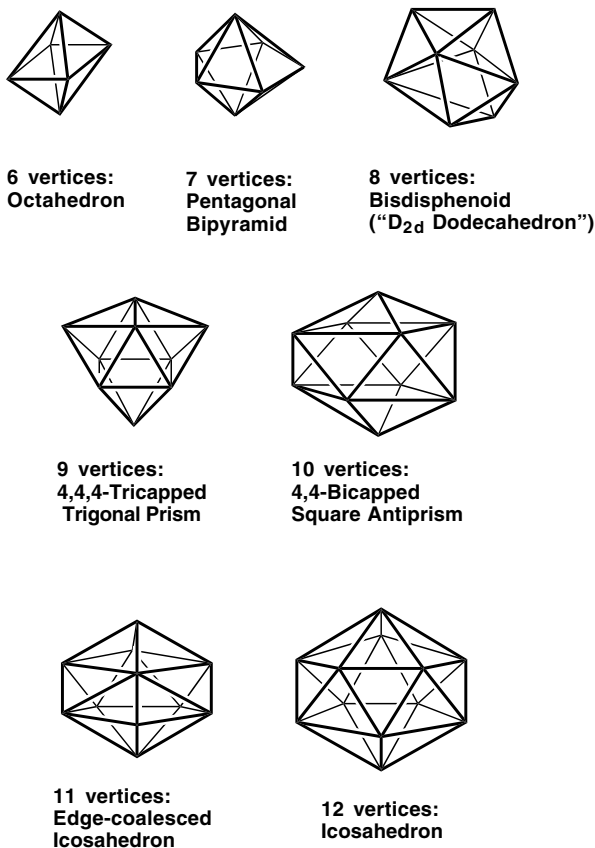


Figure 1.4 The deltahedra found in the boranes $B_nH_n^{2-}$ and isoelectronic carboranes ($6 \leq n \leq 12$).

the corresponding sets of \mathcal{P}_3 such that incidence relations are preserved. Thus if a vertex, edge, or face α of \mathcal{P}_1 is incident to or touches upon a vertex, edge, or face β of \mathcal{P}_1 , then the images of α and β under \mathcal{V} , \mathcal{E} , or \mathcal{F} are incident in \mathcal{P}_3 .

Consider a polyhedral isomerization sequence $\mathcal{P}_1 \rightarrow \mathcal{P}_2 \rightarrow \mathcal{P}_3$ in which \mathcal{P}_1 and \mathcal{P}_3 are combinatorially equivalent. Such a polyhedral isomerization sequence may be called a degenerate polyhedral isomerization with \mathcal{P}_2 as the intermediate polyhedron. Structures undergoing such degenerate polyhedral isomerization processes are often called fluxional [37]. A degenerate polyhedral isomerization with a planar intermediate ‘polyhedron’ (actually a polygon) may be called a planar polyhedral isomerization. The simplest example of a planar polyhedral isomerization is the interconversion of two enantiomeric tetrahedra

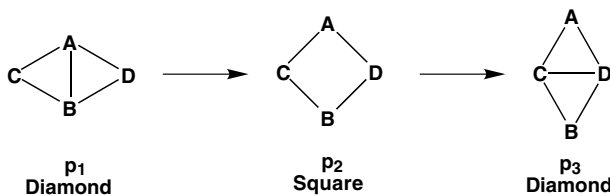


Figure 1.5 The effect of a diamond–square–diamond (dsd) process on a pair of triangular faces sharing an edge.

(\mathcal{P}_1 and \mathcal{P}_3) through a square planar intermediate \mathcal{P}_2 . Except for this simplest example, planar polyhedral isomerizations are unfavorable owing to excessive intervertex repulsion.

Microscopic approaches to polyhedral isomerizations dissect such processes into elementary steps. The most important elementary step is the diamond–square–diamond process that was first recognized in a chemical context by Lipscomb in 1966 [38] as a generalization of a process proposed earlier by Berry [39] for the degenerate isomerization of a trigonal bipyramid. Such a diamond–square–diamond process or ‘dsd process’ in a polyhedron occurs at two triangular faces sharing an edge (Figure 1.5). Thus a configuration such as p_1 can be called a *dsd situation* and the edge AB can be called a switching edge.

Let a , b , c , and d represent the degrees of the vertices A , B , C , and D , respectively, in p_1 , then the *dsd type* of the switching edge AB can be represented as $ab(cd)$. In this designation the first two digits refer to the degrees of the vertices joined by AB but contained in the faces (triangles) having AB as the common edge (i.e., C and D in p_1). The quadrilateral face formed in structure p_2 may be called a *pivot face*. If a , b , c , and d are the degrees of vertices A , B , C , and D , respectively, in the original diamond (p_1), then the requirement for a degenerate dsd process is the following:

$$c = a - 1 \quad \text{and} \quad d = b - 1 \quad \text{or} \quad c = b - 1 \quad \text{and} \quad d = a - 1 \quad (1.10)$$

A polyhedron with e edges has e distinct dsd situations; if at least one of these dsd situations is degenerate by satisfying Equation (1.10), then the polyhedron is inherently fluxional [40]. The inherent rigidity/fluxionality of the most important deltahedra including the most spherical deltahedra found in boranes (Figure 1.4) is summarized in Table 1.1.

This simple analysis indicates that in deltahedral structures the 4, 6, 10, and 12 vertex structures are inherently rigid; the 5, 8, 9, and 11 vertex structures are inherently fluxional; and the rigidity of the seven-vertex structure depends upon the energy difference between the two most symmetrical seven-vertex deltahedra [40]. From the point of view of coordination chemistry, note that the trigonal bipyramid and bisdisphenoid, which are favored coordination polyhedra for

Table 1.1 Inherent fluxionality/rigidity of deltahedra

Vertices	Deltahedron	Inherently rigid or fluxional
4	Tetrahedron	Rigid
5	Trigonal bipyramid	Fluxional
6	Octahedron	Rigid
7	Pentagonal bipyramid/ Capped octahedron	ML ₇ → Fluxional Boranes → Rigid
8	Bisdisphenoid	Fluxional
9	Tricapped trigonal prism	Fluxional
10	Bicapped square antiprism	Rigid
11	Edge-coalesced icosahedron	Fluxional
12	Icosahedron	Rigid

coordination numbers 5 and 8, respectively, are inherently fluxional whereas the octahedron found in six-coordinate complexes is inherently rigid. This relates to the stereochemical non-rigidity of five- and eight-coordinate complexes observed experimentally in contrast to the relative rigidity of six-coordinate complexes. In the case of deltahedral borane chemistry, experimental fluxionality observations by boron-11 nuclear magnetic resonance on $B_nH_n^{2-}$ ($6 \leq n \leq 12$) indicate the 6-, 7-, 9-, 10-, and 12-vertex structures to be rigid and the 8- and 11-vertex structures to be fluxional. The only discrepancy between such experiments and these very simple topological criteria for fluxionality in the deltahedral boranes arises in the nine-vertex structure $B_9H_9^{2-}$.

The discrepancy between the predictions of this simple topological approach and experiment for $B_9H_9^{2-}$ has led to the search for more detailed criteria for the rigidity of deltahedral boranes. In this connection Gimarc and Ott have studied orbital symmetry methods, particularly for the five-[41], seven-[42], and nine-[43] vertex borane and carborane structures. A topologically feasible dsd process is orbitally forbidden if crossing of occupied and vacant molecular orbitals (i.e., a 'HOMO–LUMO crossing') occurs during the dsd process as illustrated in Figure 1.6 for the single dsd process for the trigonal bipyramid, namely the so-called Berry pseudorotation [39,44]. For such an orbitally forbidden process the activation barrier separating initial and final structures is likely to be large enough to prevent this polyhedral isomerization. However, the forbidden dsd polyhedral rearrangement for the five-vertex $B_5H_5^{2-}$ and corresponding carboranes is allowed in ML_5 coordination compounds and has been observed in PX_5 derivatives such as PCl_5 and PF_5 (i.e., the single fluorine-19 resonance in PF_5) as well as $Fe(CO)_5$ (i.e., the single carbon-13 or oxygen-17 resonance). Guggenberger and Muettterties [45] point out that cage framework rearrangements such as those in the deltahedral boranes and carboranes involve bond stretches which must require more energy than bond angle changes that occur in coordination polyhedra of ligands bound to a central atom.

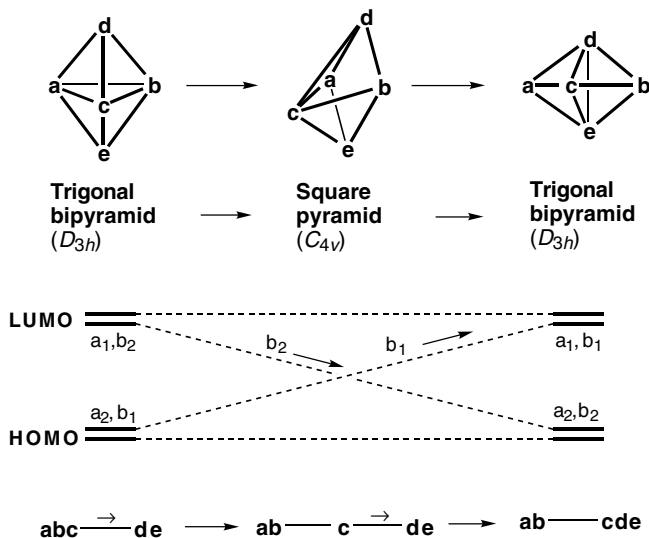


Figure 1.6 (a) The single dsd process converting a trigonal bipyramid to an isomeric trigonal bipyramid through a square pyramid intermediate (Berry pseudorotation). (b) The orbital crossing for this dsd process. (c) Gale diagrams for this polyhedral isomerization sequence.

Some selection rules have been proposed for distinguishing between symmetry-allowed and symmetry-forbidden processes in deltahedral boranes, carboranes, and related structures. Thus Wales and Stone [46] distinguish between symmetry-allowed and symmetry-forbidden processes by observing that a HOMO–LUMO crossing occurs if the proposed transition state has a single atom lying on a principal C_n rotational axis where $n \geq 3$. A more detailed selection rule was observed by Mingos and Johnston [47]. If the four outer edges of the two fused triangular faces (i.e., the ‘diamond’) are symmetry equivalent, then a single dsd process results in a pseudorotation of the initial polyhedron by 90° (Figure 1.7a) such as occurs for the trigonal bipyramid in Figure 1.6. However, if the edges are not symmetry equivalent (as indicated by the regular and bold edges in Figure 1.7b), then the rearrangement results in a pseudoreflexion of the initial polyhedron. Pseudorotations are symmetry forbidden and have larger activation energies than pseudoreflexions, which are symmetry allowed. Subsequent work by Wales *et al.* [48] has shown that a dsd process in which a mirror plane is retained throughout involves an orbital crossing and is therefore symmetry forbidden in accord with the earlier work by Gimarc and Ott [41].

The fact that a degenerate single dsd isomerization of the D_{3h} nine-vertex tricapped trigonal prismatic $B_9H_9^{2-}$ through a C_{4v} capped square antiprismatic intermediate (Figure 1.8a) is orbitally forbidden [43] has stimulated searches

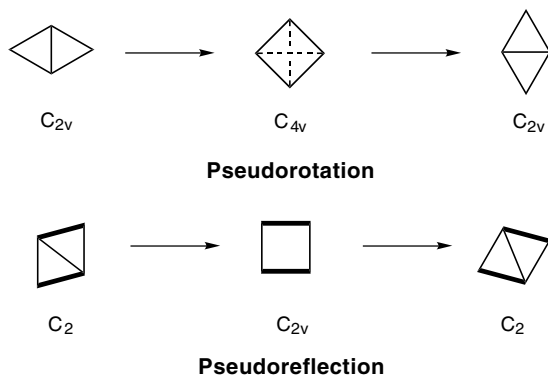


Figure 1.7 (a) A pseudorotation process involving an intermediate with a C_4 axis. (b) A pseudoreflexion process involving an intermediate without a C_4 axis.

for other isomerization mechanisms for the tricapped trigonal prism. In this connection Gimarc and Ott [43] have found a double dsd isomerization of $B_9H_9^{2-}$ (Figure 1.8b) to be orbitally allowed. However, Ceulemans *et al.* [49] have shown by computation that an analogous double dsd isomerization of the carborane $C_2B_7H_9$ passes through an intermediate with an open hexagonal face thereby preserving C_{3v} subgroup symmetry of the D_{3h} point group of the original tricapped trigonal prism.

3.2 GALE DIAGRAMS

Gale diagrams provide an elegant mathematical method for the study of microscopic aspects of rearrangement of polyhedra having relatively few vertices (i.e., for $v \leq 6$) by reducing the dimensionality of the allowed vertex motions. In a chemical context Gale diagrams can be used to study possible rearrangements of six-atom structures. Using this approach the skeletal rearrangements of the six atoms are depicted as movements of six points on the circumference of a circle or from the circumference to the center of the circle subject to severe restrictions that reduce possible such movements to a manageable number [50].

Consider a polytope \mathcal{P} in d -dimensional space \mathfrak{R}^d , where the term ‘polytope’ refers to the generalization of the concept of ‘polyhedron’ to any number of dimensions [36]. The minimum number of vertices of such a polytope is $d + 1$ and there is only one such polytope, namely the d -simplex in which each possible pair of the $d + 1$ vertices are connected by an edge corresponding to the so-called complete graph [51] K_{d+1} . The combinatorially distinct possibilities for d -dimensional polytopes having only $d + 2$ and $d + 3$ vertices (polyhedra with ‘few’ vertices) are also rather limited. They can be represented faithfully in a space of less than d dimensions through a Gale

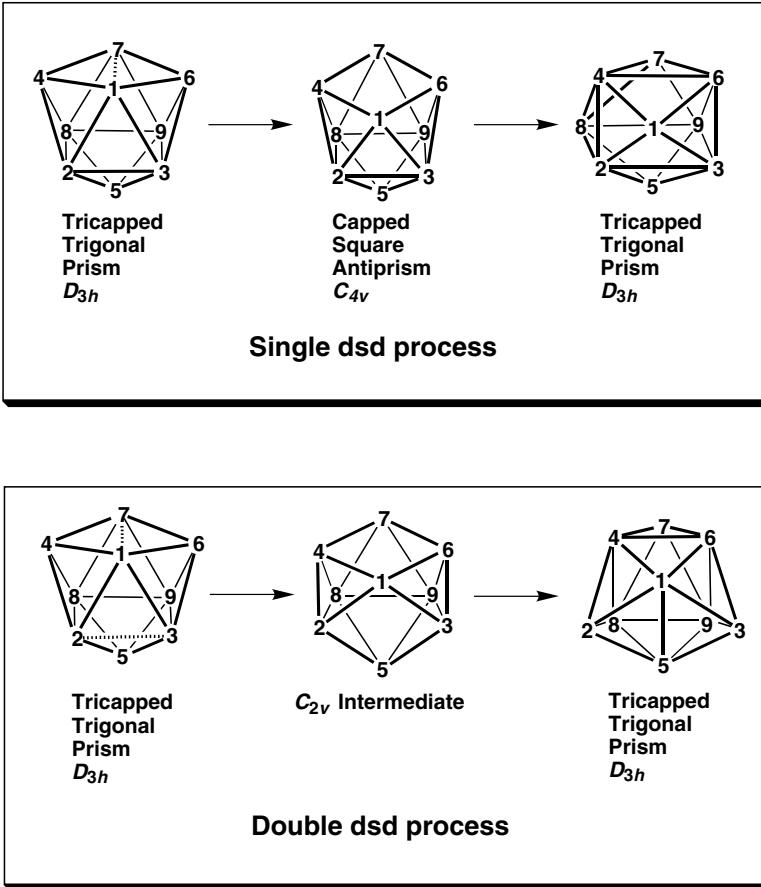


Figure 1.8 (a) A forbidden single dsd degenerate isomerization of a tricapped trigonal prism. (b) An allowed double dsd degenerate isomerization of a tricapped trigonal prism.

transformation [52]. More specifically, if \mathcal{P} is a d -dimensional polytope with v vertices, a Gale transformation leads to a Gale diagram of \mathcal{P} consisting of v points in $(v-d-1)$ -dimensional space \mathfrak{R}^{d-1} in one-to-one correspondence with the vertices of \mathcal{P} . From the Gale diagram it is possible to determine all of the combinatorial properties of \mathcal{P} such as the subsets of the vertices of \mathcal{P} that define faces of \mathcal{P} , the combinatorial types of these faces, etc. The combinatorial properties of a polytope \mathcal{P} which can be determined by the Gale diagram include all possible isomerizations (rearrangements) of \mathcal{P} to other polytopes having the same number of vertices and imbedded in the same number of dimensions as \mathcal{P} . Also of particular importance is the fact that, if v is not much larger than d (i.e., if $v \leq 2d$), then the dimension of the Gale diagram is smaller than that of the original polytope \mathcal{P} .

Now consider polyhedra in the ordinary three-dimensional space of interest in chemical structures (i.e., $d = 3$). Gale diagrams of five- and six-vertex polyhedra can be embedded into one- or two-dimensional space, respectively, thereby simplifying analysis of their possible vertex motions leading to non-planar polyhedral isomerizations of these polyhedra of possible interest in a chemical context.

In order to obtain a Gale diagram for a given polyhedron, the polyhedron is first subjected to a *Gale transformation*. Consider a polyhedron with v vertices as a set of v points X_1, \dots, X_v in three-dimensional space \mathfrak{R}^3 . These points may be regarded as three-dimensional vectors $\mathbf{X}_n = (x_{n,1}, x_{n,2}, x_{n,3})$, $1 \leq n \leq v$, from the origin to the vertices of the polyhedron. In addition, consider a set of points $\mathcal{D}(\mathbf{A})$ in v -dimensional space \mathfrak{R}^v , $\mathbf{A} = (a_1, \dots, a_v)$ such that the following sums vanish:

$$\sum_{i=1}^v a_i x_{i,k} = 0 \text{ for } 1 \leq k \leq 3 \quad (1.11a)$$

$$\sum_{i=1}^v a_i = 0 \quad (1.11b)$$

Equation (1.11a) may also be viewed as three orthogonality relationships between the v -dimensional vector $\mathbf{A} = (a_1, \dots, a_v)$ and the three v -dimensional vectors $(x_{1,k}, x_{2,k}, \dots, x_{v,k})$, $1 \leq k \leq 3$. Now consider the locations of the vertices of the polyhedron as the following $v \times 4$ matrix:

$$\mathbf{D}_0 = \begin{pmatrix} x_{1,1} & x_{1,2} & x_{1,3} & 1 \\ x_{2,1} & x_{2,2} & x_{2,3} & 1 \\ \cdot & \cdot & \cdot & \cdot \\ \cdot & \cdot & \cdot & \cdot \\ x_{v,1} & x_{v,2} & x_{v,3} & 1 \end{pmatrix} \quad (1.12)$$

Consider the columns of \mathbf{D}_0 as vectors in \mathfrak{R}^v . Since \mathbf{D}_0 has rank 4, the four columns of \mathbf{D}_0 are linearly independent. Hence the subspace $\mathcal{M}(\mathbf{X})$ of \mathfrak{R}^v represented by these four linearly independent columns has dimension 4. Its orthogonal complement $\mathcal{M}(\mathbf{A})^\perp = \{\mathbf{A} \in \mathfrak{R}^v \mid \mathbf{A} \cdot \mathbf{X} = 0 \text{ for all } \mathbf{X} \in \mathcal{M}(\mathbf{X})\}$ coincides with $\mathcal{D}(\mathbf{A})$ defined above by equations (1.11a) and (1.11b). Therefore:

$$\dim \mathcal{D}(\mathbf{A}) = \dim \mathcal{M}(\mathbf{A})^\perp = v - \dim \mathcal{M}(\mathbf{X}) = v - 4 \quad (1.13)$$

Now define the following $v \times (v - 4)$ matrix:

$$\mathbf{D}_1 = \begin{pmatrix} a_{1,1} & a_{1,2} & \cdot & \cdot & \cdot & a_{1,v-4} \\ a_{2,1} & a_{2,2} & \cdot & \cdot & \cdot & a_{2,v-4} \\ \cdot & \cdot & & & & \cdot \\ \cdot & \cdot & & & & \cdot \\ a_{v,1} & a_{v,2} & \cdot & \cdot & \cdot & a_{v,v-4} \end{pmatrix} \quad (1.14)$$

The v rows of \mathbf{D}_1 may be considered as vectors in $(v-4)$ -dimensional space; conventionally the j th row is denoted by $\bar{x}_j = (a_{j,1}, a_{j,2}, \dots, a_{j,v-4})$ for $j = 1, \dots, v$.

The final result of this construction is the assignment of a point \bar{x}_j in $(v-4)$ -dimensional space (\mathfrak{R}^{v-4}) to each vertex x_j of the polyhedron. The collection of v points $\bar{x}_1, \dots, \bar{x}_v$ in \mathfrak{R}^{v-4} is called a *Gale transform* of the set of vertices x_1, \dots, x_v of the polyhedron in question. The following features of a Gale transform of a polyhedron should be noted:

- (1) Gale transforms \bar{x}_j and \bar{x}_k of two or more vertices of a polyhedron may lead to the same point (i.e., the same $v-4$ coordinates) in $(v-4)$ -dimensional space (\mathfrak{R}^{v-4}). In other words some points of a Gale transform may have a multiplicity greater than one so that the Gale transform of a polyhedron in such cases contains fewer *distinct* points than the polyhedron has vertices.
- (2) The Gale transform depends upon the location of the origin in the coordinate system. Therefore, infinitely many Gale transforms are possible for a given polyhedron. Geometrically a Gale transform of a polyhedron corresponds to a projection of the v vertices of a $(v-1)$ -dimensional simplex [53]. Since infinitely many such projections are possible, the Gale transform for a given polyhedron is *not* unique.

In practice, it is easier to work with Gale diagrams corresponding to Gale transforms of interest. Consider a Gale transform of a (three-dimensional) polyhedron having v vertices $\bar{x}_1, \dots, \bar{x}_v$ as defined above. The corresponding Gale diagram $\hat{x}_1, \dots, \hat{x}_v$ is defined by the following relationships:

$$\hat{x}_i = 0 \quad \text{if} \quad \bar{x}_i = 0 \quad (1.15a)$$

$$\hat{x}_i = \frac{x_i}{\|\bar{x}_i\|} \quad \text{if} \quad \bar{x}_i \neq 0 \quad (1.15b)$$

In Equation (1.15b) $\|\bar{x}_i\|$ is the length (i.e., $\sqrt{a_{i,1}^2 + a_{i,2}^2 + \dots + a_{i,v-4}^2}$) of the vector \bar{x}_i . If $v-4 = 1$ (i.e., $v = 5$), Gale diagrams can only contain the points of the straight line 0, 1, and -1 of varying multiplicities m_0 , m_1 , and m_{-1} , respectively, where $m_0 \geq 0$, $m_1 \geq 2$, and $m_{-1} \geq 2$. If $v-4 = 2$ (i.e., $v = 6$) Gale diagrams can only contain the center and circumference of the unit circle. These two types of Gale diagrams (Figure 1.9) are of interest for the study of polyhedral isomerizations since they represent significant structural simplifications of the corresponding polyhedra.

The following properties of Gale diagrams corresponding to three-dimensional polyhedra are of interest since they impose important restrictions on configurations of points which can be Gale diagrams:

- (1) Any $(v-5)$ -dimensional plane passing through the central point of the Gale diagram bisects the space of the Gale diagram into two halfspaces. Each

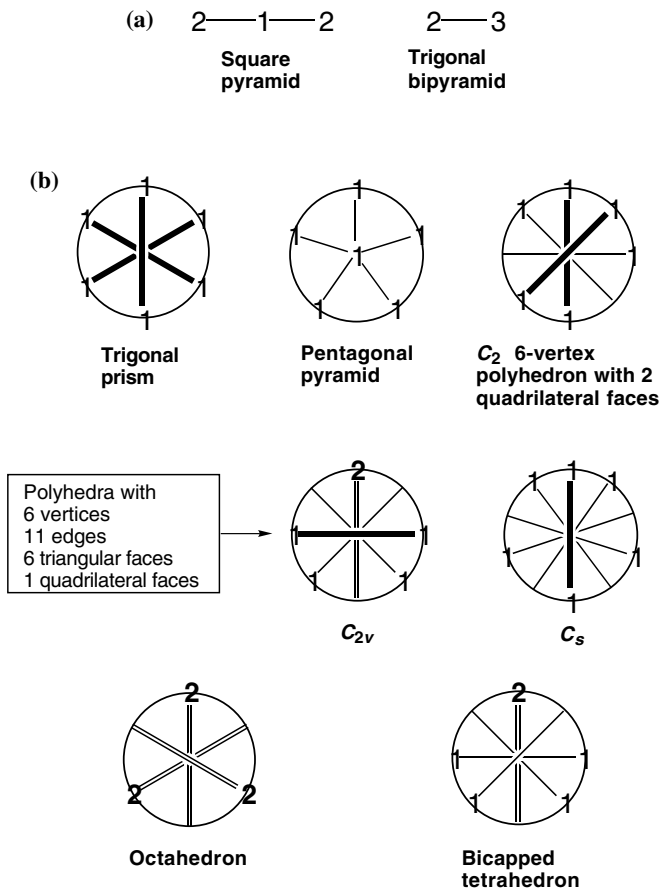


Figure 1.9 (a) Gale diagrams for the two five-vertex polyhedra. (b) Standard Gale diagrams for the seven six-vertex polyhedra.

such halfspace must contain at least two vertices (or one vertex of multiplicity 2) of the Gale diagram *not* including any vertices actually in the bisecting plane or hyperplane. Such a halfspace is called an *open* halfspace. Violation of this condition corresponds to a polyhedron with the impossible property of at least one pair of vertices *not* connected by an edge which is closer in three-dimensional space than another pair of vertices which is connected by an edge.

- (2) The set of vertices of a polyhedron *not* forming a given face or edge of the polyhedron is called a *coface* of the polyhedron. The regular octahedron is unusual since all of its faces are also cofaces corresponding to other faces. The interior of a figure formed by connecting the vertices of a Gale diagram corresponding to a coface must contain the central point.

- (3) The central point is a vertex of a Gale diagram if and only if the corresponding polyhedron is a pyramid. The central vertex of such a Gale diagram corresponds to the apex of a pyramid which is the coface corresponding to the base of the pyramid.

Nonplanar isomerizations of five- and six-vertex polyhedra correspond to allowed vertex motions in the corresponding Gale diagrams in Figure 1.9. In this context an *allowed vertex motion* of a Gale diagram is the motion of one or more vertices which converts the Gale diagram of a polyhedron into that of another polyhedron with the same number of vertices without ever passing through an impossible Gale diagram. Such impossible Gale diagrams include those with an open halfspace containing only one vertex of unit multiplicity. Since two polyhedra are combinatorially equivalent if and only if their Gale diagrams are isomorphic, such allowed vertex motions of Gale diagrams are faithful representations of all possible non-planar polyhedral isomerizations.

The application of Gale diagrams to the study of isomerizations of five-vertex polyhedra is nearly trivial but provides a useful illustration of this method. The only possible five-vertex polyhedra are the square pyramid and trigonal bipyramid. Their Gale diagrams (Figure 1.9a) are the only two possible one-dimensional five-vertex Gale diagrams which have the required two vertices in each open halfspace (i.e., $m_1 \geq 2$ and $m_{-1} \geq 2$). The only allowed vertex motion in a Gale diagram of a trigonal bipyramid involves motion of one point from the vertex of multiplicity 3 through the center point to the vertex originally of multiplicity 2 as indicated in Figure 1.6c. This process interchanges the vertices of multiplicities 2 and 3 and leads to an equivalent Gale diagram corresponding to an isomeric trigonal bipyramid. The motion through the center point of the Gale diagram corresponds to the generation of a square pyramid intermediate in the nonplanar degenerate isomerization of a trigonal bipyramid. This, of course, is the Berry pseudorotation process [39,44] that is the prototypical dsd process. The choice of three points to move away from the vertex of multiplicity 3 in the Gale diagram of a trigonal bipyramid corresponds to the presence of three degenerate edges in a trigonal bipyramid. This analysis of the Gale diagrams of the two possible five-vertex polyhedra shows clearly that the only possible nonplanar isomerizations of five-vertex polyhedra can be represented as successive dsd processes corresponding to successive Berry pseudorotations (Figure 1.6).

The Gale diagrams of six-vertex polyhedra (Figure 1.9b) can be visualized most clearly if all of the diameters containing vertices are drawn. Some Gale diagrams of six vertex polyhedra have diameters with vertices of unit multiplicity at each end. Such diameters may be called *balanced diameters* and are indicated by bold lines in Figure 1.9b. The two vertices of a balanced diameter in the Gale diagram of a six-vertex polyhedron form an edge which is a coface corresponding to a quadrilateral face. Gale diagrams drawn to maximize the

multiplicities of the vertices and the numbers of balanced diameters consistent with the polyhedral topology are called *standard Gale diagrams*. The Gale diagrams depicted in Figure 1.9b are the standard Gale diagrams for the six-vertex polyhedra in question. The number of balanced diameters in a standard Gale diagram of a six-vertex polyhedron is equal to the number of quadrilateral faces of the polyhedron. The pentagonal pyramid is the only six-vertex polyhedron for which the center of the circle is a vertex of the corresponding standard Gale diagram.

The standard Gale diagrams of the trigonal prism and octahedron illustrate another interesting feature of Gale diagrams, namely the ability to draw Gale diagrams so that all symmetry elements of the corresponding polyhedron are preserved. The C_3 symmetry elements of both the trigonal prism and octahedron are readily apparent in their standard Gale diagrams passing through the center perpendicular to the plane of the circle (Figure 1.9b). In the case of the trigonal prism, the three C_2 axes of its D_{3h} point group correspond to the three balanced diameters of the corresponding standard Gale diagram. In the case of the octahedron, which has the O_h point group, the reflection planes σ_h correspond to permuting the two vertices of an octahedron forming a vertex of multiplicity two in the corresponding standard Gale diagram while keeping the other vertices fixed. The C_2 and C_4 rotation axes of the octahedron pass through the center and a vertex of multiplicity two in the corresponding standard Gale diagram and permute the other four vertices forming the two other standard Gale diagram vertices of multiplicity two in various ways.

Alternatively the regular octahedron can be considered to be a regular $K_{2,2,2}$ tripartite graph [54]. Thus the six vertices of the octahedron are partitioned into three antipodal pairs (i.e., two vertices with a mutual *trans* relationship). Each vertex then has an edge to every vertex other than its antipode in accord with the definition of a multipartite graph [51]. Each of the three double points in the Gale diagram of a regular octahedron (Figure 1.9b) corresponds to one of the three antipodal pairs of vertices.

Polyhedral isomerizations in six-vertex polyhedra may be described by allowed motions of the vertices of their Gale diagrams along the circumference of the unit circle or through the circle center in the case of polyhedral isomerizations involving a pentagonal pyramid intermediate. However, vertex motions are not allowed if at any time they generate one or more forbidden diameters containing three or more vertices. Using these techniques all non-planar degenerate isomerizations of six-vertex polyhedra can be decomposed into sequences of eight fundamental processes, namely two processes through pentagonal pyramid intermediates, five processes which are variations of single diamond–square–diamond processes, and the triple dsd degenerate isomerization of an octahedron through a trigonal prism intermediate on which the Bailar [55] and Ray and Dutt [56] twists of $M(\text{bidentate})_3$ complexes are based.

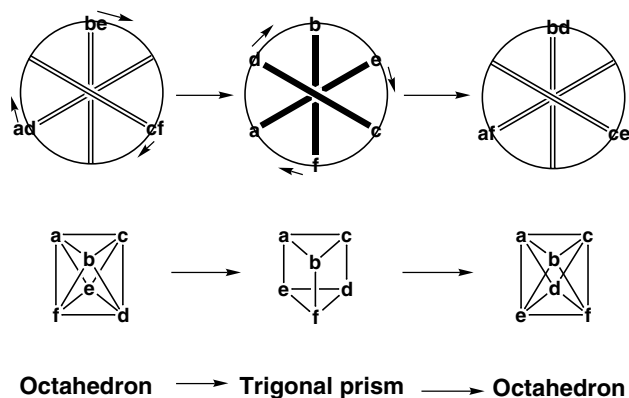


Figure 1.10 Gale diagrams for the triple dsd degenerate isomerization of an octahedron through a trigonal prismatic intermediate corresponding to the Bailar or Ray/Dutt twists.

The Gale diagrams depicting the latter processes are depicted in Figure 1.10. Note that in the first (diamond–square) stage of this triple dsd process leading from the octahedron to the trigonal prism, one vertex from each of the three vertex pairs (i.e., ad , be , and cf) in the Gale diagram of the octahedron must move in the same direction in a concerted manner preserving the C_3 axis in order to avoid violating the ‘half-space rule.’ The standard Gale diagram of the trigonal prism is reached when three balanced diameters are formed. Similarly, in the second (square–diamond) stage leading from the trigonal prism to an isomeric octahedron these three vertices continue to move in a concerted manner so as to preserve the C_3 axis.

3.3 GENERATION OF METALLABORANE STRUCTURES BY DIAMOND–SQUARE–DIAMOND TRANSFORMATIONS IN DELTAHEDRA

The basic building blocks of the most stable boranes, namely $B_nH_n^{2-}$ ($6 \leq n \leq 12$) and their isoelectronic carborane analogues $CB_{n-1}H_n^-$ and $C_2B_{n-2}H_n$, are the most spherical deltahedra (Figure 1.4). In these deltahedra all of the vertices have degrees 4 or 5 except for the topologically required single degree 6 vertex [57] in the $B_{11}H_{11}^{2-}$ deltahedron. The boron vertices in these deltahedra can be replaced by isolobal transition metal vertices bearing sufficient external ligands such as carbonyl groups or perhapto planar polygons (e.g., $\eta^5-C_5H_5$ or $\eta^6-C_6H_6$) to give the transition metal vertex a favorable electronic configuration. Initially it was assumed that the deltahedra in metallaboranes would be the same as the deltahedra in isoelectronic metal-free boranes. However, as metallaborane chemistry was developed further, particularly by Kennedy and co-workers [58–61], a variety of deltahedral metallaborane structures were

discovered based on deltahedra topologically distinct from the most spherical deltahedra found in simple metal-free boranes and carboranes (Figure 1.4). Of particular interest was the discovery of 9- and 10-vertex metallaboranes based on deltahedra with the transition metal at a degree 6 vertex whereas the metal-free borane has a most spherical deltahedral structure (Figure 1.4) with only degree 4 and 5 vertices.

The experimentally observed metallaborane deltahedra are related to the most spherical deltahedra by a series of one or more dsd processes [62,63]. For example, among the 10-vertex deltahedra a single dsd process converts the most spherical bicapped square antiprism (Figure 1.4) of four-fold D_{4d} symmetry found in $B_{10}H_{10}^{2-}$ to a deltahedron of three-fold C_{3v} symmetry with a single degree 6 vertex (Figure 1.11a). The ‘square’ intermediate in this single

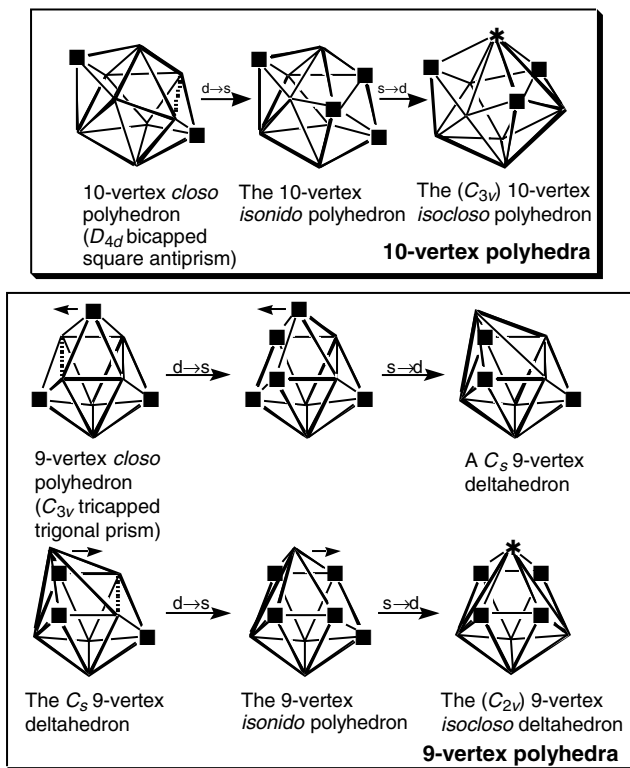


Figure 1.11 (a) Conversion of a D_{4d} bicapped square antiprism to the C_{3v} *isocloso* 10-vertex deltahedron through a dsd process. (b) Conversion of a C_{3v} tricapped trigonal prism to a C_{2v} *isocloso* 9-vertex deltahedron through a sequence of two dsd processes. For clarity the vertices of degrees 3, 4, 6, and 7 are labelled with the symbols \blacktriangle , \blacksquare , \ast , and \odot , respectively, in Figures 1.11 and 1.12. The vertices of degree 5 are not labelled in these figures.

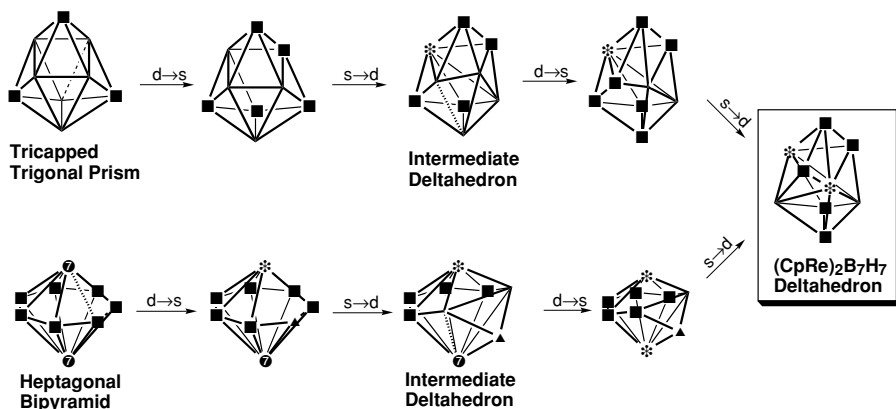


Figure 1.12 Two ways of generating the unusual 9-vertex deltahedron found in $(\eta^5\text{-C}_5\text{H}_5\text{Re})_2\text{B}_7\text{H}_7$ by sequences of two dsd processes: (a) from a D_{3h} tricapped trigonal prism; (b) from a D_{7h} heptagonal bipyramid.

dsd process is a so-called 10-vertex *isonido* polyhedron with a single quadrilateral face. In metallaboranes the transition metal occupies the degree 6 vertex. Similarly among the 9-vertex deltahedra two successive dsd processes convert the most spherical tricapped trigonal prism (Figure 1.4) to a C_{2v} deltahedron with a degree 6 vertex for a transition metal (Figure 1.11b). This 9-vertex deltahedron is observed experimentally in $(\text{Me}_3\text{P})_2\text{HfIrB}_8\text{H}_7\text{Cl}$ [64] with the iridium atom at the degree 6 vertex.

The conversion of a most spherical borane n -vertex deltahedron to a deltahedron with a degree 6 vertex for a transition metal atom leads to a change in its skeletal electron count from $2n + 2$ to simply $2n$ [58–61]. This has been attributed to a change in the skeletal bonding from a globally delocalized model with an n -center core bond to a more localized bonding model with two-center bonds along some of the deltahedral edges and three-center bonds in some of the deltahedral faces [62].

Two different sequences of dsd processes can be used to generate the rather unusual 9-vertex deltahedron found in $(\eta^5\text{-C}_5\text{H}_5\text{Re})_2\text{B}_7\text{H}_7$ with the rhenium atoms at the two degree 6 vertices (Figure 1.12) [65]. In the first such sequence, this deltahedron is obtained by a sequence of two dsd processes from the most spherical 9-vertex deltahedron, namely the tricapped trigonal prism (Figure 1.12a). This double dsd sequence generates two degree 6 vertices from a deltahedron having only degree 4 and 5 vertices. Alternatively, $(\eta^5\text{-C}_5\text{H}_5\text{Re})_2\text{B}_7\text{H}_7$ can be obtained by a sequence of two dsd process from the heptagonal bipyramid (Figure 1.12b). This double dsd sequence eliminates the two degree 7 vertices from the heptagonal bipyramid leaving two degree 6 vertices for the rhenium atoms.

4 POLYHEDRAL ISOMERIZATIONS: MACROSCOPIC MODELS

4.1 TOPOLOGICAL REPRESENTATIONS OF POLYHEDRAL ISOMERIZATIONS

Macroscopic models depict the relationship between different permutational isomers. Such models make use of topological representations (top-reps), which are reaction graphs [66,67] describing the relationships between the different permutational isomers of a given polyhedron. Thus, consider an ML_n compound having n ligands L around a central metal M or a cluster compound having n vertices. There are a total of $n!$ permutations of the ligand sites or the cluster vertices. These permutations form a group of order $n!$ called the symmetric group [68,69] and conventionally designated as S_n . The symmetric group S_n is the automorphism group corresponding to the symmetry of the complete graph K_n [51].

Now consider the symmetry point group G (or, more precisely, the framework group [70]) of the above ML_n coordination compound or n -vertex cluster compound. This group has $|G|$ operations of which $|R|$ are proper rotations so that $|G|/|R| = 2$ if the compound is achiral and $|G|/|R| = 1$ if the compound is chiral (i.e., has no improper rotations). The $n!$ distinct permutations of the n sites in the coordination compound or cluster are divided into $n!/|R|$ right cosets [71] which represent the permutational isomers since the permutations corresponding to the $|R|$ proper rotations of a given isomer do not change the isomer but merely rotate it in space. This leads naturally to the concept of *isomer count*, I , namely

$$I = n!/|R| \quad (1.16)$$

if all vertices are distinguishable. Similarly the quotient

$$E = n!/|G| = I/2 \quad (1.17)$$

for a given *chiral* polyhedron corresponds to the number of enantiomeric pairs.

Top-reps are reaction graphs [66,67] describing the relationships between polyhedral isomers. They there have I (Equation 1.16) or E vertices (Equation 1.17) depending upon whether individual isomers or enantiomeric pairs, respectively, are considered. The degree of a vertex corresponds to the number of new permutational isomers generated from the isomer represented by the vertex in a single step. This is called the connectivity, δ , of the vertex. Such reaction graphs for degenerate polyhedral isomerizations have been shown to be vertex- and edge-transitive [72].

The top-reps for the isomerizations of four- and five-vertex molecular polyhedra are quite straightforward. Thus the top-rep for four-vertex isomerizations is a graph with two degree 3 vertices and three degree 2 vertices corresponding to the unsymmetrical bipartite graph $K_{2,3}$ or to a trigonal bipyramid with the

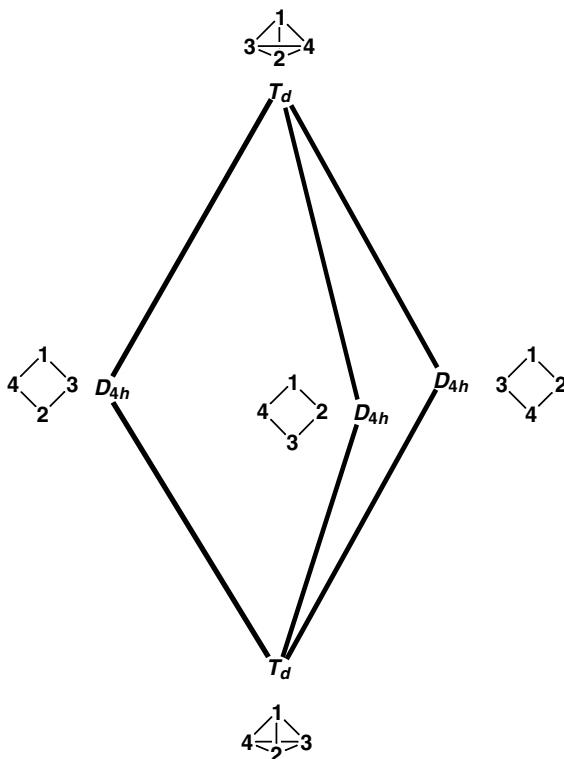


Figure 1.13 The $K_{2,3}$ bipartite graph top-rep describing isomerization of four-vertex molecular polyhedra in which the sites marked T_d and D_{4h} correspond to tetrahedral and square planar isomers, respectively. The isomers corresponding to the vertices of the $K_{2,3}$ bipartite graph are depicted next to the vertex labels.

equatorial–equatorial edges missing (Figure 1.13). The two degree 3 vertices (the axial vertices of the underlying trigonal bipyramid) correspond to the two tetrahedral isomers ($I_{\text{tet}} = 4!/|T| = 24/12 = 2$). Similarly, the three degree 2 vertices (the equatorial vertices of the underlying trigonal bipyramid) correspond to the three square planar isomers ($I_{\text{sq}} = 4!/|D_4| = 24/8 = 3$). The connectivities of the tetrahedral (δ_{tet}) and square planar (δ_{sq}) isomers are 3 and 2, respectively, in accord with the corresponding degrees of the $K_{2,3}$ graph. Thus $I_{\text{tet}}\delta_{\text{tet}} = I_{\text{sq}}\delta_{\text{sq}} = 6$. This is an example of the closure condition $I_a\delta_a = I_b\delta_b$ required for a top-rep representing more than one type of polyhedron.

In order to consider the top-reps of more complicated polyhedra, it is first instructive to consider the top-rep of four-vertex isomerizations depicted in Figure 1.13 in a different way, namely as a graph with only two vertices connected by three edges like the hydrogen-deleted molecular graph of acetylene, $\text{HC}\equiv\text{CH}$. Thus each vertex is of degree 3 and the two vertices correspond

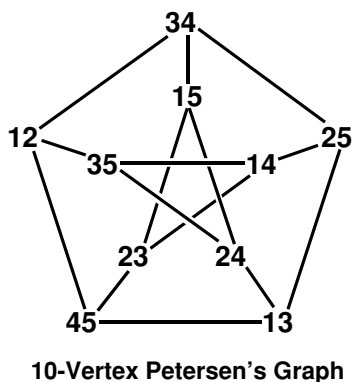
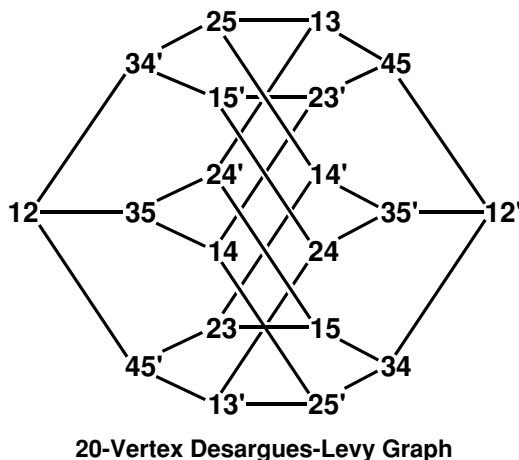


Figure 1.14 (a) The 20-vertex Desargues–Levy graph as a top-rep of the dsd isomerizations of the 20 trigonal bipyramid isomers through Berry pseudorotation processes (Figure 1.6). (b) The 10-vertex Petersen graph as a top-rep of the dsd isomerizations of the 10 trigonal bipyramid enantiomer pairs.

to the two tetrahedral isomers. The midpoints of the three edges correspond to the square planar isomers. Using this approach the top-rep of five-vertex isomerizations is a 20-vertex Desargues–Levy graph with the 20 vertices representing the trigonal bipyramid isomers, i.e. $I_{\text{tbp}} = 5!/|D_3| = 120/6 = 20$ (Figure 1.14a). The midpoints of the 30 edges represent the square pyramidal isomers, i.e., $I_{\text{sp}} = 5!/|C_4| = 120/4 = 30$. The connectivities of the trigonal bipyramidal isomers (δ_{tbp}) are 3 in accord with their locations at degree 3 vertices in the corresponding top-rep. Similarly, the connectivities of the square pyramidal isomers (δ_{sp}) are 2 in accord with their locations at edge midpoints of the top-rep. As in the case of four-vertex isomerizations, the closure condition is

met for five-vertex isomerization since $I_{\text{sp}}\delta_{\text{sp}} = I_{\text{tp}}\delta_{\text{tp}} = 6$. Travelling from one vertex to another in the Desargues–Levy graph (Figure 1.14a) corresponds to a Berry pseudorotation process [39,44] (Figure 1.6) through the square pyramidal intermediate represented by the edge midpoint.

Less complicated but still useful top-reps can be obtained by using each vertex of the graph to represent a set of isomers provided that each vertex represents sets of the same size and interrelationship and each isomer is included in exactly one set. A simple example is the use of the Petersen graph (Figure 1.14b) as a top-rep of the ten trigonal bipyramid enantiomer pairs ($E = 5!/|D_{3h}| = 120/12 = 10$) by dsd processes. The use of the Petersen graph for this purpose relates to its being the odd graph O_3 . In this connection, an odd graph O_k has vertices corresponding to subsets of cardinality $k - 1$ of a set S of cardinality $2k - 1$ (an odd number). Two vertices of O_k are adjacent if and only if the corresponding subsets are disjoint.

In six-vertex structures the process of interest is the degenerate triple dsd isomerization of the octahedron through a trigonal prismatic intermediate which is the underlying topology of both the Bailar [55] and Ray and Dutt [56] twists for $M(\text{bidentate})_3$ chelates. The isomer counts are $I_{\text{oct}} = 6!/|O| = 720/24 = 30$ for the octahedron and $I_{\text{tp}} = 6!/|D_3| = 720/6 = 120$ for the trigonal prism. A pentagonal (I_h) dodecahedron in double group form [1] can serve as the top-rep for this process (Figure 1.15). The midpoints of the 30 edges of the dodecahedron (designated by triangles in Figure 1.15) are the 30 octahedron isomers. Line segments across a pentagonal face connecting these edge midpoints correspond to triple dsd isomerization processes. The midpoints of these lines (designated by diamonds) correspond to the 120 trigonal prismatic isomers with ten such isomers being located in each of the 12 faces of the pentagonal dodecahedron. The ten lines on a face representing isomerization processes form a K_5 graph. This system is closed since the connectivities of the octahedron (δ_{oct}) and trigonal prism (d_{tp}) are 8 and 2, respectively, leading to the closure relationship $I_{\text{oct}}\delta_{\text{oct}} = I_{\text{tp}}\delta_{\text{tp}} = 240$.

Development of top-reps for isomerizations of polyhedra having more than six vertices is complicated by large isomer counts. Thus for the most symmetrical and chemically significant seven-vertex deltahedra the isomer counts are $7!/|D_5| = 5040/10 = 504$ for the pentagonal bipyramid and $7!/|C_3| = 5040/3 = 1680$. In this connection a ‘baby monster’ graph with 1680 vertices has actually been described in the chemical literature as a model for degenerate rearrangements in the seven-vertex P_7^{3-} system [73].

Among polyhedra with eight vertices the isomer counts of the cube, hexagonal bipyramid, square antiprism, and bisdisphenoid are $40\ 320/24 = 1680$, $40\ 320/12 = 3360$, $40\ 320/8 = 5040$, and $40\ 320/4 = 10\ 080$, respectively. Graphs corresponding to top-reps in systems with such large numbers of polyhedral isomers are clearly unwieldy and unmanageable. However, the problem of representing permutational isomerizations in seven- and eight-vertex polyhedra can be simplified if subgroups of the symmetric groups S_n ($n = 7, 8$) can be

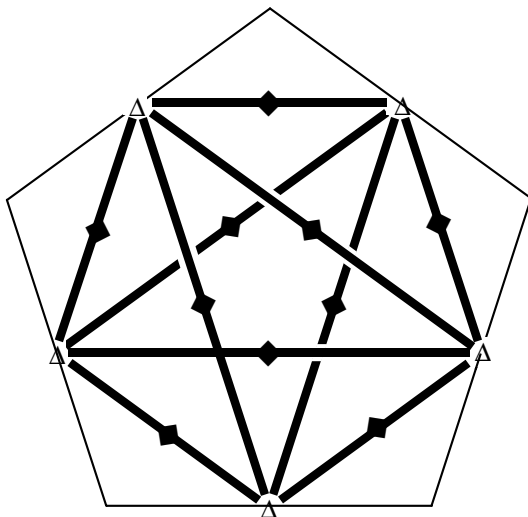


Figure 1.15 One of the 12 pentagonal faces of the I_h double group pentagonal dodecahedron used as a topological representation for the degenerate triple dsd degenerate isomerization of the octahedron through a trigonal prismatic intermediate (see Figure 1.10). The five triangles (Δ) at the midpoints of the sides of the face represent five of the 30 octahedron permutational isomers. The ten diamonds (\blacklozenge) at the midpoints of the edges of the K_5 graph drawn on the face represent 10 of the 120 trigonal prism permutational isomers.

found which contain all of the symmetries of all of the polyhedra of interest. This is *not* possible for the seven-vertex system since there is no subgroup of S_7 that contains both the five-fold symmetry of the pentagonal bipyramid and the three-fold symmetry of the capped octahedron. The situation with the eight-vertex system is more favorable since the wreath product group [74–76] $S_4[S_2]$ of order 384 contains all of the symmetries of the cube, hexagonal bipyramid, square antiprism, and bisdisphenoid [77], which are all of the eight-vertex polyhedra of actual or potential chemical interest. The major effect of reducing the symmetry by a factor of 105 ($3 \times 5 \times 7$) in going from S_8 to $S_4[S_2]$ is the deletion of five-fold and seven-fold symmetry elements. Such symmetry elements are not of interest in this context since none of the 257 eight-vertex polyhedra has five-fold symmetry elements [32,33] and the only eight-vertex polyhedron having a seven-fold symmetry element is the heptagonal pyramid, which is not of interest in this particular chemical context. Restricted isomer counts $I^* = 384/|R|$ based on subgroups of the wreath product group $S_4[S_2]$ rather than the symmetric group S_8 are the more manageable numbers 16, 32, 48, and 96 for the cube, hexagonal bipyramid, square antiprism, and bisdisphenoid, respectively [78].

The concept of restricting vertex permutations in eight-vertex systems to the wreath product group $S_4[S_2]$ rather than the fully symmetric S_8 group can

be restated in graph-theoretical terms using the hyperoctahedral graph H_4 [79]. Therefore such a restriction of permutations from S_8 to $S_4[S_2]$ can be called a hyperoctahedral restriction. The hyperoctahedral graphs underlying this restriction are designated as H_n and have $2n$ vertices and $2n(n-1)$ edges with every vertex connected to all except one of the remaining vertices so that each vertex of H_n has degree $2(n-1)$. The name ‘hyperoctahedral’ comes from the fact that an H_n graph is the 1-skeleton of the analogue of the octahedron (called the ‘cross-polytope’) in n -dimensional space [80–82]. The hyperoctahedral graphs H_2 and H_3 thus correspond to the square and octahedron, respectively. The $S_4[S_2]$ wreath product group is the automorphism (‘symmetry’) group of the hyperoctahedral graph H_4 just as the S_8 symmetric group is the automorphism group of the complete graph K_8 .

These considerations lead to a top-rep for isomerizations of eight-vertex polyhedra based on a $K_{4,4}$ bipartite graph of hexagons (Figure 1.16) with special points corresponding to the individual eight-coordinate polyhedra as follows:

- (1) The eight hexagons at the vertices of the $K_{4,4}$ bipartite graph (Figure 1.16a) correspond to the eight cube isomers.
- (2) The 16 edge midpoints of the $K_{4,4}$ bipartite graph (Figure 1.16a) correspond to the 16 hexagonal bipyramid isomers.
- (3) The 48 vertices of the eight hexagons linked by the $K_{4,4}$ bipartite graph (Figure 1.16b) correspond to the 24 square antiprism isomers.
- (4) The 48 edge midpoints of the eight hexagons linked by the $K_{4,4}$ bipartite graph (Figure 1.16b) correspond to the 48 bisdisphenoid isomers.

Moving along the circumference of a given hexagon corresponds to a sequence of double dsd processes interconverting the bisdisphenoids located at the midpoints of the two joined hexagonal edges meeting at a vertex. The vertex common to these two joined hexagonal edges corresponds to the square antiprism intermediate in this double dsd process. Since both the bisdisphenoid and square antiprism can be formed using only s, p, and d orbitals, the circumference of the hexagon is accessible in ML_8 systems in which the central atom M has the usual sp^3d^5 nine-orbital manifold. Thus in the usual situation *not* involving f orbitals, isomerizations are restricted to the circumference of a given hexagon in Figure 1.16b and cannot occur by moving from one hexagon to another along the edges of the $K_{4,4}$ bipartite graph (Figure 1.16a).

The group-theoretical aspects of top-reps can be generalized by considering a set of groups designated as G and H_1, \dots, H_n where the following apply: (1) H_1, \dots, H_n are symmetry point groups which are all subgroups of G ; (2) $|H_1| \geq |H_2| \geq \dots \geq |H_n|$; (3) R_m is the rotation subgroup of H_m . If $n = 2$, then we can seek a graph in which the number of vertices is $|G|/|H_1|$ and the number of edges is $|G|/|H_2|$. Such is the case with the $K_{2,3}$ top-rep of four-vertex isomerizations where $G = S_4(\approx T_d)$, $H_1 = T_d$, and $H_2 = D_{4h}$ (Figure 1.13) and

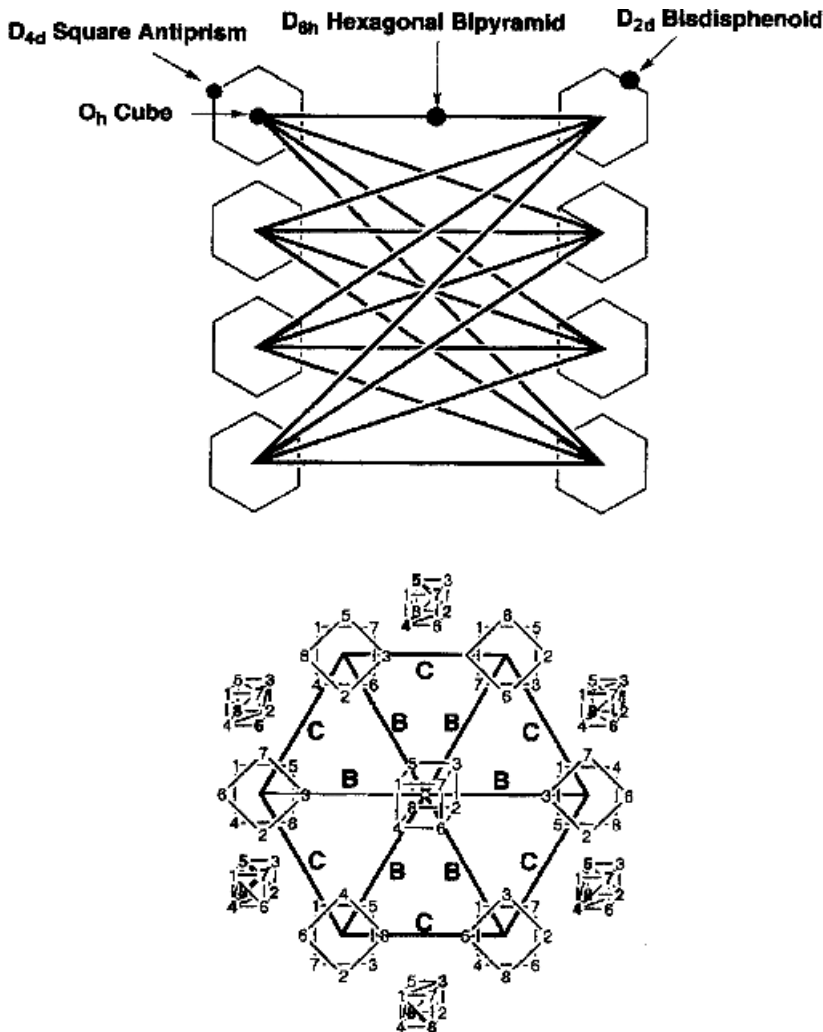


Figure 1.16 (a) The $K_{4,4}$ graph of hexagons used as a top-rep for hyperoctahedrally restricted isomerizations involving four types of eight-vertex polyhedra, namely the cube, hexagonal bipyramid, square antiprism, and D_{2d} bisdisphenoid. (b) Details of a hexagon in the top-rep in Figure 1.16a.

with the Desargues–Levy graph top-rep of five-vertex isomerizations where $G = S_5$, $H_1 = D_{3h}$, and $H_2 = C_{4v}$ (Figure 1.12a). In the case of the hyperoctahedrally restricted eight-vertex isomerizations with the $K_{4,4}$ graph of hexagons as the corresponding top-rep (Figure 1.16), G is not S_8 but instead $S_4[S_2]$, $H_1 = O_h$ (for the cube), $H_2 = D_{6h}$ (for the hexagonal bipyramid), $H_3 = D_{4d}$ (the square antiprism), and $H_4 = D_{2d}$ (the bisdisphenoid) [78].

4.2 TOPOLOGICAL REPRESENTATIONS OF JAHN–TELLER DISTORTIONS

4.2.1 Background

The Jahn–Teller (JT) theorem asserts the existence of spontaneous symmetry breaking distortions in degenerate electronic states of nonlinear molecules [21–24]. However, the amount and type of symmetry breaking is restricted by the epikernel principle [83,84]. As a result of the epikernel principle JT distortions leading to stable minima on the potential energy surface near an electronic degeneracy preserve larger symmetry groups than would be expected from an unrestricted action of the JT distorting forces. The relationships between possible JT distorted structures can be depicted by top-reps similar to those discussed in the previous section [20].

The underlying group theory for the study of JT distortions uses a direct product [85,86] $\Gamma \times \Gamma$ of a suitable irreducible representation (irrep) Γ of the symmetry group G of the undistorted nuclear configuration. The characters of $\Gamma \times \Gamma$ are the squares of the characters of the corresponding operations of G in the irrep Γ according to the following equation where g is any operation in G :

$$\chi(g : \Gamma \times \Gamma) = (\chi(g : \Gamma))^2 \quad (1.18)$$

If the dimension of Γ is d , then the dimension of $\Gamma \times \Gamma$ is d^2 . Furthermore, the direct product representation $\Gamma \times \Gamma$ can be reduced into a sum of two lower-dimensional representations, namely the symmetric part $[\Gamma \times \Gamma]_S$ of dimension $1/2d(d+1)$ and the antisymmetric part $\{\Gamma \times \Gamma\}_A$ of dimension $1/2d(d-1)$. The characters of the symmetric and antisymmetric parts of the direct product $\Gamma \times \Gamma$ can be determined by the following formulas:

$$\chi(g : [\Gamma \times \Gamma]_S) = 1/2[(\chi(g : \Gamma))^2 + \chi(g^2 : \Gamma)] \quad (1.19a)$$

$$\chi(g : \{\Gamma \times \Gamma\}_A) = 1/2[(\chi(g : \Gamma))^2 - \chi(g^2 : \Gamma)] \quad (1.19b)$$

According to the rule of the JT instability [87], the JT distortion coordinates of a degenerate electronic state corresponding to an irreducible representation (irrep) Γ must span representations Λ belonging to the non-totally symmetric part of the symmetrized direct product of Γ , i.e.

$$\Lambda \in [\Gamma \times \Gamma]_S - A_1 \quad (1.20)$$

Note that for a d -dimensional irrep Γ the total dimension of the corresponding representation Λ is $[d(d+1)/2] - 1$.

The reduction of the representation Λ to a sum of irreps depends on the symmetry point group G of the undistorted nuclear configuration. A system of JT distortions corresponding to a given Γ in a point group G is conventionally described [24] as a JT problem of the type $\Gamma \otimes \Lambda$ or $\Gamma \otimes \sum \lambda_k$ where Γ is the representation of G containing the degenerate electronic state and the λ_k s are the irreps of G contained in the representation Λ defined by Equation (1.20). The irreps for the JT problems of interest are listed in Table 1.2.

Table 1.2 The Jahn–Teller problems of interest [24]

Point group, G	Jahn–Teller problem: $\Gamma \otimes \Lambda$ or $\Gamma \otimes \sum \lambda_k$	Comments
D_{4h}	$E \otimes (b_{1g} + b_{2g})$	square \rightarrow rhombus (b_{1g}) or rectangle (b_{2g})
O_h	$E \otimes e$	octahedron \rightarrow tetragonal bipyramid (TBP)
O_h	$T \otimes (e + t_2)$	octahedron \rightarrow TBP (e) or trigonal antiprism (t_2)
I_h	$T \otimes h$	icosahedron \rightarrow pentagonal antiprism
I_h	$G \otimes (g + h)$	icosahedron \rightarrow pentagonal or trigonal symmetry (h) icosahedron \rightarrow tetrahedral symmetry (g)
I_h	$H \otimes (g + 2h)$	icosahedron \rightarrow pentagonal or trigonal symmetry (h) icosahedron \rightarrow tetrahedral symmetry (g)

In general a top-rep for the Jahn–Teller problem $\Gamma \otimes \Lambda$ is a graph embedded in a space of the same dimension as Λ , i.e., a space of dimension $[d(d+1)/2] - 1$ in which d is the dimension of Γ . However, if Λ can be reduced to a sum of irreps λ_k such that $\sum \lambda_k = \Lambda$, then the corresponding top-rep can be related to a set of complete graphs on $d_k - 1$ vertices designated as K_{d_k-1} [51]. Furthermore, a complete graph K_n can be embedded into $(n-1)$ -dimensional space to give an n -simplex. For example, a 2-simplex is a K_3 graph (i.e., a triangle) embedded into 2-dimensional space (i.e., a plane). Similarly, a 3-simplex is a K_4 graph (i.e., a tetrahedron) embedded into 3-dimensional space.

The point group symmetries for which JT distortions are of interest are the D_{4h} symmetry of the square, the T_d symmetry of the tetrahedron, the O_h symmetry of the cube or octahedron, and the I_h symmetry of the icosahedron, dodecahedron, or C_{60} . The important features of the top-reps of these JT distortions are discussed below.

4.2.2 Square Planar Molecules

JT distortions of the square are of interest from the chemical point of view in connection with distortions of cyclobutadiene derivatives from squares to rectangles (Figure 1.17a). In the D_{4h} symmetry of square planar molecules the only degenerate irreps are doubly degenerate E representations. The corresponding product $\Lambda = [E \times E]_S - A_1$ is a two-dimensional representation, which is reducible to a sum of the one-dimensional irreps b_{1g} and b_{2g} corresponding to the $E \otimes (b_{1g} + b_{2g})$ problem. The corresponding top-rep consists of two crossed straight lines, which may be regarded as diagonals of a rhombus (dashed lines in Figure 1.17b). Note that a straight line plus its endpoints is a K_2 complete graph, which is the simplex in one-dimensional space.

One of the two diagonals in this top-rep for the $E \otimes (b_{1g} + b_{2g})$ problem (the ‘vertical’ diagonal in Figure 1.17b) corresponds to the b_{1g} irrep with its endpoints corresponding to rhombus isomers of D_{2h} symmetry in which the two-fold axes are the diagonals of the rhombus. The enantiomer count

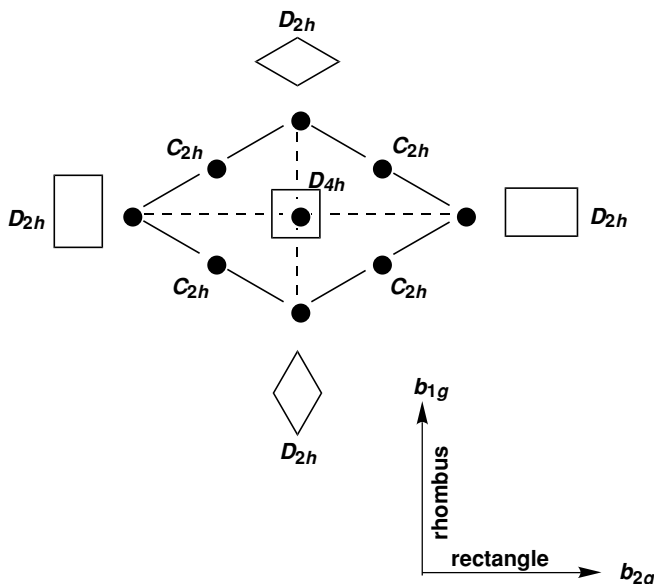
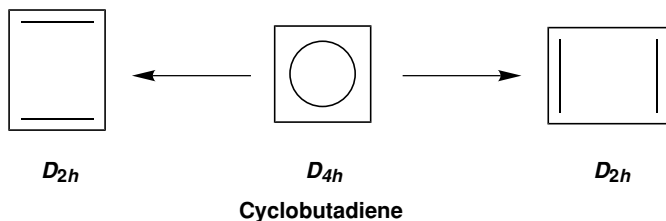


Figure 1.17 (a) The JT distortion of square (D_{4h}) to rectangular (D_{2h}) cyclobutadiene. (b) A rhombus as a top-rep for the $E \otimes (b_{1g} + b_{2g})$ problem showing the distortions from a square (D_{4h}) to rectangles (D_{2h}) and rhombi (D_{2h}).

$E_{\text{rhomb}} = |D_{4h}|/|D_{2h}| = 16/8 = 2$ by Equation (1.17) corresponds to the two endpoints of this diagonal. Similarly the other diagonal in this top-rep (the ‘horizontal’ diagonal in Figure 1.15b) corresponds to the b_{2g} irrep with its endpoints corresponding to the rectangle isomers, likewise of D_{2h} symmetry, but with the two-fold axes bisecting the midpoints of the rectangle edges. Again the enantiomer count $E_{\text{rect}} = |D_{4h}|/|D_{2h}| = 16/8 = 2$ corresponds to the two endpoints of this diagonal. The distortion of square cyclobutadiene, C_4H_4 , to the rectangular isomer (Figure 1.17a) corresponds to the latter diagonal [88,89].

The diagonals in this top-rep of the $E \otimes (b_{1g} + b_{2g})$ problem (Figure 1.17b) are drawn with different lengths corresponding to the non-equivalence (independence) of the b_{1g} and the b_{2g} components of this JT problem. Joining the

end-points of these perpendicular diagonals of nonequal lengths generates a rhombus. The midpoints of the four edges of this rhombus correspond to isomers of C_{2h} kernel symmetry [83,84] intermediate between the rectangle and rhombus joined by the edge in question. Note again that the enantiomer count of these edge midpoints $E_{C_{2h}} = |D_{4h}|/|C_{2h}| = 16/4 = 4$ corresponds to the four edges of the top-rep (Figure 1.17b).

4.2.3 Octahedral Molecules

JT distortions of octahedral molecules are of interest in coordination chemistry when the central atom (normally a d-block transition metal) has a partially filled t_{2g} or e_g shell thereby leading to degenerate electronic states. The simplest JT distortion of an octahedron arises from electronic degeneracies in the molecular orbitals represented by the doubly degenerate E representation. The corresponding product $\Lambda = [E \times E]_S - A_1$ is the irreducible two-dimensional representation e , which leads to the $E \otimes e$ JT problem. The corresponding top-rep is the 2-simplex, namely an equilateral triangle. In such a top-rep (Figure 1.18a) the vertices correspond to tetragonal bipyramidal (D_{4h}) isomers, which are either elongated or compressed along one of the original four-fold axes of the octahedron. Since there are three such four-fold axes, which are mutually perpendicular, there are necessarily three distinct tetragonal bipyramidal isomers corresponding not only to the three vertices of the triangle but also to the enantiomer count $E_{\text{tetrag}} = |O_h|/|D_{4h}| = 48/16 = 3$ by Equation (1.17). In fact these three vertices correspond to the three minima of the adiabatic potential surface considering both the linear and quadratic terms of the vibronic interaction [23,24]. The three edge midpoints correspond to orthorhombic isomers of D_{2h} kernel symmetry arising as intermediates in the conversion of one tetragonal bipyramidal isomer to another. Octahedral d^9 Cu(II) complexes such as $\text{Cu}(\text{H}_2\text{O})_6^{2+}$ provide examples of $E \otimes e$ JT distortions in which a pair of axial bonds of the octahedron is elongated to form a D_{4h} tetragonal bipyramid (Figure 1.18b) [90–92].

The other general type of JT distortion of octahedral molecules arises from electronic degeneracies in the molecular orbitals represented by the triply degenerate T representation. In this case the corresponding product $\Lambda = [E \times E]_S - A_1$ is a five-dimensional representation, which necessarily is reducible, since the octahedral point groups contain no five-dimensional irreps. Reducing this representation to a sum of irreps gives $e + t_2$ leading to the JT $T \otimes (e + t_2)$ problem. Analogy with the two-dimensional rhombus top-rep for the $E \otimes (b_{1g} + b_{2g})$ problem (Figure 1.17b) discussed above suggests a five-dimensional top-rep with a tetrahedron for the t_2 component in three of the five dimensions and a triangle for the e component in the other two dimensions of the five-dimensional space. However, the dimensionality of the top-rep can be reduced from five dimensions visualized only with considerable difficulty to a more readily visualized three-dimensional polyhedron if one type of distortion

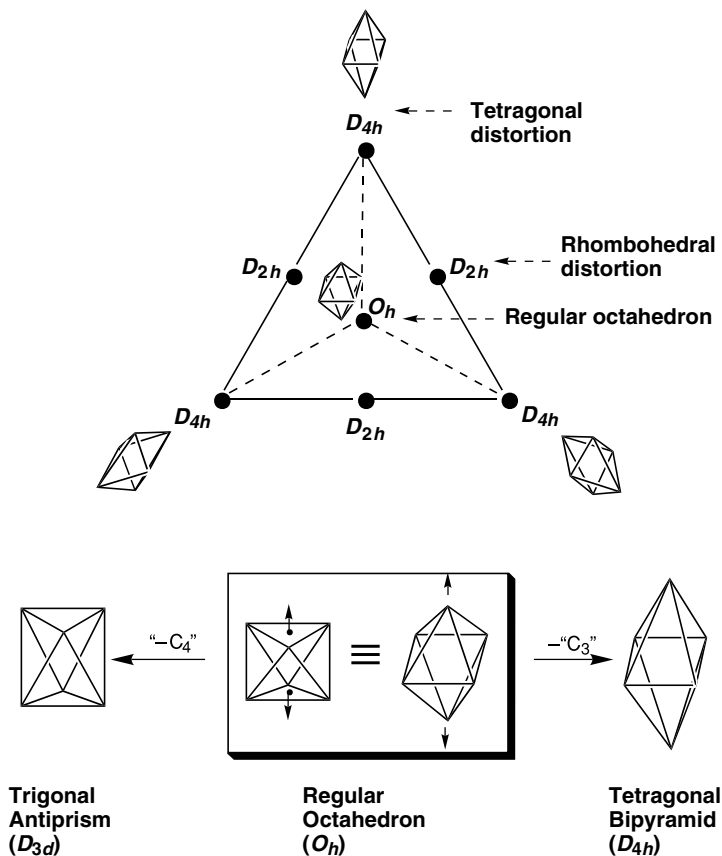


Figure 1.18 (a) Equilateral triangle top-rep for the $E \otimes e$ problem showing the distortions from a regular octahedron (O_h) to the three elongated tetragonal bipyramidal isomers (D_{4h}). (b) The JT distortions of the regular octahedron to the elongated trigonal antiprism (D_{3d}) and elongated tetragonal bipyramid (D_{4h}).

corresponds to the vertices and the other type of distortion corresponds to the face midpoints of the polyhedron in question. The edges of the polyhedron are not the actual edges of the top-rep. However, their midpoints represent polyhedral isomers of lower symmetry than the isomers represented by either the vertices or the face midpoints. The edges belonging to the top-rep connect polyhedral edge midpoints to either vertices or face midpoints. The numbers of points in such a polyhedral top-rep corresponding to a distortion of the original point group G (namely O_h in this case) to a subgroup H_k does not correspond to the enantiomer count $E = |G|/|H_k|$ (see Equation 1.17) but instead to the isomer count $I = |G|/|R_k|$ (Equation 1.16) where R_k is the rotational

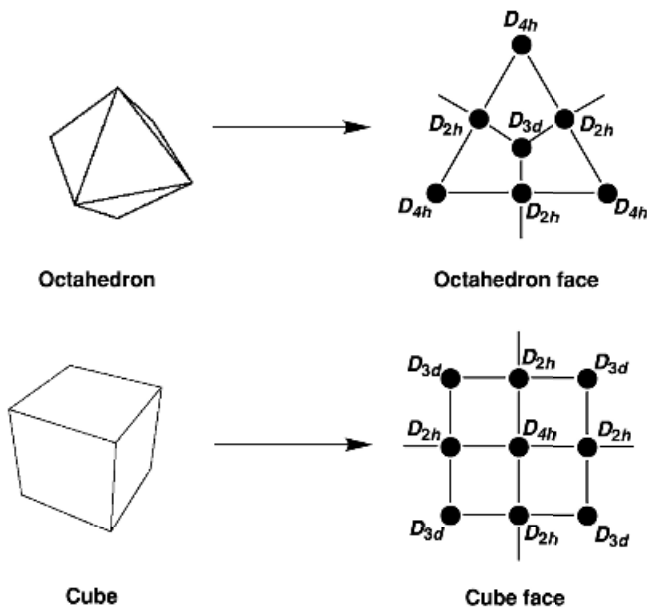


Figure 1.19 (a) The regular octahedron as a top-rep for the $T \otimes (e + t_2)$ distortions of a regular octahedron showing on a sample face the locations of the tetragonal bipyramid isomers (D_{4h}), the trigonal antiprism isomers (D_{3d}), and the rhombohedral D_{2h} isomers as vertices, face midpoints, and edge midpoints, respectively. (b) The dual of the top-rep in Figure 1.19a based on a cube with the tetragonal bipyramid isomers (D_{4h}), the trigonal antiprism isomers (D_{3d}), and the rhombohedral D_{2h} isomers as face midpoints, vertices, and edge midpoints, respectively.

subgroup of H_k . For achiral H_k (as in all of the examples discussed in this paper), $|H_k| = 2|R_k|$ so that $I = 2E$.

These considerations lead to a top-rep for the $T \otimes (e + t_2)$ problem based on a regular octahedron (Figure 1.19a) with special points corresponding to the following isomers:

- (1) The center of the octahedron corresponding to the symmetrical O_h regular octahedron before any distortion.
- (2) The six vertices of the octahedron corresponding to the three tetragonal bipyramidal D_{4h} isomers each considered as an enantiomeric pair ($I_{\text{tetrag}} = |O_h|/|D_4| = 48/8 = 6$) corresponding to the $T \otimes e$ portion of the $T \otimes (e + t_2)$ problem.
- (3) The midpoints of the eight faces of the octahedron corresponding to the four trigonal antiprismatic D_{3d} isomers each considered as an enantiomeric pair ($I_{\text{trig}} = |O_h|/|D_3| = 48/6 = 8$) corresponding to the $T \otimes t_2$ portion of the $T \otimes (e + t_2)$ problem.

- (4) The midpoints of the 12 edges of the octahedron corresponding to the six orthorhombic D_{2h} isomer intermediates between either pairs of tetragonal bipyramids (D_{4h}) or pairs of trigonal antiprisms (D_{3d}) each considered as an enantiomeric pair ($I_{D_{2h}} = |O_h|/|D_2| = 48/4 = 12$).

The dual of the octahedron, namely the cube, can also be used for a top-rep of the $T \otimes (e + t_2)$ problem in which the roles of the vertices and face midpoints are reversed from those of the octahedral top-rep. Thus for the cubic top-rep of the $T \otimes (e + t_2)$ problem (Figure 1.19b) the vertices represent the eight D_{3d} trigonal antiprismatic isomers and the face midpoints represent the six D_{4h} tetragonal bipyramid isomers. The edge midpoints of the cubic top-rep correspond to the D_{2h} orthorhombic intermediates as in the octahedral top-rep.

4.2.4 Icosahedral Molecules

JT distortions of icosahedral symmetry are of interest for understanding possible distortions in $I_h\text{-C}_{60}$ [93] or $\text{B}_{12}\text{X}_{12}^{2-}$ [94] upon reduction or oxidation. In this connection icosahedral molecules have T , G , and H molecular orbitals of degeneracies 3, 4, and 5, respectively, in which electronic degeneracies can occur. However, the non-symmetric parts of the symmetric direct products Λ (Equation 1.20) for any of these degenerate irreps never contain any triply degenerate t irreps (Table 1.2). For this reason the only possible JT distortions of icosahedra are those corresponding to the g and h irreps. The g irrep corresponds to distortions reducing the symmetry from icosahedral to tetrahedral (T_h). Similarly the h irrep corresponds to distortions reducing the symmetry from icosahedral to either trigonal (D_{3d}) or pentagonal (D_{5d}). Reasonable top-reps can be generated for both of these distortion pathways.

The simplest JT distortion of icosahedral molecules arises from electronic degeneracies in the molecular orbitals represented by the triply degenerate T representation. The corresponding product $\Lambda = [T \times T]_S - A_1$ is the five-dimensional irrep h , which leads to the $T \otimes h$ JT problem. The corresponding top-rep is the 5-simplex, which corresponds to the embedding of the complete graph on six vertices (K_6) into five-dimensional space. This simplex has $(6 \times 5)/(2 \times 1) = 15$ edges and $(6 \times 5 \times 4)/(3 \times 2 \times 1) = 20$ two-dimensional faces, which themselves are necessarily 2-simplices, i.e., triangles. Isomers are indicated by the following special points on this 5-simplex:

- (1) The center of the 5-simplex corresponding to the regular icosahedron I_h before distortion.
- (2) The six vertices of the 5-simplex corresponding to the six D_{5d} bicapped pentagonal antiprismatic isomers ($I_{D_{5d}} = |I_h|/|D_{5d}| = 120/20 = 6$).
- (3) The midpoints of the 15 edges of the 5-simplex corresponding to the 15 D_{2h} intermediates ($I_{D_{2h}} = |I_h|/|D_{2h}| = 120/8 = 15$).

- (4) The midpoints of the 20 triangular faces of the 5-simplex corresponding to the 10 D_{3d} trigonal isomers considered as enantiomeric pairs ($E_{D_{3d}} = |I_h|/|D_3| = 120/6 = 20$).

In order to avoid the complexities of five-dimensional space for a top-rep of the $T \otimes h$ problem, an alternative three-dimensional polyhedral representation can be generated based on the regular icosahedron (Figure 1.20a) analogous to the use of the regular octahedron for a top-rep of the related $T \otimes (e + t_2)$ problem. In such a representation, the special points on the icosahedron have the following significance:

- (1) The center of the icosahedron corresponds to the symmetrical I_h regular icosahedron before distortion.
- (2) The 12 vertices of the icosahedron correspond to the six bicapped pentagonal antiprismatic D_{5d} isomers each considered as an enantiomeric pair ($I_{\text{pentag}} = |I_h|/|D_5| = 120/10 = 12$).
- (3) The midpoints of the 20 faces of the icosahedron correspond to the 10 trigonal D_{3d} isomers each considered as an enantiomeric pair ($I_{\text{trig}} = |I_h|/|D_3| = 120/6 = 20$).
- (4) The midpoints of the 30 edges of the icosahedron correspond to the 15 D_{2h} isomer intermediates between either pairs of pentagonal D_{5d} isomers or trigonal D_{3d} isomers each considered as an enantiomeric pair ($I_{D_{2h}} = |I_h|/|D_2| = 120/4 = 30$).

Alternatively, analogous to the $T \otimes (e + t_2)$ problem discussed above, the dual of the icosahedron, namely the regular dodecahedron, can be used for a top-rep of the $T \otimes h$ problem (Figure 1.20b). In this case the roles of the vertices and face midpoints are reversed from those of the icosahedron top-rep (Figure 1.20a).

The next most complicated JT system of distortions for the regular icosahedron corresponds to the $G \otimes (g + h)$ problem. This problem generates a top-rep in nine-dimensional space combining a 4-simplex corresponding to the g component (i.e., a $G \otimes g$ problem) with a 5-simplex corresponding to the h component (i.e., a $G \otimes h$ problem). The $G \otimes h$ component involves distortions of I_h symmetry to the lower D_{5d} , D_{3d} , and D_{2h} symmetries leading to top-reps similar to those discussed above for the related $T \otimes h$ problem.

The $G \otimes g$ component of the $G \otimes (g + h)$ problem leads to a new simplicial top-rep which is four-dimensional in accord with the dimension of the irrep g for the corresponding distortion of the nuclear coordinates. This representation is based on the 4-simplex, which has five vertices and $(5 \times 4)/(2 \times 1) = 10$ edges. This simplex is the four-dimensional analogue of the regular tetrahedron with a skeleton corresponding to the complete graph K_5 (Figure 1.21). In this top-rep the special points on the 4-simplex have the following significance:

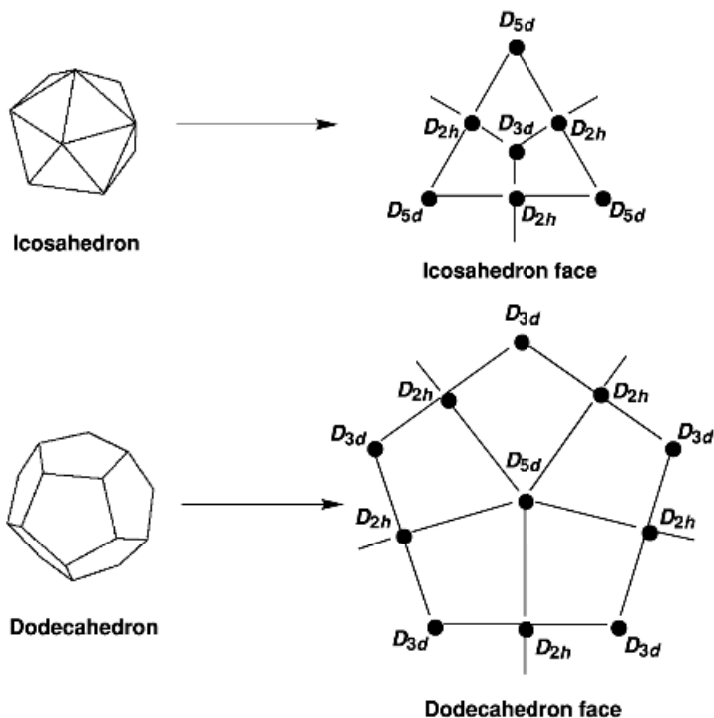


Figure 1.20 (a) The regular icosahedron as a top-rep for the $T \otimes h$ distortions of a regular icosahedron showing on a sample face the locations of the D_{5d} , D_{3d} , and D_{2h} isomers as vertices, face midpoints, and edge midpoints, respectively. (b) The dual of the top-rep in Figure 1.20a based on a regular dodecahedron with D_{5d} , D_{3d} , and D_{2h} isomers as face midpoints, vertices, and edge midpoints, respectively.

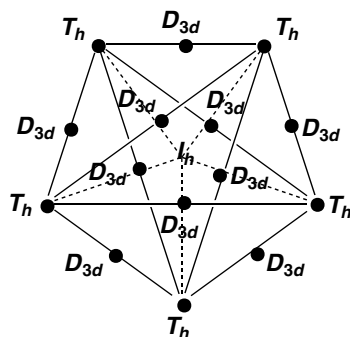


Figure 1.21 The K_5 skeleton of the 4-simplex (four-dimensional analogue of the regular tetrahedron) as a top-rep for the $G \otimes g$ distortions of an (I_h) regular icosahedron (center point) to T_h isomers (vertices) and D_{3d} intermediates (edge midpoints).

- (1) The center of the 4-simplex corresponds to the regular icosahedron I_h before distortion.
- (2) The five vertices of the 4-simplex correspond to the five T_h isomers of tetrahedral symmetry ($E_{T_h} = |I_h|/|T_h| = 120/24 = 5$).
- (3) The midpoints of the 10 edges of the 4-simplex correspond to the ten D_{3d} intermediates in the interconversions of the T_h isomers ($E_{D_{3d}} = |I_h|/|D_{3d}| = 120/12 = 10$).

The remaining JT system of distortions for the regular icosahedron corresponds to the $H \otimes (g + 2h)$ problem. A complete and rigorous top-rep of this system would require no less than 14 dimensions and is obviously impractical. The g and h components of this problem (i.e., the $H \otimes g$ and the $H \otimes h$ components) would have individual top-reps similar to those discussed above for the $G \otimes g$ and $T \otimes h$ problems, and introduce no fundamentally new features.

5 ACKNOWLEDGMENT

I am indebted to the National Science Foundation for partial support of this work under grant CHE-0209857.

6 REFERENCES

1. E. L. Muetterties, *J. Am. Chem. Soc.*, **90**, 5097 (1968).
2. E. L. Muetterties, *J. Am. Chem. Soc.*, **91**, 1636 (1969).
3. E. L. Muetterties, *J. Am. Chem. Soc.*, **91**, 4115 (1969).
4. E. L. Muetterties and A. T. Storr, *J. Am. Chem. Soc.*, **91**, 3098 (1969).
5. M. Gielen and J. Nasielski, *Bull. Soc. Chim. Belges*, **78**, 339 (1969).
6. M. Gielen and J. Nasielski, *Bull. Soc. Chim. Belges*, **78**, 351 (1969).
7. M. Gielen, C. Depasse-Delit, and J. Nasielski, *Bull. Soc. Chim. Belges*, **78**, 357 (1969).
8. M. Gielen and C. Depasse-Delit, *Theor. Chim. Acta*, **14**, 212 (1969).
9. M. Gielen, G. Mayence, and J. Topart, *J. Organometal. Chem.*, **18**, 1 (1969).
10. M. Gielen, M. de Clercq, and J. Nasielski, *J. Organometal. Chem.*, **18**, 217 (1969).
11. M. Gielen and N. Vanlautem, *Bull. Soc. Chim. Belges*, **79**, 679 (1970).
12. M. Gielen, *Bull. Soc. Chim. Belges*, **80**, 9 (1971).
13. J. I. Musher, *J. Am. Chem. Soc.*, **94**, 5662 (1972).
14. J. I. Musher, *Inorg. Chem.*, **11**, 2335 (1972).
15. W. G. Klemperer, *J. Chem. Phys.*, **56**, 5478 (1972).
16. W. G. Klemperer, *J. Am. Chem. Soc.*, **94**, 6940 (1972).
17. W. G. Klemperer, *J. Am. Chem. Soc.*, **94**, 8360 (1972).
18. J. Brocas, *Top. Curr. Chem.*, **32**, 43 (1972).
19. J. Brocas, in *Advances in Dynamic Stereochemistry*, edited by M. Gielen, Vol. 1, Freund, TelAviv, 1985, pp. 43–88.
20. R. B. King, *Mol. Phys.*, **100**, 1567 (2002).
21. I. B. Bersuker, *Coord. Chem. Rev.*, **14**, 357 (1975).
22. I. B. Bersuker, *The Jahn–Teller Effect and Vibronic Interactions in Modern Chemistry*, Plenum Press, New York, 1984.

23. I. B. Bersuker, *Electronic Structure and Properties of Transition Metal Compounds*, Wiley, New York, 1996.
24. I. B. Bersuker, *Chem. Rev.*, **101**, 1067 (2001).
25. R. B. King in *Advances in Dynamic Stereochemistry*, edited by M. Gielen, Vol. 2, Freund Publishing Co., Tel Aviv, 1988, pp. 1–36.
26. R. B. King, in *Graph Theoretical Approach to Chemical Reactivity*, edited by D. Bonchev and O. Menkenyan, Kluwer, Dordrecht, The Netherlands, 1994, pp. 109–135.
27. R. B. King, *Applications of Graph Theory and Topology in Inorganic Cluster and Coordination Chemistry*, CRC Press, Boca Raton, Florida, 1992, Chapter 12.
28. R. B. King, *J. Am. Chem. Soc.*, **91**, 7211 (1969).
29. F. Harary and E. M. Palmer, *Graphical Enumeration*, Academic Press, New York, 1973, p. 224.
30. W. T. Tutte, *J. Combin. Theory Ser. B.*, **28**, 105 (1980).
31. A. J. W. Duijvestijn and P. J. Federico, *Math. Comput.*, **37**, 523 (1981).
32. P. J. Federico, *Geom. Ded.*, **3**, 469 (1975).
33. D. Britton and J. D. Dunitz, *Acta Crystallegr.*, **A29**, 362 (1973).
34. R. B. King, *Theor. Chim. Acta*, **64**, 453 (1984).
35. R. B. King, *Inorg. Chem.*, **37**, 3057 (1998).
36. B. Grünbaum, *Convex Polytopes*, Interscience, New York, 1967.
37. F. A. Cotton, *Acc. Chem. Res.*, **1**, 257 (1968).
38. W. N. Lipscomb, *Science*, **153**, 373 (1966).
39. R. S. Berry, *J. Chem. Phys.*, **32**, 933 (1960).
40. R. B. King, *Inorg. Chim. Acta*, **49**, 237 (1981).
41. B. M. Gimarc and J. J. Ott, *Inorg. Chem.*, **25**, 83 (1986).
42. J. J. Ott, C. A. Brown, and B. M. Gimarc, *Inorg. Chem.*, **28**, 4269 (1989).
43. B. M. Gimarc and J. J. Ott, *Inorg. Chem.*, **25**, 2708 (1986).
44. R. R. Holmes, *Accts. Chem. Res.*, **5**, 296 (1972).
45. L. J. Guggenberger and E. L. Muetterties, *J. Am. Chem. Soc.*, **98**, 7221 (1976).
46. D. J. Wales and A. J. Stone, *Inorg. Chem.*, **26**, 3845 (1987).
47. D. M. P. Mingos and R. J. Johnston, *Polyhedron*, **7**, 2437 (1988).
48. D. J. Wales, D. M. P. Mingos, and L. Zhenyang, *Inorg. Chem.*, **28**, 2754 (1989).
49. A. Ceulemans, G. Goijens, and M. T. Nguyen, *J. Am. Chem. Soc.*, **116**, 9395 (1994).
50. R. B. King, *J. Mol. Struct. THEOCHEM*, **185**, 15 (1989).
51. L. W. Beinecke and R. J. Wilson, *Selected Topics in Graph Theory*, Academic Press, New York, 1978.
52. P. McMullen and G. C. Shephard, *Convex Polytopes and the Upper Bound Conjecture*, Cambridge University Press, Cambridge, England, 1971.
53. P. McMullen and G. C. Shephard, *Mathematika*, **15**, 223 (1968).
54. R. B. King, *MATCH–Commun. Math. Chem.*, **48**, 155 (2003).
55. J. C. Bailar, Jr., *J. Inorg. Nucl. Chem.*, **8**, 165 (1985).
56. P. Ray and N. K. Dutt, *J. Indian Chem. Soc.*, **20**, 81 (1943).
57. R. B. King and A. J. W. Duijvestijn, *Inorg. Chim. Acta*, **178**, 55 (1990).
58. J. Bould, J. D. Kennedy, and M. Thornton-Pett, *J. Chem. Soc. Dalton*, 563 (1992).
59. J. D. Kennedy and B. Štíbr, in *Current Topics in the Chemistry of Boron*, edited by G. W. Kabalka, Royal Society of Chemistry, Cambridge, UK, 1994, pp. 285–292.
60. J. D. Kennedy, in *The Borane–Carborane–Carbocation Continuum*, edited by J. Casanova, Wiley, New York, 1998, Chapter 3, pp. 85–116.
61. B. Štíbr, J. D. Kennedy, E. Drdáková, and M. Thornton-Pett, *J. Chem. Soc. Dalton Trans.*, 229 (1994).
62. R. B. King, *Inorg. Chem.*, **35**, 5151 (1999).
63. R. B. King, *Inorg. Chim. Acta*, **300–302**, 537 (2000).

64. J. Bould, J. E. Crook, N. N. Greenwood, J. D. Kennedy, and W. S. McDonald, *Chem. Commun.*, 346 (1982).
65. R. B. King, *Inorg. Chem.*, **40**, 2699 (2001).
66. A. T. Balaban, D. Farcaşiu, and R. Banica, *Rev. Roum. Chim.*, **11**, 1205 (1966).
67. B. M. Gimarc and J. J. Ott, in *Graph Theory and Topology in Chemistry*, edited by R. B. King and D. H. Rouvray, Elsevier, Amsterdam, 1978, pp. 285–301.
68. F. J. Budden, *The Fascination of Groups*, Cambridge University Press, London, 1972.
69. C. D. H. Chisholm, *Group Theoretical Techniques in Quantum Chemistry*, Academic Press, New York, 1976.
70. J. A. Pople, *J. Am. Chem. Soc.*, **102**, 4615 (1980).
71. S. Fujita, *Symmetry and Combinatorial Enumeration in Chemistry*, Springer, Berlin, 1991.
72. M. Randić, *Croat. Chim. Acta*, **74**, 683 (2001).
73. M. Baudler, *Angew. Chem. Int. Ed. Engl.*, **21**, 492 (1982).
74. G. Pólya, *Acta Math.*, **68**, 143 (1937).
75. N. Debruijn in *Applied Combinatorial Mathematics*, edited by E. F. Beckenbach, Wiley, New York, 1964.
76. J. G. Nourse and K. Mislow, *J. Am. Chem. Soc.*, **97**, 4571 (1975).
77. R. B. King, *Inorg. Chem.*, **20**, 363 (1981).
78. R. B. King, *Theor. Chim. Acta*, **59**, 25 (1981).
79. N. L. Biggs, *Algebraic Graph Theory*, Cambridge University Press, London, 1974.
80. B. Grünbaum, *Convex Polytopes*, Interscience, New York, 1967.
81. H. S. M. Coxeter, *Regular Polytopes*, MacMillan, New York, Second Edition, 1963.
82. H. S. M. Coxeter, *Regular Complex Polytopes*, Cambridge University Press, Cambridge, UK, Second Edition, 1991.
83. A. Ceulemans, D. Beyens, and L. G. Vanquickenborne, *J. Am. Chem. Soc.*, **106**, 5824 (1984).
84. A. Ceulemans and L. G. Vanquickenborne, *Structure and Bonding*, **71**, 125 (1989).
85. M. Orchin and H. H. Jaffé, *Symmetry, Orbitals, and Spectra*, Wiley, New York, 1971, pp. 192–194.
86. R. L. Ellis and H. H. Jaffé, *J. Chem. Educ.*, **48**, 92 (1971).
87. H. A. Jahn and E. Teller, *Proc. Soc. London Ser. A*, **161**, 220 (1937).
88. V. I. Minkin, M. N. Glukhovtsev, and B. Ya. Simkin, *Aromaticity and Antiaromaticity: Electronic and Structural Aspects*, Wiley-Interscience, New York, 1994.
89. K. B. Wiberg, *Chem. Rev.*, **101**, 1317 (2001).
90. B. Bleaney and K. D. Bowers, *Proc. Phys. Soc. (London)*, **A65**, 667 (1952).
91. R. Engelman, *The Jahn–Teller Effect in Molecules and Crystals*, Wiley-Interscience, New York, 1972.
92. K. F. Purcell and J. C. Kotz, *An Introduction to Inorganic Chemistry*, Saunders, Philadelphia, PA, 1980.
93. C. C. Chancey and M. C. M. O'Brien, *The Jahn–Teller Effect in C₆₀ and Other Icosahedral Molecules*, Princeton University Press, Princeton, N. J., 1997.
94. T. Peymann, C. B. Knobler, S. I. Khan, and M. F. Hawthorne, *Angew. Chem. Int. Ed. Engl.*, **40**, 1664 (2001).

2 NMR Studies of Intramolecular Dynamics in Allylic Type Triorganoboranes

ILYA D. GRIDNEV

COE Laboratory, Department of Chemistry, Graduate School of Science, Tohoku University, Sendai 980-8578, Japan

and

OLEG L. TOK

Anorganische Chemie II, University of Bayreuth, D-95440 Bayreuth, Germany

1 INTRODUCTION

Many σ -allylic derivatives of metals are fluxional in solution. However, most of the rearrangements responsible for this fluxionality are intermolecular. Thus, the intermolecular character of the allylic rearrangements in the derivatives of aluminium [1], cadmium [2], and zinc [3,4] has been proved experimentally. A mixed mechanism with the predominance of the intermolecular one has been initially proposed for diallylmercury [5]. However, later it was shown that an intermolecular rearrangement takes place in allylmercury derivatives that occurs only in the presence of Lewis acids [6]. The same is true for allylstannanes [7–9]. Facile intramolecular rearrangements are known for allylmagnesium compounds; however, in this case the interpretation of the experimental data is much more difficult due to ionization and Schlenk equilibria [10,11]. The activation barriers of the sigmatropic migrations in allylsilanes [12,13] and allylgermanes [14] are higher than 30 kcal mol⁻¹.

Only allylboranes exhibit a truly intramolecular allylic rearrangement in a temperature range appropriate for extensive NMR studies. This rearrangement is facilitated by easily accessible 2p-AO of the boron atom which plays a pivotal role in the formation of the transition state of the borotropic migration [15]. Facile intramolecular [1,3]-B shifts in allylic type triorganoboranes result in a reversible migration of dialkylboryl groups along the conjugated polyolefinic

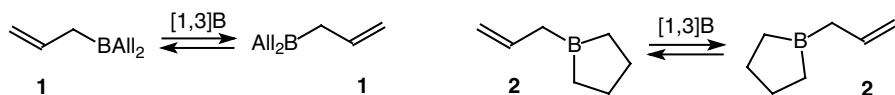
chain. This opens the possibility to construct molecules with sophisticated but predictable dynamic properties and provides an approach to structures hardly accessible by conventional synthesis. In the present chapter the known examples of fluxional allylboranes are reviewed with the emphasis on the structural and synthetic potentials of the intramolecular borotropic migrations.

2 DISCOVERY. ACTIVATION PARAMETERS OF [1,3]-B SHIFTS

It was found in 1965 that the ^1H NMR spectrum of triallylborane **1** is temperature dependent [16]. At temperatures below $-40\text{ }^\circ\text{C}$ **1** gives a A_2BX_2 spectrum. Increasing the temperature leads to the broadening of the signals of CH_2B and $\text{CH}_2=\text{}$ groups, and at $90\text{ }^\circ\text{C}$ (60 MHz) the spectrum pattern is AX_4 . These spectral changes are independent of the concentration of **1**, and testify therefore to the reversible intramolecular migrations of the diallylboryl group from the position 1 to the position 3 of the allylic moiety [16]. Very similar dynamic effects were observed in the ^1H NMR spectra of 1-allylborolene **2** (Scheme 2.1) [17].

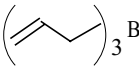
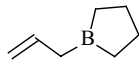
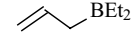
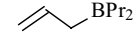
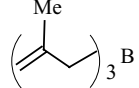
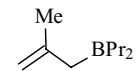
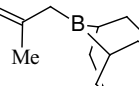
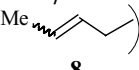
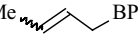
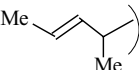
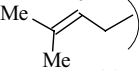
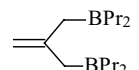
During the following decades a considerable number of fluxional allylboranes have been studied. The data on the activation parameters of the [1,3]-B shifts are collected in Table 2.1. The rearrangements in Table 2.1 are sorted in the order of their appearance in the NMR spectra in the following way.

1. The simplest case is the degenerate rearrangement, e.g. in triallylborane **1** (Scheme 2.1). Such a rearrangement results in averaging the exchanging signals in the NMR spectra producing a characteristic line-shape dependence in ^1H and ^{13}C NMR spectra. True values of activation parameters can be derived either from line-shape analysis or by 2D EXSY spectroscopy.
2. Several consecutive [1,3]-B migrations can result in a formally degenerate rearrangement (compounds **11** and **20**, e.g. Scheme 2.2). The barriers of the degenerate transformations can be measured similarly to those for the direct degenerate rearrangements. However, in this case one can obtain only effective activation parameters for the overall reaction occurring in two or several steps.
3. A special case of degenerate rearrangement takes place in cyclic conjugated molecules such as **14**, **15**, **21** and **22**. The possibility of infinite migration of



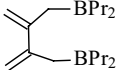
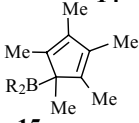
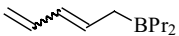
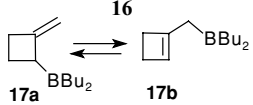
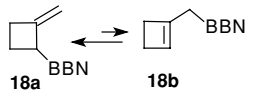
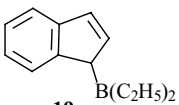
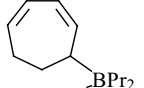
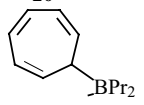
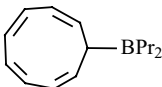
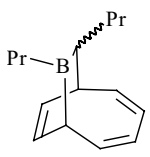
Scheme 2.1

Table 2.1 Activation parameters for the [1,3]-B shifts in allylboranes

Compound	Type of rearrangement ^a	E_A (kJ mol ⁻¹)	ΔG^\ddagger (kJ mol ⁻¹) (T , K)	Method of determination	Reference
	1	42	61.2 (312) 61.9 (298)	Line-shape ¹ H Line-shape ¹ H Line-shape ¹³ C	[16] [18] [19]
1					
	1	63		Line-shape ¹ H	[17]
2					
	1	49		Line-shape ¹ H	[20]
3					
	1		66.1 (298)	Line-shape ¹³ C	[19]
4					
	1		61.5 (311) 62.3 (298)	Line-shape ¹ H Line-shape ¹³ C	[21] [19]
5					
	1		64.0 (298)	Line-shape ¹ H	[19]
6					
	1		47.8 (303)	Line-shape ¹ H	[22]
7					
	5		80.0 (353) ^b 72.8 (298) ^c	Line-shape ¹ H Line-shape ¹³ C	[23] [19]
8					
	5		70.3 (298) ^d	Line-shape ¹³ C	[19]
9					
	1	54.7 (298)		Line-shape ¹ H	[18]
10					
	2	96.0 (425) 77.5 (298)		Line-shape ¹ H	[20] [19]
11					
	1		54.3 (298)	Line-shape ¹ H	[19]
12					

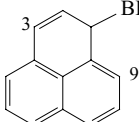
(continued)

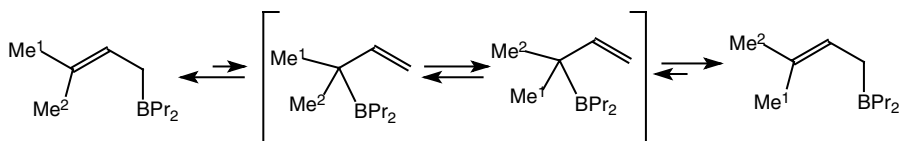
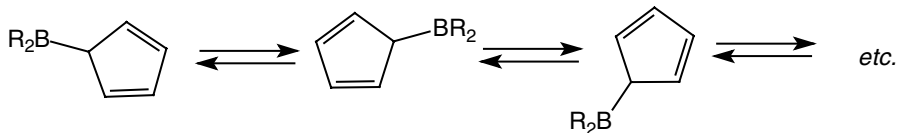
Table 2.1 (continued)

	1		74.5 (298)	Line-shape ¹ H	[19]
13					
	3	< 20 for R = Me, <i>i</i> -Pr		Line-shape ¹ H	[24]
14					
	3	< 20 for R = Cl, Me		Line-shape ¹ H	[25]
15					
	5			Line-shape ¹³ C	[26]
16					
	4	35.5 _{17a→17b} 33.8 _{17b→17a}	53.8 _{17a→17b} (298)	2D ¹³ C EXSY	[27]
17a					
17b					
	4		52.8 _{17a→17b} (298)	2D ¹³ C EXSY	[27]
18a					
18b					
	1	74.2	76.3 (298)	2D ¹ H EXSY	[28]
19					
	2	98.9	118.3 (298)	2D ¹³ C EXSY	[29]
20					
	3			DFT calculations	[30]
21					
	3	26.1	36.8 (195)	Line-shape ¹³ C	[31]
22					
	4			Line-shape ¹³ C	[32]
23					

(continued)

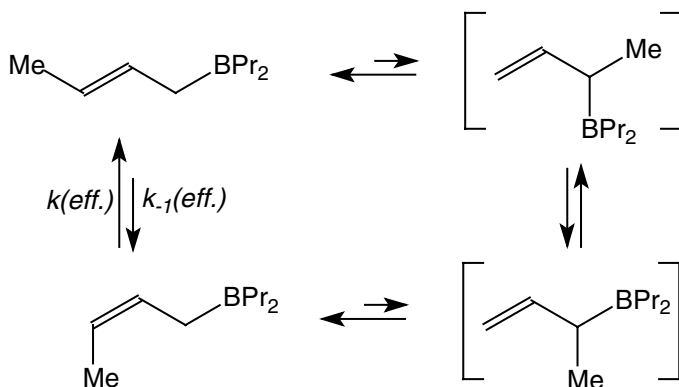
Table 2.1 (continued)

 24	1^g	80.4	63.6 (298)	2D ¹ H EXSY	[33]
--	----------------------	------	------------	------------------------	------

^a See text for explanations.^b $\Delta G^\circ_{353} = 2.95 \text{ kJ mol}^{-1}$.^c $\Delta G^\circ_{298} = 1.81 \text{ kJ mol}^{-1}$.^d $\Delta G^\circ_{298} = 1.01 \text{ kJ mol}^{-1}$.^e Multistep process.^f [1,5]-B shift was proposed.^g Both possible [1,3]-B shifts were observed, the activation parameters were determined for the faster migration to the position 9.**Scheme 2.2****Scheme 2.3**

a dialkylboryl group in one direction (Scheme 2.3) results in a specific line-shape in the ¹H and ¹³C NMR spectra of these compounds. The activation parameters of a single migration can be obtained via line-shape analysis or by quantitative 2D EXSY experiments. In these cases one must also consider the possibility of interference of other migration mechanisms.

- When the allylic fragment of the organoborane is unsymmetrical, the facile [1,3]-B shift results in the fast establishment of the thermodynamic equilibrium between all possible allylic isomers. When the stabilities of these isomers are close enough they can be simultaneously observed in the NMR spectra and the activation parameters of the 1,3-B shift can be measured by usual techniques (compounds **17**, **18** and **23**).
- The interconversion of isomers can proceed in several steps via unobservable, relatively unstable allylic isomers (e.g. Scheme 2.4). The effective rate constants for such interconversions (compounds **8**, **9** and **16**) are uniformly higher than those for direct 1,3-B shifts.



Scheme 2.4

For all rearrangements summarized in the Table 2.1 the intramolecular mechanism has been proved experimentally. The rearrangement takes place only in boranes, with a 2p-AO of boron remaining unoccupied: in amino complexes of allylic boranes the [1,3]-B shift does not proceed. The analysis of the relative values of activation parameters of allylic rearrangements indicates also that the appropriate configuration of the boron atom is important for the ease of rearrangement. Thus, in a series of simple allylboranes **1–7**, the free activation energies of the [1,3]-B migration lay within the narrow range of 60–66 kJ mol⁻¹ when the substituents on boron are alkyls or allyls (compounds **1**, **3**, **4**, **5** and **6**). Incorporation of the boron atom into a five-membered heterocycle significantly retards the rearrangement (compound **2**). On the other hand, for compounds **7** and **18** containing a boron atom incorporated into the BBN bicycle, the barriers of the [1,3]-B shifts are notably lower compared to their alkyl(allyl)-substituted analogs (**5**, **6** and **17** respectively).

Introduction of a methyl substituent into the position 2 of the allylic moiety does not affect significantly the barriers of the 1,3-B shifts (compare compounds **1** and **5**; **4** and **6**). The substitution of the position 2 with functional groups (compounds **12**, **13**) changes the activation barriers of allylic rearrangement notably. It was suggested that the [1,3]-B shift in **12** is facilitated by the participation of the 2p-AO of the second boron atom in the formation of the transition state [18]. The opposite effect for borane **13** is probably due to the decrease of electron density on the double bond due to the conjugation in the butadiene fragment. Quantum chemical calculations [15] prove the importance of the boron 2p-AO for the realisation of the sigmatropic migrations in allylboranes.

In the following sections the fluxional behavior of structurally complex triorganoboranes of the allylic type will be discussed in detail.

3 FLUXIONAL LINEAR POLYUNSATURATED ALLYLBORANES

3.1 2,4-PENTADIENYL(DI-*n*-PROPYL)BORANE

3.1.1 Synthesis and Dynamic Behavior of 2,4-Pentadienyl(di-*n*-propyl)Borane

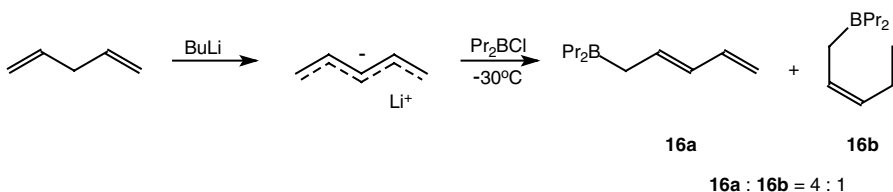
2,4-Pentadienyl(di-*n*-propyl)borane **16** was prepared by the reaction of penta-dienyllithium with chloro(di-*n*-propyl)borane in a mixture of hexane and THF at -30°C (Scheme 2.5) [26].

A reversible dependence of the line-shape on the temperature was observed in the ^{13}C NMR spectrum of borane **16** in the temperature interval 300–380 K (Figure 2.1). Thus, the C^2 , C^4 , and C^5 resonances of the *E*-isomer **16a** were notably broadened when increasing the temperature, but the C^3 signal remained sharp (Figure 2.1b–e). At 380 K the broadening was also observed for the signals of *Z*-isomer (Figure 2.1f). At this temperature the signals of C^3 in both isomers are also broadened. The appearance of the ^{13}C NMR spectrum of **16** at a certain temperature did not depend on its concentration, therefore the rearrangements taking place in **16a** and **16b** are intramolecular. Additionally the intramolecular migrations of the BPr_2 group in **16a** and **16b** were characterized by a series of 2D EXSY experiments.

The fastest rearrangement in **16** results in a formally degenerate transformation averaging the signals of C^1 / C^5 and C^2 / C^4 in the ^{13}C NMR spectrum, leaving the signal of C^3 untouched. A direct 1,5-B shift is impossible in this isomer due to geometric reasons; therefore the formally degenerate rearrangement proceeds through two consecutive 1,3-B shifts in **16a** via unstable allylic isomer **16c** (Scheme 2.6).

An estimation of the effective barriers ΔG_{EE}^{\ddagger} , ΔG_{EZ}^{\ddagger} , and ΔG_{ZZ}^{\ddagger} made by line-shape analysis of the ^{13}C NMR spectra afforded the following values:

$$\begin{aligned}\Delta G_{EZ}(366) &= 3.5 \pm 0.2 \text{ kJ mol}^{-1} \\ \Delta G_{EE}^{\ddagger}(366) &= 82.3 \pm 0.9 \text{ kJ mol}^{-1} \\ \Delta G_{EZ}^{\ddagger}(366) &= 85.5 \pm 0.9 \text{ kJ mol}^{-1} \\ \Delta G_{ZZ}^{\ddagger}(366) &= 91.5 \pm 0.9 \text{ kJ mol}^{-1}\end{aligned}$$



Scheme 2.5

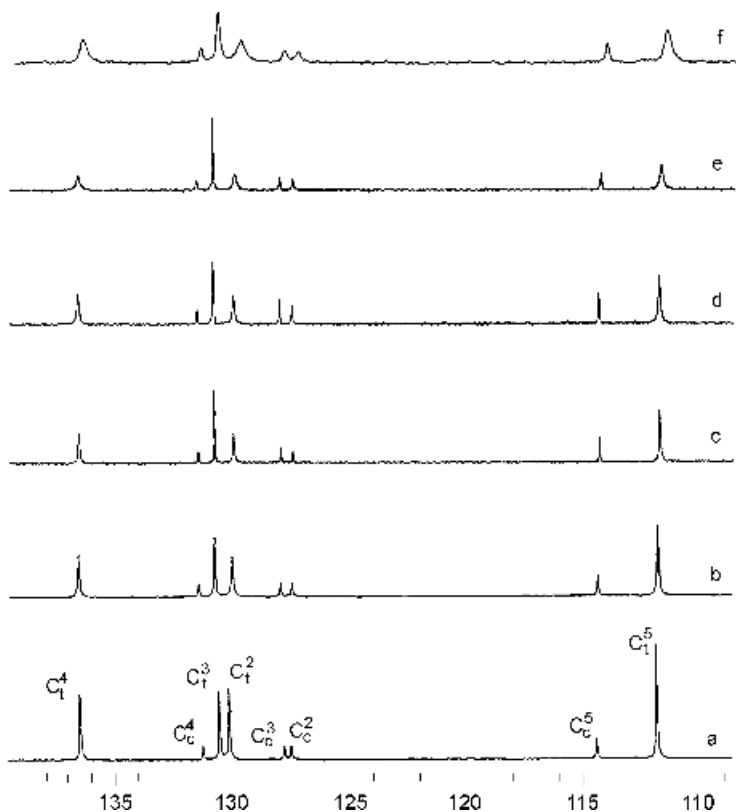


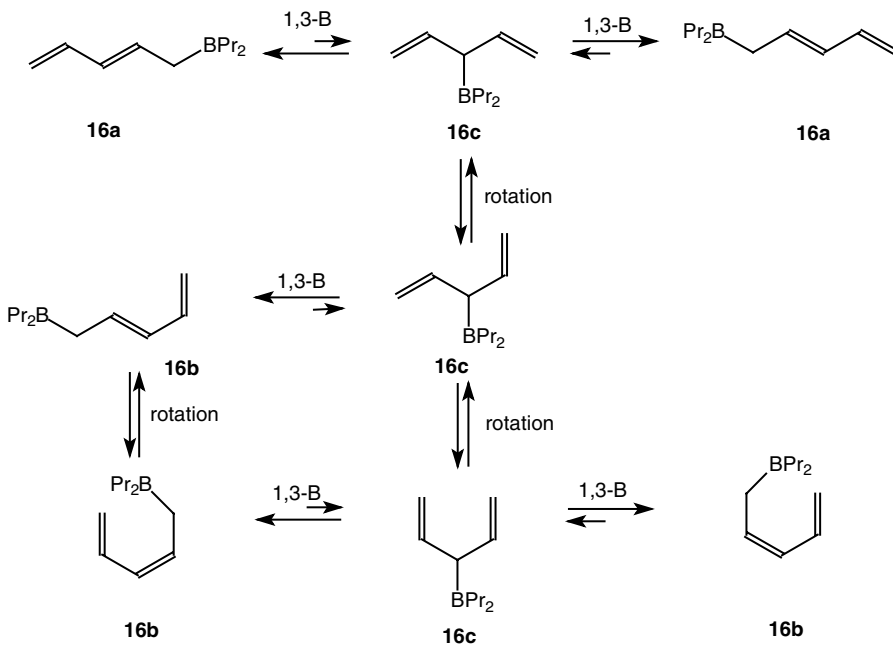
Figure 2.1 Temperature dependence of the line-shape in the ^{13}C NMR spectrum of compound **16** (50 MHz, neat liquid): (a) at 300 K; (b) at 340 K; (c) at 350 K; (d) at 360 K; (e) at 370 K; (f) at 380 K.

The lower rate of the sigmatropic 1,3-B migrations in the *Z*-isomer **16b** compared to **16a** is probably caused by the greater steric hindrance by the *cis*-allylic substituent for the formation of the transition state in **16b**.

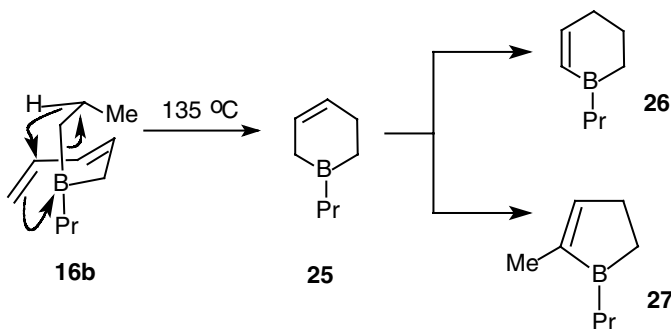
3.1.2 Thermal Cyclization of 2,4-Pentadienyl(di-*n*-propyl)Borane

At temperatures above 130 °C the pentadienyl(di-*n*-propyl)borane **16** undergoes intramolecular cyclization yielding cyclic borane **25** and propylene (Scheme 2.7) [26].

The equilibrium concentration of the *Z*-isomer **16b** is approximately 20%. Nevertheless, thermolysis of **16** gives 3-borinene **25** with 40% yield. Owing to geometric considerations only **16b** can participate in this transformation. Since the yield of **25** is greater than the equilibrium content of **16b**, it is clear that, when



Scheme 2.6



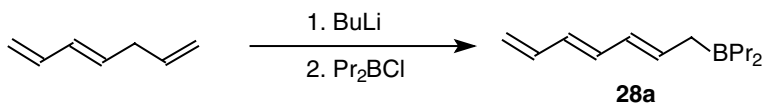
Scheme 2.7

the *Z*-isomer is consumed, it is reformed from the *E*-isomer (**16a**) by the mechanism shown in Scheme 2.6. At 160–180 °C 3-borinene **25** undergoes further transformation affording two products **26** and **27** in a ratio 1:1 (Scheme 2.7). The formation of 1-*n*-propyl-2-methyl-2-borolene **27** from **25** can be described as a consequence of dehydroboration–hydroboration. Compound **26** is formed from **25** by a [1,3]-H shift.

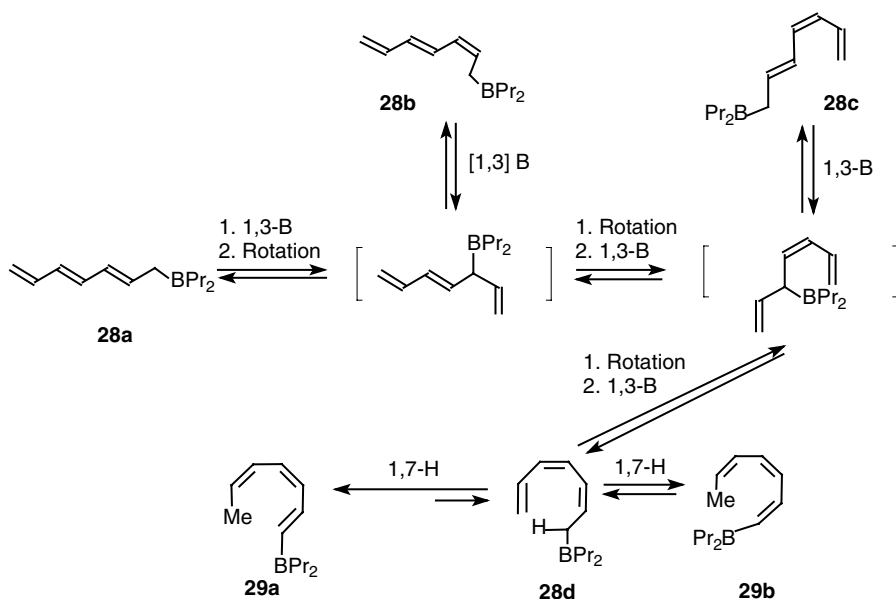
3.2 2,4,6-HEPTATRIENYL(DI-*n*-PROPYL)BORANE3.2.1 Synthesis and Dynamic Behavior of 2,4,6-Heptatrienyl(di-*n*-propyl)borane

2,4,6-Heptatrienyl(di-*n*-propyl)borane **28** was prepared from 1,3,6-heptatriene with 70% yield (Scheme 2.8). Analysis of the NMR spectra of **28** shows that all four possible isomers with a terminal di-*n*-propylboryl group **28a–d** are equilibrating in solution (the equilibrium ratio **28a**: **28b**:**28c**:**28d** is 82:12:5:1 at 298 K) [34].

The borane **28** isomerizes at elevated temperatures producing a vinyl borane **29** via a [1,7]-H sigmatropic shift in the *Z,Z*-isomer **28d** (Scheme 2.9, Figure 2.2). The content of **28d** in the equilibrium mixture is only 1%. Nevertheless due to reversible interconversions of **28a–d** taking place via 1,3-B shifts and intramolecular rotations, the 1,7-H shift proceeds until a new equilibrium is established. At room temperature, 3 weeks are required for this transformation, and at 373 K it occurs within several minutes. However, the complete



Scheme 2.8



Scheme 2.9

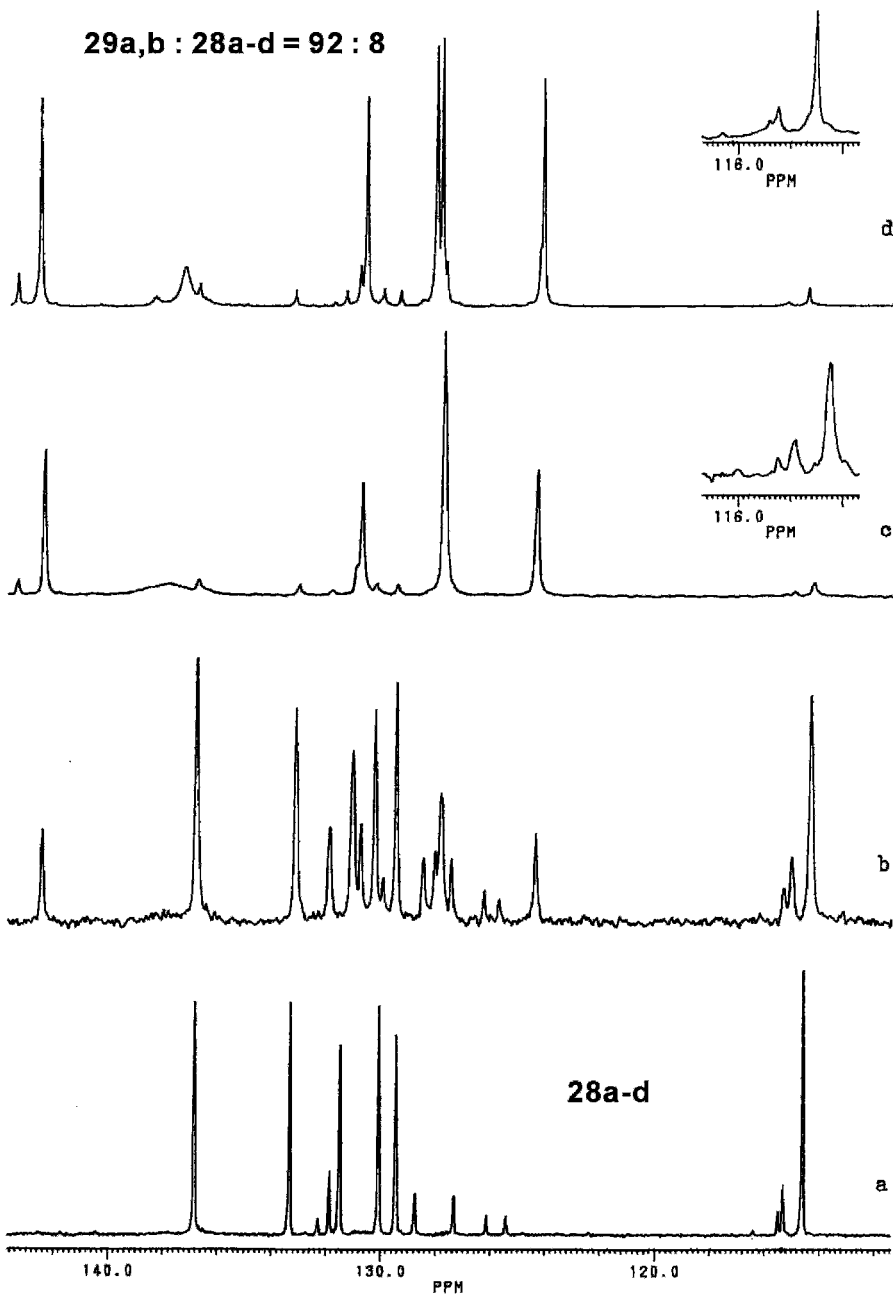


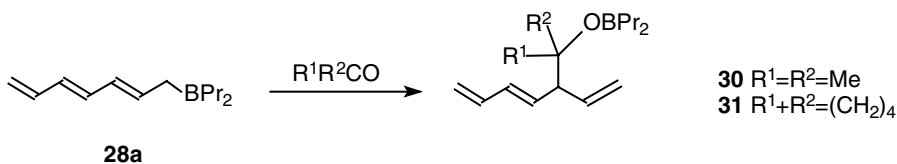
Figure 2.2 Changes in the ^{13}C NMR spectrum of **28** (low-field region) observed with the heating of the sample (50 MHz, neat liquid): (a) initial spectrum at 300 K; (b) spectrum obtained at 360 K just after heating; (c) spectrum obtained after heating for 3 h at 360 K; (d) spectrum of the same sample after cooling to 300 K.

transformation cannot be achieved due to the reversible character of the reaction – the resulting equilibrium mixture at 373 K contains 92 % of **29** (mixture of two isomers in a ratio 95:5) and 8 % of **28** (mixture of four isomers **28a–d**). Again the whole transformation proceeding via the minor isomer **28d** becomes possible due to the facile [1,3]-B migrations occurring in **28** and interconverting reversibly the isomers **28a–d**. This phenomenon was used for the first synthesis of isomerically pure *Z,Z*-1,3,5-heptatriene by the reaction of **29** with acetic acid [35].

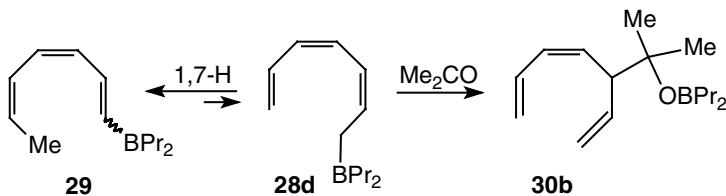
3.2.2 Reactions of Boranes **28** and **29** with Carbonyl Compounds

Allylborane **28** reacts with acetone and cyclopentanone at -30°C yielding borinic esters **30** and **31** (Scheme 2.10) [34].

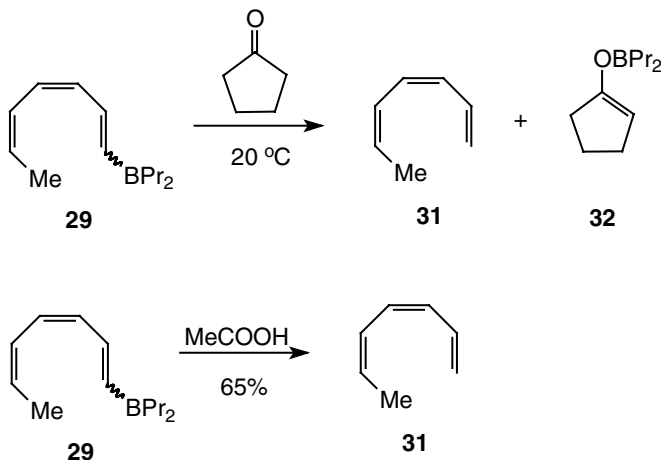
Non-fluxional vinylic boranes do not react with carbonyl compounds. Nevertheless, the vinylic borane **29** reacts with acetone (2 h under reflux) yielding the *Z*-isomer of the homoallylic borinic ester **30b**. The *cis*-configuration of the reaction product **30b** corresponds to the following sequence of transformations (Scheme 2.11). The [1,7]-H shift in the vinylic borane **29** gives the allylic *Z,Z*-isomer **28d** which immediately reacts with acetone before the equilibrium among the allylic isomers is established. On the other hand, cyclopentanone reacts directly with **29** under mild conditions yielding *Z,Z*-1,3,5-heptatriene **31** and borinic ester **32** (Scheme 2.12). Apparently **29** reacts with the enol form of cyclopentanone, and a direct splitting of the B–C_{sp}2 bond takes place. Similar reaction of **29** with acetic acid was used for the preparative synthesis of previously unknown hydrocarbon **31** (Scheme 2.12) [35].



Scheme 2.10



Scheme 2.11



Scheme 2.12

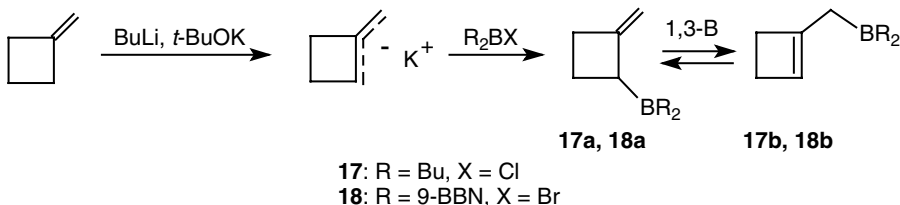
4 DYNAMIC BEHAVIOR OF CYCLIC ALLYLBORANES

4.1 DYNAMIC EQUILIBRIA BETWEEN 2-(DIALKYLBORYL)METHYLENOCYCLOBUTANES AND 1-(DIALKYLBORYL)CYCLOBUTENES

Compounds **17** and **18** were prepared by the reaction of methylenecyclobutane potassium with the corresponding dialkylhaloborane (Scheme 2.13). Both compounds **17** and **18** are fluxional in solution and in neat liquid [27].

Two sets of signals are observed in the ^1H and ^{13}C NMR spectra of borane **17** at 203 K attesting for the coexistence of 2-(di-*n*-butylboryl)-1-methylenecyclobutane (**17a**) and 1-(di-*n*-butylboryl)methyl-1-cyclobutene (**17b**) in a ratio 4:3. At 373 K the ^1H NMR spectrum of this borane is completely averaged.

The scheme of interconversion was proved by 2D EXSY spectroscopy (e.g. Figure 2.3). The activation parameters for the interconversion of **17a** and **17b** were obtained from the quantitative treatment of five 2D ^{13}C - ^{13}C EXSY spectra taken in the temperature interval 180–207 K. The rate constants for the



Scheme 2.13

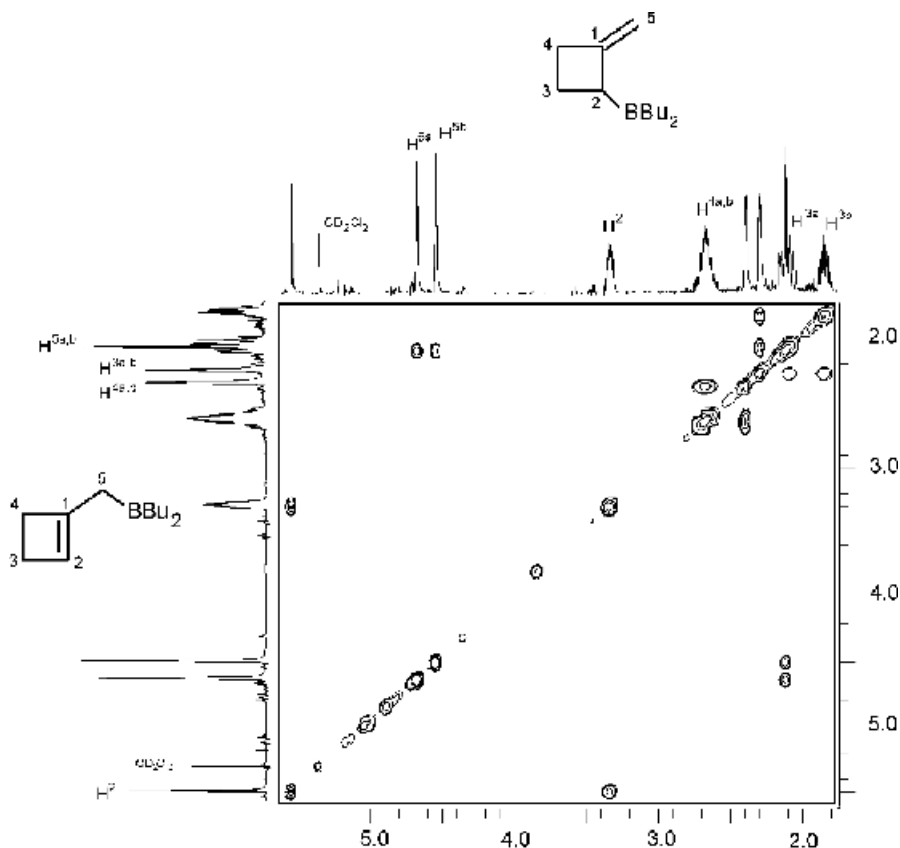


Figure 2.3 Phase-sensitive ^1H - ^1H EXSY spectrum of compound **17** (400 MHz, neat liquid, 203 K).

two-positional exchange with unequal concentrations were obtained from Equation (2.1) [36].

$$k = \frac{1}{t_m} \ln \frac{r+1}{r-1}, \quad r = 4X_A X_B \frac{I_{AA} + I_{BB}}{(I_{AB} + I_{BA}) - (X_A - X_B)^2} \quad (2.1)$$

where t_m is mixing time, X_A and X_B are the mole fractions of the isomers, I_{AA} and I_{BB} are the intensities of the corresponding diagonal peaks, I_{AB} and I_{BA} are the intensities of the corresponding cross-peaks.

The following activation parameters were obtained:

For the transformation 17a → 17b :	For the transformation 17b → 17a :
$E_A = 35.5 \pm 2.5 \text{ kJ mol}^{-1}$	$E_A = 33.8 \pm 2.5 \text{ kJ mol}^{-1}$
$\ln A = 22.0 \pm 1.6$	$\ln A = 21.6 \pm 1.5$
$\Delta G^\ddagger_{298} = 53.8 \pm 0.5 \text{ kJ mol}^{-1}$	$\Delta G^\ddagger_{298} = 52.8 \pm 0.5 \text{ kJ mol}^{-1}$

Figure 2.4 shows the temperature dependence of the ^{13}C NMR spectrum of compound **18**. Analogously to compound **17**, at a high temperature (323 K) the

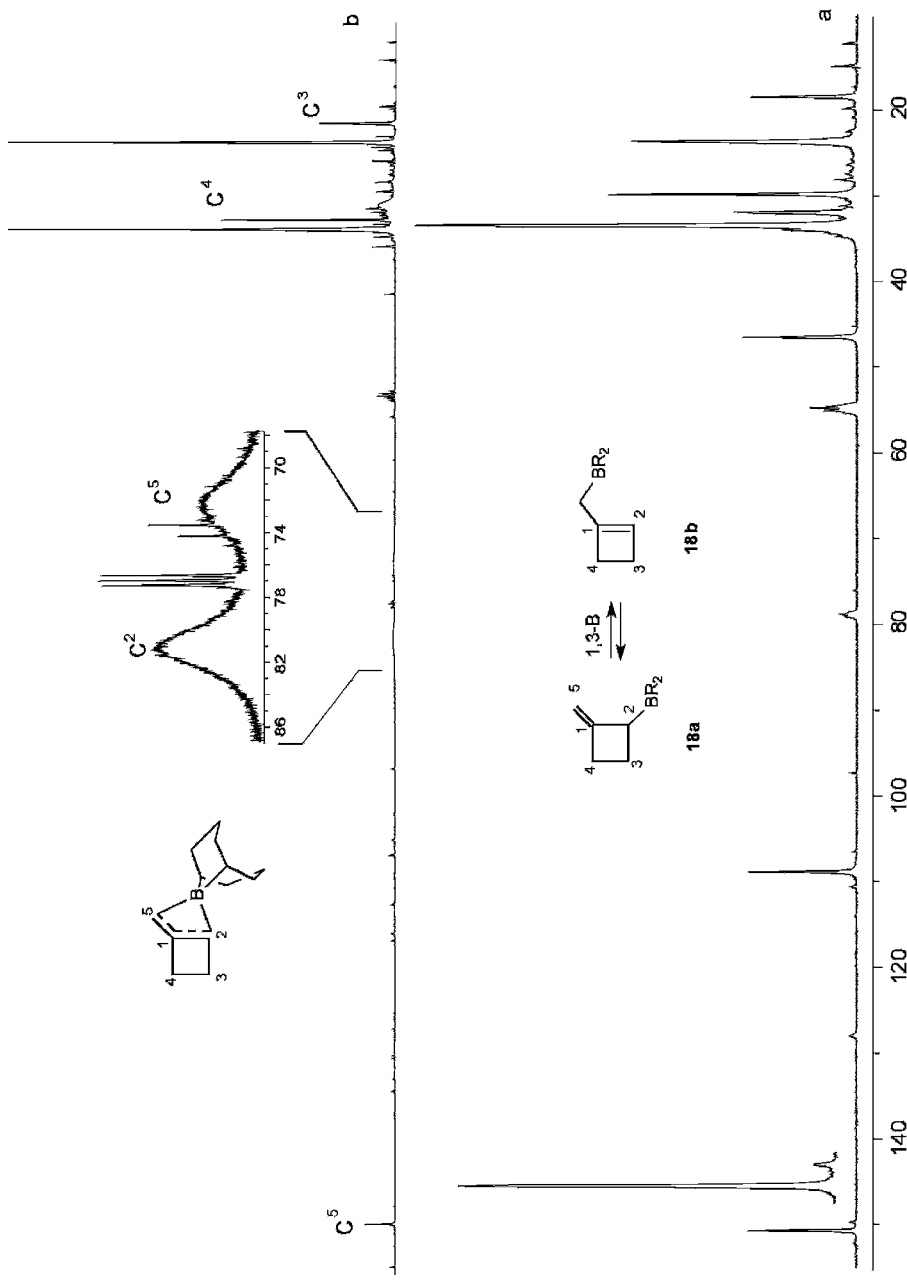


Figure 2.4 ^{13}C NMR spectrum of compound **18** (100 MHz, mixture $\text{CD}_2\text{Cl}_2\text{-CDCl}_3$ - CDCl_4 60:27:13); (a) at 163 K; (b) at 323 K.

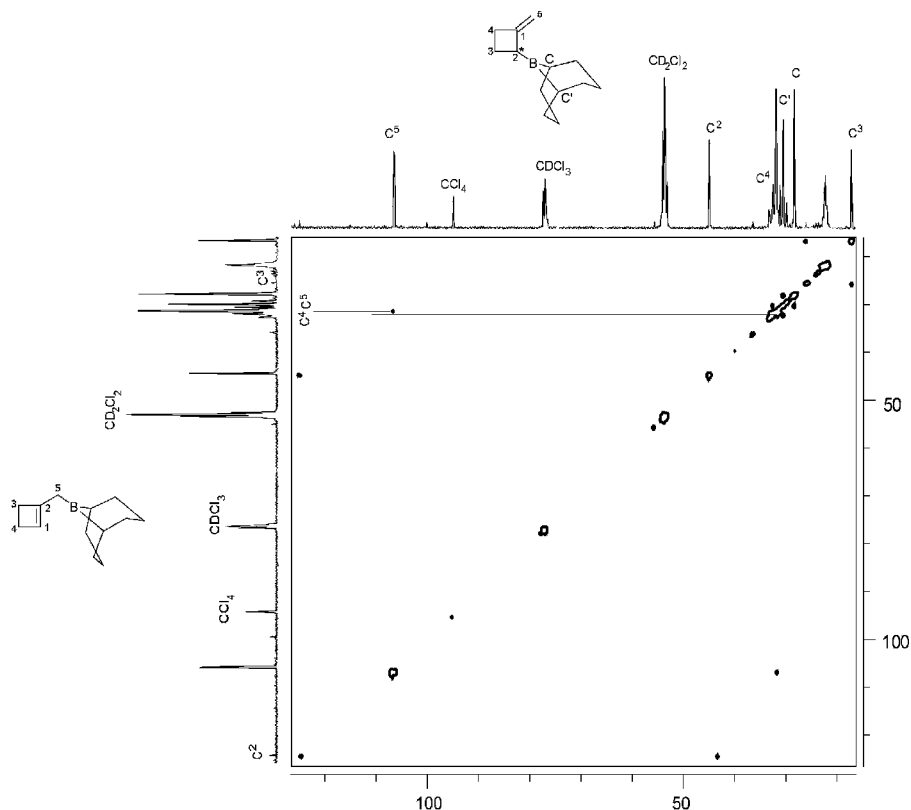


Figure 2.5 ^{13}C - ^{13}C EXSY spectrum of compound **18** (100 MHz, mixture CD_2Cl_2 - CDCl_3 - CCl_4 60:27:13, 163K), spectrum size 1024 \times 512, mixing time 0.1 s, delay 1 s.

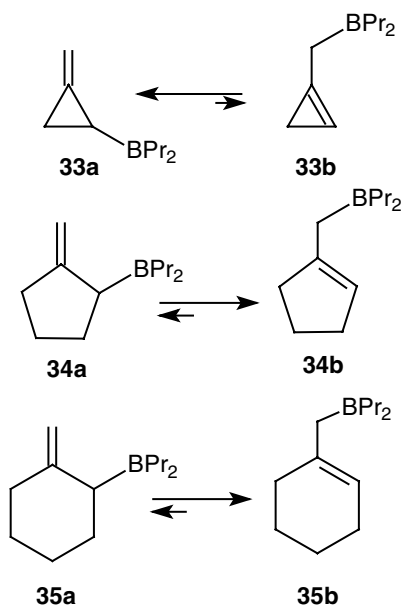
averaged spectrum corresponding to a rapid exchange between methylenecyclobutane form **18a** and methylcyclobutene form **18b** has been observed. Integration of the signals of the quaternary carbon atoms of **18a** and **18b** at 163 K gave a 24:1 ratio. Thus, the intensities of the signals of **18b** are comparable to those of impurities and the positions of some signals of **18b** could be barely detected in a one-dimensional ^{13}C spectrum. Nevertheless, the ^{13}C chemical shifts of compound **18b** could be determined from the ^{13}C - ^{13}C 2D EXSY spectrum (Figure 2.5) which confirmed the reversible interconversion of **18a** and **18b**. The signals in the ^1H NMR spectrum have been assigned on the basis of the two-dimensional ^1H - ^1H COSY, ^1H - ^1H EXSY, and ^1H - ^{13}C XHCCORR spectra of compound **18b** obtained at 163 K.

Due to the existence of an asymmetric center at position 2 in compound **18a**, carbon atoms C^1 and $\text{C}^{1'}$ in the bicyclic fragment become nonequivalent, which results in the splitting of the corresponding signals in both the ^1H and ^{13}C NMR spectra (see, for example, Figure 2.4; the C and C' signals). There

is no asymmetric center in compound **18b**; therefore the **18a** \rightarrow **18b** \rightarrow **18a** conversion results in the reversible inversion of the asymmetric center. This process is responsible for the presence of a cross-peak between the signals of C and C' in Figure 2.5.

At 323 K the ^{13}C NMR spectrum of compound **18** is completely averaged. The values of chemical shifts for C² and C⁵ in **18a** and **18b** (measured at 163 K) and the values for the same carbons in the averaged spectrum allow to calculate the ratio **18a**:**18b** at 323 K, which turned to be 65:35 (compare to 24:1 at 163 K). Thus, the equilibrium constant is strongly temperature dependent, which makes difficult the accurate kinetic analysis of this equilibrium. The rate constant for the interconversion of **18a** and **18b** at 163 K ($0.3 \pm 0.03 \text{ s}^{-1}$ for the rearrangement of **18a** to **18b** and $6.3 \pm 0.3 \text{ s}^{-1}$ for the reverse process) has been measured by 2D ^{13}C - ^{13}C EXSY spectroscopy as the slope of the linear dependence of the normalized volume of the cross-peak versus the mixing time.

In contrast to boranes **17** and **18**, no dynamic effects were found in the NMR spectra of the compounds **33–35** (Scheme 2.14). The borane with cyclopropane moiety **33** exists exclusively as 2-(di-*n*-butylboryl)-1-methylenecyclopropane. On the other hand, only *endo* isomers can be detected in the NMR spectra of the five- and six-membered boranes **34** and **35** (Scheme 2.14). The order of relative thermodynamic stability of triorganoboranes **17**, **18**, **33–35** nicely corresponds to the known order for the corresponding hydrocarbons [37].



Scheme 2.14

4.2 DYNAMIC PROPERTIES OF CYCLOPENTADIENYL AND PENTAMETHYLCYCLOPENTADIENYL DERIVATIVES OF BORON

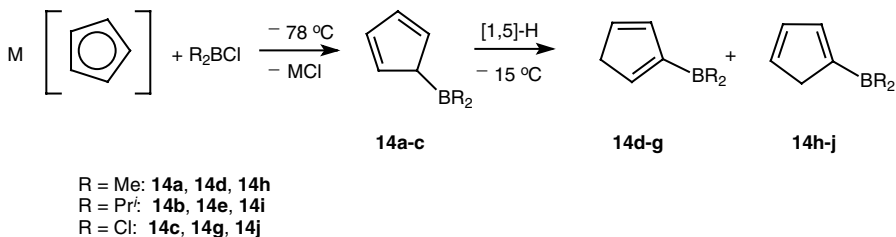
Fluxional cyclopentadienylboranes **14a–c** can be prepared by transmetalation of cyclopentadienylmetals (Li, Na, Tl, Hg) at decreased temperatures (Scheme 2.15) [24]. Fast borotropic rearrangements in **14a–c** lead to the observation of an averaged ^1H and ^{13}C NMR spectra even at -105°C . The topology of borotropic migrations is therefore unknown: the [1,5]-B shifts have been suggested by analogy to other metal cyclopentadienyls, but the experimental evidence is lacking.

At temperatures above -10°C **14a–c** rearrange to the mixtures of vinylic boranes **14d–g** and **14i–j** (Scheme 2.15).

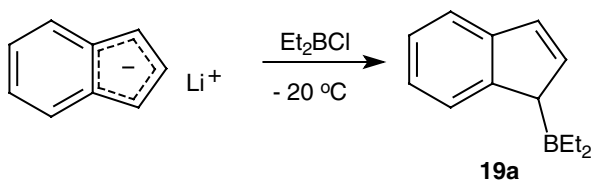
Pentamethylcyclopentadienylboranes Cp^*BR_2 **15** ($\text{R} = \text{Me}$ (**15a**), Cl (**15b**), NMe_2 (**15c**)) were prepared by transmetalation of Ge or Hg pentamethylcyclopentadienyls [25]. These compounds are thermally stable since the [1,5]-H shift is impossible. Compounds **15a** and **15b** give averaged NMR spectra till -90°C . Compound **15c** gives static spectra up to 40°C ; at higher temperatures the dynamic effects have been observed. However, the topology of the borotropic migrations in **15c** has not been studied [25a].

4.3 SYNTHESIS AND DYNAMIC PROPERTIES OF 1-INDENYL(DIETHYL)BORANE

The 1-indenyl(diethyl)borane **19a** was prepared from indenyllithium and diethylboron chloride in hexane (Scheme 2.16) [28]. In the $^1\text{H} - ^1\text{H}$ 2D EXSY



Scheme 2.15



Scheme 2.16

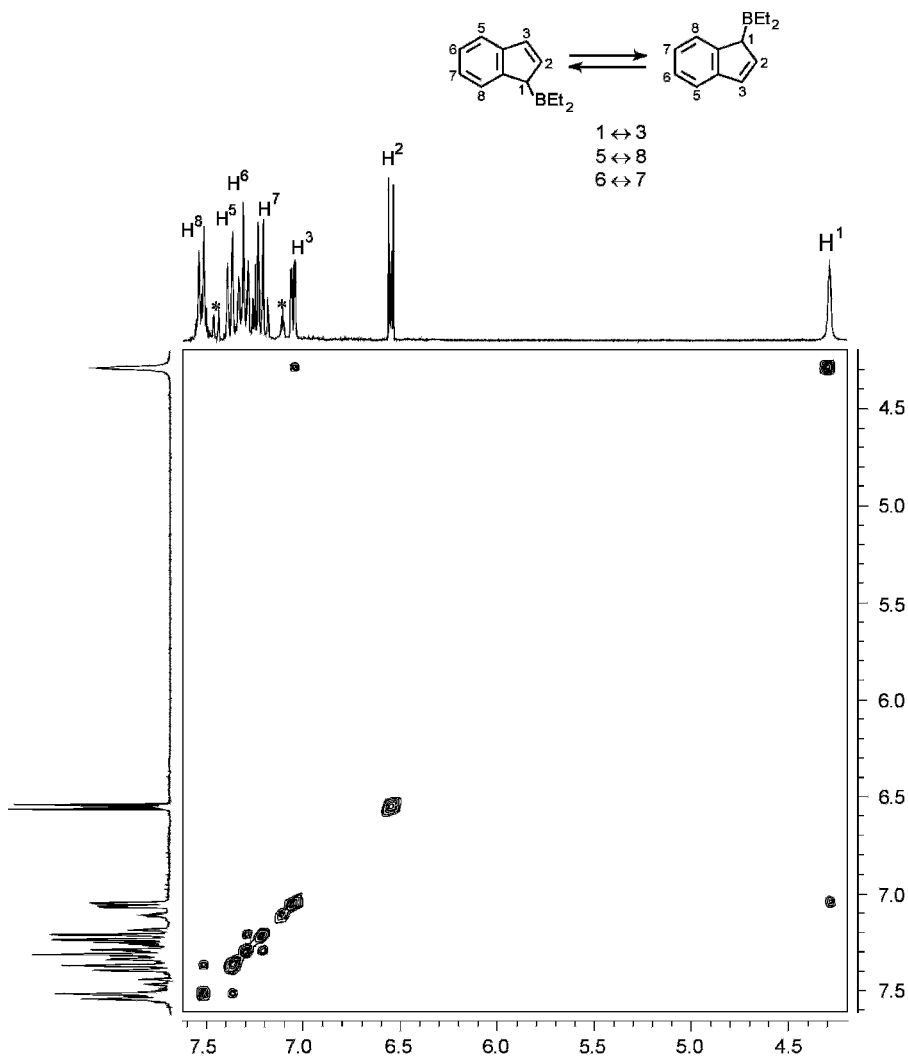
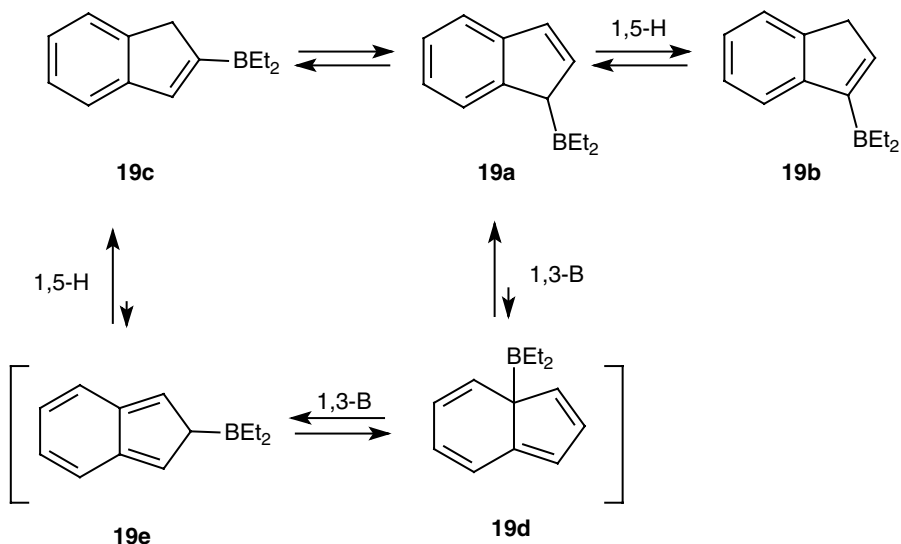


Figure 2.6 ^1H 2D EXSY NMR spectrum of **19a** (300 MHz, CDCl_3 , 313 K, mixing time 0.5 s); asterisks indicate the signals of **19b**.

NMR spectra of borane **19a** taken in the temperature interval 25–80 °C, three cross-peaks corresponding to the migrations of the diethylboryl group from position 1 to position 3 have been found (Figure 2.6).

The kinetics of the [1,3]-B sigmatropic migrations in **19a** were measured from a series of 2D ^1H - ^1H EXSY NMR spectra. For the degenerate exchange taking place in **19a** the rate constants were obtained from the intensities of the diagonal and cross-peaks corresponding to an exchanging pair of the signals



Scheme 2.17

from Equation (2.2) [36]:

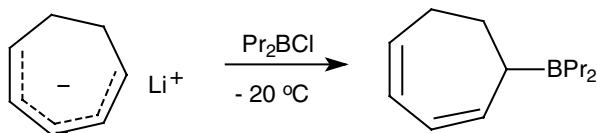
$$k = \frac{1}{t_m} \ln \frac{r+1}{r-1} \quad r = \frac{I_{AA} + I_{BB}}{I_{AB} + I_{BA}} \quad (2.2)$$

where I_{AA} , I_{BB} are the intensities of the diagonal peaks and I_{AB} , I_{BA} the intensities of the cross-peaks. The following activation parameters for the [1,3]-B shift in **19a** have been obtained: $E_A = 74.2 \pm 0.9 \text{ kJ mol}^{-1}$; $\ln A = 28.6 \pm 0.5$; $\Delta G^\ddagger(298) = 76.2 \pm 0.5 \text{ kJ mol}^{-1}$.

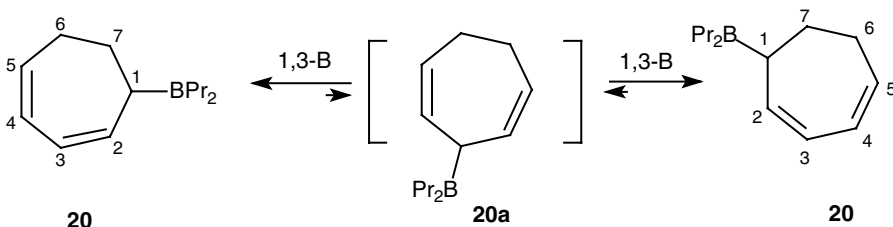
A sigmatropic migration of hydrogen takes place at elevated temperatures in **19a**. This leads to the establishment of a dynamic equilibrium between the three isomers **19a**, **19b**, and **19c** (Scheme 2.17). A small amount (about 6%) of 2-indenyl(diethyl)borane **19c** apparently appears by a [1,5]-H shift in the *iso*-indenyl intermediate **19e**, which is formed from **19a** via two consequent [1,3]-B shifts.

4.4 DYNAMIC BEHAVIOR OF CYCLOHEPTADIENYL (DI-*n*-PROPYL)BORANE

Borane **20** was prepared in 40% yield by the reaction of lithium cycloheptadienide with chloro(di-*n*-propyl)borane (Scheme 2.18) [29]. Cross-peaks corresponding to the exchange between the positions 1 and 5, 2 and 4, 6 and 7 were found in the ^1H and ^{13}C 2D EXSY NMR spectra of the compound **20**. These findings determine the topology of the rearrangement occurring in **20** as the migration of the di-*n*-propylboryl group from position 1 to position 5.



Scheme 2.18



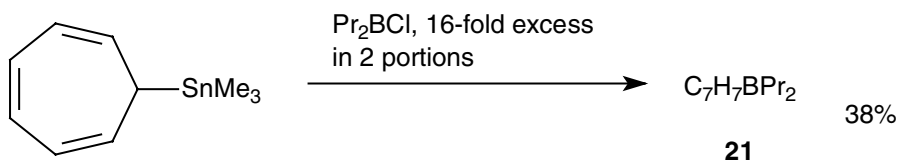
Scheme 2.19

Formally this corresponds to the [1,5] sigmatropic migration of the di-*n*-propylboryl group. However, it has been supposed that this dynamic behavior is instead caused by two consequent [1,3]-B migrations with the intermediacy of relatively unstable isomer **20a** (Scheme 2.19). This conclusion was supported by the close values of the activation barriers of borotropic migrations in **20** (found from ^{13}C 2D EXSY NMR) and structurally similar *Z*-2,4-pentadienyl(di-*n*-propyl)borane **16b** (see Table 2.1).

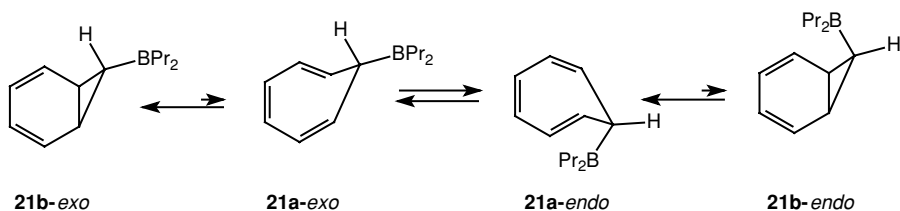
4.5 SYNTHESIS AND DYNAMIC PROPERTIES OF CYCLOHEPTATRIENYL(DI-*n*-PROPYL)BORANE EQUILIBRIUM WITH 7-(DI-*n*-PROPYLBORYL)NORCARADIENE

4.5.1 Synthesis of Cycloheptatrienyl Derivatives of Boron. Analysis of the Equilibrium Cycloheptatriene–Norcaradiene

The synthesis of cycloheptatrienylborane **21** was accomplished by repeated treatments of trimethylcycloheptatrienyltin with an excess of di-*n*-propylboron chloride without solvent (Scheme 2.20) [30].



Scheme 2.20



Scheme 2.21

Figure 2.7 displays the temperature dependence of the ^{13}C NMR spectrum of compound **21**. It corresponds to the equilibrium between cycloheptatrienyl(di-*n*-propyl)borane **21a** (*endo*- and *exo*-isomers) and its valence tautomer, 7-di-*n*-propylborylnorcaradiene **21b** (Scheme 2.21). At 153 K the spectra contain only one set of signals corresponding to the *exo*-norcaradienyl isomer **21b** (Figure 2.7).

Ab initio DFT calculations for all isomers of **21** (dimethylboryl derivatives) and the transition states for their interconversions have been used to clarify the reasons of the relative stability of **21b-*exo*** and **21b-*endo***. In the former compound the empty 2p-AO of the boron atom is ideally oriented for overlapping with the Walsh orbital of the cyclopropane ring. On the other hand, in **21b-*endo*** this interaction is effectively ‘switched off’ due to the perpendicular orientation of these orbitals emerging when the steric interactions of the alkyl groups and the cyclohexadiene ring are minimized. The thermodynamic parameters for the equilibrium between **21a** and **21b** were determined by NMR data from the linear dependence of $\ln K$ versus $1/T$: $\Delta H = 10.1 \pm 0.5 \text{ kJ mol}^{-1} \text{ L}^{-1}$, $\Delta S = -23 \pm 1 \text{ J mol}^{-1} \text{ K}^{-1}$. These values are reasonably reproduced in the calculations ($\Delta H = 8.4 \text{ kJ mol}^{-1}$; $\Delta S = -15.5 \text{ J mol}^{-1} \text{ K}^{-1}$).

Rate constants for the rearrangement of **21a** into **21b** and the reverse reaction were determined at the temperature of maximal broadening (228 K): $k_A(228) = 4.5 \times 10^3$, $k_B(228) = 6.0 \times 10^4 \text{ s}^{-1}$, $\Delta G^\ddagger_{228}(\mathbf{21a} \rightarrow \mathbf{21b}) = 8.2 \pm 0.1 \text{ kcal mol}^{-1}$ and $\Delta G^\ddagger_{228}(\mathbf{21b} \rightarrow \mathbf{21a}) = 9.4 \pm 0.1 \text{ kcal mol}^{-1}$. The computed values $\Delta G^\ddagger_{228}\{\mathbf{21a}(\textit{exo}) \rightarrow \text{TS1}\} = 3.2 \text{ kcal mol}^{-1}$ and $\Delta G^\ddagger_{228}(\mathbf{21b}(\textit{exo}) \rightarrow \text{TS1}) = 6.7 \text{ kcal mol}^{-1}$ at B3LYP/6-31G*, are in reasonable agreement with the experiment.

4.5.2 Mechanism of the Borotropic Migrations in **21**

Cycloheptatrienylborane **21** cannot be observed separately in the NMR spectra due to the fast equilibrium with its valence tautomer **21b**. Nevertheless, at temperatures above 300 K this equilibrium is fast on the NMR timescale and the concentration of **21a** is about 30%. If in **21a** a sigmatropic migration of the di-*n*-propylboryl group takes place, this rearrangement should lead to the mixing of the chemical shifts in the NMR spectra of **21a**, which inevitably

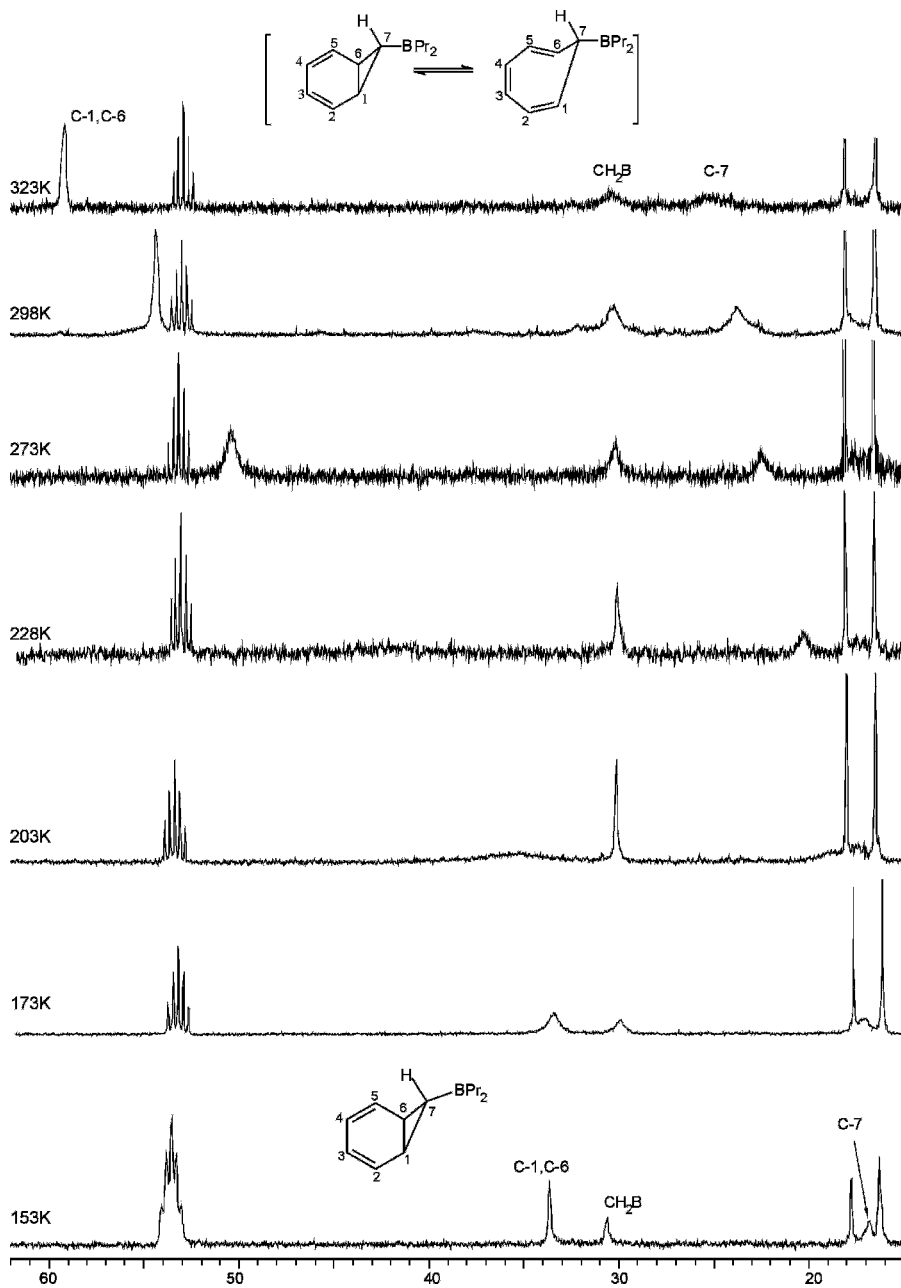
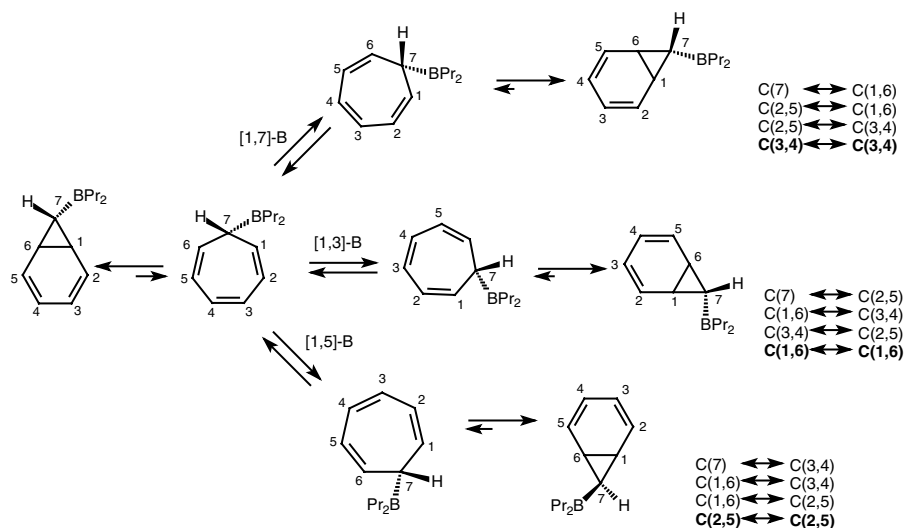


Figure 2.7 Temperature dependence of the high-field region of the ^{13}C NMR spectrum (100 MHz, $\text{CD}_2\text{Cl}_2\text{-CDCl}_3\text{-CCl}_4$) of compound **21**.

would affect the line-shape of the averaged spectra. Taking into account the data discussed above, one can conclude that the barrier to any rearrangement taking place in **21a** should be relatively high, since at temperatures below 293 K only line-shape changes attributable to the fast equilibrium between **21a** and **21b** were observed. At higher temperatures, additional effects were found. Thus, the temperature dependence of the line width of C^{1,6} passes through a minimum at 293 K and increases by 10 Hz in the temperature interval 293–313 K. The sharpening of C^{1,6} when the temperature is raised from 228 to 293 K is explained by the increasing rate of the interconversion of **21a** and **21b**. However, the notable broadening of this signal at higher temperatures can be explained only by the occurrence of another dynamic process, viz. of a sigmatropic migration of the di-*n*-propylboronyl group in **21a**. In the same temperature interval the line width of C^{2,5} changes from 4.0 to 7.5 Hz, whereas the line widths of other signals in the spectrum remain constant, 4 Hz (the signal C⁷ is broadened significantly since it is bound to the quadrupolar nucleus ¹¹B). The data on the relative broadening of the signals testify to the [1,7]-B shift mechanism in **21a**, since this topology of the migrations requires minimal broadening of C^{3,4} compared to C^{2,5} (Scheme 2.22)

The same conclusion follows from the phase-sensitive 2D ¹H EXSY spectra of the borane **21** taken at 323 K. Since the interconversion of **21a** and **21b** does not change the relative disposition of the protons (Scheme 2.21), the cross-peaks between the averaged signals directly indicate the mechanism of the borotropic migrations in **21a**. Thus, the proton H⁷ gives a cross-peak with the proton H^{1,6} that is indicative of a [1, 7]-B shift.



Scheme 2.22

The conclusive evidence for the [1,7]-B shifts in **21a** has been obtained by *ab initio* DFT calculations. The calculated relative energies of the transition states for different borotropic migrations show that the [1,7]-B shift is the most favorable energetically ($\Delta E^\ddagger = 77 \text{ kJ mol}^{-1}$). For the [1,5]-B shift the calculations give $\Delta E^\ddagger = 108 \text{ kJ mol}^{-1}$, and for the [1,3]-B shift $\Delta E^\ddagger = 115 \text{ kJ mol}^{-1}$.

4.6 THREE INDEPENDENT DYNAMIC PROCESSES IN THE IRONTRICARBONYL COMPLEX OF CYCLOHEPTATRIENYL(DI-*n*-PROPYL)BORANE

Complex **38** was synthesized by the reaction of $[\text{C}_7\text{H}_7\text{Fe}(\text{CO})_3]\text{K}$ and Pr_2BCl at -40°C in THF [38]. The chemical shift of H^7 ($\delta = 2.79$) and the values $^3J_{1,-t}(4.5 \text{ Hz})$ and $^3J_{6,1}(4.3 \text{ Hz})$ are consistent with the *exo*-configuration of the complex **38**, i.e. the $\text{Fe}(\text{CO})_3$ and BPr_2 groups are disposed at different sides of the cycloheptatriene cycle. Different [1,*j*] migrations ($j = 3, 5, 7$) of the di-*n*-propylboryl group in complex **38** lead to unique combinations of the exchanging atoms (Scheme 2.23).

All rearrangements possible for **38** are degenerate from the point of view of NMR spectroscopy (seven rearrangements marked by asterisks lead to the interconversion of stereoisomers with identical NMR spectra).

In the phase-sensitive ^1H and ^{13}C EXSY NMR spectra of complex **38** taken at 268 K three cross-peaks were detected testifying to the occurrence of a single rearrangement at this temperature, viz. of the process $\text{A} \rightarrow \text{D}$ (Scheme 2.23, Figure 2.8).

At 298–323 K, 13 cross-peaks were observed in the EXSY spectra of **38** (e.g. Figure 2.8). The three most intense cross-peaks correspond to the process $\text{A} \rightarrow \text{D}$. The nature of other dynamic processes was elucidated from a detailed analysis of the exchange cross-peaks in the EXSY spectra (Figure 2.9). The whole set of expected cross-peaks for an occurring rearrangement should be observed. If even one cross-peak from the expected combination is absent, one can conclude that this process does not take place. Comparing the expected sets of exchanges against the experimental EXSY spectra three different rearrangements were identified (Scheme 2.24; the whole set of cross-peaks was observed for two additional rearrangements, but they are most probably combinations of the fast and slow migrations). The [1,3]-B sigmatropic and the [1,3]-Fe haptotropic shifts were well known previously. However, the fastest observed process is a [1,7]-B sigmatropic shift accompanied by simultaneous [1,2]-migration of the irontricarboxyl group. In contrast to the well-studied continuous migrations of alkylmetals around the conjugated cyclic systems, the fastest rearrangement in **38** is oscillating, i.e. both migrating groups are moving towards each other, and in the next migration event they return back moving again in opposite directions. Hence, the [1,7]-B + [1,2]-Fe shift in **38** is a rare example of an *oscillating rearrangement*.

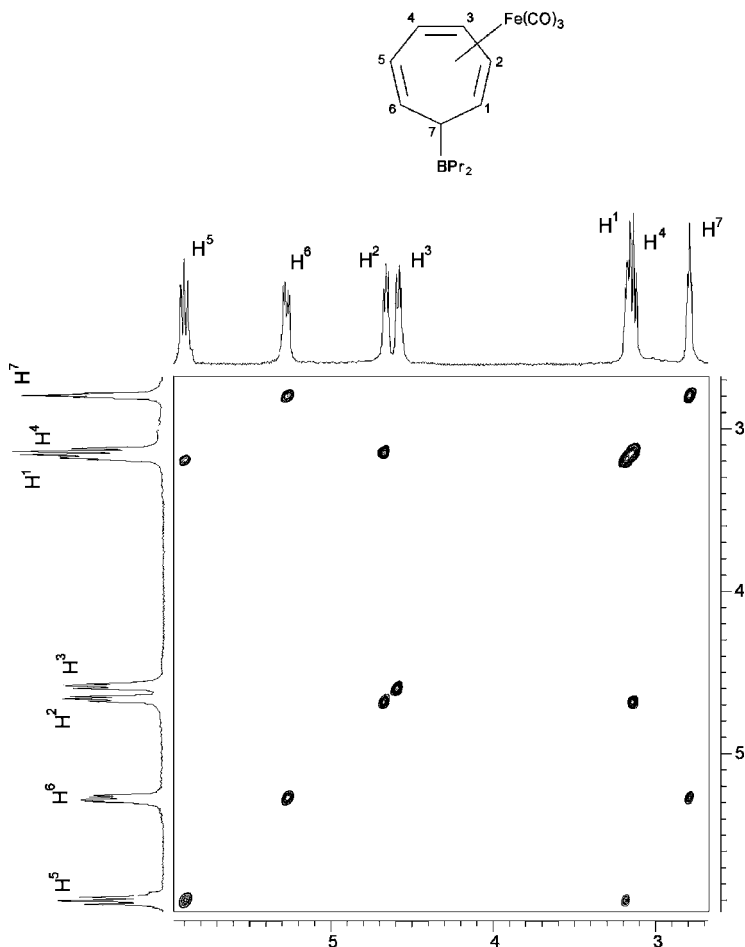


Figure 2.8 Phase-sensitive ^1H - ^1H EXSY spectrum of compound **38** (400 MHz, CDCl_3 , 268 K).

The kinetics of the [1,7]-B shift (accompanied by [1,2]-Fe migration) in compound **38** has been measured from the series of 2D ^{13}C EXSY NMR experiments by volume integration of the diagonal cross-peaks and the cross-peaks corresponding to the exchange between C^1 and C^5 . The Arrhenius treatment of the rate constants calculated using Equation (2.2) gave the following activation parameters for this rearrangement: $E_A = 71.2 \pm 2.1 \text{ kJ mol}^{-1}$; $\ln A = 32 \pm 1$.

4.7 CYCLOOCTATETRAENYL(DI-*n*-PROPYL)BORANE

The NMR spectra of cyclononatetraenyl(di-*n*-propyl)borane **39** are temperature dependent indicating the occurrence of an intramolecular rearrangement

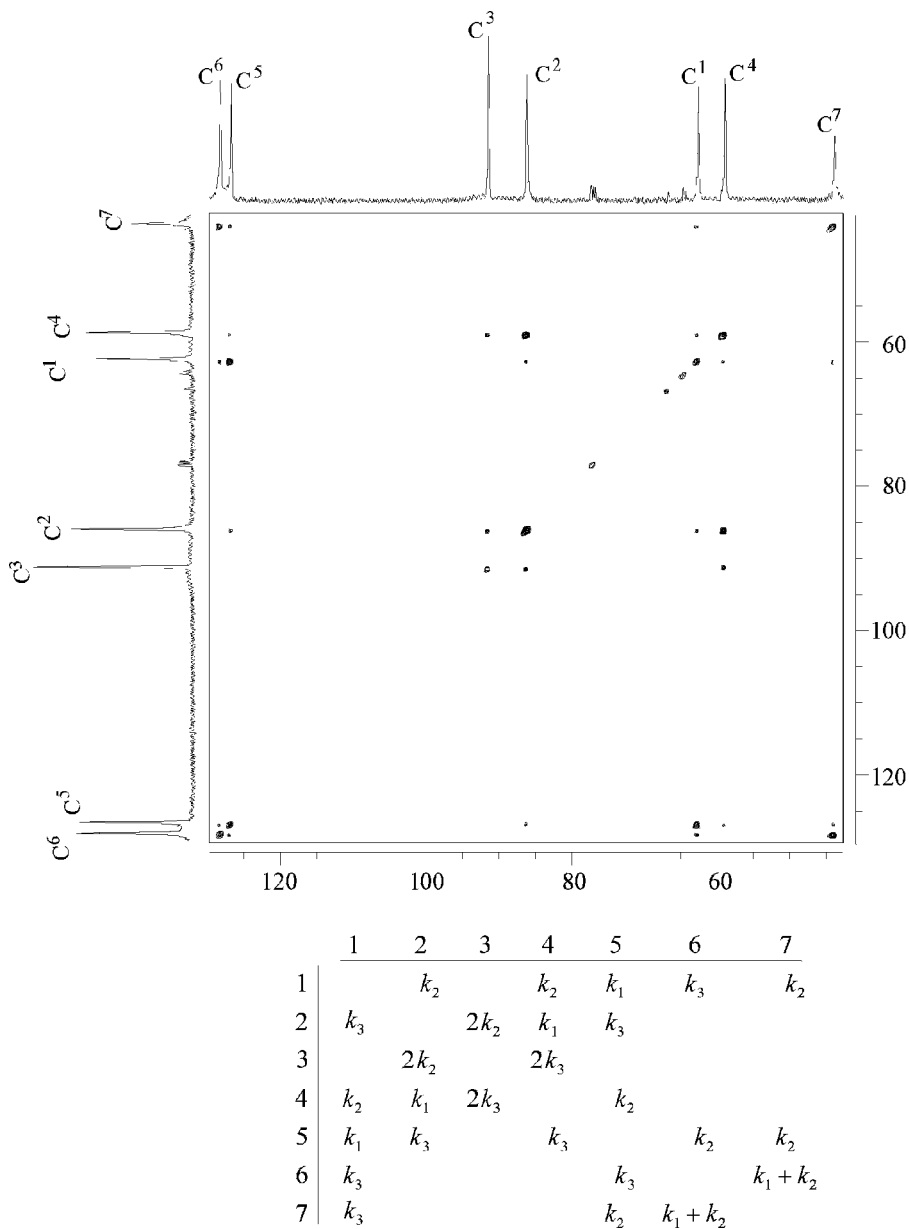
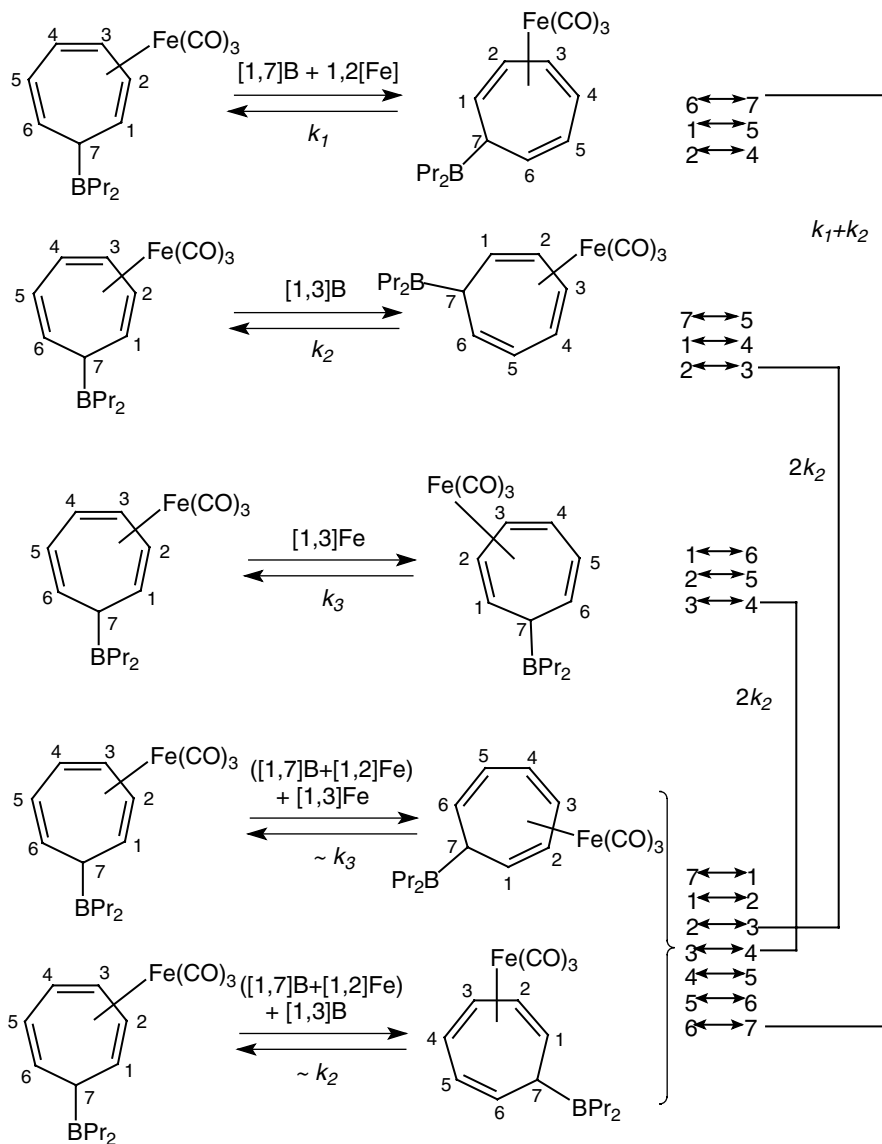
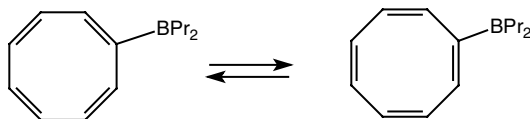


Figure 2.9 ^{13}C - ^{13}C EXSY NMR spectrum of compound **38** (100 MHz, 298 K, mixing time 1s) and analysis of rearrangements giving rise to the observed cross-peaks.



Scheme 2.24

[39]. The mechanism of this process was determined by 2D ^{13}C EXSY NMR spectroscopy. The cross-peaks between C^2 and C^8 and between C^3 and C^7 observed in the spectrum testify that a reversible bonds shifting characteristic for all cyclooctatetraenes is observed in the borane **39** (Scheme 2.25).



Scheme 2.25

The activation parameters for this rearrangement ($\Delta H^\ddagger = 58.7 \pm 0.8$ kJ mol⁻¹; $\Delta S^\ddagger = -32 \pm 5$ J mol⁻¹K⁻¹; $\Delta G^\ddagger(298) = 67.7 \pm 0.1$ kJ mol⁻¹) are close to those for the reversible double bond fluctuations in other monosubstituted cyclooctatetraenes [40]. It was concluded that the interaction of the empty 2p-AO of boron atom with the cyclic π -system of the double bonds in **39** does not notably affect the bond shifting process.

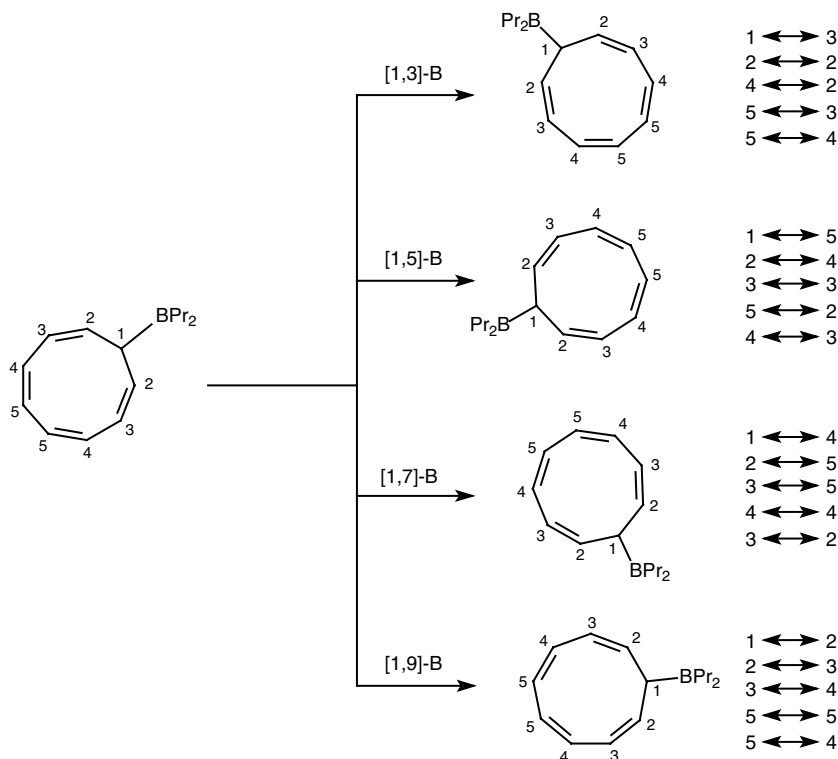
4.8 SIGMATROPIC MIGRATIONS AND THERMAL REARRANGEMENTS IN CYCLONONATETRAENYL-(DI-*n*-PROPYL)BORANE. COMPARISON WITH THE DYNAMIC PROPERTIES OF CYCLONONATETRAENYL(TRIMETHYL)TIN

4.8.1 Synthesis of Cyclononatetraenyl(di-*n*-propyl)borane **22** and Mechanism of Borotropic Migrations in this Borane. Selection Rules for the Sigmatropic Migrations of Dialkylboryl Groups

Cyclononatetraenyl(di-*n*-propyl)borane **22** was prepared by the reaction of di-*n*-propylboron chloride with lithium cyclononatetraenide at -30°C [31]. The reversible dynamic effects observed in the NMR spectra of borane **22** indicated the occurrence of a degenerate intramolecular rearrangement. The mechanism of the rearrangement was determined by 2D ¹³C EXSY NMR at 173 K. Four different migrations of the di-*n*-propylboryl group corresponding to the [1,3]-B, [1,5]-B, [1,7]-B, and [1,9]-B sigmatropic shifts are possible in **22**. Each of these migrations exchanges C¹ with C³, C⁵, C⁴ or C² respectively. Therefore the topology of the migration of the di-*n*-propylboryl group can be experimentally determined by the EXSY spectra. The expected exchanges for each rearrangement are shown in the Scheme 2.26.

Figure 2.10 displays the results of a 2D ¹³C EXSY NMR experiment for borane **22** carried out at 173 K and mixing time 0.1 s. Four intense cross-peaks are observed in the spectrum: C¹-C³, C²-C⁴, C⁵-C³, C⁵-C⁴. This attests to a [1,3]-B sigmatropic shift (Scheme 2.2). In addition, several less intense cross-peaks: C¹-C⁵, C³-C⁴ and C²-C⁵ are observed. These signals can arise due to a [1,5]-B shift, or due to the consequence of two [1,3]-B shifts. Although the latter possibility seems to be more probable, one cannot exclude completely the possibility of relatively slow [1,5]-B migrations in borane **22**.

The activation parameters of the [1,3]-B sigmatropic shift in **22** ($E_A = 26.1 \pm 2.2$ kJ mol⁻¹; $\Delta G^\ddagger(195) = 36.8 \pm 0.4$ kJ mol⁻¹) were determined by



Scheme 2.26

complete line-shape analysis of the temperature dependent ^{13}C NMR spectra. The iterative search of the activation parameters was carried out using the whole set of the experimental spectra. Figure 2.11 compares the experimental and the best-fit calculated spectra.

The borotropic rearrangements in **22** have been also studied computationally (dimethylborylcyclononatetraene **22** was computed to reduce the size of the jobs) [41]. The computed activation energy of the degenerate [1,3]-B shift in **22-exo** is 28 kJ mol^{-1} that nicely corresponds to the experimental value. Additionally a facile [1,9]-B shift has been found computationally in the **22-exo** and a nondegenerate [1,2]-B migration in **22-endo** leading to mono-*trans*-**22** (Scheme 2.27). The relatively unstable mono-*trans*-isomer **40** (it is 26.5 kJ mol^{-1} less stable than all-*cis*-**22**) is a key intermediate in further thermal rearrangements of **22** (see later).

In cyclononatetraenyl(di-*n*-propyl)borane **22** the [1,3]-B shift is the fastest rearrangement, whereas in the irontricarbonyl complex of cycloheptatrienyl(di-*n*-propyl)borane **38** the [1,7]-B shift is faster than the [1,3]-B migration. This observation corresponds to the modified least motion principle, which is recently

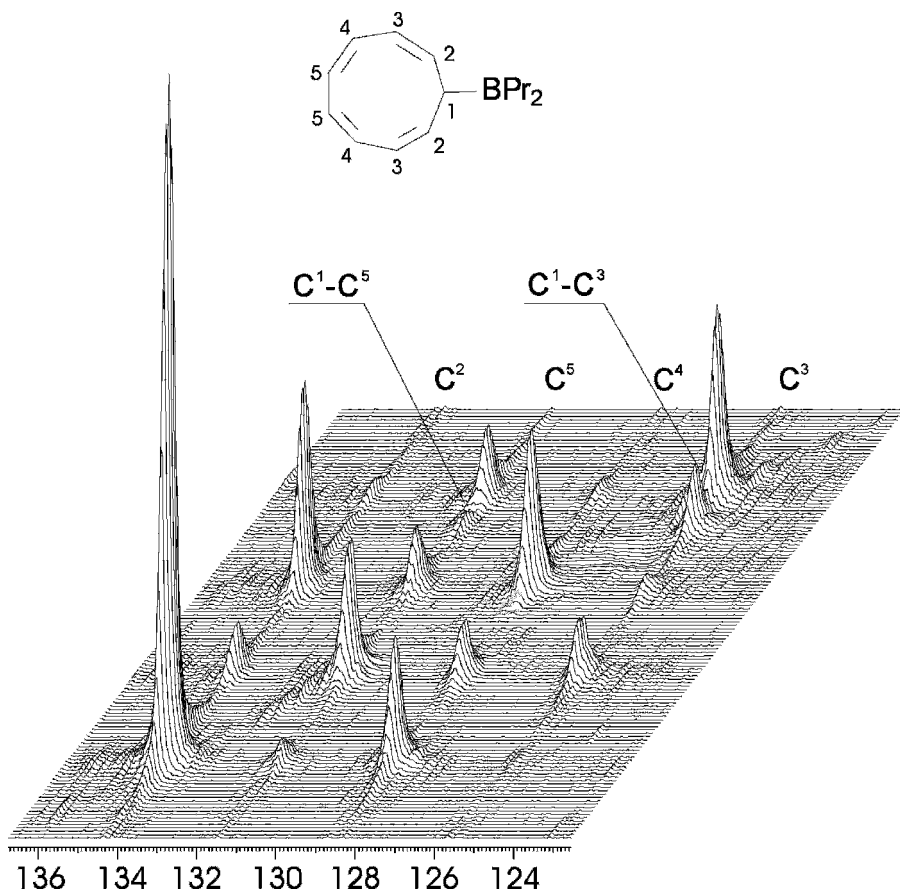


Figure 2.10 2D ^{13}C - ^{13}C EXSY NMR spectrum of compound **22** (50 MHz, CD_2Cl_2 - CDCl_3 - CCl_4 , 173 K); only the olefinic region was registered; therefore the cross-peaks C^1 - C^3 and C^1 - C^5 are reflected in F^1 .

formulated as ‘the necessity of a close relationship between the migration origin and migration terminus allowing the migrating group to be simultaneously bound to those centers as in transition state of a truly pericyclic reaction’ [42]. In cyclononatetraenyl(di-*n*-propyl)borane **22** a shorter pathway is required for the [1,3]-B shift and the migration by this mechanism occurs faster. In complex **38** the shortest migration corresponds to the [1,7]-B shift, and this rearrangement is the fastest one.

Thus, summarizing the studies of the dynamic behavior of cycloheptatrienyl- (**21a**, **38**) and cyclononatetraenyl (**22**) derivatives of boron one can elucidate the following regularities for the sigmatropic migrations of dialkylboryl groups:

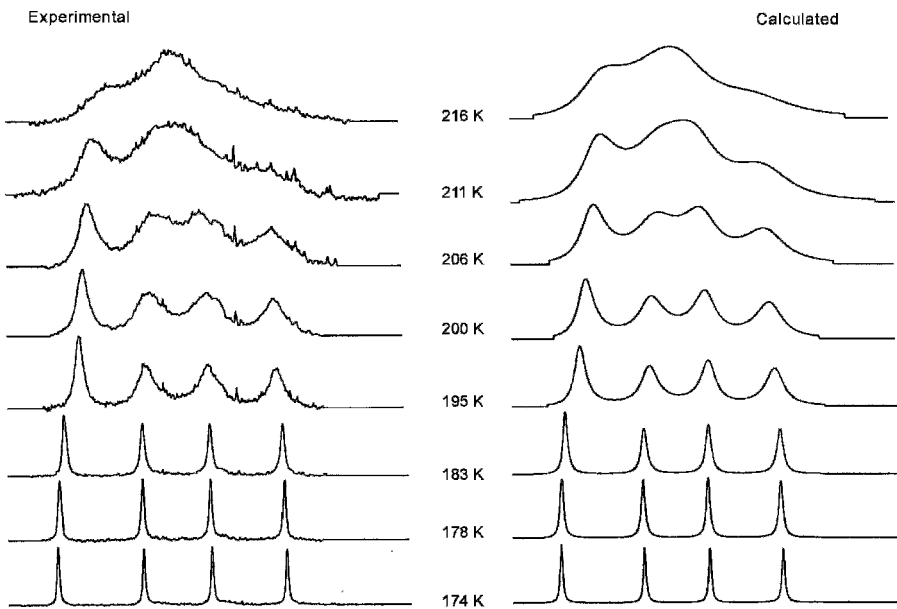
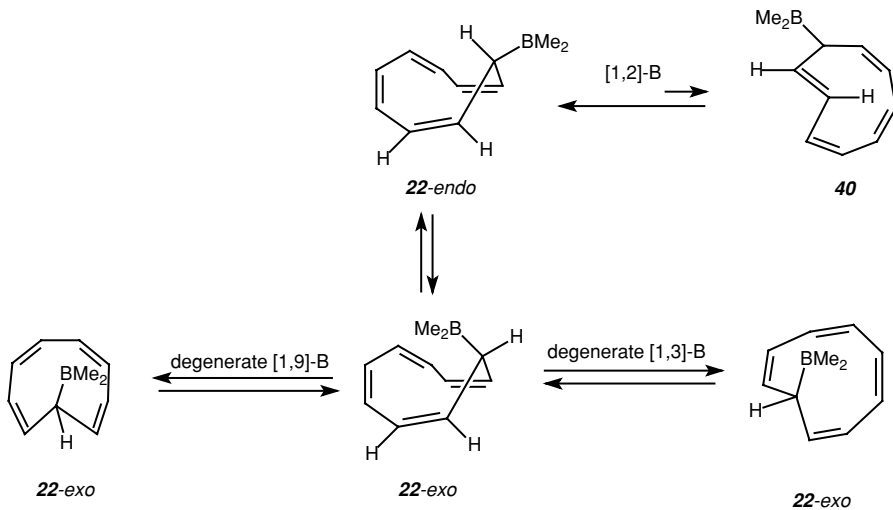


Figure 2.11 Determination of the activation parameters of the [1,3]-B shift in **22** by complete line-shape analysis.



1. [1,3] and [1,7] sigmatropic shifts of boron occur, whereas [1,5]-B shifts are not observed.
2. Among the allowed migrations those which require a minimal motion of the migrating group occur more rapidly.

Experimentally found selection rules for the borotropic migrations correspond to the sigmatropic shifts with inversion on the migrating atom according to the orbital symmetry principles [43]. This in turn corresponds to the electronic configuration of the boron atom ideal for the formation of a Moebius type transition state.

4.8.2 Mechanism of Sigmatropic Migrations in Cyclononatetraenyl(dimethyl)tin 41. Selection Rules for the Sigmatropic Migrations of Stannyl Groups

Although being beyond the scope of the present chapter, the sigmatropic migrations of trimethylstannyl group in cyclononatetraenyl(trimethyl)tin **41** are briefly discussed here in order to compare the dynamic properties of the cyclononatetraenyl derivatives of boron and tin.

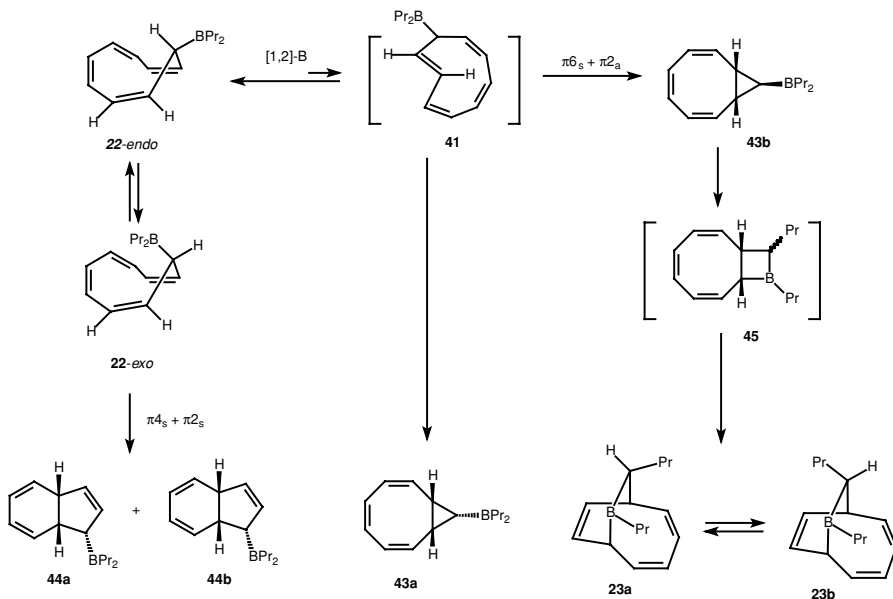
The synthesis and fluxional character of cyclononatetraenyl(trimethyl)tin **41** have been reported quite early [44]. However, due to the technical limitations, the mechanism of the rearrangement was determined experimentally only recently. The fastest rearrangement in **41** at 173 K is a [1,9]-Sn sigmatropic shift ($E_A = 25.2 \pm 2.5 \text{ kJ mol}^{-1}$) according to the 2D EXSY NMR data [45].

Thus, in cycloheptatrienyl [30] and cyclononatetraenyl (**41**) derivatives of tin the [1,5]-Sn and [1,9]-Sn sigmatropic shifts are observed. These regularities indicate that the sigmatropic migrations of trimethylstannyl groups occur with the conservation of the configuration of the migrating center.

The values of the activation barriers for the [1,3]-B ($E_A = 26.1 \pm 2.2 \text{ kJ mol}^{-1}$) and [1,9]-Sn ($E_A = 25.2 \pm 2.5 \text{ kJ mol}^{-1}$) sigmatropic shifts in cyclononatetraenyl derivatives **22** and **41** are quite close, as well as the values of the [1,7]-B ($\Delta G^\ddagger(298) = 77 \text{ kJ mol}^{-1}$) and [1,5]-Sn ($\Delta G^\ddagger_{298} = 75.2 \pm 0.2 \text{ kJ mol}^{-1}$) sigmatropic shifts in cycloheptatrienyl compounds. Since the mechanisms of the sigmatropic migrations of boron and tin are different in each case, it was concluded that the barrier of the metallotropic rearrangements is mainly determined by the nature of the hydrocarbon skeleton [46].

4.8.3 Thermal Isomerization of Cyclononatetraenyl(di-*n*-propyl)Borane **22**

Reaction of di-*n*-propylboron chloride with lithium cyclononatetraenide followed by vacuum distillation afforded the mixture of boranes **23a,b**, **43a** and **44a,b** in a 10 : 1 : 2 ratio (Scheme 2.28) [31, 47]. The reaction was carried out in an NMR tube to elucidate the mechanism of formation of the unexpected product **23**. Compounds **43a** and **43b** were the first observable products of the thermal rearrangement of cyclononatetraenyl(di-*n*-propyl)borane **22**. Apparently, the



Scheme 2.28

rearrangement of **22** to **43** proceeds via the unobservable *trans* isomer **41** characterized computationally.

The isomer **42b** rearranges to the compound **23**, whereas **43a** is thermally stable and does not exhibit dynamic properties. It is believed that the transformation of the cyclopropane derivative **43a** to the cyclobutane derivative **45** occurs by the migration of the *n*-propyl group with simultaneous ring enlargement (Scheme 2.30). Compound **45** in turn rearranges immediately to the more stable isomers **23a,b** via a [1,3]-B shift.

The two isomers of borane **23** interconvert via [1,3]-B sigmatropic shifts (Scheme 2.30). This mechanism was confirmed by a series of 2D EXSY NMR experiments for **23** and its deuteriopyridine complex [32]. The activation parameters ($\Delta G^\ddagger(298) = 52.6 \pm 0.1 \text{ kJ mol}^{-1}$; $\Delta H^\ddagger = 24.7 \pm 0.5 \text{ kJ mol}^{-1}$; $\Delta S^\ddagger = -93 \pm 10 \text{ J mol}^{-1} \text{ K}^{-1}$) were obtained by line-shape analysis of the temperature-dependent ^{13}C NMR spectra.

4.9 BOROTROPIC MIGRATIONS IN PHENALENYL(DI-*n*-PROPYL)BORANE **24**

The NMR spectra of **24** show reversible temperature dependences not affected by changes of the concentration. The mechanism of intramolecular rearrangements taking place in **24** was elucidated by 2D ^1H - ^1H EXSY NMR experiments [33]. Figure 2.12 shows the chemical exchange NMR spectrum of **24** taken at

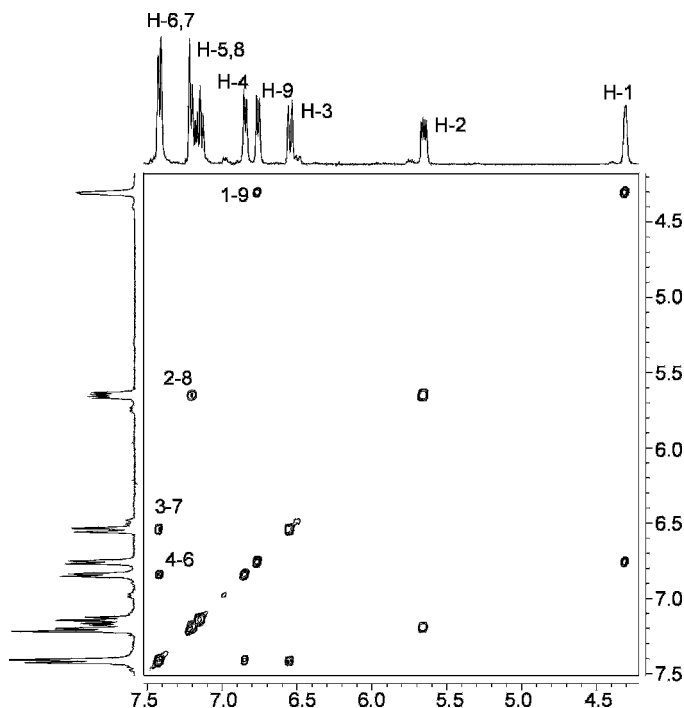
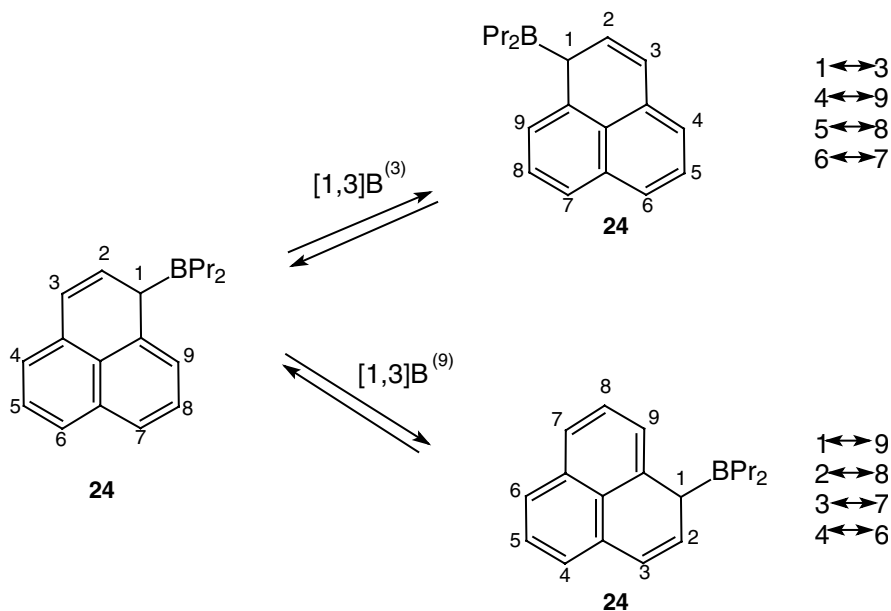


Figure 2.12 2D ^1H - ^1H EXSY spectrum (400 MHz, benzene- d_6) of phenalenyl(di-*n*-propyl)borane **24** at 298 K (mixing time 0.5 s). O. L. Tok *et al.*, *J. Chem. Soc. Chem. Commun.* 311–312 (2000). Reproduced by permission of The Royal Society of Chemistry.

298 K. Four exchange cross-peaks observed in this spectrum unequivocally prove the mechanism of [1,3]-B sigmatropic migrations from position 1 to position 9 of the phenalene ring. The 2D EXSY experiments carried out at higher temperatures also show cross-peaks of lower intensity corresponding to the second possible degenerate [1,3]-B migration from position 1 to position 3 (Figure 2.12, Scheme 2.29). Thus, both [1,3]-B shifts are observed in **24**, but their rates differ significantly.

Kinetics of the [1,3]⁽⁹⁾ sigmatropic migrations of di-*n*-propylboryl group in **24** was measured from the series of 2D ^1H EXSY spectra recorded in the temperature interval 290–318 K to give the following activation parameters: $E_A = 19.1 \pm 0.4$ kcal mol⁻¹; $\ln A = 33.0 \pm 0.7$; $\Delta H^\ddagger_{298} = 16.6 \pm 0.2$ kcal mol⁻¹; $\Delta S^\ddagger_{298} = 5.0 \pm 0.1$ cal mol⁻¹K⁻¹; $\Delta G^\ddagger_{298} = 15.1 \pm 0.2$ kcal mol⁻¹. An approximate evaluation of the available data showed that the [1,3]⁽³⁾ borotropic migration in **24** at 323 K is about 10 times slower than the [1,3]⁽⁹⁾-B shift.

Any of the two [1,3]-B shifts separately is spatially fixed to one allylic or benzylic fragment of **24** respectively. However, the *combination of both* results



Scheme 2.29 O. L. Tok *et al.*, *J. Chem. Soc. Chem. Commun.* 311–312 (2000). Reproduced by permission of The Royal Society of Chemistry.

in the possibility for the di-*n*-propylboryl group to migrate around the whole molecule. This is experimentally illustrated by difference SST ^1H NMR spectrum (Figure 2.13). Irradiation of the signal of H^1 leads to a decrease in intensities for all α -protons signals in **24** (Figure 2.13a). Similarly irradiation of H^2 shows that it is in exchange with both remaining β -protons, H^5 and H^8 (Figure 2.13b).

Since the configurations of the starting compounds and the product are equal for both observed rearrangements (more precisely, each rearrangement interconverts the enantiomers of **24**), the difference in the activation barriers is exactly the difference in the energies of the corresponding transition states. Therefore one can conclude that the spatial arrangement of the allylic fragment **A** is much nearer in configuration to the TS than that of **B** (Scheme 2.30). This conclusion is in agreement with the computational results for the [1,3]-B shift [15].

5 DIVERSE CHEMOSELECTIVITY OF CYCLIC POLYUNSATURATED ORGANOBORANES

Diverse chemoselectivity refers to the selective trapping of several different minor nonobservable tautomers in chemical reactions [48–50].

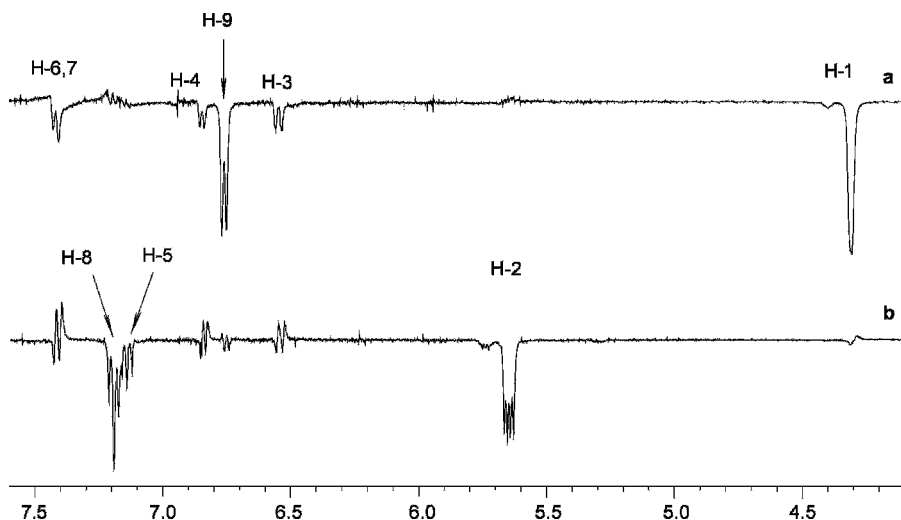
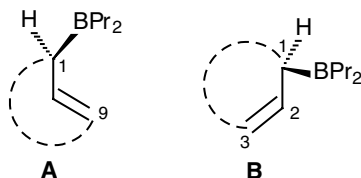


Figure 2.13 Difference ^1H SST NMR spectrum of borane **24** (400 MHz, benzene- d_6 , 313 K): (a) irradiation of H-1; (b) irradiation of H-2. O. L. Tok *et al.*, *J. Chem. Soc. Chem. Commun.* 311–312 (2000). Reproduced by permission of The Royal Society of Chemistry.

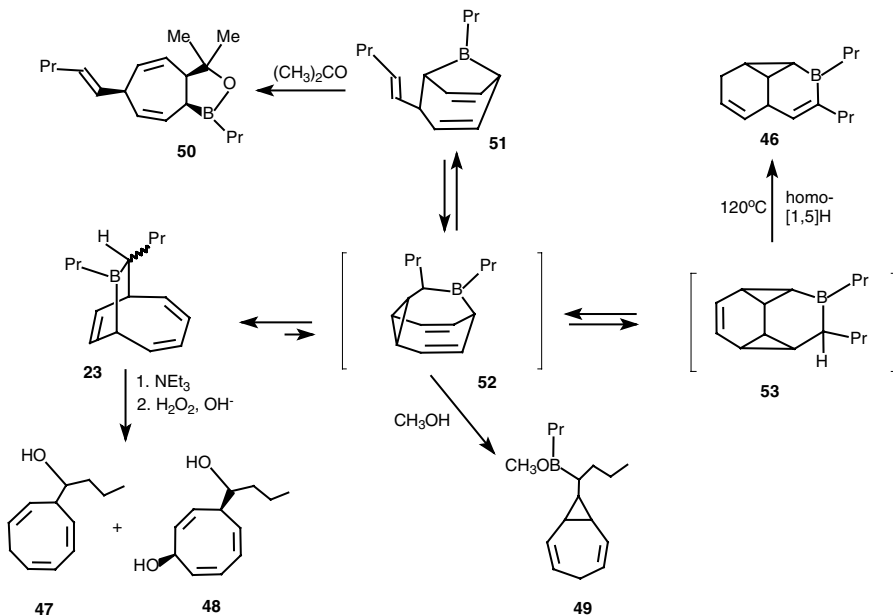
5.1 CHEMICAL BEHAVIOR OF BORANE **23**

Bicyclic borane **23** gives the products with principally different structures in various chemical reactions (Scheme 2.31) [48–50]. Thus, thermolysis of **23** yields the tricyclic borane **46**, oxidation by basic hydrogen peroxide affords the expected products with a cyclooctatriene skeleton **47**, **48** (in a 5 : 1 ratio). Methanolysis gives borinic ester **49**, whereas the single product of the reaction of **23** with acetone is cyclic borinic ester **50**.



Scheme 2.30 O. L. Tok *et al.*, *J. Chem. Soc. Chem. Commun.* 311–312 (2000). Reproduced by permission of The Royal Society of Chemistry.

The direct precursor of **50** is apparently borane **51** which can form from borabulvalene **52** by cyclopropylmethyl–butenyl rearrangement (Scheme 2.31). The same rearrangement interconverts borabulvalene **52** with the starting



Scheme 2.31

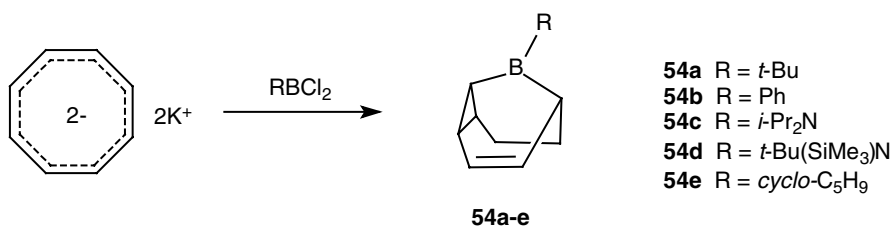
borane **23** and the derivative of bishomobenzene **53**—an apparent precursor of the thermolysis product.

Examples of the change of the carbon skeleton in the course of a reaction are known in the literature. Such effects are usually explained by an equilibrium between the reagent and its less stable unobservable valence tautomer. Following this approach, a fast equilibrium between five tautomeric forms for **23** was suggested. Two of these equilibrating compounds, viz. **52** and **51**, react selectively with methanol and acetone respectively, thus exhibiting a *diverse chemoselectivity*.

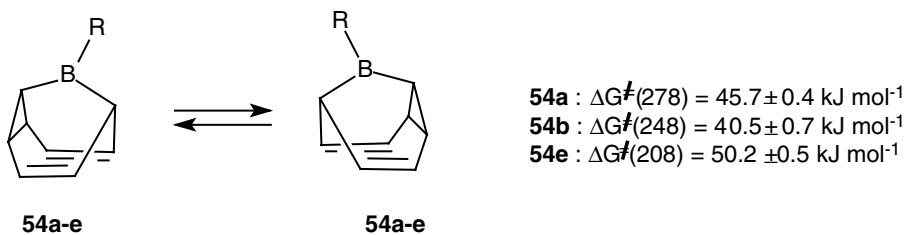
5.2 DIVERSE CHEMOSELECTIVITY OF 9-CYCLOPENTYL-9-BORABARBARALANE **54e**

A series of borabarbaralanes **54** was prepared by the reaction of $\text{K}_2\text{C}_8\text{H}_8$ with appropriate alkylboron dichlorides in hexane at -50°C (Scheme 2.32) [51,52]. Similarly to their carbon analogs, borabarbaralanes exhibit fast Cope rearrangement yielding averaged proton spectra at ambient temperature (Scheme 2.33). This rearrangement has been studied by line-shape analysis and 2D EXSY (activation parameters are listed in the Scheme 2.34).

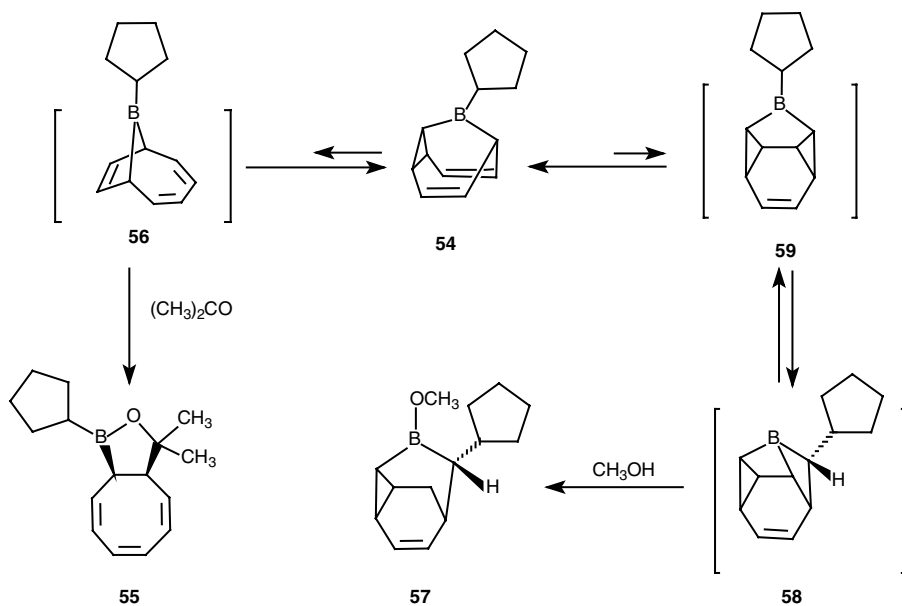
The reaction of **54e** with acetone proceeds smoothly at -10°C to give borinic ester **55** (Scheme 2.33) [50]. Since the allylboration of carbonyl



Scheme 2.32



Scheme 2.33



Scheme 2.34

compounds occurs with allylic rearrangement, the direct precursor of compound **55** should have structure **56** (Scheme 2.34). Reactions of borabarbaralane **54e** with acetaldehyde, ethoxyacetylene, trideuterioacetonitrile and tetradeuterioacetic acid proceed similarly affording exclusively the products originating from the bicyclic borane **56**. The reaction of **54e** with an excess of methanol at -30°C gave quantitatively borinic ester **57**. Formally, a direct precursor of **57** should have structure **58** (Scheme 2.34). The formation of **58** can be explained by the intermediacy of a bishomobenzene intermediate **59**; the rearrangement of **59** to **58** is a ring expansion with simultaneous alkyl group migration – a similar rearrangement has been previously found to transform **43b** into **45** (see Scheme 2.30).

Thus, similarly to its substituted homolog **23**, borabullvalene **54e** exhibits *diverse chemoselectivities* in its reactions with nucleophilic reagents. Moreover, the main interconverting tautomers (**23**, **52**, **53** and **56**, **54e**, **59**) have essentially the same carbon skeletons, but different relative stabilities. Thus, in the borabullvalene series, the most stable tautomer is **23**. This is stipulated by the possibility for the 2p-AO in **23** to conjugate with the π -system of the double bonds. In the corresponding tautomer (**56**) of the more strained borabarbaralane series such conjugation is impossible, and borabullvalene **54e** is the only observable compound.

6 CONCLUSION

The empty 2p-AO of boron atom stipulates the easiness of the [1,3]-B shift in all allylic type triorganoboranes. The activation parameters of the [1,3]-B sigmatropic migrations vary with the structure of the unsaturated fragment – the electron donation facilitates the rearrangement. The [1,3]-B shifts can manifest themselves differently in the NMR spectra, or can be nondetectable by NMR. Nevertheless, all allylic isomers of an allylic type triorganoborane are kinetically available and can react selectively with nucleophilic reagents. This type of dynamic behavior is quite rare. The results summarized in the present chapter illustrate the possibility of the application of an intramolecular dynamics for the creation of new molecular systems with unusual chemical properties, as well as for the purely synthetic purposes.

7 REFERENCES

1. H. Lehmkuhl and D. Reiner, *J. Organomet. Chem.* **23**, C25 (1970).
2. K. H. Thiele and J. Kohler, *J. Organomet. Chem.* **7**, 365 (1967).
3. K. H. Thiele and K. Zdumek, *J. Organomet. Chem.* **4**, 10 (1965).
4. E. G. Hoffmann, H. Nehl, H. Lemkuhl, K. Seevogel and W. Stempfle, *Chem. Ber.* **117**, 1363 (1984).

5. H. E. Zieger and J. D. Roberts, *J. Org. Chem.* **34**, 2826 (1969).
6. P. D. Sleezer, S. Winstein, W. G. Young, *J. Am. Chem. Soc.* **94**, 2515 (1972).
7. M. J. Hails, B. E. Mann, C. M. Spencer, *J. Chem. Soc., Dalton Trans.* 729 (1983).
8. Y. Naruta, Y. Nishigaichi, K. Maruyama, *Tetrahedron* **45**, 1067 (1985).
9. D. J. Blears, S. S. Danyluk, S. Cawely, *J. Organomet. Chem.* **6**, 284 (1964).
10. G. Wilke, B. Bogdanovic, P. Hardt, P. Heinbach, W. Keim, M. Kroener, W. Oberkirch, K. Tanaka, E. Stenrueke, D. Walter, H. Zimmermann, *Angew. Chem., Int. Ed. Engl.* **5**, 151 (1966).
11. A. Hill, W. A. Boyd, H. Desai, A. Darki, *J. Organomet. Chem.* **514**, 1 (1996).
12. Kwart, T. Slutsky, *J. Am. Chem. Soc.* **94**, 2515 (1972).
13. Takahashi, M. Kira, *J. Am. Chem. Soc.* **119**, 1948 (1997).
14. Kobayashi, N. Kobayashi, *Chem. Lett.* 385 (1986).
15. (a) M. Buehl, P. v. R. Schleyer, M. A. Ibrahim, T. Clark, *J. Am. Chem. Soc.* **113**, 2466 (1991). (b) H. Jiao, P. v. R. Schleyer, *Angew. Chem.* **105**, 1833 (1993).
16. B. M. Mikhailov, V. S. Bogdanov, G. V. Lagodzinskaya, V. F. Pozdnev, *Russ. Chem. Bull.*, 386 (1966).
17. V. S. Bogdanov, G. V. Lagodzinskaya, V. F. Pozdnev, B. M. Mikhailov *Russ. Chem. Bull.*, 944 (1966).
18. B. M. Mikhailov, V. I. Smirnov, O. D. Smirnova, V. S. Bogdanov, *Russ. Chem. Bull.*, 51 (1975).
19. (a) Y. N. Bubnov, M. E. Gurskii, I. D. Gridnev, A. V. Ignatenko, Y. A. Ustyniuk, V. I. Mstislavskii, *J. Organomet. Chem.* **424**, 127 (1992). (b) I. D. Gridnev, M. E. Gurskii, and Yu. N. Bubnov, in *Current Topics in the Chemistry of Boron*, edited by G. Kabalka, Royal Society of Chemistry Special Publication 143, Cambridge, 1994, pp. 56–59.
20. B. M. Mikhailov, Y. N. Bubnov, A. V. Tsyban', *J. Organomet. Chem.* **154**, 113 (1978).
21. B. M. Mikhailov, V. I. Smirnov, O. D. Smirnova, V. S. Bogdanov, *Russ. Chem. Bull.*, 51 (1975).
22. G. W. Kramer, H. C. Brown, *J. Organomet. Chem.* **132**, 9 (1977).
23. V. S. Bogdanov, V. F. Pozdnev, Yu. N. Bubnov, B. M. Mikhailov, *Dokl. Akad. Nauk. SSSR*, **193**, 586 (1970).
24. (a) H. Grundke, P. I. Paetzold, *Chem. Ber.* **104**, 1136 (1971). (b) G. E. Herberich, A. Fischer, *Organometallics* **15**, 58 (1996).
25. (a) P. Jutzi, A. Seufert, *Angew. Chem. Int. Ed.* **16**, 41 (1977). (b) H. D. Johnson; T. W. Hartford; C. W. Spangler *J. Chem. Soc., Chem. Commun.* 242 (1978).
26. M. E. Gurskii, I. D. Gridnev, A. V. Geiderikh, A. V. Ignatenko, Yu. N. Bubnov, V. I. Mstislavsky, Yu. A. Ustyniuk *Organometallics* **11**, 4056 (1992).
27. I. D. Gridnev, M. E. Gurskii, Yu. N. Bubnov, *Organometallics*, **15**, 3696 (1996).
28. I. D. Gridnev, A. Meller, *Main Group Metal Chem.* **21**, 121 (1998).
29. I. D. Gridnev, M. E. Gurskii, A. V. Geiderikh, Yu. N. Bubnov; *Mendeleev Commun.* 176 (1996).
30. I. D. Gridnev, O. L. Tok, N. A. Gridneva, Yu. N. Bubnov, P. R. Schreiner *J. Am. Chem. Soc.* **120**, 1034 (1998).
31. M. E. Gurskii, I. D. Gridnev, A. B. Buevich, Yu. N. Bubnov *Organometallics* **13**, 4658 (1994).
32. I. D. Gridnev, M. E. Gurskii, A. O. Krasavin, Yu. N. Bubnov *Russ. Chem. Bull.* 2243 (1996).
33. O. L. Tok, I. D. Gridnev, E. M. Korobach, Yu. N. Bubnov, *J. Chem. Soc., Chem. Commun.* 311 (2000).
34. I. D. Gridnev, M. E. Gurskii, A. V. Ignatenko, Yu. N. Bubnov, Yu. V. Il'ichev; *A Organometallics* **12**, 2487 (1993).

35. M. E. Gurskii, I. D. Gridnev, Yu. V. Il'ichev, A. V. Ignatenko, Yu. N. Bubnov *Angew. Chem., Int. Ed. Engl.* **31**, 781 (1992).
36. C. L. Perrin, T. J. Dwyer, *Chem. Rev.* **90**, 935 (1990).
37. K. B. Wiberg, R. A. Fenoglio, *J. Am. Chem. Soc.* **90**, 3395 (1968).
38. I. D. Gridnev, O. L. Tok, M. E. Gurskii, Yu. N. Bubnov *Chem. Eur. J.* **2**, 231–236, (1996).
39. M. E. Gurskii, I. D. Gridnev, A. V. Buevich, T. V. Potapova, A. O. Krasavin, V. I. Mstislavskii, Yu. N. Bubnov *Mendeleev Commun.* 221 (1994).
40. (a) L. A. Paquette, *Tetrahedron* **31**, 2855 (1975). (b) L. A. Paquette, *Pure Appl. Chem.* **54**, 987 (1982).
41. I. D. Gridnev, P. R. Schreiner, M. E. Gurskii, Yu. N. Bubnov, A. O. Krasavin, V. I. Mstislavskii, *J. Chem. Soc. Chem. Commun.* 2507 (1999).
42. C. Carpenter, *J. Am. Chem. Soc.* **117**, 6336 (1995).
43. R. B. Woodward, R. Hoffmann, *Angew. Chem.* **81**, 797 (1969).
44. (a) G. Boche, F. Heidenhain, *J. Organomet. Chem.* **121**, C49 (1976). (b) Bonny, A.; Stobart, S. R. *Inorg. Chim. Acta* **31**, L437, (1978). (c) A. Bonny, S. R. Stobart, *J. Chem. Soc., Dalton Trans.* 486 (1979).
45. I. D. Gridnev, P. R. Schreiner, O. L. Tok, Yu. N. Bubnov, *Chem. Eur. J.* **5**, 2042 (1999).
46. I. D. Gridnev, O. L. Tok, M. E. Gurskii, Yu. N. Bubnov, in: *Advances in Boron Chemistry*, edited by W. Siebert, Royal Society of Chemistry, Cambridge, 1997, pp. 100–103.
47. I. D. Gridnev, M. E. Gurskii, A. V. Buevich, Yu. N. Bubnov *Russ. Chem. Bull.* 117, (1996).
48. I. D. Gridnev, M. E. Gurskii, A. V. Buevich, T. V. Potapova; Yu. N. Bubnov; *J. Org. Chem.* **61**, 3514 (1996).
49. I. D. Gridnev, M. E. Gurskii, Yu. N. Bubnov, *J. Organomet. Chem.* **581**, 98 (1999).
50. I. D. Gridnev, P. R. Schreiner, M. E. Gurskii, O. L. Tok, A. Meller, Yu. N. Bubnov Cyclic polyunsaturated triorganoboranes. dynamic behaviour and chemical properties, in *Contemporary Boron Chemistry*, edited by M. G. Davidson, A. K. Huges, T. B. Marder, and K. Wade. The Royal Society of Chemistry, Cambridge, 2000, pp. 438–445.
51. G. E. Herberich, H.-W. Marx, S. Moss, P. v. R. Schleyer, T. Wagner, *Chem. Eur. J.* **2**, 458 (1996).
52. I. D. Gridnev, A. Meller, *J. Org. Chem.* **63**, 3699 (1998).

3 Dynamic Behavior of Group 5 and 6 Transition Metal Complexes with NMR

SERGEI G. SAKHAROV

Kurnakov Institute of General & Inorganic Chemistry, Russian Academy of Sciences, Leninskii pr. 31, Moscow, 119991 Russia

1 INTRODUCTION

Many organometallic and coordination compounds undergo fluxional rearrangements which are revealed by dynamic NMR spectroscopy [1]. These rearrangements may be detected by monitoring spectra which exhibit line broadening and line collapsing, by saturation transfer experiments [2], or by EXSY (exchange spectroscopy) technique [3]. In most cases the fluxional behavior is only reported without discussion of the molecular mechanism involved. The simple detection of the dynamic behavior is no evidence for any of suggested mechanisms. However, definitive arguments for a correct mechanistic choice may be provided by traditional lineshape analysis [4] of the resonance peaks undergoing broadening and collapse and by the kinetic parameters obtained from these. When scalar coupling between exchanging sites is absent, the lineshape calculation can be based on the classical Bloch theory as modified by McConnell and Holm [5] or, in systems of n uncoupled or loosely coupled exchanging sites, on the Anderson–Kubo–Sack theory [6]. For strongly coupled spin systems, lineshape analysis can rely on density matrix treatments [7].

The dynamic behavior of transition metal organometallic and coordination compounds, as studied by NMR, has been reviewed [8]. This chapter focuses on disclosing general tendencies in the dynamic behavior of transition metal complexes (mainly tungsten(VI), molybdenum(VI), and tantalum(V) fluoro complexes) with n -donor two-center ligands in aprotic solvents. This term implies ligands in which n -donor atoms, i.e., atoms whose donor properties are due to the presence of lone electron pairs, are linked directly to each other [9]. This type of ligand includes oximes, hydrazones, hydrazine, hydroxylamine, hydrogen peroxide, and their derivatives.

Among coordination compounds of d^0 transition metals with n -donor two-center ligands, peroxo complexes have been studied in the greatest detail; the search for methods of molecular nitrogen fixation has stimulated studies on the structures of complexes with hydrazine derivatives. As a rule, only X-ray diffraction data are available for these complexes [10].

However, these complexes in solution have not received adequate attention. The coordination ability data for oximes, hydrazones, and hydroxylamine and its derivatives are fragmentary and are normally restricted to the purposes of analytical chemistry. Data on the dynamic behavior of complexes with two-center ligands and quantitative characteristics of dynamic processes are virtually missing. Meanwhile, in our opinion, systematic studies of the coordination ability and reactivity of two-center ligands, as well as investigation and comparison of the structure, and dynamic behavior of their complexes, are not only of theoretical interest but also represent a necessary stage on the way to the application of these compounds.

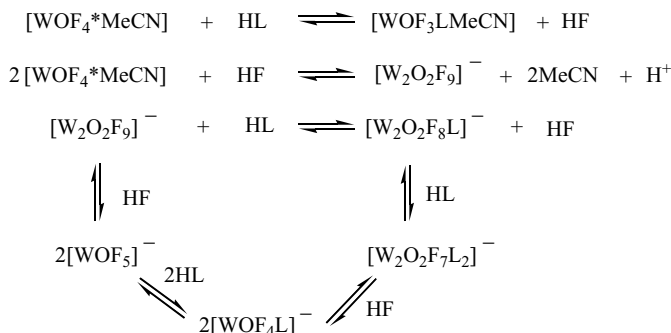
Substituted hydrazines, hydrazones, hydroxylamines and oximes can be considered to be amine derivatives. Therefore, it would be interesting to compare the data on the structure and the dynamic behavior in solution for the d^0 transition metal complexes with O,N - and N,N -two-center ligands to the complexes with amido and ketimido ligands. This will allow us to establish a correlation between the character of bonding of the organic ligand and the spectral parameters of the coordination compound. A second goal is to reveal the features of mutual transformations of stereoisomeric complexes and to determine factors affecting their stability. Thus, this chapter begins with the discussion of the dynamic behavior of transition metal amide and ketimide complexes.

2 ROTATIONAL ISOMERISM IN AMIDO AND KETIMIDO COMPLEXES

2.1 ROTATIONAL ISOMERISM IN OXOFUORAMIDO COMPLEXES OF TUNGSTEN(VI)

In an acetonitrile medium, tungsten oxyfluoride forms the octahedral complex $[WOF_4 \cdot MeCN]$, with the acetonitrile molecule *trans* to the multiple-bonded oxygen atom [11]. It is known [12] that secondary amines interacting with tungsten oxotetrafluoride substitute primarily for the fluorine atoms in *cis* position with respect to the multiply bonded oxygen atom. Buslaev and coworkers [12] have suggested that activation of the *cis* position is explained by the ability of coordinated amines to increase the multiplicity of the metal–nitrogen bond. In order to verify this assumption, we studied reactions of *N*-methylaniline and dimethylamine with WOF_4 and analyzed NMR spectra measured at various temperatures of acetonitrile solutions containing the initial reactants in differing proportions [13,14]. The study revealed that the complexation of

WOF₄ with amines (HL) proceeds by the scheme:



The final reaction product $[\text{WOF}_4\text{L}]^-$ is the octahedral complex whose equatorial plane contains a deprotonated ligand. In the case of a complex with *N*-methylaniline (HL = NHMePh) at -30°C , two isomers characterized by different stabilities were found. These isomers are characterized by two signals in the ^1H NMR spectrum, belonging to methyl protons from coordinated amides and having a 1:2 ratio of integral intensities (Figure 3.1a). The equivalence of the two equatorial fluorine atoms, as manifested in the ^{19}F NMR spectra (the A_2MX type) of the complexes, suggests that the coordinated ligand has a planar

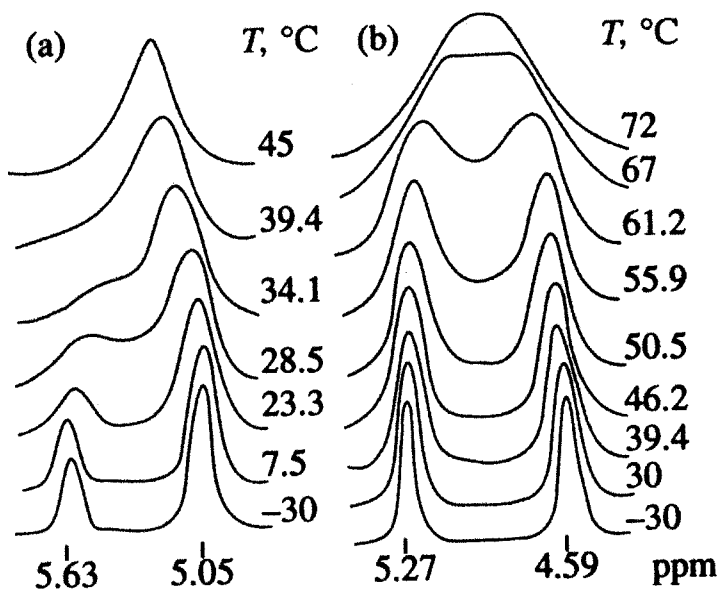
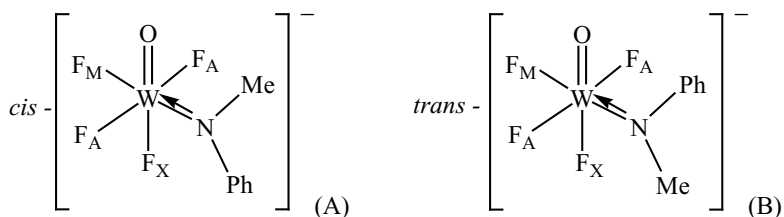


Figure 3.1 ^1H NMR spectra of complexes $[\text{WOF}_4\text{NMePh}]^-$ (a) and $[\text{WOF}_4\text{NMe}_2]^-$ (b) at various temperatures. Reproduced with permission from S. G. Sakharov and Yu. A. Buslaev, *Russ. J. Inorg. Chem.* **38**(9), 1385 (1993) [41].

structure and is oriented perpendicular to the equatorial plane of the complex. This leads to the appearance of *cis* and *trans* isomers:



The question as to which of them is more stable was clarified based on ^{13}C NMR spectra [15, p. 73]. Indeed, in the $^{13}\text{C}\{\text{H}\}$ NMR spectrum of a solution containing $[\text{WOF}_4(\text{NMePh})]^-$, the signal of the methyl ^{13}C of one of the isomers is split by a coupling to a ^{19}F nucleus, with a coupling constant of 16.5 Hz (Figure 3.2). This coupling constant is caused by the direct through-space coupling

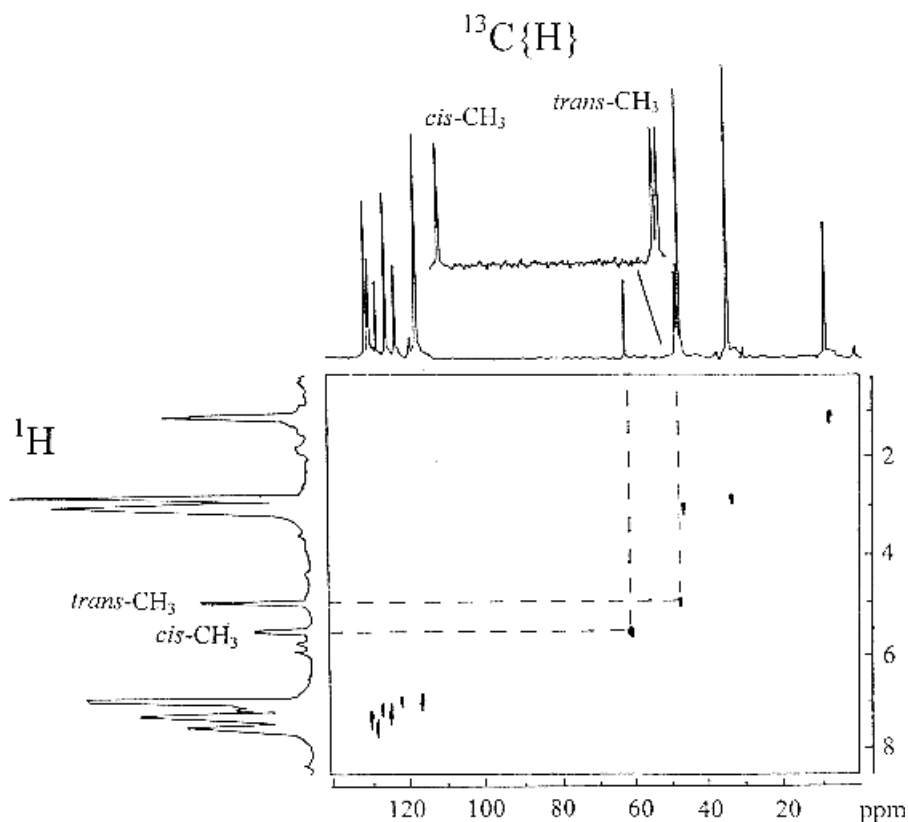


Figure 3.2 $^1\text{H},^{13}\text{C}$ - COSY spectra of a solution containing $\text{WOF}_4:\text{NHMePh}:\text{NEt}_3 = 1:2:2$ in CD_3CN at -30°C .

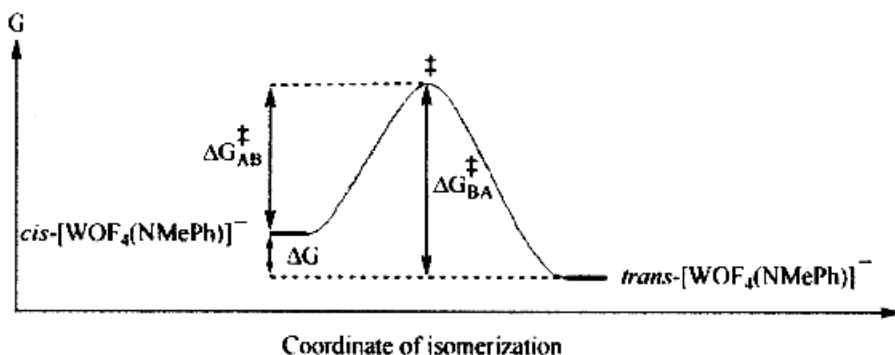
Table 3.1 Activation parameters for the $A \rightleftharpoons B$ exchange (cal = 4.184 J) [13]

Parameter	$[\text{WOF}_4\text{NMe}_2]^-$	$[\text{WOF}_4\text{NMePh}]^-$
ΔH^\ddagger_{AB} (kJ mol ⁻¹)	85.4 ± 0.8	82.0 ± 2.5
ΔH^\ddagger_{BA} (kJ mol ⁻¹)	85.4 ± 0.8	82.0 ± 2.5
ΔS^\ddagger_{AB} (J K ⁻¹ mol ⁻¹)	43.9 ± 2.9	59.4 ± 7.5
ΔS^\ddagger_{BA} (J K ⁻¹ mol ⁻¹)	43.9 ± 2.9	53.6 ± 7.5
$\Delta G^\ddagger_{AB,318}$ (kJ mol ⁻¹)	71.21 ± 0.08	63.1 ± 0.3
$\Delta G^\ddagger_{BA,318}$ (kJ mol ⁻¹)	71.21 ± 0.08	64.9 ± 0.3
$\Delta G = (\Delta G^\ddagger_{AB} - \Delta G^\ddagger_{BA})$ (kJ mol ⁻¹)	0	-1.8

of the methyl carbon nucleus to the F_X nucleus. The correspondence between the signals in ^1H and ^{13}C NMR spectra was found from the heteronuclear 2D chemical shift correlation experiment. Figure 3.2 shows the corresponding 2D ^{13}C , ^1H chemical shift correlation diagram. The projection of the ^1H spectrum is plotted along the vertical axis, while the $^{13}\text{C}\{\text{H}\}$ projection is plotted along the horizontal axis. As can be seen, the upfield methyl signal in the ^1H NMR projection, which is twice as strong as the downfield signal, corresponds to the doublet in the ^{13}C spectrum.

Thus, of the two isomers found, the *trans* isomer in which the bulkier substituent (phenyl) at the nitrogen atom points toward doubly bonded oxygen is more stable.

Corresponding signals of equal intensities from methyl groups were also observed in the ^1H NMR spectrum of a complex with dimethylamide (Figure 3.1b). In both cases, the two signals merge with increasing temperature (Figure 3.1), which indicates the exchange between the two isomers. To determine the activation parameters for the isomerism, the rates of exchange of the methyl groups were determined by calculation of the complete lineshape NMR spectra at various temperatures [13,14]. Table 3.1 gives the activation parameters of this two-position $A \rightleftharpoons B$ exchange. The analysis of their errors was carried out according to the method described [16, p. 108]. Figure 3.3 shows an

**Figure 3.3** Energy profile of isomerization of $[\text{WOF}_4(\text{NMePh})]^-$.

energy profile of isomerization in the case of a complex with *N*-methylanilide ($[\text{WOF}_4(\text{NMePh})]^-$).

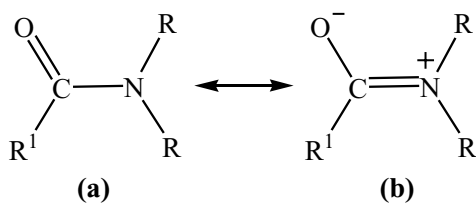
Changes in the concentration of the solutions, as well as in the ratio between the original reactants, have practically no effect on the ^1H NMR spectra. This is an indication of the intramolecular character of the exchange process studied.

The data obtained suggest that the isomerism in the amide complexes in question is caused by the essentially double character of the W–N bond. This character is due to the p_π – d_π interaction between the lone electron pair of the nitrogen atom and the vacant d_{xy} orbital of the tungsten atom. In fact, at low temperatures the amido ligand takes a flat conformation as a consequence of the sp^2 hybridization of the nitrogen atom, the plane of the ligand being oriented perpendicularly to the equatorial plane of the complex. Thus, the substituents attached to the nitrogen atom may be located in *cis* and *trans* positions relative to the doubly bonded oxygen atom. The orientation of the amido ligand indicated, under which the W, O, and N atoms, as well as both carbon atoms bonded to the nitrogen atom, are coplanar, is apparently enforced by the overlapping of the p orbitals of the oxygen atom with the d_{xz} and d_{yz} orbitals of the central atom. For this reason, the p_π – d_π interaction of the lone pair of the nitrogen atom with the orbitals just cited is more difficult than that with the vacant d_{xy} orbital.

In the case with *N*-methylanilide, the *cis* and *trans* locations of the methyl group produce different chemical environments for the fluorine atoms and cause the appearance of an 'extra' form in the ^{19}F NMR spectra. On the other hand, the isomeric complexes of WOF_4 with dimethylamide are identical, and the ^{19}F NMR spectra display signals which correspond to only one form. However, in either case, the ^1H NMR spectra display two signals for the methyl groups of the coordinated amide group, which are found in different chemical environments.

As the temperature is increased, the isomerization rate increases, and the mean lifetime of the protons of the methyl groups in different positions decreases, causing the appearance of a time-averaged spectrum. The conversion of one isomer into another apparently involves the cleavage and the subsequent formation of the π component of the metal–nitrogen bond with the simultaneous rotation of the ligand around the W–N σ bond.

Hindered rotation about (formally) single bonds, which exhibit a double character due to the conjugation effects, is typical of many organic compounds. A classic example of this type is the group of substituted amides [17], in which the double-bond character of the C–N bond may be represented by a contribution of structure **b** to a resonance hybrid:



where R^1 , $R = H$, alkyl. In such a case, the amide should have a planar conformation, which should result in the inequivalence of the different positions of the substituents attached to the nitrogen atom and, therefore, in different chemical shifts for the protons of these substituents in the 1H NMR spectra. For example, the 1H NMR spectra of dimethylformamide and dimethylacetamide at room temperature display two singlets, which are assigned to two inequivalent CH_3 groups. When the temperature is increased, the signals merge owing to the disappearance of the hindered rotation around the C–N bond [17]. Thus, according to [18], the activation enthalpy for the rotation in dimethylformamide is 84 kJ mol^{-1} (20 kcal mol^{-1}).

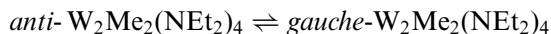
In the case of methylphenylformamide, the 1H NMR spectrum displays only one signal for the methyl group. The absence of a second signal for the methyl group in the 1H NMR spectrum of methylphenylformamide [17] is attributable to the predominant formation of only one of the two possible isomeric forms. In the case of the $[WOF_4NMePh]^-$ anion, in which the *trans* position to the doubly bonded oxygen atom is occupied by a fluorine atom, the difference between the stabilities of the two isomeric forms of the complexes is significantly lower, apparently due to the steric hindrances, and amounts to only 1.84 kJ mol^{-1} . Therefore, the observance of signals from the two isomeric forms in the 1H NMR spectrum becomes possible.

The research which has revealed the proximity of free energies for the activation of rotation in substituted amides [19] and in the corresponding oxo-fluoramide tungsten(VI) complexes (see Table 3.1) clearly shows a similarity between isomerization processes in organic compounds and those in complexes, in which the role of the acyl group is performed by the WOF_4 fragment.

2.2 RESTRICTED M–NR₂ ROTATION IN THE DINUCLEAR COMPLEXES WITH M₂⁶⁺ CORE (M = W, Mo)

The dimetal systems M_2X_6 ($M = Mo, W$; $X = R, NR_2, OR$) have been first characterized by Chisholm and coworkers [20, 21]. Two dynamic processes are typical of these molecules: rotation about the metal–metal bond, and possible restricted ligand mobility.

Electronically one would predict no barrier to rotation about the ($M \equiv M$) bond in these complexes. However, the use of sterically bulky ligands, especially dialkylamido groups, allows a sizeable rotation barrier to be imposed, resulting in the formation of *anti* and *gauche* rotamers for molecules of the type $1,2-M_2X_2(NR_2)_4$. Observation of the temperature dependence of the rate of exchange between rotamers of this type by NMR methods has allowed the steric barrier to rotation about the $Mo \equiv Mo$ bond to be evaluated [22–24]. It has been found [25] that, even at high temperatures ($60^\circ C$) *anti* \rightleftharpoons *gauche* isomerization is slow on the NMR time scale:



An approximate estimation of the free energy of activation for the *anti* / *gauche* rearrangement of $W_2Me_2(NEt_2)_4$ is as follows: $\Delta G^\ddagger_{285} = 87.9 \pm 4.2 \text{ kJ mol}^{-1}$ ($21 \pm 1.0 \text{ kcal mol}^{-1}$) [25].

Another interesting fluxional process involves dialkylamido ligands when bonded to these M_2^{6+} centers ($M = Mo, W$). The nitrogen-p to metal-d π -bonding that is a typical feature of early transition metal amido compounds involves donation to the metal d_{xy} and $d_{x^2-y^2}$ orbitals [20]. This partial double bond character to the $M-NR_2$ interaction hence imposes a preferred geometry for the ligand, with alkyl groups lying along the metal–metal axis. Hence for a $N(CH_3)_2$ ligand, one methyl group lies over the metal–metal bond (proximal) while the other lies away (distal) [24]. A large chemical shift separation, ca 2 ppm, between proximal and distal methyl proton resonances at low temperature reflects the diamagnetic anisotropy of the $M\equiv M$ triple bond [26].

In the 1H NMR spectrum, rotation about the $M-NMe_2$ bond is normally observed to be temperature dependent as seen by the broadening and collapse of the proximal and distal methyl group signals and their coalescence into a single resonance. The temperature dependence of the proton NMR spectra of the dinuclear complexes of molybdenum and tungsten was used to estimate the free energy of activation for proximal–distal exchange (see Table 3.2).

As follows from the table, the height of the barrier to rotation of the amido ligand depends on two factors: steric (the bulkiness of the R and X substituents) and electronic (the electronegativity of the X substituent).

The influence of the former is supported by the simultaneous increase in the steric volume of the substituent and the free energy of activation for proximal and distal alkyl exchange in the order: $Mo_2(NMe_2)_6$ [48.1 kJ mol^{-1}] < $Mo_2(NEt_2)_6$ [56.9 kJ mol^{-1}] < $1,2-Mo_2(OAr-Ph_2)_2(NMe_2)_4$ [66.1 kJ mol^{-1}], where $HOAr-Ph_2$ is 2,6-diphenylphenol. An analogous situation is observed for $Mo_2(NR_2)_6$. Thus, the free energy of activation rotation of amido ligand in

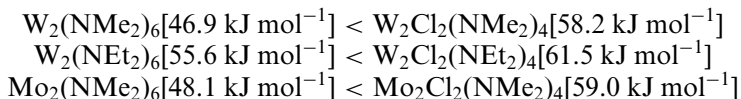
Table 3.2 Activation parameters for proximal and distal alkyl exchange in $M_2X_n(NR_2)_{6-n}$ ($M = Mo, W$; $R = Me, Et$; $X = Cl, Br, J, OAr-Ph_2$; $n = 0, 2, 3$)

Complex	ΔG^\ddagger_T [kJ mol^{-1} (kcal mol^{-1})]		$T(K)$	Reference
$W_2(NMe_2)_6$	46.9 ± 0.8	(11.2 ± 0.2)	238	[29]
$Mo_2(NMe_2)_6$	48.1 ± 0.8	(11.5 ± 0.2)	243	[26]
$W_2(NEt_2)_6$	55.6 ± 1.7	(13.3 ± 0.4)	283	[29]
$Mo_2(NEt_2)_6$	56.9 ± 2.1	(13.6 ± 0.5)	289	[26]
$W_2Cl_2(NMe_2)_4$	58.2	(13.9)	^a	[27]
$Mo_2Cl_2(NMe_2)_4$	59.0	(14.1)	^a	[27]
$W_2Cl_2(NEt_2)_4$	61.5 ± 1.7	(14.7 ± 0.4)	312	[25]
$W_2Br_2(NEt_2)_4$	64.0 ± 1.7	(15.3 ± 0.4)	343	[28]
$W_2I_2(NEt_2)_4$	64.0 ± 1.7	(15.3 ± 0.4)	343	[28]
$1,1,2-Mo_2(OAr-Ph_2)_3(NMe_2)_3$	65.3 ± 2.1	(15.6 ± 0.5)	335	[24]
$1,2-Mo_2(OAr-Ph_2)_2(NMe_2)_4$	66.1 ± 2.1	(15.8 ± 0.5)	345	[24]

^a The temperature is not indicated in the article.

$\text{Mo}_2(\text{NR}_2)_6$ is greater for $\text{R} = \text{Et}$ than for $\text{R} = \text{Me}$. This fact reflects the different steric demand of these groups [26].

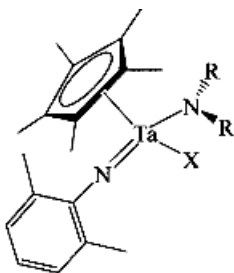
The effect of the nature of the X substituent on the barrier to rotation of the amido ligand is revealed by comparison of the activation parameters in three pairs of complexes:



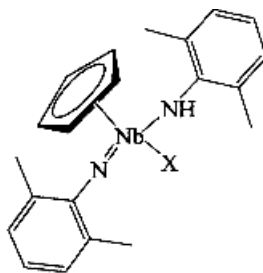
In all cases, the substitution of the more electronegative chlorine atom for NEt_2 or NMe_2 results in an increase in ΔG^\ddagger . This fact probably reflects the increase in N-to-M π bonding in $\text{M}_2\text{Cl}_2(\text{NR}_2)_4$ ($\text{R} = \text{Me}, \text{Et}$) [27].

2.3 FEATURES OF DYNAMIC BEHAVIOR OF AMIDO CYCLOPENTADIENYL COMPLEXES OF GROUP 5 TRANSITION METALS

Half-sandwich terminal early transition metal imido amido complexes have come under considerable scrutiny in recent years, in part due to their participation in C–H bond activation [30] and cycloaddition reactions [31]. According to NMR evidence, many of them are involved in dynamic processes. Compounds of this sort are exemplified by Nb(V) and Ta(V) complexes: $[(\eta^5\text{-C}_5\text{H}_5)\text{NbX}\{\text{N}(2,6\text{-Me}_2\text{C}_6\text{H})\}]$, where $\text{X} = \text{Cl}, \text{NH}(2,6\text{-Me}_2\text{C}_6\text{H}_3), \text{Me}$ [32] and $[(\eta^5\text{-C}_5\text{Me}_5)\text{TaNR}_2\text{X}\{\text{N}(2,6\text{-Me}_2\text{C}_6\text{H})\}]$, where $\text{R} = \text{Me}, \text{}^i\text{Pr}$; $\text{X} = \text{Cl}, \text{Me}$ [33].



$\text{R} = \text{}^i\text{Pr}, \text{X} = \text{Me}$ **1**;
 $\text{R} = \text{Me}, \text{X} = \text{Cl}$ **2**;
 $\text{R} = \text{Me}, \text{X} = \text{Me}$ **3**;



$\text{X} = \text{Cl}$ **4**;
 $\text{X} = \text{NH}(2,6\text{-Me}_2\text{C}_6\text{H}_3)$ **5**;
 $\text{X} = \text{Me}$ **6**;

Variable temperature NMR studies on these complexes show the presence of two dynamic processes: hindered rotation of the amido ligand around the metal–nitrogen bond and hindered rotation of the imido ligand about the $\text{N}_{\text{imido}}\text{-C}_{\text{ipso}}$ bond. For example, at 288 K the ^1H -NMR spectrum of **1** shows the coalescence of the methyl $^1\text{H}(i\text{Pr})$ H CMe_2 proton isopropyl resonances ($\Delta G^\ddagger_{288\text{K}} = 58.2 \text{ kJ mol}^{-1}$) corresponding to the slow rotation about the

Table 3.3 Kinetic parameters of rotation of the amido ligand around the $N_{\text{amido}}\text{-M}$ bond, where $M = \text{Ta}, \text{Nb}$ ($\text{cal} = 4.184 \text{ J}$)

Compound	$T(\text{K})$	$\Delta G^\ddagger (\text{kJ mol}^{-1})$	$\Delta H^\ddagger (\text{kJ mol}^{-1})$	$\Delta S^\ddagger (\text{J K}^{-1} \text{ mol}^{-1})$	Reference
1	288	58.2	—	—	[33]
2	298	50.2	55.6 ± 1.0	18.4 ± 4.0	[33]
3	298	45.2	46.9 ± 1.0	5.9 ± 4.0	[33]
4	295	60.6 ± 4.0	—	—	[32]
5	193	47.4 ± 2.5	—	—	[32]
6	183	37 (estimated value)	—	—	[32]

Ta– $N^i\text{Pr}_2$ bond [33]. Not only the electronic factor but also the steric one exerts an effect on the barrier to rotation of the amido ligand. As an illustration, let us compare the free activation energies of rotation of amido ligands in complexes **1–6** (Table 3.3). The kinetic parameters of this dynamic process for compounds **2** and **3** which were calculated on the basis of ^1H DNMR data by NMR lineshape analysis and the DNMR5 program [8(a), 34], are in good agreement with an intramolecular process which takes place without any change of the entropy factor ($\Delta S^\ddagger \approx 0$). The dynamic processes in the compounds **4** and **5** were modelled using the gNMR package [35] to obtain a series of rates for the different processes. From these rates the energy barrier to the rotations was calculated from a plot of $\ln k$ against $1/T$. Although Table 3.3 compiles the ΔG^\ddagger values determined at different temperatures and their comparison is not quite correct, certain trends of the data in going from one complex to another do persist.

Among the three tantalum compounds, complex **1** exhibits the highest barrier to rotation of the amido ligand (Table 3.3). This is evidently due to the steric crowding that emerges for the pentamethylcyclopentadienyl and isopropyl groups while the ligand rotates.

The kinetic parameters for the rotation of the NMe_2 ligand about the $N_{\text{amido}}\text{-Ta}$ bond clearly depend on the electronic and steric properties of the substituent $X = \text{Cl}$, **2**; Me , **3**. The difference between methyl and chloro groups can be assigned to their electronegativities. The high electronegativity of the chlorine atom is favorable for efficient electron transfer from the nitrogen atom of the amido ligand to the tantalum, i.e., for the increase in the order of the Ta–N bond. As a consequence, the barrier to rotation of the ligand in complex **2** (50.2 kJ mol^{-1}) is higher than in complex **3** (45.2 kJ mol^{-1}).

Analogous considerations apply to the fact that, of the two niobium compounds **4** and **6**, the higher barrier to rotation of the amido ligand is found in **4** ($X = \text{Cl}$) [32]. In the niobium complexes **4–6**, the steric volume of the substituents X is in the order $\text{NH}(2,6\text{-Me}_2\text{C}_6\text{H}_3) > \text{Cl} > \text{Me}$. Thus, from the steric point of view, compound **5** ($X = \text{NH}(2,6\text{-Me}_2\text{C}_6\text{H}_3)$) should have the highest barrier to rotation of the amido ligand. However, this is not the case for the following reasons. The crystal structures of compounds **5** and **6** indicate that

the lone pairs of the amido ligands lie in the equatorial binding plane of the imido and cyclopentadienyl groups. This is the orientation in which π donation from the amido ligand to the niobium centre is maximized [36]. Rotation of the amido ligand away from this position will lead to a loss of the π bonding interaction, giving rise to an electronic barrier to rotation of the amido ligand. This explains the low energy barrier to rotation of the amido ligands observed in **5**. The two amido ligands can only donate four electrons to the metal center between them. If each amido ligand is considered to be donating an average of one π electron the loss of the π bonding interaction on rotation of an individual amido ligand will be much reduced over that in **4** and **6**. Additionally, if the rotations of the two amido groups are out of phase with one another then the loss of π interaction from one ligand can be somewhat counterbalanced by the other [32].

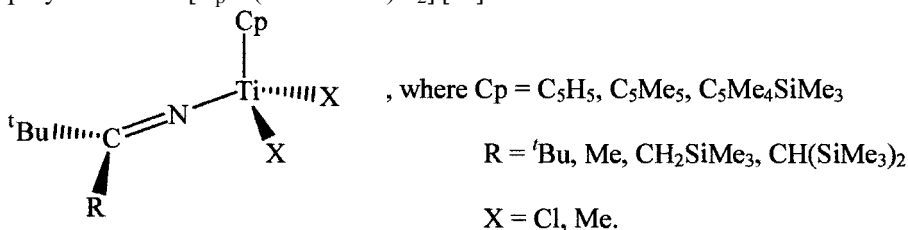
In contrast to the tantalum compounds considered above, the niobium complexes can exist as conformers of different stability at low temperatures. For example, in the ^1H NMR spectrum of complex **4**, the intensity ratio between the signals of the conformers is about 3 : 1 [32]. The crystal structures of the bis-amido compound **5** and the methylamido compound **6** all show that the lone pair of the amido ligand lies preferentially in the equatorial binding plane of the cyclopentadienyl and imido ligands, a conformation due to the π bonding interaction of the lone pair with the niobium centre. If rotation about the Nb–N_{amido} bond becomes slow on the NMR time scale then two conformers will be observed, one with the amido proton oriented toward the cyclopentadienyl ring and one with it oriented away. It is supposed that the major conformer is that with the amido proton oriented toward the cyclopentadienyl ring, which minimizes the steric interactions present [32].

2.4 INTERNAL HINDERED ROTATION OF KETIMIDO LIGANDS

2.4.1 Ketimido Complexes of Titanium

Ketimines $\text{HN}=\text{CR}^1\text{R}^2$ can be considered as formal analogs of secondary amines; however, the nitrogen atom in ketimines is sp^2 -hybridized, which can impart some specific features in the complexes of Group 4–6 d^0 transition metals.

Thus, the reaction between C_pTiX_3 and $\text{HN}=\text{C}'\text{BuR}$ (or $\text{LiN}=\text{C}'\text{BuR}$) resulted in a new class of monocyclopentadienyl titanium catalysts for olefin polymerization [$\text{C}_p\text{Ti}(\text{N}=\text{C}'\text{BuR})\text{X}_2$] [37]:



The X-ray crystal structure of the related compound $\text{Cp}-(^n\text{Bu}'\text{BuC}=\text{N})\text{TiCl}_2$ [38] showed the complex to be monomeric with a near-linear Ti–N–C linkage of $171.3(4)^\circ$. In the solid state, the plane of the ketimide ligand is approximately perpendicular to the $\text{Cp}_{\text{centroid}}\text{--Ti}$ vector. The authors noted that the relatively short Ti–N bond length of $1.872(4)$ Å was consistent with some double bond character in this linkage.

All the neutral titanium ketimido compounds described above were characterized by NMR spectroscopy. The ^1H NMR spectroscopic data for the ketimido complexes $[\text{CpTi}(\text{N}=\text{C}^t\text{BuR})\text{X}_2]$ suggest that the rotation about the Ti–N bond of the ketimido ligand is a rapid rotation. For compounds, where $\text{R} = ^t\text{Bu}$, the ^tBu groups of the ketimido ligand remain equivalent at all accessible temperatures, suggesting a perpendicular orientation of the ketimido ligand (with respect to the Cp–Ti vector) in the ground state as observed in the solid state for $\text{Cp}-(^n\text{Bu}'\text{BuC}=\text{N})\text{TiCl}_2$. With this orientation, dimethyl compounds, containing unsymmetrical ketimido ligands ($\text{Cp} = \text{C}_5\text{Me}_5$, $\text{R} = \text{Me}$, CH_2SiMe_3 , $\text{X} = \text{Me}$), should have diastereotopic methyl groups. However, the methyl groups appear as a single resonance down to -80°C in the ^1H NMR spectrum. The most reasonable explanation for this behavior is rapid rotation of the ketimido ligand about the Ti–N bond, which exchanges the titanium methyl environments. For the case of more sterically bulky groups ($\text{Cp} = \text{C}_5\text{Me}_5$, $\text{R} = \text{CH}(\text{SiMe}_3)_2$, $\text{X} = \text{Me}$), this process is observable spectroscopically. The signal for the Ti–Me groups undergoes coalescence behavior and two signals at 0.71 and 0.49 ppm emerge when the sample is cooled to -90°C . Analysis of the spectra [16, p. 93] yields a ΔG^\ddagger of 40.2 ± 2.5 kJ mol $^{-1}$ (9.6 ± 0.6 kcal mol $^{-1}$) for ketimido rotation in this compound [37]. As the size of R decreases, this free energy barrier is lowered too and the low-temperature limits are not accessible for compounds with the substituents $\text{Cp} = \text{C}_5\text{Me}_5$, $\text{R} = \text{Me}$, CH_2SiMe_3 , $\text{X} = \text{Me}$. The authors think that the low barrier to rotation of the ketimido ligand may be due to participation of the C=N π orbitals in the process, such that the π component to the Ti–N bond is not lost in the parallel orientation of the ligand, the other limiting configuration during rotation.

2.4.2 Rotational Isomerism in Oxofluoroketimido Complexes of Tungsten

Ketimines react with tungsten oxotetrafluoride according to the scheme typical of the secondary amines [39] (see Section 2.1). The final stage of the reaction is the formation of a complex anion $[\text{WOF}_4(\text{N}=\text{CR}^1\text{R}^2)]^-$ ($\text{R}^1 = \text{Ph}$, $\text{R}^2 = \text{Ph}$, Et, *para*- and *ortho*- $\text{CH}_3\text{C}_6\text{H}_4$), in which the deprotonated ketimine is coordinated in the *cis* position with respect to the double-bonded oxygen atom.

Figure 3.4 shows the ^{19}F NMR spectrum of an acetonitrile solution of $[\text{WOF}_4\{\text{N}=\text{C}(o\text{-CH}_3\text{C}_6\text{H}_4)\text{Ph}\}]^-$ at -25°C . The equatorial fluorine atoms *cis* to the organic ligand (F_C and F_M) are nonequivalent and give rise to the signals at $\delta = -47.6$ and -49.2 ppm (rel. CFCl_3), respectively. This indicates that rotation about the W–N bond is lacking at this temperature and the ligand is

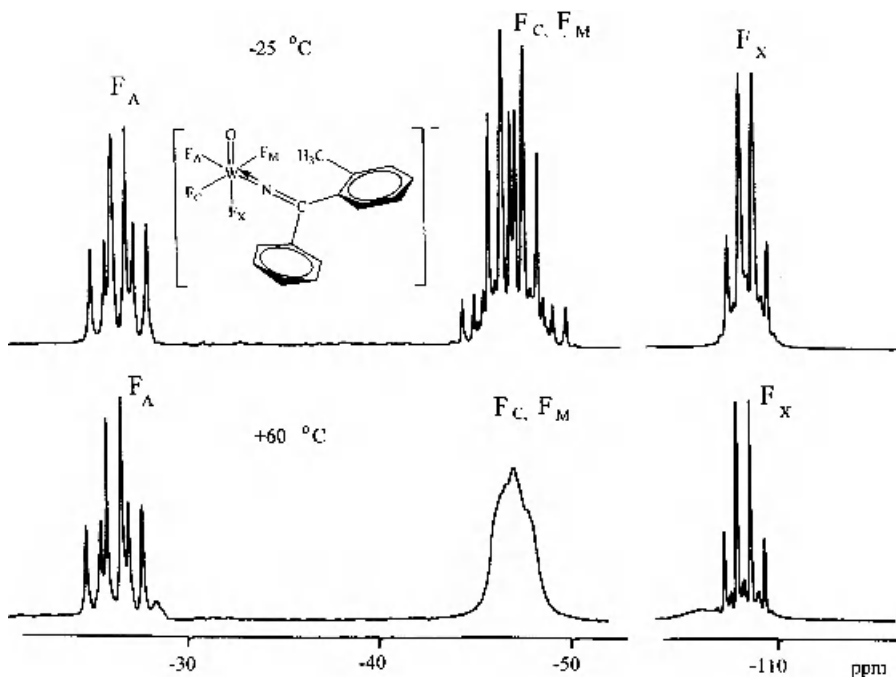
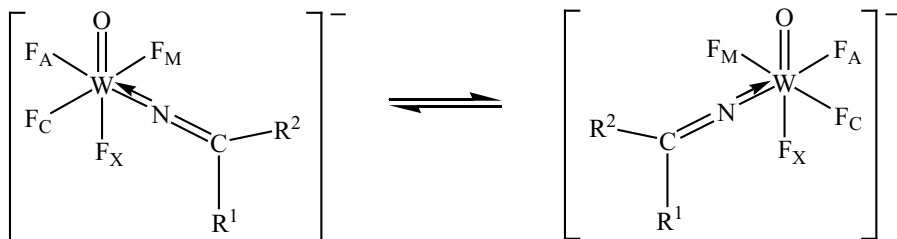


Figure 3.4 ^{19}F NMR spectra of the $[\text{WOF}_4\text{N}=\text{C}(\text{o}-\text{CH}_3\text{C}_6\text{H}_4)\text{Ph}]^-$ complexes at -25°C and $+60^\circ\text{C}$.

oriented in the equatorial plane of the complex. The equatorial fluorine atoms *cis* to the organic ligand thereby have different chemical environments and give rise to different ^{19}F signals. The fact that the substituents in phenyl *o*-tolyl ketimine are similar accounts for the small difference in chemical shift between the F_C and F_M signals.

With an increase in temperature to $+30^\circ\text{C}$, the F_C and F_M signals coalesce into one broad signal, while the F_A and F_X signals remain virtually unaltered (Figure 3.4). This spectral pattern can be caused by the hindered rotation of the ligand around the $\text{W}-\text{N}$ bond.

Just as in the case of the oxo-fluoramido complexes (see Section 2.1) the tungsten–nitrogen bond in complexes with ketimines also exhibits essentially a double bond character, which is due to the $\text{p}_\pi-\text{d}_\pi$ interaction between the lone electron pair of the nitrogen atom and the vacant d_{xy} orbital of the tungsten atom. As a result of this interaction, the nitrogen atom of the coordinated ketimine acquires a hybridization close to the sp type, an allene-like linear fragment $\text{W}=\text{N}=\text{C}$ is formed, and the ligand plane is oriented in the equatorial plane of the complex. The hindered character of rotation about the $\text{W}-\text{N}$ bond in ketimines with unlike substituents at the carbon atom leads to the appearance of two enantiomers at -30°C :



These conformations are indistinguishable in the ^{19}F NMR spectra, but as the temperature increases, the exchange between them via the internal rotation of the ligand is manifested. Using the Eyring equation for a rough estimation of the energy barrier [40] for the ligand rotation in the complex $[\text{WOF}_4\{\text{N}=\text{C}(\text{o}-\text{CH}_3\text{C}_6\text{H}_4)\text{Ph}\}]^-$ gives a value of $\Delta G^\ddagger_{333} = 66.5 \text{ kJ mol}^{-1}$ ($15.9 \text{ kcal mol}^{-1}$) for the temperature of coalescence of the signals from two equatorial fluorine atoms F_C and F_M in the ^{19}F NMR spectrum [15, p. 95; 41].

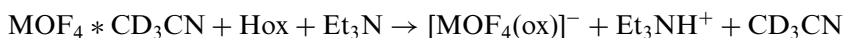
3 DYNAMIC BEHAVIOR OF d^0 TRANSITION METAL COMPLEXES WITH n -DONOR TWO-CENTER LIGANDS

3.1 ISOMERIZATION OF FLUOROCOMPLEXES OF GROUP 5–6 WITH O, N-TWO-CENTER LIGANDS

3.1.1 Dynamic Behavior of Oximate Complexes

The group of potential O,N-two-center ligands includes oximes ($>\text{C}=\text{N}-\text{OH}$), as well as hydroxylamine NH_2OH , and its derivatives. The η^2 -coordination of simple oximes and substituted hydroxylamines in d^0 transition metal complexes was reported almost simultaneously in Russia [9] and elsewhere [42,43]. More specifically, it was found [9,44,45] that the final product of the reaction between tungsten (molybdenum) oxotetrafluoride and simple oximes and β -phenylhydroxylamine is a complex anion with the deprotonated organic ligand $[\text{MOF}_4\text{L}]^-$ (where $\text{M}=\text{Mo}, \text{W}$; HL stands for acetoxime, acetaldoxime, benzaldoxime, 2- and 4-pyridinaldoxime, and β -phenylhydroxylamine).

We found [44, 46, 47] that the course of the reactions of WOF_4 (MoOF_4) with oximes is similar to that found for secondary amines and ketimines. These data and the findings reported in [45] make it possible to present the reaction of simple oximes with tungsten or molybdenum oxotetrafluorides by the overall equation



where M is Mo or W, and Hox is a simple oxime.

The presence of four multiplets of equal intensity in the ^{19}F NMR spectra (of the ACMX type) at -30°C (Figure 3.5a) indicates the formation, in the solution, of a complex with four fluorine atoms occupying nonequivalent positions.

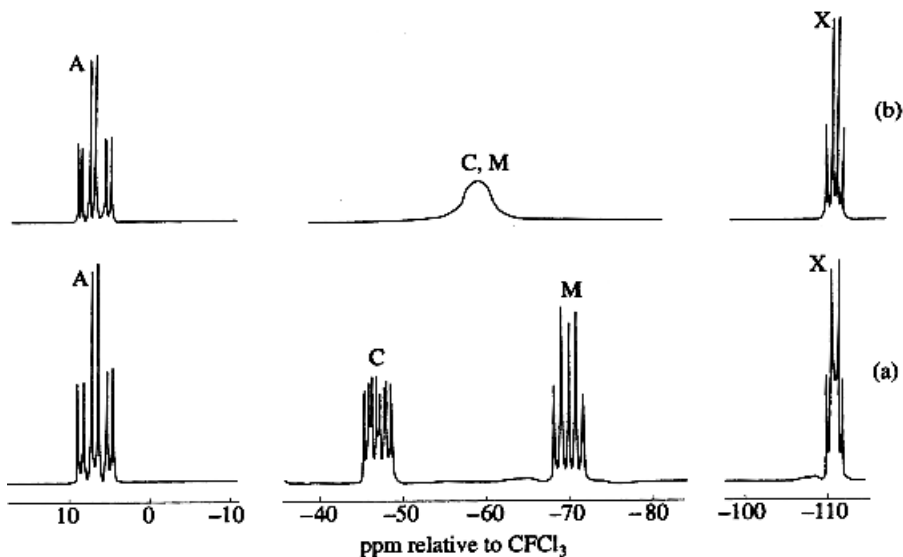
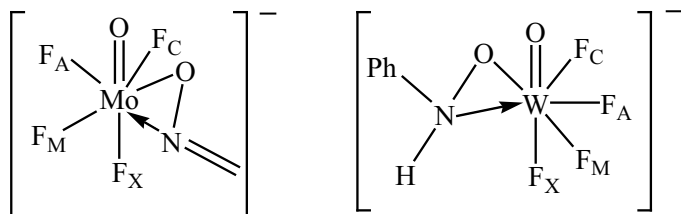


Figure 3.5 ^{19}F NMR spectra of a solution containing WOF_4 and acetoxime (1:4) in acetonitrile at (a) -30°C and (b) $+70^\circ\text{C}$. Reproduced with permission from S. G. Sakharov and Yu. A. Buslaev, *Russ. J. Inorg. Chem.* **38**(9), 1385 (1993) [41].

In this case, the nonequivalence of the F_C and F_M atoms can arise only upon the coordination of the ligand, with the N and O atoms are situated in the equatorial plane. These complexes are structurally similar to molybdenum [48, 49] and tungsten [50–53] peroxofluorides and shaped like a pentagonal bipyramid, whose equatorial plane contains three fluoro atoms (F_A , F_C , F_M) besides O and N atoms. The axial sites are occupied by a fluorine atom (F_X) and the double-bonded oxygen atom:



A comparative analysis of the ^{19}F NMR parameters of tungsten(VI) complexes with O,N-two-center ligands, amides [13,14] and ketimides [39] leads to the conclusion that the transition from the octahedral shape of the coordination compound to the pentagonal-bipyramidal structure is accompanied by a change in the mutual positions of the signals from equatorial fluorine atoms (F_A , F_C , or F_M), and by a considerable increase in the magnitude of the $^2J(^{19}\text{F}_\text{A}-^{19}\text{F}_\text{C})$ and $^2J(^{19}\text{F}_\text{A}-^{19}\text{F}_\text{M})$ coupling constants [15, p. 115] (Table 3.4).

Table 3.4 ^{19}F NMR parameters for the complexes $[\text{WOF}_4\text{L}]^-$ (HL = acetoxime, β -phenylhydroxylamine, dimethylamine, diphenylketimine) formed in a CH_3CN solution at WOF_4 : HL = 1 : 4 ($T = -30^\circ\text{C}$). Reproduced with permission from *Russ. J. Inorg. Chem.* **38**(9), 1385 (1993) [41]

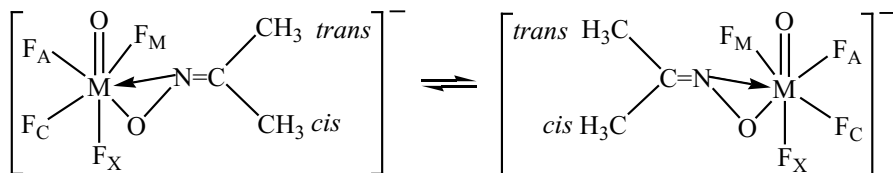
Complex	Chemical shift relative to CFCl_3 (ppm)						$J(^{19}\text{F}-^{19}\text{F})$ (Hz)					Reference
	F_A	F_C	F_M	F_X	J_{AC}	F_X	J_{AM}	J_{AX}	J_{CM}	J_{CX}	J_{MX}	
$[\text{WOF}_4(\text{ON}=\text{CMe}_2)]^-$	6.9	-47.1	-70.2	110.8	138.0	110.8	136.0	43.5	66.0	41.0	62.0	[9]
$[\text{WOF}_4(\text{ONHPh})]^-$	-19.0	-67.2	-90.0	-121.5	121.0	-121.5	121.0	44.0	52.5	35.0	64.0	[9]
$[\text{WOF}_4(\text{NMe}_2)]^-$	-80		-53.5	-96.6		-96.6	78.0	54.0			54.0	[13]
$[\text{WOF}_4(\text{N}=\text{CPh}_2)]^-$	-29.7		-49.3	-109.8		-109.8	84.9	55.7			50.4	[39]

The assumed structure of the complexes is supported also by the $^{13}\text{C}\{\text{H}\}$ NMR data. In a free planar acetoxime molecule, the methyl groups *trans* and *cis* to the OH group are nonequivalent. Both methyl groups of the complex are in the equatorial plane. However, contrary to *cis* CH_3 , the *trans* CH_3 group is in the immediate spatial proximity to one of the equatorial fluorine atoms (F_M). In the ^{13}C NMR spectrum, recorded with broad band proton decoupling at -30°C (Figure 3.6), the signal of the *trans* CH_3 group consists of a doublet with a splitting of 2.8 Hz, for the tungsten compound, and 4.1 Hz, for molybdenum.

An increase in temperature is accompanied by considerable changes in the NMR spectra of the acetoximate complexes, which are due to the occurrence of an intramolecular dynamic process in the coordination sphere. For example, in the ^{19}F NMR spectra, the signals of the equatorial F_C and F_M atoms first broaden significantly and then coalesce into one signal (Figure 3.5b). In addition, the multiplicity of the F_A and F_X signals slightly changes.

In the $^{13}\text{C}\{\text{H}\}$ NMR spectra, the signal due to the *cis* CH_3 groups remains virtually unaltered on increasing temperature, whereas the doublet from the *trans* methyl groups gradually transforms into a triplet with a coupling constant of half the constant of the doublet (Figure 3.6).

The changes observed in the ^{13}C and ^{19}F NMR spectra result from averaging a number of chemical shifts and coupling constants. This can be rationalized by the occurrence, at low temperatures, of two enantiomers, which are interconverted at elevated temperatures due to the internal rotation of the oximate ion:



where $\text{M} = \text{Mo}, \text{W}$.

In the case of a fast ligand rotation (at elevated temperature), the F_C and F_M signals in the ^{19}F NMR spectra collapse because the corresponding atoms become equivalent (Figures 3.5b, 3.7). The $^2J(\text{F}_\text{A}-\text{F}_\text{C})$ and $^2J(\text{F}_\text{A}-\text{F}_\text{M})$ constants are averaged. The $^2J(\text{F}_\text{C}-\text{F}_\text{X})$ and $^2J(\text{F}_\text{M}-\text{F}_\text{X})$ constants also become equal (Table 3.4).

To explain the changes that occur in the ^{13}C NMR spectra with increasing temperature, we can reasonably assume that the spin states of each fluorine nucleus in one complex molecule remain unaltered on the NMR time scale. Depending on the spin states of the F_C and F_M nuclei, the two types of the $[\text{WOF}_4(\text{ON}=\text{CMe}_2)]^-$ complexes (or spin isomers) are equally probable. When the spin states of F_C and F_M are the same, the dynamic process does not influence the ^{13}C NMR spectra, and the doublet from the *trans* CH_3 group is observed over the whole temperature range under consideration. In the case of the complex with opposite spin states of the F_C and F_M nuclei, an increase in temperature leads to dynamic averaging of these nuclei. As a result, the doublet

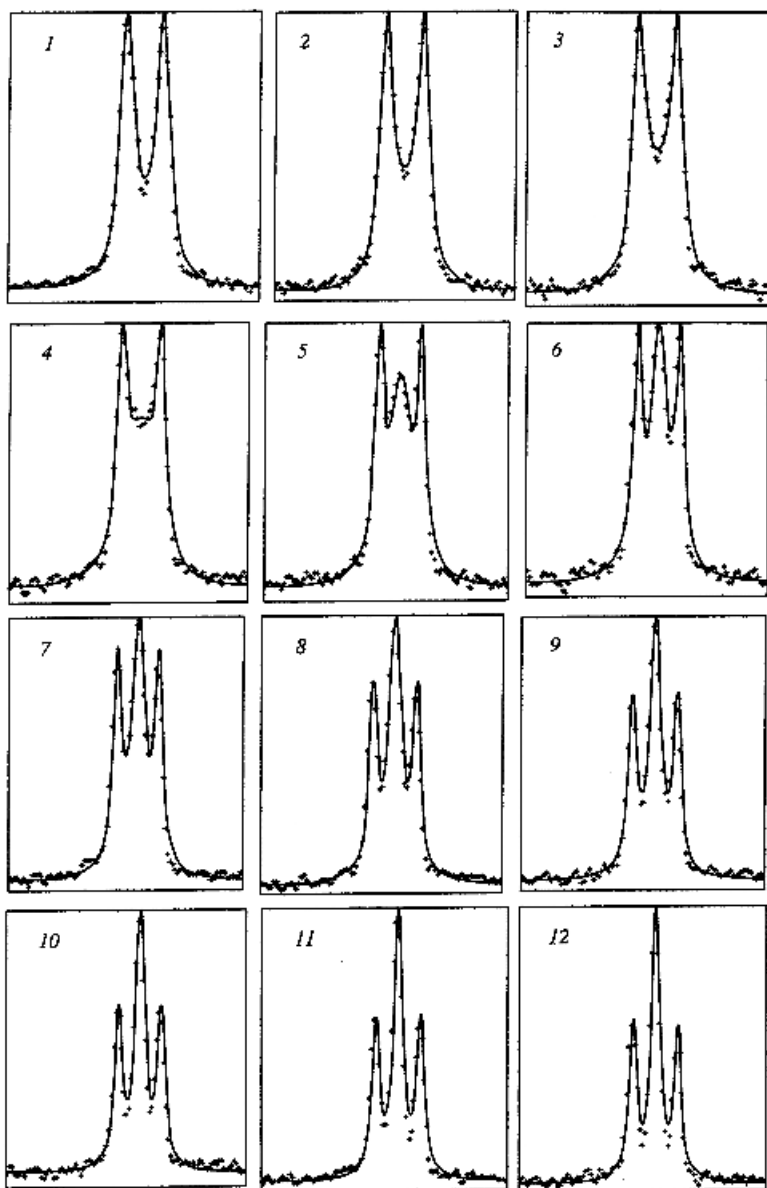


Figure 3.6 Variable-temperature $^{13}\text{C}\{\text{H}\}$ NMR spectra of *trans* CH_3 group of the $[\text{WOF}_4(\text{ON}=\text{CMe}_2)]^-$ complex.

No. of spectrum	1	2	3	4	5	6	7	8	9	10	11	12
T (K)	227	232	235	238	243	246	250	253	256	259	262	266
k (s^{-1})	1.77	3.0	4.4	7.0	12.4	20.4	28.2	44.8	59.2	91.0	135.3	184.2

(k is the rate constant of the spin-state exchange; experimental spectra are shown by dots and calculated spectra, by solid lines). Reproduced with permission from S. G. Sakharov *et al.*, *Russ. J. Inorg. Chem.* **40**(12), 1906 (1995) [46].

from the *trans* CH₃ group transforms into a singlet in the fast-exchange temperature range. The real ¹³C{H} NMR spectra, shown in Figure 3.6, are a superposition of these two subspectra, each of which corresponds to one type of the complexes.

A complete lineshape calculation of ¹⁹F and ¹³C{H} NMR spectra was carried out with the use of a program developed by us. This program is a modified version of the DNMR simulation program for noncoupled or loosely coupled systems [54] using classical formalism. Taking into account the character of the experimental ¹⁹F and ¹³C NMR spectra (the first-order spectra), we succeeded in using this program for the analysis of the complete NMR lineshape for the systems with spin–spin coupling. In so doing, we considered a change in the ¹³C NMR lineshape with increasing the temperature as the result of the four pseudo-site exchange (exchange matrix dimension was 4 × 4), which leads to a collapse of one of the two methyl doublets into a singlet. Similar changes in the ¹⁹F NMR spectra were assumed to be the result of the 16 pseudo-site exchange (exchange matrix dimension was 16 × 16), which leads to a collapse of two multiplets (eight lines in each) from F_C and F_M into a doublet of doublets with averaging of the corresponding coupling constants. Calculated spectra were fitted to the variable-temperature experimental spectra by the iterative method of conjugated directions (the Powell algorithm) [55].

Figure 3.7 shows experimental and calculated ¹⁹F NMR spectra (the F_C and F_M region) of the complex [WOF₄(ON=CMe₂)]⁻ anion at various temperatures and lists the calculated values of the rate constant of the spin state exchange. Activation parameters of the isomerization of the complex determined from the Eyring temperature dependence of the exchange rate [16, p. 93], are listed in Table 3.5. This table also contains the activation parameters of the ligand rotation in the same complex, determined by ¹³C DNMR. Figure 3.6 shows a temperature dependence of the experimental and calculated ¹³C{H} NMR spectra of the *trans* methyl group of the oximate ion.

A comparison of the activation parameters determined by two different methods is indicative of their satisfactory agreement. For example, the values of the free activation energy (ΔG^\ddagger) are virtually the same within the deviations found. This is not surprising, however, since ΔG^\ddagger is slightly affected by the systematic errors in contrast to ΔS^\ddagger and ΔH^\ddagger [16, p. 108]. Analysis of our data shows that both methods (¹⁹F DNMR and ¹³C DNMR) lead to comparable results and can be used independently of one another when studying the dynamic behavior of fluoro oximate complexes.

Studying the dynamic behavior of the [MoOF₄(ON=CMe₂)]⁻ anion showed that the barrier to the rotation of the organic ligand in the complex is more than 8.4 kJ mol⁻¹ (2 kcal mol⁻¹) higher than in the corresponding tungsten complex (Table 3.5). This indicates an influence of the electronic factor on the rotation barrier height. Indeed, effective electronegativity (and, hence, accepting ability) of a molybdenum atom in the oxo fluoro complexes is considerably higher than that of tungsten [56]. Hence, in the oximate complexes, the strength of the Mo–N bond is higher than that of the W–N bond.

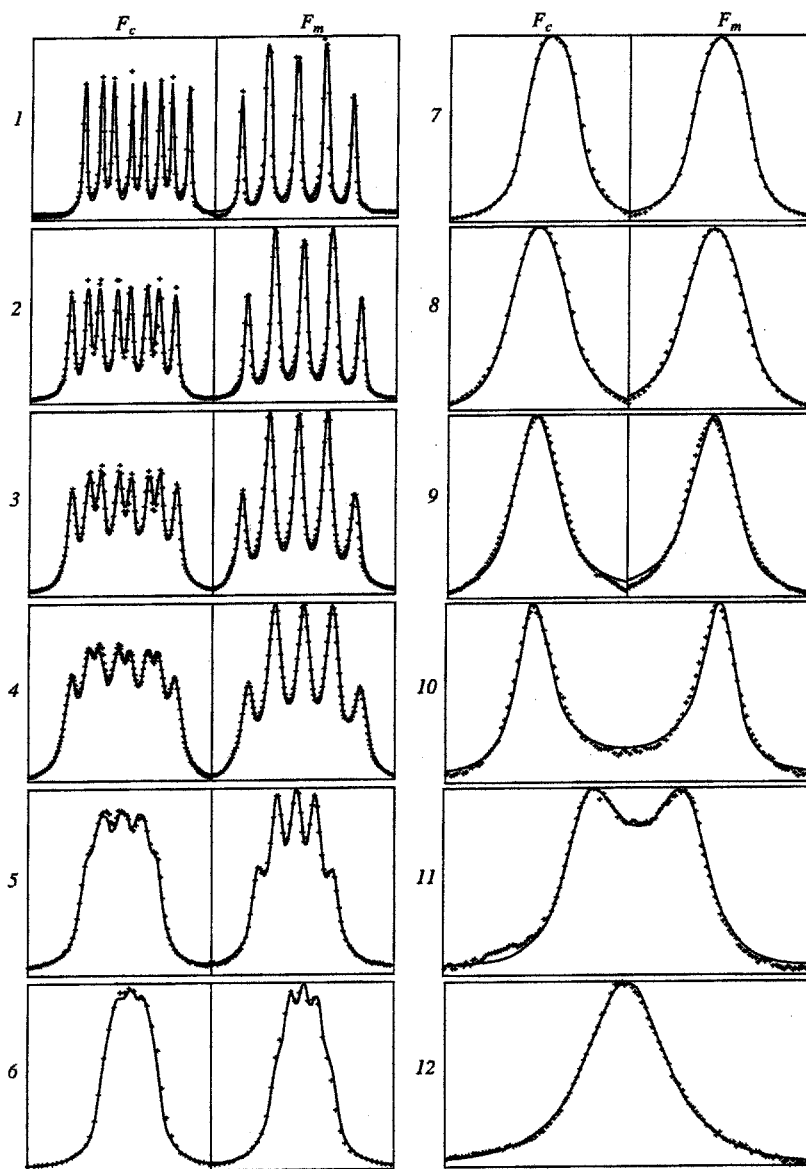


Figure 3.7 Variable-temperature ^{19}F NMR spectra of the $[\text{WOF}_4(\text{ON}=\text{CMe}_2)]^-$ complexes (the region of the equatorial F_c and F_m atoms).

No. of spectrum	1	2	3	4	5	6	7	8	9	10	11	12
T (K)	255	260	265	270	276	281	286	291	302	312	322	333
k (s^{-1})	59	100	178	300	467	724	1133	1918	3816	7917	20023	46144

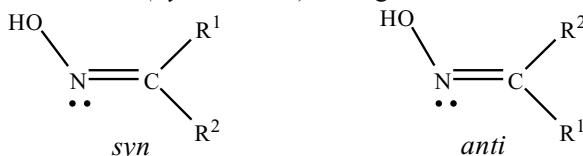
(k is the rate constant of the spin-state exchange; experimental spectra are shown by dots and calculated spectra, by solid lines). Reproduced with permission from S. G. Sakharov *et al.*, *Russ. J. Inorg. Chem.* **40**(12), 1906 (1995) [46].

Table 3.5 Activation parameters of the rotation of the oximato ligand (cal. = 4.184 J) [46,47,57,58]

Complex	Method	ΔH^\ddagger (kJ mol ⁻¹)	ΔS^\ddagger (J mol ⁻¹ K ⁻¹)	ΔG^\ddagger_{313} (kJ mol ⁻¹)
[WOF ₄ (ON=CMe ₂)] ⁻	<i>a</i>	56.40 ± 0.75	11.55 ± 2.68	52.80 ± 0.59
[WOF ₄ (ON=CMe ₂)] ⁻	<i>b</i>	59.37 ± 0.71	22.76 ± 2.80	52.26 ± 0.50
[MoOF ₄ (ON=CMe ₂)] ⁻	<i>b</i>	66.73 ± 0.84	12.55 ± 2.93	62.76 ± 0.59
[MoOF ₄ (<i>syn</i> -ON=CMeEt)] ⁻	<i>b</i>	70.70 ± 1.26	29.29 ± 4.18	61.50 ± 0.50
[MoOF ₄ (<i>anti</i> -ON=CMeEt)] ⁻	<i>b</i>	74.39 ± 1.55	32.09 ± 5.44	64.35 ± 0.67
[WOF ₄ (<i>syn</i> -ON=CHPh)] ⁻	<i>a</i>	55.31 ± 0.50	22.80 ± 1.88	48.20 ± 0.25
[WOF ₄ (<i>anti</i> -ON=CHPh)] ⁻	<i>a</i>	74.94 ± 0.33	59.41 ± 1.05	56.36 ± 0.13
[MoOF ₄ (<i>syn</i> -ON=CHPh)] ⁻	<i>a</i>	61.17 ± 0.46	14.39 ± 1.67	56.65 ± 0.25
[MoOF ₄ (<i>anti</i> -ON=CHPh)] ⁻	<i>a</i>	87.74 ± 1.84	64.60 ± 5.86	67.49 ± 0.42

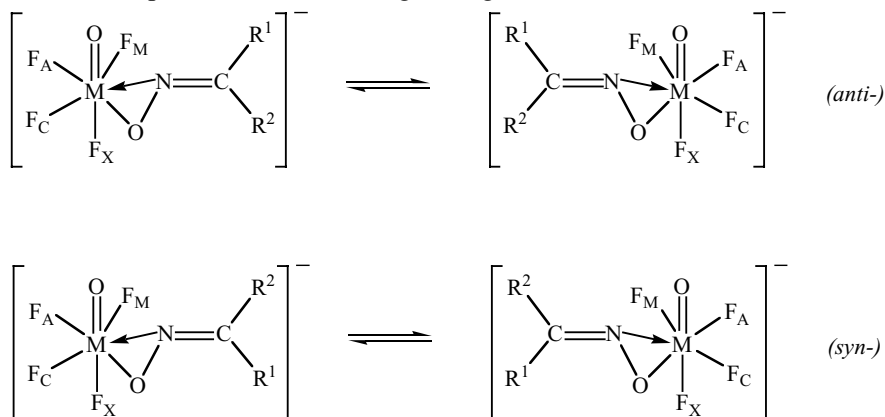
^a 19 F DNMR.^b 13 C DNMR.

Oximes bearing different substituents at the carbon atom, in particular, aldoximes, can exist as two (*syn* and *anti*) configurational isomers:



where R¹ is a less bulky substituent than R².

Therefore, they can form isomeric complexes differing in the configuration of the coordinated organic ligand. We discovered these isomers when studying the reactions of WOF₄ (MoOF₄) with pyridine-2- and 4-carbaldoximes, benzaldoxime, acetaldoxime, and methyl ethyl ketoxime [45, 57, 58]. The temperature dependence of the ¹⁹F (Figure 3.8) and ¹³C NMR spectra indicates that each of the isomeric complexes exists as two enantiomers, which are converted into each other upon rotation of the organic ligand:



where M = Mo, W, R¹ = H, R² = Ph; M = Mo, R¹ = Me, R² = Et;

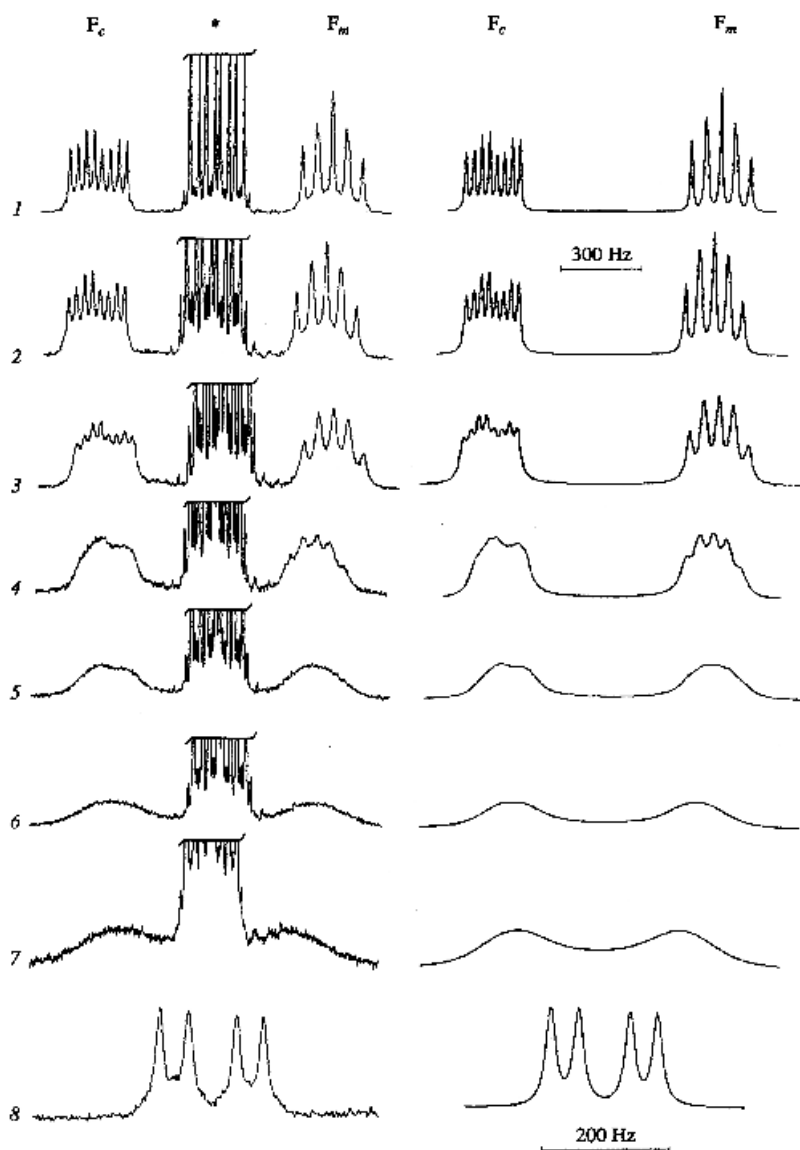


Figure 3.8 (Left) Experimental and (right) simulated ^{19}F NMR spectra of the $[\text{WOF}_4(\text{syn-ON}=\text{CHPh})]^-$ complex at various temperatures (the region of the equatorial F_C and F_M atoms).

No. of spectrum	1	2	3	4	5	6	7	8
$T(\text{K})$	233	238	244	249	255	260	266	320
$k(\text{s}^{-1})$	32	58	108	200	347	703	1151	99 621

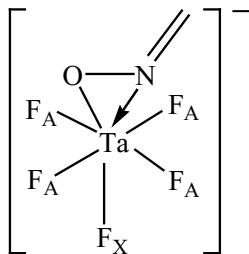
(k is the spin-state exchange rate constant; the F_C signal of the $[\text{WOF}_4(\text{anti-ON}=\text{CHPh})]^-$ complex is marked with an asterisk). Reproduced with permission from S. G. Sakharov et al., *Russ. J. Inorg. Chem.* **42**(9), 1398 (1997) [57].

An analysis of the experimental values of the activation parameters of isomerization of the oximate complexes (Table 3.5) indicates that the barrier to the hindered rotation of the ligand in the compound containing the oximate ion in *anti* conformation is higher than this barrier in the complex with *syn* conformation.

It is noteworthy that, in the case of pyridine-2-carbaldoxime, one could expect the formation of a complex with a six-membered chelate ring due to coordination through oxygen and through nitrogen of the pyridine ring. However, only the complex with the η^2 -type coordination is detected in the solution.

The dihapto coordination of oximate ligands has also been found for Ta(V) fluoro complexes in a study of the reaction of tantalum pentafluoride with acetoxime, benzaldoxime, and ethyl methyl ketoxime [59]. As in the case of the W(VI) fluoro complex, the transition from mono- to dihapto coordination of the ligand is accompanied by a change in the signals in the ^{19}F NMR spectra and by an increase in the magnitude of the spin-spin coupling constants between the fluorine nuclei. For ethyl methyl ketoxime complexes, isomeric forms with *syn* and *anti* configurations of the oximate ligand were detected.

In the complexes under consideration (e.g., $[\text{Ta}(\text{ON}=\text{CMe}_2)\text{F}_5]^-$), two heteroatoms are present in the coordinated fragment—O—N=:



which might result in the nonequivalence of the fluorine atoms in *cis* position with respect to the oximate group. However, the ^{19}F NMR spectra of tantalum fluoroximates showed equivalent fluorine atoms in the *cis* position in the entire temperature range studied [59]. This is indicative of a lower energy barrier for ligand rotation in these complexes as compared to that of $[\text{WOF}_4(\text{ON}=\text{CMe}_2)]^-$ [9].

3.1.2 Mechanism of Isomerism in Oximate Complexes

To draw a conclusion about the isomerization mechanism of the oximate complexes, one should consider the problem of the effect of the ligand coordination mode in a transition state on the ΔG^\ddagger and ΔS^\ddagger values.

For the $[\text{MOF}_4(\text{syn-ON}=\text{CR}^1\text{R}^2)]^-$ (where $\text{M} = \text{Mo}, \text{W}$) anion, three structures of the transition state are likely:

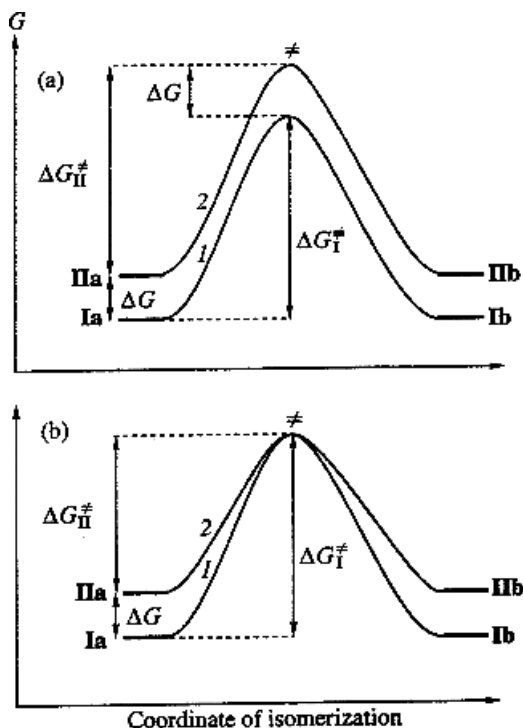


Figure 3.9 Energy profile of isomerization of $[\text{MOF}_4(\text{anti-ON}=\text{CR}^1\text{R}^2)]^-$ (I) and $[\text{MOF}_4(\text{syn-ON}=\text{CR}^1\text{R}^2)]^-$ (II) (where $\text{M} = \text{Mo}, \text{W}$; R^1 is less bulky substituent than R^2): (a) with the η^2 coordinated ligand in the transition state and (b) with the ligand coordinated only through the oxygen atom in the transition state. Reproduced with permission from S. G. Sakharov *et al.*, *Russ. J. Inorg. Chem.* **40**(12), 1906 (1995) [46].

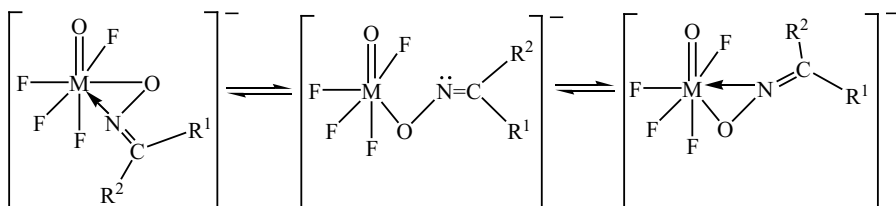
fluorine (oxygen) atom. The free energy of activation is a difference between the transition state and ground state energies. Therefore, isomerization of both **I** and **II** will be characterized by the same activation energy ($\Delta G^\ddagger_{\text{I}} = \Delta G^\ddagger_{\text{II}}$). Hence, if the coordination of the ligand in the transition state involves two chemically bonded O and N atoms, the steric factor should not markedly influence the height of barrier to rotation of the oximate ion.

If the isomerization proceeds via the open-structure complex (Figure 3.9b), the transition state energies for **I** and **II** appear to be the same due to the remoteness of the substituents in the ligand from the other ligands in the complex. Therefore, $\Delta G^\ddagger_{\text{I}} = \Delta G^\ddagger_{\text{II}} + \Delta G$ or $\Delta G^\ddagger_{\text{I}} > \Delta G^\ddagger_{\text{II}}$. Consequently, the steric factor should favor a decrease in the rotation barrier height of the oximate ligand provided that its coordination in the transition state occurs via one n-donor atom.

If the above inference is correct, the difference between the barriers to ligand rotation in compounds with the *anti* and *syn* conformation of the oximate ion should considerably increase with an increase in the difference between the

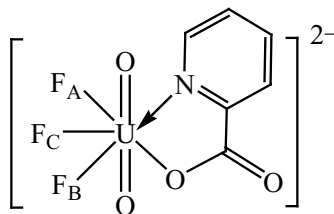
volumes of the substituents. Indeed, the difference in $\Delta G^\ddagger_{313\text{K}}$ of isomerization between the *anti* and *syn* conformations of $[\text{MoOF}_4(\text{ON}=\text{CMeEt})]^-$ is 2.9 kJ mol^{-1} ($0.7 \text{ kcal mol}^{-1}$) (Table 3.5). On the other hand, the free activation energies for the isomerism of tungsten and molybdenum complexes with the *anti* configuration of the η^2 -bonded benzaldoximato ligand are almost 8.4 and 10.9 kJ mol^{-1} (2 and $2.6 \text{ kcal mol}^{-1}$), respectively, higher than those for the complexes with the *syn* configuration [60].

Therefore, the isomerization of the oximato complexes of d^0 transition metals proceeds via an internal rotation of the η^2 -coordinated ligand with bond cleavage and following formation of the metal–nitrogen bond. In the transition state, an open-structure complex is formed [46, 57]:



This conclusion is supported by the fact that the entropy of activation of all studied molybdenum and tungsten oximato complexes is positive (Table 3.5).

This mechanism is analogous to that proposed by Grenthe *et al.* [61] for the intermolecular exchange reaction in $[\text{UO}_2(\text{pic})\text{F}_3]^{2-}$ (pic is picolinate), which was shown to be the result of opening/closing of the chelate ring, equivalent to a site exchange between the two ‘edge’ fluorides (F_A and F_B):



Thus, the chelate ring opening via N–U(VI) bond breaking is the rate-determining step of the ‘edge’ fluoride exchange.

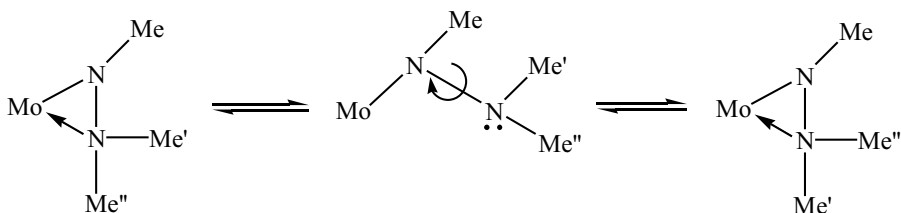
3.2 ISOMERISM OF TRANSITION METAL COMPLEXES WITH N, N-TWO-CENTER LIGANDS

3.2.1 Coordination Compounds with Substituted Hydrazines and Hydrazide(1-) Ligands

Substituted hydrazines can be considered as derivatives of amines. We may therefore expect a similar behavior for the two types of compounds in reactions with d transition metal halides, and in particular, with tungsten fluorides. The

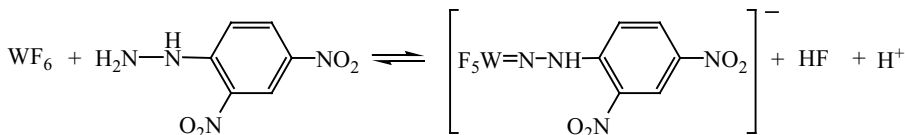
presence of two directly bonded nitrogen atoms in hydrazines implies their ability to undergo η^2 coordination to the central atom, by analogy with the O,N-two-center ligands.

The coordination mode of the hydrazide ligand (mono- or dihapto) in transition-metal complexes depends on both the nature of the substituents at the nitrogen atoms and the character of other ligands at the central atom. For instance, complexes of the general formula $[\text{Mo}(\eta^5\text{-C}_5\text{H}_5)(\text{NO})\text{I}(\text{NRNR}'\text{R}'')]$ (R , R' , and R'' are the electron-donor substituent) were prepared by treating the relevant $[\text{Mo}(\eta^5\text{-C}_5\text{H}_5)(\text{NO})\text{I}_2(\text{NHRNR}'\text{R}'')]$ compound with a stoichiometric amount of triethylamine. They contain two nitrogen atoms bonded to one another that participate in the hydrazido ligand coordination [62]. However, due to the presence of electron-acceptor substituents on hydrazine, such as C_6F_5 and $p\text{-C}_6\text{H}_4\text{NO}_2$, the donating ability of the nitrogen atom that bears these substituents drops markedly. The resulting hydrazide ligand coordination type is η^1 . An analysis of the temperature dependence of solution ^{13}C - ^1H NMR line shapes of the $[\text{Mo}(\eta^5\text{-C}_5\text{H}_5)(\text{NO})\text{I}(\text{NMeNMe}_2)]$ complex allowed us to suggest the following exchange pathway [62]:



The exchange activation energy calculated at the temperature of coalescence of NMR signals is 59 kJ mol^{-1} (14 kcal mol^{-1}). It was also pointed out that, because of the strong π -accepting ability of the NO unit, the electron density at the central atom is reduced, thereby aiding the η^2 -type coordination of the hydrazido(1-) ligands.

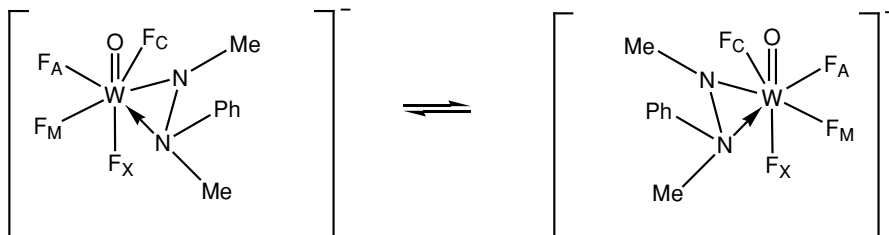
The effect of substituents in hydrazine on how the ligand is coordinated to the central atom was also noted in [63]. For example, the reaction of WOF_4 (or WF_6) with 2,4-dinitrophenylhydrazine leads to the formation of an octahedral complex with the $\text{W}=\text{N}$ bond:



Here, terminal bonding of the hydrazido ligand takes place. This is attributed to the low donor ability of the nitrogen atom bearing the electron withdrawing 2,4-dinitrophenyl moiety.

If hydrazine or hydrazone that do not contain electron-withdrawing groups are used, a different type of coordination should be expected. In fact, the study of the reaction of *N, N'*-dimethylphenylhydrazine with WOF_4 showed that a

complex with η^2 -coordinated hydrazido ligand is formed, whose structure is similar to that of W(VI) oxo fluoro complexes with O,N-two-center ligands. This complex, like the latter complexes, is characterized by hindered rotation of the ligand [64]:



This is evidenced by the changes observed in the ^{19}F NMR spectrum with increasing temperature (Table 3.6, Figure 3.10). Using the Eyring equation for

Table 3.6 Temperature dependence of ^{19}F chemical shifts and coupling constants of some W(VI) complexes with N, N-two-center ligands [64,65,69]

Complex	Chemical shift	δ (^{19}F) (ppm)		Coupling constant	$^2J(^{19}\text{F}, ^{19}\text{F})$ (Hz)		ΔG^\ddagger_T (kJ mol $^{-1}$)	T (K)
		-25 °C	+40 °C		-25 °C	+40 °C		
[WOF $_4$ (MeNNMePh)] $^-$	F $_A$	-44.1	-42.1	F $_A$ -F $_C$	125.0	111.0 a	52	273
	F $_C$	-85.4	-81.9	F $_A$ -F $_M$	96.0	111.0 a		
	F $_M$	-88.5	-81.9	F $_A$ -F $_X$	56.0	55.0		
	F $_X$	-102.0	-100.0	F $_C$ -F $_M$	39.0	b		
				F $_C$ -F $_X$	42.0	53.0 a		
[WOF $_4$ (Me $_2$ NNPh)] $^-$	F $_A$	-30.1	-29.5	F $_M$ -F $_X$	62.0	53.0 a	59	301
	F $_C$	-78.7	-79.4	F $_A$ -F $_C$	135.6	121.4 a		
	F $_M$	-95.8	-96.0	F $_A$ -F $_M$	107.1	121.4 a		
	F $_X$	-99.7	-98.0	F $_C$ -F $_M$	41.6	b		
				F $_C$ -F $_X$	42.9	54.8 a		
[WOF $_4$ (Me $_2$ NN i Pr)] $^-$	F $_A$	-46.0	-45.5	F $_M$ -F $_X$	66.7	54.8 a	64	313
	F $_C$	-79.4	-80.2	F $_A$ -F $_C$	132.5	116.5 a		
	F $_M$	-110.9	-111.4	F $_A$ -F $_M$	100.4	116.5 a		
	F $_X$	-99.7	-98.2	F $_A$ -F $_X$	52.2	53.0		
				F $_C$ -F $_M$	34.5	b		
[WOF $_4$ (PhMeNN i Pr)] $^-$	F $_A$	-42.1	-42.0	F $_C$ -F $_X$	44.2	57.5 a	>70	333
	F $_C$	-74.2	-74.5	F $_M$ -F $_X$	70.7	57.5 a		
	F $_M$	-95.4	-95.0	F $_A$ -F $_C$	132.5	132.5		
	F $_X$	-97.1	-96.7	F $_A$ -F $_M$	100.7	100.7		
				F $_A$ -F $_X$	51.4	51.4		
[WOF $_4$ (PhNN=CMe $_2$)] $^-$	F $_A$	-14.6	-14.0	F $_C$ -F $_M$	41.1	41.1	61	313
	F $_C$	-68.6	-69.3	F $_C$ -F $_X$	42.8	42.8		
	F $_M$	-87.8	\sim -88	F $_M$ -F $_X$	66.0	66.0		
	F $_X$	-108.2	-107.7	F $_A$ -F $_C$	138.3	130.0 a		
				F $_A$ -F $_M$	118.8	130.0 a		

a Splitting constant (dynamic averaged coupling).

b Not observable due to line broadening

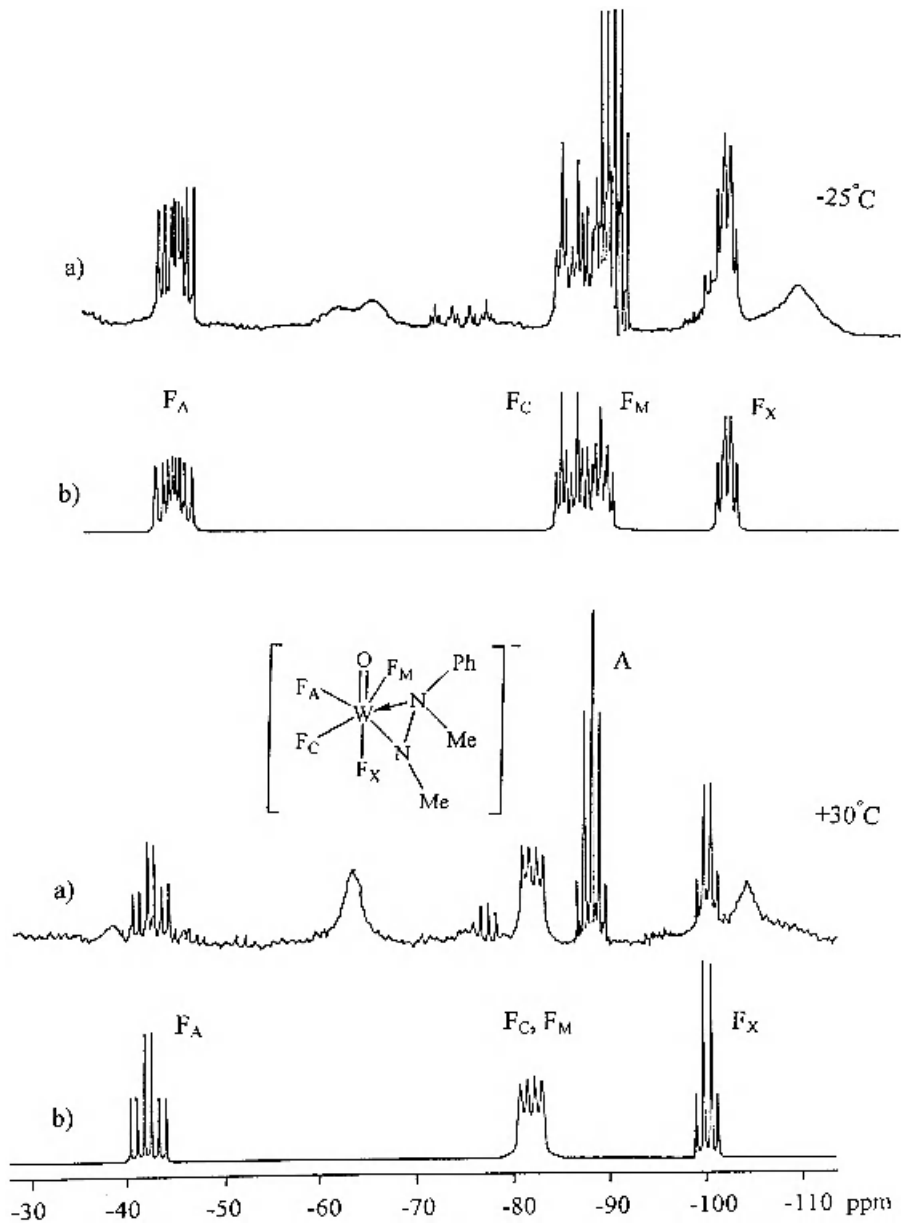


Figure 3.10 ^{19}F NMR spectra of the $[\text{WOF}_4(\text{MeNNMePh})]^-$ complexes at -25°C and $+30^\circ\text{C}$: (a) experimental spectrum; (b) theoretical spectrum; A, quintet of the axial fluorine atom from WOF_5^- .

a rough estimation of the energy barrier [40] for the ligand rotation in this complex gives a value of $\Delta G^{\ddagger}_{273} = 52 \pm 2 \text{ kJ mol}^{-1}$ ($12.4 \pm 0.5 \text{ kcal mol}^{-1}$) for the temperature of coalescence of the signals from two equatorial fluorine atoms F_C and F_M in the ^{19}F NMR spectrum.

The formation of pentagonal-bipyramidal complexes with a η^2 coordinated hydrazido(l-) ligand is also observed upon the interaction of WOF_4 with other di- and trisubstituted hydrazines in the presence of triethylamine [65]. This is indicated both by the high values of $^2J(^{19}\text{F}_A-^{19}\text{F}_C)$ and $^2J(^{19}\text{F}_A-^{19}\text{F}_M)$, and by the positions of the signals in the ^{19}F NMR spectra.

The complexes with dihapto-coordinated isopropyl-substituted hydrazido ligands are characterized by high barriers to rotation of the organic ligand. In particular, the free activation energy at the temperature of coalescence of the F_C and F_M signals for most hydrazido complexes is within $50\text{--}60 \text{ kJ mol}^{-1}$ ($\approx 12\text{--}14 \text{ kcal mol}^{-1}$), whereas for the 1,1-dimethylisopropylhydrazido complex $[\text{WOF}_4(\text{Me}_2\text{NN}^i\text{Pr})]^-$ at 313 K, only the multiplicities of these signals collapse (Table 3.6). According to the calculations in [57], this spectral pattern corresponds to $\Delta G^{\ddagger}_{313 \text{ K}} = 64.1 \text{ kJ mol}^{-1}$ ($15.3 \text{ kcal mol}^{-1}$). In the ^{19}F NMR spectrum of $[\text{WOF}_4(\text{PhMeNN}^i\text{Pr})]^-$, no indication of the rotation of the organic ligand are observed even at 333 K, which indicates that $\Delta G^{\ddagger}_{333 \text{ K}}$ is $> 70 \text{ kJ mol}^{-1}$ ($> 17 \text{ kcal mol}^{-1}$). This is presumably associated with considerable steric hindrances induced by the bulky isopropyl group as the hydrazido ligand rotates.

The complexation pattern of hydrazines largely resembles that considered for secondary amines, ketimines, and O,N-two-center ligands, with only one substantial difference: an initial reaction stage yields a neutral complex with molecular hydrazine: $[\text{WOF}_4(\text{R}^1\text{R}^2\text{N}-\text{NR}^3\text{R}^4)]$, where $\text{R} = \text{H, Me, Et, } i\text{-Pr, and Ph}$ in various combinations. The spectral parameters determined indicate that the complexes are pentagonal bipyramidal, and hydrazine is coordinated in the equatorial plane through two nitrogen atoms [66,67]. The involvement of the nitrogen lone electron pairs in the coordination to tungsten hampers the inversion of their configuration, resulting in the appearance of isomers differing in the orientation of the hydrazine substituent in the complex. The orientation of bulkier substituents toward the double-bonded oxygen atom is preferable. For none of the numerous neutral tungsten complexes with hydrazines studied thus far, temperature-induced changes in NMR spectra are observed. This points to a high barrier to rotation of the coordinated hydrazine in a complex.

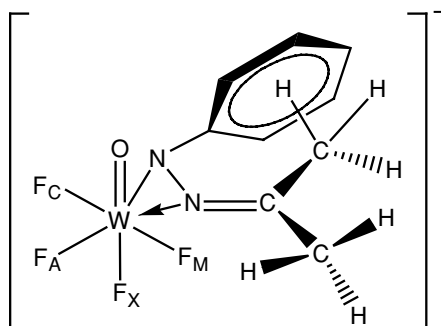
3.2.2 Isomerism of Tungsten Fluoro complexes with Mono- and Disubstituted Hydrazones

In the class of hydrazones, the properties of molecules are primarily determined by the behavior of the atomic triad $\text{N}=\text{N}=\text{C}$. In reactions with tungsten halides, these compounds behave similarly to hydrazines and simple oximes.

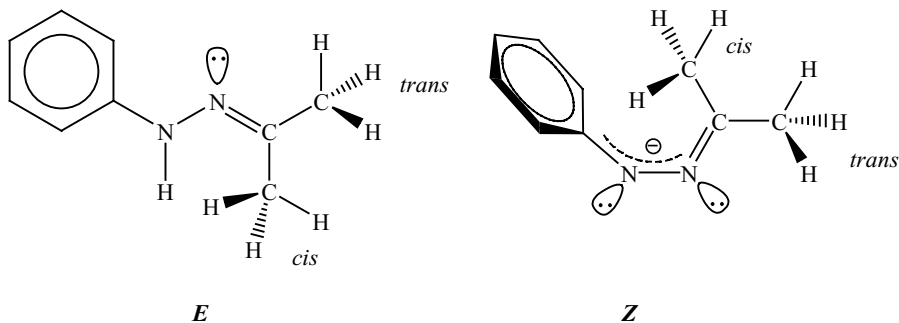
In fact, the hydrazone coordination compounds exhibit, as do the complexes with substituted hydrazines and oximes, isomer forms characterized by various orientations of the substituents at the nitrogen atom of the amine group and/or carbon atom of the carbonyl moiety [68].

The study of the interaction between WOF_4 and phenylhydrazone of acetone in acetonitrile showed [69] that the reaction proceeds similarly to the case with simple oximes [9,57,46], ketimines [39], and secondary amines [14,70].

According to the ^{19}F , ^1H , ^{13}C , and ^{15}N NMR data, the final reaction product $[\text{WOF}_4(\text{PhNN}=\text{CMe}_2)]^-$ has the shape of a pentagonal bipyramid, with both nitrogen atoms of the hydrazone ion situated in the equatorial plane [69]:



Note that, while the free hydrazone has a planar structure with *E*-configuration with respect to the N–N bond, the coordinated ligand adopts the *Z*-configuration with the phenyl ring rotated by 90° with respect to the hydrazone fragment:



This configuration is also confirmed by the fact that, in the ^{13}C NMR spectrum with broad-band proton decoupling, the signal from the *trans*- CH_3 group in the complex is a doublet with a coupling constant of 6.2 Hz, possibly caused by the direct through-space coupling between the methyl-group carbon nucleus and the F_M nucleus.

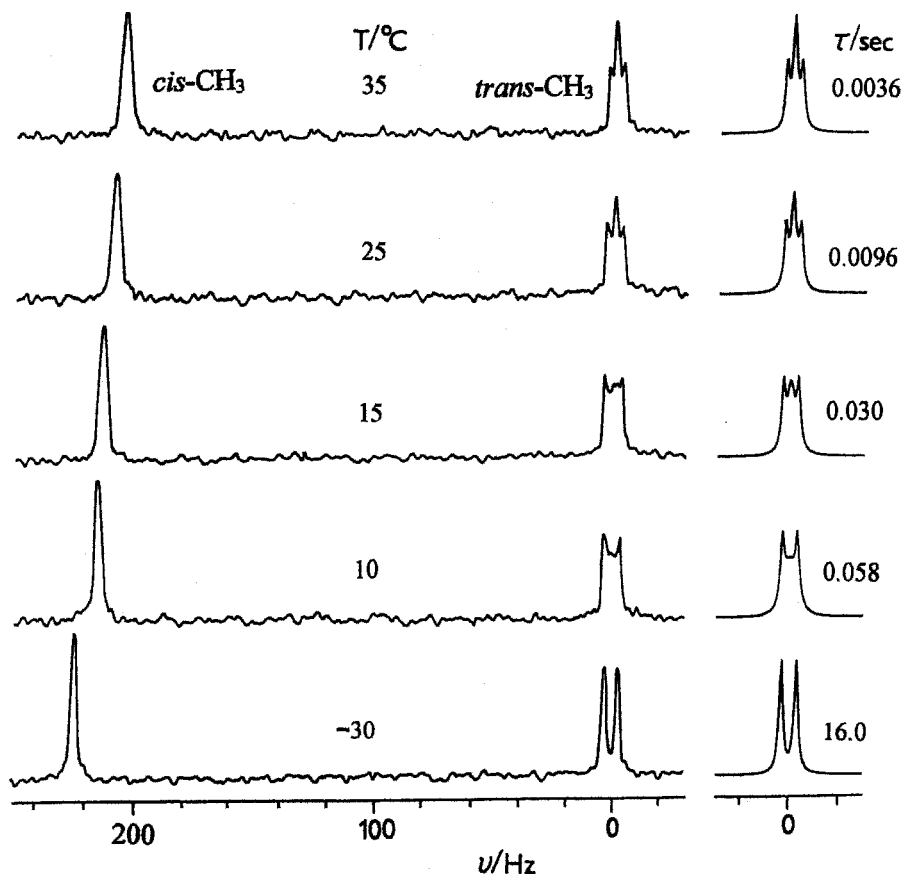
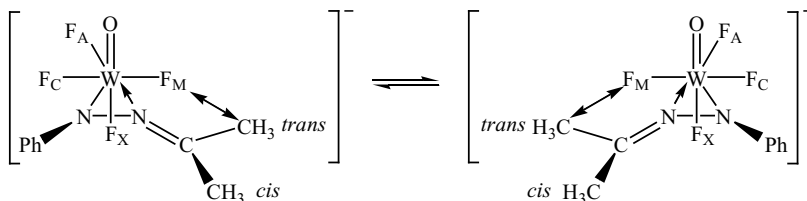


Figure 3.11 Temperature dependence of the methyl resonances in ^{13}C NMR spectra of the coordinated $(\text{PhN}=\text{N}=\text{CMe}_2)^-$ complex anion: (left) experimental spectra; (right) theoretical lineshape behavior of the trans-CH_3 resonance calculated as a function of the lifetime τ . Reproduced with permission from S. G. Sakharov *et al.*, *Inorg. Chem.* **35**(19), 5514 (1996) [69]. Copyright (1996) American Chemical Society.

Increasing the temperature leads to major changes in the ^{19}F NMR parameters of the F_C and F_M ligands (Table 3.6). The resonances of the F_C and F_M fluoro ligands are considerably broadened, and the splitting of F_A and F_X resonances due to $^2J(^{19}\text{F}, ^{19}\text{F})$ coupling with F_C and F_M is averaged. At the same time in the ^{13}C NMR spectra, the signal of the trans-CH_3 carbon gradually transforms from a doublet to a triplet (Figure 3.11). These changes in NMR spectra indicate intramolecular dynamic processes in the tungsten coordination sphere.

The $[\text{WOF}_4(\text{PhNN}=\text{CMe}_2)]^-$ complex can exist in two stereoisomeric forms, which cannot be directly distinguished by NMR spectroscopy:

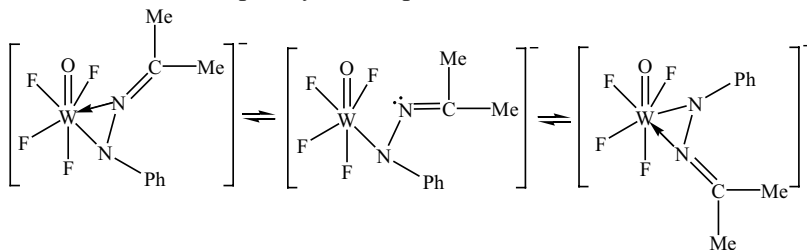


At higher temperatures, intramolecular transformation from one isomer to its mirror image occurs. The residence time of the complex in each of the stereoisomeric forms (between two successive interconversions) decreases with increasing temperature.

Changes in the ^{19}F and $^{13}\text{C}\{\text{H}\}$ NMR spectra of the $[\text{WOF}_4(\text{PhNN}=\text{CMe}_2)]^-$ anion with an increase in temperature are analogous to those observed in the spectra of molybdenum and tungsten oximate complexes described in Section 3.1.1.

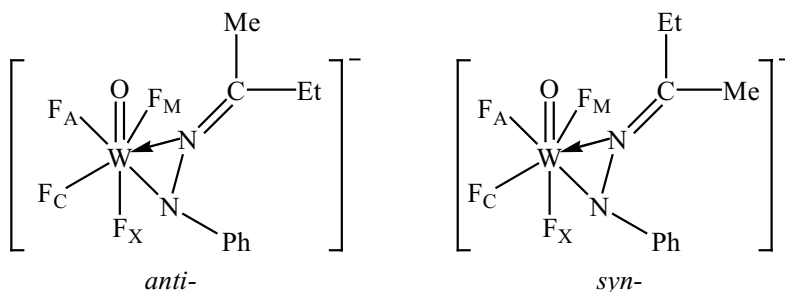
Calculated ^{13}C NMR spectra for this type of dynamic exchange with the values of averaged lifetime τ are presented in Figure 3.11. The following values of activation parameters of intramolecular rotation of the $(\text{PhNN}=\text{CMe}_2)^-$ ligand in the coordination sphere of WOF_4 are derived from the lineshape analysis: $\Delta G^\ddagger_{284} = 62.34 \pm 0.25 \text{ kJ mol}^{-1}$; $\Delta H^\ddagger = 78.5 \pm 0.5 \text{ kJ mol}^{-1}$; $\Delta S^\ddagger = 56.78 \pm 1.84 \text{ J mol}^{-1} \text{ K}^{-1}$ [69].

Considering the question of the paths of isomerization of $[\text{WOF}_4(\text{PhNN}=\text{CMe}_2)]^-$, it should be mentioned that in the ^{13}C NMR spectra the width of the signal of the phenyl *ortho* carbon atoms in the complex decreases with increasing temperature [69]. This is accounted for by the fact that, in the η^2 -coordinated ligand, free rotation of the phenyl group about the N–C bond is hindered due to spatial proximity of the protons of the *cis*-methyl group and the *ortho* protons of the phenyl ring. This may lead to a magnetic nonequivalence of the *ortho* carbon atoms in the first place and, consequently, to their broadening in the low-temperature ^{13}C NMR spectrum. With increasing temperature, the signals narrow, which may be due to free rotation of the phenyl group of the coordinated ligand. Such a situation may take place when the mechanism of isomerization of the complex with η^2 -coordinated hydrazonate ion occurs via cleavage and subsequent formation of the W–N(imine) bond with simultaneous rotation of the ligand around the W–N(amine) bond, i.e. through the formation of an intermediate open-cycle complex:



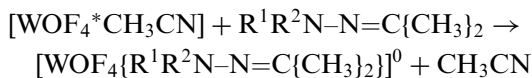
The high positive value of entropy of activation of the process that is obtained is also in accordance with this conclusion.

The structurally similar complexes with η^2 -coordinated hydrazone ion were obtained by the reaction of WOF_4 with acetone methylhydrazone, acetaldehyde phenylhydrazone, and ethylmethylketone phenylhydrazone [68]. In solution, ethylmethylketone phenylhydrazone exhibits two complex isomers of different stability, due to the *syn*- and *anti*-arrangement of the coordinated organic ligand:

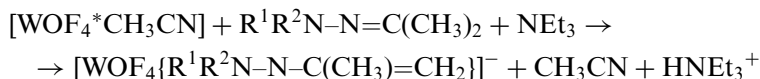


A rough estimation of the energy barrier for the ligand rotation, at the temperature of disappearance of the multiplicity of the F_C and F_M signals in the spectrum, gives the value $\Delta G^\ddagger_{318\text{K}} = 64.4 \text{ kJ mol}^{-1}$ (15.4 kcal mol⁻¹) for both isomers [68].

We studied [68] the reaction between tungsten oxotetrafluoride and the disubstituted acetone hydrazones $\text{R}^1\text{R}^2\text{NN}=\text{CMe}_2$ ($\text{R}^1 = \text{Me}$; $\text{R}^2 = \text{Me, Et, Ph}$). It was found that, if a reactant capable of accepting protons is not present in a sufficient amount, neutral complexes are formed in solution by displacing CH_3CN molecules from the coordination sphere of tungsten:



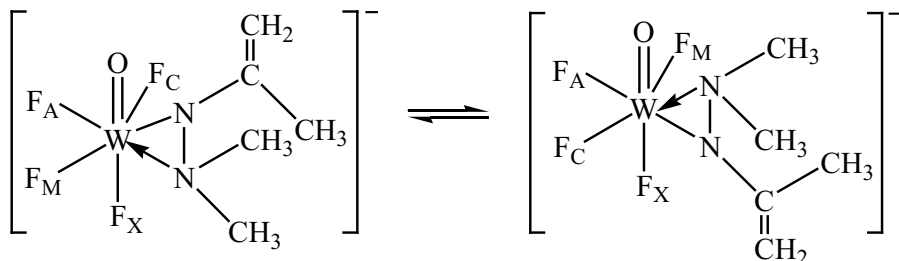
In the presence of an excess triethylamine the reaction proceeds according to the scheme:



and is accompanied by the formation of anionic complexes with deprotonated ligands present in an enehydrazine form. In each case, the complexes are pentagonal bipyramidal, with both nitrogen atoms of the coordinated ligand situated in the equatorial plane.

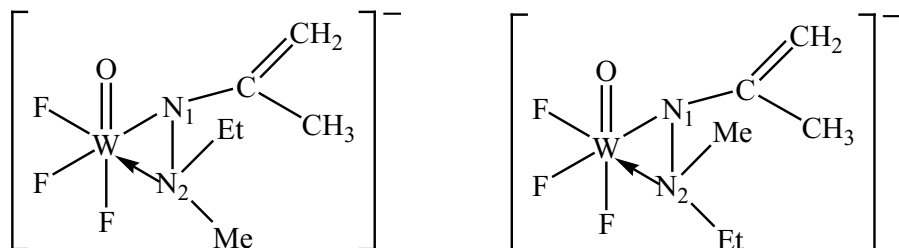
For the complex which involves the enehydrazine form of acetone dimethylhydrazone bearing two identical substituents (CH_3 groups) at the amine nitrogen atom, two NMR-indistinguishable enantiomers are possible. Nevertheless, the temperature increase brings about changes of the ¹⁹F NMR spectrum

(averaging the positions of the F_C and F_M signals, J_{AC} and J_{AM} , J_{CX} and J_{MX}), which indicates a conversion of one optical isomer into another *via* the rotation of the coordinated ligand:



The calculations in [68] showed that the barrier to isomerization is $\Delta G^{\ddagger}_{273\text{K}} = 53.6 \pm 2 \text{ kJ mol}^{-1}$ ($12.8 \pm 0.5 \text{ kcal mol}^{-1}$).

In a complex with the enhydrazine form of acetone ethylmethylhydrazone in solution, two isomers were observed at -30°C , which differ from each other with respect to orientation of the Et and Me groups at the nitrogen atom of the amine group. Here, the isomer in which the ethyl group is oriented toward the multiply bonded oxygen atom is predominant:



When the temperature increases, the ^{19}F NMR spectra exhibit changes, which indicate the mutual conversion of the isomers. The transition from one isomer to another can only occur via the breakage and the subsequent formation of the W–N(2) bond, with the simultaneous inversion of configuration of the amine nitrogen atom.

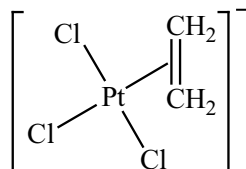
3.3 NATURE OF BONDING OF *n*-DONOR TWO-CENTER LIGANDS IN d^0 TRANSITION METAL COMPLEXES

The nature of bonding of two-center ligands with metal atoms has long been a subject of intensive discussion [9,71–77]. Thus, the bonding of molecular oxygen to a central atom is usually described in similar terms to the bonding in acetylene [78] and olefin [79] π -complexes. Here, the π -bond is formed as a result of overlap between the π -bonding orbital of oxygen and a vacant hybridized

(s, p, d) orbital of the metal. In diperoxocomplexes of chromium, the bonding of O_2^{2-} was also assumed to be analogous to that in the olefin and acetylene compounds of transition metals. The sole difference is that the central atom in peroxocomplexes acts only as an acceptor of electrons from the molecular orbitals of the O_2^{2-} ligand [72].

The data obtained on the structures of d^0 complexes with n-donor two-center ligands allow some conclusions to be drawn concerning the nature of bonds between the organic ligand and the central atom. The compounds in question possess two characteristic features: η^2 -type coordination of a two-center ligand to the central atom and the hindered internal rotation of this ligand. These structural features of complexes with two-center ligands prompt the idea that there exists an analogy between the binding of n-donor two-center ligands in these complexes and binding of olefins in π -complexes.

One of the typical examples of the transition metal π complexes is the platinum(II) complex with ethylene, $[PtCl_3(C_2H_4)]^-$, which is known as the anion in Zeise's salt:



In this complex, the molecule of coordinated ethylene occupies a single coordination site and is oriented perpendicularly to the plane of the square anion. In both complexes mentioned above (i.e., the complexes with two-center ligands and the olefin π complexes), the bonding of ligands to the central atom occurs via the *dihapto* type. Moreover, the rotation of olefin about the metal-ligand bond was observed both in Zeise's salt and in some other π complexes. Thus, the free energies for the activation of olefin (L) rotation in complexes $(PR_3)PtCl_2 - L$ and $PtCl(acac) - L$ depend on the nature of R and L, and vary within 44.4–67 kJ mol^{-1} (10.6–16 kcal mol^{-1}) [80].

For bonding to the central atom, an η^2 coordinated organic ligand uses two lone electron pairs located mainly in p orbitals. As in ethylene (Figure 3.12a), linear combinations of these orbitals can produce bonding and antibonding molecular orbitals (Figure 3.12b). However, unlike in ethylene, in which the antibonding orbital is vacant, in the case of an n-donor two-center ligand, both orbitals are occupied by electron pairs. Whereas in olefin complexes the metal accepts electrons from the bonding π orbital and functions as a donor with respect to the antibonding ligand orbital, the η^2 coordination in the complexes with two-center ligands requires that the central atom with d^0 configuration be able to accept electrons from both bonding and antibonding π orbitals of the organic ligand. Thus, the structure of the complexes with n-donor two-center ligands is similar to the structure of π complexes of the type of Zeise's salt. In this connection it would be helpful to mention a definition of π complexes given

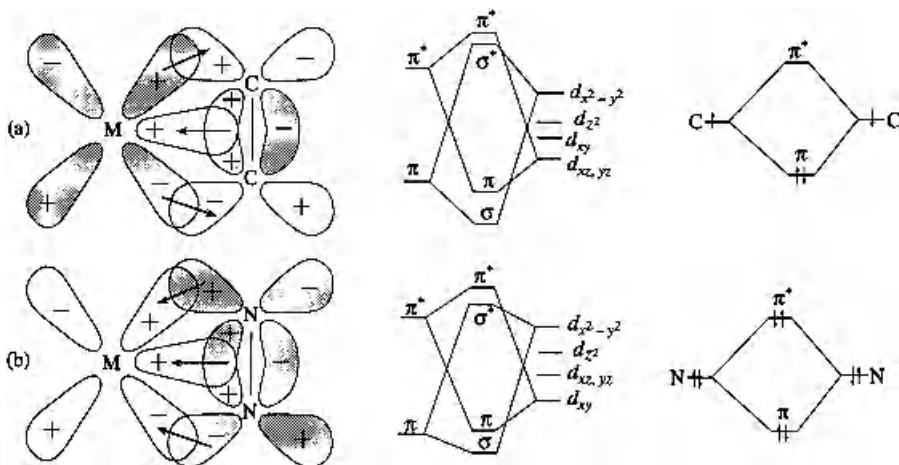


Figure 3.12 Model of bonding for olefin (a) and the N,N-two-center ligand (b) in transition metal complexes. Reproduced with permission from S. G. Sakharov and Yu. A. Buslaev, *Russ. J. Inorg. Chem.* **38**(9), 1385 (1993) [41].

by Dewar and Dougherty [81]. According to this, π complexes are compounds containing dative bonds, in which the role of a donor is played by a filled π molecular orbital.

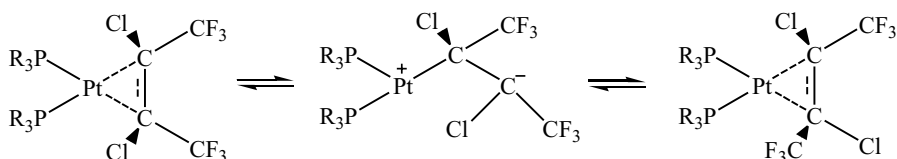
In fact, both complexes with olefins or the related compounds, and the complexes with n-donor two-center ligands exhibit a direct dative bond of the σ type (Figure 3.12). This bond forms as a result of the overlap between the vacant d AO of proper symmetry of the metal and the filled π -bonding MO of the ligand. By this definition, the complexes with n-donor two-center ligands can be treated as π complexes. The nature of the bonds in these complexes is the same as that in the classic olefin π complexes. The two systems differ only in the concept used to describe the bond formation from the component fragments. In olefin π complexes of type of Zeise's salt, the central atom acts simultaneously as a donor and acceptor of electrons with respect to the ligand. Conversely, in the complexes with n-donor two-center ligands, the central atom performs only as an acceptor.

3.4 MECHANISM OF INTERNAL HINDERED ROTATION OF η^2 -BOUND LIGANDS

The observed analogy in the nature of bonding of the η^2 coordinated ligands to the central atom in the complexes with olefins as well as in those with n-donor two-center ligands provides a better understanding of the factors responsible for the similarities and differences in the structure, properties, reactivity and dynamic behavior of these complexes. The use of the same models

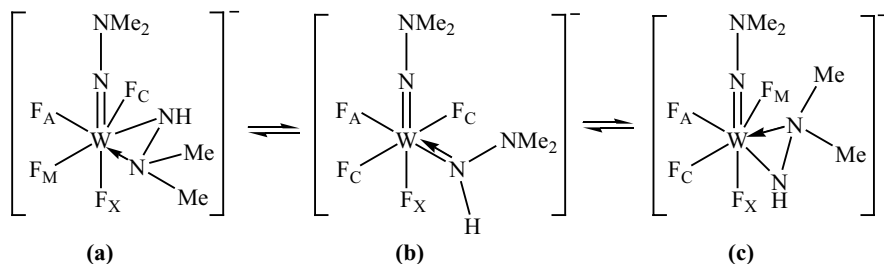
for the description of bonds in complexes of the two types allows a comparative analysis of their properties to be made and formulated in the same terms.

In complexes with η^2 coordinated ligands, two isomers may exist with their mutual interconversion occurring through the rotation of a ligand about the metal–ligand bond. There are two possible methods of isomerization. The first of these retains the η^2 coordination in the intermediate state (the propeller-like rotation of the ligand). The second involves the formation of an intermediate σ complex. It is believed that the rotation of olefin in most of the platinum π complexes proceeds by the first method. On the other hand, the *cis*–*trans* isomerization observed in some olefin complexes can only proceed via the rupture and subsequent formation of one of the metal–ligand bonds, that is, via the σ – π rearrangement [82]:



Such rearrangements are of both theoretical and practical interest, because they play an important role in homogeneous catalytic processes. Because the η^1 coordinated olefin molecules occur in a more or less excited state, the presence of the σ – π rearrangement is usually judged based on the reaction products and other indirect evidence.

The lifetime of the σ complex is normally rather short, which precludes determination of the manner of ligand coordination by spectroscopic methods. Nevertheless, in the case of the reaction of WOF_4 with the nonsymmetrical dimethyldiazine, the solution was found to contain simultaneously two isomeric complexes differing in the type of bonding (monohapto and dihapto) of the organic ligand to the central atom. In other words, keeping to the terminology accepted for the olefin π complexes, we found the σ and π isomers of the tungsten complex with hydrazido ligands [83]:

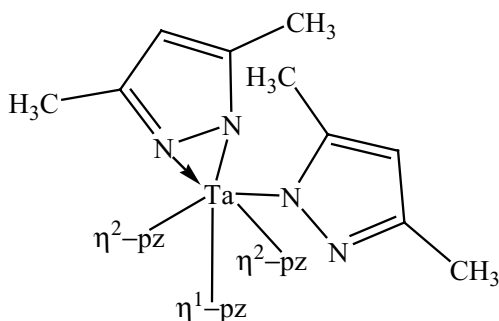


According to NMR data, the π isomer (a, c) is shaped like a pentagonal bipyramid, whose equatorial plane contains both nitrogen atoms of the

hydrazido ligand. In the σ isomer (**b**), the organic ligand is coordinated through only one nitrogen atom. The σ complex is only 3.5 kJ mol^{-1} ($0.84 \text{ kcal mol}^{-1}$) less stable than the π complex, which is due to two stabilizing factors, namely, the formation of a hydrogen bond between the NH-group proton and the axial fluorine atom (F_X) and the $p_\pi-d_\pi$ interaction between the lone electron pair of the coordinated nitrogen atom and the vacant d_{xy} orbital of tungsten.

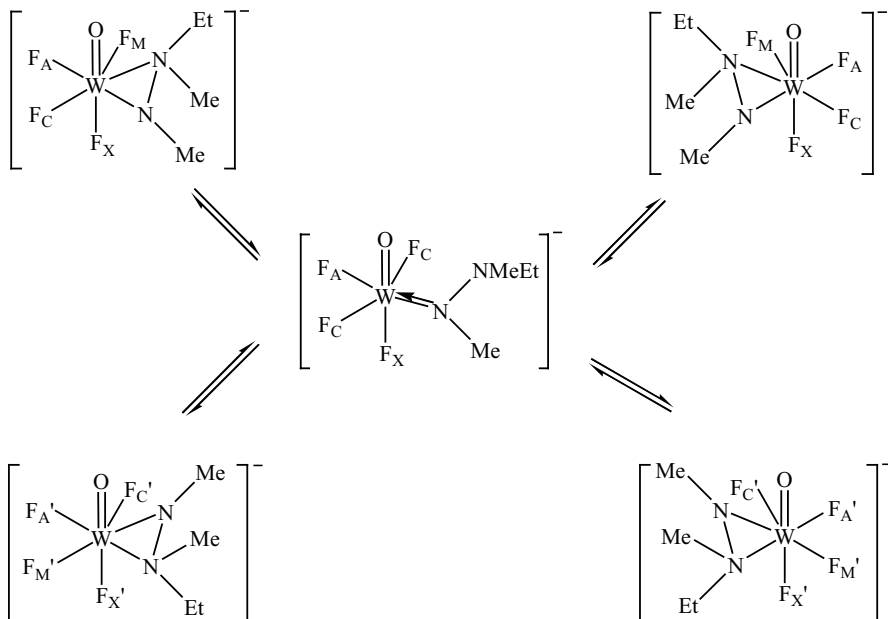
This follows from the observed fact that the bond configuration at the equatorial nitrogen atom is flattened and, hence, the four nitrogen atoms of the coordinated ligands and the proton of the NH group are located in the axial plane of the complex. The σ isomer of the hydrazido complex can be regarded as the intermediate en route from one optical π isomer (**a**) to the other (**c**). In the said example given the equilibrium between η^2 and η^1 isomers exists with $K = 4.7$, but no exchange is observed for temperatures from -25 to 30°C [83].

As shown by X-ray diffraction, the η^1 - η^2 isomerism is also observed for the tantalum(V) complex $[\text{Ta}(\eta^1\text{-pz})_2(\eta^2\text{-pz})_3]$, where pz is the pyrazolato ligand ($\text{Me}_2\text{C}_3\text{HN}_2$):

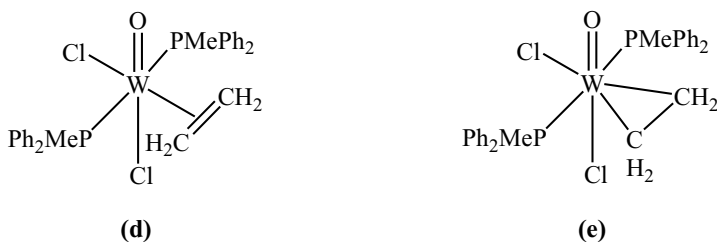


However, in contrast with the previous case, the solution apparently shows a rapid exchange between these isomers, since the ^1H NMR spectrum of this complex in toluene- d_8 between $+20$ and -80°C showed only one type of pz ligand [84].

According to these data, the mechanism of the internal rotation of the organic ligand in the hydrazido complexes includes the formation of an intermediate compound with a monohapto coordination of hydrazine, i.e. a π - σ rearrangement. This is also indicated by the fact that in the case of 1,2-dimethylethylhydrazine, isomers with different orientations of the Et and Me groups at the formally neutral nitrogen atom were detected in solution at -30°C . The isomer in which the Et group is oriented toward the doubly bonded oxygen atom proved to be more stable. We found that, as the temperature is raised, the isomers interconvert. Taking into account the fact that both isomers can exist as a pair of enantiomers, this transformation can occur via rotation of the ligand with simultaneous inversion of configuration at the amine nitrogen atom, i.e. with the intermediate formation of a complex in which the ring is opened [66]:



This mechanism accounts for the fact that the energy barrier to the ligand rotation in neutral complexes of tungsten with hydrazines is substantially higher ($>80 \text{ kJ mol}^{-1}$) than that in anionic complexes. The decrease in the barrier to ligand rotation in anionic complexes is due to the stabilization of the σ complex by the $p_{\pi}-d_{\pi}$ interaction between the lone electron pair of the coordinated nitrogen atom and the vacant d_{xy} orbital of tungsten. In the case of neutral complexes, this stabilization factor does not work because the nitrogen atom in the σ isomer has no lone electron pair. In this context, it should be noted that a high barrier to rotation of the coordinated ethylene ($>70 \text{ kJ mol}^{-1}$) was found in the tungsten π complex $[\text{W}(\text{O})\text{Cl}_2(\text{C}_2\text{H}_4)(\text{PMePh}_2)]$ [85]. According to an X-ray study the ethylene ligand lies *cis* to the oxo group and is oriented perpendicular to the tungsten–oxygen multiple bond. The ethylenic carbon–carbon bond length of 1.404 \AA is substantially longer than that of free ethylene (1.337 \AA). The complex can be represented by two equivalent structures (d, e):

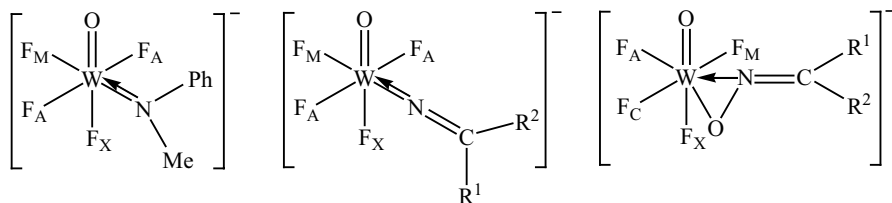


In one of these (d), the coordination geometry around the tungsten (d^2 configuration) center can be described as a distorted (the P–W–P angle is only

154.7°) octahedron with the ethylene ligand occupying one site. In the other (e), the coordination geometry about the tungsten (d^0 configuration) center can be described as a pentagonal bipyramid with the organic ligand ($C_2H_4^{2-}$) occupying two sites. Thus, the structure of the $[W(O)Cl_2(C_2H_4)(PMePh_2)]$ complex is analogous to those of the above tungsten(VI) complexes with hydrazines and other n-donor two-center ligands. Following this analogy, we can reach the conclusion that if the rotation of the olefin ligand is through the intermediate formation of a complex with an opened structure, the high barrier to rotation can be explained as in the case of neutral complexes with hydrazines by the lack of a stabilizing factor in the transition state. If the coordinated olefin experiences the 'propeller-like' rotation (with retention of η^2 bonding in the transition state), the high barrier to rotation can be due to a significant steric crowding between the phosphanes and the ethylene ligand. Moreover, according to the authors' opinion [85], the substantial barrier to ethylene rotation is indication of the importance of π back-bonding in these d^2 oxo compounds.

The orientation of the olefin in a π complex (Zeise's salt) is known [86] to be mainly defined by steric factors. In the study of tungsten complexes with n-donor two-center ligands, ketimines, and amines, we concluded that the electronic rather than steric factor exerts the crucial effect on the ligand orientation in the complex.

Thus, in the amido complexes of tungsten, the coordinated ligand has a planar structure and is oriented perpendicularly to the equatorial plane [13,14]. In the complexes with ketimines [39] the ligand is also planar, but is situated in the equatorial plane:



In both cases, the flattening of the configuration of the coordinated nitrogen atom is due to the $p_\pi-d_\pi$ interaction between its lone electron pair and the vacant d_{xy} orbital of the tungsten atom—precisely the factor that determines the ligand orientation in the complex. In the above mentioned octahedral complexes containing $W=O$ or $W=N$ groups in axial positions, the lone electron pair of the ligand nitrogen atom interacts, for the most part, with the d_{xy} orbital, rather than with the d_{xz} orbital of the tungsten atom. This is caused by the overlap of either the p orbitals of oxygen of $W=O$, or the p orbitals of nitrogen of the $W=N$ group, with the d_{xz} and d_{yz} orbitals of the central atom. This hinders the $p_\pi-d_\pi$ type interaction of the lone electron pair of the nitrogen atom of the coordinated ligand with the d_{xz} and d_{yz} orbitals, but not with the d_{xy} orbital. For the same reason, in tungsten complexes with the n-donor two-center ligands, the interaction of the π^* MO of the ligand is more favorable with the

d_{xy} orbital of tungsten than with the d_{xz} orbital. Therefore, the organic ligand is situated, irrespective of the volume of substituents at the n-donor atoms, in the equatorial plane of the complex.

Similar speculations can evidently be applied to account for both the orientation and the high barrier to rotation of the coordinated olefin in $[\text{W}(\text{O})\text{Cl}_2(\text{C}_2\text{H}_4)(\text{PMePh}_2)]$. Indeed, in propeller-like olefin rotation, the transition state (with the ethylene molecule perpendicular to the equatorial plane) appears to be destabilized due to the lack of interaction of the ligand π^* -MO with the d_{xz} orbital of tungsten.

In contrast to this, in tantalum fluoroximates, all the d orbitals of the central atom are equivalent, and the oximato group could be situated with equal probability in either the equatorial or the perpendicular plane. This produces a sharp decrease in the barrier for ligand rotation in tantalum fluorocomplexes. Correspondingly, the ^{19}F NMR spectra show equivalent signals from equatorial fluorine atoms even at -30°C [59]. Probably, the equivalence of d orbitals of the central atom also accounts for the low rotational barrier of pyrazolato ligands in the complex $[\text{Ta}(\eta^1\text{-pz})_2(\eta^2\text{-pz})_3]$ [84].

4 CONCLUSION

We considered the structure and dynamic behavior of Group 5 and 6 d^0 transition metal fluoro complexes with n-donor O,N- and N,N-two-center ligands in nonaqueous solutions, which allowed us to suggest a model of bonding of n-donor two-center ligands in d^0 transition metal complexes. The survey of available data allowed us to draw an analogy between the structure and dynamic behavior of these complexes and those of olefin π complexes.

The structures and dynamic behaviors of amido, ketimido, oximato, hydrazido, and hydrazonato complexes of Group 5 and 6 transition metals have been compared. The factors that determine the barrier to rotation of coordinated ligands have been discussed.

The formation conditions and interconversions of the stereoisomeric complexes with η^2 coordinated n-donor two-center ligands were considered. The mechanism of these transformations was elucidated, stating that a complex with open structure, i.e., a complex with ligand coordination through only one n-donor atom, is formed in the transition state.

Needless to say that the data surveyed in this review do not exhaust the whole body of information on the dynamic behavior of transition-metal complexes by NMR, but they can be a basis for further, more sophisticated investigations in this area of knowledge.

5 REFERENCES

1. L. Canovese, V. Lucchini, C. Santo, F. Visentin, and A. Zambon, *J. Organomet. Chem.* **642**, 58 (2002).

2. R. A. Hoffman and S. Forsén, *Prog. NMR Spectrosc.* **1**, 173 (1966).
3. (a) E. W. Abel, T. P. J. Coston, K. G. Orrell, V. Šik, and D. Stephenson, *J. Magn. Reson.*, **70**, 34 (1986); (b) P. S. Pregosin and R. Salzmann, *Coord. Chem. Rev.* **155**, 35 (1996); (c) K. Selvakumar, M. Valentini, P. S. Pregosin, A. Albinati and F. Eiseenträger, *Organometallics* **19**, 1299 (2000).
4. G. Binsch and H. Kessler, *Angew. Chem. Int. Ed. Engl.* **19**, 11 (1980).
5. H. M. McConnell and C. H. Holm, *J. Chem. Phys.* **28**, 430 (1958).
6. (a) R. Kubo, *J. Phys. Soc. Jpn*, **9**, 935 (1954); (b) P. W. Anderson, *J. Phys. Soc. Jpn*, **9**, 316 (1954). (c) R. A. Sack, *Mol. Phys.* **1**, 163 (1958).
7. (a) J. I. Kaplan, *J. Chem. Phys.* **28**, 278 (1958); (b) J. I. Kaplan, *J. Chem. Phys.* **29**, 462 (1958); (c) S. Alexander, *J. Chem. Phys.* **37**, 967 (1962); (d) C. S. Johnson, *J. Chem. Phys.* **41**, 3277 (1964); (e) G. Binsch, *J. Am. Chem. Soc.* **91**, no.6, 1304 (1969).
8. (a) L. M. Jackman and F. A. Cotton (eds), *Dynamic Nuclear Magnetic Resonance Spectroscopy*, Academic Press, New York, 1975. (b) B. E. Mann, in *Comprehensive Organometallic Chemistry* edited by G. Wilkinson, F. G. A. Stone, and E. W. Abel, Chapter 20, Pergamon, Oxford 1982. (c) B. E. Mann, in *Annual Reports on NMR Spectroscopy* edited by G. A. Webb, **12**, Academic Press, New York, 1982, 263; (d) S. Aime and L. Milone, *Prog. NMR Spectrosc.*, **11**, 183, (1977). (e) E. Band and E. L. Muetterties, *Chem. Rev.*, **78**, 639, (1978).
9. Yu. A. Buslaev, S. G. Sakharov, Yu. V. Kokunov, and I. I. Moiseev, *Dokl. Akad. Nauk SSSR*, **240**, no. 2, 338 (1978).
10. S. G. Sakharov and Yu. A. Buslaev, *Russ. J. Coord. Chem.* **20**, no. 1, 1 (1994).
11. Yu. A. Buslaev, Yu. V. Kokunov, and V. A. Bochkareva, *Zh. Strukt. Khim.* **13**, 611 (1972).
12. Yu. A. Buslaev, Yu. V. Kokunov, V. A. Bochkareva, and E. M. Shustorovich, *Zh. Neorg. Khim.*, **17**, no. 11, 3184 (1972).
13. S. G. Sakharov, S. A. Zarelua, Yu. V. Kokunov, and Yu. A. Buslaev, *Dokl. Akad. Nauk SSSR*, **290**, no. 1, 129 (1986).
14. S. G. Sakharov, S. A. Zarelua, Yu. V. Kokunov, and Yu. A. Buslaev, *Koord. Khim.* **13**, no. 4, 507 (1987).
15. S. G. Sakharov, Doctorate (Chem. Sci.) Dissertation, Moscow, (1992).
16. J. Sandström, *Dynamic NMR Spectroscopy*, Academic Press, London, (1982).
17. H. S. Gutowski, and C. H. Holm, *J. Chem. Phys.*, **25**, 1228 (1956).
18. Jr. R. C. Neuman, and V. Jonas, *J. Org. Chem.*, **39**, 925 (1974).
19. P. A. W. Dean, and D. F. Evans, *J. Chem. Soc.*, 1154 (1970).
20. M. H. Chisholm, F. A. Cotton, *Acc. Chem. Res.* **11**, 336 (1978).
21. M. H. Chisholm, *Polyhedron*, **2**, 681 (1983).
22. M. H. Chisholm, I. P. Rothwell, *J. Am. Chem. Soc.*, **102**, 5950 (1980).
23. M. H. Chisholm, I. P. Rothwell, *J. Chem. Soc., Chem. Commun.*, 985 (1980).
24. T. W. Coffindaffer, W. M. Westler, I. P. Rothwell, *Inorg. Chem.*, **24**, 4565 (1985).
25. M. H. Chisholm, F. A. Cotton, M. Extine, M. Millar, B. R. Stults, *Inorg. Chem.*, **15**, no. 9, 2244 (1976).
26. M. H. Chisholm, F. A. Cotton, B. A. Frenz, W. W. Reichert, L. W. Shive, B. R. Stults, *J. Am. Chem. Soc.*, **98**, 4469 (1976).
27. M. Akiyama, M. H. Chisholm, F. A. Cotton, M. W. Extine, C. A. Murillo, *Inorg. Chem.*, **16**, no. 9, 2407 (1977).
28. M. H. Chisholm, F. A. Cotton, M. W. Extine, M. Millar, B. R. Stults, *Inorg. Chem.*, **16**, no. 2, 320 (1977).
29. M. H. Chisholm, F. A. Cotton, M. Extine, B. R. Stults, *J. Am. Chem. Soc.*, **98**, no. 15, 4477 (1976).
30. (a) P. J. Walsh, F. J. Hollander, R. G. Bergman, *J. Am. Chem. Soc.*, **110**, 8729 (1988); (b) C. C. Cummins, S. M. Baxter, P. T. Wolczanski, *J. Am. Chem. Soc.*, **110**, 8731 (1988); (c) D. S. Glueck, J. Wu, F. J. Hollander, R. G. Bergman, *J. Am. Chem. Soc.*, **113**, 2041

- (1991). (d) C. C. Cummins, C. P. Schaller, G. D. Van Duyne, P. T. Wolczanski, A. W. E. Chan, R. Hoffman, *J. Am. Chem. Soc.*, **113**, 2985 (1991).
- (e) P. J. Walsh, A. M. Baranger, R. G. Bergman, *J. Am. Chem. Soc.*, **114**, 170 (1992).
- (f) T. R. Cundari, *J. Am. Chem. Soc.*, **114**, 10557 (1992).
- (g) J. de With, A. D. Horton, *Angew. Chem. Int. Ed. Engl.*, **32**, 903 (1993).
31. (a) D. S. Glueck, F. J. Hollander, R. G. Bergman, *J. Am. Chem. Soc.*, **111**, 2719 (1989). (b) M. H. Schofield, T. P. Kee, J. T. Anhaus, R. R. Schrock, K. H. Johnson, W. M. Davis, *Inorg. Chem.*, **30**, 3595 (1991). (c) R. I. Michelman, R. A. Andersen, R. G. Bergman, *J. Am. Chem. Soc.*, **113**, 5100 (1991).
32. M. J. Humphries, M. L. H. Green, R. E. Douthwaite, L. H. Rees, *J. Chem. Soc., Dalton Trans.*, 4555 (2000).
33. A. Castro, M. V. Galakhov, M. Gómez, F. Sánchez, *J. Organomet. Chem.*, **580**, 161 (1999).
34. S. Abragam, *The Principles of Nuclear Magnetism*, Clarendon, Oxford, (1961)
35. P. H. M. Budzelaar, in *gNMR*, Cherrwell Scientific Ltd., The Magdalen Centre, Oxford Science Park, Oxford, (1995)
36. V. C. Gibson, *Angew. Chem., Int. Ed. Engl.*, **33**, 1565 (1994).
37. S. Zhang, W. E. Piers, X. Gao, M. Parvez, *J. Am. Chem. Soc.* **122**, 5499 (2000).
38. I. A. Latham, G. J. Leigh, G. Huttner, I. Jibril, *J. Chem. Soc., Dalton Trans.* 377 (1986).
39. S. G. Sakharov, S. A. Zarelua, Yu. V. Kokunov, and Yu. A. Buslaev, *Dokl. Akad. Nauk SSSR*, **294**, no. 5, 1132 (1987).
40. H. Günter, *NMR Spectroscopy*, Wiley, Chichester, 1980.
41. S. G. Sakharov, Yu. A. Buslaev, *Russ. J. Inorg. Chem.*, **38**, No. 9, 1385 (1993).
42. (a) L. S. Liebeskind, K. B. Sharpless, R. D. Wilson, and J. A. Ibers, *J. Am. Chem. Soc.*, **100**, 7061 (1978); (b) D. A. Muccigrosso, S. E. Jacobson, P. A. Apgar, and F. Mares, *J. Am. Chem. Soc.*, **100**, 7063 (1978).
43. (a) K. Wieghardt, U. Quilitzsch, B. Nuber, and J. Weiss, *Angew. Chem.*, **90**, 381 (1978); (b) H. Mimoun, *Israel. J. Chem.*, **23**, 451 (1983). (c) G. P. Khare, and R. J. Doedens, *Inorg. Chem.*, **16**, no. 4, 907 (1977). (d) R. B. King, and K. N. Chen, *Inorg. Chem.*, **16**, no. 5, 1164 (1977).
44. Yu. V. Kokunov, S. G. Sakharov, I. I. Moiseev, and Yu. A. Buslaev, *Koord. Khim.*, **5**, no. 2, 207 (1979).
45. S. G. Sakharov, S. A. Zarelua, Yu. V. Kokunov, and Yu. A. Buslaev, *Dokl. Akad. Nauk SSSR*, **301**, no. 4, 909 (1988).
46. S. G. Sakharov, N. A. Ovchinnikova, and Yu. A. Buslaev, *Rus. J. Inorg. Chem.*, **40**, no.12, 1906 (1995).
47. S. G. Sakharov, N. A. Ovchinnikova, and Yu. A. Buslaev, *Dokl. Akad. Nauk*, **334**, no. 5, 1 (1995).
48. D. Grandjean, and R. Weiss, *Bull. Soc. Chim. Fr.*, 3044 (1967).
49. I. Larking, and R. Stromberg, *Acta Chem. Scand.*, **24**, 2043 (1970).
50. Z. Ruzic-Toros, B. Kojic-Prodic, F. Gabela, and M. Sljukis, *Acta Crystallogr., Ser. B: Struct. Sci.*, **33**, 692 (1977).
51. D. F. Evans, W.P. Griffith, and L. Pratt, *J. Chem. Soc.*, 2182 (1965).
52. Yu. A. Buslaev, S. P. Petrosyants, and V. P. Tarasov, *Dokl. Akad. Nauk SSSR*, **193**, 611 (1970).
53. Yu. A. Buslaev, S. P. Petrosyants, and V. P. Tarasov, *Zh. Strukt. Khim.*, **11**, 1023 (1970).
54. M. L. Martin, G. J. Martin, and J. J. Delpuech, *Practical NMR Spectroscopy*, Heyden, London, 442 (1980).
55. D. Himmelblau, *Applied Nonlinear Programming*, McGraw-Hill, New York, (1971)
56. A. Neuhaus, A. Veldkamp, and G. Frenking, *Inorg. Chem.*, **33**, 5278 (1994).
57. S. G. Sakharov, V. D. Butskii, and Yu. A. Buslaev, *Russ. J. Inorg. Chem.*, **42**, no. 9, 1398 (1997).

58. S. G. Sakharov, V. D. Butskii, N. A. Ovchinnikova, M. S. Dolmat, Yu. A. Buslaev, *Dokl Akad. Nauk*, **353**, no. 5, 634 (1997).
59. S. G. Sakharov, Yu. V. Kokunov, M. P. Gustyakova, I. I. Moiseev, and Yu. A. Buslaev, *Dokl Akad. Nauk SSSR*, **247**, no. 5, 1197 (1979).
60. S. G. Sakharov, *Russ. J. Inorg. Chem.*, **44**, No.11, 1694 (1999).
61. Z. Szabó, W. Aas, and I. Grenthe, *Inorg. Chem.*, **36**, 5369 (1997).
62. P. D. Frisch, M. M. Hunt, W. G. Kita, *et al.*, *J. Chem. Soc., Dalton Trans.*, no.11, 1819 (1979).
63. S. G. Sakharov, Yu. V. Kokunov, M. P. Gustyakova, and Yu. A. Buslaev, *Koord. Khim.*, **8**, no. 12, 1669 (1982).
64. S. G. Sakharov, Yu. V. Kokunov, M. P. Gustyakova, and Yu. A. Buslaev, *Dokl. Akad. Nauk SSSR*, **278**, no. 3, 637 (1984).
65. Sakharov, S. G., Zarelua, S. A., Kokunov, Yu. V, and Buslaev, Yu. A., *Koord. Khim.*, **17**, no. 9, 1224 (1991).
66. S. G. Sakharov, S. A. Zarelua, Yu. V. Kokunov, and Yu. A. Buslaev, *Z Anorg. Allg. Chem.*, **577**, 223 (1989).
67. S. G. Sakharov, S. A. Zarelua, Yu. V. Kokunov, and Yu. A. Buslaev, *Koord. Khim.*, **17**, no. 3, 330 (1991).
68. S. G. Sakharov, S. A. Sarelua, Yu. V. Kokunov, and Yu. A. Buslaev, *Rus. J. Coord. Chem.*, **19**, no.8, 565 (1993).
69. S. G. Sakharov, Yu. A. Buslaev, and I. Tkáč, *Inorg. Chem.*, **35**, no. 19, 5514 (1996).
70. Yu. V. Kokunov, V. A. Bochkareva, S. G. Sakharov, and Yu. A. Buslaev, *Koord. Khim.*, **11**, no. 1, 36 (1985).
71. D. Begin, F. W. B. Einstein, and J. Field, *Inorg. Chem.*, **14**, 1785 (1975).
72. D. G. Tuck, and R. M. Walters, *Inorg. Chem.*, **2**, no. 2, 428 (1963).
73. R. Hoffmann, M. M. -L. Chen., and D.L. Thorn, *Inorg. Chem.*, **16**, 503 (1977).
74. J. S. Valentine, *Chem. Rev.*, **73**, 235 (1973).
75. A. Muller, W. Jaegermann, and J. H. Enemark, *Coord. Chem. Rev.*, **46**, 245 (1982).
76. S. Sakaki, and M. Ieki, *Inorg. Chem.*, **30**, no. 22, 4218 (1991).
77. G. Frenking, and N. Fröhlich, *Chem. Rev.*, **100**, 717 (2000).
78. E. G. Greaves, C. J. L. Lock, and P.M. Maitlis, *Can. J. Chem.*, **46**, 3879 (1968).
79. J. S. Griffith, *Proc. R. Soc. London* **A235**, 23 (1956).
80. J. Ashley-Smith, Z. Kouek, B. F. G. Johnson, and J. Lewis, *J. Chem. Soc., Dalton Trans.*, 128 (1974).
81. M. Dewar, and R. Dougherty, *The PMO Theory of Organic Chemistry*, Plenum, New York, 1975.
82. M. Tsutsui, and A. Courtney, *Adv. Organomet. Chem.*, **16**, 241 (1977).
83. S. G. Sakharov, S. A. Zarelua, Yu. V. Kokunov, and Yu. A. Buslaev, *Inorg. Chem.*, **31**, 3302 (1992).
84. I. A. Guzei, G. P. A Yap, C. H. Winter, *Inorg. Chem.*, **36**, 1738 (1997).
85. F. -M. Su, C. Cooper, S. J. Geib, A. L. Rheingold, J. M. Mayer, *J. Am. Chem. Soc.*, **108**, 3545 (1986).
86. J. D. Ashley-Smith, *J. Chem. Soc., Dalton Trans.*, 128 (1974).

4 Conformational Mobility in Chelated Square-planar Rh, Ir, Pd, and Pt Complexes

PABLO ESPINET AND JUAN A. CASARES

Química Inorgánica, Facultad de Ciencias, Universidad de Valladolid. E-47005 Valladolid (Spain)

1 INTRODUCTION

The stereoselectivity of ligand coordination and its influence on metal mediated reactions is a most important matter in organometallic chemistry [1]. In catalysts using chiral chelate L–L ligands bonded to square planar metals, ligand conformation is responsible for the chiral induction. High enantiomeric excess (ee) in asymmetric catalysis is a major target of modern synthesis [2–4]. Chiral ligands and their use in enantioselective reactions are frequently reviewed in the literature [5].

The study of preferred conformations by computational methods has established some general trends, such as the lower energy of puckered ring (for five members) or chair-like (for six members) compared to envelope or boat-like conformations, and the general preference of substituents in the metallacycle for equatorial positions [1,6–9]. These trends are strongly favored in five-member chelating rings, but slightly less in six-member rings (Figure 4.1), for which a skew conformation is not very different in energy from the chair. The use of molecular mechanics methods continues to be a useful tool to understand the conformational preferences of ligands, and the results of these studies are reviewed periodically [10–13].

The easy availability of X-ray structures in the last decade has helped with the understanding of preferred conformations, and is a valuable complement of the computational methods. Comparatively less material is available on detailed experimental studies in solution, but very often their results differ from the results found in the solid state, or calculated for the gas phase.

Several NMR conformational studies were based on the determination of $J(^1\text{H}-^1\text{H})$ values and the application of Karplus equations, and are well

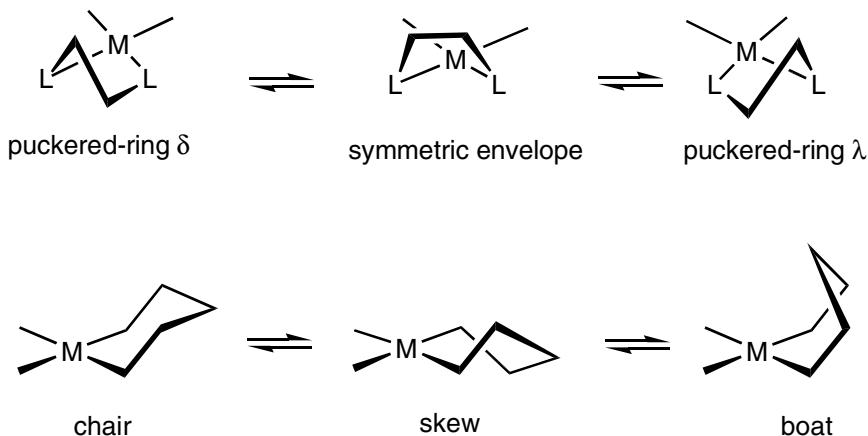


Figure 4.1 Main conformations for five-member and six-member metallacycles.

summarized in the review by Hawkins and Palmer [14]. This is still the most used method to establish the more probable conformations in cycles with very fast conformational change. The initial ^1H - ^1H data available for conformational analysis have now been extended to ^1H - ^{195}Pt , ^1H - ^{103}Rh , and especially ^1H - ^{31}P coupling constants in square-planar complexes. The study of coalescence processes is also frequent. However, not many studies in the literature are complete and quantitative. More often, only ΔG^\ddagger at Tc is given, and sometimes Tc is not even specified. This reduces the utility of the literature data. More sophisticated experiments are much less frequent. Thus magnetization transfer (MT) experiments or line shape analysis (LSA) are rarely used. Phase sensitive NOESY and ROESY experiments have become more popular recently, but they are used qualitatively. Only exceptionally are rates for the conformational change obtained. Fortunately, a number of excellent studies are available that should serve as examples for further research. This chapter collects some of these studies applied to investigate the conformations and conformational exchange in Rh, Ir, Pd and Pt complexes with chelating ligands. The material is classified by the number of members in the chelated cycle. In each section, the cases are ordered by type of ligand (e. g. amines, phosphines, etc) as far as it is possible.

2 CONFORMATIONAL CHANGES IN FIVE-MEMBER METALLACYCLES

Five-member metallacycles have two possible conformations (Figure 4.1). One is called pucker-ring (or twist), and is chiral with λ and δ enantiomers. The other is a 'meso' symmetric envelope. The envelope form is less stable than

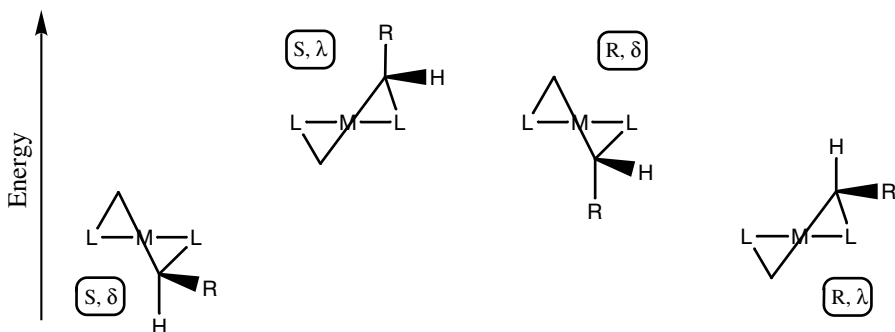


Figure 4.2 Relationship between configuration and conformational stability in five-member metallacycles with a chiral carbon.

the puckered-ring conformations, but it is often proposed as an intermediate in the exchange between λ and δ conformations.

In cycles lacking substituents (typically in ethylenediamine complexes) the λ/δ interconversion is often extremely fast on the NMR timescale but the preferred conformations can be assigned measuring J values and applying Karplus equations, as described in the review by Hawkins and Palmer. The rate of conversion could be measured in CD_3OD solution for the paramagnetic complex $[\text{Fe}(\text{CN})_4(\text{en})]^-$ (taking advantage of the large paramagnetic shift of the signals, which increases T_c) [15], and in the solid state for some Pt complexes [16].

When the cycle bears substituents, the free activation energy of the conformational change increases. Thus, the exchange process in diamagnetic TMEDA complexes in solution can be studied by NMR. As a general rule, the configuration determines the most stable conformation, which is always that with the substituent in equatorial position. Figure 4.2 shows five-member chelate complexes with one stereogenic carbon ($R = \text{alkyl}$). The complex with an S carbon prefers a δ conformation. In contrast the complex with an R carbon prefers the λ conformation. The exchange between conformers is usually very fast. When there is interaction of the metallacycle with other ligands in the coordination sphere, the previous rule can be broken. Thus, in $[\text{Pt}(\text{bipy})(\text{men})]^{2+}$ ($\text{men} = N\text{-methyl-1,2-ethanediamine}$) the conformations with the Me substituent in equatorial position are destabilized by repulsion by the external H^6 atom of the bipy ligand, and the conformer with axial Me is the one observed [14]. A recent review discusses the relationship between conformation and ee in catalytic asymmetric hydrogenation reactions for five-member metallacycles [17].

Inversion of configuration of atoms with electron lone pairs is a common process for chelates containing thioethers and related groups [18–20]. Depending on the symmetry of the complex, the pyramidal inversion can produce a conformational change, or a change of configuration at the atom, inducing therefrom a conformational change. For five- or six-member metallacycles with dithioethers

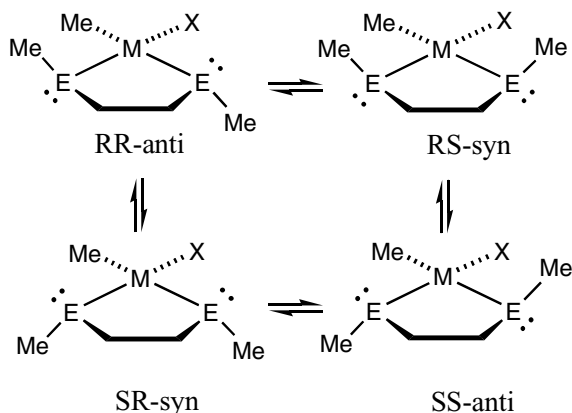


Figure 4.3 The four possible conformations associated with the configuration of the electron pair-containing atoms for $[\text{PtX}(\text{Me})(\text{MeECH}_2\text{CH}_2\text{EMe})]$ complexes.

not heavily substituted, the conformational changes are fast compared to the inversion of configuration at sulfur, and only the configurational changes need to be discussed. For instance, complexes $[\text{PtX}(\text{Me})(\text{MeECH}_2\text{CH}_2\text{EMe})]$ ($\text{E} = \text{S}, \text{Se}, \text{Te}$) can give rise to four isomers related by inversion of the E-donor atoms (Figure 4.3).

The process is particularly sensitive to the *trans* influence of the other ligands: The more they weaken the M–S bond, the easier the inversion. For instance, changing a halogen for a Me group reduces the inversion activation energy for an S atom in a *trans* position by about 15–20 kJ mol^{-1} [18].

If the ring conformations are taken into account, the number of pair, conformational change, or both. The left and right pairs represented in Figure 4.4, for example, are related by conformational change. There are few examples of observation of conformational change in thioether derivatives. The first observation was made on the complex $[\text{PtI}_2(\text{meso-MeSCH}(\text{CF}_3)\text{CH}(\text{CF}_3)\text{SMe})]$ [21].

Other configurational changes involve ligand decooordination. For chelating ligands, the decooordination of one stereogenic end and its recoordination in an inverted conformation brings about a conformational change in the metallacycle. An example of this process is provided by the complex in Figure 4.5, which has an enantiomerically pure P,N donor ligand [22].

The X-ray structure reveals a δ -twist conformation for the complex, with the $i\text{-Pr}$ and the R^2 substituents in equatorial positions. However, in solution two isomers are detected, in 9.4:1 ratio, which undergo slow exchange. The major isomer corresponds to that found in the solid state. The minor isomer could be either the λ conformer of the major isomer, or a diastereomer. NOESY experiments and analysis of the coupling constants prove it to be the δ conformation

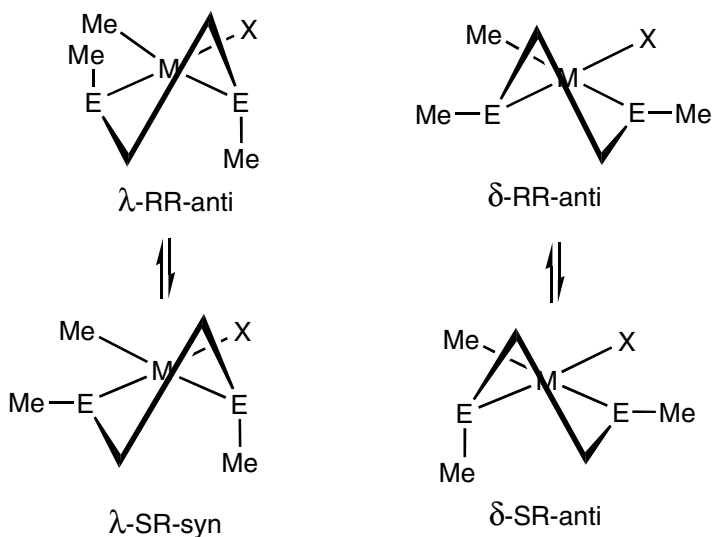


Figure 4.4 The two ring conformations give rise to two species for each of the complexes shown in Figure 4.3. Here only two of the forms shown in Figure 4.3 are considered.

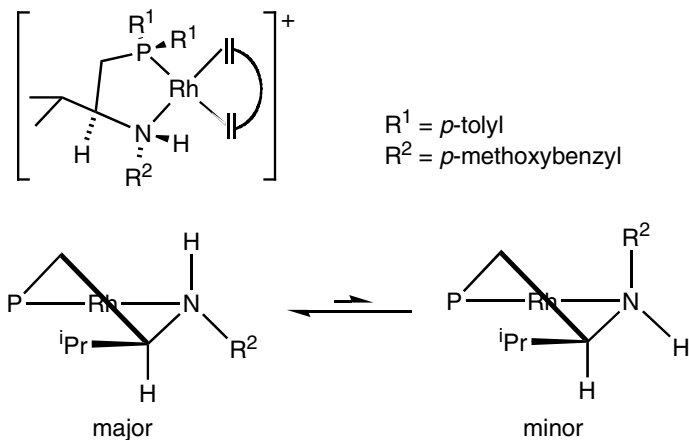


Figure 4.5 Isomerization change by decooordination, inversion, and recoordination of a pyramidal chiral nitrogen atom. The δ conformation is recovered at the end of the reaction.

of the other isomer. Hence inversion of the nitrogen has occurred bringing the N(*p*-methoxybenzyl) group to an axial position, which requires necessarily N decooordination. Probably this preference is due to the high steric requirements of *i*Pr compared to the aromatic ring and also to the steric strain caused by other ligands in the coordination plane.

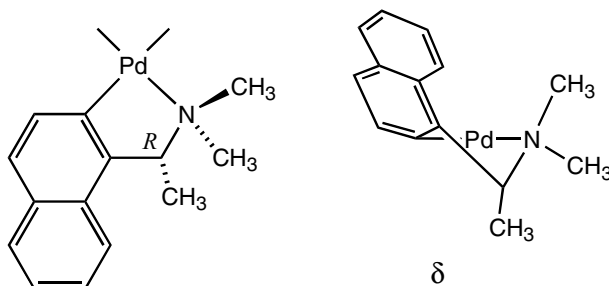


Figure 4.6 Coordination of orthometallated dimethyl(1-(α -naphthyl)-ethyl)amine.

Pd(II) complexes with enantiomerically pure orthometallated benzylamines have been studied in detail because they are used for the resolution of chiral ligands. For dimethyl(1-(α -naphthyl)-ethyl)amine it is clear that the chelate prefers the conformation with the benzylic Me in axial position, thus avoiding interactions with the naphthyl ring. This leads to a δ conformation for the *R* amine (Figure 4.6), and to a λ conformation for the *S* amine [23–26].

The effect of the conformation of this orthopalladated ligand on the other ancillary ligands has been studied using *S*-dimethyl(1-(α -naphthyl)-ethyl)amine and the three isomers (*RR*, *SS*, and *RS*) of *N,N,N',N'*-tetramethyl-2,3-butanediamine [27]. The conformation chosen by the diamine depends on two factors: (i) the preference of the Me groups in the diamine for equatorial positions, and (ii) the tendency to minimize interligand interactions, which means that the *N*-methyl groups of the orthometallated ligand, and those in the diamine end *cis* to it should ideally be staggered. For the *RR* diamine the two factors favor a λ conformation of the diamine. In fact, only one *SRR* isomer is observed by NMR at -80°C . The ^1H NMR δ and *J* values found fully support this conformation. For the *SS* diamine the first factor (i) favors a δ conformation of the diamine, whereas the second (ii) favors λ . The ^1H NMR data support a δ conformation for this *SSS* isomer, which was confirmed by X-ray crystallography. This indicates that the intraligand interactions impose over the interligand repulsions in this case.

A cross-experiment mixing equal amounts of the enantiomers *RRR* and *SSS* (the first letter corresponds to the configuration of the orthometallated amine) prepared independently showed, in the equilibrium, a mixture of diastereomers (Figure 4.7) containing (*RRR* + *SSS*):(*RSS* + *SRR*) = 1:19.

For the *RS* diamine there is always one axial and one equatorial Me. Hence the configuration (selection of the chiral center *cis* to N) and the conformation are determined by interligand interactions, and this leads to a λ conformation. In this case there are two possible diastereomers, both in λ conformations, depending on whether the *R* carbon of the diamine is *trans* or *cis* to the orthometallated carbon. Both are found in CD_2Cl_2 solution by ^1H NMR in a 1:6

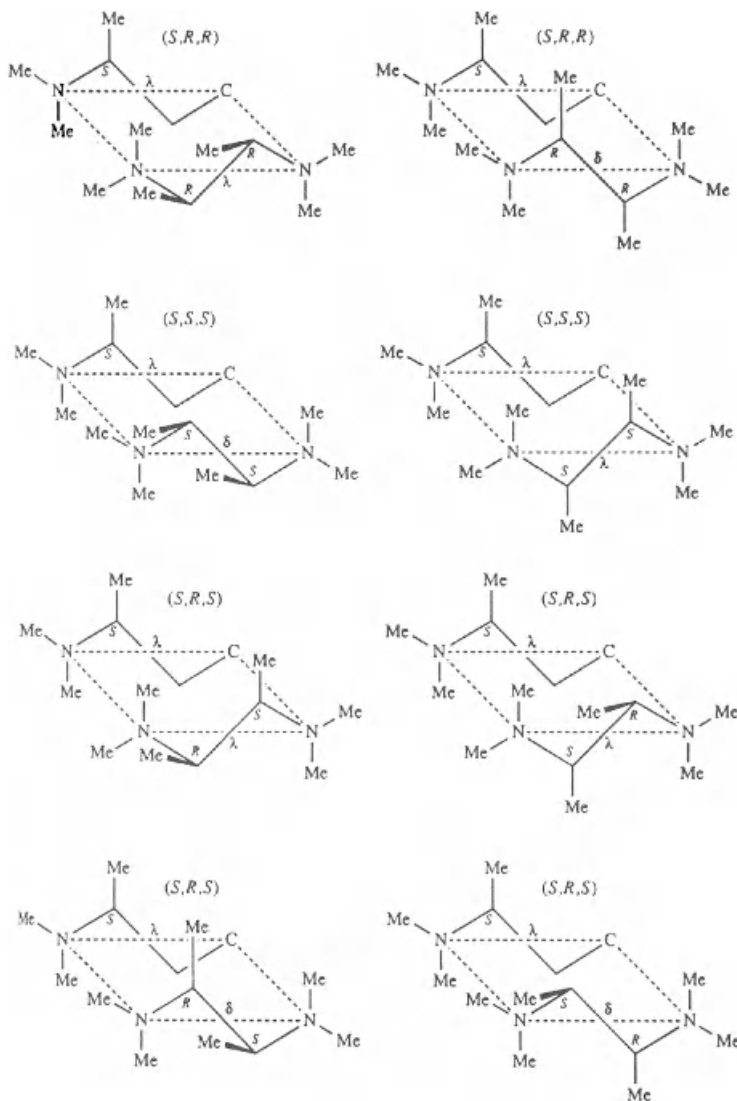


Figure 4.7 Possible isomers of a square-planar complex with orthometallated dimethyl(1-(α -naphthyl)ethyl)amine and N, N, N', N' -tetramethyl-2,3-butanediamine. Reproduced with permission from S. Y. M. Chooi *et al. Inorg. Chem.* **33**, 3097 (1994) [27]. Copyright (1993) American Chemical Society.

ratio at 25 °C. Based on X-ray diffraction studies, the most stable was proposed to be the *SRS*, but this was not studied by NMR.

McFarlane has studied the orthopalladated complexes of enantiomerically pure 1-phenyl-1-(N,N -dimethylamino)ethane and Chiraphos, shown in

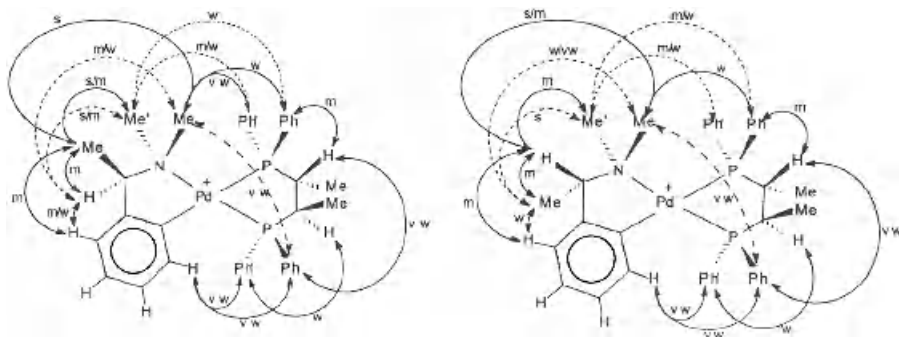


Figure 4.8 Patterns of NOE interactions in the orthopaladated complexes of enantiomerically pure 1-phenyl-1-(*N,N*-dimethylamino)ethane and Chiraphos derived from volume integrals of off-diagonal peaks in proton ROESY spectra at 500 MHz with a mixing time of 130 ms, *s* = strong, *m* = medium, *w* = weak, *vw* = very weak. W. McFarlane *et al.*, *J. Chem. Soc. Dalton Trans.* 3233 (1988) [28]. Reproduced by permission of the Royal Society of Chemistry.

Figure 4.8 [28]. ROESY was applied to establish unambiguously the stereochemistry of the orthometallated chelates. Exchange cross peaks were observed for *N*-methyl exchange in one of the isomers, and MT was utilized to determine the rate of this exchange process ($\Delta G^\ddagger_{295} = 100.5 \text{ kJ mol}^{-1}$). The conformation of the diphosphine was assigned based on the cross-peaks in the ROESY and on an analysis of the $^3J(\text{H-H})$ and $^3J(^{31}\text{P-H})$ values. Finally, quantitative NOE experiment was used to determine the relative population of the two conformations observed for the five-member orthometallated cycle, which are undergoing a fast exchange process.

Using 1-phenyl-1-(*N,N*-dimethylamino)ethane instead of dimethyl(1-(α -naphthyl)-ethyl)amine, the conformational preference of the orthometallated metallacycle is still for axial C–Me avoiding the interaction with the aromatic ring, but less marked. In fact the two conformers can be seen in CDCl_3 solution [28]. The interaction of (*R,R*)-Chiraphos with the two enantiomers of this orthometallated system has been studied, examining the ratio of δ and λ conformers arising from each orthometallated (*R* or *S*) by coordination of the (*R,R*)-Chiraphos. This ratio has been established from the ratio of NOE effects of the benzylic H and the C–Me with each of the N–Me of the amine, as observed in ROESY experiments. Both enantiomers of the orthometallated amine prefer a λ conformation. In the *R* enantiomer ($\lambda:\delta = 55:45$) the λ conformation has the benzylic Me group in equatorial position ((ii) in Figure 4.9). In contrast, in the *S* enantiomer ($\lambda:\delta = 90:10$) the λ conformation places the Me group axial ((iii) in Figure 4.9). This is interpreted as a consequence of the preference to minimize interactions between the *N*-methyl groups of the orthometallated moiety and the Ph groups of the phosphine: the λ conformation corresponds to a staggered arrangement of these substituents. In the *R* enantiomer this con-

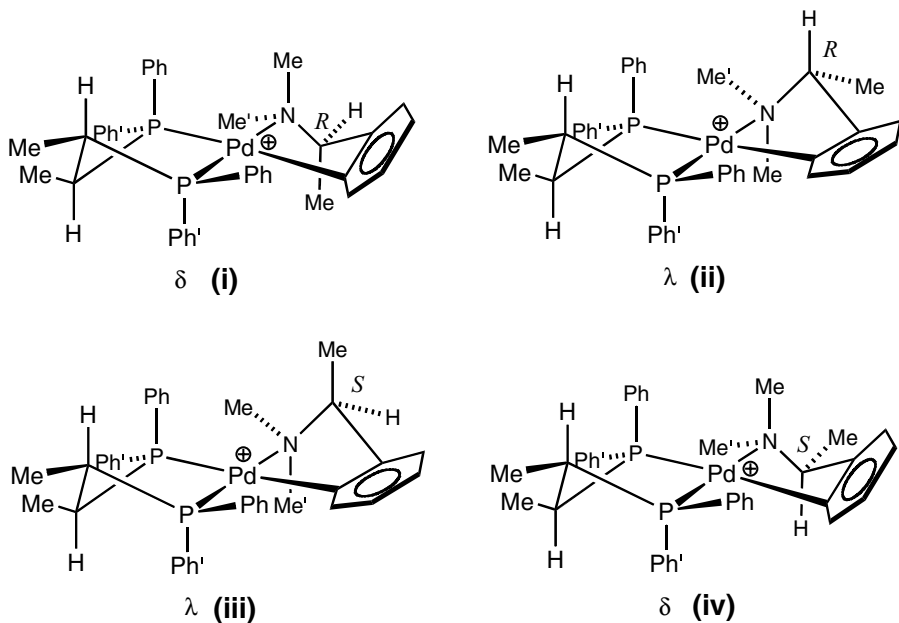


Figure 4.9 Overall conformations of the complexes of *R* and *S* orthopaladated 1-phenyl-1-(*N,N*-dimethylamino)ethane with (*R,R*)-Chiraphos.

formation brings the C–Me to a close repulsive encounter with one C–H of the orthometallated aromatic ring ((ii) in Figure 4.9). This seems to be the reason for the easy decoordination of the amine end in the orthometallated *R* isomer (measured by magnetization transfer, $\Delta G^\ddagger = 100.5 \text{ kJ mol}^{-1}$), which is not observed for the complex with the *S* enantiomer.

Increasing the steric requirement of the substituent at the benzylic carbon (*t*Bu for Me) produced clear improvement in the resolution of monodentate phosphines chiral at the P atom [29]. The stereochemistry and conformation of these complexes (Figure 4.10) was determined by monodimensional NOE experiments and by analysis of *J* values. The palladacycle with *S* configuration for the stereogenic C atom showed exclusively the λ conformation with both enantiomers of the phosphine.

The complexes $[\text{PtCl}_2(\text{L-L})]$ and $[\text{Rh}(\text{diolen})\text{(L-L)}]^+$ ($\text{L-L} = p\text{-aryl substituted } (S,S)\text{-chiraphos, } (S,S)\text{-BDPP, and } (S,S)\text{-diop}$, Figure 4.11), are examples of five-, six-, and seven-member metallacycles, respectively [30]. Their conformation in solution have been established by ^1H , ^{13}C and ^{31}P NMR, according to the ^{13}C chemical shifts, the anisotropic effects on the ^1H chemical shifts, and $^1J(\text{P-C})$, $^3J(\text{P-C})$, $^3J(\text{P-H})$, and $^3J(\text{H-H})$, as well as variable temperature measurements. The experimental data suggest a rigid, or highly preferred conformation, with a δ arrangement for the rhodium complexes with Chiraphos

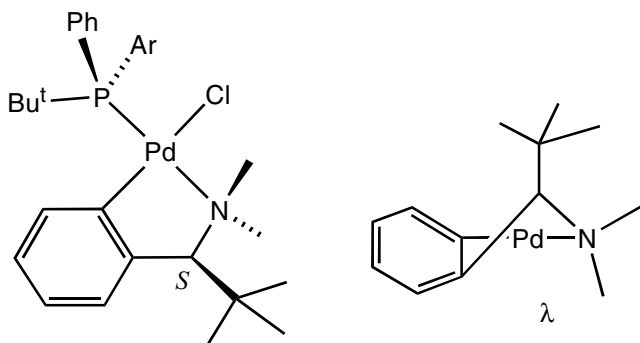


Figure 4.10 An orthopalladated complex with a phosphine chiral at the P atom.

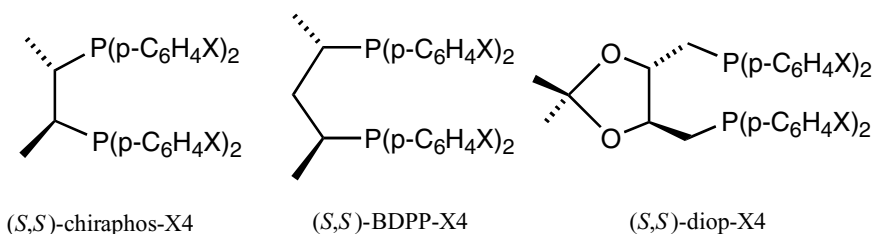


Figure 4.11 Structure of the ligands (*S,S*)-chiraphos, (*S,S*)-BDPP, and (*S,S*)-diop.

or BDPP. The P–aryl groups of these complexes are fixed in quasi-axial and quasi-equatorial arrangements. In contrast, $\text{PtCl}_2(\text{diop})$ is conformationally labile, and more than one conformer is detected at low temperature, although the exact geometry was not determined. This difference is attributed to the stabilizing effect of the bulky diene ligands on the former.

The presence of intramolecular hydrogen bonds can stabilize a particular conformation [31]. However, there are cases when conformational flexibility can be maintained in presence of hydrogen bonds. For instance, in the complex $[\text{PtCl}_2\{\textit{meso}$ -1,2-bis(2-hydroxyphenyl)-ethylenediamine}] (I in Figure 4.12), the aryl rotation is locked by the formation of hydrogen bonds between the OH and the amino groups [32]. The compound has been studied in DMF-d_7 by 1D NOE experiments (Figure 4.12). The fast exchange between δ and λ conformations results in an apparent C_s symmetry for the complex, simplifying the spin system (trace A). In both conformations one of the aryl groups is in an axial position almost perpendicular to the coordination plane, allowing a close interaction of the O–H with the coordinated amino group. The saturation of the benzylic signals (trace B) results in an intensive response of one N–H signal and the aromatic H^d , as well as a small effect on the phenol hydrogens. This is interpreted as the effect of the restricted rotation of the aryl rings. Irradiation of the OH protons reveals chemical exchange with one amino H atom, and NOE with the

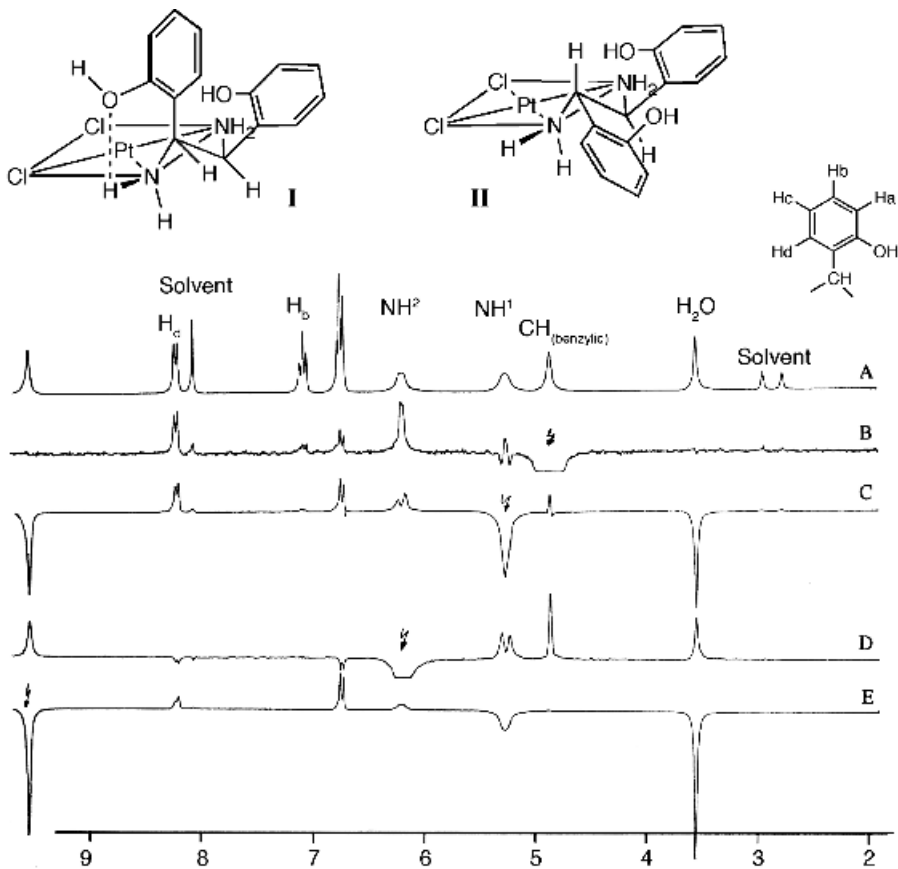


Figure 4.12 Structures of $[\text{PtCl}_2\{\text{meso-1,2-bis(2-hydroxyphenyl)-ethylenediamine}\}]$ (**I**) and $[\text{PtCl}_2\{(S,S(-))-1,2-bis(2-hydroxyphenyl)-ethylenediamine}\}]$ (**II**). Below, 250 MHz ^1H NMR spectra of **I** in DMF-d_7 and 250 MHz (A); and NOE difference spectra due to the irradiation of $\text{CH}_{\text{benzylic}}$ (B), NH^1 (C), NH^2 (D), and OH (E). Reproduced with permission from R. Gust *et al.*, *Inorg. Chem.* **32**, 5944 (1993) [32]. Copyright (1993) American Chemical Society.

other (trace E). This is confirmed by irradiation on the N–H protons (traces C and D).

In contrast, in the C_2 complex $[\text{PtCl}_2\{(S,S(-))-1,2-bis(2-hydroxyphenyl)-ethylenediamine}\}]$ both aryls are in equatorial position in the puckered ring (**II** in Figure 4.12). In order to enforce proximity of the NH_2 and OH groups, the aryls should be almost in the coordination plane, which increases the steric hindrance between H^d protons. In the 1D difference NOE spectra, neither NOE nor exchange is observed between O–H and N–H protons.

3 CONFORMATIONAL CHANGES IN SIX-MEMBER METALLACYCLES

These systems are very common and include ligands with equal or different donor atoms, as well as metal-containing ligands (e.g. ferrocenyl derivatives, pyrazolyl borates). In these cycles three conformations are considered (Figure 4.9). In flexible systems calculations suggest that the chair, and skew (or twist) conformations are more stable, but in practice, depending on the substituents or when some rigidity is imposed in the metallacycle, the boat conformation is found. The skew conformation is chiral, while the chair and boat conformations are not. When one lateral substituent is introduced in the chelate (L–L' in place of L–L in Figure 4.13), or in some low symmetry complexes, the chair and boat conformations become chiral. When the chelating ligand has two different donor atoms (as in the numerous complexes with P,N ligands), the skew λ and δ , the chair, and the boat conformers are enantiomers.

Imposing restrictions on the chelate, the number of conformers decreases, and the conformational changes become slower, facilitating the kinetic NMR studies. For instance, in $[\text{Rh}(\text{COD})(\text{PN}_1)](\text{BF}_4)$ ($\text{PN}_1 = \text{PPh}_2(o\text{-phosphino-}N,N\text{-dimethylbenzylamine})$), with an aromatic ring in the metallacycle, the PN_1 ligand can adopt two distorted boat conformations (Figure 4.14). In the room temperature ^1H NMR spectra the benzylic hydrogen atoms and the N -methyl groups appear equivalent due to fast conformational change, but they become nonequivalent at -60°C [33]. The same process, with very similar activation energies, has been observed for other complexes with this PN_1 ligand [34–36].

Huttner *et al.* have studied complexes $[\text{Rh}(\text{COD})(\text{PR}_2\text{CH}_2\text{CH}(\text{OH})\text{CH}_2\text{PR}_2)](\text{PF}_6)$ with enantiomerically pure phosphines [37]. With bulky R and

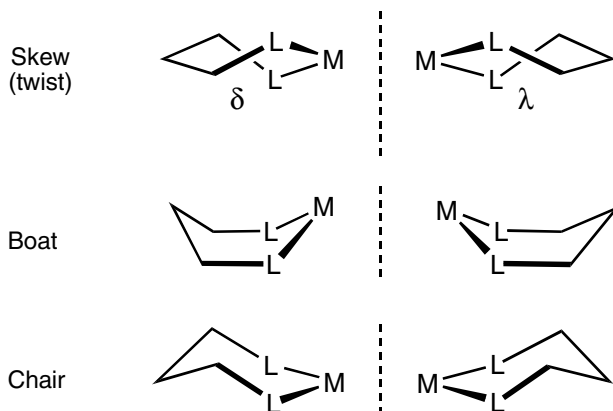


Figure 4.13 Main conformations for six-member metallacycles.

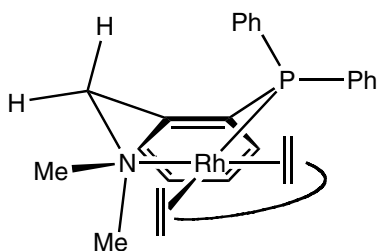


Figure 4.14 Structure of $[\text{Rh}(\text{COD})(\text{PNi})](\text{BF}_4)$ showing the nonequivalence of the benzylic hydrogen atoms and the *N*-methyl groups.

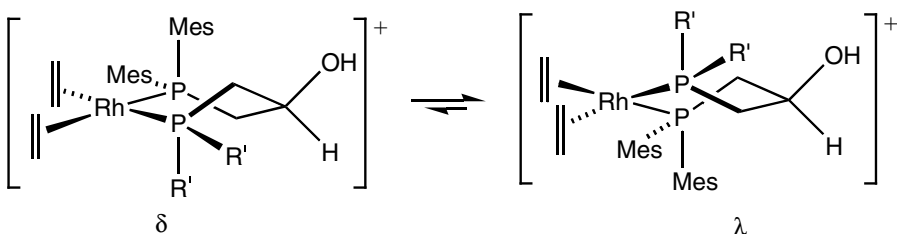


Figure 4.15 Conformations observed for the cation in complexes $[\text{Rh}(\text{COD})(\text{PMes}_2\text{CH}_2\text{CH}(\text{OH})\text{CH}_2\text{PR}'_2)](\text{PF}_6)$ in CD_2Cl_2 .

R' substituents the twist conformation is preferred, but the chair is more stable if these substituents are small. A detailed study was carried out on the solution behavior in CD_2Cl_2 for complexes $[\text{Rh}(\text{COD})(\text{PMes}_2\text{CH}_2\text{CH}(\text{OH})\text{CH}_2\text{PR}'_2)](\text{PF}_6)$ [38]. The twist conformation (δ and λ) is observed (Figure 4.15). The rotation of the mesityl groups about the C–P bond is hindered in each conformer, and only takes place during the conformational change. This can be seen in the EXSY spectrum of the complex with $\text{R}' = \text{Ph}$ where each of the *o*-Me groups at one mesityl group of one isomer exchanges with both of the *o*-Me groups of the other mesityl group in the other conformer. The equilibria at 298 K for the λ/δ isomerization lie on the side of the λ conformer, and the corresponding reaction enthalpies range from -8 to -2 kJ mol^{-1} , and the reaction entropies from -10 to $8 \text{ J K}^{-1} \text{ mol}^{-1}$ [38]. The activation barriers for the isomerization δ to λ correspond to ΔG^\ddagger_{298} with values ranging from 68.6 to 73.6 kJ mol^{-1} .

In Rh(I) complexes with (–)-(2*S*,4*S*)-2,4-bis(diphenylphosphino)pentane and diolefins as ancillary ligands the metallacycle is conformationally very flexible in solution [39]. The X-ray diffraction solid state structures show a chair conformation for the complex with NBD, and a skew conformation for the complex with COD, but in solution both complexes show fast conformational exchange and behave as having C_2 symmetry.

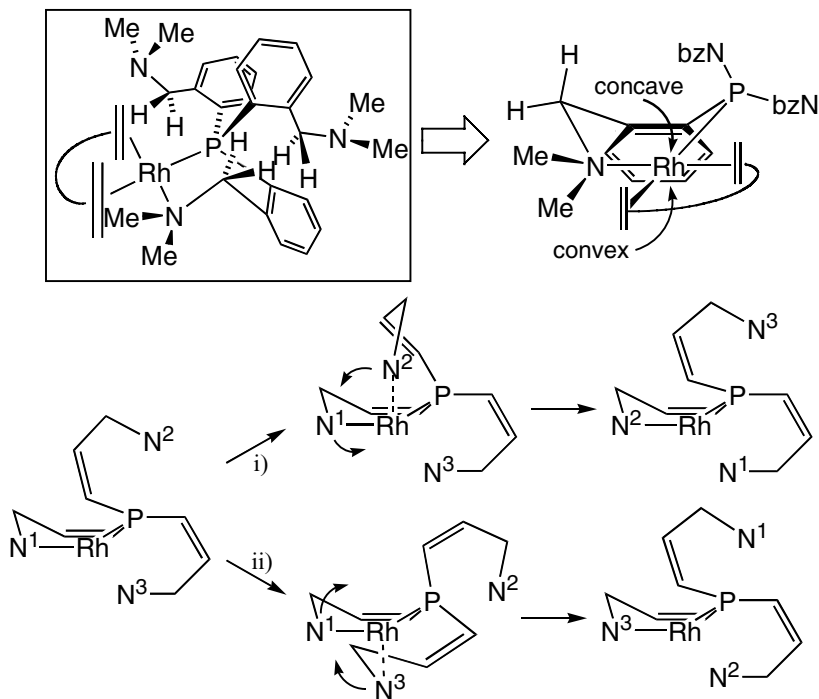


Figure 4.16 Structure and ligand substitution mechanism for the complexes $[\text{Rh}(\text{diolefin})(\text{PN}_3)]\text{BF}_4$.

Six-member P,N donor chelating ligands have been profusely used in coordination chemistry and catalysis. The simplest ligands of these series are the derivatives $\text{P}(o\text{-phosphino-}N,N\text{-dimethylbenzylamine})_n\text{Ph}_{3-n}$ (labeled PN_1 , PN_2 and PN_3). The successive substitution of phenyl by benzylamine groups at the phosphorus slows down noticeably the conformational inversion.

The complexes $[\text{Rh}(\text{diolefin})(\text{PN}_3)]\text{BF}_4$ feature P,N-coordinated chelated ligands with two pendant amino groups. The corresponding metallacycle has a boat like conformation (racemic chiral), which defines concave and convex sites for the attack of the pendant ligands in an associative ligand substitution process of the coordinated by the pendant amino groups (Figure 4.16) [40].

These complexes undergo exchange of the coordinated for pendant amino groups with complete retention of the configuration of the ring. It might be said that the molecule keeps memory of the configuration of the ring during the exchange process. This is clearly seen in the ^1H EXSY of $[\text{Rh}(\text{COD})(\text{PN}_3)]\text{BF}_4$ at room temperature (Figure 4.17), which is consistent only with an associative substitution where the incoming ligand adopts the same configuration as that of the leaving group. This is due to the fact that conformational exchange is much slower than the ligand exchange, and its conformation is retained in the penta-

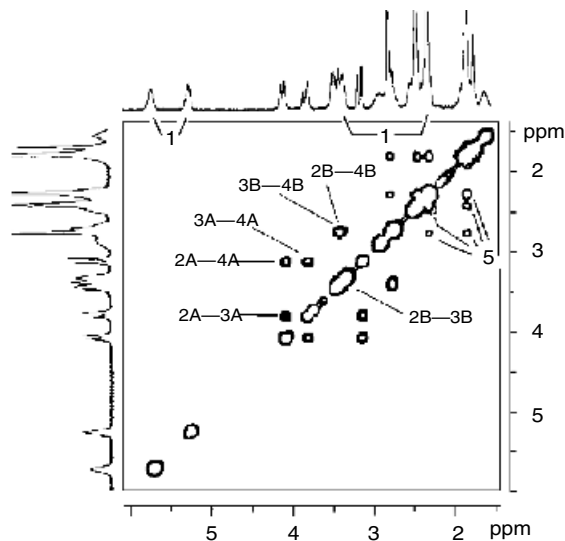


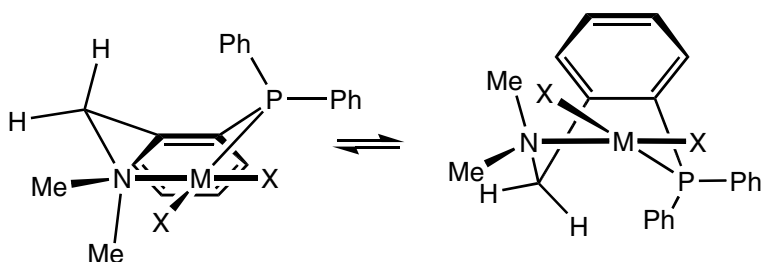
Figure 4.17 ^1H EXSY spectrum (300 MHz, CDCl_3 , room temperature) of $[\text{Rh}(\text{COD})(\text{PN}_3)]\text{BF}_4$ Olefinic protons *cis* to the coordinated N (at left) and *cis* to the coordinated P (at right); note the marked anisotropic shielding of the latter by the aromatic rings of the pendant arms. (2A–2B), (3A–3B), and (4A–4B) are the three methylenic groups, each giving rise to an AB spin system. (5) Cross peaks of the methyls. M. A. Alonso *et al.*, *Angew. Chem. Int. Ed. Engl.* **38**, 533 (1999) [40]. Reproduced by permission of Wiley-VCH.

coordinated intermediate formed during the amino exchange reaction, allowing for the conservation of the conformation of the chelate ring during the substitution process (Figure 4.16). Both processes, ligand exchange and conformational exchange, were measured independently for $[\text{Rh}(\text{TFB})(\text{PN}_3)]\text{BF}_4$. The rate of ligand exchange was measured by LSA of the singlets of the methyl groups, affording $\Delta G^\ddagger_{298} = 55.7 \text{ kJ mol}^{-1}$ ($\Delta H^\ddagger = 51.5 \pm 2.7 \text{ kJ mol}^{-1}$; $\Delta S^\ddagger = -14 \pm 10 \text{ J K}^{-1} \text{ mol}^{-1}$). The boat inversion was studied by MT on the F atoms of the TFB ligand, affording $\Delta G^\ddagger_{298} = 66.9 \text{ kJ mol}^{-1}$ ($\Delta H^\ddagger = 49.6 \pm 2.7 \text{ kJ mol}^{-1}$; $\Delta S^\ddagger = -58 \pm 10 \text{ J K}^{-1} \text{ mol}^{-1}$). This means that, at 298 K, the rate of exchange of pendant for coordinated amine is about 100 times faster than the boat inversion. Although it appears that concave and convex sites are very differently hindered, both attacks occur at the same rate. Otherwise there would be a preferred sense of rotation, but this cannot happen when movement is converting degenerate states.

Square-planar complexes with PN_1 (Figure 4.18) are involved in a fast conformational inversion of the metallacycle formed by the chelating ligand, which is plane-averaged on the NMR time scale. Values of ΔG^\ddagger are collected in Table 4.1.

Table 4.1 Selected values of activation free energy at Tc for the conformational inversion of the ligand PN₁ in square planar complexes of different metals.

Complexes	ΔG^\ddagger (kJ mol ⁻¹)	Tc (K)	Reference
[RhCl(CO)(PN ₁)]	36.7	221	[34]
[Pd(Me)(OCH(CF ₃) ₂)(PN ₁)]	41.7	215	[35]
[Pd(Me)(OC ₆ H ₅)(PN ₁)]	41.7	215	[35]
[Pt(o-Me ₂ Si(C ₆ H ₄))(PN ₁)]	51.0	266	[36]
[Pt(Me) ₂ (PN ₁)]	55.0	276	[36]
[Pt](Me)(PN ₁)]	57.0	289	[36]
[Rh(TFB)(PN ₁)]BF ₄	41.5	211	[33]
[Rh(COD)(PN ₁)]BF ₄	51.6	253	[33]

**Figure 4.18** Boat-to-boat conformational change in square-planar complexes with PN₁.

The coordination of the ligand PN₂ through the phosphorus and only one nitrogen, renders nonequivalent the coordinated and the noncoordinated amino groups and converts the P atom to a stereogenic center. The substitution of the coordinated N end by the noncoordinated amine in [Rh(diolefin)(PN₂)]BF₄ complexes, provides an energetically accessible pathway for the exchange of enantiomers [33]. These complexes have been studied by phase sensitive NOESY. The preferred conformer has the free benzylamino group occupying an axial site. For [Rh(TFB)(PN₂)]BF₄ the equilibrium between the two diastereomeric boat conformers (33:1; $k_{\text{major-minor}} = 300 \text{ s}^{-1}$; $\Delta G^\ddagger_{242} = 47.2 \pm 0.2 \text{ kJ mol}^{-1}$) occurs at a rate similar to the ligand exchange process ($\Delta G^\ddagger_{211} = 41.7 \pm 0.2 \text{ kJ mol}^{-1}$) measured at the coalescence temperature.

Ligands PePy_n (PePy_n = P(CH₂CH₂(2-pyridyl))_nPh_{3-n}) also form a six-member metallacycle containing three sp³ and two sp² atoms. The complexes [PdXRf(PePy_n)] (Rf = C₆F₅, C₆Cl₂F₃; X = halide; $n = 1, 2, 3$) and [Rh(diolefin)(PePy_n)]⁺ ($n = 1, 2$) are very flexible and their conformational change is not detected to have slowed down in the temperature range available with common solvents (by ¹H NMR at 300 MHz) [41,42].

Other comparable ligands, but chiral, are those bearing *o*-substituted *N,N*-dimethylbenzylamine (P^{*}N_n = P(α-methyl-*N,N*-dimethylbenzylamine-*o*)_nPh_{3-n}) [33,43,44]. Solid state structures of transition metal complexes (e.g. of

Rh, Pd, Pt, Ni) with similar ligands indicate that the preferred conformations are those minimizing steric repulsions between the methyl group on the α -carbon and the equatorial methyl group of the coordinated *syn*-amine group [45–48]. The conformations of cationic complexes $[\text{Rh}(\text{diolefin})(\text{P}^*\text{N}_n)]^+$ ($\text{P}^*\text{N}_n = \text{P}^*\text{N}_1, \text{P}^*\text{N}_2$ or P^*N_3) in solution have been established by NOESY experiments [33, 44]. Often all the diastereomeric conformations are observed. The major isomer in solution is always the same as that found in the solid state, with the methyl group on the α -carbon in axial position. The conformational inversion rates are much slower than in analogous complexes with the corresponding nonchiral ligands PN_n . For instance the conformational inversion for the complex $[\text{Rh}(\text{TfB})(\text{P}^*\text{N}_1)]\text{BF}_4$ is so slow that the coalescence in acetone- d_6 of the olefin signals of the major with those of the minor isomer occurs, at 300 MHz, above room temperature. For $[\text{Rh}(\text{TfB})(\text{PN}_1)]\text{BF}_4$ the coalescence temperature is 213 K. Therefore an important effect of the C–Me substituent in the P^*N_n ligands is to increase the activation energy for the exchange between the two conformers.

These results are in agreement with the work of Crociani on iminophosphane-rhodium derivatives $[\text{Rh}(\text{diolefin})(\text{P},\text{N})](\text{BF}_4)$ (Figure 4.19, diolefin = COD, NBD) [49]. For $\text{R} = 2, 6\text{-C}_6\text{H}_3(\text{tPr})_2$ only two olefinic signals are seen, indicating fast conformational exchange. For $\text{R} = \text{tBu}$ the conformational exchange is slow at room temperature for COD but fast for NBD, although the latter exchange becomes slow at 183 K. LSA for the latter process gave $\Delta G^\ddagger_{208} = 41 \text{ kJ mol}^{-1}$, $\Delta S^\ddagger = -60 \text{ J K}^{-1} \text{ mol}^{-1}$ and $\Delta H^\ddagger = 28.5 \text{ kJ mol}^{-1}$.

Less studied are the P,S donor ligands, although they have been used in homogeneous catalysis [50]. Pregosin *et al.* have reported a spectroscopic study of Pt, Rh and Ir complexes with the P,S chiral ligand depicted in Figure 4.20 [51]. The corresponding complex with PtCl_2 shows two conformers in CDCl_3 solution (93:7), which equilibrate slowly at room temperature and have been characterized after careful analysis of their $J(^{195}\text{Pt}-^1\text{H})$, $J(^{31}\text{P}-^1\text{H})$, $J(^{13}\text{C}-^1\text{H})$ and $J(^1\text{H}-^1\text{H})$ constants, HMQC $^{195}\text{Pt}-^1\text{H}$ correlation and 2D-NOE spectroscopy. The conclusion is that the chelate ring disposes the sulfur substituent in a pseudoaxial position, and the isomers result from simultaneous inversion of the sulfur configuration and conformational change. When coordinated to

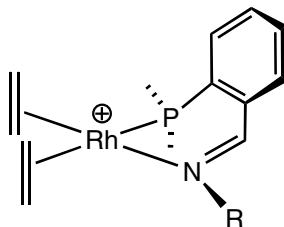


Figure 4.19 Coordination of iminophosphines.

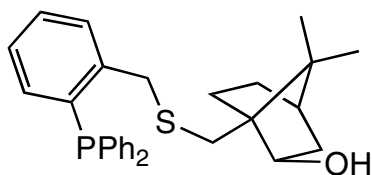


Figure 4.20 Structure of the chiral ligand *exo*-8-((*o*-(diphenylphosphino)benzyl)thio)borneol.

η^3 -allylplatinum instead of PtCl_2 , the 1D ^1H and 2D TOCSY NMR spectra in CD_2Cl_2 at 323 K reveal two complexes in solution, which have been assigned the *exo* and *endo* orientations of the allyl ligand in slow exchange. At 233 K the spectra show four isomers in solution, due to conformational changes in the chelate ring. For $[\text{Rh}(\text{P,S})(\text{COD})]^+$ in CD_2Cl_2 the coupling constants as well as the observed NOE signals reveal that the conformational change is fast at room temperature. At 173 K two separate isomers in 2:1 ratio are observed. Finally, the Ir(III) complex $[\text{IrH}_2\text{L}_2(\text{P,S})]^+$ ($\text{L} = \text{P}(p\text{-XC}_6\text{H}_4)_3$, $\text{X} = \text{Cl, F, H, OMe}$), in which geometrical isomers are possible and the Ir is a stereogenic center, shows in the ^{31}P NMR more than 16 resonances in CD_2Cl_2 .

Recent reviews on pyrazolylborate complexes are available [52–55]. Their solution study is complicated by the occurrence of equilibria between pentacoordinated and square-planar species, and by fast pyrazolyl exchange in the square-planar complexes. These fast phenomena are difficult to distinguish as they lead to spectroscopically equivalent results when followed by ^1H NMR only.

The first detection of two boat conformers was due to Venanzi *et al.* in $[\text{Tp}^{i\text{Pr},4\text{Br}}\text{Rh}(\text{CO})_2]$ (Figure 4.21) [56]. The compound with **B** geometry, with pseudoaxial Pz^{R} , undergoes fast exchange of free and coordinated Pz^{R} . The exchange of **A** and **B** isomers is very slow. Other $[\text{Tp}^{\text{R}}\text{Rh}(\text{CO})_2]$ systems give geometries **A**, **B**, **C**, or mixtures, depending on the pyrazolyl substituents. A similar behavior has been found for olefin complexes $[\text{Tp}^{\text{R}}\text{Rh}(\text{di-olefin})]$, where some general trends have been observed: Bulky substituents in R^3 disfavor pentacoordination, and substituents in position 5 destabilize geometry **A**. ^{103}Rh NMR spectra (indirect detection, HMQC experiments) show almost identical chemical shifts for **A** and **B** isomers, while isomers **C** are shifted to lower field. The ^{13}C resonances for the olefinic carbons are slightly more shifted to lower frequencies in the pentacoordinated complexes **C** than in square-planar

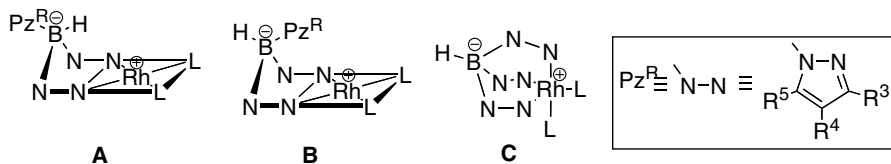


Figure 4.21 Possible geometries for tris(pyrazolyl) Rh(I) complexes.

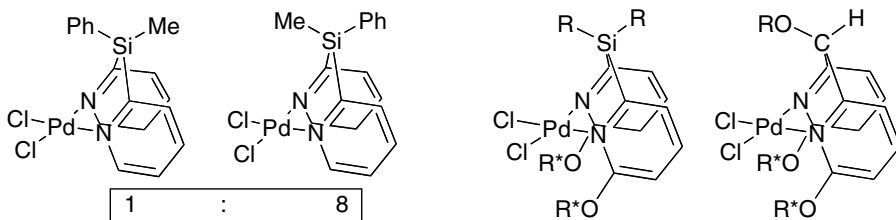


Figure 4.24 Complexes with bispyridylsilanes.

to bis- or tris-pyrazolyl borates (Figure 4.21) with O, S, or $(C_6F_5)_3Pt$ in place of H. Palladium complexes κ^2 -N-coordinated with $EPPy_nPh_{3-n}$ ($E = O, S$; $Py = 2$ -pyridyl; $n = 2, 3$) always prefer the conformation with the aromatic P substituent in axial position (conformation **E** in Figure 4.23) No conformational change **D/E** has been detected [62–64]. The bimetallic complexes $[(C_6F_5)_3Pt(\mu-PPy_n)RhL_2]$ ($L_2 = 2 CO, COD, \text{ or } TFB$) give conformers **D** and **E**, but never the pentacoordinated **J**. The complexes appear static in the ^{19}F and ^{31}P NMR. Conformations **D** and **E** can be distinguished by other fluxional processes in the molecule. The complexes were fully characterized at variable temperature by ^{31}P , ^{19}F and 1H RMN, COSY and NOESY, and HMQC ^{195}Pt – ^{19}F and ^{13}C – 1H NMR experiments [65].

The bispyridylsilane in Figure 4.24 (left) gives rise to a 1:8 mixture of conformers. The major isomer has the Me group towards the M and the Ph group pseudoequatorial. No exchange is observed at $65^\circ C$ [66]. Similar complexes with bis(6-substituted)-2-pyridylsilanes and bis(2-pyridyl)methanol ligands have been reported (Figure 4.24, right). The complexes also behave as conformationally rigid and show hindered rotation for the O–R substituents [67,68].

Studies on related complexes $PdMe_2(L-L)$ and $PdIME(L-L)$ with $(L-L) = Pz_3CH, Py_3CH, Pz_2(mim)CH, Pz_2PyCH, Py_2(mim)CH, \text{ and } Py(mim)_2CH$ ($mim = \text{methylimidazol}$; $Py = 2$ -pyridyl; $Pz = \text{pyrazolyl}$), show systematically boat structures with the aromatic ring pointing towards the metal (Figure 4.25) [69]. In other complexes of the type $[MR_2(\kappa^2-L_3CH)]$ ($R = \text{alkyl, aryl or halogen}$; $L = \text{pyrazolyl, 2-pyridyl, 2-imidazolyl, etc}$), in which the N-donor chelate has a boat conformation, the bulky substituent of the cycle is in an axial position, above the metal center [70–73]. However, for $[PdMe_2(Pz_2CH-CH_3)]$ and related complexes with methylbispyrazolylmethane the inversion of the boat conformation is observed by NMR. Tc and ΔG^\ddagger were not measured, but the signals for the two conformers are well resolved at $-10^\circ C$ [74].

Ferrocenyldiphosphanes are very flexible ligands. The ligand dppf in chelated *cis* complexes can be compared to chelates giving rise to six-member rings, having the possibility of boat-like structures (with eclipsed Cp rings) and skew-like structures with staggered Cp rings, which can interconvert in solution (Figure 4.26) [75].

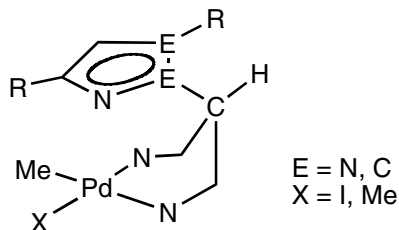


Figure 4.25 Boat structure for complexes $PdMe_2(L-L)$ and $PdIme(L-L)$.

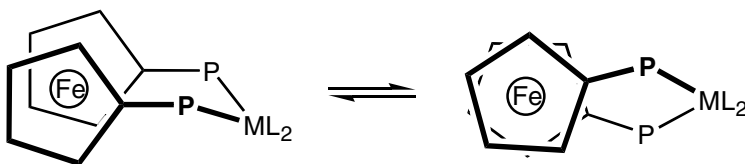


Figure 4.26 Conformational change in dppf cis square planar complexes.

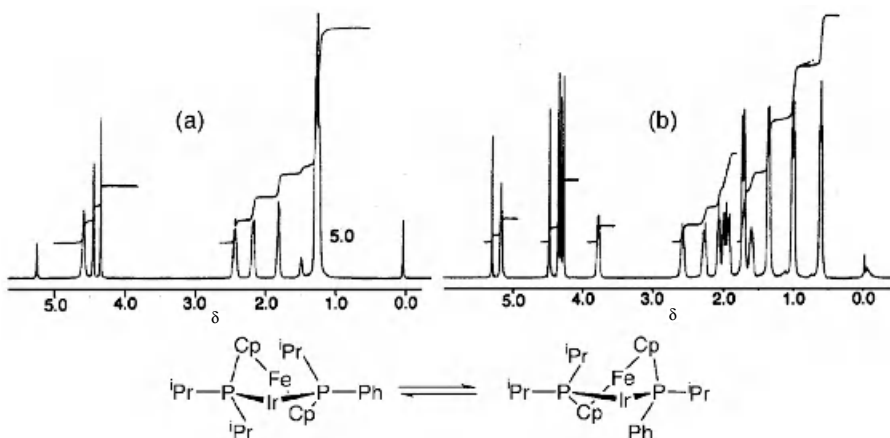


Figure 4.27 The 500 MHz 1H NMR spectra of $[Ir(COD)(1,1'-bis(diisopropylphosphine)ferrocene)](PF_6)$ recorded at (a) 298, and (b) 186 K. A. G. Avent *et al.*, *J. Chem. Soc. Dalton Trans.*, 4633 (1996) [76]. Reproduced by permission of the Royal Society of Chemistry.

Complexes $[M(\text{diolefin})(\text{diphosphane})]^+$ ($M = Rh, Ir$; diphosphane = diisopropyl- and diphenyl-ferrocenylphosphane) have been studied in CD_2Cl_2 solution by Chaloner *et al.* [76]. The NMR spectra of $[Ir(COD)(1,1'-bis(diisopropylphosphane)ferrocene)](PF_6)$ at 500 MHz reveal exchange between skew conformations in solution (Figure 4.27), with ΔG^\ddagger at Tc (206 K) = 39.3 kJ

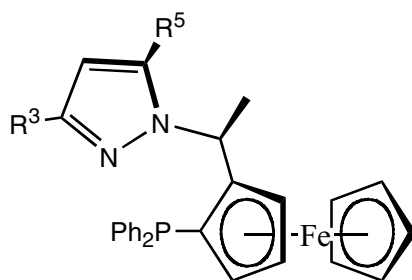


Figure 4.28 General structure of phosphinopyrazoles.

mol^{-1} . For $[\text{Ir}(\text{COD})(\text{dppf})]\text{PF}_6$, ΔG^\ddagger is 36.1 kJ mol^{-1} , and for $[\text{Ir}(\text{COD})((\text{Ph}_2\text{P})(\text{Pr}_2\text{P})\text{Fc})]\text{PF}_6$, 34.3 kJ mol^{-1} .

An important class of ferrocene-based compounds contains chiral ferrocenyl phosphanes with planar chirality. Togni *et al.* have studied the behavior of phosphinopyrazoles (Figure 4.28) [77], in which the ferrocene moiety in the chelate ring restricts the conformational flexibility [78]. When the ligand is chelated to allyl-palladium fragments, it adopts two boat conformations in THF- d_8 or CDCl_3 solution. The dynamic equilibrium has been studied with phase sensitive NOESY experiments. In addition, for each conformer two rotational isomers are possible depending on the relative orientation of the allyl and the P,N ligand. This is the situation observed for the complex with the β -pinene allyl: The four possible conformers are seen at 253 K, and the ^{31}P EXSY (THF- d_8) shows that only conformational exchange is involved in the process.

Complexes with $\text{M}(\text{C}_6\text{F}_5)_2$ or $\text{M}(\text{C}_6\text{F}_5)\text{X}$ ($\text{X} = \text{Cl}, \text{Br}; \text{M} = \text{Pt}$) fragments and dppf have been reported, with dppf acting as bridging or as chelating ligands. Since the rotation of the C_6F_5 groups is restricted, these groups act as reporters and the conformational change in solution can be seen in the variable temperature ^{19}F NMR spectra. A similar spectroscopic behavior is observed for the ligand 1,1'-bis(phenylthiolate)ferrocene (dtpf), where a further source of fluxionality is the pyramidal inversion of sulfur [79]. A complete analysis of the fluxionality in ferrocenyldisulphide complexes has been carried out on $[\text{MX}_2(\text{Fe}(\text{C}_5\text{H}_4\text{SR})_2)]$ $\text{M} = \text{Pd}, \text{Pt}; \text{X} = \text{Cl}, \text{Br}; \text{R} = \text{Ph}, ^i\text{Pr}, ^t\text{Bu}$ [80]. A variable temperature NMR study of the complexes resolved the pyramidal inversion of the S atoms at about -100°C . ΔG^\ddagger values for this process were in the range 47 to 65 kJ mol^{-1} . The reversal of the metallacycle remained fast (at 100 MHz) at that low temperature.

4 CONFORMATIONAL CHANGES IN FIVE- OR SIX-MEMBER METALLACYCLES INVOLVING COORDINATED OLEFINS

A configurational change is also produced if a prochiral olefin initially coordinated by its *Re* face decoordinates and recoordinates through its *Si* face. An

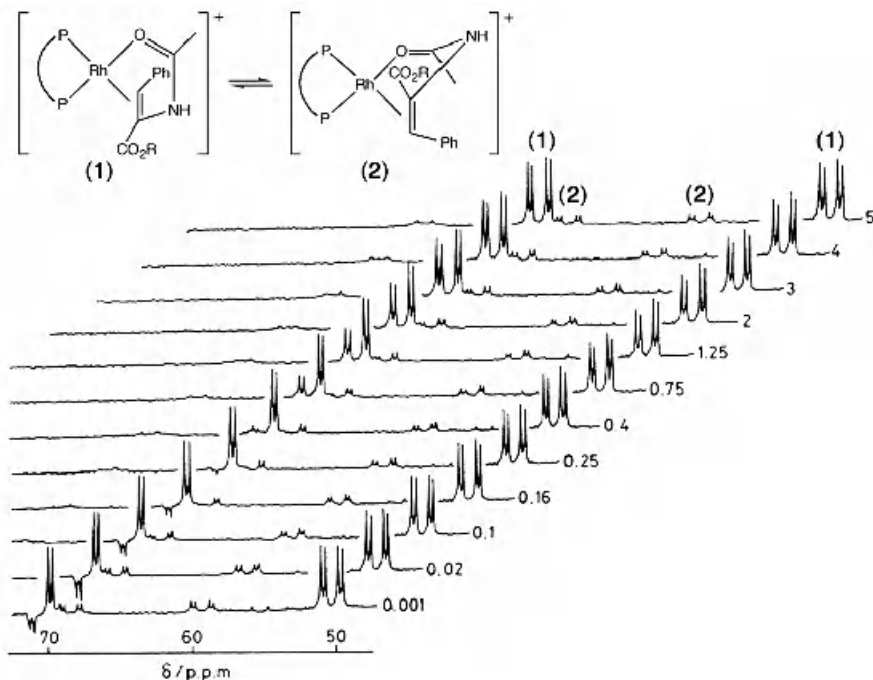


Figure 4.29 Mixture of isomers obtained by coordination of cinnamic acid to a diphosphine complex (P–P = (*S,S*)-2,3-bis(diphenylphosphino)butane). In the lower part, MT experiments in ^{31}P NMR. J. M. Brain *et al.*, *J. Chem. Soc. Chem. Commun.* **12**, 664 (1983) [81]. Reproduced by permission of the Royal Society of Chemistry.

interesting case (Figure 4.29), has been studied by Brown *et al.* using MT [81]. The selective excitation was achieved using DANTE. The experiments demonstrate that the face by which the olefin coordinates changes from *Si* (taking as reference the terminal carbon) in **1** to *Re* in **2**. The exchange rate constant at 325 K is 0.65 s^{-1} . Using the same technique in ^{13}C , with a sample containing excess enamide labeled at the carbonyl group, the authors could determine the rate constant for the complete decoordination of the enamide, to give the complex with two moles of solvent (ethanol) coordinated. This rate constant was 0.45 s^{-1} .

The conformational isomers of the Rh complexes shown in Figure 4.30 are photochemically equilibrated, but the thermal isomerization of **2** into **1** is slow and can be monitored by ^1H NMR in toluene- d_8 solution. This isomerization requires olefin decoordination, and the activation parameters reflect the energetic cost of breaking the Rh–olefin bond ($\Delta H^\ddagger = 114 \pm 1\text{ kJ mol}^{-1}$ (**2a**); $123.2 \pm 2\text{ kJ mol}^{-1}$ (**2c**); $124.2 \pm 2\text{ kJ mol}^{-1}$ (**2d**) and $\Delta S^\ddagger = 41 \pm 4\text{ J K}^{-1}\text{ mol}^{-1}$ (**2a**); $72 \pm 8\text{ J K}^{-1}\text{ mol}^{-1}$ (**2c**); $66 \pm 6\text{ J K}^{-1}\text{ mol}^{-1}$ (**2d**) [82]. The activation enthalpy is similar to the ethene dissociation enthalpy in $[\text{CpRh}(\text{C}_2\text{H}_4)_2]$ (about 129 kJ mol^{-1}) [83].

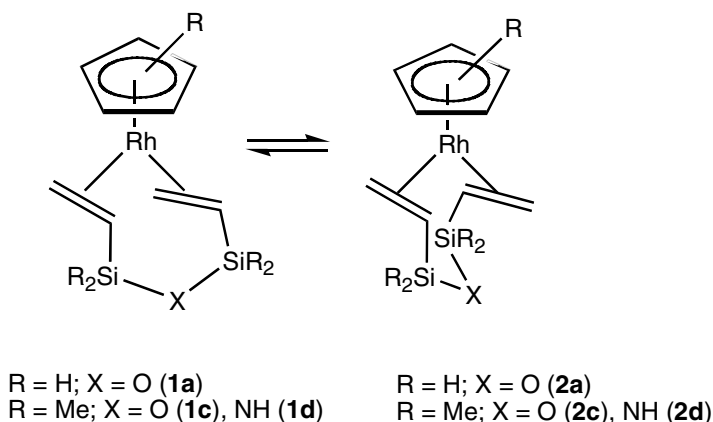


Figure 4.30 Conformational change by *Re* or *Si* olefin coordination.

5 CONFORMATIONAL CHANGES IN SEVEN-MEMBER METALLACYCLES

The behavior of tetrahedral $M(0)$ complexes $Pt(\text{diop})_2$ and $Pd(\text{diop})_2$ is used in enantioselective catalysis and has been studied by Brown and Chalener [84,85] and Campi *et al.* [86]. More recently Kadyrov *et al.* have examined square planar complexes $[Rh(L-L)(COD)]^+$ with $L-L = \text{dppb}$ (1,4-bis(diphenylphosphanyl)butane), *R*-diop and (*HO*-diop) (Figure 4.31) using theoretical calculations, a Cambridge X-ray data search, and NMR studies at low temperature [87]. In their theoretical study they identify two types of conformations: twist-chair (four different, three of them as pairs of enantiomers), and boat (two different, one as a pair of enantiomers). The metallacycles are always very flexible and the coalescence temperatures are below the temperatures accessible in usual solvents. However, working in CD_2Cl_2/CH_2Cl_2 at 161.98 MHz for ^{31}P , they could detect two independent processes, as illustrated for $[Rh(\text{diop})(COD)](PF_6)$ (Figure 4.31). A coalescence occurs in the range 210–180 K, which separates two families of conformers, chair and boat. The boat conformation is entropically favored, whereas the chair conformation is enthalpy stabilized, so the ratio of isomers changes noticeably with temperature.

The fluxionality of the boat stops in the range 165–123 K, and the two P atoms become nonequivalent. The conditions required to resolve the interconversion of the chairs was not reached, and the chair conformer shows an apparent C_2 symmetry. The activation free energy for the boat interconversion is 33.5 kJ mol⁻¹ for dppb and 36.0 kJ mol⁻¹ for diop (for Ni, Pd and Pt complexes the values cover a range from 40.2 to 48.9 kJ mol⁻¹) [84–86]. The activation free energy for the chair interconversion was estimated to be only of about 12.5 kJ mol⁻¹.

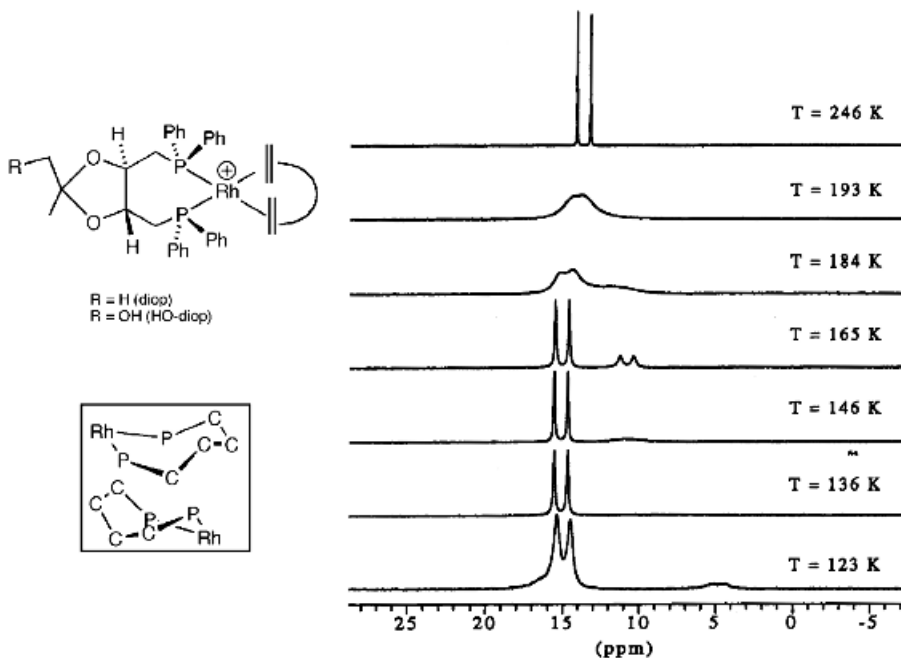


Figure 4.31 Structure of complexes $[\text{Rh}(\text{L-L})(\text{COD})]^+$ with $\text{L-L} = \text{diop}$ and (HO-diop) . Twist-chair (left), and boat (right) conformations of the $\text{Rh}(\text{L-L})$ metallacycle with $\text{L-L} = \text{dppb}$, R-diop and (HO-diop) are shown in the box. At the right, ^{31}P variable temperature study on $[\text{Rh}(\text{diop})(\text{COD})](\text{PF}_6)$ in $\text{CD}_2\text{Cl}_2/\text{CHFCl}_2$. R. Kadyrov *et al.*, *Eur. J. Inorg. Chem.* 705 (1999) [87]. Spectrum reproduced by permission of Wiley-VCH.

Cationic Rh complexes with dppb and dienes are catalysts for the hydrogenation of itaconate. In chiral analogs of the type shown in Figure 4.32, the incorporation of OMe diminishes the rate of the reaction compared to dppb , and the selectivity observed is low. The use of OH in place of OMe gives rise to a further loss in reactivity, but yields a significant gain in selectivity by approximately 35 % ee. An X-ray diffraction study of the complexes reveals the existence of one $\text{O} \cdots \text{Rh}$ interaction for OH , but not for OMe (Figure 4.32, right). The low temperature ^{31}P NMR spectrum in CD_3OD of the complex with OH (diolefin = NBD) is consistent with the presence of only the same O -bonded pentacoordinated complex as observed in the solid. At room temperature the two oxygens undergo fast exchange, associated with a fast conformational inversion. The complex with OMe and diolefin = COD , gives at 177 K a mixture of square-planar and O -bonded (pentacoordinated) complexes, which are in fast equilibrium at room temperature. This suggests that the conformational flexibility (and therefrom the asymmetric induction) might be modulated by the use of different O -donor substituents [88].

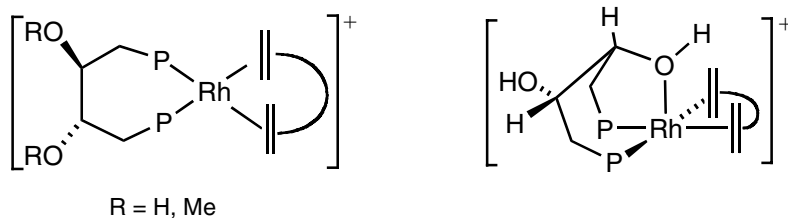


Figure 4.32 Possible square-planar and pentacoordinated isomers for Rh complexes with ligands derived from dppb.

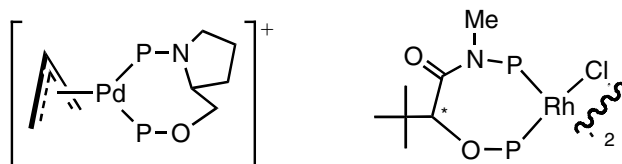


Figure 4.33 Complexes with diphosphines giving metallacycles with additional heteroatoms.

Other seven-member metallacycles with diphosphanes include heteroatoms in the cycle. This is the case of the systems reported by the groups of Pregosin (Figure 4.33, right) [89], and Cesarotti (Figure 4.33, left) [90]. These systems are very complex. In some of the compounds reported by Cesarotti *et al.* up to five different species are seen in solution at low temperature. For the complexes of Pregosin *et al.* the diphosphane was reported to act as chelating towards Rh(μ -Cl) or Rh(COD), but also as bridging ligand between Rh atoms. Equilibria between dimers and monomers were detected by EXSY.

6 CONFORMATIONAL CHANGES IN HIGHER METALLACYCLES

Complexes with a derivative of oxazolyphosphane (Figure 4.34, left) [91], or a diphosphane derived from 2,2' diphenylmethane (Figure 4.34, right) [92], have boat structures in the solid state, and show no boat inversion at room temperature.

Tsuji has studied the complexation behavior of a diphosphane based on a calix[4]arene scaffold, 5,17-bis(diphenylphosphanyl)-25,26,27,28-tetrabenzoyloxycalix[4]arene (diphoscalix, Figure 4.35) [93]. This ligand acts as chelating in spite of the fact that it forms a 14-member metallacycle, due to geometrical constraints. It chelates in a *cis* fashion in the mononuclear [PtCl₂(diphoscalix)] and [Pd(η^3 -allyl)(diphoscalix)](BF₄). The mononuclear Pt and Pd complexes exhibit C₁ symmetry at -80 °C, the latter as a mixture

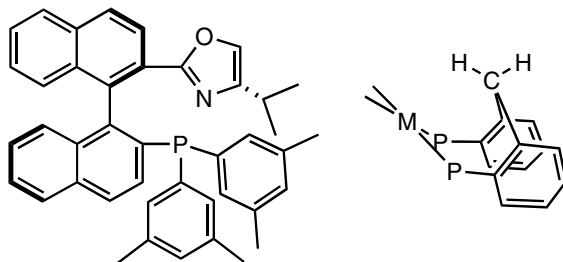


Figure 4.34 Some eight-member metallacycles.

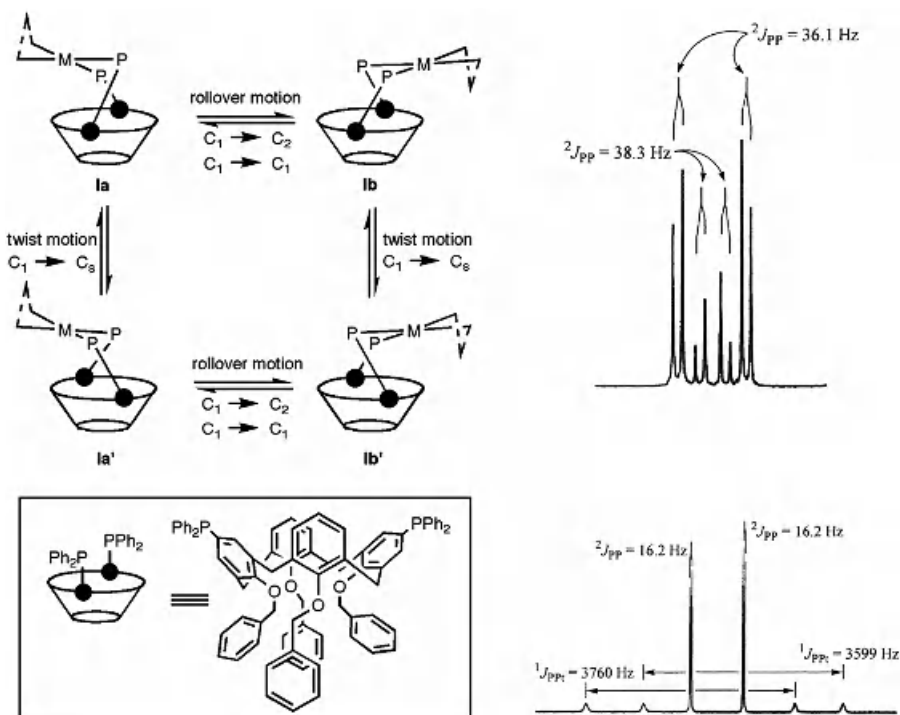


Figure 4.35 Schematic representation of 5,17-bis(diphenylphosphino)-25,26,27,28-tetrabenzyloxycalix[4]arene, and low temperature spectra of their complexes $[\text{PtCl}_2(\text{diphoscalix})]$ (down) and $[\text{Pd}(\eta^3\text{-allyl})(\text{diphoscalix})](\text{BF}_4)$ (up). Spectra reproduced with permission from K. Takenaka *et al.*, *Organometallics* **21**, 1162 (2002) [93]. Copyright (1993) American Chemical Society.

of two stereoisomers both possessing C_1 symmetry, corresponding to the two possible arrangements of the allyl-*endo* and *exo*-with respect to the coordination plane. However, their NMR spectra measured at 20°C indicate a higher, time-averaged, C_{2v} symmetry for the Pt dichloro complex, and a C_s symmetry

for the Pd allyl. [PtCl₂(diphoscalix)] produces an AB system in the ³¹P NMR spectrum at -80 °C because in the λ or δ conformations the two P atoms are nonequivalent. [Pd(η³-allyl)(diphoscalix)](BF₄) gives two AB systems (5:2) at low temperature, because, in addition to the nonequivalence observed for the Pt complex, the allyl group can be *exo* or *endo*. (Figure 4.35).

This fluxional behavior is caused by the two separable motions shown in Figure 4.35, rollover motion of the coordination plane, and twist motion of the calix[4]arene scaffold. Both are needed to produce the equivalence observed at room temperature. The twist motion is a δ/λ conversion while the rollover motion is a kind of boat inversion through an intermediate where the coordination plane is parallel to the axis of the calixarene. The activation parameters (by LSA) are $\Delta H^\ddagger_{\lambda/\delta}$ (twist motion) = 43 ± 1.5 kJ mol⁻¹, and ΔH^\ddagger boat inversion (rollover motion) = 41 ± 1.4 kJ mol⁻¹ for [Pd(η³-allyl)(diphoscalix)](BF₄). For [PtCl₂(diphoscalix)] the overall value (λ/δ + boat inversion) is $\Delta H^\ddagger = 41 \pm 0.9$ kJ mol⁻¹.

7 ACKNOWLEDGMENT

We thank the Ministerio de Ciencia y Tecnología (Project BQU2001–2015) and the Junta de Castilla y León (Project VA120-01) for financial support of our research in this area.

8 REFERENCES

1. E. J. Corey and J. C. Bailar, *J. Am. Chem. Soc.* **81**, 2620 (1959).
2. W. S. Knowles, *Angew. Chem. Int. Ed. Engl.* **41**, 1998 (2002). *2001 Nobel Lecture in Chemistry*.
3. R. Noyori, *Angew. Chem. Int. Ed. Engl.* **41**, 2008 (2002). *2001 Nobel Lecture in Chemistry*.
4. K. B. Sharpless, *Angew. Chem. Int. Ed. Engl.* **41**, 2024 (2002). *2001 Nobel Lecture in Chemistry*.
5. See for instance the monographic volume *Enantioselective Catalysis*, edited by C. Bolm and J. Gladysz, *Chem Rev.* **8**, (2003).
6. J. R. Gollgoly and C. J. Hawkins, *Inorg. Chem.* **9**, 576 (1970).
7. J. R. Gollgoly and C. J. Hawkins, *Inorg. Chem.* **8**, 1168 (1969).
8. J. R. Gollgoly and C. J. Hawkins, *Inorg. Chem.* **11**, 156 (1972).
9. L. J. DeHayes and D. H. Busch, *Inorg. Chem.* **12**, 1505 (1973).
10. G. R. Brubaker and D. W. Johnson, *Coord. Chem. Rev.* **53**, 1 (1984)
11. P. Comba, *Coord. Chem. Rev.* **186**, 81 (1999).
12. P. Comba, *Coord. Chem. Rev.* **182**, 343 (1999).
13. B. P. Hay, *Coord. Chem. Rev.* **126**, 177 (1993).
14. C. J. Hawkins and J. A. Palmer, *Coord. Chem. Rev.* **44**, 1 (1982).
15. Y. Kuroda, N. Tanaka, M. Goto, and T Sakai, *Inorg. Chem.* **28**, 997 (1989).
16. Z. J. Guo, A. Habtemariam, P. J. Sadler, R. Palmer, B. S. Potter, *New J. Chem.* **22-1**, 11 (1998).

17. L. Dahlenburg, *Eur. J. Inorg. Chem.* **15**, 2733 (2003).
18. E. W. Abel, S. K. Bhargava, and K. G. Orrell, *Prog. Inorg. Chem.* **32**, 1 (1984).
19. K. G. Orrell, *Coord. Chem. Rev.* **96**, 1 (1989).
20. W. Levason, S. D. Orchard, and G. Reid, *Coord. Chem. Rev.* **225**, 159 (2002).
21. R. J. Cross, D. S. Rycroft, D. W. A. Sharp, H. Torrens, *J. Chem. Soc. Dalton Trans.* 2434, (1980).
22. H. Berger, R. Nesper, P. S. Pregosin, H. Rügger, M. Worle, *Helv. Chim. Acta* **76**, 1520 (1993).
23. D. G. Allen, G. M. McLaughlin, G. B. Robertson, W. L. Steffen, G. Salem, S. B. Wild, *Inorg. Chem.* **21**, 1007 (1982).
24. J. W. L. Martin, J. A. L. Palmer, S. B. Wild, *Inorg. Chem.* **23**, 2664 (1984).
25. P. H. Leung, G. M. McLaughlin, J. W. L. Martin, S. B. Wild, *Inorg. Chem.* **25**, 3329 (1986).
26. P. H. Leung, A. C. Willis, S. B. Wild, *Inorg. Chem.* **31**, 1406 (1992).
27. S. Y. M. Chooi, M. K. Tan, P.-H. Leung, K. F. Mok, *Inorg. Chem.* **33**, 3096 (1994).
28. W. McFarlane, J. D. Swarbrick, J. L. Bookham, *J. Chem. Soc. Dalton Trans.* 3233, (1998).
29. V. V. Dunina, L. G. Kuz'mina, M. Y. Rubina, Y. K. Grishin, Y. A. Veits, E. I. Kazakova, *Tetrahedron: Asymm.* **10**, 1483 (1999).
30. I. Toth, B. E. Hanson, *Organometallics* **12**, 1506 (1993).
31. T. G. Appleton, J. R. Hall, *Inorg. Chem.* **11**, 117 (1972).
32. R. Gust, H. Schönenberger, J. Kritzenberger, K.-J. Range, U. Klement, T. Burgemeister, *Inorg. Chem.* **32**, 5939 (1993).
33. M. A. Alonso, J. A. Casares, P. Espinet, K. Soulantica, *Inorg. Chem.* **33**, 3856 (2003).
34. T. B. Rauchfuss, F. T. Patino, D. M. Roundhill, *Inorg. Chem.* **14**, 652 (1975).
35. G. M. Kapteijn, M. P. R. Spee, D. M. Grove, H. Kooijman, A. L. Spek, G. van Koten, *Organometallics* **15**, 1405 (1996).
36. J. Pfeiffer, G. Kickelbick, U. Schubert, *Organometallics* **19**, 62 (2000).
37. J. Karas, G. Huttner, K. Heinze, P. Rutsch, L. Zsolnai, *Eur. J. Inorg. Chem.* 405, (1999).
38. A. Frick, V. Schulz, G. Huttner, *Eur. J. Inorg. Chem.* 3129 (2002).
39. J. Bakos, I. Tóth, B. Heil, G. Szalontai, L. Párkányi, V. Fülöp, *J. Organomet. Chem.* **370**, 263 (1989).
40. M. A. Alonso, J. A. Casares, P. Espinet, K. Soulantica, *Angew. Chem. Int. Ed. Engl.* **38**, 533 (1999).
41. J. A. Casares, P. Espinet, K. Soulantica, I. Pascual, A. G. Orpen, *Inorg. Chem.* **36**, 5251 (1997).
42. M. A. Alonso, J. A. Casares, P. Espinet, K. Soulantica, J. P. H. Charmant, A. G. Orpen, *Inorg. Chem.* **39**, 705 (2000).
43. N. C. Payne, D. W. Stephan, *Inorg. Chem.* **21**, 182 (1982).
44. I. Yamada, M. Ohkouchi, M. Yamaguchi, T. Yamagishi, *J. Chem. Soc., Perkin Trans. 1*, 1869 (1997).
45. I. D. McKay, N. Payne, *Can. J. Chem.* **64**, 1930 (1986).
46. W. R. Cullen, F. W. B. Eisentein, C. H. Huang, A. C. Willis, E. SanYeh, *J. Am. Chem. Soc.* **102**, 988 (1980).
47. I. D. McKay, N. Payne, *Acta Crystallogr., Sect. C.: Cryst. Struct. Commun.* **42**, 307 (1986).
48. N. C. Payne, G. R. Tobin, *Acta Crystallogr.* **C48**, 45 (1992).
49. B. Crociani, S. Antonaroli, M. L. Di Vona, S. Licoccia, *J. Organomet. Chem.* **631**; 1–2, 117 (2001).
50. D. A. Evans, K. R. Campos, J. S. Tedrow, F. E. Michael, M. R. Gagné, *J. Am. Chem. Soc.* **122**, 7905 (2000), and references therein.

51. A. Albinati, J. Eckert, P. Pregosin, H. R egger, R. Salzmann, C. St ssel, *Organometallics* **16**, 579 (1997).
52. S. Trofimenko, *Scorpionates: The Coordination Chemistry of Polypyrazolylborate Ligands*, Imperial College Press, London, 1999.
53. S. Trofimenko, *Chem. Rev.* **93**, 943 (1993).
54. N. Kitajima, W. B. Tolman, *Prog. Inorg. Chem.* **43**, 419 (1995).
55. C. Slugovc, I. Padilla-Mart nez, S. Sirol, E. Carmona, *Coord. Chem. Rev.* **213**, 129 (2001).
56. U. E. Bucher, A. Currao, R. Nesper, H. R egger, L. M. Venanzi, E. Younger, *Inorg. Chem.* **34**, 66 (1995).
57. T. O. Northcutt, R. J. Lachicotte, W. D. Jones, *Organometallics* **17**, 5148 (1998).
58. M. Akita, K. Ohta, Y. Takahashi, S. Hikichi, Y. Moro-oka, *Organometallics* **16**, 4121 (1997).
59. A. Albinati, M. Bovens, H. R egger, L. M. Venanzi, *Inorg. Chem.* **36**, 5991 (1997).
60. D. Sanz, M. D. Santa-Maria, R. M. Claramunt, M. Cano, J. V. Heras, J. A. Campo, F. A. Ruiz, E. Pinilla, A. Monge, *J. Organomet. Chem.* **526**, 341 (1996).
61. M. C. Keyes, V. G. Young Jr., W. B. Tolman, *Organometallics* **15**, 4133 (1996).
62. J. A. Casares, S. Coco, P. Espinet, Y.-S. Lin, *Organometallics* **14**, 3058 (1995).
63. J. A. Casares, P. Espinet, J. M. Mart nez-Irarduya, Y.-S. Lin, *Organometallics* **16**, 770 (1997).
64. M. A. Alonso, J. A. Casares, P. Espinet, J. M. Mart nez-Irarduya, C. P rez-Briso, *Eur. J. Inorg. Chem.* 1745, (1998).
65. J. A. Casares, P. Espinet, J. M. Mart n-Alvarez, V. Santos, *Inorg. Chem.*, **43**, 189 (2004).
66. M. E. Wright, C. K. Lowe-Ma, *Organometallics* **9**, 347 (1990).
67. M. E. Wright, S. A. Svejda, M.-J. Jin, M. A. Peterson, *Organometallics* **9**, 136 (1990).
68. M. E., Wright, *Tetrahedron Letters* **28**, 2322 (1987).
69. P. K. Byers, A. J. Canty, R. T. Honeyman, *J. Organomet. Chem.* **385**, 417 (1990).
70. P. E. Rush, J. D. Oliver, *J. Chem. Soc., Chem. Commun.* 996, (1974).
71. A. J. Canty, N. J. Minchin, P. C. Healy, A. H. White, *J. Chem. Soc. Dalton Trans.* 1795, (1982).
72. A. J. Canty, N. J. Minchin, L. M. Engelhardt, B. W. Skelton, A. H. White, *J. Chem. Soc. Dalton Trans.* 1253, (1983).
73. P. K. Byers, A. J. Canty, N. J. Minchin, J. M. Patrick, B. W. Skelton, A. H. White, *J. Chem. Soc. Dalton Trans.* 1183, (1985).
74. P. K. Byers, A. J. Canty, *Organometallics* **9**, 210 (1990).
75. I. R. Butler, W. R. Cullen, T. J. Kim, S. J. Rettig and J. Trotter, *Organometallics* **4**, 972 (1985).
76. A. G. Avent, R. B. Bedford, P. A. Chaloner, S. Z. Dewa, P. B. Hitchcock, *J. Chem. Soc. Dalton Trans.* 4633, (1996).
77. A. Togni, C. Breutel, A. Schnyder, F. Spindler, H. Landert, A. Tijani, *J. Am. Chem. Soc.* **116**, 4062 (1994).
78. U. Burkhardt, V. Gramlich, P. Hofmann, R. Nesper, P. S. Pregosin, R. Salzmann, A. Togni, *Organometallics* **15**, 3496 (1996).
79. S. Coco, P. Espinet, *J. Organomet. Chem.* **484**, 113 (1994).
80. K. G. Orrell, V. Sik, C. H. Brubaker, Jr., B. McCulloch, *J. Organomet. Chem.* **276**, 267 (1984).
81. J. M. Brown, P. A. Chaloner, G. A. Morris, *J. Chem. Soc. Chem. Commun.* **12**, 664 (1983).
82. S. S. D. Brown, S. N. Heaton, M. H. Moore, R. N. Perutz, G. Wilson, *Organometallics* **15**, 1392 (1996).
83. R. Cramer, *J. Am. Chem. Soc.* **94**, 5681 (1972).
84. J. M. Brown, P. A. Chaloner, *J. Am. Chem. Soc.* **100**, 4307 (1978).

85. J. M. Brown, P. A. Chaloner, *J. Organomet. Chem.* **217**, C-29 (1981).
86. E. M. Campi, P. S. Elmes, W. R. Jackson, R. J. Thomson, J. A. Weigold, *J. Organomet. Chem.* **371**, 393 (1989).
87. R. Kadyrov, A. Börner, R. Selke, *Eur. J. Inorg. Chem.* 705, (1999).
88. S. Borns, R. Kadyrov, D. Heller, W. Baumann, A. Spannenberg, R. Kempe, J. Holz, A. Börner, *Eur. J. Inorg. Chem.* 1291, (1998).
89. N. Feiken, P. Pregosin, G. Trabesinger, *Organometallics* **17**, 4510 (1998).
90. E. Cesarotti, M. Grassi, L. Prati, F. Demartin, *J. Chem. Soc. Dalton Trans.* 2073, (1991).
91. K. Sevakumar, M. Valentini, P. S. Pregosin, A. Albinati, F. Eisenträger, *Organometallics* **19**, 1299 (2000).
92. W. Lesueur, E. Solari, C. Floriani, *Inorg. Chem.* **36**, 3354 (1997).
93. K. Takenaka, Y. Obora, L. H. Jiang, Y. Tsuji, *Organometallics* **21**, 1158 (2002).

5 Dynamic and Kinetic Aspects of Metallodrugs by NMR

FEI LI AND HONGZHE SUN

*Department of Chemistry and Open Laboratory of Chemical Biology,
the University of Hong Kong, Pokfulam Road, Hong Kong. Key Laboratory for
Supramolecular Structure and Materials, Jilin University, P. R. China*

1 INTRODUCTION

The use of metal containing compounds in medicine and health applications has been practiced for several centuries [1]. The Egyptians used copper to sterilize water in 3000 BC and the Chinese were using gold in a variety of medicines 3500 years ago. In fact, the first modern chemotherapeutic agent was an organoarsenic compound (Erlich606 or salvarsan), for the treatment of syphilis, although modern pharmaceuticals are dominated by organic compounds. The success of cisplatin (*cis*-[Pt(NH₃)₂Cl₂]) as an anticancer drug has largely stimulated the modern use of metal compounds for therapeutic and diagnostic purposes. Beside platinum, clinically useful metal complexes include gold as antiarthritic agents, lithium for manic depression, antimony as antileishmaniasis agents, bismuth as antiulcer drugs, gadolinium (Gd³⁺) as magnetic resonance imaging contrast agents and technetium (^{99m}Tc) as radio-diagnostic agents [1–4]. Recently, arsenic trioxide (As₂O₃, Trisenox[®]), an active component in various traditional Chinese medicines for several hundred years, was approved for clinical use for the treatment of patients with acute promyelocytic leukemia (APL) only within three years since the first study of the drug in the United States [5,6]. Not only do inorganic compounds extend the range of drugs available, but also they are successful in treating some diseases where organic compounds are not.

In contrast to organic compounds, both the metal and the bound ligand(s) determine the biological activity of metallodrugs, not just the metal itself. The ligand is often, but not always, an organic (chelate) compound that binds to the metal ion(s) and modifies the chemical (e.g., reactivity) and biochemical (e.g., tissue uptake and biodistribution) properties. The active species may not be the one that is administered or tested *in vitro*, and it may be biotransformed

by ligand substitution (exchange) and/or redox reactions before it reaches the target sites. It is important to investigate both kinetic (ligand-exchange dynamics, mechanism and pathway) and dynamic aspects of the reactivity of a metal complex since biological systems are rarely at thermodynamic equilibrium. For example, it is known that kinetics are crucial to antitumor activities of platinum drugs and possibly other metallo-anticancer complexes (e.g., Ru(II)/Ru(III)), and ligand-exchange kinetics of metal complexes are found in the same order of magnitudes as the division of tumor cells [7]. Modern multinuclear and multidimensional NMR spectroscopy offers a very powerful method to allow the kinetics and dynamics of metallodrugs in solution, and to a lesser extent in the solid state to be followed, and is also applicable for studying the interaction of metal compounds with biomolecules under physiologically relevant conditions. In this chapter, we describe examples of the application of NMR spectroscopy to the kinetics and dynamics of metallopharmaceuticals in solutions including biofluids and cells, and complexation to biomolecules (nucleic acids, peptides and proteins). Since the topic is vast, we do not intend to be comprehensive but rather focus on platinum, titanium and ruthenium anticancer drugs, gold antiarthritic, vanadium antidiabetic, antimony antiparasitic, bismuth antiulcer drugs and MRI contrast agents. The reader is referred to related papers elsewhere [8].

2 METHODS OF STUDY BY NMR

Most medicinally relevant metals are quadrupolar nuclei. Only those in highly symmetric complexes give relatively sharp resonances. This situation may be improved at very high fields (e.g., ≥ 14.1 T), which are expected to dramatically sharpen the central transition ($m = \frac{1}{2}$ to $-\frac{1}{2}$) of half-integer quadrupolar nuclei such as ^{27}Al ($I = \frac{5}{2}$), ^{45}Sc ($I = \frac{7}{2}$) and ^{71}Ga ($I = \frac{3}{2}$) [9]. In the limit of slow isotopic molecular motion, as is the case for moderate- to high-frequency nuclei bound to proteins ($\omega\tau_c \gg 1$), the central transition ($m = \frac{1}{2} \rightarrow -\frac{1}{2}$) gives rise to a relatively narrow signal and the linewidth ($\Delta\nu_{\frac{1}{2}}$) also decreases with increasing magnetic field:

$$\Delta\nu_{\frac{1}{2}} = k\chi^2/(\tau_c\nu_0^2) \quad (5.1)$$

where χ is the quadrupolar coupling constant, τ_c is the correlation time of fluctuations in the electric field gradient at the nucleus and ν_0 is the resonance frequency which is proportional to the magnetic field.

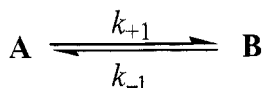
^1H NMR spectroscopy will continue to be the most widely used method for monitoring the behavior of ligands and biomolecules. Other spin $I = \frac{1}{2}$ nuclei such as ^{13}C , ^{15}N , ^{31}P , ^{119}Sn and ^{195}Pt , and weak quadrupolar nuclei (e.g., ^6Li , ^7Li , ^{27}Al and ^{51}V) have also quite often been used. Similar to study of organic drugs by NMR spectroscopy, almost all of the available NMR techniques have been used for studying the kinetic aspect of metallodrugs, from one-

two-dimensional NMR techniques, such as COSY, TOCSY, ROESY, HMQC and HSQC-TOCSY [10]. There is an increasing interest in the use of indirect (or inverse) detection (e.g., [^1H , X] HSQC and HSQC-TOCSY, where X = ^{13}C , ^{15}N or ^{119}Sn) for kinetic study due to the significantly enhanced sensitivity by a theoretical maximum $\{|\gamma_{\text{H}}|/|\gamma_{\text{X}}|\}^{5/2}$, with respect to direct detection. This technique, in combination with isotopic labeling of specific nucleus (e.g., ^{13}C or ^{15}N) of the ligand, has been successfully used in the kinetic investigation of platinum anticancer agent activation (hydrolysis), metabolism, DNA and protein binding [8,11,12].

Due to the ligand ‘wrapping’ around the metal in an asymmetric conformation (e.g., MRI contrast agent) or the metabolism of metallodrugs in biological systems, more than one metal environment (species) can normally be present for metallodrugs. A nucleus will exchange between two or more environments in which its NMR parameters, such as chemical shift or relaxation, differ. These may be either intramolecular (e.g., conformational/configurational equilibria) or intermolecular exchanges (e.g., binding of metallodrugs to biomolecules, protonation/deprotonation equilibrium of ionizable groups). Dynamic NMR methods are especially suited to characterize kinetic and dynamic processes that take place at equilibrium. Even degenerate equilibria, in which exchange leads to metallodrugs or their biomolecule complexes indistinguishable from the original ones, can be investigated by NMR spectroscopy.

Dynamic NMR methods are well established and have been described in numerous books and reviews [13–16]. We only summarize briefly those methods that are most widely used and their range of applications. In all these cases, the effect of a dynamic process on the NMR spectrum depends on its exchange rate with respect to the magnitude of the accompanying change in the corresponding NMR parameters such as chemical shift and spin–spin coupling, and three different states can be distinguished: slow, fast and intermediate exchange (Table 5.1).

In slow exchange, separate resonances with sharp linewidths are observed for the nucleus of interest on the NMR spectrum. In contrast, only a singly averaged resonance is observed in fast exchange, while in intermediate exchange, a complex series of changes in appearance of the spectrum from separate broad resonances coalescing into one (broad) is seen. The effect of exchange on NMR spectra can be illustrated by a two-site first-order exchange:



The lifetimes (τ) of state A and B are, $\tau_{\text{A}} = 1/k_{+1}$ and $\tau_{\text{B}} = 1/k_{-1}$, respectively. For the slow exchange, the exchange rate (k) can readily be measured from the linewidth ($\Delta\nu_{1/2} = (\pi T_2)^{-1}$) of the resonance, which is derived from the apparent spin–spin relaxation rates, $1/T_{2,\text{obs}}$, based on the following equation (for

Table 5.1 Rate constants for the hydrolysis of selected platinum(II)–am(m)ine anticancer complexes by NMR

Complexes	$k/10^{-5}(\text{s}^{-1})$	$t_{1/2}$ (h)	I (M)	Temperature (°C)	Reference
Cisplatin	$k_1: 7.66^a$ $k_2: 7.51$	2.51 2.56	0.01	37	49
<i>cis</i> -[Pt(NH ₃)(2-Py)Cl ₂] (AMD473) ^c	$k_{1a}: 3.19; k_{1b}: 3.68$ $k_{2a}: 7.30; k_{2b}: 0.35$	6.03; 5.23 2.64; 55.0	0.1	37	57
1,1/ <i>t,t</i> ($n = 6$)	$k_1: 7.9$ $k_2: 7.9$	2.44 2.44	0.002	37	62
1,0,1/ <i>t,t,t</i> ($n = 6$) (BBR3464)	$k_1: 7.1$ $k_2: 7.1$ $k_1: 9.2$ $k_2: 9.2^a$	2.71 2.71 2.09 2.09	0.1 0.015	25 25	64

^a Rate constants determined during the reaction of cisplatin with DNA.

^b Determined by other methods.

^c Corresponds to the hydrolysis of Cl⁻ *trans* to the 2-methyl pyridine (2-Py).

first-order exchange),

$$\frac{1}{T_{2A,\text{obs}}} = \frac{1}{T_{2A}} + \frac{1}{\tau_A} = \frac{1}{T_{2A}} + k_{+1} \quad \text{and} \quad \frac{1}{T_{2B,\text{obs}}} = \frac{1}{T_{2B}} + \frac{1}{\tau_B} = \frac{1}{T_{2B}} + k_{-1} \quad (5.2)$$

Where $1/T_{2A}$ and $1/T_{2B}(= \pi \Delta\nu_{1/2})$ represent the spin–spin relaxation rates and $(\pi T_{2A})^{-1}$ and $(\pi T_{2B})^{-1}$ are the natural linewidth.

For fast exchange, a weighted average resonance at $\delta_{\text{obs}} = p_A \delta_A + p_B \delta_B$ for two-site exchange (and $\delta_{\text{obs}} = \sum p_i \delta_i$ for multi-site exchange, is observed. Where p_A and p_B are the fractional populations of states A and B, with $p_A + p_B = 1$ (or $\sum p_i = 1$ for multi-site exchange). The exchange process causes an additional broadening of the linewidth by $4\pi^2 p_A p_B^2 (\delta_A - \delta_B)^2 / k_{+1}$, and the observed relaxation rate (linewidth) for moderate fast exchange, is described by:

$$\begin{aligned} \frac{1}{T_{2,\text{obs}}} &= \frac{p_A}{T_{2A}} + \frac{p_B}{T_{2B}} + \frac{p_A p_B^2 [2\pi (\delta_A - \delta_B)]^2}{k_{+1}} \\ &= \frac{p_A}{T_{2A}} + \frac{p_B}{T_{2B}} + \frac{p_A^2 p_B [2\pi (\delta_A - \delta_B)]^2}{k_{-1}} \end{aligned} \quad (5.3)$$

Therefore, the faster the exchange reaction or the smaller the frequency difference ($(\delta_A - \delta_B)$ in Hz), the narrower the linewidth. Such an increase in exchange rate can be accompanied by either a temperature increase or a decrease in frequency separation on a lower magnetic field. For very fast exchange, the above equation can be simplified as: $1/T_{2,\text{obs}} = p_A/T_{2A} + p_B/T_{2B}$.

For the intermediate exchange where the resonances change upon passing from a slow into a fast regime, the lineshape can be described by McConnell's modification of the Bloch equations [17]. For a first-order two-site exchange without homonuclear scalar coupling, for example, the lineshape is given by:

$$g(\nu) = \frac{2\tau_A(\nu_A - \nu_B)^2}{[\nu - (\nu_A + \nu_B)/2]^2 + \pi^2\tau_A^2(\nu - \nu_A)^2(\nu - \nu_B)^2} \quad (5.4)$$

A number of approximate methods have been proposed to extract rate constants from NMR spectra. By far, the most commonly used method is the lineshape simulation since the lineshape is determined by the parameters of each site and the exchange rates as discussed above. Each site has chemical shifts, scalar couplings and linewidths which are determined by spin-spin relaxation rates, and populations with respect to other site(s). The description of these lineshapes in the presence of spin-spin coupling requires the use of density matrix theory which is rather complicated [18]. Complete lineshape analysis therefore normally needs computer simulation and various computer programs (e.g., gNMR and MEX/MEXICO) are available for this purpose [19]. Exchange in an equally populated two-site system formed by uncoupled nuclei can also be addressed simply by using the coalescence temperature, where the lineshape is characterized by a flat top and the corresponding rate constant (k_A^c) can be obtained from

$$k_A^c = k_{+1} = k_{-1} = \frac{\pi(\nu_A - \nu_B)}{\sqrt{2}} = 2.22(\nu_A - \nu_B) \quad (5.5)$$

For an unequally populated system, the rate constant, $k_A^c = \frac{\pi(\nu_A - \nu_B)}{X}$, where X is the solution of the equation: $X^6 - 6X^4 + [12 - 27(\Delta p)^2]X^2 - 8 = 0$, and $\Delta p = p_A - p_B$ [20].

When the exchange is slow, and separate resonances can be observed for the nucleus in two or more states, magnetization transfer is also a useful technique to trace the exchange pathway. Both saturation transfer and inversion transfer have been used in chemical and biochemical studies [16b,21,22]. The former has the advantage of simplicity, in terms of experimental design and data analysis, since the magnetization transfer can be described by a single exponential function. However, the latter has good sensitivity and covers a fairly wide range of exchange rate, in contrast to the saturation transfer experiment, with a smaller dynamical and temporal range.

The effect of exchange processes can be observed in two-dimensional spectrum and be analyzed in a very similar way. The 2D exchange spectroscopy (EXSY) is in principle, identical to the NOESY experiment. Cross peaks in 2D EXSY experiments arise from noncoherent magnetization transfer between sites with different resonances. Noncoherent magnetization transfer takes place either by exchange of nuclei between different sites or by cross-relaxation (NOE). However, the mixing time in EXSY is usually chosen to be shorter,

since the exchange rate is normally much faster than the cross-relaxation rate. Exchange rates can be extracted from EXSY spectra at a single mixing time based on the following equation:

$$\mathbf{I}(\tau_m) = \exp(\mathbf{L}\tau_m) \cdot \mathbf{P} \quad (5.6)$$

where \mathbf{I} is the integrated intensity matrix of the 2D absorption peak; $\mathbf{L} = -\mathbf{R} + \mathbf{K}$, is the dynamic matrix which expresses the effect of spin–lattice relaxation, cross-relaxation (relaxation matrix \mathbf{R}) and chemical exchange (kinetic matrix \mathbf{K}); τ_m is the mixing time and \mathbf{P} is the relative populations of the sites. The dynamic matrix \mathbf{L} can be obtained directly from the normalized experimental intensity (\mathbf{A}) by taking the logarithm of \mathbf{A} and dividing by the mixing time τ_m . In practice, it can be readily carried out with a general-purpose program such as Mathematica [23], by diagonalization of the matrix \mathbf{A} . Again, computer programs (e.g., D2D program) are available for the determination of the rate constants from 2D EXSY data, and vice versa [24].

For the simplest case of the first-order two-site exchange with equal populations and equal relaxation rates (\mathbf{R}), the diagonal peaks: $I_{AA} = I_{BB} = \frac{1}{2}[1 + \exp(-2k\tau_m)]\exp(-\tau_m/T_1)$ and the cross-peaks, $I_{AB} = I_{BA} = \frac{1}{2}[1 - \exp(-2k\tau_m)]\exp(-\tau_m/T_1)$.

The exchange rate can be determined directly from the ratio of the peak intensities at short mixing times [25]

$$\frac{I_{AA}}{I_{AB}} = \frac{1 + \exp(-2k\tau_m)}{1 - \exp(-2k\tau_m)} \approx \frac{1 - k\tau_m}{k\tau_m} \quad (5.7)$$

There are several advantages of the 2D EXSY over other methods such as saturation transfer and inversion transfer. The major advantage of this technique is its ability to provide an entire exchange ‘map’ of the exchange system, which allows all exchange pathways to be observed simultaneously. All the exchange rate constants, in principle, can be extracted from one experiment at one temperature. This is extremely important in multi-site exchange systems and in those with limited range of temperature change, particularly in aqueous solutions. In addition, it helps to resolve the exchanging spin in the 2D matrix and avoid potential overlapping with other non-exchanging spins. This technique is very valuable in the study of the dynamics of complex formations and metal/metallo-drug translocations. For example, the dynamic matrix was solved and the activation parameters of the intra- and intermolecular dynamic processes that occur in the lanthanide–DOTA complex were obtained with the use of 2D EXSY at different temperatures [26]. However, 2D EXSY covers a small dynamic range and is only suitable for slow exchange. In addition, measurement of 2D EXSY spectra is time consuming and sometimes, 1D selective EXSY can be used instead [27].

The rates from NMR data, as a function of temperature, will allow the activation parameters of the dynamic process to be determined. The activation energy (E_a) for an exchange process can be extracted according to the Arrhenius

equation:

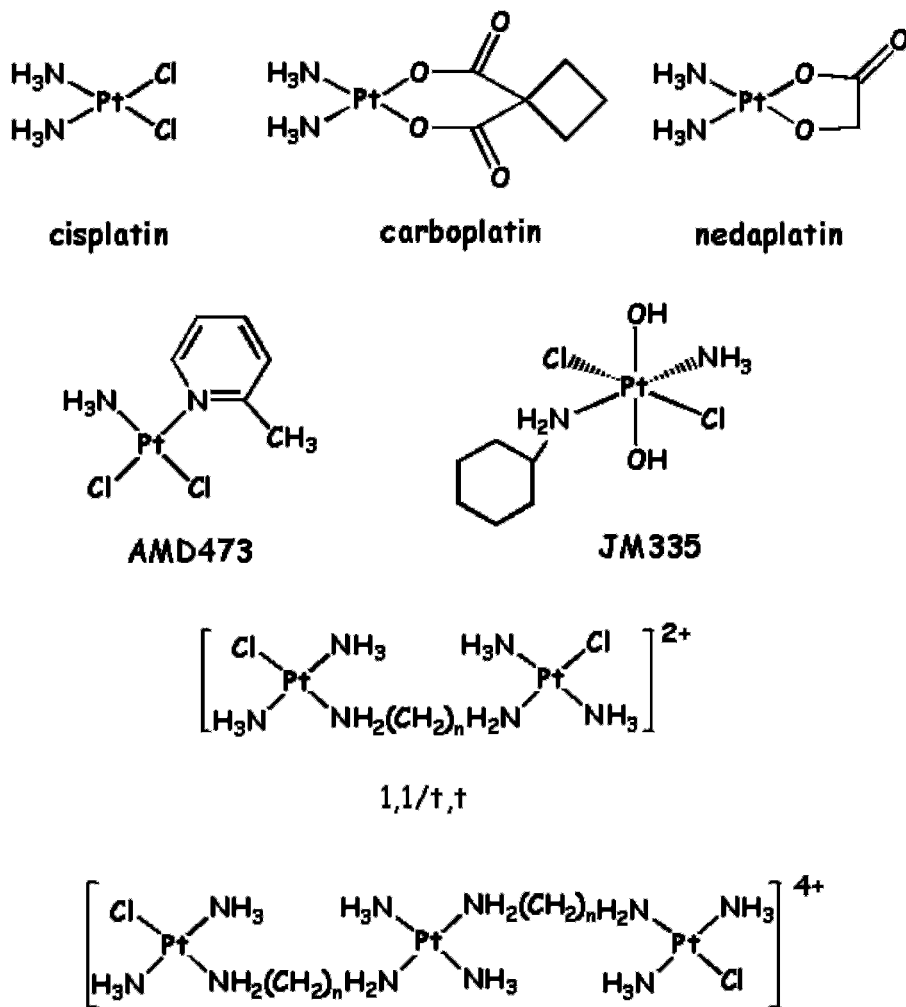
$$\ln k = -\frac{E_a}{RT} + \ln A \quad (5.8)$$

An Eyring plot of $\ln(k/T)$ versus $1/T$ should give a straight line with slope $(-\Delta H^\ddagger/R)$ and intercept $(23.76 + \Delta S^\ddagger/R)$. The activation enthalpy (ΔH^\ddagger), activation entropy (ΔS^\ddagger) and activation free energy ($\Delta G^\ddagger = \Delta H^\ddagger - T\Delta S^\ddagger$) can be obtained.

3 PLATINUM ANTICANCER DRUGS

Since Rosenberg first revealed anticancer properties of *cis*-dichlorodiammine-platinum (II) [*cis*-Pt(NH₃)₂Cl₂ or *cis*-DDP] [28], which is widely utilized today in clinical practice as the pharmaceutical agent cisplatin, many platinum complexes with different oxidation states (II–IV) have been successfully synthesized and tested [29–34]. To date, more than 3000 platinum compounds have been prepared and tested to improve their cytostatic activities and reduce their toxicities [35,36], about 30 of these compounds have entered clinical trials [37]. After the first-generation antitumor drug cisplatin, the second-generation antitumor drugs such as carboplatin (*cis*-Pt(CBDCA)(NH₃)₂, where CBDCA is 1,1-dicarboxy-cyclobutane, Scheme 5.1) and the third-generation cisplatin derivatives such as *cis*-[amminedichloro(2-methylpyridine)] platinum(II) (AMD473), which belong to the ‘classical’ mononuclear platinum compounds, multinuclear platinum compounds comprising di- or tri-nuclear platinum centers linked by variable length diamine chains constitute a new and discrete class of platinum-based anticancer agents [34]. The trinuclear [(*trans*-PtCl(NH₃)₂)₂{ μ -*trans*-Pt(NH₃)₂(NH₂(CH₂)_nNH₂)₂}]⁴⁺ (1,0,1/*t,t,t* (*n* = 6) or BBR3464, Scheme 5.1), is the first genuinely ‘nonclassical’ platinum derivative to enter phase II clinical trials now. The compounds of this class exhibit significantly enhanced antitumor activities relative to cisplatin and its derivatives [11].

It is widely believed that the principal target of platinum anticancer agents in cells is DNA and the resulting DNA lesions are responsible for their biological activities [34,38–41]. However, some substantial biomedical and chemical evidences have indicated that the attack of platinum complexes on other non-DNA cellular targets could also play roles in the antitumor activity of platinum drugs. The known candidates among them are RNA, membrane phospholipids, cytoskeleton microfilaments, albumin, tubulin and other proteins [36,38,42,43]. In order to understand the mechanism of action of platinum antitumor activity, it is important to investigate the kinetic and structural aspects of the DNA or other targets binding to platinum agents. ¹H, ¹⁵N and ¹⁹⁵Pt NMR have been widely used in studying the mode of action of platinum anticancer drugs, including the detection of intermediates arising during the hydrolysis process



Scheme 5.1 Structures of cisplatin and other platinum drugs.

and the dynamics and kinetics in reactions with either DNA or proteins, and metabolites in body fluids [8a,86,10].

3.1 ^{195}Pt , ^{15}N AND INVERSE [^1H , ^{15}N] NMR SPECTROSCOPY

^{195}Pt ($I = \frac{1}{2}$) is a reasonably sensitive nucleus for NMR detection with natural abundance of 33.8% and a receptivity relative to ^1H of 3.4×10^{-3} . The

relaxation time of ^{195}Pt is rather short, usually in the range from 1.4×10^{-2} to 8.3 s, with most values less than 2 s [44]. The short relaxation time is mainly attributed to the chemical shift anisotropy (CSA) contribution, which is given by [8a]:

$$[T_1(\text{Pt})]^{-1}(\text{CSA}) = \frac{6}{7}[T_2(\text{Pt})]^{-1}(\text{CSA}) = \frac{2}{15}\gamma_{\text{Pt}}^2 B_0^2 \Delta\sigma^2 \tau_c \quad (5.9)$$

In general, ^{195}Pt resonances are sharper for the complexes with higher symmetry (smaller anisotropy $\Delta\sigma$), e.g., Pt(IV) complexes, which are six coordinate and hence more symmetrical. They are broader at higher fields of measurement (B_0) and in larger molecules (longer correlation time τ_c).

In the DNA adducts of platinum anticancer compounds, the relaxation time is further shortened by quadrupolar effects of ^{14}N from both the ammine and the guanine ligands. The short relaxation time has the advantage of allowing short relaxation delay and rapid transient accumulation without saturation effects. The advantage of the increased sensitivity achievable at high magnetic field for ^{195}Pt is offset by the increase in linewidths due to CSA relaxation. For natural abundance ^{195}Pt , the detection limit is about 10 mM, which is much higher than those under biologically relevant conditions. So samples of ^{195}Pt isotopic enrichment are usually used in the study of platinum compounds.

The chemical shift range of ^{195}Pt is large, generally from -6000 to 9000 ppm, and often allows readily differentiation between Pt(II) and Pt(IV) [8a, 10] because the resonances tend to occur at high field and low field ends of the range for Pt(II) and Pt(IV), respectively. The chemical shift differences between geometrical isomers and diastereomers are also usually distinguishable [45]. In addition, the ^{195}Pt chemical shift in monomeric compounds is usually sensitive to the nature of bound donor atoms and can be used to distinguish various types of ligand binding to platinum [10]. ^{195}Pt NMR spectroscopy was successfully used to follow the binding of cisplatin to DNA although the aqation process could not be separated from monofunctional adduct formation [46].

^{15}N NMR is a powerful method for identifying the *trans* ligands in the coordination spheres of both Pt(II) and Pt(IV) complexes because both ^{15}N (and ^1H) chemical shifts and $^1J(^{195}\text{Pt}-^{15}\text{N})$ coupling constants are sensitive to the nature of the *trans* ligand in platinum am(m)ine complexes. For example, the ^{15}N resonances of $\text{Pt}^{\text{II}}-\text{NH}_3$ complexes shift up- and down-field, respectively when the *trans* ligands change from Cl/N to O and S (Figure 5.1). A similar picture was observed for $\text{Pt}^{\text{II}}-\text{NH}_2$ and $\text{Pt}^{\text{II}}-\text{NH}$ complexes. Beside difference in ^{15}N chemical shifts, the ^1H NMR resonances in $\text{Pt}^{\text{IV}}-\text{NH}_3$ complexes (5–7 ppm) shift to lower field compared to those of Pt^{II} .

The low receptivity of ^{15}N (3.85×10^{-6} relative to ^1H) limits its usefulness for direct detection of platinum complexes in biofluids. However, the sensitivity of detection can be improved by ^{15}N isotopic enrichment and further enhanced by polarization transfer from ^1H , e.g., $^{15}\text{N}-\{^1\text{H}\}$ DEPT and INEPT experiments. The maximum enhancement in ^{15}N signal intensity achievable via polarization

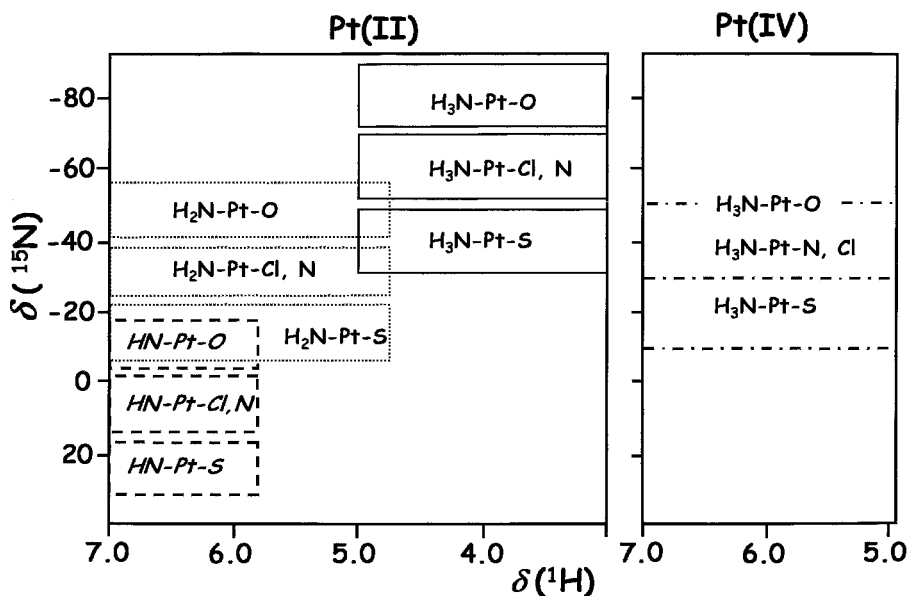


Figure 5.1 Variation of ^1H and ^{15}N chemical shifts with the *trans*-ligand in Pt^{II} and Pt^{IV} am(m)ine complexes.

transfer is 9.8 ($|\gamma_{\text{H}}|/|\gamma_{\text{N}}|$). However, since the repetition time of the pulse sequence is governed by the ^1H rather than the longer ^{15}N spin-lattice relaxation time, there is an additional advantage of allowing more rapid pulsing.

In recent years, the inverse [^1H , ^{15}N] heteronuclear single quantum coherence (HSQC) NMR method has been widely used to study the aequation of cisplatin [47,48] and its interactions with nucleotides and DNAs [49–52]. The major advantage of the technique is the sensitivity of detection, which is enhanced by a theoretical maximum of 306 ($\{|\gamma_{\text{H}}|/|\gamma_{\text{N}}|\}^{5/2}$) with respect to directly detected ^{15}N , such that signals can be detected from platinum complexes in aqueous solutions at concentrations of physiological relevance ($\leq \text{mM}$). In addition, the inverse [^1H , ^{15}N] HSQC also brings the simplification of complicated spectra since it selectively detects those protons directly attached to the labeled ^{15}N in samples and gives rise to a sharp ^1H NMR singlet for each distinct type of Pt–NH resonance together with the broadened ^{195}Pt satellites if ^{15}N decoupling (e.g. the GARP method) is employed during acquisition. This is of particularly valuable in studies of body fluids or cell culture media, where it is possible to follow the kinetics and dynamics of the speciation of the platinum complexes without interference from thousands of other overlapping ^1H resonances which are completely filtered out. The use of the pulsed field gradient not only enhances the S/N (by $\sqrt{2}$ times), but also greatly improves solvent suppression (e.g., H_2O) so that NH peaks can readily be detected even very close to the water signal. It takes just a few minutes to obtain a 2D [^1H , ^{15}N]

HSQC spectrum at mM concentrations and it is possible to detect ^{15}N -labeled species at concentrations as low as μM at high field NMR spectrometers.

In the 2D [^1H , ^{15}N] HSQC spectra of platinum complexes with *trans* ligand, both the Pt(II) and Pt(IV) ammine/amine complexes can be distinguished by the combination of ^1H and ^{15}N chemical shifts. Each distinct type of Pt–HN (i.e. ammine, primary and secondary amines) can be identified by their specific $^1\text{H}/^{15}\text{N}$ resonances and the shifts move gradually to lower field from ammine to primary amine, then to secondary amine in each dimension (Figure 5.1).

The inverse [^1H , ^{15}N] NMR spectroscopy is particularly useful in the kinetic studies of the aquation of platinum complexes and the interaction of platinum anticancer drug with DNA or other target agents. It allows the quantification of all intermediate and product species that form simultaneously and provides detailed information on individual species at the molecular level without the need for trapping out reaction intermediates or chromatographic separation of products. The NH_3 , NH_2 and NH regions of [^1H , ^{15}N] 2D NMR spectra are well separated and reaction courses can be followed independently in each region. The kinetic analysis of the reaction is normally undertaken by measuring peak volumes or intensities in the Pt–NH regions of the [^1H , ^{15}N] 2D NMR spectra (or sometimes 1D ^{15}N -edited ^1H spectra) and calculating relative concentrations of the various Pt species at each time point. The rate constants are determined by fitting the data to appropriate models.

3.2 ACTIVATION OF PLATINUM ANTICANCER DRUGS: KINETICS AND EQUILIBRIA OF AQUATION

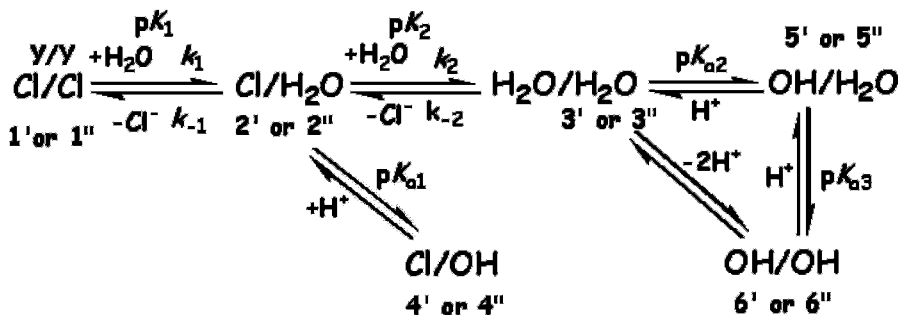
Cisplatin has been extensively used for the treatment of testicular and ovarian cancers and increasingly against other types of solid tumors (head/neck, lung, cervical, and bladder) [53]. The mechanism of action is believed to involve its aquation to the more reactive aqua-chloro complex, *cis*-[PtCl(NH₃)₂(OH₂)]⁺ prior to binding to DNA *in vivo* [50,51,54–56]. Therefore, it is important to determinate the rates of hydrolysis and $\text{p}K_{\text{a}}$ values of the hydrolysis products.

The detailed kinetics of the aquation of cisplatin have been investigated by [^1H , ^{15}N] HSQC NMR technique [47,48]. The aquation of a 1.5 mM solution of cisplatin in 9 mM NaClO₄ was monitored for 40 h at 298 K and the amounts of all species formed are followed and the rates of aquation, diaquation, and related anation processes are determined. The reaction commences with no significant concentrations of any species other than cisplatin. The mono-aquated complex *cis*-[Pt($^{15}\text{NH}_3$)₂Cl(OH₂)]⁺ is the first new species to be observed, comprising 8% of the total Pt within 2 h and reaching 65% after 40 h. The first indication of the diaquated complex *cis*-[Pt($^{15}\text{NH}_3$)₂(OH₂)₂]²⁺ occurs after 3.5 h and never accounts for more than 7% of the total Pt. The bridged dinuclear Pt complexes [*cis*-Pt($^{15}\text{NH}_3$)₂]₂(μ -Cl)(μ -OH)²⁺ and [*cis*-Pt($^{15}\text{NH}_3$)₂(OH₂)]₂(μ -OH)³⁺, appear at 10.5 and 26 h, respectively,

and account for less than 5% of the Pt after 30 h, and 23% of the cisplatin still remains in solutions after 30 h. The mono-aquated complex, $cis\text{-}[\text{Pt}(\text{}^{15}\text{NH}_3)_2\text{Cl}(\text{OH}_2)]^+$, was found to be dominant over the diaquated complex $cis\text{-}[\text{Pt}(\text{}^{15}\text{NH}_3)_2(\text{OH}_2)_2]^{2+}$ in the aquation. Low concentrations of phosphate do not significantly influence the early stage of hydrolysis of cisplatin. In contrast, the presence of DNA slows the aquation of cisplatin by 30–40% compared to that observed in 9 mM either phosphate or NaClO_4 , probably due to the association between cisplatin and DNA which limits solvent access to the metal. The kinetics of hydrolysis of $cis\text{-}[\text{PtCl}_2(\text{NH}_3)(2\text{-Py})]$ (Py = 2-methyl pyridine, AMD473), was also investigated by 2D NMR and it was found that the sterically hindered anticancer agent AMD473 hydrolyzes more slowly than cisplatin (Table 5.1). The effect of 2-methyl pyridine on the rate of hydrolysis of Cl^- *trans* to NH_3 (*cis* to 2-Py) is dramatic, being about five times as slow as the analogous Cl^- ligand in the nonsterically hindered 3-Py complex [57]. The slower hydrolysis and lower pK_a values of the mono-aqua and diaqua adducts compared with cisplatin adducts are likely to result in a reduced intracellular activity and may account for AMD473's high activity against cisplatin-resistant cell lines.

Dinuclear and trinuclear platinum complexes represent a unique class of anticancer agents. The first representative of this class, BBR3464, entered phase II clinical trials in 2000 for ovarian, gastric, and lung cancer, after showing responses in colon and pancreatic cancers in phase I trials [58–60]. Preclinical evaluation indicates that BBR3464 is consistently more effective than cisplatin. Extensive studies have shown that the DNA binding profiles for the multinuclear platinum complexes differ significantly from those reported for mononuclear platinum compounds [61].

The hydrolysis profile of the bifunctional dinuclear platinum complex [$\{trans\text{-PtCl}(\text{}^{15}\text{NH}_3)_2\}_2(\mu\text{-}^{15}\text{NH}_2(\text{CH}_2)_6^{15}\text{NH}_2)]^{2+}$ (1,1/*t,t* ($n = 6$), **1'**), the prototype of a novel class of potential antitumor complexes, has recently been studied by using [^1H , ^{15}N] HSQC NMR spectroscopy [62]. The process of the hydrolysis is sketched in Scheme 5.2. An interesting finding is that the position of the



Scheme 5.2 Aquation processes of 1,1/*t,t* ($n = 6$) (**1'**) and 1,0,1/*t,t,t* ($n = 6$) (BBR3464, **1''**).

equilibrium for **1'** favors the dichloro form to a much greater extent than does the aquation equilibrium of cisplatin under similar concentrations. When dissolved in aqueous solution, aquation of the dichloride form **1'** occurs rapidly to give the monoaqua monochloro form **2'** and equilibrium is achieved more rapidly ($t_{1/2} = 23$ min) than for cisplatin ($t_{1/2} = 165$ min) [63], under similar conditions. For a 5.4 mM aqueous solution of nitrate salt of **1'**, the coordinated chloride is only aquated to 15% at 25 °C. The equilibrium constant ($pK_1 \approx 4.0$) is comparable to those reported previously for $[\text{PtCl}(\text{dien})]^+$ ($pK_1 = 3.9$) and $[\text{PtCl}(\text{NH}_3)_3]^+$ ($pK_1 = 4.1$), which also belong to PtClN_3 systems. These complexes are aquated in aqueous solutions with rate constants in the 10^{-5} s^{-1} range, but the extent of aquation is limited by the relatively high chloride anation rate constants $\sim 10^{-1} \text{ M}^{-1} \text{ s}^{-1}$, which is in the magnitude of $10^{-3} \text{ M}^{-1} \text{ s}^{-1}$ for cisplatin. The relatively small extent of hydrolysis and the evidence of high DNA affinity (and rapid DNA binding) suggest that the formation of aqua species may not be a necessary step in DNA adduct formation for this class of compounds and other factors such as DNA interactions may be more important [62].

The kinetics of the aquation of the trinuclear platinum anticancer complex BBR3464 (1,0,1/t,t,t ($n = 6$), **1''**) is similar to that of its binuclear analogue **1'** (1,1/t,t ($n = 6$)), based on the [^1H , ^{15}N] HSQC NMR spectroscopy studies [64]. The equilibrium conditions were found to be established much more rapidly for **1''** (2 h) than for cisplatin (30 h) and the equilibrium constant for the aquation ($pK_1 = 3.4$) is slightly lower than that of the related dinuclear complex **1'** under similar conditions, indicating that the equilibrium for **1''** lies further toward the dichloro species and the dichloro form of **1''** is still strongly favored over the aquated forms. An Arrhenius analysis for the temperature dependence of rate constants in combination with the equilibrium constant at 298 K gave an activation energy (ΔG^\ddagger_{298}) of $93 \pm 3 \text{ kJ mol}^{-1}$ and other thermodynamic parameters for the aquation of BBR3464 (in 15 mM NaClO_4). The entropy value ($\Delta S^\ddagger_{298} = -19.1 \text{ J K}^{-1} \text{ mol}^{-1}$) is consistent with an associative mechanism, as expected for square planar Pt^{II} [64].

The pK_a values for the **2'** and **2''** of the multinuclear platinum complexes 1,1/t,t ($n = 6$) and 1,0,1/t,t,t ($n = 6$) are lower than that for *cis*- $[\text{Pt}(\text{NH}_3)_2\text{Cl}(\text{H}_2\text{O})]^+$, and is also lower than the reported values for $[\text{Pt}(\text{dien})(\text{H}_2\text{O})]^{2+}$ and $[\text{Pt}(\text{NH}_3)_3(\text{H}_2\text{O})]^{2+}$ (Table 5.2) [62,64]. It is inferred that the smaller extent of hydrolysis and lower pK_a values (about 5.62) of the monoaqua chloro species compared to cisplatin (6.41) will have a major influence on the differences in the speciation and reactivity of these platinum antitumor complexes under biological conditions. The lower pK_a value suggests that the monoaqua monochloro complex **2'**, the major hydrolysis product of **1'**, will be mainly in the less reactive hydroxo form **4'** under physiological pH [62].

It is assumed that the aquation of cisplatin to the more reactive monoaquated complex *cis*- $[\text{Pt}(\text{NH}_3)_2\text{Cl}(\text{OH}_2)]^+$ does not occur readily in the blood stream or in the extracellular environment since the high chloride concentration (> 100 mM) favors the dichloro complex [54–56,65]. It had frequently been argued that

Table 5.2 pK_a values of H_2O ligands for some platinum complexes

Complexes	pK_a	H_2O (<i>trans</i> to)	Reference
<i>cis</i> -[Pt(NH ₃) ₂ (H ₂ O) ₂] ²⁺	5.37	NH ₃	47
<i>cis</i> -[PtCl(H ₂ O)(NH ₃) ₂] ⁺	6.41	NH ₃	
<i>cis</i> -[Pt(NH ₃)(2-Py)(H ₂ O) ₂] ²⁺	5.22		57
	7.16		
<i>cis</i> -[Pt(NH ₃)(2-Py)Cl(H ₂ O)] ⁺	6.49	NH ₃	
	6.13	2-Py	
[Pt (dien) (H ₂ O)] ²⁺	6.0	NH	^a
1,1/ <i>t,t</i> (<i>n</i> = 6) (H ₂ O/H ₂ O)	5.62	NH ₂	62
1,0,1/ <i>t,t,t</i> (<i>n</i> = 6) (H ₂ O/H ₂ O)	~5.62	NH ₂	64
[Pt(NH ₃) ₃ (OH ₂)] ²⁺	6.0		^b

^a Data from Z. Guo, Y. Chen, E. Zang, and P. J. Sadler, *J. Chem. Soc. Dalton Trans.* 4107 (1997).

^b Data from F. Gonnet, F. Reeder, J. Kozelka, and J.-C. Chottard, *Inorg. Chem.* **35**, 1653 (1996).

the low chloride (Cl^-) concentrations (~ 4 mM) inside the cell allow hydrolysis to occur [56,65], facilitating binding of the Pt(II) to the DNA [54–56, 66]. The investigation of the influence of chloride concentrations on the kinetics of the reactions between ¹⁵N-labeled cisplatin and 14-mer duplex oligonucleotides has been carried out by [¹H, ¹⁵N] HSQC 2D NMR spectroscopy [52]. Indeed, it has been found that the presence of Cl^- at the concentration of 60–80 mM (within the range of values obtained in biological media and only slightly higher than the chloride concentration in cancer cells [67]) results in a fivefold decrease in the rate of hydrolysis of *cis*-[Pt(NH₃)₂Cl(OH₂)]⁺ and a 2–20-fold decrease in the rate of monofunctional adduct formation. The effects on the rate of closure from monofunctional to bifunctional adducts are less well established but some of these rates appear not to be significantly reduced by the presence of added Cl^- [52].

3.3 PLATINATION OF NUCLEOTIDES AND DNA

DNA has been considered as the major cellular target of platinum anticancer drugs. This idea comes from the numerous experiments on cisplatin showing that the percentage of platinum atoms bound per molecules is the highest for DNA [36,68]. It is not yet clear what determines the adduct profile, but Pt(II) binding to nucleobases is kinetically controlled and the bifunctional adducts are believed to be stable on the time scale of days up to weeks.

Following and determining the rates of the manifold reactions that occur in the formation of even a single adduct are difficult tasks. Using [¹H, ¹⁵N] 1D/2D HSQC to monitor the reaction between ¹⁵N-labeled platinum complexes and nucleobases or DNA is particularly attractive because species can be acquired quickly (in as little as 3–4 min) and all platinated species are observed at micromolar concentrations. The interaction between ¹⁵N-cisplatin

and guanosine-5'-monophosphate (5'-GMP) has been investigated and the short-lived active species $cis\text{-[Pt(NH}_3)_2\text{Cl(H}_2\text{O)]}^+$ was detected during the early stage of the reaction, followed by the formation of mono- and bis-GMP complexes [69]. Hydrogen-bonding may form between NH protons in Pt-NH₃ and deprotonated 5'-monophosphate of GMP. The detailed kinetics for the interaction of cisplatin with a 14-mer duplex, d(ATACATGGTACATA)-d(TATGTACCATGTAT) has been investigated by [¹H, ¹⁵N] NMR technique [49,50,70]. The mono-aqua intermediate, which is usually present at micromolar concentrations, was readily monitored in these experiments and its lifetime was determined (only $t_{1/2} \approx 8$ min at 310 K) directly for the first time. The kinetic data obtained by [¹H, ¹⁵N] 2D HSQC are in close agreement with those determined by ¹⁹⁵Pt NMR spectroscopy (with ¹⁹⁵Pt-enriched cisplatin) [46]. However, no mono-aqua intermediate was detected previously using ¹⁹⁵Pt NMR during the course of the reaction with DNA.

The reaction between ¹⁵N-cisplatin and a self-complementary 14-mer oligonucleotide 5'-d(AATTGGTACCAATT)-3', having a GpG intrastrand bind site, has been investigated in an aqueous solution at pH 6, at 298 K for over 2 weeks (Figure 5.2) [48]. Under the experimental conditions, $cis\text{-[Pt(}^{15}\text{NH}_3)_2\text{Cl(OH}_2)]^+$

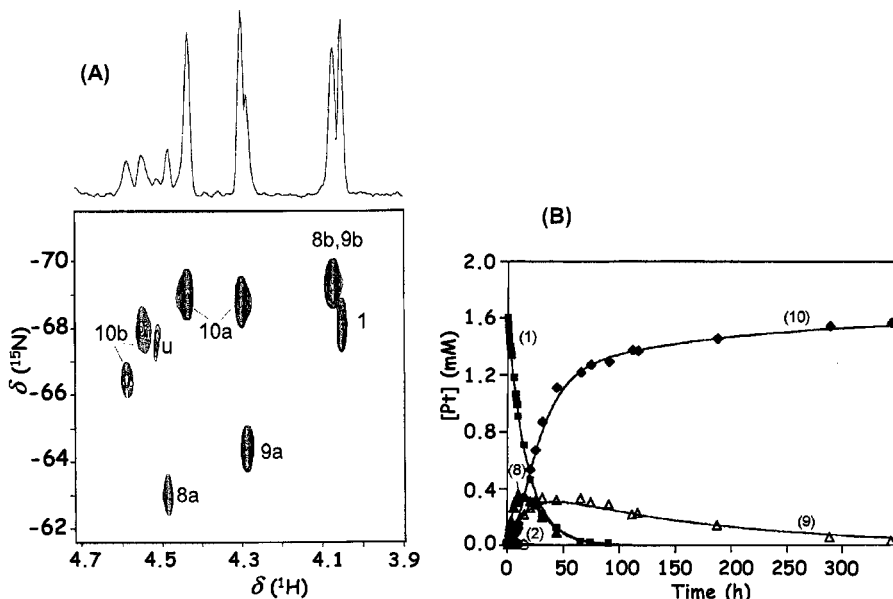
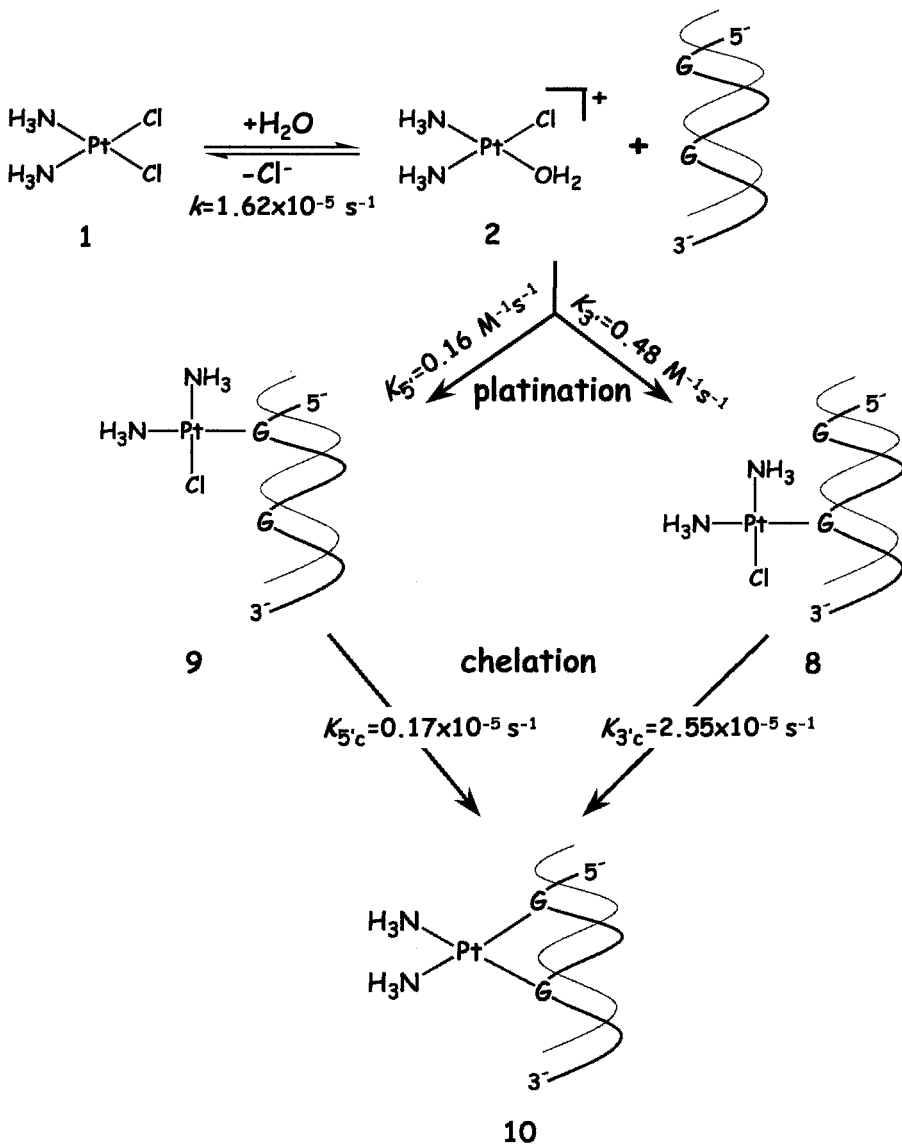


Figure 5.2 [¹H, ¹⁵N] HSQC NMR spectrum of ¹⁵N-cisplatin at 298 K after reaction with 5'-d(AATTGGTACCAATT)-3' for 31 h (left) and plots of the relative concentrations of species observed during the reaction (right). Peaks are assigned to ¹⁵NH₃ in structures **1**, **8**, **9**, and **10** (see Scheme 5.3). Adapted with permission from M. S. Davies *et al.*, *Inorg. Chem.* **39**, 5603 (2000) [48]. Copyright (2000) American Chemical Society.

never accumulates to more than 1.1 % of the total Pt and its concentration decreases steadily until it becomes undetectable after 20 h of the reaction. The resonance of $cis\text{-[Pt}^{(15}\text{NH}_3)_2(\text{OH}_2)_2]^{2+}$ is not observed. Two monofunctional DNA adducts, $cis\text{-[Pt}^{(15}\text{NH}_3)_2\text{Cl(G6-N7)]}$ (3' adduct) and $cis\text{-[Pt}^{(15}\text{NH}_3)_2\text{Cl(G5-N7)]}$ (5' adduct), are formed with the former formed more rapidly than the latter (Scheme 5.3). The monofunctional adducts undergo ring closure to form the bifunctional species $cis\text{-[Pt}^{(15}\text{NH}_3)_2(\text{G5-N7})(\text{G6-N7})]$, which exists as two conformers. This experiment supports the assumption that the monoaquated complex, $cis\text{-[Pt}^{(15}\text{NH}_3)_2\text{Cl(OH}_2)]^+$, is largely responsible for the binding of cisplatin to DNA, whereas the diaquated species $cis\text{-[Pt}^{(15}\text{NH}_3)_2(\text{OH}_2)_2]^{2+}$ makes only a minor contribution to this binding process. This is because the diaquated species, even in the absence of DNA, only reaches significant levels after 2–3 h of aquation, and by then the reaction between the monoaquated species and DNA is well under way [48].

It has been known that, when cisplatin binds to DNA, the major adducts are --GG-- and --AG-- intrastrand crosslinks, but not --GA-- . Binding of Pt to DNA is known to be kinetically determined. Therefore, by determining the rates of platination of DNA, one can get an insight into the factors that influence Pt–DNA interactions and prevent formation of the bifunctional GpA adduct. The kinetics of the reactions between ^{15}N -cisplatin and two 14-mer oligonucleotides, 5'-d(AATTAGTACTAATT)-3' (--AG--) and 5'-d(AATTGATACTAATT)-3' (--GA--), have been investigated by [^1H , ^{15}N] NMR spectroscopy [51]. Together with the results of --GG-- [48], it was found that the rate of hydrolysis of cisplatin to $cis\text{-[Pt}(\text{NH}_3)_2\text{Cl(OH}_2)]^+$ decreases from --GG-- ($1.62 \times 10^{-5} \text{ s}^{-1}$) [48] to --AG-- ($1.57 \times 10^{-5} \text{ s}^{-1}$) to --GA-- ($1.23 \times 10^{-5} \text{ s}^{-1}$), Table 5.3. Monofunctional binding of $cis\text{-[Pt}(\text{NH}_3)_2\text{Cl(OH}_2)]^+$ to --GA-- sequence occurs at a greatly diminished rate compared to those of both --GG-- and --AG-- . The rate of binding to the 3' base, the preferred site of attack in --GG-- and --AG-- , is 80–200-fold lower for --GA-- (~ 1.0 , 0.48 [48] and $0.0054 \text{ M}^{-1} \text{ s}^{-1}$ for --AG-- , --GG-- and --GA-- , respectively). Ring closure to form the bifunctional adduct is more rapid in the case of --AG-- ($9.8 \times 10^{-5} \text{ s}^{-1}$) than --GA-- ($0.69 \times 10^{-5} \text{ s}^{-1}$). It is concluded that the bifunctional intrastrand adduct profile observed when cisplatin binds to DNA is substantially controlled by the rate of formation of monofunctional adducts at the different X–purine–purine–X sequences. A slow rate of closure also contributes to the nonformation of the bifunctional GpA adduct.

To compare the DNA-binding profile of a typical dinuclear platinum anticancer drug with that of cisplatin, the kinetics and mechanism of formation of site-specific long-range 1,4-interstrand cross-links by interaction between the dinuclear platinum complex $\{[trans\text{-PtCl}^{(15}\text{NH}_3)_2]_2(\mu\text{-}^{15}\text{NH}_2(\text{CH}_2)_6^{15}\text{NH}_2)\}^{2+}$ (1,1/t,t ($n = 6$)) and a 12-mer duplex $d(\text{ATATGTACATAT})_2$ were studied [11]. Interstrand cross-linking is a potent and varied lesion which is responsible for the cell-killing effects of many anticancer drugs [71]. The results show that the bifunctional adduct formation is about 10–55-fold faster



Scheme 5.3 The kinetic pathway for the reaction between ^{15}N -cisplatin and intrastrand $-\text{GG}-$. The self-complementary 14-mer, $5'\text{-d}(\text{AATTG}^5\text{G}^6\text{TACCAATT})\text{-3}'$, is used as an example [48].

Table 5.3 Cisplatin half-lives ($t_{1/2}$) for reaction with duplexes having specific binding sites and percentage of total platinated DNA adducts^a

Sequence	$t_{1/2}$ (h)	Total adducts (%)
In 9 mM ClO ₄ ⁻ or phosphate	8.1	
5'-d(AATTGGTACCAATT)-3' (-GG-)	11.9	50
5'-d(ATACATGGTACATA)-3'	10.5	50
5'-d(TATGTACCATGTAT)-3' (-GG-)		
5'-d(AATTAGTACTAATT)-3' (-AG-)	12.3	28
5'-d(AATTATGTGTATAT)-3'	12.5	6-10
5'-d(ATATACACATAATT)-3' (-GTG-)		
5'-d(AATTAACGTTAATT)-3' (-CG-) ^b	13.7	<1
5'-d(AATTATGCATAATT)-3' (-GC-) ^b	15.1	1-4
5'-d(AATTGATATCAATT)-3' (-GA-)	15.7	<1

^a Data taken from references 48 and 51, and the half-life of hydrolysis in the absence of duplex is listed for comparison.

^b Forms a 1,2-interstrand -GG- adduct.

than closure of 5' and 3'G monofunctional adducts generated by the diaqua form of cisplatin (at 288 K) [70], which is attributed to a higher rate of aquation and more rapid bifunctional fixation of monofunctional adduct. The NMR analysis confirms the conformational flexibility of the cross-linking, a feature expected to contribute to the distinct differences in a biological profile between those dinuclear and mononuclear platinum anticancer drugs.

The kinetics and mechanism of the reaction between the dinuclear Pt complex [*trans*-PtCl(¹⁵NH₃)₂]₂(μ-¹⁵NH₂(CH₂)₆¹⁵NH₂)²⁺ (**1'**) and a 14-mer duplex d(ATACATG(7)G(8)TACATA)·d(TATG(25)TACCATG(18)TAT) has been investigated recently [72]. The sequence offers three possible bifunctional binding modes for the dinuclear Pt complex, a 1,2-intrastrand G(7)G(8) adduct and two 1,4-interstrand G(8)G(18) and G(7)G(25) adducts that differ in the direction (5'-5' versus 3'-3') of the cross-link. Therefore, it provides the opportunity to examine the preference of the drug towards formation of these adducts in a competitive manner. [¹H, ¹⁵N] HSQC was used to follow the reaction at 298 K, pH 5.4, at various time points and the rate constants for various steps were obtained and the kinetic pathway is proposed (Figure 5.3). It is noteworthy from the competition experiments that the dinuclear platinum complex preferentially forms a 1,4-interstrand GG adduct orientated in the 5'-5' direction on binding to the 14-mer duplex. A minor product (<10%) is likely to be the 3'-3' 1,4-interstrand GG cross-link and not the 1,2-GG intrastrand adduct. An initial electrostatic association of the drug with the DNA could play a role in the 5'-5' specificity. The specificity is also attributed to more rapid binding to the 3'G of the -GG- binding site than 5'G ($k_{3'} = 1.5 \pm 0.7$ and $k_{5'} = 0.24 \pm 0.11$ M⁻¹ s⁻¹) and the inability of the Pt complex to span more than five base pairs. The overall formation of the 1,4-interstrand cross-link is faster than that observed for the self-complementary 12-mer sequence 5'-{d(ATATGTACATAT)₂} [11], largely a consequence of more rapid monofunctional binding due to the enhanced

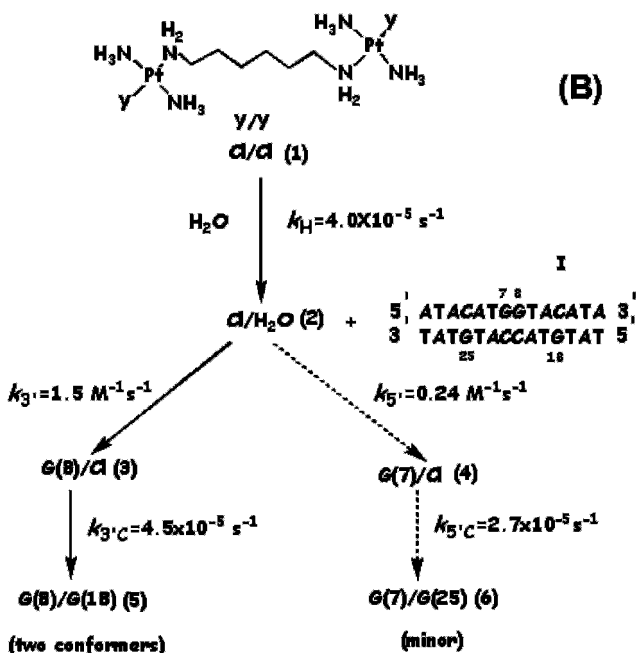
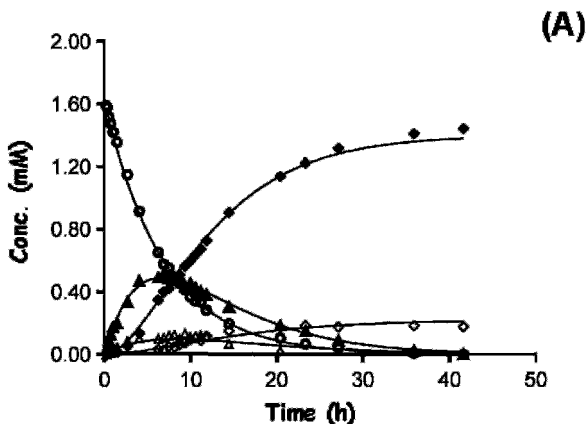


Figure 5.3 Plot of the relative concentration of species observed during the reaction between the dinuclear Pt^{II} anticancer agent and 14-mer duplex at 298 K (A) and proposed reaction scheme (B). (Labels: ○, complex 1; ●, complex 2; ▲, complex 3; △, complex 4; ◆, complex 5; ◇, complex 6. Adapted with permission from S. J. Berners-Price *et al.*, *Chem. Eur. J.* 9, 713 (2003) [72]. Reproduced by permission of Wiley-VCH.

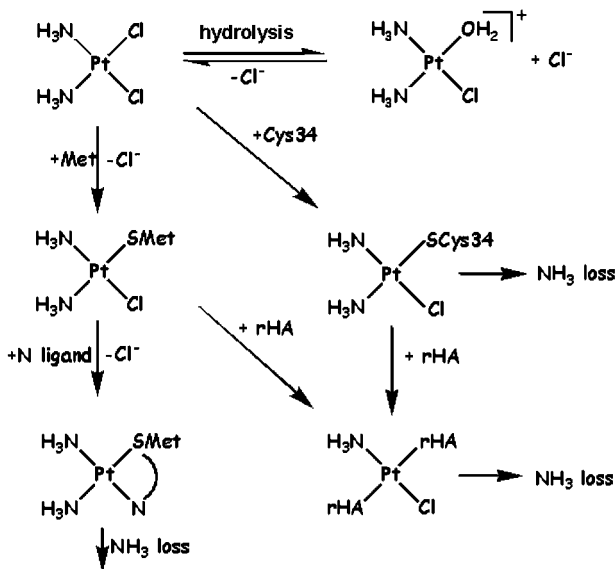
nucleophilicity associated with the GG binding site relative to an isolated guanine residue. There are two conformational forms of the 1,4-interstrand cross-link which differ in the orientation of the bound G(18) residue.

3.4 INTERACTION OF PLATINUM AGENTS WITH AMINO ACIDS, PEPTIDES AND PROTEINS

Although attack on DNA is responsible for the antitumor activity, platinum complexes can interact with many other biomolecules. One day after rapid intravenous infusion of cisplatin, 65–98 % of platinum in blood plasma is protein-bound, while no unbound platinum has been detected at any time in blood plasma of patients after slow infusions over 20 h [53]. A full understanding of the modes of action of platinum drugs requires the study of their interactions with all possible biological targets, including amino acids, hormones, peptides and proteins. However, relatively few detailed mechanistic studies have been performed on such interactions, in comparison to studies with DNA and nucleobases. It is known that sulfur donors bind strongly to platinum(II). Sulfur-containing biomolecules, including amino acids such as cysteine (Cys) and methionine (Met), peptides such as glutathione, and proteins such as metallothionein and many others, are therefore likely to be important in the metabolism of platinum drugs.

Albumin is one of the most abundant proteins in plasma (~0.63 mM) and it is reasonable to assume that any injected metallodrug will present certain interactions with this macromolecule, which could largely determine its bioavailability and toxicology [42]. A comprehensive study of the reactions of the ^{15}N -labeled cisplatin with intact and chemically modified recombinant human albumin (rHA) as well as human serum albumin (HSA) has been performed by 1D ^1H and [^1H , ^{15}N] 2D HSQC NMR spectroscopy [53]. Recombinant albumin is similar to serum albumin but has a higher thiol content (~0.9 –SH per rHA and only ~0.4 –SH per HSA) and is structurally more homogeneous. NMR studies showed that the major sulfur-containing binding site involves Met in the form of an S, N chelate but not Cys-34, which is commonly believed to be the major platination site of HSA (Scheme 5.4) [73].

The reactions of $\text{cis}[\text{Pt}(\text{NH}_3)_2\text{Cl}(\text{OH}_2)]^+$ with L-methionine under an acidic condition and at $\text{pH} \approx 7$ have been investigated by 1D ^{195}Pt and ^{15}N NMR as well as 2D [^1H , ^{15}N] HSQC NMR [74]. When the platinum complex is in excess in an acidic solution, the initial product, $\text{cis}[\text{Pt}(\text{NH}_3)_2\text{Cl}(\text{Met-S})]^+$ undergoes slow ring closure to $\text{cis}[\text{Pt}(\text{NH}_3)_2(\text{Met-N,S})]^{2+}$. Slow ammine loss occurs to produce the isomer of $\text{cis}[\text{Pt}(\text{NH}_3)\text{Cl}(\text{Met-N,S})]^+$ with chloride *trans* to sulfur. When methionine is in excess, a reaction sequence is proposed in which $\text{trans}[\text{Pt}(\text{NH}_3)\text{Cl}(\text{Met-S})_2]^+$ isomerizes to the *cis* isomer, with subsequent ring closure reactions leading to the formation of $\text{cis}[\text{Pt}(\text{Met-N,S})_2]^{2+}$. In contrast to methionine which is unreactive toward $\text{cis}[\text{Pt}(\text{NH}_3)_2\text{Cl}(\text{OH})]$ at $\text{pH} \approx 7$,



Scheme 5.4 Stepwise interaction of cisplatin with recombinant albumin (rHA). Adapted with permission from A. I. Ivanov *et al.*, *J. Biol. Chem.* **273**, 14721 (1998) [53].

L-cysteine reacts readily with *cis*-[Pt(NH₃)₂Cl(OH)], giving various reaction products including bridged species.

A new insight into molecular mechanisms of antitumor activity of platinum complexes has been provided by a recent study of the effect of cisplatin on the process of tubulin assembly *in vitro* [75]. Based on electron microscopic studies, it has been found that the platination of tubulin leads to the formation of highly stable and inert closed tubulin rings rather than microtubules. Such platinum-bound tubulin aggregates are unable to participate in the process of chromosome separation during the mitosis, thus blocking cell division in living cells. The dynamic ¹⁹⁵Pt NMR study has proved that the blockage of tubulin assembly is due to the binding of cisplatin to N7 of guanosine triphosphate (GTP) in the GTP center of tubulin. The GTP substitution for (Met-N7) GTP, a (N7) methyl analogue of GTP which is not accessible to the attack of platinum on N7 but slightly differs from GTP in the structure and therefore can fully bind with tubulin, leads to a complete disappearance of the signals that appear during the reaction of diaqua complex *cis*-[Pt(NH₃)₂(H₂O)₂]²⁺ with tubulin GTP and are assigned to the monoadduct (MA) and biadduct (BA) of cisplatin bound tubulin, respectively. The calculated rate constants for mono- and bi-adduct bindings are 1.7×10^{-2} and $1.1 \times 10^{-2} \text{ s}^{-1}$, respectively, which are close to those reported in the cisplatin–DNA interaction. The interaction of tubulin GTP with *cis*-[Pt(NH₃)₂(H₂O)₂]²⁺ increases the total rate of hydrolysis of GTP to guanosine diphosphate (GDP), and results in breaking the balance

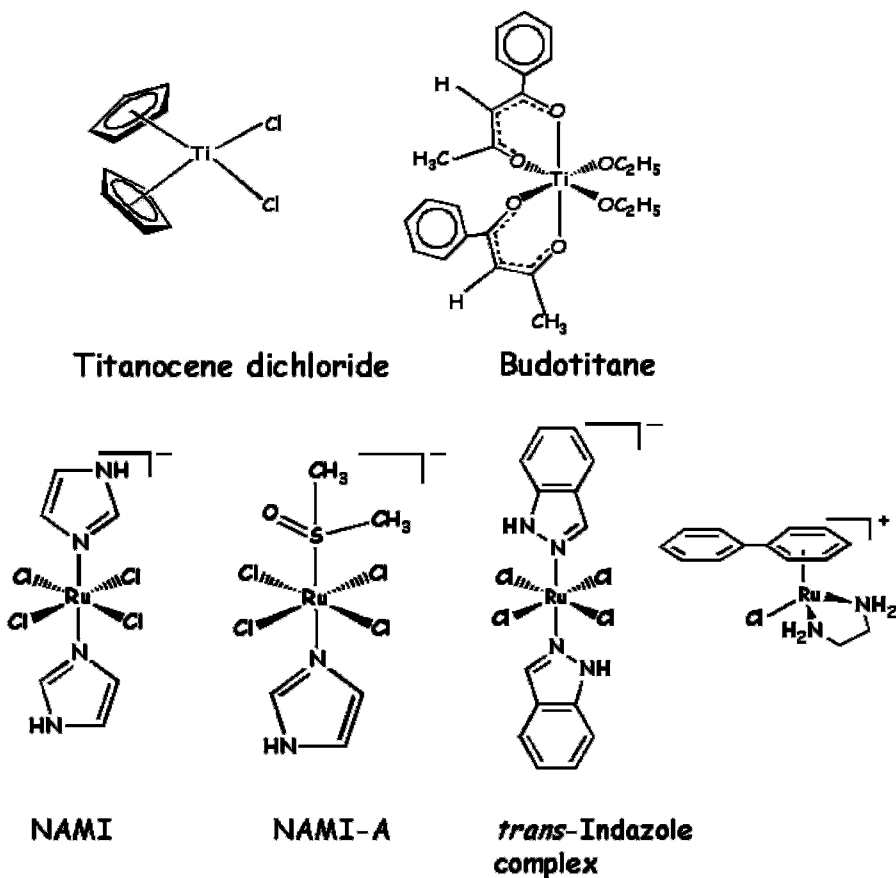
between the dynamics of GTP and GDP tubulin assembly, a trimolecular and bimolecular process, respectively. The change from the trimolecular to bimolecular mechanism of assembly leads to the production of closed rings rather than microtubulins [75].

Reactions of widely used second-generation platinum anticancer drug carboplatin (^{15}N -labeled) with a variety of sulfur-containing amino acids, namely, *N*-acetyl-L-cysteine, glutathione (GSH), *N*-acetyl-L-Met, L-HMet, have also been investigated by [^1H , ^{15}N] NMR spectroscopy [76]. The kinetics of the formation of adducts between carboplatin and these sulfur-containing amino acids, are followed through the time course of the reactions. Surprisingly, it has been found that the reactions between carboplatin with thiols are very slow. This accounts for the observation that, even though thiols such as GSH have high concentrations *in vivo*, only very small amounts of Pt–thiolate complexes were detectable in the urine of mice after they were administered with ^{15}N -carboplatin [77]. In contrast, the reactions of carboplatin with thioethers are much more rapid (for the initial stages of the reaction with L-methionine, the rate constant of $k = 2.7 \times 10^{-3} \text{ M}^{-1} \text{ s}^{-1}$). The ring-opened complexes that are initially formed are unexpectedly stable with half-life of about 24 h at 310 K, and are apparently detectable in the urine of mice after they are administered with ^{15}N -carboplatin [76]. It has been shown that platinum species can initially bind to thioether groups and then migrate to N7 of guanine [78–81]. Surprisingly, L-methionine increases the rate of reaction of cisplatin with guanosine 5'-monophosphate (5'-GMP) at pH 7 [82]. Such a migration of Pt from an S ligand to a purine N7 may be possible *in vivo*. These discoveries have raised the possibility that alternative pathways for DNA platination may exist for carboplatin.

There is an increasing interest in the development of oxygen-independent photochemotherapeutic agent [83–85]. Photoactive Pt^{IV} analogues of the active drug cisplatin are of special interest. It has been shown that nucleotide (5'-GMP) platination by Pt^{IV} -diiododiamine complex can be slowly induced by visible light and this photoactivation can be controlled by the axial ligands, which allow fine-tuning of the photoreactivity. However, slow photoreactions and low stability against biological reducing agents, such as glutathione, prevent its further application. Recently, the photoreactions of the ^{15}N -labeled Pt^{IV} complexes *cis,trans*- $[\text{Pt}^{\text{IV}}(\text{N}_3)_2(\text{OH})_2(\text{NH}_3)_2]$ and *cis,trans*- $[\text{Pt}^{\text{IV}}(\text{en})(\text{N}_3)_2(\text{OH})_2]$ (en = ethylenediamine, N_3^- = azide) in water and in the presence of 5'-GMP and d(GpG), have been studied [86]. The two Pt^{IV} complexes are potential photochemotherapeutic agents with their low chemical reactivities under physiological conditions. They react only slowly with the intracellular reducing agent glutathione (GSH) over a period of weeks and no reactions at all were observed in human blood plasma. Both 5'-GMP and d(GpG) do not react with these complexes over a period of 1 week at 298 K in the dark. The kinetics of the photoreactions were followed by 1D ^1H , 2D [^1H , ^{15}N] HSQC and HSQC-TOCSY NMR spectroscopy. These data suggest that Pt^{IV} -diazido complexes could be selectively activated by photoirradiation in cancer cells, side-effects might therefore be avoided.

4 TITANIUM AND RUTHENIUM ANTICANCER AGENTS

Bis(β -diketonato)-Ti^{IV} complexes and biscyclopentadienyl-Ti^{IV} complexes have been shown to exhibit high anticancer activities against a wide range of murine and human tumors with less toxic side effects than cisplatin [87–89]. Two of them, titanocene dichloride (Cp₂TiCl₂) and budotitane (Ti(bzac)₂(OEt)₂, where bzac = 1-phenylbutane-1,3-dionato) (Scheme 5.5), are currently undergoing clinical trials. Recent studies have shown that titanocene dichloride significantly overcomes cisplatin resistance in ovarian carcinoma cell lines [90]. The mechanism of antitumor activity of titanocene is believed to result from the interaction of a hydrolyzed titanocene species with DNA [88,91]. Titanium derived from titanocene accumulates in cellular nucleic acid-rich regions and



Scheme 5.5 Selected titanium and ruthenium anticancer compounds.

nucleic acid synthesis, particular DNA synthesis, is inhibited after administration with titanocene dichloride both *in vitro* and *in vivo* [92].

It has been shown that Ti^{IV} binds strongly to the serum transferrin [93,94] and the protein may therefore serve to deliver Ti^{IV} from the anticancer drug Cp_2TiCl_2 or budotitan into tumor cells, which are known to have a higher density of transferrin receptors than normal cells [95,96]. The interaction of human transferrin and titanocene dichloride (Cp_2TiCl_2) has been studied by NMR spectroscopy and other techniques recently [97]. Although the 1H NMR spectrum is complicated due to the overlap of a large number of resonances from this large molecule (80 kDa), some regions of the 1H NMR spectrum are relatively sensitive to the metal binding to the specific iron sites of the protein [98]. The displacement of a Cp ligand during the reaction of Cp_2TiCl_2 with hTF at various time intervals was monitored by 1H NMR spectroscopy. A decrease in intensity of the resonance for bound Cp (singlet at 6.42 ppm) and an increase in intensities of the resonances for free Cp (CpH) (two multiplets at 6.57 and 6.62 ppm and a weak multiplet at 2.95 ppm) were observed which indicated that the Cp ligands are released from the drug. It is known that the chloride ligands are readily displaced from Cp_2TiCl_2 in aqueous solution (e.g., by H_2O/OH^- upon hydrolysis) [99,100] and therefore only the Ti^{IV} ion from the drug is taken up by the protein. The 2D [1H , ^{13}C] HSQC NMR experiments on ϵ -[^{13}C]-Met-hTF showed that only the cross peaks for Met residues (e.g., Met464) in the C-lobe of the protein are perturbed upon addition of 1 mol equiv of Cp_2TiCl_2 in apo-hTF at pH 7.4 in the presence of 10 mM $NaHCO_3$ and those of N-lobe are perturbed only after addition of the second mol equiv of Cp_2TiCl_2 , suggesting that preferential binding of Ti^{IV} occurred to the C-lobe of hTF. Based on the observation of the changes of 2D [1H , ^{13}C] HSQC NMR spectra at different time intervals after addition of $Fe^{III}(NTA)_2$ into Ti_2 -hTF solution, the order of displacement of Ti^{IV} from the lobes by Fe^{III} was established. Unexpectedly, Fe^{III} displaces Ti^{IV} much more rapidly from the C-lobe (<5 min) than from the N-lobe (days).

The kinetics of the binding of Cp_2TiCl_2 to the phenolic ligand *N,N'*-ethylenebis(*o*-hydroxyphenylglycine) (EHPG), a model compound for transferrin, was also studied [101]. It has been shown that the monomeric complex of EHPG with Cp_2TiCl_2 , $[Ti(EHPG)(H_2O)]$ is stable over the pH range of 1.0–7.0, while the dimeric complexes $[\{Ti(HEHPG)(H_2O)\}_2O]$ is stable only between pH 2.5 and 5.5. Interaction of Cp_2TiCl_2 and EHPG at neutral pH value leads to the formation of only the monomeric complex with a half-life of about 50 min at 298 K. At pH* 3.7, the reaction becomes much slower: the monomeric and dimeric complexes form with half-lives of about 2.5 days and 2 weeks, respectively.

The interaction of Cp_2TiCl_2 with nucleotides and their analogues at different pH values were investigated by both 1H and ^{31}P NMR [102,103]. Based on the shape of the pH titration curves and the pK_a values, the binding sites

of Ti^{IV} on nucleoside monophosphates were proposed. It has been shown that the S-shaped titration curves from ^{31}P NMR indicate the effects of protonation/deprotonation at the phosphate group, while the sigmoidal curves of H8 of GMP from ^1H NMR reveal the effects of protonation/deprotonation at the guanine N7 site. These results show that the anticancer drug Cp_2TiCl_2 binds strongly to the phosphate groups of nucleotides at low pH values in aqueous solution and weakly at a neutral pH, and N7 is not directly coordinated to Ti^{IV} .

The metal ruthenium possesses several favorable chemical properties and it may be a strong candidate to form a basis for rational anticancer drug design [104,105]. For instance, several ruthenium(II) and ruthenium(III) complexes (Scheme 5.5) exhibit a high antitumor activity both *in vitro* and *in vivo* [2,106,107]. Therefore, the reactions of Ru^{II} and Ru^{III} complexes with DNA and sulfur-containing amino acids as well as proteins has been studied by NMR and other spectroscopic methods (e.g. HPLC). Such studies may facilitate the development of an additional structure–activity relationship and allow more selective, potent and less toxic anticancer drugs to be designed.

It has shown that Ru^{III} complexes, such as *trans*-indazolium(bisindazole) tetrachloro-ruthenate(III) (Ru-Ind), *trans*-imidazolium(bisimidazole) tetrachloro-ruthenate(III), and *trans*- $\text{RuCl}_4(\text{Me}_2\text{SO})(\text{Im})(\text{ImH})$ [NAMI-A] (Scheme 5.5), demonstrate similar ligand exchange kinetics to those of platinum (Pt^{II}), while displaying only low toxicity, which in part is believed to be due to the ability to mimic iron in binding strongly to plasma proteins including transferrin and albumin [105,106,108]. Transport and sequestration of Ru^{III} into tumor cells may be mediated via the transferrin/transferrin receptor pathway due to the large number of transferrin receptors on the surface of tumor cells [95,96]. Reactions with the sulfur-containing amino acids L-cysteine and L-methionine appear to play key roles in the biological activity of Ru^{III} anticancer agents. In contrast, Ru^{II} complexes, such as $[(\eta^6\text{-Bip})\text{Ru}(\text{II})(\text{en})\text{Cl}]$ (en = ethylenediamine and Bip = biphenyl) and their analogues, interact only weakly with transferrin and react slowly with sulfur-containing amino acids [107]. Ru^{III} antitumor complexes are thought to bind more strongly to protein than to DNA, while Ru^{II} complexes have higher reactivity toward the DNA and can form adducts with DNA even in the presence of amino acids, peptides and proteins [107]. It is suggested that the mechanism of action of Ru^{II} arene complexes, a class of novel ruthenium anticancer agents, may be different from that of Ru^{III} complexes.

The thermodynamics and kinetics of the binding of $[(\eta^6\text{-arene})\text{Ru}(\text{II})(\text{en})\text{X}]^{n+}$ complexes (arene = benzene (Ben), biphenyl (Bip), di-, tetrahydroanthracene (DHA, THA), *p*-cymene (Cym); en = ethylenediamine; X = Cl or H_2O , Scheme 5.5) to mononucleosides (G, I, A, C and T) and mononucleotides have been studied in detail by ^1H , ^{31}P and ^{15}N NMR spectroscopy [109,110]. Based on the changes of the chemical shifts, $\text{p}K_a$ values are obtained and

the binding sites of $[(\eta^6\text{-arene})\text{Ru(II)(en)X}]^{n+}$ complexes to nucleosides and nucleotides are identified. Reactions of the chloro Ru^{II} (arene) complexes with nucleotides (5'-GMP, 5'-IMP, 5'-AMP, 5'-CMP, and 5'-TMP) proceed via hydrolysis in water to give more reactive aqua Ru^{II} -arene species followed by rapid binding to the phosphate monoester group (Figure 5.4). In contrast, binding to the phosphodiester group of nucleotides (e.g., cGMP and cAMP) is weak and was not detected. Bound phosphate groups are then readily displaced by nitrogens from the base. Studies of the kinetics of binding of $[(\eta^6\text{-Bip})\text{Ru(II)(en)X}]^{n+}$ to N7 of GMP showed that the rate of reaction depends on whether Cl^- , H_2O , OH^- , or phosphate occupies the available coordination position (X). The slower reaction of Ru-OH and Ru-Cl compared to Ru-OH_2 is attributed to the lower reactivity of Ru-OH and Ru-Cl than Ru-OH_2 . The rates of reaction of $[(\eta^6\text{-arene})\text{Ru(II)(en)X}]^{n+}$ ($\text{X} = \text{H}_2\text{O}$, Cl) complexes with c-GMP depends markedly on the nature of the arene, decreasing by over an order of magnitude in the series: $\text{THA} > \text{Bip} > \text{DHA} \gg \text{Cym} > \text{Ben}$, and obeys second-order kinetics. The faster reaction of complexes containing the arenes THA, Bip, and DHA, which can take part in π stacking interactions, than that of complexes containing the arenes Cym and Ben, which cannot, implies that hydrophobic interaction between the arene groups of the complexes and the nucleobase (e.g., purine), plays a significant role in stabilizing the transition state in the associative substitution reactions. Such a kinetic effect could play a role in the biological activity of this class of anticancer complexes.

5 GOLD ANTIARTHRITIC DRUGS

Gold-based drugs (chrysotherapy) have been used in the treatment of rheumatoid arthritis for over 60 years [111,112] with a 70% success rate. Auranofin ($\text{Et}_3\text{P-Au-SATg}$, where SATg is 2,3,4,6-tetra-*o*-acetyl-1-thio- β -D-glucopyranosato-S, Scheme 5.6) is an orally active drug, while myocrisin (aurothiomalate; AuStm) and solganol (aurothioglucose; AuStg) are only active by injection. Gold(I) is a soft metal and therefore has a very high affinity for soft ligands such as thiolate sulfurs, it also binds to nitrogen of histidine imidazole in proteins (e.g., cyclophilin) [113], and hardly to oxygen. Consequently, proteins and enzymes containing thiolate groups (Cys residues, and possibly His imidazole) are targets for Au^{I} . It has been shown that when triple-labeled auranofin (^{195}Au , ^{35}S , ^{32}P) was injected, 82% of the gold, but only 10% of the sulfur and 42% of the phosphorus, remained in the blood after 20 min [114]. Therefore, the gold circulates probably as metabolites and not as the original gold complex.

One feature of the gold-based drugs is that ligands undergo facile thiolate exchange reactions with components in biofluids and cells in the body. For example, auranofin reacts rapidly with serum albumin with gold binding to

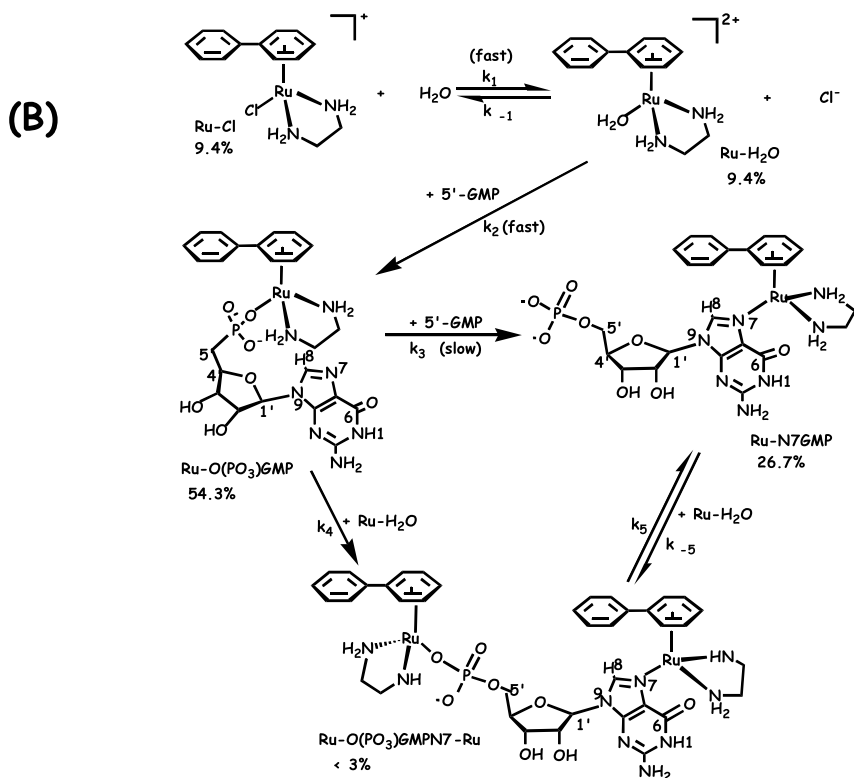
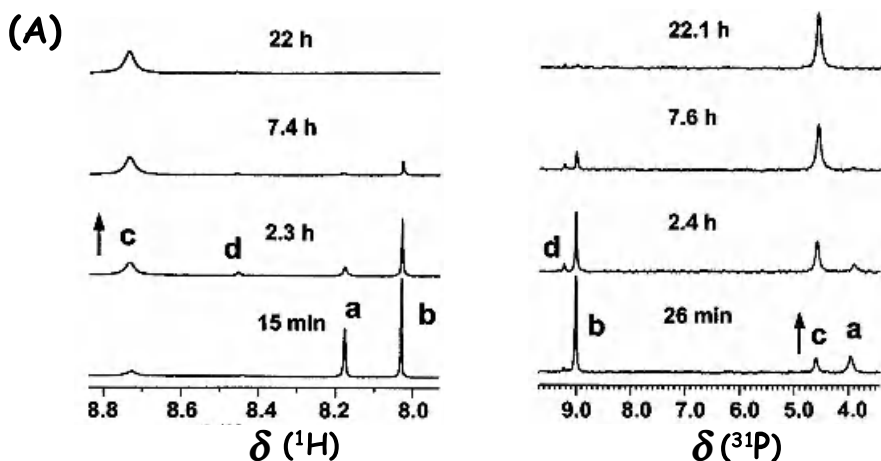
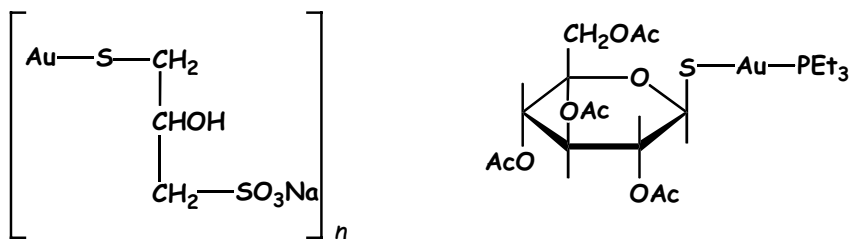
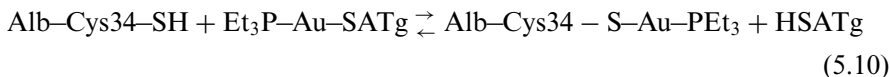


Figure 5.4 The time dependences of ^1H and ^{31}P NMR spectra for the reaction of 5'-GMP with $[(\eta^6\text{-Bip})\text{Ru}(\text{en})\text{Cl}]^+$ in aqueous solution at pH 7.15, 298 K (A), and the proposed kinetics pathway with species distribution after 55 min reaction (B). Peak assignments in (A): a, free 5'-GMP; b, $\text{Ru-O}(\text{PO}_3)\text{GMP}$; c, Ru-N7GMP ; d, $\text{Ru-O}(\text{PO}_3)\text{GMPN7-Ru}$. Adapted with permission from H. Chen *et al.*, *J. Am. Chem. Soc.* **125**, 173 (2003) [109]. Copyright (2003) American Chemical Society.

**Sodium thiopropanolsulfonate-S-Au(I)****Auranofin****Scheme 5.6** Gold antiarthritic drugs.

Cys34 and STAg being displaced (Equation 5.10).



A displacement of gold-bound phosphine can also occur but is much slower, accompanied with the slow oxidation of the phosphine moiety to Et_3PO . In order to gain an insight into the mechanism of action of gold drugs with intracellular ligands, it is important to assess independently the interchange reaction of these ligands with gold(I) drugs. ^1H , ^{13}C , and ^{31}P NMR spectroscopy has been widely used to study the kinetics and mechanism of the reaction of gold drugs with serum albumin (Alb-SH), thiolates ligands in red blood cells (RBCs) such as ergothionine (ErS, 0.15–0.6 mM in RBCs) and GSH, and their analogues [115–122]. The ^{31}P chemical shift of bound phosphine (XAu-PEt_3) is sensitive to the nature of the coordinated ligands (X) and the release of PEt_3 can readily be detected. In addition, the ^{31}P chemical shift of bound phosphine in RS-Au-PR_3 was found to correlate with the $\text{p}K_a$ values of thiolates (SR) [123].

^1H and ^{31}P NMR studies have shown that the rate of binding of gold drugs to albumin appears to be determined by the rate of opening of the cleft where Cys34 is situated [120,121]. Surprisingly, binding of auranofin and related gold compounds to Cys34 of albumin induces a structural transition, the effect of which can readily be observed by imidazole ϵCH ^1H NMR resonances of His3 of the protein (Figure 5.5) [119–121]. Such a communication between His3 and Cys34 may be explained by small changes in the arrangement of intervening helices 1 and 2 of domain I of the protein. This may be mediated by a *cis-trans* isomerization of a proline (Pro35), changing the environment of Cys34 from a buried to an exposed form. The rapid exchange of $\text{R}_3\text{P-Au-SATg}$ at the exposed Cys34 residue was observed under an

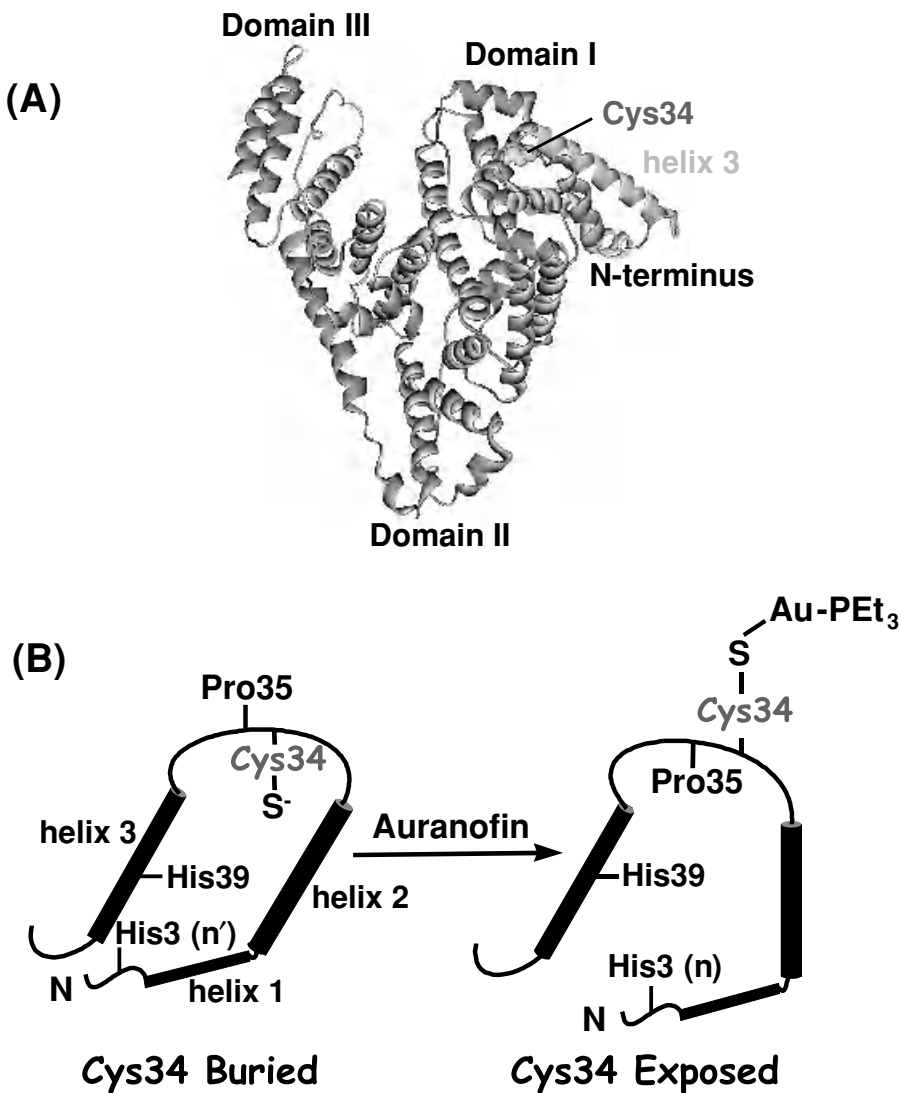


Figure 5.5 (Plate 1) (A) Crystal structure of human albumin (PDB ID: 1AO6) with helix 1–3 and Cys34 (space-filling model) highlighted. Color code: cyan, residues 5–61 (containing helix 10–3); yellow, Cys34. (B) A model for structural changes induced by the Au^I drug in domain I of albumin. Adapted with permission from J. C. Christodoulou *et al.*, *FEBS Lett.* **376**, 1 (1995) [119].

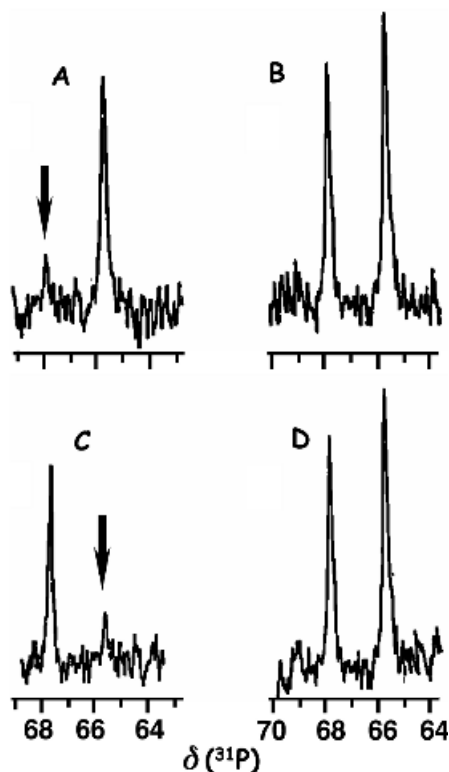


Figure 5.6 ^{31}P NMR saturation transfer on the reaction mixture of Alb-S-Au- $i\text{Pr}_3\text{P}$. Selective saturation was applied on the carrier frequencies: (A) 68 ppm (Alb-S-Au- $i\text{Pr}_3\text{P}$); (B) 64 ppm (as a control for A); (C) ca 66 ppm ($i\text{Pr}_3\text{P}$ -Au-SATg) and (D) 71 ppm (as a control for C). Adapted with permission from J. R. Roberts *et al.*, *Inorg. Chem.* **35**, 424 (1996) [116]. Copyright (1996) American Chemical Society.

equilibrium condition by ^{31}P NMR saturation transfer experiments using $i\text{Pr}_3\text{P}$ -Au-SATg, a tri-isopropylphosphine analogues of auranofin (Figure 5.6) [116]. The second-order rate constants for both the forward and reverse directions are 1.2×10^2 and $3.9 \times 10^1 \text{ M}^{-1} \text{ s}^{-1}$, respectively. A multistep mechanism involving a conformationally altered albumin species was proposed. Domain I of albumin opens with concomitant Cys34 rearrangement, allowing facile Au^{I} binding and exchange, and then closes. The rate of Au^{I} is governed by the rate of opening of the cleft containing Cys34 [116].

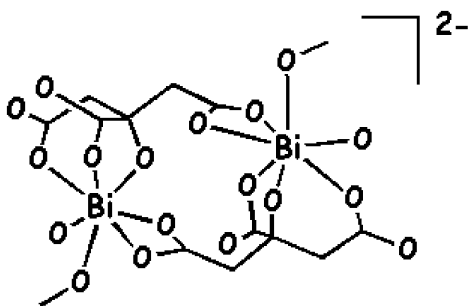
The interaction of auranofin (Et_3P -Au-SATg) with ergothioneine (ErS), imidazolidine-2-thione (Imt), diazinane (Diaz) and thiourea (Tu) has been studied by ^{13}C and ^{31}P NMR spectroscopy [117,118]. It was shown that these thiones are able to replace both Et_3P and SATg^- ligands simultaneously from auranofin, forming $>\text{C}=\text{S}-\text{Au}-\text{SATg}$ and $[\text{Et}_3\text{P}-\text{Au}-\text{S}=\text{C}<]^+$ complexes. The

displaced SATg^- is then oxidized to its disulfide form $(\text{SATg})_2$. Whereas some of the displaced Et_3P is oxidized to Et_3PO , the remaining reacts with thiones to form $\text{Et}_3\text{P-S=C<}$ species. The Et_3PO ^{31}P resonance signals appeared after 4–19 days of the addition of these thiones, indicative of a slow reaction.

Cyanide appears to play an important role in the metabolism of gold drugs. It can readily replace the thiomalate ligand from aurothiomalate *in vitro* and dicyanoaurate(I) ion $\text{Au}(\text{CN})_2^-$ has been shown to be a metabolite of chrysotherapy agents *in vivo* [124]. The $\text{Au}(\text{CN})_2^-$, formed probably from gold drugs and thiocyanate during the oxidative burst of macrophages [125–127], can inhibit the oxidative burst of polymorphonuclear leukocytes, which may be one of the mechanisms of action of the gold drugs. Interaction of aurothiomalate and cyanide (^{13}C -enriched CN^-) was followed by ^1H and ^{13}C NMR spectroscopy [128]. The mixed-ligand complex $[(\text{Stm})\text{Au}(\text{CN})]^-$ (Stm = S-bound thiomalate) readily forms as an intermediate when $[\text{CN}^-]/[\text{aurothiomalate}] < 2$, and $\text{Au}(\text{CN})_2^-$ is the major species at a higher ratio. The binding of $\text{Au}(\text{CN})_2^-$ to bovine serum albumin (BSA), which may modulate the *in vivo* activity of $\text{Au}(\text{CN})_2^-$, was investigated by ^{13}C NMR spectroscopy and other techniques. This study revealed two distinct binding mechanisms. The dominant mechanism is reversible association (nonspecific binding) of intact $\text{Au}(\text{CN})_2^-$, characterized by a sharp resonance at 156.4 ppm, to albumin to form $\text{Alb}\cdot[\text{Au}(\text{CN})_2^-]_n$, a broad resonance at $\delta_{^{13}\text{C}} = 154.7$ ppm. The second binding mechanism is a ligand exchange reaction at Cys34 to form $\text{Alb-S-Au}(\text{CN})$, which accounts for only a minor fraction of the bound gold (~11 %). Mixed-ligand complexes of aurocyanide with other thiolates molecules such as glutathione, cysteine and captopril have also been reported [128–131]. Both thiols and cyanide bind to Au^{I} , although as expected cyanide binds more strongly. Under biological conditions where $[\text{thiols}] \gg [\text{HCN}]$, substantial displacement of cyanide may take place. This may facilitate the accumulation of gold in red cells where the intracellular glutathione concentration is high (mM).

6 ANTIMONY ANTIPARASITIC AND BISMUTH ANTIULCER DRUGS

Interestingly, all of the elements in group 15 in the periodic table (N, P, As, Sb and Bi) are directly or indirectly related to the maintenance of human life as either essential elements (e.g., N and P) or therapeutic/toxic elements (e.g., As, Sb and Bi). Currently antimony compounds (e.g., sodium stibogluconate, Pentostam[®]) are used clinically for the treatment of leishmaniasis and bismuth compounds (e.g., bismuth subsalicylate (BSS), colloidal bismuth subcitrate (CBS) and ranitidine bismuth citrate (RBC)) are widely used for the treatment of ulcer and *Helicobacter pylori* infection [1–3c,10,132,133]. Recently, clinical



Scheme 5.7 The basic Bi^{3+} citrate dimer found in the antiulcer drugs, colloidal bismuth subcitrate (CBS, DE-Nol[®]) and possibly ranitidine bismuth citrate. Assembly of these building block leads to the formation of polymeric anion.

studies in China have demonstrated that the classical inorganic compound, arsenic trioxide (As_2O_3) can induce remission in patients with acute promyelocytic leukemia (APL, a rare blood cancer) [5,134]. The induction of apoptosis and partial differentiation may be responsible for the activity of this metalloid [135]. Progress in the understanding the mode of action and design of drugs based on these elements is being greatly held up due to the lack of a suitable probe for the metal itself. NMR studies of these complexes have therefore relied on the observation of ligand nuclei such as ^1H and ^{13}C .

The binding of citrate to Bi^{III} in antiulcer complexes has been studied by ^1H , ^{13}C and [^1H , ^{13}C] NMR spectroscopy [136–139]. Citrate is a good bridging ligand and polymeric species are formed in solution and in solid-state. The basic building block is dinuclear unit $[\text{Bi}(\text{citrate})_2\text{Bi}]^{2-}$ (Scheme 5.7) in most bismuth citrate structures [132,133,140]. The structures of bismuth citrate complexes are complicated, being dependent on pH, concentrations, $[\text{Bi}:\text{citrate}]$ ratios and even the counter cations. Different bismuth citrate species are in fast exchange on the NMR time scale at $\text{pH} < 6$. 2 and therefore only an averaged resonance was observed corresponding to each carbon or proton. The exchange rate decreases at $\text{pH} > 6$, and different bound species can be observed [136,137]. By means of diffusion-ordered 2D [^1H , ^{13}C] HSQC NMR spectroscopy together with isotopic labeling of citrate ($^{13}\text{C}2/^{13}\text{C}4$), a wide range of different types of bound citrate can readily be detected at low Bi concentrations (5 mM) in aqueous solutions of ranitidine bismuth citrate at $\text{pH}^* 7.4$ (Figure 5.7). There appears to be an equilibration between free citrate, dinuclear species $[\text{Bi}(\text{citrate})_2\text{Bi}]^{2-}$ and multinuclear bismuth citrate clusters at physiological pH values.

Both Sb^{III} and Bi^{III} form stable complexes with the tripeptide glutathione (GSH) with a stoichiometry $[\text{Bi}(\text{GS})_3]$ or $[\text{Sb}(\text{GS})_3]$. The rate of uptake of these metals into red blood cells and complexation with intracellular glutathione as determined by spin-echo ^1H NMR, is rapid for Sb^{III} (minutes) and

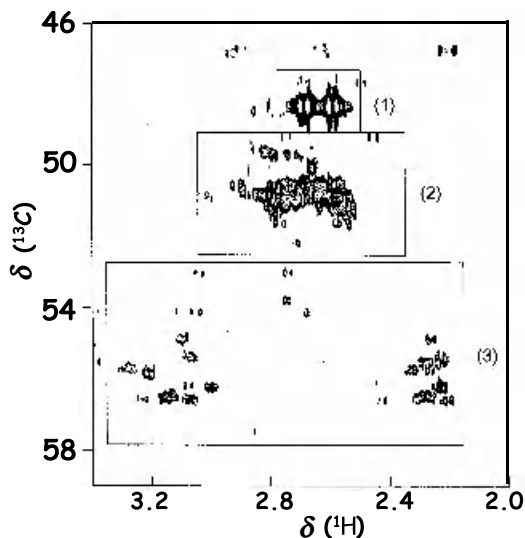


Figure 5.7 2D [^1H , ^{13}C] HSQC NMR spectrum of 5 mM ranitidine bismuth citrate showing different forms of bound citrate. Adapted with permission from J. A. Parkinson *et al.*, *Chem. Commun.* 881 (1998) [138]. Reproduced by permission of The Royal Society of Chemistry.

relatively slow for Bi^{III} (hours) [141,142]. Strong binding of Sb^{III} to trypanothione ($\text{T}(\text{SH})_2$) was chemically characterized for the first time by electrospray ionization mass spectrometry (ESI-MS) and NMR spectroscopy. In contrast to the glutathione complex, each Sb^{III} coordinates to only one $\text{T}(\text{SH})_2$ with two sulfurs provided by Cys residues and probably an oxygen from a water molecule [143]. Similar to the Sb^{III} in the ArsA ATPase complex where Sb^{III} acts as a soft metal and coordinates to three donate atoms with two of them from the protein residues and one from a nonprotein ligand (Cl^-) [144], Sb^{III} (TS_2) is probably an intermediate. A ternary complex between Sb^{III} –trypanothione and other monothiol ligands such as glutathione and cysteine can readily form [145]. In spite of being thermodynamically stable, both the Sb^{III} (TS_2) and the ternary complexes are kinetically labile, and the free and bound forms of either trypanothione or cysteines/glutathione exchange on the ^1H NMR time scale (Figure 5.8). This exchange is also pH dependent, from slow exchange at low pH (~ 4) to fast exchange at pH 7. Such a facile exchange may be important for the transport and delivery of Sb^{III} *in vivo*.

Bismuth and zinc are known to be potent inducers of renal metallothionein (MT) synthesis, and pretreatment with bismuth significantly reduces the renal and lethal toxicity of cisplatin without affecting its anticancer activity in human patients [146]. The protection probably involves Bi^{III} induction of metallothionein synthesis. UV and NMR studies have shown that Bi^{III} binds very strongly

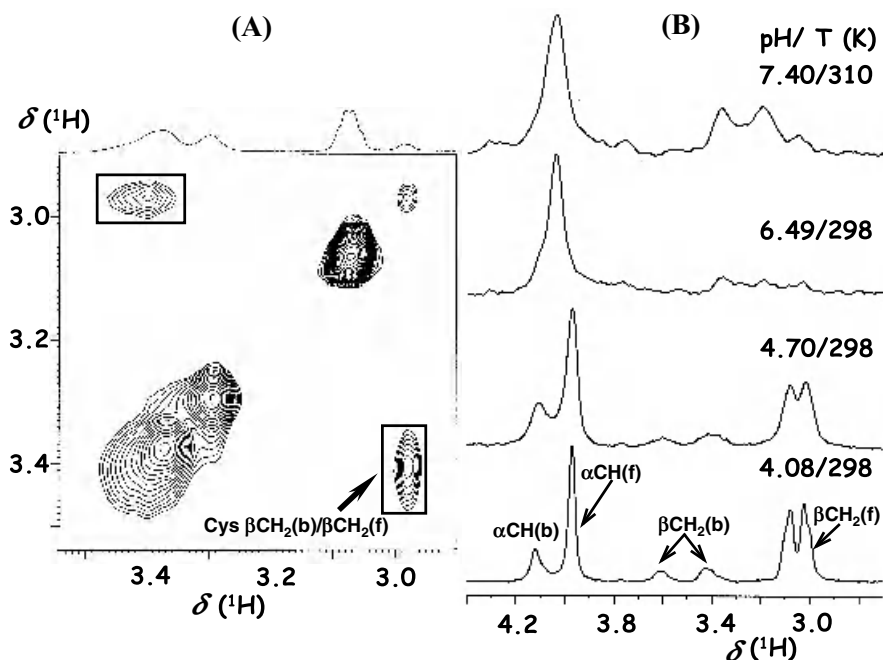


Figure 5.8 (A) A 2D EXSY showed exchange of trypanothione between its bound and free forms (mixing time 500 ms) and (B) ^{13}C edited ^1H NMR spectra showed the exchange of ^{13}C -labeled cysteine between its bound and free forms in the ternary complex. Adapted with permission from S.-C. Yan *et al.*, *J. Biol. Inorg. Chem.* **8**, 689 (2003) [145]. Copyright (2003) Springer Verlag.

to metallothionein with a stoichiometry Bi_7MT , and can readily displace Zn^{II} and Cd^{II} in biphasic processes [147]. ^1H NMR data show that displacement of Zn^{II} is very rapid (<3 min), while displacement of Cd^{II} is relative slow (>4 h). Zn^{II} and Cd^{II} from $\text{Zn}_2\text{Cd}_5\text{MT}(\text{II})$ are replaced much faster from the β -domain (three metal cluster) than from the α -domain.

Binding of bismuth to human transferrin was unexpectedly strong [148,149]. The uptake of Bi^{III} by apo-transferrin from bismuth citrate complexes is very slow (hours at 310 K) and occurs in at least two steps, whereas transfer from bismuth nitrilotriacetate is rapid (minutes). ^{13}C NMR suggests that bismuth binds to transferrin along with carbonate (CO_3^{2-}) as the synergistic anion, which is similar to Fe^{III} . Binding of Bi^{III} occurs preferentially to the C-lobe of transferrin. This order of lobe loading has been confirmed by 2D [^1H , ^{13}C] heteronuclear multiple-quantum coherence (HMQC) NMR studies using recombinant ϵ - ^{13}C Met-hTF (ca 0.3 mM) in which all Met residues are enriched with ^{13}C at the $-\text{SCH}_3$ group. The changes in shift of the ^1H and ^{13}C NMR resonances of Met can be used not only as a probe for determining the order of

lobe loading of transferrin with metal ions, but also as fingerprints of conformational changes induced by Bi^{III} and other metal ions. Bi^{III} , Fe^{III} , Ga^{III} and Al^{III} probably induce similar conformational changes in hTF, since the changes in shifts of SCH_3 resonances (Met) are almost identical [150]. Due to the ^{13}C labeling of Met and the sensitivity enhancement by inverse detection, the possible metal binding (e.g., Bi^{3+}) to transferrin (ϵ - ^{13}C]Met-hTF) can readily be detected in the presence of large excess of other proteins and even in blood plasma by 1D and 2D [^1H , ^{13}C] NMR spectroscopy [151]. Both NMR and other techniques have shown that transferrin is a potential mediator for Bi^{III} transport in blood plasma, which may have implications for the mechanism of neurotoxicity of Bi^{III} drugs [152].

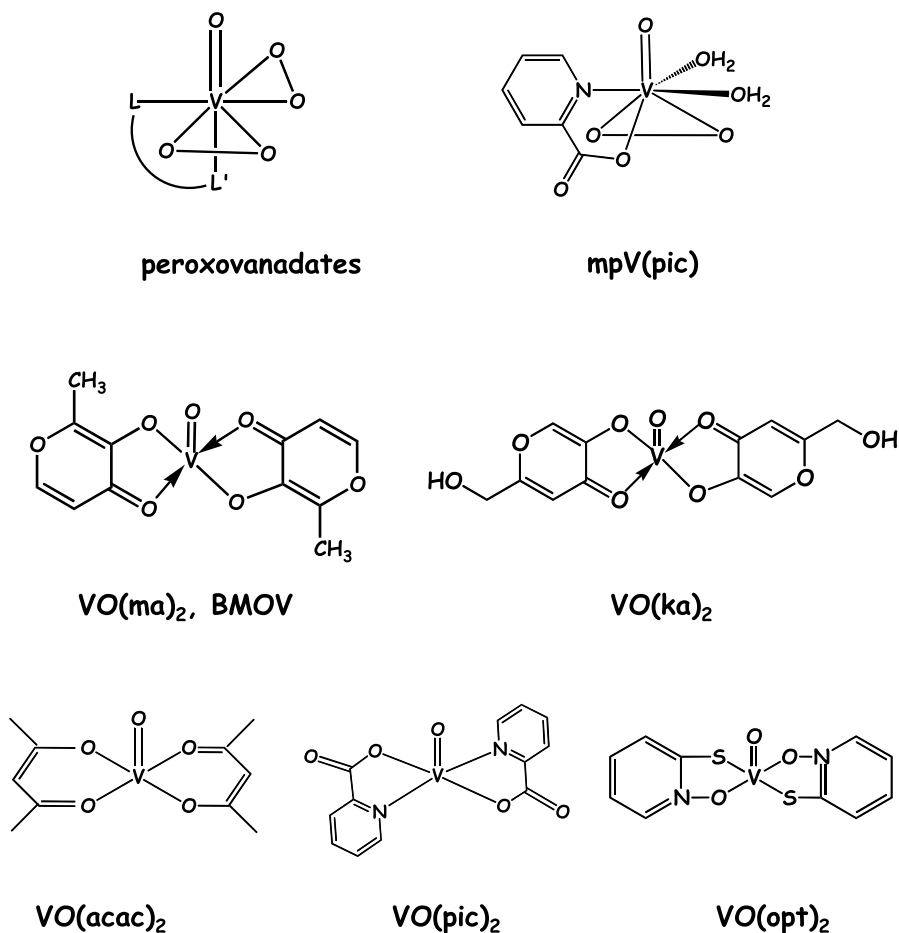
7 VANADIUM ANTIDIABETIC MIMETICS

Diabetes mellitus is a heterogeneous disorder, which can lead to cardiovascular disease, blindness, kidney disease, and even death. It is characterized by hyperglycemia, alterations in carbohydrate and lipid metabolism, and vascular and neurological complications. The number of patients suffering from diabetes mellitus is over 140 million throughout the world and has become one of the most significant diseases in the 21st century. Diabetes is caused by either an underlying insufficiency of insulin (type 1 or insulin-dependent diabetes mellitus) or defective insulin utilization (type 2 or noninsulin-dependent diabetes mellitus). The insufficiency of insulin for type 1 results from inadequate pancreatic production and can be corrected therapeutically only by daily subcutaneous injections of insulin to patients to lower their high glucose levels in blood to normal values and interrupt an otherwise fatal disorder. For the patients of type 2, which accounts for about 90% of diabetic patients, the pancreas continues to produce insulin, yet patients remain hyperglycemic as muscle, liver and adipose tissues fail to respond efficiently to insulin. This phenomenon, known as insulin resistance, is a major contributing factor in hyperglycemia in type 2 diabetic patients. Because type 2 diabetes is characterized at least initially by hyperinsulinemia and insulin resistance, not insulin deficiency, it is treated by several types of drugs with different pharmacological functions [153–155].

The discovery of the insulinomimetic effect of vanadium ions and their complexes as potential agents for treatment of diabetes has been considered as the most remarkable progress in the diabetic therapy over the last two decades [2,4c]. Since a series of landmark studies in 1979 and 1980 demonstrated the ability of vanadate and vanadyl to have insulin-like biological effects of glucose uptake and metabolism in skeletal muscle and adipose tissue *in vivo*, much work has been focused on exploring the insulin-mimetic properties of vanadate and vanadyl both *in vitro* and *in vivo* and on developing new vanadium compounds as potential insulin alternatives in diabetes treatment [156–162], which

was dramatically accelerated when the oral insulin-like effects of vanadate *in vivo* were first reported in 1985 [163].

Three general classes of vanadium-containing compounds are of interest for their utility as insulin-mimetic agents: (1) inorganic vanadium salts, both anionic (vanadates $[\text{VO}_4]^{3-}$) and cationic (vanadyl VO^{2+}); (2) complexes resulting from combination of vanadium(V) and hydrogen peroxide(s) (mono- and di-peroxovanadates, $[\text{VO}(\text{O}_2)_2(\text{H}_2\text{O})_2(\text{L}^-)]^{n-}$ ($n = 0, 1, 2$) and $[\text{VO}(\text{O}_2)_2(\text{L}^-)]^{n-}$ ($n = 1, 2, 3$, and $\text{L} = \text{e.g., bipyridil, oxalate, phenanthroline, picolinate}$), and (3) chelated vanadium(IV) complexes (Scheme 5.8) [160]. Vanadyl,



Scheme 5.8 Insulin-mimetic vanadium complexes. In the peroxovanadate complex, $\text{L} =$ bipyridine (bipy), oxalate (ox), phenanthroline (phen) and picolinate (pic). BMOV represents bis(maltolato)oxovanadium(IV).

vanadate and bis(ethylmaltolato)oxovanadium(IV) (BEOV) have all proceeded to phase I clinical trials in recent years [164].

^{51}V is essentially a 100% abundant natural isotope with a nuclear spin of $\frac{7}{2}$. The typical linewidths for this nucleus (V) are between 50 and a few hundred Hz broadened due to the electric quadrupole moment. But the linewidths often do not result in a great hindrance to interpreting spectra relative to a large chemical shift range of about 2000 ppm for vanadium (V) and the line-broadening factors of 40 Hz or more can be applied to the spectra without degradation of the information content. Furthermore, the fast nuclear relaxation corresponding to such linewidths means the shorter delay needed before each acquisition, often 30 or more acquisitions per second can be accumulated without perturbing the resultant spectrum [165].

The speciation of vanadate in aqueous systems is found to be both concentration and pH dependent. The ^{51}V NMR spectrum of the vanadate solution contains four main peaks at -542, -564, -574 and -582 ppm, which are attributed to vanadate monomer, dimer, tetramer and pentamer, respectively [166,167]. A dynamic analysis combined with exchange rates determined by using the 2D EXSY ^{51}V NMR spectrum, allowed quantification of exchange pathways, and has yielded information about the kinetic stability of the vanadate oligomers (Figure 5.9) [167]. The major pathway for monomer formation is unimolecular decomposition of the dimer; conversely, the major pathway for

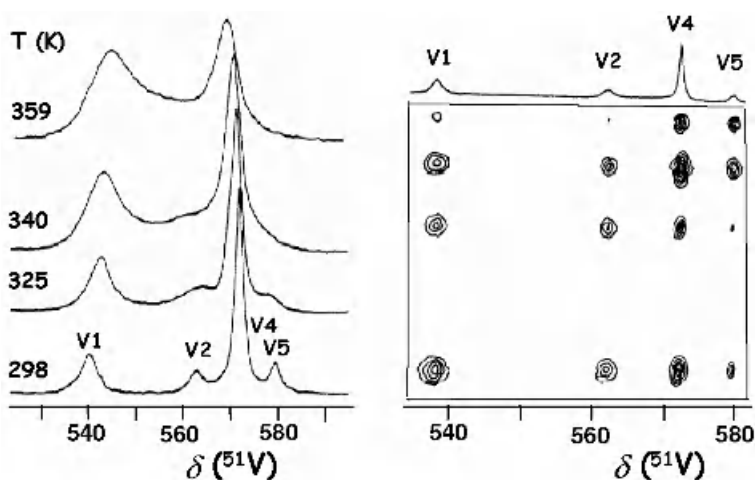


Figure 5.9 (A) Different vanadate species are observed in a 10 mM vanadate solution (pH 8.6), and various temperature ^{51}V NMR spectra show the exchange between them. (B) 2D EXSY NMR spectrum shows the entire exchange 'map' of the vanadates. V1, V2, V4 and V5 represent vanadate monomer, dimer, tetramer and pentamer, respectively. Adapted with permission from D. C. Crans *et al.*, *J. Am. Chem. Soc.* **112**, 2901 (1990) [167]. Copyright (1990) American Chemical Society.

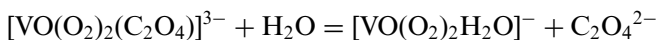
dimer formation is dimerization of the monomer. The tetramer forms mainly from two monomers and one dimer. At low vanadate concentrations, the pentamer forms from a tetramer and either a monomer or a dimer with similar rates. At high vanadate concentrations, the pentamer exchanges more rapidly with the tetramer. The monomer is found to be the most reactive vanadate derivative and is involved in exchange reactions with all vanadate oligomers, and the rates are all significant. The dimer is inherently more labile than the tetramer and pentamer.

In order to understand the insulin-mimetic properties of vanadate *in vivo*, the action of vanadate on intact human erythrocytes was studied by ^{51}V and ^1H spin-echo NMR spectroscopy [168]. Upon addition of vanadate (1 mM) to a suspension of intact erythrocytes, ^{51}V NMR shows a decrease in the total V^{V} over a period of 400 min. This change was thought to be cell-mediated reduction of diamagnetic NMR-active V^{V} to paramagnetic NMR-silent V^{IV} intracellularly, where sufficient quantities of glutathione and reductase enzymes are present. However, the component of the ^{51}V NMR signal which is derived from intracellular vanadate was not observed after dysprosium salts were added to the cellular suspension to paramagnetically shift the NMR resonance from the extracellular vanadate. This suggests that reduction of vanadate to vanadyl within the thiol-rich erythrocyte is rapid and that membrane transport of vanadate as an anion ($[\text{HVO}_4]^{2-}/[\text{H}_2\text{VO}_4]^-$) is the rate-limiting step. The anion transport cross the cell wall was confirmed by the inhibition of the vanadate reduction on addition of the blocking agent 4,4'-diisothio-cyanantostilbene-2,2'-disulfonic acid (DIDS), which specifically blocks the anion transport. The effects of membrane on the action of vanadate in intact cells were detected by following the time dependence of the signal intensities of ^1H spin-echo NMR spectra of intact human erythrocytes mixed with an equivalent volume of fresh cell haemolysate in the presence of vanadate. The possible influences of vanadate on glutathione reductase were also studied. This study generates a model for the behavior of vanadium complexes *in vivo*. Basically, vanadium is transported across the membrane as V^{V} , is reduced *in situ* by glutathione, and forms complexes to a wide range of intracellular ligands. Thiol exchange between glutathione and other biomolecules such as haemoglobin and membrane leads to the depletion of glutathione from cytosol [168].

The oral active bis(maltolato)oxovanadium(IV) complex ($\text{VO}(\text{ma})_2$ or BMOV) has a five-coordinate square-pyramidal geometry with the oxo ligand in the axial position and *trans* maltol ligands in the solid state. Upon dissolved in water or methanol under anaerobic conditions, $\text{VO}(\text{ma})_2$ binds to solvent molecule in a position *cis* to the oxo ligand and becomes six coordinate. The aqueous chemistry of $\text{VO}(\text{ma})_2$ has been investigated by ^{51}V NMR as a function of pH [169], since the oral activity of this complex may be related to its chemical properties in water. The diamagnetic V^{V} species (NMR active) produced via aerial oxidation in solutions of the paramagnetic $\text{V}^{\text{IV}}\text{OL}_2$ complexes (NMR silent) were probed. At pH 10, only the peak of

$[\text{VO}_4]^{3-}$ (-537 ppm) was left in the ^{51}V NMR spectrum of a solution of $\text{VO}(\text{MA})_2$. As the pH was lowered, both bis- and mono-maltolato complexes (-496 and -510 ppm, respectively) appeared and the $[\text{VO}_4]^{3-}$ (at $-538 \sim -560$ ppm in various pH) decreased. Similar results were also obtained from the chemical analogue of $\text{VO}(\text{ma})_2$, bis(kojato)oxovanadium(IV) ($\text{VO}(\text{ka})_2$) [170]. The oxidation of $\text{VO}(\text{ma})_2$ can be slowed down dramatically in the presence of good donor ligands such as pyridine (py) via the formation of six coordinate adducts (e.g., $\text{VO}(\text{ma})_2$ py), and it could be indefinitely suppressed with 5–10 equiv of ascorbic acid. The oxidation could be speeded up significantly by either iodobenzene or hydrogen peroxide [169].

It has been suggested that the biological activity of the V^{V} peroxo complexes, a new class of powerful insulin mimetic agents, might be related to their involvement in oxidation processes of cysteine residues at the active site of protein tyrosine phosphatases [171,172]. Therefore, the oxidation process of cysteine of V^{V} oxo diperoxo complexes $[\text{VO}(\text{O}_2)_2\text{L}]^{n-}$ ($n = 1, 2, 3$, and $\text{L} =$ bipyridil (bipy), oxalate (oxa), phenanthroline (phen), and picolinate (pic), Scheme 5.8) has been investigated by ^{51}V NMR [173]. These complexes (pic, phen and bipy) in solution show a unique signal at -743.7 , -746.1 and -748.5 ppm, respectively, unaffected by concentration variations, and the oxidant species present in solution are the starting peroxo complexes except in the case of oxalate, which loses the ligand completely and yields the $[\text{VO}(\text{O}_2)_2(\text{H}_2\text{O})]^-$. Unlike other oxo diperoxo complexes, $[\text{VO}(\text{O}_2)_2(\text{oxa})]^{3-}$ undergoes a ligand dissociation in aqueous solution. When the concentration of the complex in aqueous solution was low (0.5 mM), only the signal due to $[\text{VO}(\text{O}_2)_2\text{H}_2\text{O}]^-$ (-691.3 ppm) appeared and the original oxalate ligand has been replaced by water. With increasing concentrations of $[\text{VO}(\text{O}_2)_2(\text{oxa})]^{3-}$ in solution, a new signal (-737.2 ppm), which is assigned to the starting peroxo complex $[\text{VO}(\text{O}_2)_2(\text{oxa})]^{3-}$ or $[\text{VO}(\text{O}_2)_2(\text{C}_2\text{O}_4)]^{3-}$, appeared and became more intense. The addition of potassium oxalate to the solution caused a large increase in intensity of a peak at -737.2 ppm while a remarkable decrease in intensity of the peak at -691.3 ppm. Therefore, it was suggested that $[\text{VO}(\text{O}_2)_2(\text{C}_2\text{O}_4)]^{3-}$ in the aqueous solution experiences the following ligand dissociation reaction:



which leads to the complete lose of the ligand and yields the $[\text{VO}(\text{O}_2)_2\text{H}_2\text{O}]^-$ species in the small concentration of $[\text{VO}(\text{O}_2)_2(\text{C}_2\text{O}_4)]^{3-}$.

Oxidation of cysteine to cystine was carried on under a pseudo-first order condition in the presence of excess of cysteine on the oxidant:



It was suggested that ligands exert a large modulatory role in determining the oxidative ability of these vanadium oxo diperoxo complexes affecting both the coordination of cysteine and the reduction potentials of the oxidants.

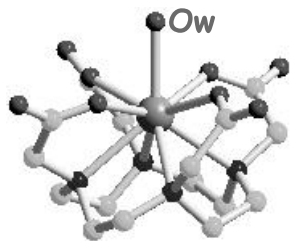
8 MRI CONTRAST AGENTS

The use of heavy elements (metals) as contrast agents, for example, organoiodide and BaSO₄, can be traced back to 19th century. Magnetic resonance imaging (MRI) is a powerful technique in clinical diagnosis. Diseases can be detected based on the differences in ¹H NMR relaxation (mainly H₂O) between normal and abnormal tissues. Addition of external paramagnetic compounds, the so-called ‘magnetic resonance imaging contrast agents’, shortens the proton relaxation times and therefore provides improved *contrast* in image. The most effective MRI contrast agents are the high-spin transition metal ions, Mn^{II}: [Ar]3d⁵ and Fe^{III}: [Ar]3d⁵, and the lanthanide ion Gd^{III}: [Xe]4f⁷, which have a large number of unpaired electrons (5, 5 and 7, respectively) and long electron-spin relaxations. Among them, Gd^{III} is highly favored due not only to its highest unpaired electrons, but also to its unique coordination chemistry (coordination number: 9) and very rapid exchange of bound water with bulk water ($k_{\text{ex}} = 8 \times 10^8 \text{ s}^{-1}$).

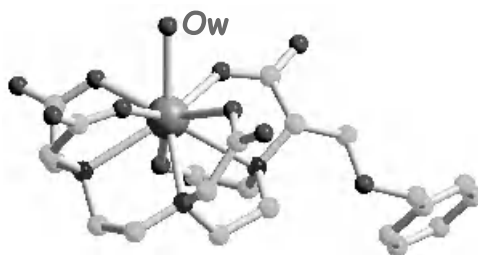
Since the Gd^{III} aqua ion is highly toxic and binds tightly to calcium binding sites, chelate of Gd^{III} by a multidentate ligand is necessary. Therefore an important requirement that a Gd^{III} complex must meet for *in vivo* applicability is high stability, both thermodynamic and kinetic. In practice, this means that suitable ligands are generally octadendate, leaving a vacant site for coordination of water. Most of the Gd^{III} complexes are nine-coordinate in the solid state and contain one bound water, Scheme 5.9. Several complexes of Gd^{III} with DTPA (diethylenetriamine-*N, N, N', N', N'*-pentaacetate) and DOTA (1,4,7,10-tetraazacyclododecane-1,4,7,10-tetraacetate) and their derivatives have been approved for clinical use as extracellular imaging agents (Table 5.4).

Crystal structures of Ln^{III} complexes of DTPA and DOTA derivatives show that Ln³⁺-bound diethylenetriamine moieties in these complexes always occur either in the δδ or in the λλ conformation (Scheme 5.10). In these complexes, the steric interactions are always minimized. Upon coordinated by a metal ion, the central nitrogen atom is chiral. The inversion is precluded if the nitrogen is coordinated to the metal. A common feature of cyclen-based macrocyclic Gd^{III} (and other Ln^{III}) is the formation of various isomers which display dynamic behavior (interconvert/exchange) on the NMR time scale in aqueous solution [174,175]. However, the long electronic relaxation time of Gd^{III} ion prevents the observation of the NMR spectra of its complexes and its solution structure has been inferred from the ¹H and ¹³C NMR spectra of its related Ln^{III} complexes.

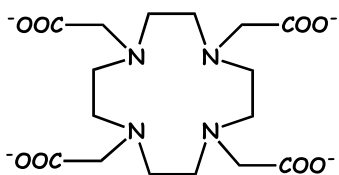
At low temperature, the ¹H NMR spectra for [Ln(DTPA)]⁻, where Ln = Pr, Eu and Yb, display 18 signals, which coalesced to 9 signals upon the increase of temperature. The exchange was studied by EXSY spectroscopy [176,177]. Ln^{III} binding of the three nitrogens of the diethylenetriamine backbone results in chirality of the central nitrogen, the two enantiomers cannot be discriminated



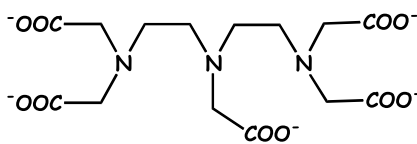
$[Gd^{III}(DOTA)]^-$



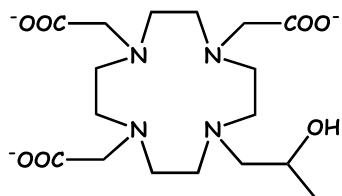
$[Gd^{III}(BOPTA)]^{2-}$



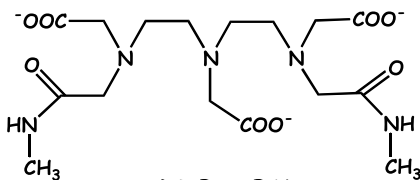
DOTA



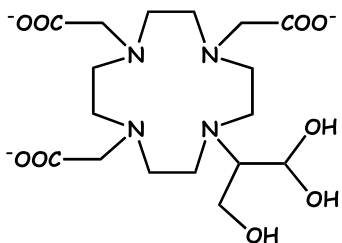
DTPA



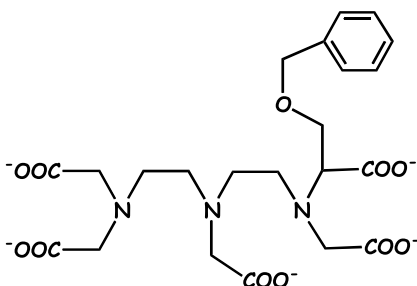
DO3A-HP



DTPA-BMA



DO3A-butrol



BOPTA

Scheme 5.9 (Plate 2) Crystal structures of Gd^{III} contrast agents $[Gd(DOTA)]^-$ and $[Gd(BOPTA)]^{2-}$, and structures of DOTA and DTPA and their derivatives. The bound water (Ow) in the crystal structures is shown.

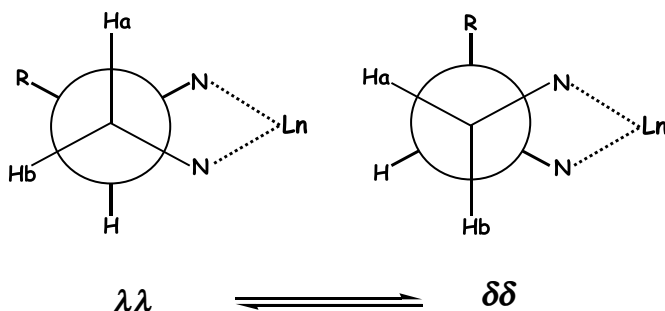
Table 5.4 Some clinically used Gd^{III} MRI contrast agents

Complex	Commercial name	k_{ex}^{298} (10^6 s^{-1}) ^a	Log K ^b
[Gd(DTPA)(H ₂ O)] ⁻	Magnevist	3.3	22.5
[Gd(DOTA)(H ₂ O)] ⁻	Dotarem	4.8	25.8
[Gd(DTPA-BMA)(H ₂ O)]	Omniscan	0.45	16.9
[Gd(DO3A-HP)(H ₂ O)]	ProHance		23.8
[Gd(BOPTA)(H ₂ O)] ²⁻	MultiHance		22.5
[Gd(DO3A-butrol)(H ₂ O)]	Gadovist		
MS-325 ^c	AngioMARK		

^a k_{ex}^{298} = the water exchange rate at 298 K (s^{-1}).

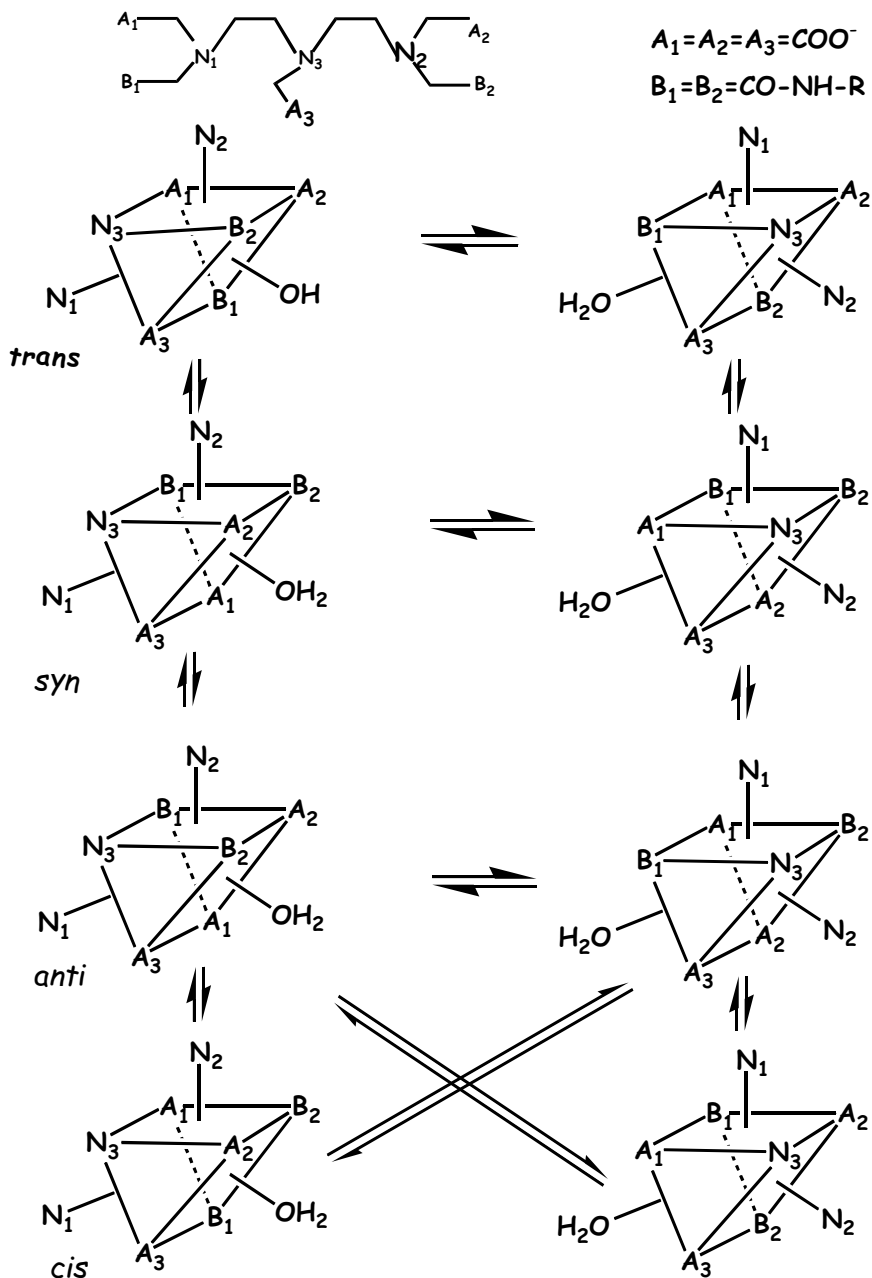
^b K = stability constant.

^c Phase III clinical trial.



Scheme 5.10 Equilibrium between the two gauche conformations of the ethylenediamine moieties in polyaminocarboxylates.

by NMR directly. However, the NMR data suggested that the $\delta\delta$ and the $\lambda\lambda$ enantiomers interconvert, which leads to average situation at high temperature with an effective mirror plane through the central glycine unit [177,178]. The ^{13}C NMR spectra of Ln^{III} complexes of DTPA-bis(amides) showed a large number of resonances, indicative of the presence of various isomers [179,180]. ^{17}O NMR data indicate that the coordination sphere is completed by one water molecule. If it is assumed that the coordination polyhedron of the nine-coordinated Ln^{III} in these complexes can be described by a tricapped trigonal prism, this gives the eight enantiomeric forms as shown in Scheme 5.11. The dynamics of the interchange of the various isomers in these complexes have been investigated by lineshape analysis. Two isomerization processes can be discerned: (i) a relatively rapid racemization of the central nitrogen atom via the interconversions of **1-4** and **1'-4'**, which are associated with the interconversions of the two gauche conformations of the ethylenediamine bridges ('wagging'); (ii) a slow racemization at the terminal decoordination of a nitrogen and its two neighboring oxygens (Scheme 5.11). The occurrence of various isomers



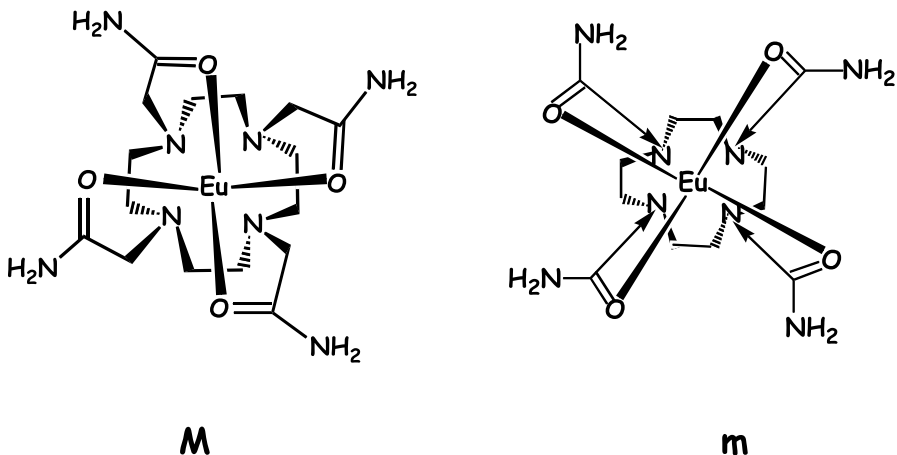
Scheme 5.11 Coordination polyhedra of the eight enantiomers of $\text{Ln}^{\text{III}}[\text{DTPA-bis}(\text{amide})]$ complexes, assuming that the geometry is a tricapped trigonal prism. Interconversions between the two columns (mirror image) correspond to the 'wagging' process (racemization at N_3), while the interconversions between rows in a column result in racemization at N_1 and N_3 . Adapted with permission from H. Lammers *et al.*, *Inorg. Chem.* **36**, 2527 (1997) [180]. Copyright (1997) American Chemical Society.

in solution has also been observed in diamagnetic Ln^{III} (e.g., La^{III} and Lu^{III}) complexes of DTPA derivatives, which showed the presence of several isomers under slow exchange on ^1H and ^{13}C NMR time scales [181–184]. The water exchange rate ($k_{\text{ex}} = 0.2 \times 10^6$ to $0.5 \times 10^6 \text{ s}^{-1}$) of Gd^{III} DTPA-bis(amides) is typically one order of magnitude smaller than that of the $\text{Gd}(\text{DTPA})$ ($3.3 \times 10^6 \text{ s}^{-1}$) complex and shows a trend toward lower rates upon the increase of bulkiness of the amide functional groups [180].

The contrast agent $[\text{Gd}(\text{BOPTA})]^{2-}$ (Gadobenate[®]) has been proved not only to be useful for the imaging of the hepatocytes but also to be more effective than $[\text{Gd}(\text{DTPA})]^-$ (Magnevist[®]), giving rise to a twofold enhancement of liver tumor *in vivo* [185]. The introduction of the benzyloxymethyl group on a terminal acetic acid residue has little effect on the stability and relaxivity of $[\text{Gd}(\text{BOPTA})]^{2-}$ compared to its parent complex [186]. NMR study of La^{III} and Lu^{III} complexes of BOPTA indicated that the structures of $[\text{Gd}(\text{BOPTA})]^{2-}$ in solution and solid state are identical. ^{13}C NMR spectra of the diamagnetic complexes $[\text{M}(\text{BOPTA})]^{2-}$ ($\text{M} = \text{La}^{\text{III}}$ and Lu^{III}) at various temperatures showed the presence of two couples of isomers interconverting through a dynamic process which is similar to other DTPA related complexes.

NMR studies of $[\text{Ln}(\text{DOTA})(\text{H}_2\text{O})]^-$ in solution have shown that the hydration number is one across the lanthanide, in agreement with the crystal structures [187]. The bound water ligand has a preferred location in the complex. Two sets of peaks have been observed in ^1H and ^{13}C NMR spectra at room temperature, indicative of the presence of two isomers (**M** and **m**) interconverting slowly on the NMR time scale. Isomers **M** and **m** adopt the same square conformation of the macrocyclic ring, but with a different layout of the acetate arms, through change of the four torsion angles $\text{Ln}-\text{N}-\text{C}-\text{COO}$. This difference leads to a square antiprismatic and a twisted antiprismatic geometry for **M** and **m**, respectively. Both the intra- and inter-molecular exchanges within and between the two isomeric forms of $[\text{Yb}(\text{DOTA})(\text{H}_2\text{O})]^-$ have been observed and the dynamic behavior was investigated through quantitative analysis of 2D EXSY spectra of the complex at various temperatures by completely solving the dynamic matrix. The activation energy (ΔG_{298}^\ddagger) for the major \rightarrow minor species (and arm rotation and ring inversion) exchange is higher than for the minor to major species exchange (65.6 and 61.4 kJ mol^{-1} , respectively), probably due to the greater steric crowding of the minor isomer [26]. The corresponding value for enantiomerization in $[\text{Yb}(\text{DOTA})]^-$ is 65.9 kJ mol^{-1} . The relative concentrations of the two species depend on the individual Ln^{III} ion, temperature, pressure and on the concentration of added inorganic salts.

For the α -substituted DOTA derivatives, the introduction of the chiral centers of equal configuration to all four acetate arms of the DOTA results in four possible diastereomers (*RRRR* and *SSSS*) upon metal binding. However, the occurrence of only two isomers appears to be features of Ln^{III} complexes of such DOTA derivatives. Both Yb^{III} and Eu^{III} complexes of DOTAM (DOTAM = 1,4,7,10-tetrakis(carbamoylmethyl)1,4,7-tetraazacyclododecane)



Scheme 5.12 Schematic structure of the two diastereoisomers of the complexes $[\text{Eu}(\text{DOTAM})(\text{H}_2\text{O})]^{3+}$. The coordinated water, in the apical position above the plane of the four oxygens, has been omitted for clarity [189].

show only two species in solution [188,189]. Bound water is directly observed in two isomers (**M** and **m**, Scheme 5.12) of $[\text{Eu}(\text{DOTAM})(\text{H}_2\text{O})]^{3+}$ by ^{17}O NMR. It was found that the rate (k_{ex}) of water exchange is dependent on the conformation of the complexes, k_{ex} for **m** being about 40 times faster than for **M** ($327(\pm 50) \times 10^3$ and $8.3(\pm 0.3) \times 10^3 \text{ s}^{-1}$ at 298 K, respectively). The interconversion between the two isomers happens mainly through a rotation of the amide arms in an interchange activated mechanism, with the interconversion rate to be 60 ± 10 (**M** \rightarrow **m**) and $260 \pm 50 \text{ s}^{-1}$ (**m** \rightarrow **M**) at 250 K, respectively, based on magnetization transfer experiments. 2D EXSY shows the strong cross-peaks due to the arm rotation, and only a very weak interaction due to the enantiomerization is observable, indicative of the arm rotation being much faster than other processes. The exchange due to ring conversion is not observed (Figure 5.10) [189]. The contribution of **m** to the overall exchange rate is 90%. Water exchange rates in the Gd^{III} tetra(carboxyethyl)-DOTA complexes have been determined by ^{17}O NMR and correlate well with the proportion of the twisted square antiprismatic isomer [190]. Exchange is the fastest for the *RRRR* complex which contains the highest proportion of the **m** isomer in solution. These studies show that it is necessary to synthesize DOTA-like complexes which mainly exist in the fast exchange form (twisted square antiprismatic isomer, **m**) in solution.

The success of $[\text{Gd}(\text{DOTA})]^-$ as an MRI contrast agent has stimulated an extensive search for derivatives with improved properties. Both $[\text{Gd}(\text{DO3A-HP})]$ and $[\text{Gd}(\text{DO3A-butrol})]$ (Table 5.4) are neutral complexes and their low osmolarity dramatically decreases the pain of the injection. X-ray crystal structure shows that Gd^{III} in $[\text{Gd}(\text{DO3A-HP})]$ complex is again nine coordinates, with eight coordinated sites occupied by the ligand and the ninth (apical) occupied

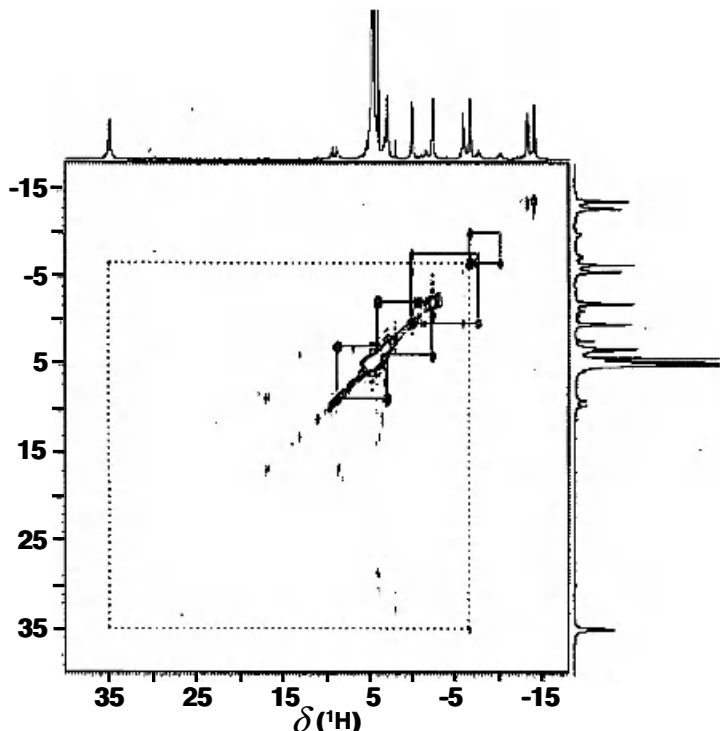


Figure 5.10 2D EXSY of $[\text{Eu}(\text{DOTAM})(\text{H}_2\text{O})]^{3+}$ at 250 K (mixing time 20 ms). The strong cross-peaks are due to the arm rotation (solid lines) while the weak cross-peaks are due to the enantiomerization. No cross-peaks coming from ring inversion is observed. Adapted with permission from F. A. Dunand *et al.*, *J. Am. Chem. Soc.* **122**, 1506 (2000) [189]. Copyright (2000) American Chemical Society.

by a water molecule [191]. Both the capped square antiprism ($\theta = 38^\circ$) and twisted capped square antiprism ($\theta = -26^\circ$) geometries are present, whereas the $[\text{Gd}(\text{DO3A-butrol})]$ complex has the nine-coordinate metal exclusively in the twisted capped square antiprism ($\theta = -28^\circ$) geometry [192]. The two diastereoisomers are also found in solution, and interconvert by ring inversion. Replacement of an acetate by a hydroxypropyl group, which contains a chiral carbon, leads to eight possible stereoisomers or four pairs of enantiomers. The presence of multiple species in $[\text{Y}(\text{DO3A-HP})]$ was confirmed by 2D ROESY spectra. Quantitative analysis of the cross-peaks in terms of the exchange dynamics gave the rates of various exchange processes [193]. It was found that the rate of exchange of the methylene groups ($91\text{--}119\text{ s}^{-1}$) during ring inversion is faster than the exchange of pendant arms ($20\text{--}30\text{ s}^{-1}$), while the exchange of the hydroxypropyl pendant arm ($\sim 33\text{ s}^{-1}$) is faster than for the acetate arms ($\sim 21\text{ s}^{-1}$) at 293 K.

It was elegantly demonstrated that the rate of water exchange at the Ln^{III} is dependent on the nature and composition of the isomers of a given complex [188,194]. The water exchange rate also depends on the extent of second sphere hydration which is determined by complex hydrophobicity and the nature of counter-anions [195,196].

9 CONCLUDING REMARKS

Studies of mechanism of action of metallodrugs provide not only the basis of drug design but also profound understanding of the biological processes. Biological systems are rarely at equilibria and it is crucial to understand both the kinetic and dynamic aspects of metallodrug–biomolecule interactions although thermodynamic study is equally important. It has become clear that the kinetics is crucial to all properties of platinum anticancer drugs (and other metallo-anticancer agents), from activation (ligand exchange) and DNA binding to even antitumor activities [7]. Trafficking of metal ions and metallodrugs in cells is probably via a ligand exchange process.

NMR spectroscopy is a very powerful technique for the study of interactions of metallodrugs with molecules of biological importance. The chemical shifts (and J -coupling constants) of some nuclei such as ^{195}Pt are sensitive to either the oxidation state or to the coordination sphere, and provide information on the binding site of the metallodrug–biomolecule complex. With the rapid development of NMR techniques and currently available high fields (e.g., $>17\text{ T}$), more information is expected to be obtainable from NMR experiments. The use of inverse detection of ^{13}C or ^{15}N (e.g. 2D/3D HSQC, HSQC-TOCSY, HSQC-NOESY) together with isotopically labeled metallodrugs or biomolecules, allows the kinetics and dynamics of metallodrug–biomolecule interactions to be readily followed at physiologically relevant concentrations without separation. The use of new NMR technology such as cyroprobe and new methods (TROSY) on a high-field NMR spectrometer significantly enhances the sensitivity of NMR. In combination with other techniques such as chromatography (LC-NMR and HPLC-NMR) should it offer a valuable tool for the investigation of the kinetics and dynamics of metallodrugs under physiologically relevant conditions [197].

10 ABBREVIATIONS

A, adenosine; 5'-AMP, adenosine 5'-monophosphate; AMD473, *cis*-[ammine-dichloro(2-methyl pyridine)] platinum(II); cAMP, cyclic adenosine monophosphate; BBR3464, $[[\textit{trans}\text{-PtCl}(\text{NH}_3)_2]_2\{\mu\text{-}\textit{trans}\text{-Pt}(\text{NH}_3)_2(\text{NH}_2(\text{CH}_2)_n\text{NH}_2)_2\}]^{4+}$; Ben, benzene; BEOV, bis(ethylmaltolato)oxovanadium(IV); Bip, biphenyl; bipy, bipyridine; BMOV, bis(maltolato) oxovanadium(IV);

C, cytidine; CBDCA, 1,1-dicarboxy-cyclobutane; cGMP, cyclic guanosine monophosphate; 5'-CMP, cytidine 5'-monophosphate; CSA, chemical shift anisotropy; Cym, *p*-cymene; DDP, *cis*-dichloro diammineplatinum (II); DEPT, distortionless enhancement by polarization transfer; DHA, dihydroanthracene; Diaz, diazinane; DIDS, 4,4'-diisothio-cyanantostilbene-2,2'-disulfonic acid; DNA, deoxyribonucleic acid; DOTA, 1,4,7,10-tetraazacyclododecane-1,4,7,10-tetraacetate; DTPA, diethylenetriamine-*N, N, N', N', N''*-pentaacetate; EHPG, *N, N'*-ethylenebis(*o*-hydroxyphenylglycine); en, ethylenediamine; ErS, ergothionine; EXSY, exchange spectroscopy; G, guanosine; 5'-GMP, guanosine 5'-monophosphate; GSH, glutathione; GDP, guanosine diphosphate; GTP, guanosine triphosphate; Met, methionine; HMQC, heteronuclear multiple quantum coherence; HPLC, high performance liquid chromatography; HSA, human serum albumin; HSQC, heteronuclear single quantum coherence; hTF, human transferrin; I, inosine; 5'-IMP, inosine 5'-monophosphate; Imt, imidazolidine-2-thione; INEPT, insensitive nuclei enhanced by polarization transfer; MRI, magnetic resonance imaging; *N*-acetyl-L-Cys, *N*-acetyl-L-cysteine; *N*-acetyl-L-Met, *N*-acetyl-L-methionine; NAMI-A, Na[*trans*-RuCl₄(Me₂SO)(Im)]; NOESY, nuclear overhauser enhancement spectroscopy; oxa, oxalate; phen, phenanthroline; pic, picolinate; RBCs, red blood cells; rHA, recombinant human albumin; RNA, ribonucleic acid; ROESY, rotating frame overhauser enhancement spectroscopy; Ru-Im, *trans*-imidazolium(bisimidazole) tetrachloro-ruthenate(III); Ru-Ind, *trans*-indazolium(bisindazole) tetrachloro-ruthenate(III); T, thymidine; THA, tetrahydroanthracene; 5'-TMP, thymidine 5'-monophosphate; TOCSY, total correlation spectroscopy; TROSY, transverse relaxation-optimized spectroscopy; Tu, thiourea; 5'-UMP, uridine 5'-monophosphate; UV, ultraviolet; VO(ka)₂, bis(kojato)oxovanadium(IV); VO(ma)₂, bis(maltolato)oxovanadium(IV).

11 ACKNOWLEDGEMENTS

We thank the generous support by the Hong Kong Research Grants Council (RGC, HKU7110/02P), NSFC/RGC, the Area of Excellence Scheme of the University Grants Committee (Hong Kong), Livzon Pharmaceutical Ltd and the University of Hong Kong. We acknowledge the use of the Protein Data Bank (<http://www.rcsb.org/pdb/>) and the Cambridge Structural Database (Cambridge, UK) for access to some of the structural data shown in this paper.

12 REFERENCES

1. (a) P. J. Sadler, *Adv. Inorg. Chem.* **36**, 1 (1991). (b) *Metallopharmaceuticals (Top. Biol. Inorg. Chem., Vols 1 and 2)*, edited by M. J. Clarke and P. J. Sadler, Springer, Heidelberg,

1999. (c) *Uses of Inorganic Chemistry in Medicine*, edited by N. P. Farrell, Royal Society of Chemistry, Cambridge, 1999. (d) *Metal Ions and Their Complexes in Medication and Metal Complexes in Tumor Diagnosis and as Anticancer Agents (Met. Ions Biol. Syst. Vols 41 and 42)*, edited by A. Sigel and H. Sigel, Marcel Dekker, New York, 2004, in press.
2. (a) Z. Guo and P. J. Sadler, *Angew. Chem. Int. Ed. Engl.* **38**, 1512 (1999). (b) Z. Guo and P. J. Sadler, *Adv. Inorg. Chem.* **49**, 183 (2000).
 3. *Medicinal Inorganic Chemistry*, special issue of *Chem. Rev.* **99**, 2201 (1999).
 4. (a) M. J. Abrams and B. A. Murrer, *Science* **261**, 725 (1993). (b) J. Reedijk, *Curr. Opin. Chem. Biol.* **3**, 236 (1999). (c) K. H. Thompson, and C. Orvig, *Science* **300**, 936 (2003).
 5. G. Q. Chen, X. G. Shi, W. Tang, S. M. Xiong, J. Zhu, X. Cai, Z. G. Han, J. H. Ni, G. Y. Shi, P. M. Jia, M. M. Liu, K. L. He, C. Niu, J. Ma, P. Zhang, T. D. Zhang, P. Paul, T. Naoe, K. Kitamura, W. Miller, S. Waxman, Z. Y. Wang, H. de The, S. J. Chen, and Z. Chen, *Blood* **89**, 3345 (1997).
 6. X. H. Zhu, Y. L. Shen, Y. K. Jing, X. Cai, P. M. Jia, Y. Huang, W. Tang, G. Y. Shi, Y. P. Sun, J. Dai, Z. Y. Wang, S. J. Chen, T. D. Zhang, S. Waxman, Z. Chen, and G. Q. Chen, *J. Natl. Cancer Inst.* **91**, 772 (1999).
 7. J. Reedijk, *Proc. Natl. Acad. Sci. USA* **100**, 3611 (2003).
 8. (a) S. J. Berners-Price and P. J. Sadler, *Coord. Chem. Rev.* **151**, 1 (1996). (b) Y. Chen, Z. J. Guo, P. J. Sadler, in *Cisplatin—Chemistry and Biochemistry of a Leading Anticancer Drug*, edited by B. Lippert, Wiley-VCH, Weinheim, 1999, p. 293. (c) S. O. Ana, Z. Kuklenyik, and L. G. Marzilli, in *Cisplatin – Chemistry and Biochemistry of a Leading Anticancer Drug*, edited by B. Lippert, Wiley-VCH, Weinheim, 1999, p. 247.
 9. (a) J. M. Aramini and H. J. Vogel, *Biochem. Cell. Biol.* **76**, 210 (1998). (b) M. W. Germann, J. M. Aramini, and H. J. Vogel, *J. Am. Chem. Soc.* **116**, 6971 (1994).
 10. H. Sun, in *Encyclopedia of Nuclear Magnetic Resonance: Advances in NMR*, Vol. 9, edited by D. M. Grant and R. K. Harris, John Wiley & Sons, Inc. New York 2002, p. 413.
 11. J. W. Cox, S. J. Berners-Price, M. S. Davies, Y. Qu, and N. Farrell, *J. Am. Chem. Soc.* **123**, 1316 (2001).
 12. T. Peleg-Shulman and D. Gibson, *J. Am. Chem. Soc.* **123**, 3171 (2001).
 13. J. Sandström, *Dynamic NMR Spectroscopy*, Academic Press, London, 1982.
 14. J. I. Kaplan and G. Fraenkel, *NMR of Chemically Exchanging Systems*, Academic Press, New York, 1980.
 15. K. G. Orrell, *Annu. Rep. NMR Spectroscosc.* **19**, 79 (1987).
 16. (a) B. D. Nageswara, in *Methods in Enzymology*, Vol. 176, edited by N. J. Oppenheimer and T. L. James, Academic Press, London, 1989, p. 279. (b) J. J. Led, H. Gesmar and F. Abildgaard, in *Methods in Enzymology*, Vol. 176, edited by N. J. Oppenheimer and T. L. James, Academic Press, London, 1989, p. 311.
 17. H. M. McConnell, *J. Chem. Phys.* **28**, 430 (1958).
 18. E. R. Johnston, *Concepts Magn. Reson.* **7**, 219 (1995).
 19. (a) <http://www.exetersoftware.com/cat/gnmr.html>. (b) <http://www.chemistry.mcmaster.ca/~bain/mexmanc.html>.
 20. M. Pons and O. Millet, *Prog. Nucl. Mag. Reson. Spectrosc.* **38**, 267 (2001).
 21. (a) S. Forsén and R. A. Hoffmann, *J. Chem. Phys.* **39**, 2892 (1963). (b) S. Forsén and R. A. Hoffmann, *J. Chem. Phys.* **40**, 1189 (1964).
 22. R. L. Vold, J. S. Waugh, M. P. Klein, and D. E. Phelps, *J. Chem. Phys.* **48**, 3831 (1968).
 23. S. Wolfram, *Mathematica. A System for Doing Mathematics by Computer*, Addison-Wesley, Redwood City, 1991.

24. E. W. Abel, T. P. J. Coston, K.G. Orrell, V. Sik, and D. Stephenson, *J. Magn. Reson.* **70**, 34 (1986).
25. R. R. Ernst, G. Bodenhausen, and A. Wokaun, *Principles of Nuclear Magnetic Resonance in One and Two Dimensions*, Oxford University Press, New York, 1987.
26. V. Jacques and J. F. Desreux, *Inorg. Chem.* **33**, 4048 (1994).
27. H. Kessler, S. Mronga, and G. Gemmecker, *J. Magn. Reson.* **29**, 527 (1991).
28. B. Rosenberg, L. Van Camp, and T. Krigas, *Nature* **205**, 698 (1965).
29. F. Raynaud, F. E. Boxall, and L. R. Kelland, *Clin. Cancer Res.* **3**, 2063 (1997).
30. C. M. Giandomenico, M. J. Abrams, B. A. Murrer, J. T. Vollano, and M. T. Rheinheimer, *Inorg. Chem.* **34**, 1015 (1995).
31. M. Galanski and B. K. Keppler, *Inorg. Chem.* **35**, 1709 (1996).
32. E. Wong and C. M. Giandomenico, *Chem. Rev.* **99**, 2451 (1999).
33. H. M. Pinto and J. H. Schornagel, in *Platinum and Other Coordination Compounds in Cancer Chemotherapy*, Plenum, New York, 1996.
34. L. Randaccio and E. Zangrando, in *Cisplatin—Chemistry and Biochemistry of a Leading Anticancer Drug*, edited by B. Lippert, Wiley-VCH, Weinheim, 1999, p. 379.
35. T. W. Hambely, *Coord. Chem. Rev.* **166**, 181 (1997).
36. E. R. Jamieson and S. J. Lippard, *Chem. Rev.* **99**, 2467 (1999).
37. D. Lebwohl and R. Canetta, *Eur. J. Cancer* **34**, 1522 (1998).
38. J. Reedijk, *Chem. Rev.* **99**, 2499 (1999).
39. A. Zakovska, O. Novakova, Z. Balcarona, U. Blerbach, N. V. Farrell, and V. Brabec, *Eur. J. Biochem.* **254**, 547 (1998).
40. B. Lippert, *BioMetals* **15**, 195 (1992).
41. L. G. Marzilli, J. S. Saad, Z. Kuklenyik, K. A. Keating, and Y. Xu, *J. Am. Chem. Soc.* **123**, 2764 (2001).
42. B. P. Espósito and R. Najjar, *Coord. Chem. Rev.* **232**, 137 (2002).
43. A. A. Tulub and V. E. Stefanov, *Int. J. Biol. Macromol.* **28**, 191 (2001).
44. P. S. Pregosin, *Annu. Rep. NMR Spectrosc.* **17**, 285 (1986).
45. R. E. Norman, J. D. Ranford, and P. J. Sadler, *Inorg. Chem.* **31**, 877 (1992).
46. D. P. Bancroft, C. A. Lepre, and S. J. Lippard, *J. Am. Chem. Soc.* **112**, 6860 (1990).
47. S. J. Berners-Price, T. A. Frenkiel, U. Frey, J. D. Ranford, and P. J. Sadler, *Chem. Commun.* 789 (1992).
48. M. S. Davies, S. J. Berners-Price, and T. W. Hambley, *Inorg. Chem.* **39**, 5603 (2000).
49. K. J. Barnham, S. J. Berners-Price, U. Frey, T. A. Frenkiel, and P. J. Sadler, *Angew. Chem. Int. Ed. Engl.* **34**, 1874 (1995).
50. S. J. Berners-Price, K. J. Barnham, U. Frey, and P. J. Sadler, *Chem. Eur. J.* **2**, 1283 (1996).
51. M. S. Davies, S. J. Berners-Price, and T. W. Hambley, *J. Am. Chem. Soc.* **120**, 11380 (1998).
52. M. S. Davies, S. J. Berners-Price, and T. W. Hambley, *J. Inorg. Biochem.* **79**, 167 (2000).
53. A. I. Ivanov, J. Christodoulou, J. A. Parkinson, K. J. Barnham, A. Tucker, J. Woodrow, and P. J. Sadler, *J. Biol. Chem.* **273**, 14721 (1998).
54. J. Reedijk, *Inorg. Chim. Acta* **198–200**, 873 (1992).
55. A. Eastman, *Pharmacol. Ther.* **34**, 155 (1987).
56. S. E. Sherman and S. J. Lippard, *Chem. Rev.* **87**, 1153 (1987).
57. Y. Chen, Z. Guo, S. Parsons, and P. J. Sadler, *Chem. Eur. J.* **4**, 672 (1998).
58. P. M. Calvert, M. S. Highley, A. N. Hughes, E. R. Plummer, A. S. T. Azzabi, M. W. Verrill, M. G. Camboni, E. Verdi, A. Bernareggi, M. Zucchetti, A. M. Robinson, J. Carmichael, and A. H. Calvert, *Clin. Cancer Res.* **5**, 3796 (1999).
59. G. Pratesi, P. Perego, D. Polizzi, S. C. Righetti, R. Supino, C. Caserini, C. Manzotti, F. C. Giuliani, G. Pezzoni, S. Tognella, S. Spinelli, N. Farrell, and F. Zunino, *Br. J. Cancer* **80**, 1912 (1999).

60. P. Perego, C. Caserini, L. Gatti, N. Carenini, S. Romanelli, R. Supino, D. Colangelo, I. Viano, R. Leone, S. Spinelli, G. Pezzoni, C. Manzotti, N. Farrell, and F. Zunino, *Mol. Pharmacol.* **55**, 528 (1999).
61. Y. Qu, N. J. Scarsdale, M.-C. Tran, and N. P. Farrell, *J. Biol. Inorg. Chem.* **8**, 19 (2003).
62. M. S. Davies, J. W. Cox, S. J. Berners-Price, W. Barklage, Y. Qu, and N. Farrell, *Inorg. Chem.* **39**, 1710 (2000).
63. K. Hindmarsh, D. A. House, and M. M. Turnbull, *Inorg. Chim. Acta* **257**, 11 (1997).
64. M. S. Davies, D. S. Thomas, A. Hegmans, S. J. Berners-Price, and N. Farrell, *Inorg. Chem.* **41**, 1101 (2002).
65. M. C. Lim and R. B. Martin, *J. Inorg. Nucl. Chem.* **38**, 1191 (1976).
66. F. Legrendre, J.-C. Chottard, in *Kinetics and Selectivity of DNA-Platination*, edited by B. Lippert, Wiley-VCH, Zürich, 1999, p. 223.
67. P. A. Andrews and M. Jennerwein, *Drug Metab. Dispos.* **23**, 178 (1995).
68. S. Neidle, *Chem. Br.* **4**, 27 (2000).
69. S. J. Berners-Price, T. A. Frenkiel, J. D. Ranford, and P. J. Sadler, *J. Chem. Soc. Dalton Trans.* 2137 (1992).
70. F. Reeder, Z. Guo, P. del S. Murdoch, A. Corazza, T. W. Hambley, S. J. Berners-Price, J.-C. Chottard, and P. J. Sadler, *Eur. J. Biochem.* **249**, 370 (1997).
71. S. R. Rajsiki and R. M. Williams, *Chem. Rev.* **98**, 2723 (1998).
72. S. J. Berners-Price, M. S. Davies, J. W. Cox, D. S. Thomas, and N. Farrell, *Chem. Eur. J.* **9**, 713 (2003).
73. S. V. Pizzo, M. W. Swaim, P. A. Roche, and S. L. Gonias, *J. Inorg. Biochem.* **33**, 67 (1988).
74. M. El-Khateeb, T. G. Appleton, L. R. Gahan, B. G. Charles, S. J. Berners-Price, and A. Bolton, *J. Inorg. Biochem.* **77**, 13 (1999).
75. A. A. Tulub and V. E. Stefanov, *Int. J. Biol. Macromol.* **28**, 191 (2001).
76. K. J. Barnham, M. I. Djuran, P. del S. Murdoch, J. D. Ranford, and P. J. Sadler, *Inorg. Chem.* **35**, 1065 (1996).
77. K. J. Barnham, U. Frey, P. del S. Murdoch, J. D. Ranford, and P. J. Sadler, *J. Am. Chem. Soc.* **116**, 11175 (1994).
78. S. S. G. E. van Boom and J. Reedijk, *J. Chem. Soc., Chem. Commun.* 1397 (1993).
79. K. J. Barnham, M. I. Djuran, P. del S. Murdoch, and P. J. Sadler, *J. Chem. Soc., Chem. Commun.* 721 (1994).
80. J. M. Teuben, S. S. G. E. van Boom, and J. Reedijk, *J. Chem. Soc. Dalton Trans.* 3979 (1997).
81. Z. Guo, T. W. Hambley, P. del S. Murdoch, and P. J. Sadler, *J. Chem. Soc. Dalton Trans.* 469 (1997).
82. K. J. Barnham, M. I. Djuran, P. del S. Murdoch, J. D. Ranford, and P. J. Sadler, *J. Chem. Soc. Dalton Trans.* 3721 (1997).
83. L. Milgrom and S. MacRobert, *Chem. Br.* **34**, 45 (1998).
84. N. A. Kratochwil, M. Zabel, K.-J. Range, and P. J. Bednarski, *J. Med. Chem.* **39**, 2499 (1996).
85. N. A. Kratochwil, J. A. Parkinson, P. J. Bednarski, and P. J. Sadler, *Angew. Chem. Int. Ed. Engl.* **38**, 1460 (1999).
86. P. Müller, B. Schröder, J. A. Parkinson, N. C. Kratochwil, R. A. Coxall, A. Parkin, S. Parsons, and P. J. Sadler, *Angew. Chem. Int. Ed. Engl.* **42**, 335 (2003).
87. P. Köpf-Maier and H. Köpf, *Chem. Rev.* **87**, 1137 (1987).
88. P. Köpf-Maier and H. Köpf, in *Metal Compounds in Cancer Therapy*, edited by S. P. Fricker, Chapman & Hall, London, 1994, p. 109.
89. B. K. Keppler, C. Friesen, H. Vongerichten, and E. Vogel, in *Metal Complexes in Cancer Chemotherapy*, edited by B. K. Keppler, VCH, Weinheim, 1993, p. 297.

90. C. V. Christodoulou, A. G. Eliopoulos, L. S. Young, L. Hodgkins, D. R. Ferry, and D. J. Kerr, *Br. J. Cancer* **77**, 2088 (1998).
91. P. Köpf-Maier, *J. Struct. Biol.* **105**, 35 (1990).
92. P. Köpf-Maier and R. Martin, *Virch. Arch. B Cell Pathol.* **57**, 213 (1989).
93. H. Sun, H. Li, R. Weir, and P. J. Sadler, *Angew. Chem. Int. Ed. Engl.* **37**, 1577 (1998).
94. L. Messori, P. Orioli, V. Banholzer, I. Pais, and P. Zatta, *FEBS Lett.* **442**, 157 (1999).
95. E. Wagner, D. Curiel, and M. Cotton, *Adv. Drug. Delivery Rev.* **14**, 113 (1994).
96. Z. M. Qian, H. Li, H. Sun, and K. Ho, *Pharmacol. Rev.* **54**, 561 (2002).
97. M. Guo, H. Sun, H. J. McArdle, L. Gambling, and P. J. Sadler, *Biochemistry* **39**, 10023 (2000).
98. H. Sun, M. C. Cox, H. Li, and P. J. Sadler, *Struct. Bonding* **88**, 71 (1997).
99. P. Yang and M. Guo, *Coord. Chem. Rev.* **186**, 189 (1999).
100. J. H. Toney and T. J. Marks, *J. Am. Chem. Soc.* **107**, 947 (1985).
101. M. Guo, H. Sun, S. Bihari, J. A. Parkinson, R. O. Gould, S. Parsons, and P. J. Sadler, *Inorg. Chem.* **39**, 206 (2000).
102. J. H. Murray and M. M. Harding, *J. Med. Chem.* **37**, 1936 (1994).
103. M. Guo, Z. Guo, and P. J. Sadler, *J. Biol. Inorg. Chem.* **6**, 698 (2001).
104. M. J. Clarke, F. Zhu, and D. R. Frasca, *Chem. Rev.* **99**, 2511 (1999).
105. C. S. Allardyce and P. J. Dyson, *Platinum Met. Rev.* **45**, 62 (2001).
106. F. Kratz, M. Hartmann, B. Keppler, and L. Messori, *J. Biol. Chem.* **269**, 2581 (1994).
107. F. Wang, H. Chen, J. A. Parkinson, P. del S. Murdoch, and P. J. Sadler, *Inorg. Chem.* **41**, 4509 (2002).
108. R. E. Aird, J. Cummings, A. A. Ritchie, M. Muir, R. E. Morris, H. Chen, P. J. Sadler, and D. I. Jodrell, *Br. J. Cancer* **86**, 1652 (2002).
109. H. Chen, J. A. Parkinson, R. E. Morris, and P. J. Sadler, *J. Am. Chem. Soc.* **125**, 173 (2003).
110. H. Chen, J. A. Parkinson, S. Parsons, R. A. Coxall, R. O. Gould, and P. J. Sadler, *J. Am. Chem. Soc.* **124**, 3064 (2002).
111. C. F. Shaw III, *Chem. Rev.* **99**, 2589 (1999).
112. S. L. Best and P. J. Sadler, *Gold Bull.* **29**, 87 (1996).
113. J. Zou, P. Taylor, J. Dornan, S. P. Robinson, M. D. Walkinshaw, and P. J. Sadler, *Angew. Chem. Int. Ed. Engl.* **39**, 2931 (2000).
114. A. P. Intoccia, T. L. Flanagan, D. T. Walz, L. Gutzait, J. E. Swagdis, J. Flagiello, B. Y-H Hwang, R. H. Dewey and H. J. Noguchi, *Rheumatol.* **9**, 90 (1982).
115. A. A. Isab, A. L. Hormann, M. T. Coffler, and C. F. Shaw III, *J. Am. Chem. Soc.* **110**, 3278 (1988).
116. J. R. Roberts, J. Xiao, B. Schliesman, D. J. Parsons, and C. F. Shaw III, *Inorg. Chem.* **35**, 424 (1996).
117. A. A. Isab and S. Ahmad, *J. Inorg. Biochem.* **88**, 53 (2002).
118. S. Ahmad and A. A. Isab, *J. Inorg. Biochem.* **88**, 44 (2002).
119. J. C. Christodoulou, P. J. Sadler, and A. Tucker, *FEBS Lett.* **376**, 1 (1995).
120. C. F. Shaw III, A. A. Isab, J. D. Hoeschele, M. Starich, J. Locke, P. Schulteis, and J. Xiao, *J. Am. Chem. Soc.* **116**, 2254 (1994).
121. O. M. N. Dhubhghail, P. J. Sadler, and A. Tucker, *J. Am. Chem. Soc.* **114**, 111 (1992).
122. J. C. Christodoulou, P. J. Sadler, and A. Tucker, *Eur. J. Biochem.* **225**, 363 (1994).
123. C. F. Shaw III, *Comments Inorg. Chem.* **8**, 233 (1989).
124. R. C. Elder, Z. Zhao, Y. Zhang, J. G. Dorsey, E. V. Hess, and K. Tepperman, *J. Rheumatol.* **20**, 268 (1993).
125. G. G. Graham and M. M. Dale, *Biochem. Pharmacol.* **39**, 1697 (1990).
126. R. Rudkowski, G. G. Graham, G. D. Champion, and J. B. Ziegler, *Biochem. Pharmacol.* **39**, 1687 (1990).
127. G. G. Graham, G. D. Champion, and J. B. Ziegler, *Met. Based Drugs* **1**, 395 (1994).

128. G. G. Graham, J. R. Bales, M. C. Grootveld, and P. J. Sadler, *J. Inorg. Biochem.* **25**, 163 (1985).
129. G. Lewis, and C. F. Shaw III, *Inorg. Chem.* **25**, 58 (1986).
130. M. N. Akhtar, I. H. Gazi, A. A. Isab, A. R. Al-Arfaj, M. I. N. Wazzer, and M. S. Hussain, *J. Coord. Chem.* **36**, 149 (1995).
131. A. A. Isab, I. H. Gazi, and A. R. Al-Arfaj, *J. Chem. Soc. Dalton Trans.* 841 (1993).
132. G. G. Briand and N. Burford, *Chem. Rev.* **99**, 2601 (1999).
133. (a) H. Sun, L. Zhang, and K. Y. Szeto, *Met. Ions Biol. Syst.*, **41**, 333 (2004). (b) H. Sun and P. J. Sadler, *Top. Biol. Inorg. Chem.* **2**, 159 (1999).
134. Z. X. Shen, G. Q. Chen, J. H. Ni, X. S. Li, S. M. Xiong, Q. Y. Qiu, J. Zhu, W. Tang, G. L. Sun, K. Q. Yang, Y. Chen, L. Zhou, Z. W. Fang, Y. T. Wang, J. Ma, P. Zhang, T. D. Zhang, S. J. Chen, Z. Chen, and Z. Y. Wang, *Blood* **89**, 3354 (1997).
135. S. J. Soignet, P. Maslak, Z. G. Wang, S. Jhanwar, E. Calleja, L. J. Dardashti, D. Corso, A. De Blasio, J. Gabrilove, D. A. Scheinberg, P. P. Pandolfi, and R. P. Warrell, *New Engl. J. Med.* **339**, 1341 (1998).
136. P. J. Sadler and H. Sun, *J. Chem. Soc. Dalton Trans.*, 1395 (1995).
137. E. Asato, K. Katsura, M. Mikuriya, T. Fujii, and J. Reedijk, *Inorg. Chem.* **32**, 5322 (1993).
138. J. A. Parkinson, H. Sun, and P. J. Sadler, *Chem. Commun.* 881 (1998).
139. P. J. Barrie, M. I. Djuran, M. A. Mazid, M. McPartlin, P. J. Sadler, I. J. Scowen, and H. Sun, *J. Chem. Soc. Dalton Trans.* 2417 (1996).
140. W. Li, L. Jin, N. Zhu, X. Hou, F. Deng, and H. Sun, *J. Am. Chem. Soc.*, **125**, 12408–12409 (2003).
141. P. J. Sadler, H. Sun, and H. Li, *Chem. Eur. J.* **2**, 701 (1996).
142. H. Sun, S.-C. Yan, and W.-S. Cheng, *Eur. J. Biochem.* **267**, 545 (2000).
143. S.-C. Yan, K. Ding, L. Zhang, and H. Sun, *Angew. Chem. Int. Ed.* **39**, 4260 (2000).
144. T. Zhou, S. Radaev, B. P. Rosen, and D. L. Gatti, *EMBO J.* **19**, 4838 (2000).
145. S.-C. Yan, F. Li, K. Ding, and H. Sun, *J. Biol. Inorg. Chem.* **8**, 689–697 (2003).
146. (a) A. Naganuma, M. Satoh, and N. Imura, *Cancer Res.* **47**, 983 (1987). (b) M. Satoh, A. Naganuma, and N. Imura, *Toxicology* **53**, 231 (1988).
147. H. Sun, H. Li, and P. J. Sadler, *J. Biol. Chem.* **274**, 29094 (1999).
148. H. Li, P. J. Sadler, and H. Sun, *J. Biol. Chem.* **271**, 9483 (1996).
149. H. Sun, H. Li, A. B. Mason, R. C. Woodworth, and P. J. Sadler, *Biochem. J.* **337**, 105 (1999).
150. H. Sun, M. C. Cox, H. Li, A. B. Mason, R. C. Woodworth, and P. J. Sadler, *FEBS Lett.* **422**, 315 (1998).
151. H. Sun, H. Li, A. B. Mason, R. C. Woodworth, and P. J. Sadler, *J. Biol. Chem.* **276**, 8829 (2001).
152. H. Sun and K. Y. Szeto, *J. Inorg. Biochem.* **94**, 114 (2003).
153. L. C. Y. Woo, V. G. Yuen, K. H. Thompson, J. H. McNeill, and C. Orvig, *J. Inorg. Biochem.* **76**, 251 (1999).
154. Y. Shechter, I. Goldwasser, M. Mironchik, M. Fridkin, and D. Gefel, *Coord. Chem. Rev.* **237**, 3 (2003).
155. B. Zhang, G. Salituro, D. Szalkowski, Z. Li, Y. Zhang, I. Royo, D. Vilella, M. T. Diez, F. Pelaez, C. Ruby, R. L. Kendall, X. Mao, P. Griffin, J. Calaycay, J. R. Zierath, J. V. Heck, R. G. Smith, and D. E. Moller, *Science* **284**, 974 (1999).
156. E. I. Tolman, E. Barris, M. Burns, A. Pansini, and R. Partridge, *Life Sci.* **25**, 1159 (1979).
157. Y. Shechter and S. J. D. Karlish, *Nature* **284**, 556 (1980).
158. G. R. Dubyak and A. Kleinzeller, *J. Biol. Chem.* **255**, 5306 (1980).
159. H. Yasui, A. Tamura, T. Takino, and H. Sakurai, *J. Inorg. Biochem.* **91**, 327 (2002).
160. K. H. Thompson, J. H. McNeill, and C. Orvig, *Chem. Rev.* **99**, 2561 (1999).

161. K. H. Thompson and C. Orvig, *Coord. Chem. Rev.* **219–221**, 1033 (2001).
162. E. Tsiani and I. G. Fantus, *Trends Endocrinol. Metab.* **8**, 51 (1997).
163. C. E. Heyliger, A. G. Tahiliani, and J. H. McNeill, *Science* **227**, 1474 (1985).
164. S. A. Dikanov, B. D. Liboiron, and C. Orvig, *J. Am. Chem. Soc.* **124**, 2969 (2002).
165. A. S. Tracey, *Coord. Chem. Rev.* **237**, 113 (2003).
166. E. Heath and O. W. Howarth, *J. Chem. Soc. Dalton Trans.* 1105 (1981).
167. D. C. Crans, C. D. Rithner, and L. A. Theisen, *J. Am. Chem. Soc.* **112**, 2901 (1990).
168. M. Garner, J. Reglinski, W. E. Smith, J. McMurray, I. Abdullah, and R. Wilson, *J. Biol. Inorg. Chem.* **2**, 235 (1997).
169. P. Caravan, L. Gelmini, N. Glover, F. G. Herring, H. Li, J. H. McNeill, S. J. Rettig, I. A. Setyawati, E. Shuter, Y. Sun, A. S. Tracey, V. G. Yuen, and C. Orvig, *J. Am. Chem. Soc.* **117**, 12759 (1995).
170. V. G. Yuen, P. Caravan, L. Gelmini, N. Glover, J. H. McNeill, I. A. Setyawati, Y. Zhou, and C. Orvig, *J. Inorg. Biochem.* **68**, 109 (1997).
171. A. Shaver, J. B. Ng, D. A. Hall, B. S. Lum, and B. I. Posner, *Inorg. Chem.* **32**, 3109 (1993).
172. A. Shaver, J. B. Ng, D. A. Hall, and B. I. Posner, *Mol. Cell Biochem.* **153**, 5 (1995).
173. F. P. Ballistreri, E. G. M. Barbuzzi, G. A. Tomaselli, and R. M. Toscano, *J. Inorg. Biochem.* **80**, 173 (2000).
174. L. Frullano, J. Rohovec, J. A. Peters, and C. F. G. C. Geraldes, *Top. Curr. Chem.* **221**, 25 (2002).
175. J. A. Peters, E. Zitha-Bovens, D. M. Corsi, and C. F. G. C. Geraldes, in *The Chemistry of Contrast Agents in Medical Magnetic Resonance Imaging*, edited by A. E. Merbach and É. Tóth, John Wiley & Sons, Ltd, Chichester, 2001, p. 315.
176. B. G. Jenkins and R. B. Lauffer, *J. Magn. Reson.* **80**, 328 (1988).
177. B. G. Jenkins and R. B. Lauffer, *Inorg. Chem.* **27**, 4730 (1988).
178. J. A. Peters, *Inorg. Chem.* **27**, 4686 (1988).
179. C. F. G. C. Geraldes, A. M. Urbano, M. A. Hoefnagel, and J. A. Peters, *Inorg. Chem.* **32**, 2426 (1993).
180. H. Lammers, F. Maton, D. Pubanz, M. W. van Laren, H. van Bekkum, A. E. Merbach, R. N. Muller, and J. A. Peters, *Inorg. Chem.* **36**, 2527 (1997).
181. E. N. Rizkalla, G. R. Choppin, and W. Cacheris, *Inorg. Chem.* **32**, 582 (1993).
182. E. Bovens, M. A. Hoefnagel, E. Boers, H. Lammers, H. van Bekkum, and J. A. Peters, *Inorg. Chem.* **35**, 7679 (1996).
183. D. H. White, L. A. de Learie, T. J. Dunn, E. N. Rizkalla, H. Imura, and G. R. Choppin, *Invest. Radiol.* **26**, S229 (1991).
184. S. Aime, F. Benetollo, G. Bombieri, S. Colla, M. Fasano, and S. Paoletti, *Inorg. Chim. Acta* **254**, 63 (1997).
185. C. Petre, Y. C. Ni, G. Marchal, J. Yu, M. Wevers, R. B. Lauffer, and A. L. Baert, *Magn. Reson. Med.* **35**, 532 (1996).
186. F. Uggeri, A. Aime, P. L. Anelli, M. Botta, M. Brocchitta, C. de Haen, G. Ermindi, M. Grandi, and P. Paoli, *Inorg. Chem.* **34**, 633 (1995).
187. C. C. Bryden, C. C. Reilley, and J. F. Desreux, *Anal. Chem.* **53**, 1418 (1981).
188. S. Aime, A. Barge, D. Parker, and A. S. de Sousa, *Angew. Chem. Int. Ed. Engl.* **37**, 2673 (1998).
189. F. A. Dunand, S. Aime, and A. E. Merbach, *J. Am. Chem. Soc.* **122**, 1506 (2000).
190. M. Woods, A. Aime, M. Botta, J. A. K. Howard, J. M. Moloney, M. Navet, D. Parker, M. Port, and O. Rousseaux, *J. Am. Chem. Soc.* **122**, 9781 (2000).
191. K. Kumar, C. A. Chang, L. C. Francesconi, D. D. Dischino, M. F. Malley, J. Z. Gougoutas, and M. F. Tweedle, *Inorg. Chem.* **33**, 3567 (1994).
192. J. Platzek, P. Blaszkiewicz, H. Gries, P. Luger, G. Michl, A. Müller-Fahrnow, B. Radüchel, and D. Sülzle, *Inorg. Chem.* **36**, 6086 (1997).

193. R. B. Shukla, *J. Magn. Reson. Ser. A* **113**, 196 (1995).
194. S. Aime, A. Barge, J. I. Bruce, M. Botta, J. A. K. Howard, J. M. Moloney, D. Parker, A. S. de Sousa, and M. Woods, *J. Am. Chem. Soc.* **121**, 5762 (1999).
195. S. Aime, A. Barge, A. S. Batsanov, M. Botta, D. D. Castelli, F. Fedeli, A. Mortillaro, D. Parker, and H. Puschmann, *Chem. Commun.* 1120 (2002).
196. A. Barge, M. Botta, D. Parker, and H. Puschmann, *Chem. Commun.* 1386 (2003).
197. J. C. Lindon, J. K. Nicholson, and I. D. Wilson, *J. Chromatogr. B* **748**, 233 (2000).

6 Dynamics by EPR: Picosecond to Microsecond Time Scales

SABINE VAN DOORSLAER

*SIBAC Laboratorium Universiteit Antwerpen – Dept. Natuurkunde,
Universiteitsplein 1, 2610 Wilrijk, Belgium*

and

GUNNAR JESCHKE

*Max Planck Institute for Polymer Research, Postfach 3148, 55021 Mainz,
Germany*

1 INTRODUCTION

Electron paramagnetic resonance (EPR) spectroscopy [1,2] is the most versatile technique for characterizing structure and dynamics of paramagnetic systems and can also be applied to macromolecular or supramolecular diamagnetic systems by using spin probes or spin labels [3–6]. For materials that can be crystallized, EPR spectroscopy provides detailed information on symmetry and distribution of the singly occupied molecular orbital and hence on electronic structure. Furthermore, it can be used to detect and characterize dynamic processes, such as Jahn–Teller dynamics or methyl group rotation, that are averaged on the time scale of X-ray crystallography. Being a local method, EPR spectroscopy can be applied as well to systems that lack long range order, such as glasses and frozen solutions, and in many cases also to liquid solutions. For such disordered systems EPR spectroscopy compares favorably to any competing techniques for determining the geometric structure of paramagnetic systems. On length scales between 1 nm and 10 nm, EPR spectroscopy is also competitive for structural characterization of bulk diamagnetic materials, since few alternative techniques exist, and these techniques either also depend on labeling (fluorescence energy transfer), or are less sensitive and selective (neutron scattering) [7]. On time scales between 10 ps and a few microseconds, simple, fast and highly sensitive continuous-wave (CW)

EPR experiments reveal details about dynamic processes such as reorientation of the whole molecule or of side groups. As energies involved in EPR transitions are much smaller than bond energies and energies of electronic excitation, experiments do not induce any changes in the investigated material, except for the occasional need to perform certain measurements at low temperatures.

Not all the information can be obtained by the basic CW experiment that is considered by many chemists as all there is to EPR. Elucidating geometric structure or small spin densities requires the separation of small hyperfine couplings or dipole–dipole couplings between electron spins from larger interactions. This can be achieved by double resonance experiments, such as electron nuclear double resonance (ENDOR) [8,9] and electron electron double resonance (ELDOR) spectroscopy and further pulse-EPR techniques [10] such as electron spin echo envelope modulation (ESEEM). Pulse-EPR techniques may also provide more information on dynamic processes than simple CW experiments and may access longer time scales.

Standard EPR and ENDOR spectrometers operate at a microwave frequency of about 9 GHz (X-band), although spectrometers working at lower (e.g. S-band, 3–5 GHz) and higher microwave frequencies (Q-band, 35 GHz; W-band, 95 GHz) are often used. Recently, spectrometers operating at even higher frequencies (180 GHz and above) have been developed. Higher microwave frequencies usually lead to enhanced resolution and sensitivity, but imply higher magnetic fields, more sophisticated electronics and pseudo-optical components.

Here we want to give a broad overview of the opportunities that EPR spectroscopy offers for studies on organometallic systems and coordination compounds. We do not restrict ourselves to those techniques that have already been applied to such systems in the past, but also discuss approaches that have proved to be useful in other contexts and could be adapted to problems in organometallic chemistry. The chapter is organized as follows. In Section 2, we discuss which systems are accessible to EPR spectroscopy. The basic knowledge on spin interactions and on spin relaxation is presented in Section 3 to an extent that should be sufficient to estimate whether a given problem can be tackled by EPR methods. This section also provides basic knowledge on the selection of techniques, on required concentrations of paramagnetic species and amounts of sample. Approaches for the characterization of dynamic processes are discussed in some more depth in Section 4, which also points to selected literature on their application. Finally, Section 5 is intended to illustrate how several techniques are combined to obtain insight into a more complex problem. We discuss this on the example of binding of nitric oxide to iron porphyrin complexes [11,12], which is a biologically important process but which may also be of interest in the context of biomimetic catalysis.

2 SCOPE OF EPR SPECTROSCOPY

2.1 NATIVE PARAMAGNETIC CENTERS

EPR spectroscopy is based on excitation of electron-spin transitions by electromagnetic radiation. For such transitions to exist, the total electron spin quantum number S of a many-electron system has to be larger than zero (paramagnetic system). This is always the case for systems with an odd number of electrons, for which $S = \frac{1}{2}$ in the low-spin case and $S > \frac{1}{2}$ in the high-spin case or, in some systems, in intermediate spin cases. Many transition metals have stable oxidation states with an odd number of electrons (Kramers systems), for example Ti^{III} , V^{IV} , Mo^{V} ($3d^1$, $S = \frac{1}{2}$), Cr^{III} ($3d^3$, $S = \frac{3}{2}$), Mn^{II} ($3d^5$, $S = \frac{5}{2}$), Fe^{III} ($3d^5$, low spin: $S = \frac{1}{2}$, intermediate spin: $S = \frac{3}{2}$, high spin: $S = \frac{5}{2}$), Co^{II} ($3d^7$, low spin: $S = \frac{1}{2}$, high spin: $S = \frac{3}{2}$), Cu^{II} ($3d^9$, $S = \frac{1}{2}$). For transition metal ions in the absence of any coordination, high-spin states are expected according to Hund's rule. The ligand field introduces a splitting of the originally degenerate d orbitals, and when this splitting exceeds the electron-pairing energy, low-spin states are attained. The energy difference between low-spin and high-spin states may be of the same order of magnitude as thermal energies, so that both states may be populated. EPR experiments on species with $S = \frac{1}{2}$ often result in a larger amount of information and a more reliable interpretation of the spectra than experiments on high-spin species, since the zero-field splitting present for the latter species complicates spectral analysis and often causes faster relaxation that prevents the application of more sophisticated experiments or requires measurements at very low temperatures (< 5 K).

Non-Kramers systems with an even number of electrons have low-spin states with $S = 0$ that are inaccessible to EPR spectroscopy, but may have high-spin states with integer $S > 0$ that can be investigated by EPR under certain circumstances. Important examples are Mn^{III} ($3d^4$, $S = 2$), Fe^{II} ($3d^6$, $S = 2$), and Ni^{II} ($3d^8$, $S = 1$). Such species are often termed 'EPR-silent' as no signals are observable with conventional spectrometers with a frequency of approximately 9.6 GHz in the field range between 0 and 1 T. Whether or not transitions can be detected depends on the magnitude of the zero-field splitting compared to the electron-Zeeman splitting and to the energy of the microwave quanta. Non-Kramers systems can thus be studied by EPR when the zero-field splitting at least in one direction is small (cubic or axial symmetry) or when large fields and/or microwave frequencies are available (high field/high frequency EPR) [13,14].

For rare-earth metal ions, the situation is characterized by strong coupling of spin and orbital angular momentum of the electrons. In a number of cases, such as Ce^{3+} ($4f^1$), Nd^{3+} ($4f^3$), Dy^{3+} ($4f^9$), and Er^{3+} ($4f^{11}$), ground-state doublets of spin states arise when a crystal field removes other degeneracies. The ground-state doublet exhibits a splitting that is proportional to the magnetic

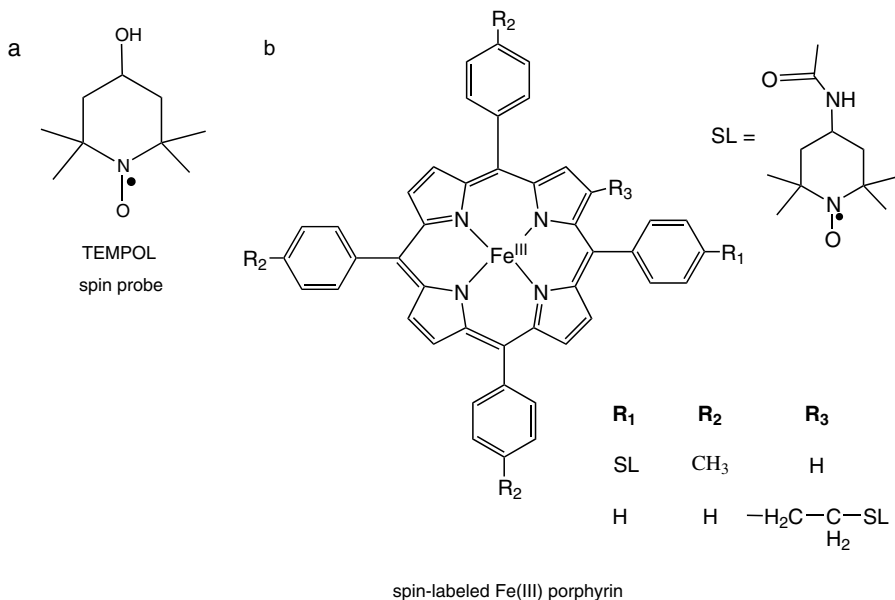


Figure 6.1 (a) Example of a commonly used spin probe: 4-hydroxy-2,2,6,6-tetramethyl piperidiny-1-oxy (TEMPOL). (b) Example of spin-labeled Fe(III) tetraphenylporphyrin (TPP) complexes (see also Section 5).

field and can thus be considered as a Kramers doublet with an effective spin $S = \frac{1}{2}$.

If the metal has zero total electron spin, a complex is EPR active only if one of the ligands has an odd number of electrons, important examples being NO (see Section 5), NO₂ [15], and semiquinone radicals [16].

2.2 SPIN LABELS AND SPIN PROBES

Much research in the field of EPR is currently devoted to the structure, dynamics, and function of *diamagnetic* systems. In such studies EPR is used as a probe technique by employing stable free radicals, usually nitroxide radicals, or paramagnetic transition metal ions that can substitute for diamagnetic metal ions without disturbing the structure [3–6]. If the radical is attached by covalent bonds to a specific site it is called a spin label; if it is just mixed into the system, it is called a spin probe. Figure 6.1 shows an example of a spin probe and of a spin-labeled metal complex. Spin probes are particularly useful when they mimic an integral component of a supramolecular system, such as a surfactant or lipid molecule, or if they attach themselves to specific sites by noncovalent interactions such as hydrogen bonding [17] or electrostatic interactions [18,19].

Site-directed spin labeling of proteins [20] is based on point mutations of one or two selected amino acids to cysteine and reaction with nitroxide radicals with an additional functional group that is reactive specifically to thiol groups. It is also possible to engineer metal ion binding sites in a protein and use a paramagnetic transition metal ion as the spin label [21]. The substitution of paramagnetic for diamagnetic metal ions is a viable technique for metalloenzymes, in particular for those ones that depend on Mg^{2+} , as this ion is closely mimicked by Mn^{2+} so that the biochemical activity of the enzyme is usually retained [22].

In general, spin probes and labels are well suited for large macromolecules or biomacromolecules and complex supramolecular systems where other techniques may have difficulties in distinguishing signals due to the site of interest from background signals. As the dynamics of the matrix couples to the dynamics of spin probes and labels, observation of the latter can provide indirect information on the former. As far as the motion of whole domains of a biomacromolecule with respect to each other on millisecond time scales is concerned, the information can even be considered as direct [23].

3 A BRIEF PRIMER ON EPR SPECTROSCOPY

3.1 INTERACTIONS OF ELECTRON SPINS WITH THEIR ENVIRONMENT

Spins are local probes of structure and dynamics that couple only weakly to their environment. A total electron spin $S = \frac{1}{2}$ can be considered as a magnetic dipole and interacts only with magnetic fields which may be external (static field of the EPR magnet and oscillatory field of the electromagnetic irradiation) or local (fields induced by other spins in the vicinity). This interaction with magnetic fields exists also for $S > \frac{1}{2}$ and in general shifts levels by an energy that is proportional to the magnetic quantum number $m_S = -S, -S + 1, \dots, S$. A total electron spin $S > \frac{1}{2}$ also has an electric quadrupole moment and thus experiences an additional zero-field splitting. In this case the shift of the levels is proportional to m_S^2 . All these interactions contribute to the spin Hamiltonian, which can, at least in principle, be derived from the Hamiltonian of the many-electron system by considering only the spin degrees of freedom [24]. The magnetic parameters of the system can thus be computed from its known wave function. In the following, we discuss this in only a qualitative way that is sufficient to understand how dynamic processes can influence spectra. Figure 6.2 shows schematically the interactions that can be observed with EPR for a system of molecules with total electron spin $S = \frac{1}{2}$.

The electron Zeeman interaction with the static external field B_0 scales with the g value, which is $g_e = 2.002319$ for a free electron. For bound electrons, the electron spin slightly (light elements) or strongly (heavy elements) couples to

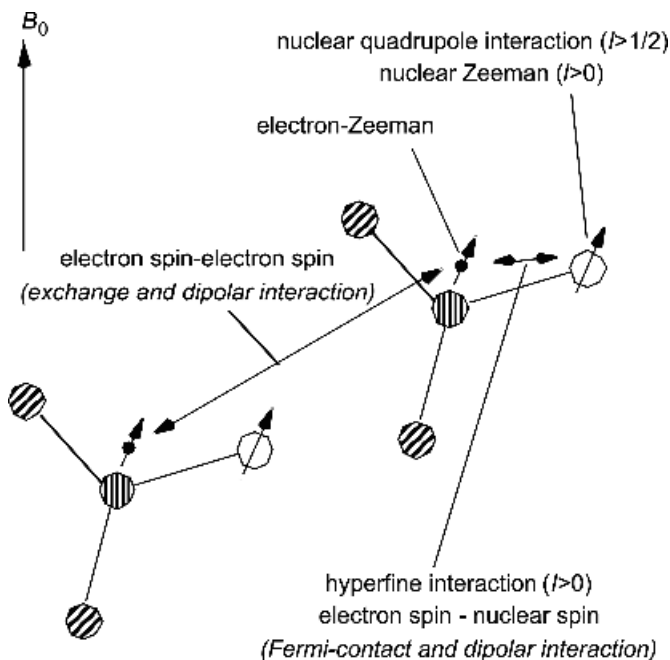


Figure 6.2 Schematic representation of the interactions that can be observed by EPR techniques in a system of paramagnetic molecules with $S = 1/2$.

orbital angular momentum. This spin-orbit coupling not only causes a shift of the g value with respect to g_e , but also induces an orientation dependence of the g value as the singly occupied molecular orbital generally does not have spherical symmetry. In this situation the electron Zeeman interaction is described by a g tensor, i.e., by three principal values and the corresponding principal directions. As a consequence of this g anisotropy, molecules with different orientations with respect to the magnetic field have different resonance frequencies. A reorientation of the molecule thus causes a shift in the resonance frequency. This is one of the mechanisms by which dynamics influences EPR spectra.

Local fields at the site of the observed electron spin S are induced by nuclear spins and other electron spins in the vicinity. The nuclear spins are much more abundant and are usually of more interest. The hyperfine coupling to a nuclear spin I results in a local field that is proportional to the magnetic quantum number m_I , so that each level with magnetic quantum number m_S splits into $2I + 1$ hyperfine sublevels. Accordingly, each allowed EPR transition with $|\Delta m_S| = 1$ splits into $2I + 1$ transitions that give rise to the lines of a hyperfine multiplet. The hyperfine coupling consists of the Fermi-contact contribution caused by spin density of the electron at the site of the nucleus and a dipolar contribution that acts through space. As only s orbitals have nonzero spin density at

the site of the nucleus, the Fermi-contact contribution is isotropic. It provides information on the spatial extent of the singly occupied molecular orbital and thus on the bonding situation. If the electron spin is well localized on the length scale of its distance r to the nucleus, the dipolar contribution scales with r^{-3} and can be used to infer this distance r . Typical length scales are between 2 and at most 8 Å [10]. The dipolar contribution is then also proportional to the second Legendre polynomial $(3 \cos^2\theta - 1)/2$ of the angle θ between the direction of the external magnetic field and the vector connecting the electron and nuclear spin. Thus, bond angles can also be determined in favorable cases. If the electron spin is distributed on the length scale of r , the dipolar part is still purely anisotropic (its average over all orientations vanishes), but analysis becomes more complicated and generally requires quantum-chemical computation of the hyperfine coupling. Further information on the hyperfine-coupled nucleus can be gained through the observation of the nuclear Zeeman interaction (interaction between the nuclear spin and the static external field B_0) and for $I > \frac{1}{2}$ through the observation of the nuclear quadrupole coupling, which gives information on the electric field gradient sensed at the nucleus [10]. CW EPR usually does not allow for the detection of these interactions, so that more sophisticated EPR and ENDOR techniques have to be used [8–10].

Electron spins interact with each other by orbital overlap (Heisenberg exchange) or through space. The dipolar contribution through space is analogous to the dipolar part of the hyperfine coupling, but, due to the larger magnetic moment of electron spins, it can be used to characterize structure at longer distances between 1 and 8 nm [25]. The exchange coupling lowers the energy of a pair of antiparallel spins and increases the energy of a pair of parallel spins if the orbital overlap is bonding (antiferromagnetic coupling). In the opposite case of antibonding overlap, parallel spins are favored (ferromagnetic coupling). In fully conjugated systems, exchange coupling can be significant at distances between the paramagnetic centers as large as 3.6 nm [26]. Otherwise, the exchange coupling through space or through matrix is relevant, which can be neglected with respect to the dipolar part at distances larger than 1.5 nm in nonconducting matrices. The exchange coupling between two centers is related to the rate of electron transfer between these centers by Marcus theory.

Strong exchange coupling between electron spins effectively combines them to a large spin system extended over a long range. It partially destroys the local character of EPR spectroscopy, can average anisotropic interactions, and often complicates spectrum analysis tremendously. For these reasons it is advisable to dilute the electron spins to an extent that renders intermolecular exchange coupling insignificant. Measurements in solutions and frozen solutions are therefore performed at concentrations of 2 mmol L⁻¹ or lower. For measurements on frozen solutions it is advantageous to use solvents that easily form glasses since otherwise phase separation of the solute and solvent may occur. For weakly polar species, toluene is often a good choice, for polar

species, methanol, ethanol, or water–glycerol mixtures with a glycerol fraction of at least 25 vol% can be used. Species with both polar and nonpolar moieties may dissolve best in 1:1 mixtures of ethanol with a less polar solvent such as dichloromethane. This mixture also forms glasses easily. Studies on crystalline compounds are best performed by dilution of up to 2 % of the paramagnetic compound into an isostructural diamagnetic crystal.

3.2 RELAXATION

The magnetic parameters discussed in the previous section are not static, they can be modulated by dynamical processes. Reorientation of the paramagnetic center, even by only a small angle, causes a change in the anisotropic contribution to the local field at the spin. Any motion of the nuclei, for instance vibrational motion, causes changes in the electronic wavefunction and thus modulates all magnetic parameters, including their isotropic contributions. The modulation of local magnetic fields couples to the spin in the same way as electromagnetic fields, it may induce spin transitions if the modulation frequency coincides with the transition frequency.

For an external magnetic field B_0 along the z direction, the electron spins are oriented parallel or antiparallel to the z direction. Modulation of the components of the local field in the xy plane due to a stochastic process then induces stochastic electron spin transitions (spin flips) that contribute to longitudinal relaxation with time constant T_1 . For historical reasons longitudinal relaxation is often termed spin–lattice relaxation. The relaxation rate T_1^{-1} is proportional to the spectral density $J(\omega)$ of the stochastic process at the resonance frequency ω_0 of the transition under consideration. This spectral density is maximum for a correlation time τ_c of the stochastic process that fulfils the condition $\omega_0\tau_c = 1$. As correlation times usually are a monotonic function of temperature, there is a temperature for which the relaxation rate attains a maximum and T_1 attains a minimum. Measurements of T_1 as a function of temperature can thus be used to infer the correlation time of a dynamic process. By varying the external field B_0 and thus ω_0 , the time scale can be shifted to which EPR experiments are most sensitive.

Modulation of the z component of the local field cannot influence the z component of the spin magnetization and thus cannot induce spin flips. However, the x and y components of the magnetization that stem from coherent superposition of spin states with $|\Delta m_S| = 1$ are influenced, as the modulation of the z component can induce a cooperative flip-flop of two spins. The energy change during such a flip-flop is close to zero, as the two transition frequencies are almost equal. Such transverse or spin–spin relaxation with time constant T_2' is thus related to spectral density $J(0)$ at zero frequency. This spectral density $J(0)$ increases with increasing τ_c , i.e., with a slowdown of the process. The total rate of transverse relaxation includes a contribution of spin flips, so that $T_2^{-1} = (T_2')^{-1} + (2T_1)^{-1}$.

The considerations above apply to fast dynamic processes in the sense that the amplitude of the modulation of the resonance frequency $\Delta\omega_0$ (induced by modulation of the local field) multiplied with the correlation time τ_c is much smaller than unity. This Redfield regime [27] is usually attained in solutions with low viscosity [2], but may also apply to small-amplitude libration in solids [28]. For slower reorientation in solutions with high viscosity or in soft matter above the glass transition temperature (slow tumbling), spectral lineshapes are directly influenced by exchange between different orientations of the molecule (Section 4.1). Relaxation times in solids outside the Redfield regime cannot be predicted from first principles except for a few crystalline systems with very simple structure and few defects [29]. In such systems, qualitative or semi-quantitative analysis of relaxation data can still provide some information on dynamics.

At sufficiently low temperatures, usually below 10–20 K for transition metal complexes with $S = \frac{1}{2}$ and below 50 K for free radicals, transverse relaxation of electron spins is dominated by fluctuation of dipolar hyperfine fields from distant protons. These fluctuations are driven by coupling among the protons, so that in this regime, T_2 is not sensitive to dynamics.

3.3 MEASUREMENT TECHNIQUES

The most widely used and in many cases most sensitive way of recording EPR spectra is continuous-wave (CW) EPR. In this experiment, microwave with constant frequency is irradiated with relatively weak power (typically between 1 μ W to 200 mW) and the magnetic field is swept to bring the transitions into resonance. As broadband microwave detection by diodes is used, the detection bandwidth has to be limited by other means to avoid accumulation of excessive noise over a wide frequency range. This is achieved by low-frequency (typically 100 kHz) modulation of the magnetic field with an amplitude of 0.01–1 mT and phase-sensitive detection of the signal component modulated with this frequency. As a result, the derivative of an absorption lineshape is measured, which is better resolved than the absorption lineshape itself. The technique is disadvantageous if all features of the absorption lineshape are much broader than the maximum modulation amplitude that can be technically achieved.

The sensitivity of CW EPR is maximized by separately increasing modulation amplitude and microwave power as long as the increase of the signal is still linear to the modulation amplitude and to the square root of the microwave power. Further increase causes lineshape distortions. Under optimum conditions spectra of sufficient quality can be acquired within 1 h down to concentrations of approximately 1–10 $\mu\text{mol L}^{-1}$ at microwave frequencies between 2 and 35 GHz. Higher concentrations may be required for transition metal complexes where the maximum technically possible modulation amplitude is insufficient to optimize sensitivity. At lower and higher frequencies, concentration sensitivity declines somewhat. Typical sample volumina with standard equipment are

150 μL at X-band (9.5 GHz) and 1 μL at W band (95 GHz), however, when using special loop-gap resonators sample volumina of approximately 5 μL are sufficient even at X band. For solid samples, 1 μL roughly corresponds to 1 mg.

The maximum available microwave power sets a lower limit to the transverse-relaxation time T_2 for which CW EPR is still possible. Typically, T_2 must be at least in the nanosecond range to detect a signal. For shorter T_2 lifetime broadening would also lead to extremely low resolution and thus render the spectrum practically useless even if it could be acquired. Certain samples have to be cooled to temperatures of approximately 4 K to achieve sufficiently long T_2 , prominent examples being high spin Fe^{3+} and many rare earth ions.

The CW EPR spectrum may not be sufficient for detailed analysis of the spin interactions and the dynamics in cases where the paramagnetic center, or its approximate geometric and electronic structure is not known *a priori*. In such situations, where it is necessary to separate the different spin interactions, or different dynamic contributions or the relaxation times T_1 and T_2 from each other, pulse EPR techniques are the methods of choice [10]. After a high-power microwave pulse (typically 100 W–1 kW) there is a deadtime of 60 to 100 ns during which the pulse rings down and no signal can be detected. In most pulse EPR experiments, the signal is shifted to later times by echo formation, but it is also possible to use pulses that are longer than the deadtime, so that a significant part of the free induction decay (FID) can still be detected. In any case, the application of such techniques requires transverse-relaxation times T_2 of at least 100 ns, so that studies may have to be conducted at lower temperatures than are required for CW EPR studies. If only the absorption EPR spectrum is to be recorded, fast repetition can partially compensate for shorter T_2 down to approximately 10 ns.

Hyperfine interactions of the electron spin with nuclear spins outside the first coordination sphere of a localized paramagnetic center or for strongly delocalized centers are usually unresolved in solid-state EPR spectra and may lead to complicated multiline patterns in solution. Simpler spectra and strongly enhanced resolution are obtained by measuring the nuclear frequencies, i.e., by measuring an NMR spectrum with the electron spin serving only as polarization source and more sensitive observer spin. In electron nuclear double resonance (ENDOR) experiments, polarization is transferred from electron spin to nuclear spin transitions, the nuclear transitions are excited by irradiation with resonant radio frequency, and the resulting change in the population of the involved levels is again detected on an electron spin transition. Such experiments can be performed with continuous irradiation of both microwave and radio frequency (CW ENDOR) [8,9], but are nowadays mostly based on more versatile pulse techniques [10]. The nuclear transitions can also be indirectly excited by relying on microwave excitation of forbidden electron–nuclear spin transitions. Such electron spin echo envelope modulation (ESEEM) techniques and related spectral hole-burning techniques can be advantageous for small hyperfine couplings and for those cases where electron–nuclear mixing and thus the amplitude

of forbidden transitions is significant (e.g., protons and weakly coupled ^{14}N at X-band frequencies, strongly coupled ^{14}N at W-band frequencies). Probably the most valuable ESEEM experiment is the two-dimensional HYSORE experiment [30], which simplifies spectral assignment in situations where signals from different isotopes overlap in one-dimensional spectra and when nuclear frequencies are influenced by both hyperfine and nuclear quadrupole coupling. In favorable cases the HYSORE experiment or related experiments [31] can also be used to separate isotropic and anisotropic contributions to the hyperfine coupling and thus to infer the distance between the electron spin and nuclear spins.

4 DETECTION OF DYNAMIC PROCESSES BY EPR

4.1 SLOW TUMBLING

Due to the anisotropy of spin interactions such as the electron Zeeman and hyperfine interaction and the zero-field splitting, the EPR spectrum of a paramagnetic species depends on its orientation with respect to the external magnetic field. Consider the case of a square-planar copper complex with four equivalent ligands, electron spin $S = \frac{1}{2}$ and nuclear spin $I = \frac{3}{2}$ for the copper isotopes ^{63}Cu and ^{65}Cu (Figure 6.3a). Both isotopes give rise to only slightly different EPR spectra, and for simplicity we restrict ourselves to one of them. At any given orientation the EPR spectrum then consists of $(2S + 1)(2I + 1) = 4$ lines that are separated by the hyperfine splitting A (Figure 6.3).

The complex has a C_4 symmetry axis perpendicular to the plane and thus g and copper hyperfine tensors with axial symmetry. The orientation of the complex with respect to the magnetic field can then be characterized by a single angle β between the magnetic field vector \mathbf{B}_0 and the symmetry axis, which is also the unique axis of the g and copper hyperfine tensors. Both the g value $g(\beta)$ and the hyperfine splitting $A(\beta)$ are maximum along the unique axis. The orientation dependence of the spectrum is depicted in Figure 6.3b. Note that a large g value corresponds to a low resonance field, $B_0 = h\nu_{\text{mw}}/(g \mu_B)$. The overlap of derivative lineshapes leads to partial cancellation of the signal, as is apparent in the trace for $\beta = 90^\circ$.

In a macroscopically disordered system such as a microcrystalline powder or a glassy frozen solution, all possible orientations β occur with weighting factors $\sin \beta$. The EPR spectrum of such a disordered system depends on whether reorientation by rotational diffusion is very slow, moderate, or very fast on the EPR timescale. In the following we assume isotropic Brownian rotational diffusion with an isotropic value R_{iso} of the diffusion tensor and a transverse relaxation time of 150 ns.

The rotational correlation time τ_r is then given by $1/(6R_{\text{iso}})$. Rotational diffusion is very slow (rigid limit) for $T_2 R_{\text{iso}} \ll 1$. In this regime, the spectrum

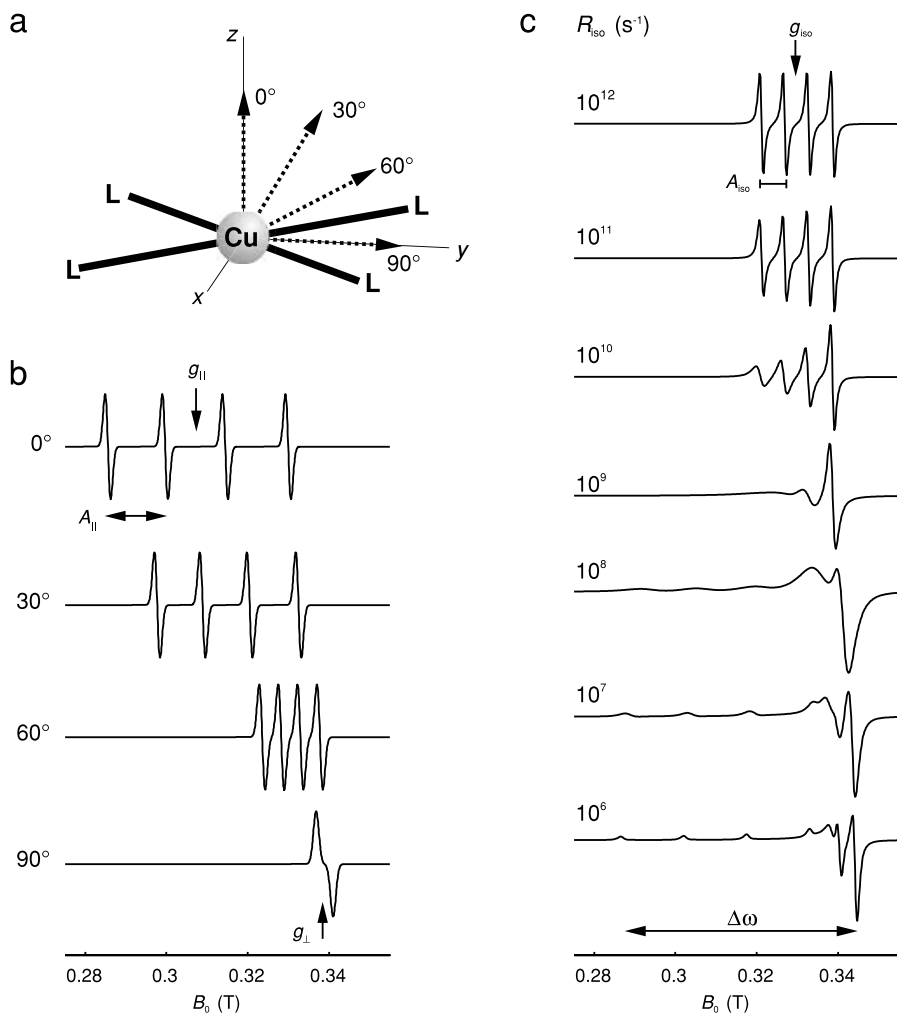


Figure 6.3 Orientation dependence of the EPR spectrum of a planar copper(II) complex and lineshapes in the slow tumbling regime (simulations). (a) Geometry of the complex, molecular coordinate frame, and orientations of the magnetic field vector B_0 corresponding to the spectra in (b). (b) EPR spectra at four selected orientations simulated with EasySpin 1.3 (<http://www.esr.ethz.ch>). (c) Slow tumbling spectra assuming isotropic Brownian diffusion with rotational correlation time $\tau_r = 1/(6R_{\text{iso}})$ simulated with the Schneider–Freed suite of programs [32].

is simply an additive superposition of the spectra of all possible orientations (bottom trace in Figure 6.3c). Rotational diffusion is very fast (isotropic limit) for $R_{\text{iso}}/\Delta\omega \gg 1$, where $\Delta\omega$ is the total width of the spectrum. In this regime, the anisotropy of all interactions is averaged and a simple four-line spectrum

with parameters $g_{\text{iso}} = (g_{\parallel} + 2g_{\perp})/3$ and $A_{\text{iso}} = (A_{\parallel} + 2A_{\perp})/3$ is observed (top trace in Figure 6.3c). The regime in between these two limits is the slow tumbling regime. As can be seen in Figure 6.3c the lineshape depends strongly on the rotational correlation time in this regime. In particular in the vicinity of the condition $R_{\text{iso}}/\Delta\omega = 1$ the lineshape is also sensitive to specifics of the rotational diffusion process, such as anisotropy of the rotational diffusion tensor, jump diffusion, or a reorienting potential in a microscopically ordered matrix such as a liquid crystal [32]. It is often difficult to obtain a perfect fit of simulated to experimental lineshapes in this regime, but estimates of the rotational correlation time are usually reliable.

Rakhimov *et al.* [33] showed nicely that, even when different dynamical processes are taking place simultaneously, CW EPR may be able to separate them. They investigated the dynamics of the bis(triphenylphosphine)-3,6,-di-*tert*-butyl-4,5-dimethoxy-*o*-semiquinone complex of copper(I) in viscous media with EPR at 9.6 GHz and 140 GHz and could unravel the two dynamical processes influencing the EPR spectra: the overall reorientation (tumbling) of the complex and an intramolecular exchange (see Section 4.2) of the PPh_3 ligands in the coordination sphere of the complex. The key to characterizing the complex despite the diamagnetic state of the central ion is the strong interaction of the unpaired electron of the paramagnetic *o*-semiquinone ligand with the metal ion and the phosphine ligands. A partial transfer of spin density to the central ion results in significant anisotropy of the g tensor and of the hyperfine interactions, which makes the EPR lineshapes sensitive to the rates of rotational diffusion of the complex, analogous as described above for the Cu(II) case. Furthermore, the intramolecular exchange leads to a variation of the linewidth for the components of the ^{31}P hyperfine multiplet.

4.2 EXCHANGE PROCESSES

Dynamic equilibria can be characterized by EPR spectroscopy if at least one educt and one product are paramagnetic and if the rate of exchange between products and educts is on the EPR timescale (nanoseconds to microseconds). As such systems are rare and the theory is basically the same as in the case of dynamic NMR [34], we refrain from a detailed discussion. The characteristic time of electron transfer in mixed-valence dioxolene manganese complexes at a temperature of 5 K has been estimated to be shorter than 1.77×10^{-11} s and longer than 5.6×10^{-13} s by analyzing EPR spectra acquired in the temperature range between 5 and 50 K at frequencies of 9.23, 190, and 285 GHz [35]. For the adsorption of NO onto the zeolites H-ZSM-5, Na-ZSM-5, and Na-A homogeneous EPR line broadening could be used to derive estimates of the lifetime of the adsorbed states in the range of a few hundred picoseconds in the temperature range between 110 and 150 K [36]. Arrhenius plots of the homogeneous linewidth provided activation energies of desorption in the range between 4 and 20 kJ mol^{-1} . Note that such lifetime broadening can be used

to estimate the exchange rate in a dynamic equilibrium even if only one of the involved species is paramagnetic.

A special case in EPR, which is not covered by the theory of dynamic NMR, is spin exchange due to collision of like paramagnetic molecules in solution [37–39]. The influence on the lineshape and line position arises from the fact that the nuclear spin magnetic quantum numbers and hence the local hyperfine fields acting on the electron spin may be different in the two colliding molecules. The spectra can be analyzed in terms of diffusion coefficients and local concentrations of the paramagnetic species.

In a similar way collisional spin exchange between unlike species can be studied, as has been demonstrated for Cu^{II} and Ni^{II} complexes of crown ethers and the nitroxide radical TEMPO [40]. Comparison of the rate constant of spin exchange with the rate constant of diffusion collisions gave information on the steric factor, which characterizes the accessibility of the ligated transition metal ion to the nitroxide radical.

4.3 DYNAMIC JAHN–TELLER EFFECT

According to the Jahn–Teller theorem ‘any nonlinear molecular system in a degenerate electronic state will be unstable and will undergo distortion to form a system of lower symmetry and lower energy thereby removing the degeneracy’ [41]. This is not necessarily manifest in crystal structures at room temperature, as electron–vibration coupling may cause fast exchange between different low-symmetry states and thus result in an average high-symmetry structure on the time scale of X-ray crystallography. In other words, at room temperature an excited vibronic state may be preferentially populated that corresponds to a dynamic rather than static Jahn–Teller effect. Although the time scale of EPR spectroscopy is much faster than that of X-ray crystallography, such Jahn–Teller dynamics still corresponds to the fast-exchange limit of EPR spectroscopy, as the time scale of vibrations is yet much faster. The spectrum in the excited vibronic state thus also reflects the high-symmetry situation with the g and hyperfine tensors averaged over the set of low-symmetry states.

At sufficiently low temperatures only the vibronic ground state is populated and the EPR spectrum reflects the static Jahn–Teller distortion [42]. In an intermediate temperature range, both the vibronic ground state (for $\text{Cu}(\text{II})$: an elongated octahedron that is static) and the first excited state (for $\text{Cu}(\text{II})$: oscillation between two elongated octahedrals with perpendicular long axes) are populated (see Figure 6.4a) and transitions between these states are also fast on the EPR time scale. The observed principal values of the g and hyperfine tensor are thus Boltzmann-weighted averages over the two vibronic states and depend on the ratio $K = n_0/n_1$ of the populations of these states.

By measuring the principal values of the g tensor as a function of temperature (Figure 6.4b), one can thus derive the temperature dependence of K . In this

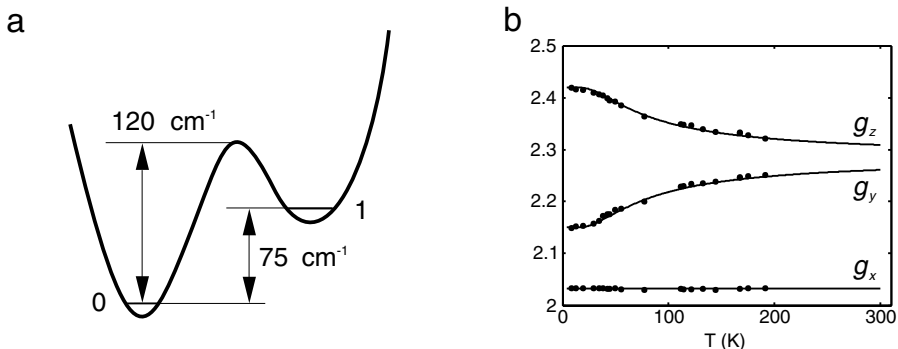


Figure 6.4 Dynamic Jahn–Teller effect in Cu^{II} -doped Tutton's salt (data taken from Ref. 42). (a) Schematic plot of the part of the potential energy surface relevant at temperatures below 310 K. (b) Dependence of the experimental g tensor principal values on temperature (full circles) and fit by the Silver–Getz model (solid lines).

model, a plot of $\ln K$ against $(kT)^{-1}$ is linear, with the slope corresponding to the energy difference between the two vibronic levels. In the case of the $\text{Cu}^{2+}(\text{H}_2\text{O})_6$ complex in copper-doped zinc Tutton's salt the temperature dependence of K in the range between 30 and 300 K was nicely fit by this Silver–Getz model, and an energy difference of 75 cm^{-1} between the vibronic levels was found.

The modulation of the g and hyperfine tensor during the transitions governs the transverse relaxation time of the electron spin and is thus manifest in the linewidths. The linewidths depend on the magnetic spin quantum number m_I of ^{63}Cu , the population ratio K defined above, and the average reciprocal lifetime P in the vibrational ground state. A plot of $\ln P$ against $(kT)^{-1}$ is again linear, with the slope corresponding to the barrier height for passing from the vibrational ground state to the first excited state (120 cm^{-1} for $\text{Cu}^{2+}(\text{H}_2\text{O})_6$ in zinc Tutton's salt).

Recent work on deuterated pure copper Tutton's salt [43] and on $\text{Cu}^{\text{II}}-(2, 2':6', 6''\text{-terpyridine})_2(\text{PF}_6)_2$ [44] demonstrated that the energy difference between the two vibronic levels may itself depend on temperature due to cooperativity of the Jahn–Teller dynamics. In the case of Tutton's salt this cooperativity is believed to be mediated by a hydrogen-bond network.

The situation described above applies to complexes packed in a crystal lattice. We have recently found that the situation is drastically different for the $\text{Cu}^{\text{II}}-(2, 2':6', 6''\text{-terpyridine})_2$ complex in glassy matrices of frozen ethanol or frozen ethanol–dichloromethane mixtures and the same complex isolated in a matrix of crystalline ethanol. In these cases, only small amplitude librations along the Jahn–Teller active mode are observable below the melting point of ethanol. Above the melting point, averaging of the g and hyperfine tensor by the Jahn–Teller effect is complete [45].

4.4 CHEMICALLY INDUCED DYNAMIC ELECTRON POLARIZATION (CIDEP)

Time-domain experiments in EPR spectroscopy have response times down to tens of nanoseconds, which makes them suitable to study the processes initiated by light excitation of a molecule. In many such photochemical processes bond cleavage occurs, often from a triplet state, and a pair of radicals is formed. The spins of the two radicals are correlated, since bond cleavage is a spin-conserving process due to conservation of angular momentum. If the spin-correlated radical pair (SCRIP) is formed from a triplet-state molecule it is thus also in a pure triplet state; if it is formed from a single-state molecule it is in a pure singlet state. In the presence of an external magnetic field, pure triplet and singlet states are not eigenstates of the system and their exclusive polarization does not correspond to thermal equilibrium polarization of the EPR transitions. Rather the SCRIP is born in a state of large non-equilibrium polarization corresponding to a strong signal enhancement with respect to EPR on equilibrium species.

The nonequilibrium polarization is not directly observable at the instant after SCRIP formation if the radical pair is formed from a singlet precursor (formally diamagnetic pair with $S = 0$) or from a triplet precursor in which all the triplet sublevels T_{-1} , T_0 , and T_{+1} were equally populated. In these cases there are as many molecules with emissively polarized transitions in the ensemble as there are molecules with absorptively polarized transitions.

Two major mechanisms break this balance and lead to observable signals [46]. A triplet precursor is normally generated by intersystem crossing from an excited singlet state and as the rate constants for this process differ among the triplet sublevels, these sublevels are not initially equally populated. Longitudinal electron spin relaxation equalizes these populations on the time scale of T_1 in the triplet state, which is typically in the nanosecond range. However, if dissociation of the triplet state molecule proceeds on a faster or comparable time scale, an excess of emissive polarization is created for preferential polarization of T_+ compared to T_- sublevels and an excess of absorptive polarization for the opposite case. This triplet mechanism of chemically induced dynamic electron polarization (CIDEP) leads to net polarization, i.e., all the lines are either emissive or absorptive (Figure 6.5a).

In the radical pair mechanism of CIDEP the observable polarization is created by an interplay of spin dynamics, diffusion, and chemical reactions. As the singlet state S and the triplet sub-state T_0 are not eigenstates of the radical pair, they are interconverted by spin dynamics during the time after SCRIP formation. This does not influence net polarization of any transition directly, but it leads to different reactivity on diffusional reencounter of the two radicals. Normally, recombination of triplet pairs is spin forbidden as the triplet energy hypersurface has no minimum corresponding to the bond that was broken during SCRIP formation. On the other hand, singlet pairs readily recombine. The

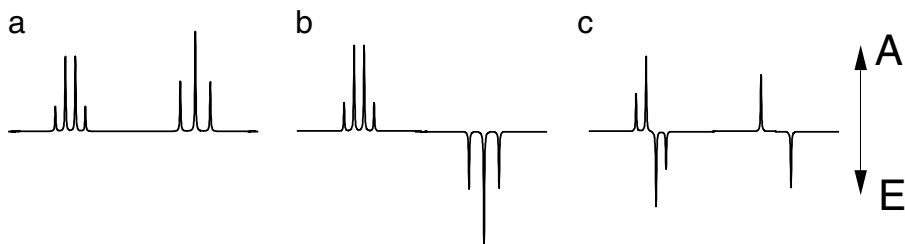


Figure 6.5 Schematic CIDEP patterns for a radical pair consisting of one radical with three equivalent protons (left) and one radical with two equivalent protons (right). (a) Triplet mechanism. (b) Radical pair mechanism, contribution due to g value difference. (c) Radical pair mechanism, contribution due to hyperfine couplings.

interconversion of S and T_0 states can be either due to a difference in the g values of the two radicals or due to hyperfine couplings. In the former case, one radical exhibits only emissive lines, the other one only absorptive lines (Figure 6.5b). For radical-pair mechanism CIDEP caused by hyperfine couplings there are absorptive and emissive lines in the spectrum of each radical, the lines above the center frequency of the multiplet having a different sign from the lines below the center frequency (Figure 6.5c). Detailed sign rules for both mechanisms, considerations on kinetic equations, and a discussion of further mechanisms of minor importance can be found in Ref. [46]. The variation of CIDEP spectra with solvent viscosity or when going from solubilized to micellized radical pairs can provide valuable information on solvent cage effects or micelle supercage effects in the diffusion of molecules.

CIDEP spectra in solution can be observed after initiation of the reaction with a flash lamp or by laser pulses. CW observation with boxcar integration over a certain time window after the light pulse can be used, while slow field modulation is not usually applied as it considerably decreases time resolution. Maximum resolution in both frequency and time domain is obtained by detecting the FID of the SCRIP after a short high-power microwave pulse (FT EPR). Both techniques have been applied to investigate homolysis of metal–carbon bonds [47–49]. In the study on methylaquocobaloxime the CIDEP pattern could be unequivocally assigned to a methyl radical. Simulation of this pattern revealed that the polarization must be mainly from the triplet mechanism, thus establishing that cleavage of the metal–carbon bond originates from the triplet state of the complex [47].

A more complicated behavior was observed for complexes of the types $[\text{Ru}^{\text{I}}(\text{R})(\text{CO})_2(\alpha\text{-diimine})]$ and $[\text{Re}(\text{R})(\text{CO})_3(\alpha\text{-diimine})]$ with $\text{R} = \text{ethyl, isopropyl, or benzyl}$ [48]. In this case, the CIDEP patterns varied strongly with R , the metal ion, and the solvent. Again, metal–carbon bond homolysis was demonstrated by assigning the spectra to radicals $\text{R}\cdot$. However, the CIDEP patterns exhibited varying contributions due to the radical-pair mechanism and the triplet mechanism. Possible involvement of a third mechanism allowing for

backreaction of triplet pairs under conditions of significant spin-orbit coupling for these heavy transition metal ions was also discussed. In a related study of $[\text{Re}(\text{R})(\text{CO})_3(4,4'\text{-Me}_2\text{-bpy})]$ with $\text{R} = \text{methyl, methyl-d}_3$ the sign of the CIDEP pattern of methyl radicals and the net emissive CIDEP effect for the deuterated methyl radical proved that metal-carbon bond cleavage originates from the triplet excited state of the complex and that bond dissociation is complete 50 ns after the laser pulse.

The situation is somewhat different in the solid state [50], where stable radical pairs are usually formed by electron transfer over a distance of more than 1 nm and are then localized rather than diffusing. In this case it becomes significant that the T_0 state is a coherent superposition of spin eigenstates of the pair; the same is true for the S state [51]. Evolution of this zero-quantum coherence can be observed indirectly, and information on the coupling between the two spins can be obtained from out-of-phase ESEEM experiments [52]. In photosynthetic reaction centers, this technique was used to measure distances between the radicals up to approximately 3 nm [53]. In a cascade of electron transfers, out-of-phase ESEEM spectra depend on the couplings in both the primary and secondary pair and on the time constant for the secondary electron transfer [54].

5 APPLICATION EXAMPLE: HOW TO COMBINE DIFFERENT EPR TECHNIQUES

In the following, we illustrate how a combination of EPR techniques can be applied to obtain a wealth of information on the structure and dynamics of complex materials. As an example we use heme proteins, such as hemoglobin (Hb) or myoglobin (Mb) that are important in oxygen transport and storage and are also known to bind NO. EPR allows for the detection of the ferric forms of the proteins (low spin $S = \frac{1}{2}$ or high spin $S = \frac{5}{2}$) and for the observation of NO binding to the native Fe(II) form. The ability of heme proteins to bind nitric oxide in their native form has been recognized and studied over a long period. Recently, however, the interest in these analyses increased enormously after the discovery that myoglobin not only acts as an O_2 buffer and facilitates O_2 diffusion, but that the protein is also involved in the removal of toxic NO in the cardiac and striated muscle [55]. The EPR spectra of MbNO show an interesting temperature dependence [56,57]. At 300 K an axial species (denoted state II) is the only species observed with X-band EPR. Analysis of its development with decreasing temperature shows a partial transformation into a rhombic state I. At an intermediate temperature (240–100 K) irregular line shapes are apparent indicating disordered geometries of the Fe-NO-heme group. Regular rhombic line shapes develop increasingly at temperatures below 70 K. At 5–10 K, the rhombic state I dominates the EPR spectra but state II is still present. Based on EPR and ENDOR studies, state I has been assigned to a hexacoordinated structure with the nitroso ligand coordinated in a bent end-on orientation with

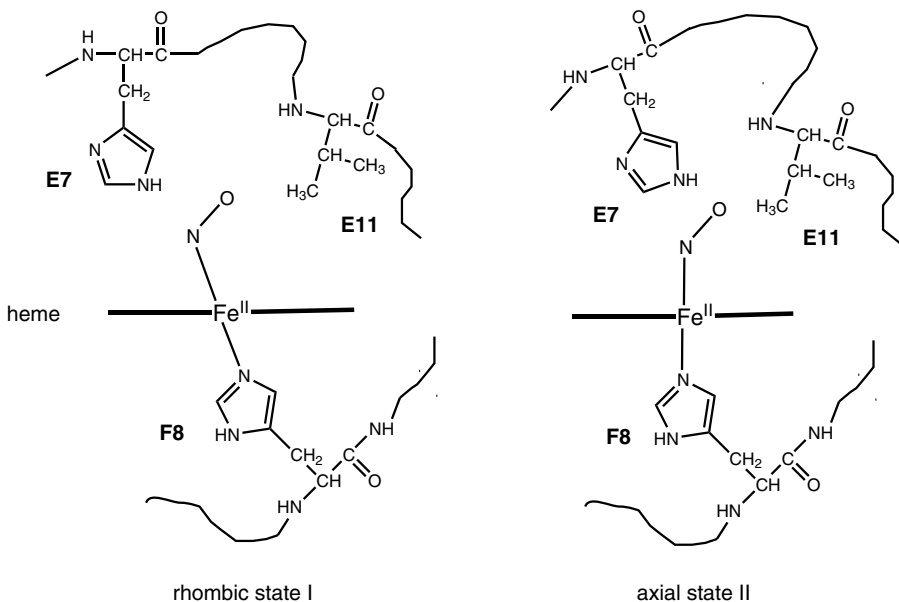


Figure 6.6 Schematic representation of the two MbNO forms identified using EPR. The rhombic state I is dominant at very low temperature (<30 K), whereas the axial state II dominates the EPR spectra at higher temperature.

the proximal histidine F8 as second axial ligand (see Figure 6.6) [56]. In this configuration the N(His)–Fe–N(NO) axis does not coincide with the porphyrin plane normal. The nature of state II is still somewhat controversial. Several authors have ascribed state II at low temperature to a species with the N(His)–Fe–N(NO) axis aligned with the normal of the porphyrin ligand (Figure 6.6) [56]. ENDOR studies of the two states suggest that in both cases the E7-His and E11-Val residues are present in the heme pocket and stabilize the bound NO [58,59]. Using ESEEM, an interaction with the N_e nitrogen of the distal E7-His could be found for NO-ligated heme proteins of state II, where this interaction was not observed for state I [60]. The development of state I from state II in MbNO with decreasing temperature must be invoked by protein conformational changes which force an increasing fraction of the NO ligand out of the axial hydrogen-bonded state, combined with a respective movement of the proximal histidine. A large variety of new Fe–NO configurations appear to be adopted between 240 and 100 K, which very probably lack hydrogen bonding [56]. The fact that the plot of the relative fraction of axial to rhombic species as a function of $1/T$ deviates from the linear behavior points again to the existence of more than two conformational states [57].

At this point, it would be interesting to compare the temperature behavior of MbNO with that of oxygenated Mb. However, oxygenated heme proteins

are EPR silent, but it is found that Co(II) porphyrin complexes can reversibly bind oxygen, analogous to their ferrous analogues and both the oxy and deoxy forms are EPR active. The chemical substitution of ferrous protoporphyrin IX by cobaltous porphyrin in Mb thus opens a way to infer the motional behavior of the dioxygen moiety by EPR [61]. Single-crystal EPR measurements of oxycobalt Mb show two distinct forms at the lowest temperature, which change into one form at room temperature [61,62]. This can be interpreted in terms of an increased hopping between the two forms with an additional wobbling of the O₂ fragment at higher temperatures [63,64]. The existence of two forms at low temperature is again related to the amino acids in the heme pocket [61–63]. An EPR study of the temperature dependence of simple oxygenated Co(II) porphyrin complexes lacking a distal pocket, but with a nitrogen ligand coordinating at the proximal site showed that the dioxygen fragment has increased mobility at higher temperature, but that it is not freely rotating around the Co–O bond [64]. This suggests that the proximal ligand also has an influence on the mobility of the dioxygen fragment. It still has to be determined how big the influence of the proximal histidine is on the position of the NO moiety in MbNO.

Using the CW saturation method, the temperature dependence of the spin–lattice relaxation rate T_1^{-1} was determined for native MbNO in solution, powdered MbNO and denatured MbNO [65,66]. The results below 70 K could be described using the relation $T_1^{-1} = AT^n + C$. For the native MbNO in solution and for powdered MbNO n was found to be 2.4 and $C = 0$. The n value is too low to be described by a normal Raman process and comparison with glassy systems revealed that the temperature dependence of the spin–lattice relaxation can best be described by a tunneling localized state (TLS) model. The tunneling system was identified as the two different binding conformations of the NO relative to the heme plane (states I and II). The relaxation mechanism can then be induced by the TLS modulation of the crystal field since the paramagnetic center belongs to the tunneling system [65]. For denatured MbNO, C was found to differ from 0 and n lies between 3.5 and 4.5. For temperatures lower than 11 K, the principal contribution to the relaxation of the denatured sample is that from the constant term [66]. This behavior could be explained by considering that in the unfolded structure of the denatured samples, the interheme distances are sufficiently short to allow spin–lattice relaxation to be dominated at low temperatures by cross-relaxation between hemes. From the value of the cross-relaxation rates an interheme distance of 1.2 nm could be estimated for denatured MbNO. Estimates of the interheme distance in cases of dehydration of the protein can be obtained from volume changes (3 nm). The observed fast cross-relaxation for denatured MbNO thus shows that the denaturation process goes further than mere dehydration.

Not only can the ferrous Mb bind NO, also its related Fe(III) form binds NO, giving rise to an EPR-silent complex. Upon illumination (photolysis) of ferric MbNO EPR-active products become detectable [67]. Upon photolysis at low

temperature, the photoinduced intermediates trapped in the distal heme cavity exhibit new EPR spectra due to the interaction between the photodissociated NO ($S = \frac{1}{2}$) and the ferric high-spin heme ($S = \frac{5}{2}$). Temperature-dependent EPR revealed that the photodissociated NO is still trapped in the distal heme pocket of Mb in multiple intermediate states and cannot leave the protein matrix at temperatures below 100 K. The influences of the distal E7 (His64) and E11 (Val68) were tested by selective mutations. The EPR spectra of the photoproducts were closely related to the size and/or the polarity of the distal pocket residues. The distal pocket of the E7 mutants seemed to be sterically crowded even when the side-chain volume or hydrophobicity at amino acid position 64 was changed. The mobility of the photodissociated NO molecule in the heme pocket was found to be strongly governed by the nature of the amino acid residue at the E11 position. These results are analogous to the earlier ENDOR results indicating an important effect of E7-His and E11-Val on the stabilization of Fe(II)–NO [59].

The ability of Fe(II) and Fe(III) complexes to bind NO and spin–spin interaction between NO and Fe(III) can be exploited in a more general way to obtain structural information about all sorts of iron complexes. NO can then be seen as a probe to detect the molecular environment of the Fe(III). In a further step, one could think of attaching nitroxyl spin labels to Fe(III) complexes and use the specific interactions between the spin label and the Fe(III) ion. This idea was investigated by Rakowsky *et al.* [68] who spin labeled low-spin Fe(III)TPP(1-MeIm)₂ complexes (see Figure 6.1b, axial bases: 1-MeIm = 1-methylimidazole). The nitroxyl free radical electron spin relaxation times of the spin-labeled complexes were measured between 8 and 70 K by two-pulse spin-echo spectroscopy (ESE) and between 9 and 120 K by saturation recovery (SR). The relaxation times for the Fe(III) were determined between 10 and 28 K by SR and between 10 and 25 K by ESE. At low temperature the iron electron spin relaxation rates are slow relative to the electron–electron spin–spin splitting. As temperature is increased, the relaxation rates for the Fe(III) become comparable to and then greater than the spin–spin splitting, which collapses the splitting in the continuous wave EPR spectra and causes an increase and then a decrease in the nitroxyl spin-echo decay rate. Throughout the examined temperature range, the spin–lattice relaxation rate ($1/T_1$) for the nitroxyl was found to increase by interaction with Fe(III). The measured relaxation times for the Fe(III) allowed for an analysis of the temperature-dependent changes in the ESE and SR data of the interacting nitroxyl. Interspin distances (1.05–1.5 nm range) consistent with other data could be determined. Furthermore, the analysis of the nitroxyl ESE and SR data provided values of the iron relaxation rates at temperatures where the rates are too fast to be measured directly. It was shown that the effect of the low-spin Fe(III) on T_1 for an interacting nitroxyl radical can be interpreted quantitatively to obtain the interspin distances. This opens interesting possibilities for selectively probing the environment of paramagnetic metal centers.

6 ACKNOWLEDGEMENT

G. J. gratefully acknowledges financial help by a Dozentenstipendium of Fonds der Chemischen Industrie.

7 REFERENCES

1. J. A. Weil, J. R. Bolton, and J. E. Wertz, *Electron Paramagnetic Resonance of Transition Ions*, Clarendon Press, Oxford, 1970.
2. N. M. Atherton, *Principles of Electron Spin Resonance*, Ellis Horwood, New York, 1993.
3. L. J. Berliner (Ed.), *Spin Labeling: Theory and Applications*, Academic Press, New York, 1976.
4. L. J. Berliner (Ed.), *Spin Labeling II: Theory and Applications*, Academic Press, New York, 1979.
5. L. J. Berliner and J. Reuben (Eds), *Biological Magnetic Resonance*, Vol. 8, Plenum, New York, 1989.
6. L. J. Berliner (Ed.), *Biological Magnetic Resonance*, Vol. 14, Plenum, New York, 1998.
7. G. Jeschke, *Macromol. Rapid Commun.* **23**, 227–246 (2002).
8. L. Kevan and L. D. Kispert, *Electron Spin Double Resonance Spectroscopy*, John Wiley & Sons, Inc., New York, 1976.
9. H. Kurreck, B. Kirste, and W. Lubitz, *Electronic Nuclear Double Resonance Spectroscopy of Radicals in Solution*, VCH, New York, 1988.
10. A. Schweiger and G. Jeschke, *Principles of Pulse Electron Paramagnetic Resonance*, Oxford University Press, Oxford, 2001.
11. M. Hoshino, L. E. Laverman, and P. C. Ford, *Coord. Chem. Rev.* **187**, 75–102 (1999).
12. J. K. S. Moller and L. H. Skibsted, *Chem. Rev.* **102**, 1167–1178 (2002).
13. A. K. Hassan L. A. Pardi, J. Krzystek, A. Sienkiewicz, P. Goy, M. Rohrer, and L. C. Brunel, *J. Magn. Reson.* **142**, 300–312 (2000).
14. J. Krzystek, J. H. Park, M. W. Meisel, M. A. Hitchman, H. Stratemeier, L. C. Brunel, and J. Telser, *Inorg. Chem.* **41**, 4478–4487 (2002).
15. D. Biglino, H. T. Li, R. Erickson, A. Lund, H. Yahiro, and M. Shiotani, *Phys. Chem. Chem. Phys.* **1**, 2887–2896 (1999).
16. C. W. Lange, B. J. Conklin, and C. G. Pierpont, *Inorg. Chem.* **33**, 2176–1283 (1994).
17. M. D. Pace and A. W. Snow, *Macromolecules* **28**, 5300–5305 (1995).
18. G. Tsagaropoulos, J. S. Kim, and A. Eisenberg, *Macromolecules* **29**, 2222–2228 (1996).
19. D. Hinderberger, G. Jeschke, and H. W. Spiess, *Macromolecules* **35**, 9698–9706 (2002).
20. W. L. Hubbell and C. Altenbach, *Curr. Opin. Struct. Biol.* **4**, 566–573 (1994).
21. J. Voss, L. Salwinski, H. R. Kaback, and W. L. Hubbell, *Proc. Natl Acad. Sci. USA* **92**, 12295–12299 (1995).
22. R. M. Petrovich and E. K. Jaffe *Biochemistry* **36**, 13421–13427 (1997).
23. N. Radzwill, K. Gerwert, and H. J. Steinhoff, *Biophys. J.* **80**, 2856–2866 (2001).
24. A. Abragam and B. Bleaney, *Electron Paramagnetic Resonance of Transition Ions*, Clarendon Press, Oxford, 1970.
25. G. Jeschke, *Chem. Phys. Chem.* **3**, 927–932 (2002).
26. P. Wautelet, A. Bieber, P. Turek, J. LeMoigne, and J. J. Andre, *Mol. Cryst. Liq. Cryst.* **305**, 55–67 (1997).
27. A. G. Redfield, *Adv. Magn. Res.* **1**, 1–32 (1965).
28. M. Rohrer, P. Gast, K. Möbius, and T. Prisner, *Chem. Phys. Lett.* **259**, 523–530 (1996).

29. S. Geschwind (Ed.), *Electron Paramagnetic Resonance*, Plenum, New York, 1972.
30. P. Höfer, A. Grupp, N. Nebenführ, and M. Mehring, *Chem. Phys. Lett.* **132**, 279–282 (1986).
31. A. Schweiger, *Angew. Chem. Int. Ed. Engl.* **30**, 265–292 (1991).
32. D. J. Schneider and J. H. Freed in L. J. Berliner and J. Reuben (Eds), *Biological Magnetic Resonance*, Vol. 8, Plenum, New York, 1989, pp. 1–75.
33. R. R. Rakhimov, N. P. Benetis, A. Lund, J. S. Hwang, A. I. Prokof'ev, and Y. S. Lebedev, *Chem. Phys. Lett.* **255**, 156–162 (1996).
34. J. I. Kaplan and G. Fraenkel, *NMR of Chemically Exchanging Systems*, Academic Press, New York, 1980.
35. A. Dei, D. Gatteschi, C. Sangregorio, L. Sorace and M. G. F. Vaz, *Chem. Phys. Lett.* **368**, 162–167 (2003).
36. T. Rudolf, W. Böhlmann, and A. Pöpl, *J. Magn. Reson.* **155**, 45–56 (2002).
37. D. Kivelson, *J. Chem. Phys.* **33**, 1094–1106 (1960).
38. B. L. Bales and M. Peric, *J. Phys. Chem. B* **101**, 8707–8716 (1997).
39. B. L. Bales and M. Peric, *J. Phys. Chem. A* **106**, 4846–4854 (2002).
40. V. A. Livshits, B. B. Meshkov, A. L. Mikhailov, and M. V. Alfimov, *Russ. Chem. Bull. Int. Ed.* **51**, 2207–2215 (2002).
41. H. A. Jahn and E. Teller, *Proc. R. Soc. London Ser. A*, **161**, 220 (1937).
42. B. L. Silver and D. Getz, *J. Chem. Phys.* **61**, 638–650 (1974).
43. M. A. Hitchman, W. Maaskant, J. van der Plas, C. J. Simmons, and H. Stratemeier, *J. Am. Chem. Soc.* **121**, 1488–1150 (1999).
44. W. Bietsch, A. Mirea, T. Kamleiter, M. Weiss, U. S. Schubert, C. H. Weidl, C. Eschbaumer, I. Ovchinnikov, and N. R. Domracheva, *Mol. Phys.* **100**, 1957–1968 (2002).
45. E. Narr, H. Zimmermann, A. Godt, D. Goldfarb, and G. Jeschke, *Phys. Chem. Chem. Phys.*, **5**, 3959–3967 (2003).
46. K. A. McLauchlan, in L. Kevan, and M. K. Bowman (Eds), *Modern Pulsed and Continuous-wave Electron Spin Resonance*, John Wiley & Sons, Inc., New York, 1990, Chapter 7.
47. Y. Sakaguchi, H. Hayashi, Y. J. and I' Haya, *J. Phys. Chem.* **94**, 291–293 (1990).
48. C. J. Kleverlaan, D. M. Martino, H. vanWilligen, D. J. Stufkens, and A. Oskam, *J. Phys. Chem.* **100**, 18607–18611 (1996).
49. C. J. Kleverlaan, D. J. Stufkens, I. P. Clark, M. W. George, J. J. Turner, D. M. Martino, H. van Willigen, and A. Vleck A; *J. Am. Chem. Soc.* **120**, 10871–10879 (1998).
50. M. C. Thurnauer and J. R. Norris, *Chem. Phys. Lett.* **76**, 557–561 (1980).
51. K. M. Salikhov, Yu. E. Kandrashkin, and A. K. Salikhov, *Appl. Magn. Reson.* **3**, 199–216 (1992).
52. S. A. Dzuba, P. Gast, and A. J. Hoff, *Chem. Phys. Lett.* **236**, 595–602 (1995).
53. S. G. Zech, W. Lubitz, and R. Bittl, *Ber. Bunsenges. Phys. Chem.* **100**, 2041–2044 (1996).
54. G. Jeschke and R. Bittl, *Chem. Phys. Lett.* **294**, 323–331 (1998).
55. M. Brunori, *Trends Biochem. Sci.* **26**, 209–210 (2001).
56. P. P. Schmidt, R. Kappl, and J. Hüttermann, *Appl. Magn. Reson.* **21**, 423–440 (2001).
57. M. Flores, E. Wajnberg, and G. Bemski G., *Biophys. J.* **73**, 3225–3229 (1997).
58. R. Kappl, and J. Hüttermann, *Isr. J. Chem.* **29**, 73–84 (1989).
59. M. Flores, E. Wajnberg and G. Bemski, *Biophys. J.* **78**, 2107–2115 (2000).
60. A. M. Tyryshkin, S. A. Dikanov, E. J. Reijerse, C. Burgard, and J. Hüttermann, *J. Am. Chem. Soc.* **121**, 3396–3406 (1999).
61. L. C. Dickinson and J. C. W. Chien, *Proc. Natl Acad. Sci. USA* **77**, 1235–1239 (1980)
62. H. Hori, M. Ikeda-Saito, and T. Yonetani, *Nature* **288**, 501–502 (1980).
63. L. C. Dickinson and M. C. R. Symons, *Chem. Soc. Rev.* **12**, 387–414 (1992).
64. S. Van Doorslaer and A. Schweiger, *J. Phys. Chem. B* **104**, 2919–2927 (2000).

65. O. R. Nascimento, L. M. Neto, and E. Wajnberg, *J. Chem. Phys.*, **95**, 2265–2268 (1995).
66. E. Wajnberg and O. C. Alves. *J. Magn. Reson. B*, **113**, 119–124 (1996).
67. H. Hori, F. Masuya, Y. Dou, and M. Ikeda-Saito, *J. Inorg. Biochem.*, **82**, 181–187 (2000).
68. M. H. Rakowsky, K. M. More, A. V. Kulikov, G. R. Eaton, and S. S. Eaton, *J. Am. Chem. Soc.* **117**, 2049–2057 (1995).

7 μ SR Studies of Molecular Dynamics in Organometallics

UPALI A. JAYASOORIYA

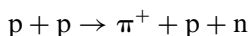
*School of Chemical Sciences and Pharmacy, University of East Anglia, Norwich
NR4 7TJ, UK*

1 INTRODUCTION

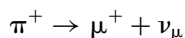
μ SR spectroscopies have unique advantages when it comes to the study of dynamic processes. Almost always it is the open shell compound, resulting from the addition of an electron during the spectroscopy, that is probed. The dynamic rates accessible to muon spectroscopies cover an exceptionally wide range bridging the gap between nuclear magnetic resonance (NMR) and quasielastic neutron scattering (QENS) time windows with a particularly good overlap of the latter. The present chapter will first introduce μ SR spectroscopy [1–3], followed by the examples of its application to the study of the dynamic processes in organometallic compounds [4–6].

2 MUON

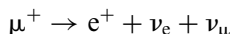
The muon, which belongs to the lepton family of fundamental particles, is the dominant constituent of the cosmic rays arriving at sea level, with roughly one muon per square centimeter of the earth's surface, every minute [7]. However these muon fluxes are insufficient for muon spectroscopy and hence the need for higher intensities of muons that require the development of particle accelerators. The process of muon generation involves the bombardment of a light element target such as graphite with a high energy proton beam, produced using a synchrotron or a cyclotron. This generates pions (π^\pm), which have a radioactive half-life of 26.03 ns.



Muons are the radioactive decay products of the pions.



where ν_μ is a muon-neutrino. (Only the positive muon, which is the more commonly used spectroscopic probe of condensed matter research, is discussed in this article.) This being a two body decay, by selecting pions that are at rest in the production target at the time of decay, it is possible to produce muon beams of almost 100 % spin polarization. The muons (with the well-defined spin direction) are then stopped in the sample of interest, where they precess in the local magnetic fields within the sample, prior to radioactive decay after a mean lifetime $\tau_\mu = 2.2 \mu\text{s}$, to a positron and two neutrinos.



This decay process is mediated by the ‘weak interaction’, thus involves no conservation of parity, and as a consequence the emitted positron emerges predominantly along the direction of the muon spin at the moment of decay [8]. The decay positrons are easily detected, as sparks of light in scintillators placed around the sample, and give the direction of the muon spin at the moment of decay. This therefore provides a way of monitoring the evolution of the muon spin well within the sample, and is the basis of μSR .

3 MUON IN MATTER

Muons, when implanted into matter, may exist in three forms. A muon on its own as the positive ion, mimicking the interstitial proton, precessing in the local magnetic fields is one of the most sensitive microscopic magnetometers available. It may pick up an electron and form muonium, the analogue of a hydrogen atom. The muonium thus formed may then add to unsaturated centers in the molecules of the sample to form muoniated radical species that are charge neutral. The interaction of the muon with the unpaired electron is the main hyperfine interaction that is probed in μSR of such radical species. There is also the possibility of the addition of the bare muon to molecules, analogous to protonation, giving a positively charged muonated species.

What happens to the muon from the moment of implantation into the sample? The implanted muon rapidly loses energy first by ionization of atoms and scattering of electrons followed by a series of electron capture and loss reactions within about a nanosecond of implantation. At the end of the radiolysis track, the muon/muonium still has sufficient energy to propagate a distance of about $1 \mu\text{m}$ through the sample, before any data acquisition can commence. Therefore the region of the sample measured is further down stream from any region of radiation damage [9].

A comparison of the properties of the muon with that of the electron and proton shows that the positive muon can be considered as a light proton, with approximately 1/9th the mass of a proton, Table 7.1. This analogy is further

Table 7.1 Properties of the electron, muon and proton

	Charge/unit of electronic charge	Spin	Mass	Magnetic moment	Magnetogyric ratio, $\gamma/2\pi$ (kHz G ⁻¹)	Lifetime (μ s)
e	-1	$\frac{1}{2}$	$m_e = 0.51$ MeV	$657 \mu_p$	2800	∞
μ	± 1	$\frac{1}{2}$	$207 m_e = 105.7$ MeV $= 0.113 m_p$	$3.18 \mu_p$	13.5	2.19
p	+1	$\frac{1}{2}$	$1836 m_e = 938$ MeV	μ_p	4.26	∞

Table 7.2 Muonium as an isotope of hydrogen

Isotope	Mass (m_e)	Reduced mass (m_e)	Bohr radius (nm)	Ionization energy (eV)
Tritium (^3H)	5498	0.9998	0.05290	13.603
Deuterium (^2H)	3675	0.9997	0.05293	13.602
Hydrogen or protium (^1H)	1847	0.9995	0.05292	13.599
Muonium (Mu)	208	0.9952	0.05315	13.541

reinforced by a comparison of the properties of muonium (μ^+e^-) with that of hydrogen and other isotopes as shown in Table 7.2. The close similarity of the reduced masses, Bohr radii and the ionization energies clearly justifies muonium's claim to be a light isotope of hydrogen (or protium). The light mass of muonium manifests itself, for example, with strong quantum tunneling effects and some of the largest kinetic isotope effects observed up to date [10].

In materials containing molecules with unsaturated centers, muonium that is formed at the end of the radiation track can react chemically to give radical species. The simplest case of a reaction with a double bond is illustrated in Figure 7.1 where the addition of muonium opens the carbon-carbon double bond to give a C-Mu bond and a radical electron.

In its simplest form μ SR is essentially the study of the interaction between the resulting unpaired electron and the muon nucleus, similar to electron nuclear

**Figure 7.1** Muonium addition to an ethene molecule.

double resonance, ENDOR. The definition of the acronym μ SR was given in the first issue of the μ SR Newsletter in 1974 as: ‘ μ SR stands for **M**uon **S**pin **R**elaxation, **R**otation, **R**esonance, **R**esearch or what have you. The intention of the mnemonic acronym is to draw attention to the analogy with NMR and ESR, the range of whose applications is well known. Any study of the interactions of the muon spin by virtue of the asymmetric decay is considered μ SR, but this definition is not intended to exclude any peripherally related phenomena, especially if relevant to the use of the muon’s magnetic moment as a delicate probe of matter.’

Out of the many variants of μ SR, it is the Muon Spin Relaxation that has been utilized up to now for the study of dynamic processes in organometallic systems, and therefore only this aspect will be discussed here. Interested readers should find ample descriptions of the other aspects of μ SR in the references provided at the end of this chapter. For the unpaired electron occupying a 1s hydrogenic orbital about the muon, the electron spin **S** and muon spin **I** are coupled by a scalar product to give the Hamiltonian for the so-called hyperfine, Fermi or contact interaction.

$$H = Ah \mathbf{S} \cdot \mathbf{I}$$

This magnetic interaction, between the muon and the electron for the spherically symmetrical s state, sums to zero except where the electronic wavefunction overlaps the nucleus, hence the name ‘contact interaction’. Therefore the resulting hyperfine interaction constant, *A*, is a measure of the electron density at the nucleus.

The hyperfine constant for the free-atom or vacuum-state muonium is, $A_0 = 4.46$ GHz. This is approximately equal to the value for hydrogen, when scaled by the ratio of magnetic moments of the muon and the proton, i.e. 3.18. This implies essentially the same electron spin density at the nucleus for muonium and hydrogen, providing further justification for considering muonium as an isotope of hydrogen.

Molecular dynamics information from spin resonance spectroscopies is obtained by the measurement of the spin–lattice relaxation contribution. Spin–lattice relaxation information can be extracted from longitudinal field μ SR experiments while the transverse field experiments provide information on spin–spin relaxation.

4 EXPERIMENT

The experimental arrangement for a longitudinal field experiment is shown as a schematic in Figure 7.2. What follows is based on the discussions of Cox [1,11] on the theoretical aspects of longitudinal field relaxation of muon spins of most relevance to the present topic.

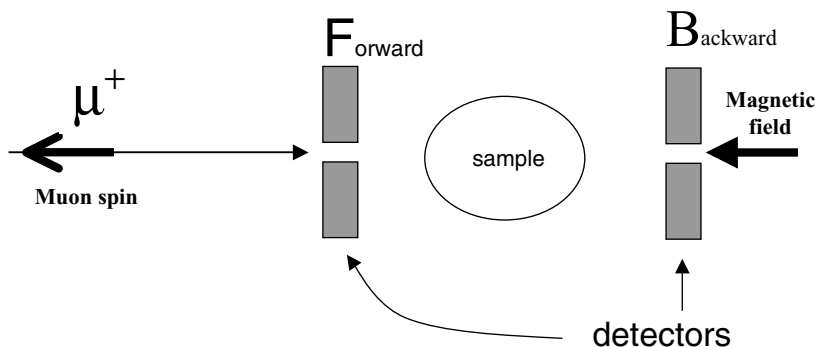


Figure 7.2 A schematic of the longitudinal field μ SR experimental setup. Note that the direction of muon spin polarization is opposite to the direction of propagation.

5 MUON IN A LONGITUDINAL MAGNETIC FIELD

Some of the important aspects may be demonstrated by considering the simplest case of a single muon in a longitudinal magnetic field. This is similar to any spin $\frac{1}{2}$ particle such as an electron or a proton, and the energetics of such a situation are shown in Figure 7.3. The energy difference between the spin-up and spin-down states is the so-called Zeeman energy and is given by the following, two equivalent, expressions.

$$\delta E = g_{\mu} \beta_n B \tag{7.1}$$

$$\delta E = \hbar \gamma_{\mu} B \tag{7.2}$$

where the muon g -factor is similar to that of the electron and is close to 2, β_n is the nuclear magneton and $\gamma_{\mu} \approx 2\pi \times 13.6 \text{ kHz/G}$ is the magnetogyric ratio. Note that the latter is specific to the muon and is 3.18 times the proton value.

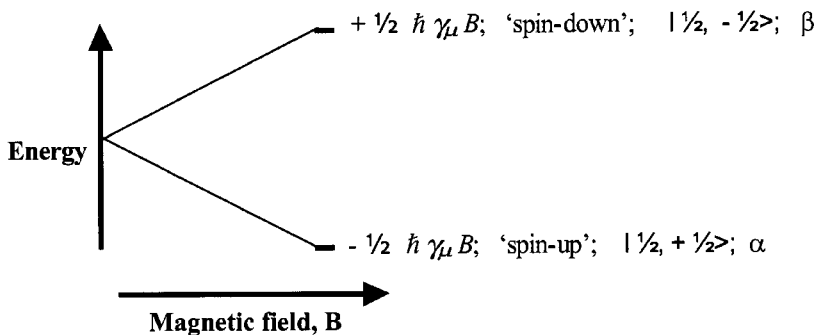


Figure 7.3 Energy level splittings (Zeeman energies) of a muon in a magnetic field. Also indicated are the common notations used for these levels [12].

The so called ‘surface muon’ beams, where the beam energies are ca 4 MeV, are almost 100 % spin polarized. If the fractional populations of the Zeeman energy levels shown in Figure 7.3 are indicated by n_- and n_+ , at the time of implantation into the sample these populations are either $n_- = 1$ and $n_+ = 0$ or $n_- = 0$ and $n_+ = 1$, depending on the direction of the longitudinal magnetic field with respect to the muon spin direction. The net polarization:

$$P = \frac{n_- - n_+}{n_- + n_+} = \pm 1 \quad (7.3)$$

Compare this with the situations encountered with EPR and NMR (except with dynamic nuclear polarization) where it is the difference in population between these levels at thermal equilibrium that is relevant. Then the population differences are given by the Boltzmann factor. Thus,

$$\frac{n_+}{n_-} = \exp\left(\frac{-\delta E}{k_B T}\right) \quad (7.4)$$

and in terms of the net polarization,

$$P_\infty = \tanh\left(\frac{h\gamma_\mu B}{4\pi k_B T}\right) \quad (7.5)$$

Thermal equilibrium polarization is very small, because the Zeeman energy is very much smaller than the thermal energy. Therefore this equation may be approximated to

$$P_\infty \approx \frac{h\gamma_\mu B}{8\pi k_B T} \quad (7.6)$$

The thermal equilibrium polarization given by this formula is negligibly small when compared to the almost 100 % starting polarization. For example, at room temperature and at a magnetic field of 1 T, thermal equilibrium polarization $P \approx 0.0005\%$. Therefore from the moment of implantation with almost 100 % polarisation, the muons will try to attain the thermal equilibrium value of almost zero polarization. However, this would require a mechanism that would assist the muon spins to flip in a longitudinal magnetic field. In a purely longitudinal field of sufficient magnitude to be away from any resonance conditions, and in the absence of any other molecular processes, one would not expect any observable relaxation. Of the several types of processes that may influence the transitions between muon spin-down and spin-up eigenstates, only molecular dynamics will be discussed here.

Assuming the upward and downward transition probabilities to be W_\uparrow and W_\downarrow respectively, it is possible to obtain the type of relaxation to be expected by writing the simple rate equations for the change of the two populations.

$$\frac{dn_+}{dt} = -W_\downarrow n_+ + W_\uparrow n_- \quad (7.7)$$

$$\frac{dn_-}{dt} = +W_\downarrow n_+ - W_\uparrow n_- \quad (7.8)$$

Equations (7.7), (7.8) and (7.3) together give

$$\frac{d}{dt}\delta P = -(W_{\uparrow} + W_{\downarrow})\delta P \tag{7.9}$$

where $\delta P = P(t) - P_{\infty}$ is the difference between the instantaneous and thermal equilibrium polarization. Solving this differential equation gives,

$$\begin{aligned} \delta P(t) &\propto e^{-(W_{\uparrow}+W_{\downarrow})t} \\ &= e^{-\lambda t} \end{aligned} \tag{7.10}$$

Therefore a simple exponential decay is expected with a relaxation rate λ , equal to the sum of the upward and downward transition probabilities. One can also define a relaxation time, in analogy with notation used in conventional magnetic resonance, as $T_1 = \lambda^{-1}$. Under experimental conditions it is often necessary to consider situations where the initial polarization is less than 100%. This may be represented by the following equation.

$$P(t) = p_1 G_{\parallel}(t) + p_2 \tag{7.11}$$

Or in terms of the asymmetries or amplitudes of the μSR signals

$$a(t) = a_1 G_{\parallel}(t) + a_2 \tag{7.12}$$

where $G_{\parallel}(t)$ is called the *relaxation function*, defined so that $G_{\parallel}(0) = 1$, the subscript specifying that this is longitudinal relaxation.

For a molecular dynamic process to influence the relaxation of a muon spin, it is essential to satisfy two main conditions. First it should cause some fluctuation of the muon’s magnetic environment. Further these fluctuations must have a component transverse to the main or static average longitudinal field because any fluctuations parallel to the muon beam polarization is not effective in bringing about a transition between the two stationary states of the muon shown in Figure 7.3. The second condition is the need for a quantum of energy equal to the Zeeman splitting, so as to bring about a transition between the spin-down and spin-up states. The implication is that the power spectrum of the molecular fluctuations must contain a significant density of states at the Larmor frequency, the frequency corresponding to the Zeeman splitting.

$$\omega_{\mu} = \delta E / \hbar = \gamma_{\mu} B \tag{7.13}$$

The time-dependent perturbation theory in the form of the Fermi’s Golden Rule may now be used to obtain W the transition probability between the two spin states, assuming $W_{\uparrow} = W_{\downarrow}$ for simplicity, so that $\lambda = 2W$.

$$W \approx (\gamma_{\mu} B_{\perp})^2 J(\omega_{\mu}) \tag{7.14}$$

where B_{\perp} is the rms amplitude of transverse fluctuations of the local field and $J(\omega_{\mu})$ is the spectral density function or power spectrum of the fluctuations. Spin-lattice relaxation samples this spectrum at the Larmor frequency,

$\omega = \omega_\mu$. The usual form of the spectral density function is a simple Lorentzian, characterized by a single correlation time τ_c .

$$J(\omega) = \frac{\tau_c}{\pi(1 + \omega^2\tau_c^2)} \quad (7.15)$$

This gives the relaxation rate as,

$$\lambda = T_1^{-1} \propto (\gamma_\mu B_1)^2 \frac{\tau_c}{1 + \omega_\mu^2 \tau_c^2} \quad (7.16)$$

This was first formulated by Bloembergen, Purcell and Pound [13] and is commonly known as the BPP expression.

6 MUON-ELECTRON (MUONIUM LIKE) SYSTEM

Consider the case of an isotropic, static (or time averaged) hyperfine interaction between the muon and the electron, that is represented by the following Hamiltonian, which includes the Zeeman energy terms of the electron and the muon.

$$H = Ah \mathbf{S} \cdot \mathbf{I} + \hbar\omega_e S_z + \hbar\omega_\mu I_z \quad (7.17)$$

Cox [11] has discussed the relaxation mechanisms in this type of system in detail with experimental results and simulations to clearly demonstrate the various aspects. The most likely candidate that would account for the relaxation due to molecular dynamics is shown to be the fluctuation of the hyperfine interaction or the so called Fermi contact term. The hyperfine constant is in fact a thermal average over the different vibrational modes of the molecule. Therefore the molecular vibrations or librations will modulate the hyperfine constant. Hyperfine interaction is in general anisotropic, except in the gas or liquid state when the fast molecular tumbling averages out the anisotropy leaving the isotropic part. One can think of two separate mechanisms of relaxation depending on the modulation of either the isotropic part or the anisotropic part.

Modulation of the *isotropic* hyperfine interaction has the same spin operator ($\mathbf{I} \cdot \mathbf{S}$) as the time-average hyperfine interaction, thus making this mechanism ineffective in zero field. In an applied field it will only induce the flip-flop transition $2 \leftrightarrow 4$ (Figure 7.4). The contribution of this mechanism to the observed relaxation rate begins by increasing quadratically with field, reaching a plateau region until eventually quenched by the $J(\omega_{2 \leftrightarrow 4})$ spectral density term. The modulation of the *anisotropic* hyperfine interaction was shown to induce the other transitions $1 \leftrightarrow 2$, $1 \leftrightarrow 4$, $2 \leftrightarrow 3$ and $3 \leftrightarrow 4$ (Figure 7.4).

Cox [11] has also shown that, even though the μ SR response is in principle a superposition of several exponential terms, in practice they appear in combinations such that, whenever the eigenvalues differ greatly in magnitude, only one of these has significant weight. Alternatively, when the different eigenvalues have

comparable weight, they have very similar magnitudes. Therefore the muon relaxation function is in practice indistinguishable from a single exponential from which one can extract an effective relaxation rate $\lambda = T_1^{-1}$.

7 MOLECULAR DYNAMICS

Molecular dynamic information is obtained from a study of the variation of the muon spin relaxation rate with temperature. Reorientation depolarizes the muons by causing anisotropic or dipolar terms in the electron–muon hyperfine interaction to fluctuate. Peaks in the relaxation rate (analogous to T_1 minima in NMR) occur when the reorientation rate matches the frequency of the dominant transition between the coupled muon–electron spin states. The correlation time, τ , at each temperature can be obtained using the derivations of Cox and Sivia [14]. The measured relaxation rate λ is given by the following expression:

$$\lambda = 2(2\pi\delta A)^2 \frac{x^2}{1+x^2} \frac{\tau}{1+\omega^2\tau^2} \tag{7.18}$$

where $(2\pi\delta A)^2 x^2/(1+x^2)$ is the matrix element responsible for the transition, x is the reduced field in units of hyperfine field, and $\tau/(1+\omega^2\tau^2)$ is the spectral density function. The transition frequency $\omega (= 2\pi A\sqrt{1+x^2})$ used to extract the correlation times τ is that between states $|2\rangle = \cos\theta|+-\rangle + \sin\theta|-+\rangle$ and $|4\rangle = \cos\theta|-+\rangle - \sin\theta|+-\rangle$, in the Breit–Rabi diagram, Figure 7.4. This is the only transition induced in the spin relaxation mechanism involving modulation of the isotropic hyperfine interaction. Thus the relaxation rate can be described by a single transition probability, $\omega_{2\leftrightarrow 4}$. The modulation of the anisotropic hyperfine interaction makes other transitions possible. However, it is possible to determine unique activation parameters so long as one transition is dominant.

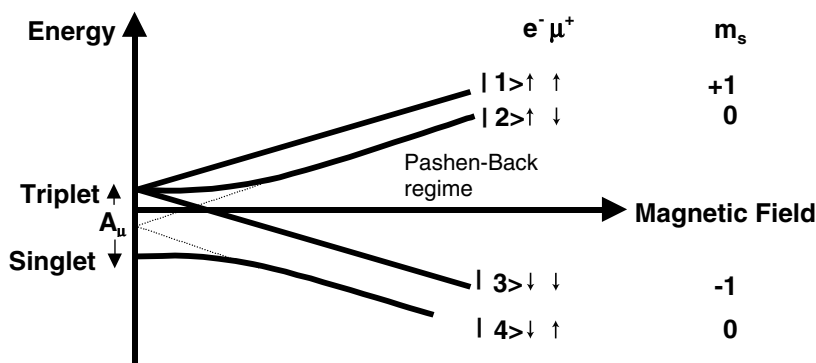


Figure 7.4 Breit–Rabi energy level diagram for a muonium like (or a muoniated radical) system. A_μ is the muon–electron hyperfine constant and m_s is the total quantum number.

If the process under scrutiny shows Arrhenius behavior, a plot of $\ln(1/\tau)$ versus $1/T$ should reveal the activation parameters. As the activation energy is determined from the gradient of such a plot, its value is independent of the chosen transition frequency, but the attempt frequency will vary.

An approximate value of the hyperfine coupling constant and hence the type of radical formed can be deduced using repolarization curves. These are plots of the initial amplitude of the muon relaxation signal, which increases as the hyperfine interaction is decoupled by an applied magnetic field. However, these estimates can be distorted by anisotropic terms and motional effects and more accurate values of the hyperfine coupling constants would be given by TF- μ SR (transverse field) and ALC- μ SR (avoided level crossing) measurements.

8 STUDIES OF ORGANOMETALLICS

8.1 TETRAPHENYL METALS

The first studies of molecular dynamics of organometallics using μ SR were by Stride [15], who investigated the series of tetraphenyl metals, $M(C_6H_5)_4$ where $M = Pb, Sn, Ge$. Clear maxima were observed when longitudinal muon spin relaxations were plotted against sample temperature, Figure 7.5. Repolarization curves showed the muonium addition sites to be the phenyl rings. Further, these spin-lattice relaxation processes were found to show Arrhenius behavior, and the activation parameters estimated, Figure 7.6. It was also found that the activation energies correlated very well with the size of the central atom, Figure 7.6 [4,11].

However, both structural data and NMR data of these compounds show that the phenyl groups are too restricted for these μ SR measured values to correspond to the phenyl group rotations if these are assumed to be unchanged in their bonding in going from the closed shell compound to the open shell radical. The μ SR investigations of other organometallics since these early studies now appear to throw light on this problem, to which we return later in this chapter.

8.2 BENZENE CHROMIUM TRICARBONYL

The first publication in a journal of μ SR of organometallics was in 1997 by Jayasooriya *et al.* [4], where studies of tetraphenyl lead, benzene chromium tricarbonyl and ruthenocene were discussed.

The most complete conclusions were drawn from the results on benzene chromium tricarbonyl. This compound crystallizes in the monoclinic space group $P2_1/m$ with two symmetry related molecules per unit cell, with almost undistorted benzene rings at room temperature [16]. Measurements at 78 K using both X-ray and neutron diffraction showed a lowering of the benzene

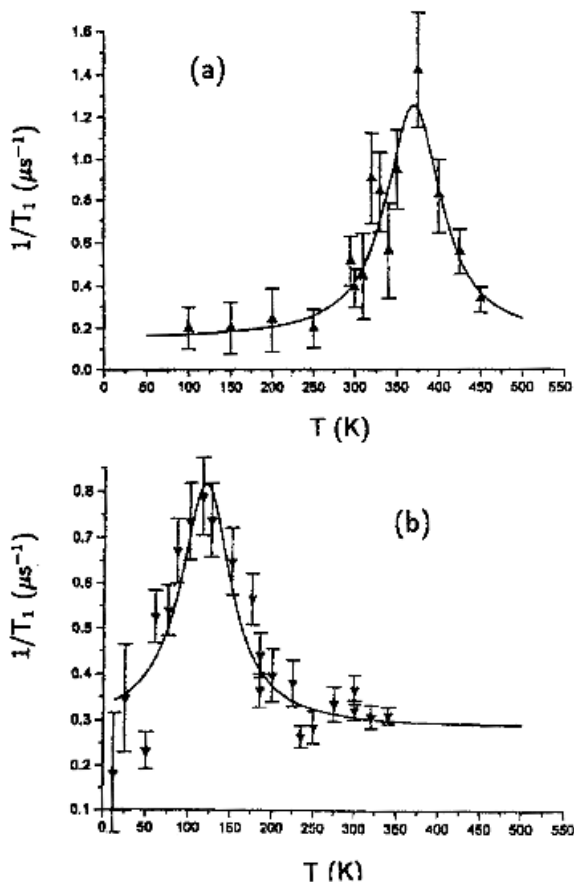


Figure 7.5 Temperature dependences of the muon spin relaxation rate in (a) $\text{Ge}(\text{C}_6\text{H}_5)_4$ and (b) $\text{Pb}(\text{C}_6\text{H}_5)_4$, showing the T_1 minimum condition or the spin-lattice relaxation maximum [15].

ring symmetry to C_{3v} with the hydrogen atoms displaced by an average of 0.03 Å towards the chromium atom [17]. No evidence for any phase changes was found using heat capacity measurements.

A magnetic field of 1500 G was used in the μ SR measurements, high enough to be in the Paschen-Back regime, thus avoiding any level crossings and other processes that would complicate the mixing between the energy levels. It was shown that it is possible to treat the muon spin relaxation measurements made under these conditions with the Cox and Sivia [14] approach described above [18]. A minimum of two relaxations was found to be necessary to simulate the observed muon spin relaxation data. This suggests the generation of two distinct radical species under muon implantation. The slower relaxing of these

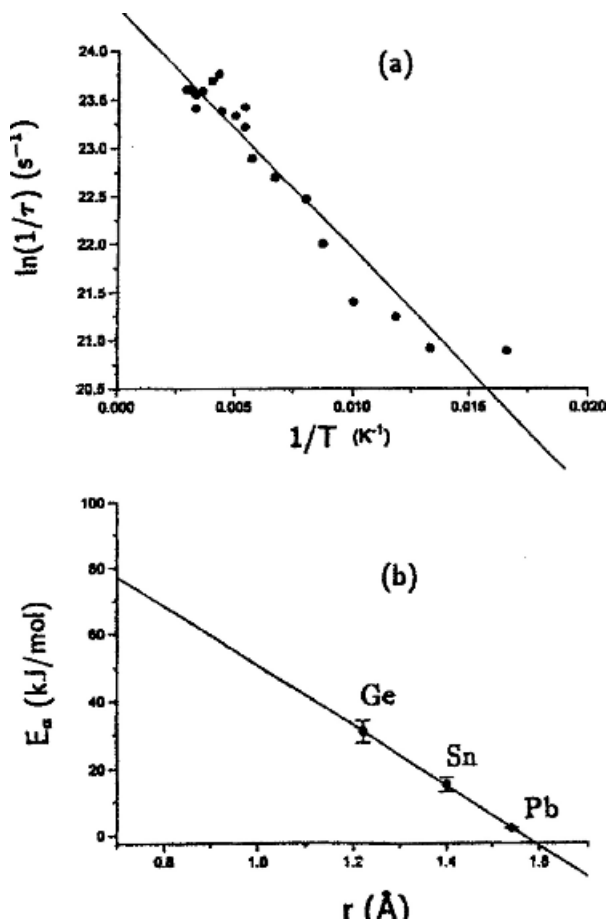


Figure 7.6 (a) Arrhenius plot from the muon spin relaxation rates shown in Figure 7.5 for $\text{Pb}(\text{C}_6\text{H}_5)_4$. (b) The correlation of activation energies calculated with muon spin relaxation with the size of the central atom for the tetraphenyl metallates [15].

two components was found to repolarize at a hyperfine field corresponding to an adduct to the benzene ring, and showed a peak in the temperature dependence of the relaxation at a temperature of about 300 K. The Arrhenius plot of estimated correlation times against the reciprocal of the sample temperature for this relaxation maximum was shown to be in excellent agreement with that for benzene ring rotation independently measured from quasielastic neutron scattering, QENS, Figure 7.7 [4,19]. Note that the range of correlation times covered by μSR in this case is from ca 10^{-8} to 10^{-11} s. This when compared with the range for QENS of ca 10^{-10} to 10^{-11} s clearly illustrates one of the advantages of the μSR technique.

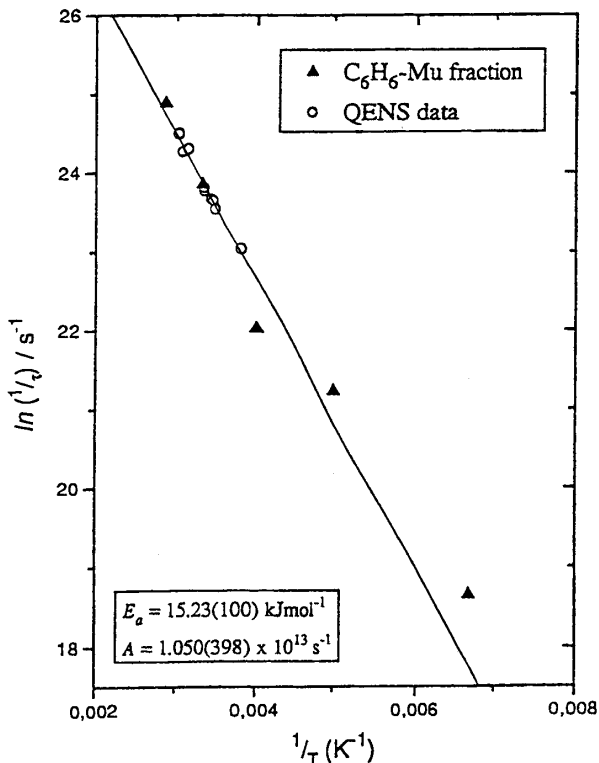


Figure 7.7 Arrhenius plot of reciprocal correlation times extracted from the longitudinal muon spin relaxation measurements of benzene chromium tricarbonyl compared with QENS data [4]. Reproduced from *Hyperfine Interactions* **106**, 27–32 (1997), U. A. Jayasooriya, J. A. Stride, G. M. Aston, G. A. Hopkins, S. F. J. Cox, S. P. Cottrell and C. A. Scott, Figure 2, © Kluwer, with kind permission of Kluwer Academic Publishers.

The faster relaxing component was not further investigated at the time [18]. These additional radicals that are formed showing Arrhenius parameters which have no closed-shell counterparts are discussed later in this chapter.

8.3 CYCLOPENTADIENYL MANGANESE TRICARBONYL

Similar set of experiments with a polycrystalline sample of cyclopentadienyl manganese tricarbonyl has shown very similar patterns of data to the above compound [18]. Longitudinal field relaxation of muons implanted into cyclopentadienyl manganese tricarbonyl was studied within the field range 0–400 mT at 300 K, and the temperature range 375–25 K at an applied field of 200 mT. The latter showed a relaxation maximum around 275 K, which was shown to be due to an Arrhenius process with an activation energy of

7.7 ± 0.6 kJ mol⁻¹ and an attempt frequency of 1.50×10^{12} s⁻¹. These values are to be compared with the literature values using other techniques that measure the cyclopentadienyl ring rotation. NMR spin lattice relaxation time measurements by Gilson *et al.* [19] gave a value of 7.24 kJ mol⁻¹ of activation energy for the cyclopentadienyl ring rotation and an attempt frequency of 1.55×10^{12} s⁻¹. The μ SR estimate is also close to a value estimated from Raman spectroscopy [20] of 10 kJ mol⁻¹, but lower than a somewhat tentative QENS estimate [21] of 16.8 kJ mol⁻¹ using only three temperatures. Therefore the μ SR measurements in this case are clearly assigned to the restricted rotation of the cyclopentadienyl ring.

8.4 RUTHENOCENE

The data reported [4] for the metallocene ruthenocene, show that there are two distinct relaxations present, suggesting the presence of at least two different muoniated radicals. The amplitude of the slower relaxing component was found to repolarize at ca 250 G, suggesting a ring adduct, while the faster relaxing component repolarizes at a rather high field of ca 600 G. Muon spin relaxation of this metallocene was also studied all the way to a high field of 4 T, and two peaks were observed [11,18]. Cox in his review of 'muon spin relaxation studies of interstitial and molecular motion', has shown that motional perturbations of both the isotropic as well as the anisotropic parts of the hyperfine interaction are needed to simulate both these peaks [11]. This simulation gave two distinct correlation times for the two peaks, 100 ps for the broad peak ca 60 mT, and a value of 2 ns for the sharper peak ca 2 T. Most recent work on the metallocene ferrocene, seems to shed more light on these observations.

8.5 FERROCENE

The most detailed investigation of muon implantation into an organometallic is that of the classic metallocene ferrocene [5,6]. The field of organometallic chemistry was transformed by the recognition in 1952 of the 'sandwich' structure of what has become the most famous of this family of compounds, dicyclopentadienyl iron or ferrocene [22]. A wealth of knowledge now exists on its structure and dynamics, including NMR [23] and QENS [24] studies, and for that reason ferrocene was chosen to explore the use of μ SR for the investigation of organometallics. Ferrocene undergoes several phase transitions, with the most important to the reported μ SR studies being that at 163.9 K [25]. X-ray crystal structures done at 295 and 173 K show the high temperature phase to be monoclinic, space group $P2_1/a$ with $Z = 2$. This phase was found to be rotationally disordered, and the transition to the low temperature phase takes a long time (ca 1h) to achieve. μ SR investigation of molecular dynamics of the high temperature phase was reported in Ref. 5, and the findings are summarized below.

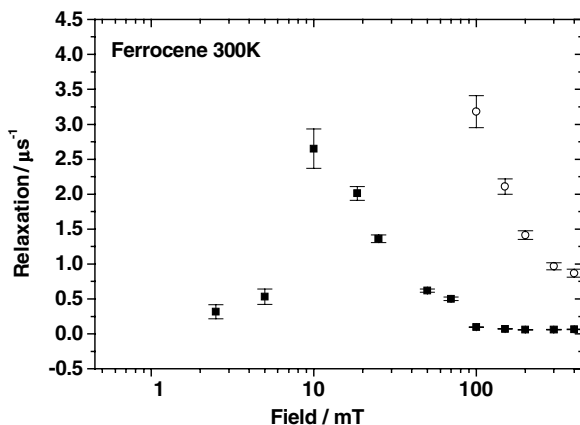


Figure 7.8 Longitudinal muon spin relaxation versus magnetic field for polycrystalline ferrocene at 300 K, showing the two distinct relaxations [5,6]. Reproduced from U. A. Jayasooriya *et al.*, *Appl. Magn. Resonance* **13**, 165–171 (1997) with permission from Springer–Verlag KG.

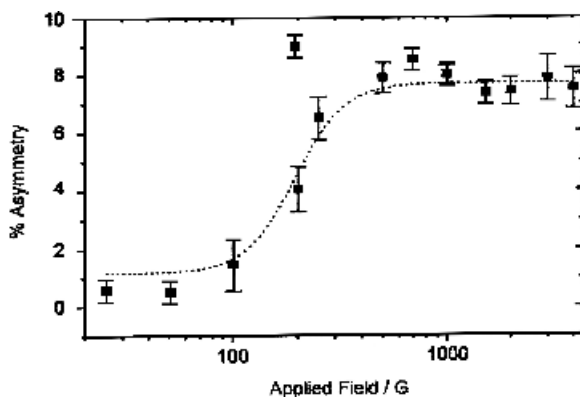


Figure 7.9 Plot of initial asymmetry against the applied field for the slow relaxing component of the longitudinal muon spin relaxation of ferrocene measured at 300 K [5,6]. Reproduced from U. A. Jayasooriya *et al.*, *Appl. Magn. Resonance* **13**, 165–171 (1997) with permission from Springer–Verlag KG.

A minimum of two distinct relaxations were needed to simulate the muon spin relaxation data up to ca 400 mT, Figure 7.8. The slower relaxing component was found to repolarize at ca 20 mT, Figure 7.9, a hyperfine field similar to that observed for muoniated benzene and therefore assigned to muonium addition to the cyclopentadienyl ring [26].

The temperature dependence of this slower relaxing component showed a relaxation maximum around 225 K from which the extracted correlation times

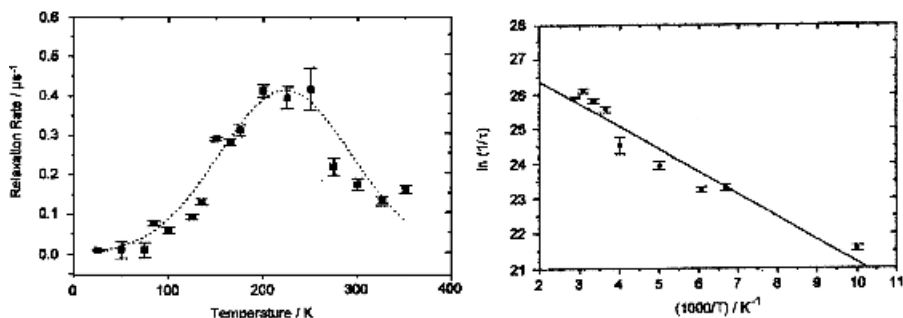


Figure 7.10 Temperature dependence of the longitudinal muon spin relaxation of the slow relaxing component of ferrocene measured at 200 mT (on the left). An Arrhenius plot of inverse correlation time giving the activation parameters of the dynamic process (on the right) [5,6]. Reproduced from U. A. Jayasooriya *et al.*, *Appl. Magn. Resonance* **13**, 165–171 (1997) with permission from Springer–Verlag KG.

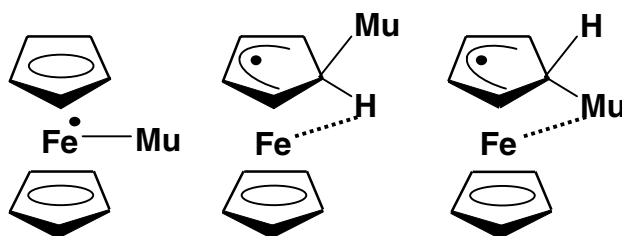


Figure 7.11 The metal and ring adducts of muoniated ferrocene.

indicated Arrhenius behavior giving an activation energy of $5.4 \pm 0.5 \text{ kJ mol}^{-1}$ and an attempt frequency (pre-exponential factor) of $(1.03 \pm 0.43) \times 10^{12} \text{ s}^{-1}$, Figure 7.10.

The activation parameters for the ring rotation in ferrocene have been estimated in the literature using NMR [23] and QENS [24]. Activation energies of 5.4 ± 0.5 and $4.4 \pm 0.5 \text{ kJ mol}^{-1}$, and an attempt frequency of 3.16×10^{12} and $1.25 \times 10^{12} \text{ s}^{-1}$ respectively were reported. Close agreement between these independently estimated values and those obtained from muon spin relaxation is evidence that the same dynamic process is measured in all three techniques.

The more detailed study [6] shows that there are three distinct radicals formed. Two with the muon located on a cyclopentadienyl ring, with either the muon or the hydrogen attached to the carbon being on the side of the iron atom. These two radicals are called ‘muon-agostic’ and ‘hydrogen-agostic’ respectively, Figure 7.11. The third radical is that where muonium is bonded directly to the iron atom. The latter is the first observed case of a muoniated radical where there is a muonium to metal bond. The faster relaxing component of the muon spin relaxation is assigned to that radical. Muon spin relaxation

versus temperature of this radical was also investigated and found to show a relaxation maximum, around 175 K, and Arrhenius behavior giving an activation energy of ca 2.43 kJ mol^{-1} and an attempt frequency of $2.56 \times 10^{11} \text{ s}^{-1}$. This is a most interesting observation, since it raises the question of what is the dynamic process that is measured in this case? Here the activation energy is almost half the value that is confidently assigned to the cyclopentadienyl ring rotation in ferrocene [6].

It should be remembered that it is a radical species that results from the addition of muonium to the close-shell compound that is studied in μ SR. In studies of molecular, 'whole body' dynamics where the muon appears to be an almost passive observer, it is the very light mass of the muon that makes possible for the observation of properties which are almost identical to those of the parent molecule. There are a number of such studies of organic systems [1]. μ SR studies of the dynamics of fullerenes C_{60} and C_{70} are particularly interesting examples of such whole body motions where the change in the moment of inertia because of the added muonium is negligible [27,28]. However the use of μ SR to study intramolecular dynamics presents at least two distinct scenarios.

- (1) The radical electron may have a *passive role* with regards to the dynamic process that is investigated. This will be due to this electron occupying an orbital, such as a *nonbonding* molecular orbital, that plays no role in bonding with respect to the bonds directly involved in this dynamic process.
- (2) The radical electron may have an *active role* with regards to the dynamic process that is investigated. This may be achieved by this electron occupying, either a *bonding* or an *antibonding* molecular orbital with respect to the bonds directly involved in this dynamic process.

In the case of ferrocene, there are several calculations in the literature of its molecular orbital energy levels [29]. There is a general consensus as to the energy ordering of the molecular orbitals up to the HOMO. However, the precise ordering of the LUMO and higher levels is still uncertain; with the most recent work having assigned the antibonding e_{1g} (xz , yz pair) as the LUMO, closely followed by the nonbonding e_{2u} pair localized within the cyclopentadienyl rings. It would not be surprising to see a modification of this energy ordering with muonium adduct formation. Therefore, the excellent agreement between the muon spin relaxation activation parameters of the ring adduct radical and those measured for the closed shell ferrocene itself using NMR and QENS spectroscopies is evidence for the occupation of a nonbonding orbital, with respect to the metal to ring bond, by the unpaired electron of the muonium adduct. This gives the assignment of the lowest partially occupied molecular orbital in the case of the muonium to cyclopentadienyl ring adduct to the nonbonding e_{2u} pair, Figure 7.12. This therefore is an example of the radical electron playing a *passive role*.

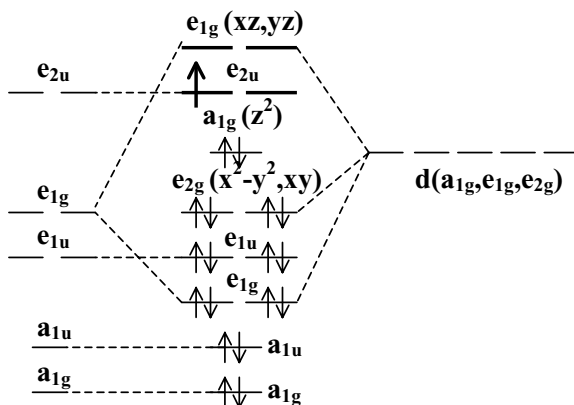


Figure 7.12 Approximate molecular orbital energy level diagram for ring adduct radicals.

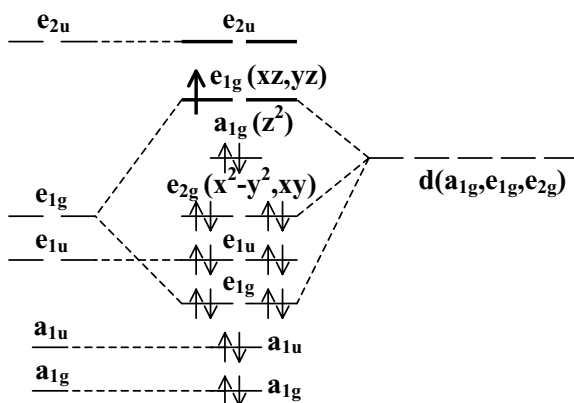


Figure 7.13 Approximate molecular orbital energy level diagram for metal adduct radical.

An assignment of the unpaired electron in the muonium to metal adduct radical to the antibonding $e_{1g}(xz, yz)$ orbitals is expected to result in a substantial reduction in the bonding between the iron atom and the rings. This then provides an explanation for the reduction of the activation energy for the ring rotation, which is almost halved in magnitude, as a result of the muonium addition to the metal atom, Figure 7.13. This therefore is an example of the radical electron playing an *active role*.

This investigation has also shown the importance of spin-orbit coupling in the case of the metal-Mu adduct, where strong orbital angular moments are expected for the case of electrons in transition metal atoms. Of particular interest in this case is an apparently subtle interplay between the molecular

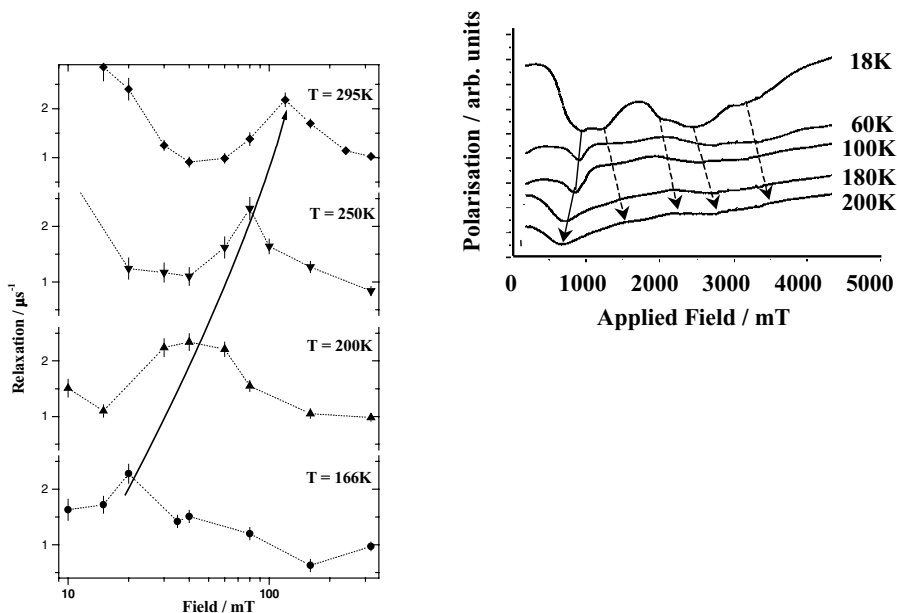


Figure 7.14 Field and temperature dependence of fast relaxing component (left). High-field time integral spectra at different temperatures (right). The errors in polarization measurements are within the width of the trace [6].

dynamics and the quenching of the spin-orbit coupling. An exceptional temperature dependence was observed between the two level crossing resonances of the metal-Mu adduct, Figure 7.14. This observation was explained by theory development which correlates the two extreme situations of complete ring localization at low temperature when the crystal field effects dominate and the completely free ring rotation at high temperatures when the e_{1g} (xz, yz) degeneracy is expected to be complete, when the spin-orbit coupling dominates, Figure 7.15. A change in sample temperature was found to probe a range of values of this correlation, in the case of ferrocene. This appears to be the first such observation of an interplay between spin-orbit coupling and molecular dynamics, and the accessibility of this phenomenon is a result of the time window of μ SR. One would anticipate the other metallocenes too to probe this correlation, probably different regions of it.

8.6 FERROCENE ENCAPSULATED IN ZEOLITE

There is much interest in the reorientation dynamics of guest molecules in zeolite hosts. This is mainly because the mobility of the guests is of importance to the catalytic properties of these materials. Kaiser and Gubbens [30] at TU-Delft have recently applied μ SR to the investigation of ferrocene encapsulated in

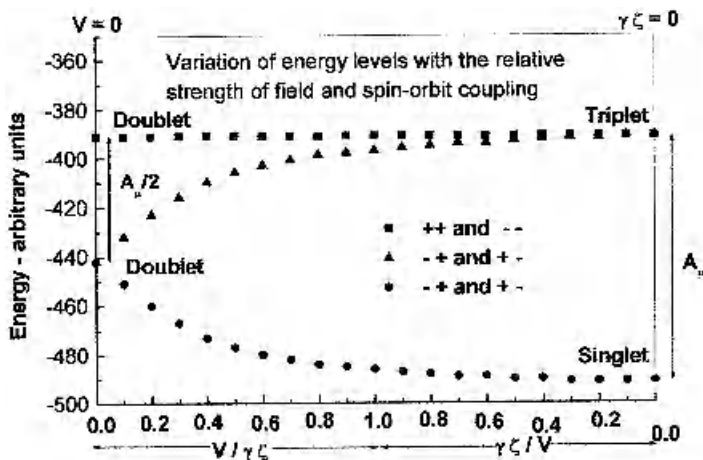


Figure 7.15 Energy level dependence on the interplay between spin-orbit coupling and crystal field effects [6].

KY zeolite. It was found that ferrocene loses its stability to air when encapsulated in zeolite readily oxidizing, when exposed to air, to give ferricinium ion. It was shown, by neutron diffraction measurements, that at saturation encapsulation there are two molecules of ferrocene per supercage of the zeolite [31]. Quasielastic neutron scattering experiments of zeolite-encapsulated ferrocene have shown [32] a fivefold jump orientation of the cyclopentadienyl rings around the symmetry axis of the ferrocene molecule with an activation energy of 5.96 kJ mol^{-1} , somewhat higher than the value of 4.4 kJ mol^{-1} reported from QENS measurements of pure ferrocene [24]. Longitudinal field muon spin relaxation measurements, however, have shown the cyclopentadienyl rings to be much more hindered when encapsulated giving an activation energy of $9.7 \pm 0.7 \text{ kJ mol}^{-1}$, compared with the μSR value for pure ferrocene of $5.4 \pm 0.5 \text{ kJ mol}^{-1}$, a significant increase [30].

The HOMO–LUMO energy gap of a material is one of the properties that will influence its chemical reactivity. Data from NMR and QENS measurements of the ring rotation dynamics of ferrocene will reflect only effects of any interaction of the ferrocene molecule with the zeolite cage up to the HOMO level of the ferrocene molecule. This is because the LUMO is empty of electrons and any interaction of this level with the zeolite cage orbitals, to a first approximation, will have no effect on the QENS measured dynamic parameters, unless electron density flows into this orbital from the zeolite host. Such a transfer of a small amount of electron density will explain the slightly higher activation energy measured by QENS for ferrocene when encapsulated in zeolite. However, the μSR measurements are made of a molecule of ferrocene with an additional electron introduced into the LUMO. Thus any interaction of the LUMO with the

cage orbital will show up more strongly, as an additional bonding interaction by the cyclopentadienyl ring, hence a substantial increase in the activation energy as observed. Therefore, μ SR measurements show a substantial interaction of the LUMO with the cage orbitals. Further this should result in a depression of the energy of the LUMO when in the zeolite cavity in comparison to that of pure ferrocene. This indicates a significant decrease in the HOMO–LUMO energy gap as a result of encapsulation, thus explaining the increase in reactivity of ferrocene when in the encapsulated state.

9 CONCLUSION

The examples where μ SR provides Arrhenius parameters similar in magnitude to those measured by NMR and QENS are summarized in Table 7.3. The μ SR measured dynamic process in all these cases is likely to be the same as that measured by the other two techniques, namely the metallocene (benzene or cyclopentadienyl) ring rotation. The detailed investigation of ferrocene illustrates how this can be rationalized on the basis of the occupancy of a nonbonding orbital, with respect to the dynamic process, by the unpaired electron of the radical species. These were named as the electron playing a *passive role*.

With the other examples such as the Mu–Fe adduct of ferrocene and all the tetraphenyl compounds, the μ SR measures unique dynamic processes which are only to be found in the radical species. Here the partially occupied molecular orbital by the additional electron is an antibonding orbital, thus reducing the strength of the bond involved. The only case that was studied in detail, ferrocene, illustrates the weakening of the iron to cyclopentadienyl ring by providing an activation energy closer to half that for the close shell molecule. Tetraphenyl metals must also belong to this category, where the unpaired electron plays an *active role* in reducing the strength of a bond between the central metal and a phenyl group. This bond will then elongate so that the phenyl group with the attached muon will move away from the highly crowded four-phenyl shell. The Arrhenius parameters that were measured using μ SR are therefore

Table 7.3 Arrhenius parameters measured by μ SR, NMR and QENS

Compound	μ SR	NMR	QENS
Benzenechromium tricarbonyl [4]	$E_a = 15.23 \text{ kJ mol}^{-1}$ $A = 1.05 \times 10^{13} \text{ s}^{-1}$	$E_a = 17.6 \text{ kJ mol}^{-1}$ $A = 2.38 \times 10^{13} \text{ s}^{-1}$	$E_a = 15.5 \text{ kJ mol}^{-1}$ $A = 1.04 \times 10^{13} \text{ s}^{-1}$
Cyclopentadienyl- manganese tricarbonyl [18]	$E_a = 7.69 \text{ kJ mol}^{-1}$ $A = 1.05 \times 10^{12} \text{ s}^{-1}$	$E_a = 7.2 \text{ kJ mol}^{-1}$ $A = 1.5 \times 10^{12} \text{ s}^{-1}$	$E_a = 16.8 \text{ kJ mol}^{-1}$ $A = 4.21 \times 10^{13} \text{ s}^{-1}$
Ferrocene [5]	$E_a = 5.39 \text{ kJ mol}^{-1}$ $A = 1.03 \times 10^{13} \text{ s}^{-1}$	$E_a = 5.3 \text{ kJ mol}^{-1}$ $A = 3.2 \times 10^{12} \text{ s}^{-1}$	$E_a = 4.4 \text{ kJ mol}^{-1}$ $A = 1.2 \times 10^{12} \text{ s}^{-1}$

those encountered by the phenyl group with this elongated metal–phenyl bond. Even the relatively small number of studies that report μ SR measurements of molecular dynamics shows that this is a very powerful technique, which can produce almost unique data on radical species, not easily accessible to other techniques.

10 ACKNOWLEDGEMENTS

Contributions to μ SR research on molecular dynamics in my group by the following colleagues are gratefully acknowledged. Steve Cox, John Stride, Gina Aston, Penny Hubbard, Roger Grinter, Steve Cottrell, Ivan Reid and Dierk Herlach. EPSRC is thanked for funding, and ISIS-RAL and PSI for generous beamtime and the facilities to do the experiments.

11 REFERENCES

1. See for example: *Muon Science. Muons in Physics, Chemistry and Materials*, edited by S. L. Lee, S.H. Kilcoyne, and R. Cywinski, Proceedings of the Fifty First Scottish Universities Summer School in Physics and A NATO Advanced Study Institute, Institute of Physics, Bristol, 1998.
2. E. Roduner, The positive muon as a probe to free radical chemistry, *Lecture Notes Chem.* **49**, (1988).
3. S. J. Blundell, Spin-polarized muons in condensed matter physics, *Contemp. Phys.*, **40**, 175–192 (1999).
4. U. A. Jayasooriya, J. A. Stride, G. M. Aston, G. A. Hopkins, S. F. J. Cox, S. P. Cottrell, and C. A. Scott, Muon spin relaxation as a probe of molecular dynamics of organometallic compounds, *Hyperfine Interactions*, **106**, 27–32 (1997).
5. U. A. Jayasooriya, G. M. Aston, and J. A. Stride, Molecular dynamics of organometallic compounds using μ SR, *Appl. Magn. Reson.* **13**, 165–171 (1997).
6. (a) U. A. Jayasooriya, R. Grinter, P. L. Hubbard, G. M. Aston, J. A. Stride, G. A. Hopkins, L. Camus, I. D. Reid, S. F. J. Cox, and S. P. Cottrell, Muon implantation studies of organometallics: ferrocene, *J. Chem. Phys.* submitted (b) P. L. Hubbard, PhD Thesis, University of East Anglia, 2003.
7. C. Caso *et al.*, The 1998 Review of Particle Physics., *Eur. Phys. J.*, **C3**, 1 (1998).
8. R. L. Garwin, L. M. Lederman, and M. Weinrich, *Phys. Rev.*, **105**, 1415 (1957).
9. J. Chappert, in *Muons and Pions in Materials Research*, edited by J. Chappert and R.I. Grynspan, Elsevier Amsterdam, 1984.
10. E. Roduner and K. Münger, *Hyperfine Interactions*, **17–19**, 793 (1984).
11. S. F. J. Cox, Muon spin relaxation studies of interstitial and molecular motion, *Solid State Nucl. Magn. Reson.*, **11**, 103–121 (1998).
12. A. Carrington and A. D. McLaclan, *Introduction to Magnetic Resonance, with Applications to Chemistry and Chemical Physics*, Harper International, 1967, pp. 3–5.
13. N. Bloembergen, E. M. Purcell, and R. V. Pound, *Phys. Rev.* **73**, 679 (1948).
14. (a) S. F. J. Cox and D. S. Sivia, *Hyperfine Interactions* **87**, 871 (1994). (b) S. F. J. Cox and D. S. Sivia, *Appl. Magn. Reson.* **12**, 213 (1997).
15. J. A. Stride, PhD Thesis, University of East Anglia, 1995.
16. M. F. Bailey and L. F. Dahl, *Inorg. Chem.* **4**, 1314 (1965).

17. B. Rees and P. Coppens, *Acta Crystallogr.* **B29**, 2515 (1973).
18. G. M. Aston, PhD Thesis, University of East Anglia, 1997.
19. D. F. R. Gilson, G. Gomez, I. S. Butler, and P. J. Fitzpatrick, *Can. J. Chem.* **61**, 737 (1983).
20. K. Chhor and G. Lucazeau, *Inorg. Chem.* **23**, 462 (1984).
21. G. Lucazeau, K. Chhor, C. Sourisseau, and A. J. Dianoux, *Chem. Phys.* **76**, 307 (1983).
22. (a) E. O. Fischer and W. Z. Pfab, *Naturforsch. B*, **7** (1952). (b) P. F. Eland and R. Pepinsky, *J. Am. Chem. Soc.* **74**, 4971 (1952). (c) J. D. Dunitz and L. E. Orgel, *Nature* **171**, 121 (1953).
23. A. Kubo, R. Ikeda, and D. Nakamura, *J. Chem. Soc., Faraday Trans. II* **82**, 1543 (1986).
24. A. B. Gardner, J. Howard, T. C. Waddington, R.M. Richardson, and J. Tomkinson, *J. Chem. Phys.* **57**, 453 (1981).
25. J. W. Edwards, G. L. Kingston, and R. Mason, *Trans. Faraday Soc.* **56**, 660 (1960).
26. (a) D. Yu, P. W. Percival, J. Borodovitch, S. Leung, R. F. Keifl, K. Venkateswaram, and S. F. J. Cox, *Chem. Phys.* **142**, 229 (1990). (b) D.G. Fleming, D.J. Arseneau, J. Pan, M. Y. Shelley, M. Senba, and P. W. Percival, *Appl. Magn. Reson.* **13**, 181 (1997).
27. E. Roduner, *Chem. Soc. Rev.* **22**, 337 (1993).
28. (a) E. J. Ansaldo, J. Boyle, Ch. Niedermeyer, G. D. Morris, J. H. Brewer, C. E. Stronach, and R. S. Carey, *Z. Phys. B Condens. Matter* **86**, 317 (1992). (b) R. F. Kiefl, J. W. Schneider, A. MacFarlane, K. Chow, T. L. Duty, T.L. Estle, B. Hitti, R. L. Lichti, E. J. Ansaldo, C. Schwab, P. W. Percival, G. Wei, S. Wlodek, K. Kojima, W. J. Pomanow, J. P. McCauley Jr., N. Coustel, J. E. Fischer, and A. B. Smith III, *Phys. Rev. Lett.* **68**, 1347 (1992). (c) E. Roduner *et al.*, *J. Chem. Phys.* **102**, 5989 (1995).
29. See for example: (a) J. C. Green, *Struct. Bonding (Berlin)* **43**, 37 (1981). N. Fey, *J. Chem. Technol. Biotechnol.* **74**, 852 (1999).
30. (a) C. T. Kaiser, PhD Thesis, TU-Delft, 2001. (b) C. T. Kaiser, P. C. M. Gubbens, E. Kemner, A. R. Overweg, U.A. Jayasooriya and S. P. Cottrell, *Chem. Phys. Lett.* **381**, 292 (2003).
31. E. Kemner, A. R. Overweg, L. van Eijck, A. N. Fitch, E. Suard, I. M. de Schepper, G. J. Kearley, *J. Chem. Phys.* **116**, 10838 (2002).
32. E. Kemner, I. M. de Schepper, A. J. M. Schmets, H. Grimm, A. R. Overweg, and R. A. van Santen, *J. Phys. Chem. B* **104**, 1560 (2000).

8 Proton Dynamics in Solids: Vibrational Spectroscopy with Neutrons

FRANÇOIS FILLAUX

*LADIR-CNRS and Université Pierre et Marie Curie, UMR 7075, 2 rue
H. Dunant, 94320 Thiais, France*

1 INTRODUCTION

Vibrational spectroscopy techniques are routinely used for chemical analysis, characterization and process control. Besides, they are also powerful for probing forces between atoms, molecules and ions, in various states of the matter. Vibrational frequencies are related to electronic structures via multidimensional potentials that govern the dynamics. To determine such potential surfaces is a major prospect for fundamental research aiming to rationalize the interplay of structure and dynamics. However, there are fundamental and technical limitations to the determination of potential hypersurfaces from vibrational spectra of complex systems. Our understanding of vibrational dynamics of systems with increasing complexity has benefited from development of mathematical models and quantum chemistry methods. But, in spite of spectacular progress, the confrontation of experiments with theory is far from being free of ambiguities and the interpretation of vibrational spectra remains largely based on experiments. In the present chapter, we wish to highlight the contribution of advanced neutron spectroscopy techniques to vibrational dynamics leading to determination of effective potential functions. Whenever possible, we shall emphasize the contribution to organometallic and metal–organic systems.

Since the very beginning, almost a century ago, spectroscopy has revealed that vibrational dynamics are quantal in nature: the energy is quantized and dynamics are described in terms of eigenstates. The quantum theory has developed predominantly within the harmonic approximation, that is the simplest expansion, to quadratic terms, of the potential hypersurface around the equilibrium position. Vibrational dynamics can be thus represented with harmonic oscillators (normal modes) corresponding to coherent oscillations of all degrees

of freedom at the same frequency. Since the main source of information is the interaction of matter with light, spectra are largely related to symmetry. Group theory and symmetry-related selection rules have emerged as very efficient tools. For example, they are widely used to determine the symmetry of ligands linked to a metallic centre [1]. From this long history, paved with remarkable successes, the interpretation of vibrational spectra with normal modes is largely prevailing.

However, in some cases, vibrations with large amplitudes show great anharmonicity, or even nonlinearity in the extreme cases where perturbation theory no longer holds. This occurs primarily for protons, the lightest nuclei, provided their displacements are decoupled from the surrounding heavy atoms. In solids, this is observed mainly for hydrogen bonds and for rotation of light hydrogenated rotors. The breakdown of the harmonic approximation for these oscillators with large amplitude gives rise to a manifold of transitions conveying a wealth of information. These systems are unique to understanding nonlinear quantum dynamics in a complex environment. However, the interpretation of the infrared and Raman spectra is hampered by the complexity of the interaction of light and matter. With advanced neutron sources, we are now able to perform vibrational spectroscopy by measuring inelastic neutron scattering (INS). Because the interaction of neutrons and matter is simpler, and can be rationalized more rigorously, the interpretation of INS spectra provides complementary information. A new view of proton dynamics in solids is emerging progressively from INS studies.

Apart from great advantages, INS has limitations. Experiments can be performed only at a very limited number of sources. Large amounts of samples are necessary. Best spectra are obtained for samples at very low temperature. Special chemistry for isotope substitution has to be carried out, because deuterium atoms scatter very much less than hydrogen atoms. Therefore, INS studies on organometallic complex systems are very rare and, as far as it can be foreseen, they will remain largely hampered by neutron beam intensities, even at advanced sources, and by the presence of complex hydrogenated ligands. Nevertheless, INS studies of simple models, possibly designed on purpose, reveal new aspects of proton dynamics that can be tentatively transposed to more complex systems.¹

The organization of this chapter is the following. After definition of some physical constants to be kept in mind and an abstract presentation of infrared and Raman spectroscopy, inelastic neutron scattering spectroscopy is featured in Section 2. In Section 3, the long lasting problem of force-field calculation is enlightened by comparison of calculated and observed INS profiles. By direct comparison, unrealistic dynamical models can be eliminated quite safely.

¹ Neutron scattering techniques are also unique to observing magnetic transitions which may occur in organometallic or metal-organic compounds. For the sake of clarity, magnetic studies are not considered in this chapter.

The case of the potassium hydrogen carbonate crystal (KHCO_3) is presented as a tutorial. It is shown in Section 3.2 that INS experiments performed on single crystals provide the most detailed view ever obtained of proton dynamics. INS is unparalleled for studies of the fascinating tunnel effects of light hydrogenous entities in the solid state (see Section 4). We can distinguish linear tunnelling, typically proton transfer along hydrogen bonds, and rotational tunnelling for light quantum rotors. The impact of INS on rotational tunnelling in organometallic complexes is emphasized in Section 4.2.

2 VIBRATIONAL SPECTROSCOPY TECHNIQUES

Before presenting the basics of optical (Section 2.2) and neutron scattering techniques (Section 2.3), let us recall the definition of some physical parameters that should be borne in mind.

2.1 SOME DEFINITIONS

For vibrational spectroscopists, energies of eigenstates are traditionally expressed in ‘wavenumber’ units ($\tilde{\nu}$) or ‘ cm^{-1} ’, that is the number of wavelengths (λ) per cm:

$$\tilde{\nu} = \frac{\nu}{c} = \frac{1}{\lambda} \quad (8.1)$$

where ν is the frequency and c the velocity of light. It is very important to keep in mind that the wavenumber and frequency are different parameters, yet these two terms are often used interchangeably. Thus, an expression such as ‘frequency shift of 10 cm^{-1} ’ is used conventionally by infrared and Raman spectroscopists and this convention will be used hereafter.

If an electromagnetic field or neutrons interact with a molecule or a crystal, a transfer of energy can occur only when Bohr’s frequency condition is satisfied:

$$\Delta E = h\nu = \hbar\omega = h\frac{c}{\lambda} = hc\tilde{\nu} \quad (8.2)$$

ΔE is the difference in energy between two eigenstates, usually expressed in cm^{-1} units, h is Planck’s constant, $\hbar = h/2\pi$, and $\omega = 2\pi\nu$. Thus, $\tilde{\nu}$ is proportional to the energy of the transition. Most of the vibrational first-eigenstates occur in the range from 1 to 5000 cm^{-1} and spectrometers commonly used for condensed matter studies operate with a resolution on the order of 1 cm^{-1} . (High-resolution spectroscopy in the gas phase can go very far beyond this value, by several orders of magnitude.)

Routine infrared spectroscopy measures the absorption of an incident radiation as a function of the frequency or, equivalently, of the energy transferred

from the beam to the sample. The incident beam spans the whole frequency range and the wavelength is in the range 2–1000 μm ($1 \mu\text{m} = 10^{-6} \text{m}$). Raman spectroscopy measures the light scattered by a sample irradiated with a sharp monochromatic laser beam, very often in the visible region ($\lambda_i \approx 0.5 \mu\text{m}$).

The neutron is a dimensionless particle whose kinetic momentum \mathbf{p} is related to the de Broglie wavelength λ_n as

$$|\mathbf{p}| = \frac{h}{\lambda_n} = \hbar|\mathbf{k}| \quad (8.3)$$

where \mathbf{k} is the wavevector parallel to the beam direction and such that $|\mathbf{k}| = 2\pi/\lambda_n$, usually express in \AA^{-1} units. The kinetic energy is

$$E = \frac{\hbar^2 k^2}{2m_n} \approx 2.08k^2 \quad (8.4)$$

where m_n is the neutron mass. From particle physics, E is traditionally given in meV or terahertz units ($1 \text{ THz} \equiv 10^{12} \text{ Hz} \equiv 33.356 \text{ cm}^{-1}$):

$$1 \text{ meV} \equiv 10^{-3} \text{ eV} \equiv 10^3 \mu\text{eV} \equiv 0.24 \text{ THz} \equiv 8.07 \text{ cm}^{-1} \equiv 11.61 \text{ K} \quad (8.5)$$

The neutron velocity is

$$v(\text{ms}^{-1}) \approx 3.95610^3 k(\text{\AA}^{-1}) \quad (8.6)$$

and the neutron wavelength is

$$\lambda_n(\text{\AA}) = \sqrt{\frac{\hbar^2}{2m_n E}} \approx \frac{9.04}{\sqrt{E}} \quad (8.7)$$

with E in meV units. Therefore, incident neutrons with an energy ranging from 1 to 500 meV ($\approx 8\text{--}4000 \text{ cm}^{-1}$) have wavelengths in the range about 9–0.4 \AA . Wavevectors are in the range 0.7–16 \AA^{-1} and velocities from 60 to 3 km s^{-1} . With time resolution $\approx 10^{-6} \text{ s}$, it is possible to estimate the neutron kinetic energy from the time of flight over a distance of a few meters.

2.2 OPTICAL TECHNIQUES

Detailed presentations of the theoretical framework for infrared and Raman spectroscopy can be found in many textbooks [1–6]. Here, we give only a few definitions for further comparison with INS.

Light is an electromagnetic wave having electric and magnetic field components. Hereafter, only interaction of the electric field and matter is considered and we shall ignore the magnetic component. Nuclei and electrons determine the distribution of electric charges in a sample. The barycentres of positive and negative charges define the dipole moment vector \mathbf{M} . In the cases of interest herein, infrared spectroscopy measures the interaction of an incident light beam with the derivatives of the dipole

moment with respect to the various vibrational degrees of freedom:

$$\left. \begin{aligned} \mathbf{M} &= \mathbf{M}_0 + \sum_i \frac{\partial \mathbf{M}}{\partial x_i} x_i + \frac{1}{2} \sum_{ij} \frac{\partial^2 \mathbf{M}}{\partial x_i \partial x_j} x_i x_j + \dots \\ \text{or } \mathbf{M} &= \mathbf{M}_0 + \sum_i \mathbf{M}_i x_i + \frac{1}{2} \sum_{ij} \mathbf{M}_{ij} x_i x_j + \dots \end{aligned} \right\} \quad (8.8)$$

The transition between an initial state $|\varphi_0\rangle$ at energy E_0 and a final state $|\varphi_f\rangle$ at E_f occurs at frequency $\hbar\omega_{0f} = E_f - E_0$ and the intensity is proportional to the square amplitude of the transition matrix element: $|\langle\varphi_0|\mathbf{M}|\varphi_f\rangle|^2$. Only vibrations generating a change of the dipole moment are infrared active.

The origin of Raman [7] spectra is markedly different from that of infrared spectra. In Raman, the sample is irradiated with an intense laser beam at frequency ν_0 , usually in ranges of energy corresponding to ultraviolet, visible or near infrared radiations. In ‘normal’ Raman, ν_0 does not correspond to any eigenstate. The interaction of the incident radiation with the sample is represented as a ‘virtual’ state that can be represented as a linear combination of vibronic eigenstates. The lifetime of virtual states is supposed to be virtually zero. The scattered light consists of *Rayleigh* scattering, very intense elastic scattering at ν_0 , and Raman scattering, very weak inelastic scattering, normally $\approx 10^{-5}$ of the incident beam intensity. The *Stokes* and *anti-Stokes* Raman lines are observed at $\nu_0 + \nu_i$ and $\nu_0 - \nu_i$, respectively.

Normal Raman spectroscopy probes the variations of the polarizability tensor with respect to the degrees of freedom, in the ground electronic state. When an electrical field is applied to a system the electron distribution is modified and the sample acquires an induced dipole moment as the barycenters of the charges are displaced. The polarizability tensor $[\alpha]$ defines the correspondence between the incident electrical field \mathbf{E} and the induced dipole moment $\mathbf{M}' = [\alpha]\mathbf{E}$. The polarizability tensor can be expanded in a Taylor series analogous to Equation (8.8):

$$[\alpha] = [\alpha]_0 + \sum_i [\alpha]_i x_i + \frac{1}{2} \sum_{ij} [\alpha]_{ij} x_i x_j + \dots \quad (8.9)$$

and the intensity is proportional to $|\langle\varphi_0|[\alpha]|\varphi_f\rangle|^2$.

Because the interaction of photons with matter is quite complicated and depends strongly on the electronic structure, the various derivatives of the dipole moment and polarizability tensor cannot be estimated easily. Even calculations with the most advanced quantum methods are far from providing reliable estimations. Therefore, a major drawback of optical techniques is that intensities cannot be interpreted with confidence.

2.3 NEUTRON SCATTERING TECHNIQUES

Vibrations in solids can also be probed with neutrons. An incident monochromatic beam is scattered by a sample and analysed with a detector at a general position

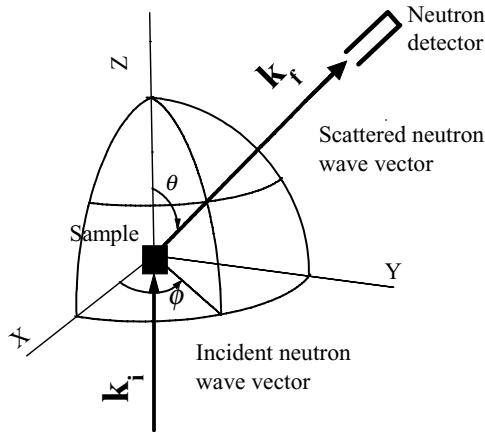


Figure 8.1 Schematic view of a neutron scattering experiment.

in space (see Figure 8.1). The incident and scattered neutrons are represented by plane waves whose wavevectors are \mathbf{k}_i and \mathbf{k}_f , respectively. The momentum transfer vector is

$$\mathbf{Q} = \mathbf{k}_i - \mathbf{k}_f \quad (8.10)$$

One can distinguish elastic–inelastic and coherent–incoherent scattering processes [8]. Indeed, neutron sources are very expensive and quite rare compared to optical sources such as black bodies or lasers. However, neutrons give information that cannot be obtained with other techniques. Some interesting properties are featured below.

2.3.1 Nuclear Cross-sections

The interaction of neutrons and matter is extremely weak, for the neutron has no electric charge. It is essentially *spin–spin* interaction with nuclei, whilst interaction with electron spins is negligible. Nuclei can be treated as dimensionless scattering centres (Fermi potential). The nuclear cross-sections are strictly independent of the electronic surrounding (ionic or neutral, chemical bonding, etc.). Therefore, the scattering cross-section of any sample can be calculated exactly, from the known cross-section of each constituent. Compared to optical techniques, INS intensities can be fully exploited and the spectra can be interpreted with more confidence. They are related to nuclear displacements involved in each vibrational eigenstate.

2.3.2 Coherent versus Incoherent Scattering

For each nucleus, one can distinguish coherent and incoherent scattering cross-sections. Elastic coherent scattering by a crystal gives rise to Bragg diffraction, analogous to what is more routinely measured with X-rays. A great advantage of neutron diffraction is the possibility to locate protons that are normally barely seen

with X-rays. Inelastic coherent scattering performed on single crystals probes the frequency dispersion of phonons in momentum space. For the sake of simplicity, and because coherent scattering by protons is very weak, these measurements will not be presented any further. Inelastic incoherent scattering, namely INS, probes the phonon density of states over entire Brillouin zones (reciprocal space). This effect is exploited to study proton dynamics in solids.

2.3.3 Contrast

The incoherent scattering cross-section of the hydrogen nucleus (proton) is more than one order of magnitude greater than for any other atom. Therefore, neutrons scattered by protons largely dominate INS intensities for hydrogenous samples (see below Section 2.4). In many systems the nonhydrogenous matrix environments can be regarded as virtually transparent. This great sensitivity to proton motions can be further exploited because the incoherent cross-section for deuterium atoms (or deuterons, ^2H) is about 40 times weaker. Therefore, isotope substitution at specific sites greatly simplifies the spectra. Skilled chemists can thus assign bands with great confidence. Isotope labelling is also extremely useful to interpreting infrared and Raman spectra. However, whereas some band frequencies are shifted quite significantly, the spectra of deuterated samples are not greatly simplified, regarding the number of bands and their intensities.

2.3.4 Penetration Depth

As a consequence of the weak interaction with matter, neutrons can penetrate many samples over rather long distances and probe the bulk material. In contrast, light can hardly penetrate samples with high refractive indices and optical techniques probe only a very thin layer at the surface. On the other hand, INS requires much greater amounts of samples in the beam and longer measuring times.

2.3.5 Wavelength

With optical techniques, vibrational dynamics are probed on spatial scales much greater than molecular sizes, or unit cell dimensions in crystals, commonly encountered. The scale is directly related to the wavelength of the incident radiation (in the range from 1 to 1000 μm in the infrared or about 0.5 μm for Raman). Oscillators at very short distances, compared to the wavelength, are excited exclusively in phase. For molecules, only overall variations of the dipole moment or polarizability tensor can be probed. In crystals, only a very thin slice of reciprocal space about the centre of the Brillouin zone ($\mathbf{k} \approx 0$) can be probed. This corresponds to in-phase vibrations of a virtually infinite number of unit cells. With optical techniques, band intensities are largely determined by symmetry-related selection rules, although these rules hold only in the harmonic approximation.

With the INS technique, wavelengths compare to chemical bonds or unit cells in crystals. Therefore, collective oscillations can be excited and, simultaneously, the

phase correlation of oscillators can be controlled via the momentum transfer. Consequently, symmetry-related selection rules are irrelevant.

2.3.6 Scattering Function

In order to appreciate the particular impact of INS on vibrational spectroscopy, it is necessary to consider the role of momentum transfer in more detail. For optical techniques, the momentum transfer range is smaller than 10^{-3} \AA^{-1} . It can be as large as 30 \AA^{-1} with neutrons, for an energy of 500 meV. Consequently, whereas infrared and Raman spectroscopy measures an intensity as a function of energy ($I(\nu)$), the INS intensity depends on energy *and* momentum transfer. This is traditionally represented with the scattering function, $S(\mathbf{Q}, \omega)$. Consequently, the intensity measured at each frequency (usually termed energy transfer or $\hbar\omega$) depends on the orientation and magnitude of the final wavevector. Because the wavelength of neutrons is similar to the spatial extension of vibrational wavefunctions of bound atoms, the dependence on \mathbf{Q} provides additional information on the vibrational states that cannot be obtained with optical techniques.

In order to be practical, we present below the oversimplified textbook example of the isolated harmonic oscillator in one dimension with mass m . The Hamiltonian

$$H = -\frac{\hbar^2}{2m} \frac{d^2}{dx^2} + \frac{1}{2} m \omega_0^2 x^2 \quad (8.11)$$

can be solved analytically [9,10]. The first term is the kinetic energy and the second term is a parabolic potential. Energy levels and wave functions are

$$\left. \begin{aligned} E_n &= \left(n + \frac{1}{2} \right) \hbar \omega_0 \\ \Psi_n(x) &= \frac{1}{\sqrt{2^n n!}} H_n \left(\sqrt{\frac{m \omega_0}{\hbar}} x \right) \exp \left(-\frac{m \omega_0}{2 \hbar} x^2 \right) \end{aligned} \right\} \quad (8.12)$$

where H_n is the Hermite polynomial of order n . The frequency is $\omega_0/2\pi$. Eigenstates are equidistant in energy (see Figure 8.2). The neutron scattering function accounts for the coupling of the initial and final states via the neutron plane wave:

$$S(Q_x, \omega) = |\langle \Psi_i(x) | \exp(i Q_x x) | \Psi_f(x) \rangle|^2 \delta(\omega - \omega_{if}) \quad (8.13)$$

Q_x is the momentum transfer along the x direction. The scattering function can be calculated analytically for transitions arising from the ground state as:

$$S_{0 \rightarrow n}(Q_x, \omega) = \frac{(Q_x u_x)^{2n}}{n!} \exp(-Q_x^2 u_x^2) \delta(\omega - n \omega_0) \quad (8.14)$$

where

$$u_x^2 = \langle \Psi_0(x) | x^2 | \Psi_0(x) \rangle = \frac{\hbar}{2m\omega_0} \quad (8.15)$$

is the mean square amplitude of the oscillator in the ground state.

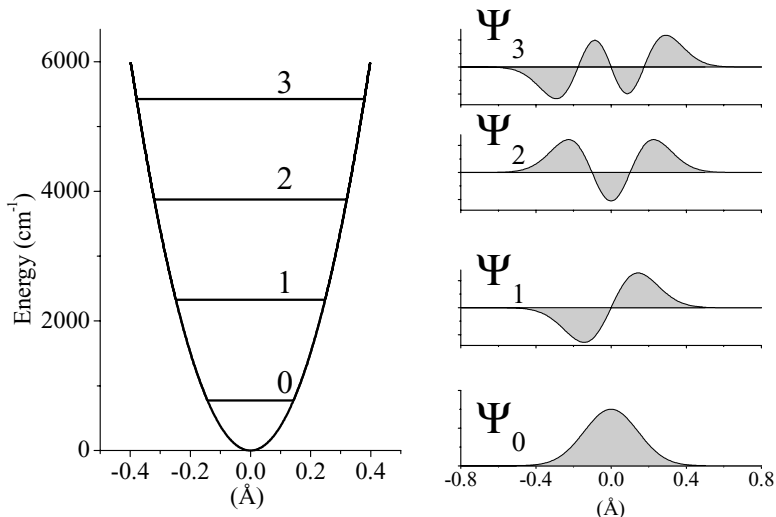


Figure 8.2 The harmonic oscillator: energy levels and wavefunctions. $\hbar\omega_0 = 1600 \text{ cm}^{-1}$, $m = 1 \text{ amu}$.

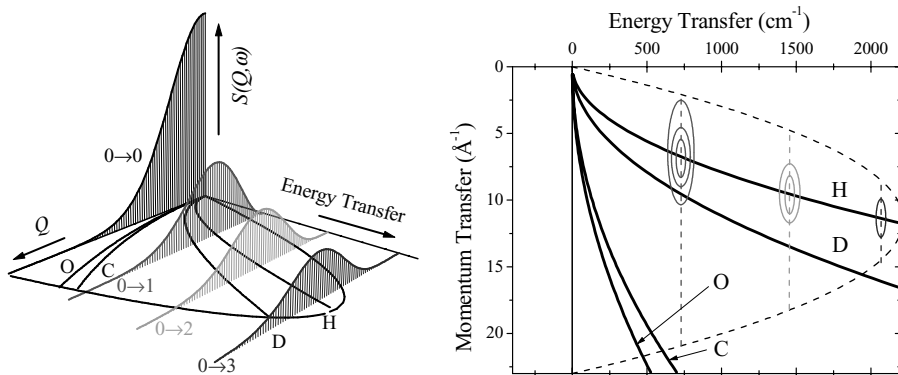


Figure 8.3 (a) Landscape and (b) isocontour map representations of the incoherent neutron scattering function for the proton harmonic oscillator. The intensity is a maximum along the recoil line labelled H. Recoil lines for oscillators with masses corresponding to D, C and O atoms are shown. For a fixed incident energy, only momentum transfer values inside the parabolic area can be measured.

It is thus possible to observe all transitions $|0\rangle \rightarrow |n\rangle$ arising from the ground state (see Figure 8.3). The intensity is a maximum at $Q_x^2 u_x^2 = n$. In the $S(Q_x, \omega)$ map of intensity, each transition appears as an island of intensity, thanks to unavoidable broadening in energy. Profiles along Q_x are directly related to the effective oscillator mass, via u_x^2 . The maxima of intensity occur along the *recoil line* for the corresponding

oscillator mass:

$$E \approx \frac{\hbar^2 Q^2}{2m} \quad (8.16)$$

Equations (8.13) and (8.14) can be generalized for a set of harmonic oscillators. Then, combination bands can be observed, in addition to transitions for each oscillator. As opposed to this, intensities measured for higher transitions with optical techniques are proportional to

$$|\langle \Psi_m | x^p | \Psi_n \rangle|^2 \neq 0 \quad \text{if } m = n \pm p \quad (8.17)$$

For most of the active transitions, the high order derivatives of the dipole moment or polarizability tensor are very weak and optical spectra are largely dominated by $|0\rangle \rightarrow |1\rangle$ transitions. Overtones and combination bands are usually very weak.

2.4 POTASSIUM HYDROGEN BISTRIFLUOROACETATE

In order to illustrating at a very qualitative level the complementarity of infrared, Raman and INS techniques, let us examine the spectra of potassium hydrogen bistrifluoroacetate, whose chemical formula is $(\text{H}(\text{CF}_3 \text{ COO})_2)^-$. In the crystal, hydrogen bistrifluoroacetate ions (namely $(\text{H}(\text{CF}_3 \text{ COO})_2)^-$, see Figure 8.4), are surrounded by potassium ions [11]. Two trifluoroacetate entities, $\text{CF}_3 \text{ COO}^-$, are linked by a very short (strong) and centrosymmetric hydrogen bond with $\text{O} \cdots \text{O}$ distance of 2.435 Å. This sample is extremely well suited to INS studies as there is only one hydrogen atom with large incoherent cross-section. The contribution from other atoms is largely negligible. Proton dynamics in such strong symmetrical hydrogen bonds are of interest to many fields.

The infrared, Raman and INS spectra compared in Figure 8.4 reveal different aspects of the vibrational dynamics of the $(\text{H}(\text{CF}_3 \text{ COO})_2)^-$ dimers [12]. The infrared spectrum is dominated by a very broad and intense band whose absorption is a maximum (the transmittance is a minimum) at $\approx 800 \text{ cm}^{-1}$. This band extends almost continuously from ≈ 300 to 2000 cm^{-1} . This spectacular infrared intensity is distinctive of the centrosymmetric hydrogen bond which can be regarded as essentially ionic in nature. The two oxygen atoms share the electron of the H atom. This is conventionally written as: $\text{O}^{0.5-} \cdots \text{H}^+ \cdots \text{O}^{0.5-}$. By symmetry, there is no permanent electric dipole. However, the derivative of the dipole moment with respect to the displacements of the neat charge of the proton is very large along the H bond (stretching or ν_a OHO) and very weak perpendicular to the bond, either parallel to the plane defined by the COO groups (in-plane bending or δ OHO) or perpendicular to the same plane (out-of-plane bending or γ OHO). The broad infrared band can be thus assigned to the stretching mode, whereas the bending modes are barely visible.

The Raman spectrum is dominated by very sharp bands due to the COO and CF_3 entities. These entities contain many electrons and the variation of the polarizability tensor with atomic displacements is a maximum. On the other hand, there is no visible counterpart to the huge infrared band. Because of its pronounced ionic character,

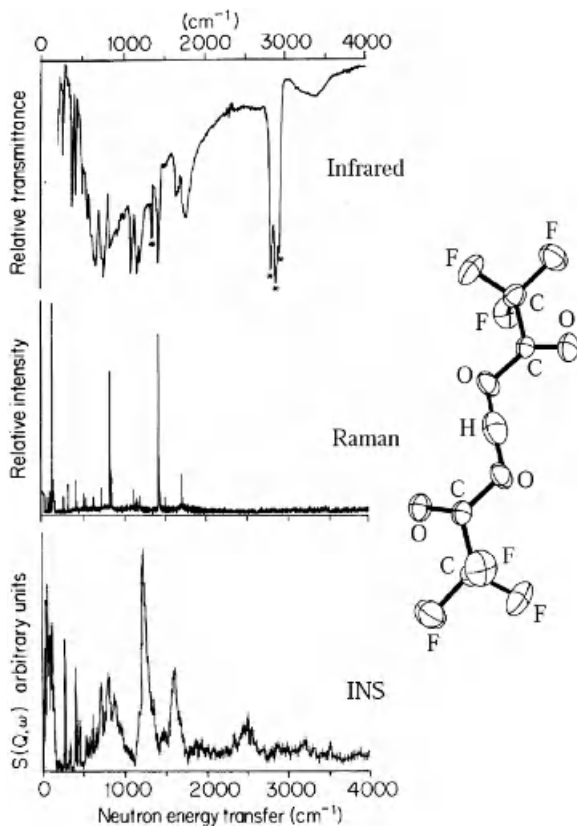


Figure 8.4 Schematic view of the hydrogen bistrifluoroacetate complex and infrared (Nujol® mull), Raman and INS spectra (from top to bottom) at 20 K*, Nujol® band; C, carbon; H, hydrogen; O, oxygen; F, fluorine. Reproduced with permission from Chem. Phys. **158**, F. Fillaux and J. Tomkinson, *An inelastic neutron scattering study of the proton dynamics in KH (CF₃COO)₂ and CsH(CF₃COO)₂*, 113, Copyright (1991) Elsevier.

there is virtually no deformation of the electronic orbitals for proton displacements and the derivatives of the polarizability tensor are very small.

The INS profile represents a cut of the scattering function $S(Q, \omega)$ along the recoil line for the proton mass (see Figure 8.3). Along this trajectory, the intensity arises from vibrational modes involving proton displacements. The band intensity for H-free vibrations is much weaker for two reasons. First, the scattering cross-sections of C, O and F atoms are small. Second, the maximum of the scattering function for these heavy oscillators occurs along recoil lines located at much greater Q values, beyond the actually accessible Q range (see Figure 8.3). Consequently, most of the observed INS intensity arises from proton motions and the assignment scheme is straightforward, for there is only one proton in the dimer and all dimers are indistinguishable. The three bands at ≈ 800 , 1200 and 1600 cm^{-1} can be safely attributed to the three

degrees of freedom of the proton. The weaker band at $\approx 2500\text{ cm}^{-1}$ is the overtone of the sharp band at 1200 cm^{-1} . Then, back to the infrared spectrum, there is a clear correspondence between the INS band at $\approx 800\text{ cm}^{-1}$ and the broad proton stretching band. Furthermore, it is easy to identify the weak infrared bands due to the proton bending modes, at about the same frequencies as in INS.

The strong INS intensity of the proton modes indicates that the proton vibrations are largely decoupled from the other internal degrees of freedom. This is primarily due to the very light mass of the proton compared to the other atoms. However, the very sharp INS bands in the $200\text{--}500\text{ cm}^{-1}$ range, with counterparts in Raman, reveal weak but significant coupling of the proton displacements with the CF_3 modes. Finally, below 200 cm^{-1} , the INS spectral profile arises from the density of states of the crystal lattice (phonons). In this low frequency range, the dynamics can be represented, to a good level of approximation, with translational and librational (rotational) motions of rigid CF_3COO^- entities.

3 VIBRATIONAL DYNAMICS OF PROTONS IN SOLIDS

3.1 FORCE-FIELD CALCULATIONS: NORMAL VERSUS LOCALIZED MODES

It is widely accepted that vibrational dynamics of atoms and molecules are reasonably well represented by harmonic force fields. The resolution of the secular equation transforms a set of (say N) coupled oscillators into (N) independent oscillators along orthogonal (normal) coordinates. Eigenvalues of the dynamical matrix are normal frequencies and eigenvectors give atomic displacements for each normal mode [3,4,13]. If band intensities cannot be fully exploited, as it is normally the case for infrared and Raman spectra, these vectors are unknown and force fields refined with respect to observed frequencies only are largely underdetermined. For complex systems, symmetry consideration or/and isotopic substitutions may remove only partially this under determination.

With the INS technique, force fields can be refined with respect to the full spectral profiles including both frequencies and intensities [14,15]. This technique is most powerful for hydrogenous samples for which intensities are dominated by modes involving large proton displacements. Contributions from other atoms are much weaker and can be easily overlooked.

When harmonic force fields are used to represent local atom–atom interactions in molecular crystals, the mean positions of the protons oscillating at high frequency (internal modes) follow adiabatically the slow lattice vibrations. This proton riding effect should give rise to large intensities for lattice modes at low frequency. Moreover, intensities for internal molecular vibrations should be depressed dramatically by an exponential term referred to as the Debye–Waller factor, $\exp[-\langle(\mathbf{Q}\cdot\mathbf{u})^2\rangle]$, where \mathbf{u} is the displacement vector for atoms and $\langle \rangle$ means ‘averaged over the density of states’. Consequently, it has been speculated that internal modes at high frequency (say above $\approx 1000\text{ cm}^{-1}$) and large momentum transfer values should be almost invisible with INS. However, this is largely in error. For example, CH stretching

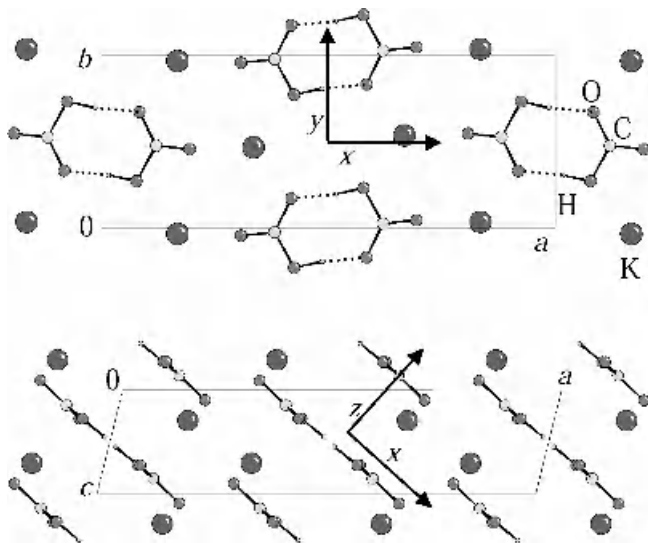


Figure 8.5 Schematic view of the crystalline structure of KHCO_3 at 14 K. Reproduced with permission from F. Fillaux, A. Cousson and D. Keen, *Phys. Rev B* **67**, 054301. Copyright (2003). American Physical Society.

modes were observed at $\approx 3000 \text{ cm}^{-1}$ and the role of the Debye–Waller factor had to be reconsidered [16].

Potassium hydrogen carbonate (KHCO_3) is another ideal system for proton dynamics studies with INS, along with potassium hydrogen bistrifluoroacetate, because the spectra are largely dominated by a small number of vibrational modes involving proton displacements with large amplitudes. The crystal contains centrosymmetric dimer entities $(\text{HCO}_3^-)_2$ and this structure remains unchanged from 298 K to 14 K (see Figure 8.5) [17–19]. The hydrogen bond with length $\text{O} \cdots \text{O} = 2.559 \text{ \AA}$ at 14 K (2.607 \AA for KDCO_3) is moderately strong. At 298 K protons are disordered between two sites located at $\pm 0.3 \text{ \AA}$ off centre of the hydrogen bond, with population ratio of $\approx 1:4$. However, diffraction studies cannot distinguish statistical and dynamical disorders.

The INS spectrum along the recoil line for protons (see Figure 8.6) is dominated by sharp bands arising from out-of-plane ($\gamma \text{ OH} \approx 960 \text{ cm}^{-1}$) and in-plane ($\delta \text{ OH} \approx 1400 \text{ cm}^{-1}$) proton modes [20]. Weaker bands at $\approx 640 \text{ cm}^{-1}$ ($\delta \text{ CO}_3$) and $\approx 1620 \text{ cm}^{-1}$ ($\nu \text{ CO}_3$) reveal weak coupling of the carbonate entities with OH modes. Bands at high frequency correspond to overtones and combinations of the bending modes, superimposed on the broad and ill-defined $\nu \text{ OH}$ mode centred at $\approx 2800 \text{ cm}^{-1}$. Below 200 cm^{-1} , the lattice density of states forms a quasicontinuum with a maximum at $\approx 100 \text{ cm}^{-1}$.

As previously for the potassium hydrogen bistrifluoroacetate crystal, INS clearly evidences the decoupling of the proton bending modes from the carbonate entities. This is largely confirmed by a simulation of the spectral profile with valence-bond force-field models of the dimers. With force fields based on infrared and Raman

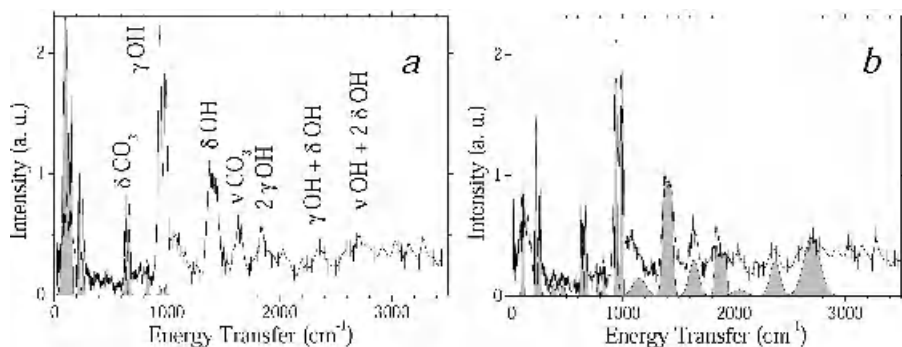


Figure 8.6 The INS spectrum of KHCO_3 at 20 K, tentative assignment scheme, and calculation of intensity profiles. (a) Valence-bond force-field. (b) Localized modes. Reproduced with permission from Chem. Phys. **124**, F. Fillaux, J. Tomkinson and J. Penfold, Chem. Phys., *Proton Dynamics in the Hydrogen Bond. The Inelastic Neutron Scattering Spectrum of Potassium Hydrogen Carbonate at 5K*, 425, Copyright (1988) Elsevier.

spectra [21], there is a spectacular difference between observed and calculated profiles (see Figure 8.6(a)). As the observed intensities for lattice modes below 200 cm^{-1} are smaller than those calculated by at least one order of magnitude, conventional harmonic force fields must be rejected. The discrepancy arises essentially from the riding effect, because the proton is bound by strong forces to the oxygen atom. It is straightforward to conclude that protons are almost totally decoupled from the surrounding heavy atoms. Dynamics are better represented with localized proton modes defined with respect to a ‘fixed’ (laboratory) referential frame. From the standpoint of the INS technique, KHCO_3 can be regarded as a crystal of protons so weakly coupled to the surrounding atoms that the framework of carbonate and potassium ions can be virtually ignored. Dynamical models are thus greatly simplified and the calculated profile reasonably fits the observed spectrum (see Figure 8.6(b)). In addition, this view is not specific to the ionic nature of the crystal [22]. These results severely undermine the representation of vibrational spectra with usual normal modes.

3.2 THE PROTON CRYSTAL MODEL

The $S(Q, \omega)$ maps of intensity measured with the MARI spectrometer at the ISIS pulsed neutron source (Rutherford Appleton Laboratory, Chilton, UK) show islands of intensity corresponding to the eigenstates involving large proton displacements (see Figure 8.7). In these experiments, one has to compromise with the energy E_i of the incident neutron beam, which determines both energy and momentum transfer ranges to be probed, and the resolution ($\Delta E_i/E_i \approx 2\%$).

Islands of intensity are observed for the out-of-plane and in-plane bending modes at about 1000 and 1400 cm^{-1} , respectively, for the overtone $2 \times \gamma\text{ OH}$ at $\approx 1850\text{ cm}^{-1}$ and for the broad stretching mode at $\approx 2800\text{ cm}^{-1}$. The maxima of intensity for all observed eigenstates are very close to the recoil line for the proton mass, with only one exception for the in-plane bending $\delta\text{ CO}_3$ at $\approx 650\text{ cm}^{-1}$. A more quantitative analysis

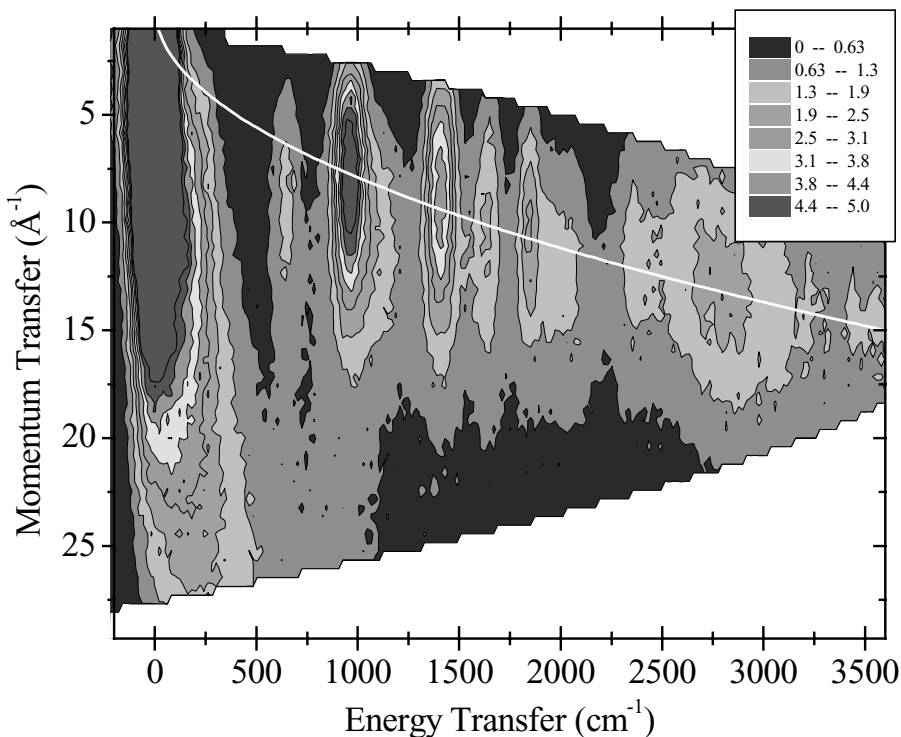


Figure 8.7 (Plate3) $S(Q, \omega)$ for powdered KHCO_3 at 20 K measured with a fixed incident energy of 500 meV. The recoil line for protons is superimposed (white line).

of cuts along the Q axis confirms that effective oscillator masses are virtually equal to 1 amu for the proton modes. It can be thus concluded that coupling of the proton modes with the heavy atoms is marginal. More surprising is the band at $\approx 1600 \text{ cm}^{-1}$ that is traditionally attributed to the CO stretching mode: this band is quite intense in the infrared and shows very weak frequency shift upon deuteration. However, this eigenstate appears as a virtually pure proton mode on the map of INS intensity.

For a more detailed understanding of the coupling between the $\delta \text{ OH}$ and $\nu \text{ CO}_3$ coordinates, it is necessary to measure the scattering function of properly oriented single crystals to probe the orientation of the eigenvectors with respect to the crystal referential [23–25]. Then, it transpires that the local mode representation for the proton modes fully applies to the ground state, but, for symmetry reasons, anharmonic coupling mixes the first excited states of the $\delta \text{ OH}$ and $\nu \text{ CO}_3$ coordinates. This graphic case emphasizes that different techniques may support different representations of a particular eigenstate. Straightforward assignment schemes from infrared and Raman can be misleading.

As a conclusion for this section, when INS techniques can be fully exploited, as is possible for a rather simple system such as KHCO_3 , they provide the most detailed view of proton dynamics ever obtained. They emphasize that with optical techniques

we have only a limited amount of information. Apparently straightforward representations, sometime given for sure in text books on vibrational spectroscopy, must be severely revised. However, it is obvious that INS measurements such as those presented in this section would be totally irrelevant if they were performed on organometallic complexes with large ligands.

4 TUNNELLING

Light particles moving in a potential with topological degeneracy manifest their quantum nature via tunnelling, one of the manifestations of the profound difference between classical and quantal worlds. Owing to the spatial extension of the wavefunction, the degenerate ground state in the classical regime splits into sublevels. In condensed matter, the observation of tunnelling sheds light onto fundamental problems of quantum mechanics in a complex environment.

As the proton is the lightest nucleus, it may show marked quantum effects. Tunnel effects are observed essentially for proton transfer between proton donors and acceptors, most frequently along hydrogen bonds, and for rotation of hydrogenated rotors.

4.1 PROTON TRANSFER

Proton transfer along hydrogen bonds, say $XH \cdots Y$, is of fundamental importance to many physical, chemical and biochemical processes [26–35]. There is a general agreement that proton transfer dynamics have properties characteristic of a light particle in a heavy framework that can be represented with an effective potential along a local reaction coordinate coupled to the motions of heavy atoms. In simple linear systems the potential energy for the hydrogen atom along the hydrogen bond may have two inequivalent minima corresponding to the schematic structures $XH \cdots Y$ and $X^- \cdots H^+ Y$, respectively. The top of the potential barrier corresponds to the transition state. Only in symmetric systems $AH \cdots A$ can the two wells be equivalent and proton transfer mediated by tunnelling may take place, even at very low temperature. Indeed, there is a manifold of intermediate cases between perfectly symmetric and highly asymmetric systems. In all cases, the key parameters for proton transfer dynamics are the distance between the two wells (R), the barrier height (E_a), the potential asymmetry (ΔU) and the tunnelling matrix element (ν_{0t}). The latter determines the transfer rate in the quantum regime. In addition, proton transfer occurs in a complex multidimensional environment and strong coupling with the surrounding degrees of freedom is also regarded as a major factor determining the transfer rate. According to the great complexity of the microscopic mechanism for proton transfer an accurate determination of these parameters from experimental and theoretical studies is not easy.

From the theoretical viewpoint, there is no unique way to partition the binding energy resulting from simultaneous changes of the electronic and vibrational wavefunctions upon hydrogen bond formation (see for example Ref. 33). Modelling

of proton transfer dynamics with quantum chemistry is further hampered by the complexity of treating thermal and quantum fluctuations in complex systems with high accuracy [34,36–38]. On the other hand, the characterization of hydrogen bonds and proton transfer by experimental means is often ambiguous as each particular approach highlights a different view. Structural studies emphasize bond lengths and angles [39, 40]. NMR and quasi-elastic neutron scattering (QENS) are mainly concerned with dynamics at a rather long time scale (typically longer than $\sim 10^{-10}$ s) [41,42] whilst quantum effects are observed with vibrational spectroscopy [43,44]. Consequently, quite different views of the proton transfer mechanism have emerged from previous works.

Proton transfer along the $\text{OH} \cdots \text{O}$ bonds in KHCO_3 is responsible for proton disordering at room temperature. In order to determine the double minimum potential function, the OH stretching vibration is of particular interest since quantum proton transfer (tunnelling) is best observed for vibrations along the reaction path. In the infrared and Raman this mode gives broad bands, with several submaxima between 1800 and 3500 cm^{-1} [45,46]. Although various models have been proposed for hydrogen bond dynamics, and extensive quantum-mechanical calculations have been performed [30,33,38], a detailed understanding of the band shaping mechanism is still lacking. In spite of these limitations, a quasi-symmetric double minimum potential along the proton stretching mode coordinate has been proposed (Figure 8.8), based on a quantitative analysis of the ν OH profiles in the infrared and Raman [47,48]. The ‘tunnelling’ transition associated with quantum transfer of a single proton was estimated at 213 cm^{-1} , but the intensity is so weak that it is not observed with optical techniques.

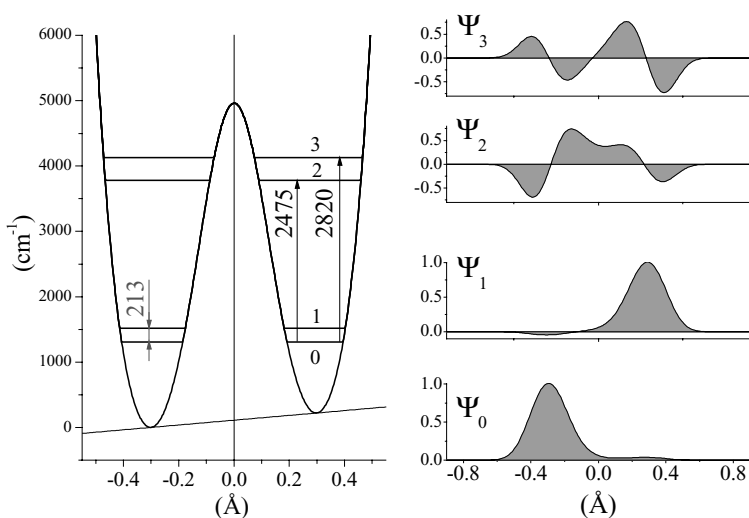


Figure 8.8 (Plate 4) Potential function and wavefunctions for the KHCO_3 crystal at 10 K. Reproduced with permission from Chem. Phys. **74**, F. Fillaux, *Calculation of infrared and Raman band profiles of strong hydrogen bonds. OH stretching bands and proton dynamics in crystalline potassium hydrogen carbonate*, 405, Copyright (1983) Elsevier.

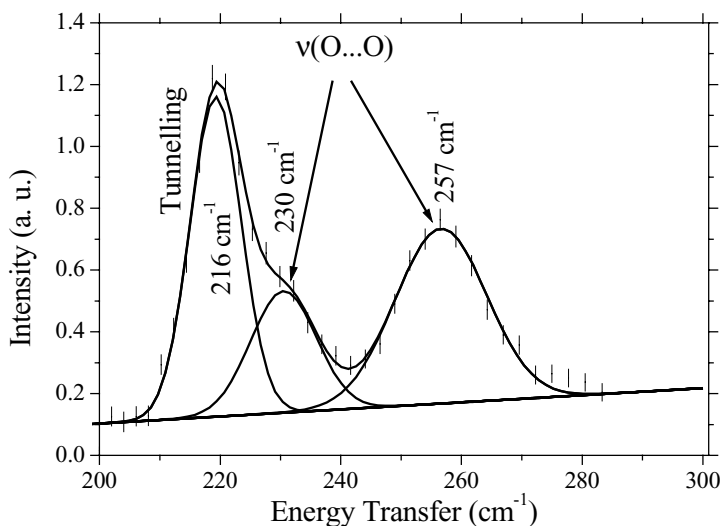


Figure 8.9 INS spectrum of KHCO_3 at 4 K in the tunnelling region and band decomposition into Gaussian profiles. Reproduced with permission from Chem. Phys. **124**, F. Fillaux, J. Tomkinson and J. Penfold, Chem. Phys., *Proton Dynamics in the Hydrogen Bond. The Inelastic Neutron Scattering Spectrum of Potassium Hydrogen Carbonate at 5K*, 425, Copyright (1988) Elsevier.

However, thanks to the great sensitivity of the INS technique to proton displacements with large amplitudes, this transition was observed at 216 cm^{-1} , close to the $\text{O}\cdots\text{O}$ stretching bands (see Figure 8.8). The dynamical nature of the proton disorder was thus established. If the potential were symmetrical, the tunnelling matrix element corresponding to the splitting of the ground state would be equal to 18 cm^{-1} . The observed splitting of 216 cm^{-1} is largely due to the potential asymmetry.

Surprisingly, the ‘tunnelling’ band is rather sharp. The measured full width at half maximum (FWHM) of $\approx 10\text{ cm}^{-1}$ is probably greater than the real bandwidth. This is clear evidence that proton transfer is also totally decoupled from heavy atom dynamics, in line with the remainder of the spectrum. Therefore, the prevailing idea that proton transfer should occur along a complex multidimensional reaction path due to rearrangement of the heavy atoms [34,38,41,42,49] is not confirmed. The double minimum potential in Figure 8.9 corresponds to the transfer of a single proton within dimers. The positions of the potential minima at $\approx \pm 0.3\text{ \AA}$ off the hydrogen bond centre are in agreement with the crystal structure. Therefore, tautomerization and proton disordering arise from uncorrelated transfer of each proton (see Figure 8.10).

This view is quite at variance with the direct interconversion between I and II proposed on the basis of NMR studies [41]. These different views correspond to measurements performed at different time scales. NMR and QENS measure only probabilities averaged over rather long time scales, compared to the transfer rate of a single proton. Only vibrational spectroscopy can probe the quantum regime and distinguish intermediate configurations. Similar double minimum potentials have

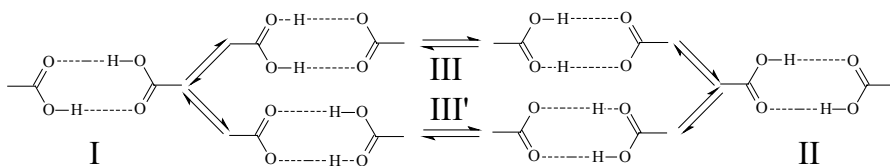


Figure 8.10 Schematic representation of the proton transfer dynamics and tautomerization in the KHCO_3 dimer. For the sake of clarity, the electric charges of I and II are not shown.

been reported for other bicarbonates [12] and for benzoic acid [50]. In all cases, potential barriers, distances between the minima, ν OH frequencies and tunnelling transitions are quite similar.

The potential barrier of $\approx 5000 \text{ cm}^{-1}$ between the two minima is so high that the probability of a semiclassical proton jump over the barrier is negligible at any temperature. Therefore, the quantum regime prevails, even at room temperature. This is also quite at variance with the phenomenological model proposed by Skinner and Trommsdorff [42]. This phonon-assisted tunnelling model gives a potential barrier about ten times smaller and semiclassical jumps dominate at room temperature. This conclusion can be rejected safely upon quick examination of the ν OH frequency at about 3000 cm^{-1} . The potential barrier is necessarily significantly greater than this frequency.

Clearly, the opportunity to observe tunnelling transitions with INS is an important step toward a better understanding of proton transfer dynamics. Further improvements of the spectrometer resolution should allow us to analyse tunnelling band shapes in more details.

4.2 ROTATIONAL TUNNELLING

For light quantum rotors such as H_2 , CH_3 , NH_3 , CH_4 or NH_4^+ , topological degeneracy arises from the intrinsic periodicity of the angular coordinate. In principle, rotational tunnelling should occur in all systems containing such rotors. However, the tunnel splitting decreases exponentially as the potential barrier between degenerate orientations increases linearly. The splitting cannot be observed if it is below the maximum resolution of a given instrument. With INS, the lower limit is $\sim 1 \mu\text{eV}$. At the other extreme, free rotation is the upper limit for tunnel splitting. For a presentation of tunnelling spectroscopy, it is thus convenient to consider first free rotation.

For a free rotor with a fixed axis, the rotational levels are given by a very simple formula: $E_j = j^2 B$ [51]. The rotational constant $B = \hbar^2/2I_r$ depends on I_r , the moment of inertia of the rotor. The rotational quantum number is $j = 0, \pm 1, \pm 2, \dots$. The wavefunctions are also extremely simple and can be written as:

$$\left. \begin{aligned} \varphi_0(\theta) &= (2\pi)^{-1/2} \\ \varphi_{j+}(\theta) &= \pi^{-1/2} \cos j\theta \\ \varphi_{j-}(\theta) &= \pi^{-1/2} \sin j\theta \end{aligned} \right\} \quad (8.18)$$

In the ground state $E_0 = 0$. The wavefunction is a constant, for there is no preferred orientation. In the upper states, the kinetic momentum is nonzero and levels at $E_{\pm j} = j^2 B$ are degenerate, as clockwise and anticlockwise rotations are indistinguishable.

The rotational constants for the free H_2 molecule rotating around a fixed axis perpendicular to the H–H bond and passing through the centre is ≈ 7.4 meV (or 59.6 cm^{-1}) [51]. For rotors with a ternary axis of inertia supposed to be fixed, the rotational constant is ≈ 780 μeV (6.3 cm^{-1}) for NH_3 (gas-phase geometry) or ≈ 675 μeV (5.5 cm^{-1}) for CH_3 groups [52]. For tetrahedral rotors, the rotational constant depends on the choice of the rotational axis.

For rotors chemically bound to a molecular frame, the effective potential in the crystalline state is the sum of two contributions: the intramolecular potential arising from chemical bonding and additional terms due to the crystal environment. It is extremely unlikely that free rotation in the solid state could arise from exact cancellation of the different contributions. Therefore, a vanishing intramolecular potential barrier is a prerequisite for free rotation in the solid state. This occurs only for methyl groups bound to planar conjugated frames such as aromatic rings or acetate ions. For these free molecular rotors, and for small molecules such as NH_3 or CH_4 inserted in a lattice, tunnelling is a very sensitive probe of the local potential arising from the environment.

In many molecular crystals the frequency range for tunnelling is well separate from internal vibrations and from the optical phonon density of states. On the time scale of the tunnelling frequency, the lattice can be regarded as static and the dynamical interaction of tunnelling with the lattice is normally very weak. Therefore, tunnelling transitions are specific to rotational coordinates and dynamics can be represented by rather simple Hamiltonians ignoring other degrees of freedom. For hydrogenated tops, this specificity can be fully exploited with the INS technique, because of the cross-section of H atoms. Any intensity arising from the crystal density of states can be regarded as a virtually flat background.

Nowadays, transitions above ≈ 1 μeV are observed with advanced spectrometers available at various neutron sources (for a recent compilation, see Ref. 52). However, the observation of tunnelling transitions for deuterated analogues is hampered by the much weaker cross-section of D atoms and by the dramatic decrease of the splitting upon deuteration. This is a limitation for modelling rotational dynamics. Unfortunately, the hope that advanced methods of quantum chemistry and molecular dynamics simulation could provide realistic modelling of the effective potential experienced by methyl rotors is not yet realized [53,54]. As long as tunnelling frequencies cannot be calculated with good accuracy (say to within a few μeV), experiments remain the best source of knowledge of these quantum dynamics. In this section, we present a few examples to highlight the impact of rotational tunnelling in organometallic science.

4.2.1 Rotational Dynamics of the Dihydrogen Ligand in Metal Complexes

In 1984 G. J. Kubas demonstrated the existence of coordinated molecular hydrogen in certain metal complexes, involving an entirely new type of chemical bonding to metals

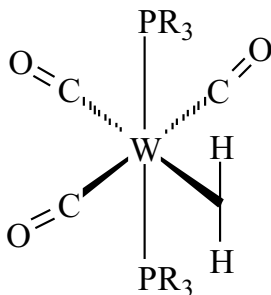


Figure 8.11 Schematic representation of the metal–hydrogen bond.

(σ -bond complexes, see Figure 8.11) [55]. Activity in this new area has expanded greatly and the importance of the role of dihydrogen in several catalytic processes has been recognized [56].

One of the key indicators for the so-called nonclassical coordination in the solid state has been the observation of rotational transitions by INS [57,58]. These studies have led to a value for the rotational barrier of the dihydrogen ligand under the assumption of a model for this rotation. The barrier in turn was then tentatively analysed in terms of distinctive interactions by theoretical calculations or a series of experiments where one or more of these factors were changed.

The simplest model for the rotation of a dumbbell molecule is planar reorientation about a fixed axis perpendicular to the midpoint of the H–H bond. The potential function has necessarily twofold symmetry and the model Hamiltonian for rotational dynamics can be written as:

$$H_2 = -B \frac{d^2}{d\theta^2} + \frac{V_2}{2}(1 - \cos 2\theta) \quad (8.19)$$

The first term represents the kinetic rotational energy. This equation is amenable to Mathieu's equation and analytical formulae for the eigenstates are known. However, with computer facilities available nowadays, it is faster to calculate numerically both eigenvalues and eigenfunctions [59]. If necessary, these calculations can be performed for potential functions including several Fourier terms.

The energy level diagram and wavefunctions for a moderately high potential barrier are shown in Figure 8.12. For a free rotor, levels $|\pm 1\rangle$ or $|\pm 2\rangle$ in Equation (8.18) are degenerate. As the potential barrier is increased, E_{+1} decreases whilst E_{-1} increases toward E_{-2} . For an infinitely high potential barrier the level degeneracy is twofold. The potential barrier V_2 in Equation (8.19) can be estimated from the observed tunnelling frequency $\nu_t = (E_{-1} - E_0)/\hbar$.

As the hydrogen molecule has no permanent dipole moment, rotational transitions are inactive in the infrared, but not necessarily in Raman (see Section 2.2). However, as the molecule is composed of two indistinguishable fermions, the nuclear spins are correlated to the symmetry of the rotational states. According to the Pauli

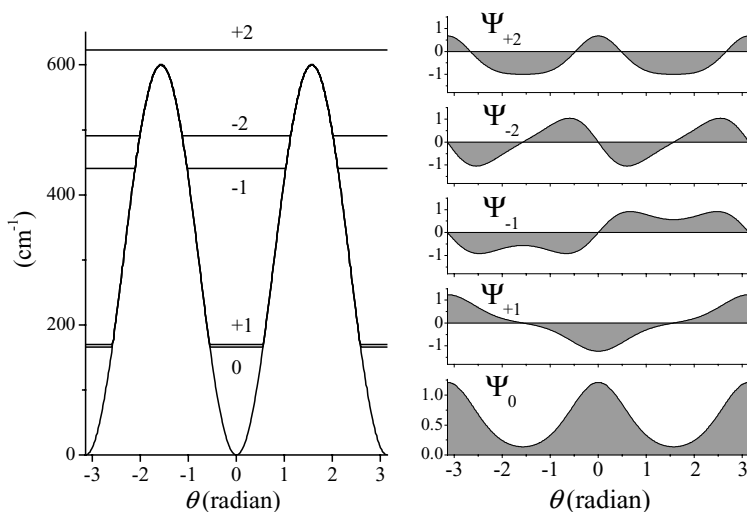


Figure 8.12 (Plate 5) Potential function (left) and wavefunctions for hindered rotation of a H_2 molecule. The rotational constant was set to 56 cm^{-1} and the potential barrier to 600 cm^{-1} . The $|0\rangle$ – $|1\rangle$ splitting is $\approx 3.7 \text{ cm}^{-1}$.

principle, the total wavefunction, including nuclear spins, must be antisymmetric with respect to permutation of the nuclei. The $|0\rangle$ and $|-2\rangle$ states are singlets (the total nuclear spin $S = 0$), whilst the states $|+1\rangle$ and $|+2\rangle$ are triplets ($S = 1$). Consequently, transitions between states with different rotational symmetries, for example the tunnelling transition $|0\rangle \rightarrow |+1\rangle$, that may have optical activity, cannot be observed in the case of H_2 molecules, as they involve a change in the total nuclear spin. This is analogous to the *ortho*–*para* transition of the hydrogen molecule itself. These transitions can be probed exclusively with INS techniques, because in addition to exchanging energy and momentum, neutrons can also induce spin flip for protons.

At first glance, higher order terms in the Fourier expansion of the potential function in Equation (8.19) might arise from the local environment. Inspection of the structure of many of the dihydrogen complexes would suggest the presence of at least one additional set of potential minima. However, these terms are usually small and cannot be determined with INS. The reason why the simplest picture of the rotation of the dihydrogen ligand seems to be a good description is likely to be the fact that the dynamics arise primarily from a strong three-center H–M–H chemical bond which keeps the ligand essentially in a plane as it rotates [57].

The observation of tunnelling transitions in metal complexes can be hampered by the other hydrogen-containing ligands (e.g., isopropyl, ethyl, or phenyl groups) that are usually present in these complexes. In addition, large counterions needed to crystallize ionic complexes may contain many protons. Even if these ligands have no observable excitations at low temperatures in the tunnelling energy range of the dihydrogen ligand, they give rise to an extremely intense elastic peak centred at zero

frequency, whose intensity is proportional to the total number of protons in the beam. The relative intensity for tunnelling can be much less than 1 %. Furthermore, as dynamical disordering of the ligands significantly broadens the elastic peak, it may overlap the tunnelling band at low frequency and the measurements is then problematic.

The measurements of higher transitions (usually referred to as rotational transitions) are of great interest to determine the contribution of higher order terms in the Fourier expansion of the potential function. However, in the frequency range of rotational transitions ligands may have intense transitions arising from their many methyl groups. INS experiments on these complexes involve a subtraction of the vibrational spectrum of a sample with O₂ ligands (regarded as a background) from that of a sample with H₂ ligands. This is based on the assumption that the vibrational modes of the other proton-containing ligands on the metal do not couple strongly with those of the dihydrogen ligand. They are supposed to be essentially unaffected by the isotope substitution.

In spite of these difficulties, the ground-state rotational tunnel splitting, as well as the two transitions to the split excited librational states could be observed in some cases [57,58]. Because the tunnel splitting ($\sim 1 \text{ cm}^{-1}$) can be measured with much better accuracy than the librational transitions, the value for the twofold barrier height was estimated from the former. Additional minor higher terms in the expansion of the potential were adjusted to improve the agreement between observed and calculated transitions.

Another difficulty is the change of the rotational constant upon activation of the dihydrogen ligand. The rotational constant of activated dihydrogen is smaller than that for molecular hydrogen because of the lengthening of the H–H bond. Only in cases where the H–H bond length has been obtained by neutron diffraction is B known. For example, for the Kubas' tungsten complexes $B = 49.5 \text{ cm}^{-1}$ was derived from the bond length of 0.82 \AA determined by neutron diffraction [60]. If this bond length is unknown, modelling and quantum chemistry methods are necessary. However, this may cast some doubt on the final result.

Tunnelling transitions for the dihydrogen ligand in various complexes have been observed with INS between 17 cm^{-1} ($\approx 2 \text{ meV}$) and 0.6 cm^{-1} ($\approx 75 \text{ \mu eV}$) [57,58]. In several cases tunnel splitting was unobservable and was therefore supposed to be in the range below $\sim 0.01 \text{ cm}^{-1}$ ($\sim 1 \text{ \mu eV}$). The associated barriers to rotation range from about 0.6 to $2.4 \text{ kcal mol}^{-1}$ ($200\text{--}800 \text{ cm}^{-1}$).

Owing to large distances between dihydrogen ligands in crystallized complexes, the likely contributions to the rotational barrier are primarily of intramolecular origin. One can distinguish the direct electronic interactions between the dihydrogen and the metal, and the nonbonded (mostly van der Waals forces) interactions between the hydrogen atoms and the neighbouring atoms on the same complex. Both experiments and theoretical calculations agree that the major factor is direct electronic interaction of H₂ with the metal. There is a pronounced effect of the metal centre itself. The ratios of the tunnel splitting are approximately 1 : 3 : 5 for W/Mo/Cr. As opposed to this, the change in the phosphine ligands was found to shift the mean tunnelling transition by only $\sim 20 \%$. This conclusion is also strongly supported by theoretical calculations.

Finally, many details on the interactions between the dihydrogen ligand, the metal and the coligands have emerged from these INS studies of the hindered rotation. The potential barrier is largely the result of the $M-(H_2)$ bonding. It reflects the degree of back bonding from the metal to $\sigma-(H_2)$ in cases where barriers are compared for complexes that differ only in the metal centre. However, large changes in the ligand sets on a metal are of consequence to the back-donation and the barrier height and it is not easy to distinguish different contributions. A very delicate balance of the interactions between dihydrogen and the metal leads to stable dihydrogen binding.

4.2.2 Free Rotation of NH_3 Molecules in Hofmann Clathrates

Hofmann-type clathrates have the general chemical formula $M(NH_3)_2M'(CN)_4 \cdot 2G$, usually abbreviated as $M-M'-G$ [61]. M (Ni, Fe, Co, Cd) is a six-coordinated and M' (Ni, Pt, Pd) is a four-coordinated divalent metal ion. The guest molecule is mostly an aromatic molecule (benzene, aniline, pyrrole).

The crystal structure of the Ni–Ni–Bz derivative is composed of layers containing metal ions cross linked by $C\equiv N$ groups (see Figure 8.13) [62,63]. Two ammonia

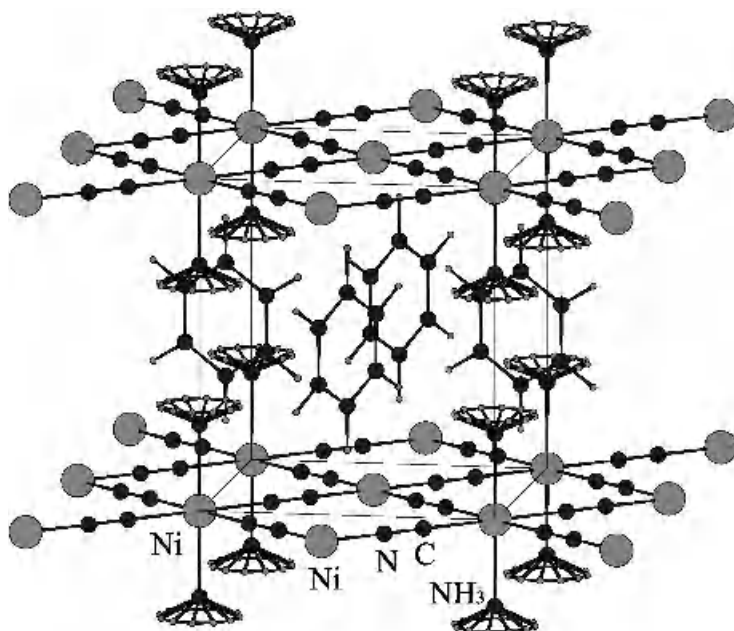


Figure 8.13 Schematic view of the structure of the Ni–Ni Hofmann clathrate with benzene as guest molecule. The planes of the benzene guest molecules are perpendicular to the plane of the metal ions cross-linked by $C\equiv N$ entities. The disordered NH_3 groups are represented as a superposition of four crystallographically equivalent configurations. Reproduced with permission of the International Union of Crystallography.

Table 8.1 Free rotor $|0\rangle \rightarrow |1\rangle$ rotational transitions of NH_3 in various M–Ni– C_6D_6 Hofmann clathrates at 2 K, after Ref. 68, and M–N(H_3) stretching frequencies, after Ref. 69.

	Zn–Ni	Ni–Ni	Mn–Ni	Fe–Ni	Cu–Ni
$ 0\rangle \rightarrow 1\rangle$ (μeV)	710	710	703	681	698
M–N(H_3) stretch (cm^{-1})	350	372	—	—	460

molecules are bound, via their N atoms, to M ions. $\text{H}_3\text{N–M–NH}_3$ entities are in a *trans* configuration perpendicular to the layers. The guest molecules are caged between the layers. There are four crystallographically equivalent H atom positions around each N atom. The crystal structure suggests rotationally disordered NH_3 groups with a virtually isotropic distribution of protons [62].

INS experiments performed with the Ni–Ni– C_6D_6 derivative have revealed a series of transitions that fit exactly with those anticipated for a free uniaxial rotor with $B \approx 0.71$ meV [64]. More recently, INS spectra of the Ni–Ni clathrate with caged biphenyl molecules ($\text{C}_{12}\text{H}_{10}$) gave the same result [65]. Compared to the molecular geometry of NH_3 in the gas phase, the rotational constant is decreased by $\sim 10\%$. This increase of the gyration radius can be easily attributed to a structure closer to planarity due to coordination with the metal ion. Alternatively, the apparent decrease of the rotational constant has been tentatively attributed to a coupling of the rotational coordinate with displacements of the N atom [66,67]. Rather sophisticated dynamical models have been developed but they do not yield convincing results compared with the ‘chemical’ interpretation. To the best of our knowledge, there is no unquestionable evidence for this coupling. As opposed to that, neutron diffraction measurements performed with a powdered Ni–Ni– C_6D_9 sample at 25 K suggest that the structure of the NH_3 entities is consistent with the rotational constant of ~ 0.71 meV [62].

INS spectra of a series of Hofmann clathrates M–Ni– C_6D_6 with M=Zn, Mn, Fe and Cu give very similar frequencies (see Table 8.1) [68]. The averaged value is $B = (700 \pm 10)$ μeV . The nature of the metal ion has little effect on the rotational constant. Nevertheless, the possible correlation with the M–N(H_3) stretching frequencies [69], suggests a small decrease of the rotational constant for the higher stretching frequency. This is consistent with an increased planarity for the stronger M– NH_3 binding.

4.2.3 The Single Methyl Rotor

The simplest model for methyl rotation is the single rigid rotor in a threefold potential. The Hamiltonian can be written as

$$H_3 = -B \frac{d^2}{d\theta^2} + \frac{V_{03}}{2} (1 - \cos 3\theta) \quad (8.20)$$

Eigenstates $E_{n\sigma}$ and wave functions $\Psi_{n\sigma}(\theta)$ depend on two quantum numbers: the

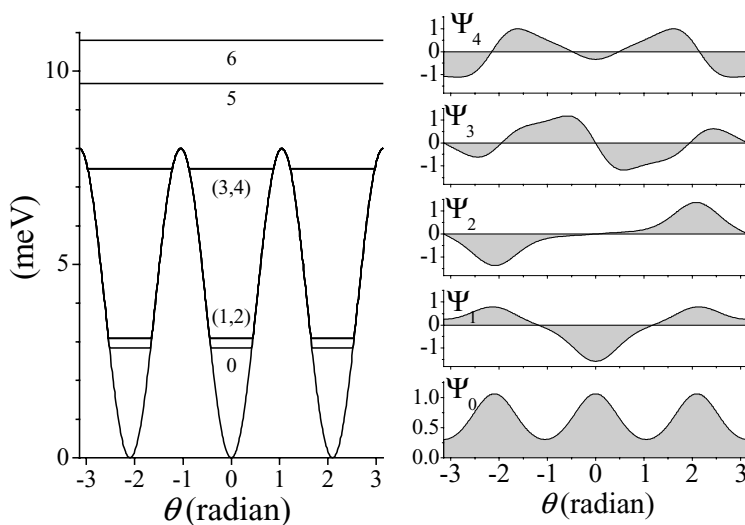


Figure 8.14 Eigenstates and eigenfunctions for a methyl rotor in a threefold potential.

principal rotational quantum number n for the oscillator limit with full degeneracy and a sublevel index σ , which gives the symmetry of the wavefunction. As there is no analytical solution for the eigenvalues, numerical calculations using the basis set of the free rotor are carried out with the variational method (Figure 8.14) [59,70]. In this simple model, there is only one tunnelling transition and it is straightforward to estimate the threefold potential barrier from measurements. Experimental values can be compared with those estimated with various models (for example quantum chemistry methods) [53,54].

A graphic example is the crystal of manganese diacetate tetrahydrate, $\text{Mn}(\text{CH}_3\text{COO})_2 \cdot 4\text{H}_2\text{O}$, which contains three crystallographically inequivalent methyl groups [71]. The INS spectrum of a powdered sample at 1.5 K reveals three tunnelling transitions at 1.2, 50 and 137 μeV , with equal intensities [72]. The corresponding potential barriers (49.0, 17.5 and 11.5 meV, respectively), according to Equation (8.20), emphasize the great sensitivity of the tunnelling frequency to the local potential. However, effective potentials arising from the crystal environment at each site cannot be calculated with sufficient accuracy to propose a firm assignment scheme for the tunnelling frequency to the proper rotor site.

The structure of manganese diacetate tetrahydrate determined with X-ray diffraction reveals the orientations of the rotational axes of the methyl groups (see Figure 8.15) [73–75]. Then, with properly oriented single crystals, the INS intensity of the tunnelling transitions can be probed as a function of the orientation of the momentum transfer vector \mathbf{Q} with respect to the rotational axes. The intensity is a maximum when \mathbf{Q} is perpendicular to the axis of rotation and it vanishes if \mathbf{Q} is parallel. According to such measurements, the tunnelling frequencies at 1.2, 50 and 137 μeV are attributed to sites C, B and A, respectively.

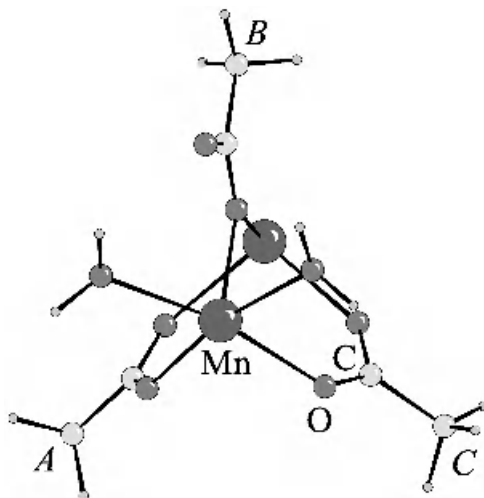


Figure 8.15 Schematic representation of the arrangement of the three inequivalent methyl groups in the manganese diacetate tetrahydrate crystal at 14 K. Reproduced with permission of the International Union of Crystallography.

The neutron diffraction technique is complementary to X-ray diffraction. The scattering cross-section of electrons is negligible and Bragg peaks arise from scattering by nuclei. This technique is unique to determine the position of H atoms because the nuclear cross-sections are on the same order of magnitude for all nuclei. For example, the orientation of the methyl groups and of the water molecules were determined for manganese diacetate tetrahydrate, as partially shown in Figure 8.15 [71].

With the Fourier difference method, data obtained from single-crystal neutron diffraction provide a full view of the probability density of the H(D) atoms. For this purpose, once the crystal structure has been determined, Bragg peak intensities can be calculated for an ideal crystal in which the scattering cross-section of the H(D) atoms of the methyl groups is set to zero. The difference from the original pattern contains specific information on the methyl H(D) atoms. Further Fourier back-transformation gives the probability density distribution in direct space (see Figure 8.16).

Because diffraction arises from coherent scattering by a large number of atoms in a regular lattice, disorder appears as a perturbation of the lattice periodicity averaged over space and time. It is impossible to distinguish statistical and dynamical disorder. However, the dynamical orientational disorder of a methyl group is so large compared to disorder arising from other vibrations that the angular probability density is quite representative of the wave function and can be related to the potential.

The different rotational dynamics of the three methyl groups in the manganese diacetate tetrahydrate crystal at 14 K are immediately recognized by visual inspection of the Fourier difference maps (Figure 8.16). The highest potential barrier (lowest tunnelling frequency) occurs for the methyl group C whose protons are quite localized.

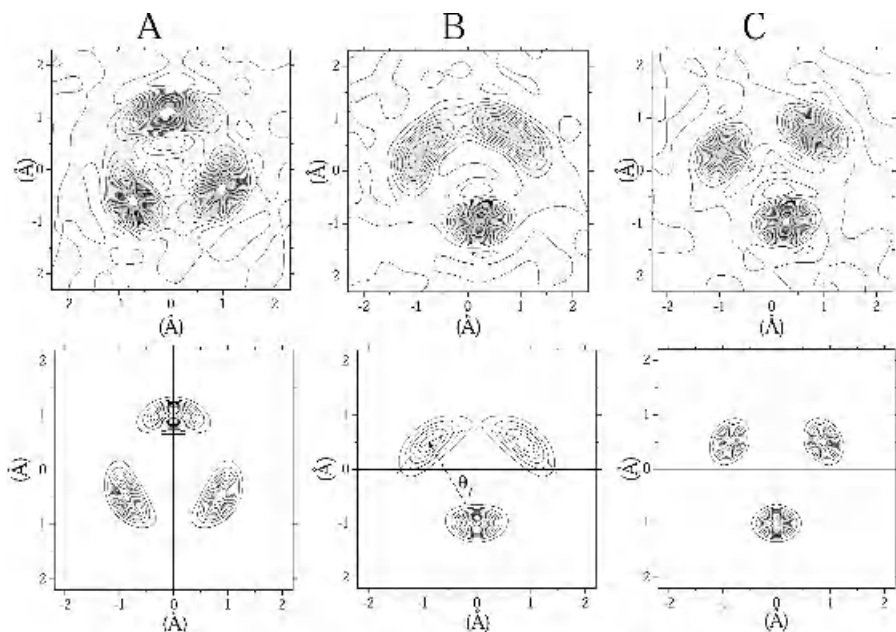


Figure 8.16 Top: measured probability density distributions for the three inequivalent methyl groups in the manganese diacetate tetrahydrate crystal measured at 14 K. Labels A, B and C refer to those in Figure 8.15. Bottom: calculated maps (see text). (A) $V_3 = 11.5$ meV, $u_r^2 = 0.05 \text{ \AA}^2$. (B) $V_3 = 17.6$ meV, $u_r^2 = 0.05 \text{ \AA}^2$, $\theta_L^2 = 0.06 \text{ rad}^2$. (C) $V_3 = 49.0$ meV, $u_r^2 = 0.05 \text{ \AA}^2$. Reproduced with permission of the International Union of Crystallography.

The more delocalized protons for the methyl group A correspond to the lowest potential barrier (highest tunnelling frequency).

The map for the methyl group B is much more intriguing. Whereas the distributions for A and C have clearly the threefold symmetry anticipated for rigid methyl groups with fixed axes, the probability densities at the three proton sites are quite different for methyl B. Of course, the three protons are indistinguishable. As each proton is totally delocalized the total probability is the same for each site. The probability density is actually a comprise of several contributions arising from both the methyl groups and the crystal lattice. It is necessary to analyze these maps more thoroughly in order to highlight rotational dynamics.

One can distinguish three contributions to the probability density: (i) the rotational dynamics; (ii) the deformation of the methyl groups due to internal vibrations; (iii) the lattice dynamics and/or disorder. Because the tunnelling occurs at a very low frequency, lattice dynamics and internal vibrations can be represented with time/space-averaged distributions. It is convenient to distinguish isotropic and anisotropic contributions. The former, as opposed to the latter, does not disturb the threefold symmetry.

- (i) From the tunnelling frequency and Equation (8.20) the temperature-dependent angular probability density is determined by the Boltzmann distribution:

$$P_d(\theta, T) = \frac{\sum_{n\sigma} \Psi_{n\sigma}^2(\theta) \exp(-E_{n\sigma}/kT)}{\sum_{n\sigma} \exp(-E_{n\sigma}/kT)} \quad (8.21)$$

- (ii) Methyl groups are not perfectly rigid. The eight degrees of freedom for internal motions give rise to complex vibrations that can be represented with a static distribution for the H atoms. The projection onto the rotational plane gives an isotropic distribution with a Gaussian-like profile. The variance (mean square amplitude) of $\sim 0.01 \text{ \AA}^2$ is largely temperature independent.
- (iii) Similarly, lattice vibrations give rise to an isotropic Gaussian distribution for the C atom with a variance of $\sim 0.02 \text{ \AA}^2$ at a low temperature. This value may increase significantly as the temperature approaches the melting point. The mean square displacements in the rotational plane are further multiplied by a factor of ~ 2 due to the distance between the rotational plane and the C atom.

Altogether, the observed angular distribution for a given methyl group is a convolution of the density distribution for the rotational coordinate with those for internal and external vibrations. Dynamical models suggest that the probability densities measured for the A and C rotors are directly related to the square of the rotational wave functions, with minor contribution from other dynamics (see Figure 8.16). For the B rotor, the dynamical probability density is convoluted with an anisotropic distribution of the angular coordinate θ_L representing the orientational disorder of the methyl axis with respect to one of the potential minima.

Tunnelling bands are well observed only at very low temperature, usually below 50 K. At higher temperatures, bandwidths increase and transitions merge into the huge peak due to elastic scattering. The prevailing interpretation is that the quantum dynamics switches to classical diffusion at high temperature. Nowadays, density distributions obtained at any temperature compatible with the stability of the crystal shed light onto the rotational dynamics at high temperature.

At room temperature, the proton distributions for rotors A and B are almost isotropic (see Figure 8.17). Nearly free rotation arises mainly from thermal population of rotational levels close to, or above, the top of the potential barrier. (The rather modest anisotropic features may arise from convolution with lattice displacements.) For the C rotors, partial localization of the protons due to hindered rotation is still observed and the effective potential barrier still exists at 300 K. In addition, a marked anisotropic contribution from the lattice dynamics is observed. The quantum dynamics is likely to survive even at room temperature and mixing of higher rotational states with phonons may take place.

4.2.4 Hexamine Complexes

Evidence for rotational dynamics at very low energy in $\text{Ni}(\text{NH}_3)_6\text{X}_2$ complexes, with $\text{X} = \text{I, Br or Cl}$, was first obtained from specific heat measurements down to

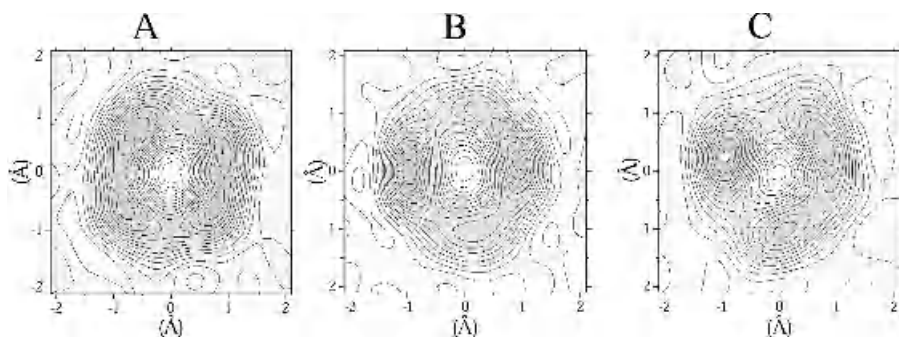


Figure 8.17 Measured probability density distributions for the three inequivalent methyl groups in the manganese diacetate tetrahydrate crystal at 300 K. Labels A, B and C refer to those in Figures 8.15 and 8.16. Reproduced with permission of the International Union of Crystallography.

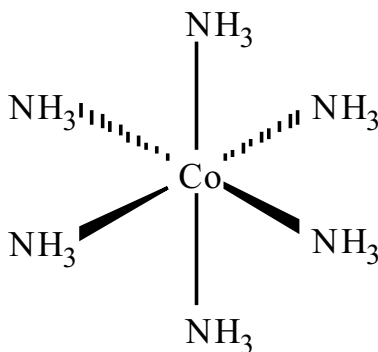


Figure 8.18 Schematic view of the structure of the cobalt hexamine complex.

~ 0.1 K [76]. Schottky anomalies were attributed to a two-level system with a small energy separation of 62, 10.5 and 3–4 μeV for I, Br and Cl, respectively. Tunnelling transitions have been directly observed with INS at 63 ± 2 and 8.0 ± 0.3 μeV for the I and Br derivatives [77]. However, for the Cl derivative, the tunnel splitting could not be resolved. It is presumably smaller than 1 μeV .

Nearly free rotation of NH_3 ligands has also been observed for a cobalt hexamine complex: $\text{Co}(\text{NH}_3)_6(\text{PF}_6)_2$ [78]. In the crystalline state, there is a considerable uncertainty surrounding the relative orientations of the NH_3 groups. At low temperature, (below ~ 20 K) the NH_3 groups are supposed to take up preferred orientations, which however could not be determined with crystallographic techniques. The INS spectra reveal a series of transitions that differ significantly from those of the free rotor (see Table 8.2). Close inspection of the spectra under high resolution and very low temperature suggests that all rotors are equivalent.

Table 8.2 Rotational transitions observed with INS and assignments for $\text{Co}(\text{NH}_3)_6(\text{PF}_6)_2$ at 1.7 K, after Ref. 78

Frequency (meV)	0.54	1.09	1.40	1.88	2.44	2.98
Assignment	$ 0\rangle \rightarrow 1\rangle$	$2 \times (0\rangle \rightarrow 1\rangle)$	$ 1\rangle \rightarrow 2\rangle$	$ 0\rangle \rightarrow 2\rangle$	$ 1\rangle \rightarrow 3\rangle$	$ 0\rangle \rightarrow 3\rangle$

The $|0\rangle \rightarrow |1\rangle$ transition at 540 μeV is smaller than the rotational constant by $\sim 35\%$. This decrease is too large to be attributed to a change of the NH_3 geometry. Moreover, the upper transitions do not fit the simple progression anticipated for a free rotor. It has been found that the observed frequencies are well fitted with a simple sixfold potential with a rather high barrier, $V_6 = 15.0 \text{ meV}$ (120 cm^{-1}). However, this is rather disturbing since there is apparently no direct correlation between the sixfold periodicity and the environment of the NH_3 rotors. It was noticed that it is not possible to arrange the NH_3 groups such that each of the six groups is in an environment of rigorous C_2 symmetry generated only by its neighbouring entities. Consequently, the crystal field is likely to play a dominant role in the potential symmetry. Moreover, temperature effects suggest that dynamical coupling could occur between neighbouring rotors. It is thus clear that the apparently straightforward interpretation of the tunnelling transition brings new questions to the front of the scene. Further experimental and theoretical progress is needed.

4.2.5 Quantum Rotational Dynamics for Pairs of Coupled Rotors

Pioneering INS works with rather modest resolution have first revealed single tunnelling transitions and dynamical models for single rotors were sufficient to interpreting the spectra [77,79]. With better spectrometer resolution, multicomponent spectra due to dynamical coupling were observed and different models were proposed to account for local or collective rotational dynamics. The diversity of models is partly due to the lack of information and this is a long lasting source of polemics that keep the field lively.

The lithium acetate dihydrate ($\text{CH}_3\text{COOLi}\cdot 2\text{H}_2\text{O}$ or Liac-h) crystal is a typical example to emphasize the need to utilize simultaneously the most advanced neutron diffraction and INS techniques, along with isotope substitution, to rationalize complex rotational dynamics beyond the isolated methyl group approximation.

For the fully hydrogenated derivative the crystal symmetry ($Cmmm$) remains unchanged upon cooling from room temperature to 1 K [54,80]. The methyl groups are arranged in infinite chains, along the a crystal axis, of face-to-face coaxial pairs parallel to b (see Figure 8.19). The distances between consecutive axes of rotation ($a/2 \approx 3.4 \text{ \AA}$) and between the methyl-carbon atoms within pairs ($0.3b \approx 3.3 \text{ \AA}$) are significantly shorter than the van der Waals radii and significant interactions along the chains and within pairs are schematically represented as a honeycomb-like structure in 2D,

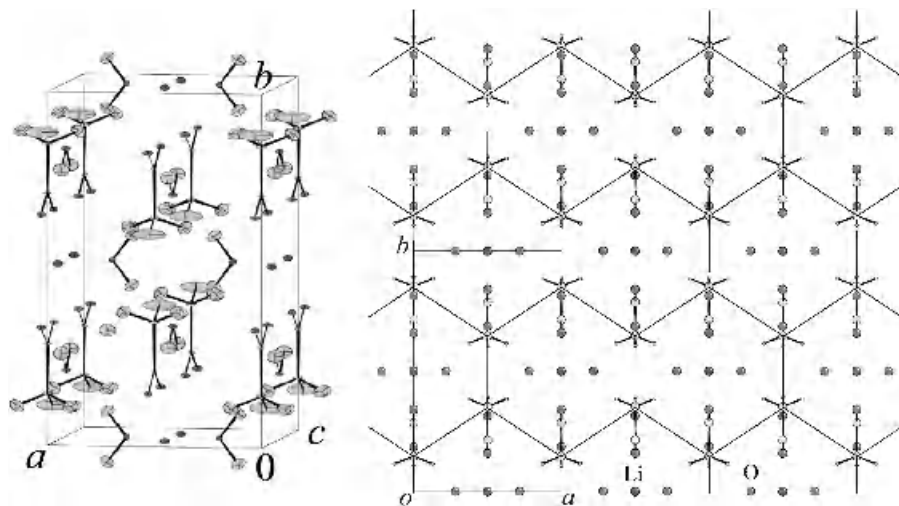


Figure 8.19 Crystal structure of the methyl deuterated lithium acetate dihydrate. Left: view of the unit cell with thermal ellipsoids. Right: projection onto the (a, b) plane. The lines along nearest neighbour interactions are guides for the eye. For clarity, the hydrogen atoms of the water molecules are hidden. Reproduced with permission from Chem. Phys. **290**, B. Nicolai, A. Cousson and F. Fillaux, *The effect of methyl deuteration on the crystalline structure in Lithium acetate dihydrate*, 101, Copyright (2003) Elsevier.

parallel to the (a, b) planes. The interlayer distances of $\sim 6.56 \text{ \AA}$ between (a, b) planes are much greater and interaction between methyl groups along the *c* axis is negligible.

For Liac-h the methyl groups are totally disordered at any temperature and the angular probability density is totally isotropic, even at $\sim 1 \text{ K}$ [54]. Quite surprisingly, the methyl deuterated derivative ($\text{CD}_3\text{COOLi}\cdot 2\text{H}_2\text{O}$ or Liac- d_3, h_4) undergoes a phase transition at 17.5 K , from *Cmmm* to *Pman* symmetry. The ordering of the centrosymmetric pairs of methyl groups is clearly observed with the neutron diffraction technique (Figure 8.20) [81,82]. As all other atomic coordinates remain virtually unchanged, there is no significant variation of the effective potential arising from heavy atoms and the phase transition is entirely due to mass effects on the quantum dynamics.

In the ordered phase at 14 K the localization of the probability density distribution is consistent with a rather high potential barrier (see Figure 8.20). The two methyl groups in centrosymmetric pairs are indistinguishable and their images are superimposed in the Fourier difference. (The three peaks do not mean that the two methyl groups are in the eclipsed conformation.) At 300 K , the disorder is fully established. At 40 K , there is a mixture of ordered and disordered methyl groups which means that the potential barrier does not vanish at the phase transition. The density is a superposition of angular distributions for delocalized ($\sim 50 \%$) and localized deuterium atoms ($\sim 50 \%$). The six maxima do not mean that the rotational potential changes progressively from threefold to sixfold symmetry and then to free rotation upon increasing the temperature. At 40 K deuterium atoms are still partially ordered

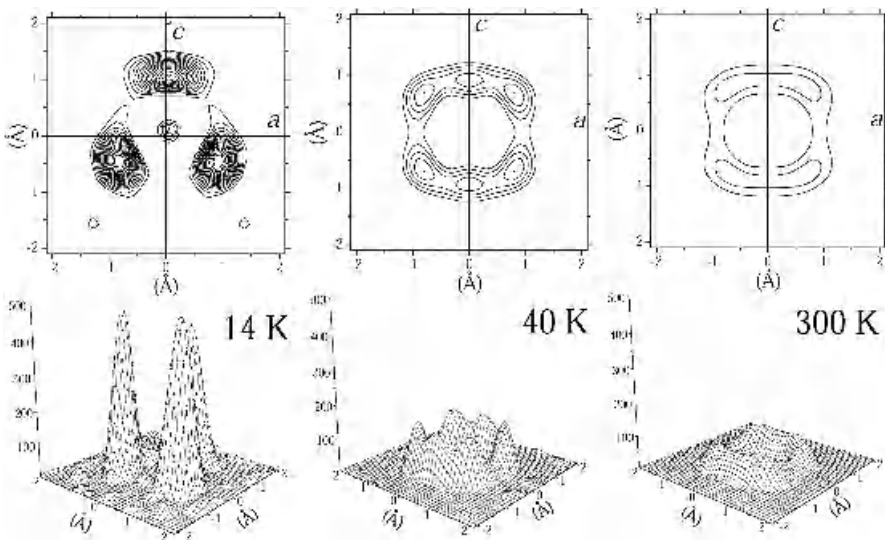


Figure 8.20 Probability density distributions of the deuterium atoms in the methyl deuterated lithium acetate dihydrate ($\text{CD}_3 \text{COOLi} \cdot 2\text{H}_2\text{O}$) at 14 K in the ordered phase $Pm\bar{a}n$, 40 K in the $Cmmm$ phase, slightly above the transition, and, in the same phase, at room temperature. Reproduced with permission from Chem. Phys. **290**, B. Nicolai, A. Cousson and F. Fillaux, *The effect of methyl deuteration on the crystalline structure in Lithium acetate dihydrate*, 101, Copyright (2003) Elsevier.

but face-to-face methyl groups are no longer indistinguishable in the $Cmmm$ phase and give six maxima of density.

Early measurements of the proton spin–lattice relaxation revealed almost free rotation of the methyl groups [83]. However, the tunnelling bands observed in the $300 \mu\text{eV}$ range (see Figure 8.21) are quite below the frequency anticipated for almost free rotation ($\sim 675 \mu\text{eV}$). Moreover, since all methyl groups in the crystal experience the same effective potential the rather complex spectrum must be interpreted in terms of dynamical correlation between indistinguishable quantum rotors.

In the low-resolution limit, the threefold potential barrier for a single transition at $\sim 250 \mu\text{eV}$ in Equation (8.20) is about 8 meV. Then, the proton density should be quite localized at a low temperature, but this is in conflict with the full delocalization experimentally observed.

For the CD_3 derivative the tunnelling frequency calculated at $33 \mu\text{eV}$ with the same potential barrier is actually observed at $12.5 \mu\text{eV}$ [84]. There is a significant increase of the effective barrier to ~ 11.6 meV. This may contribute to the ordering of the CD_3 at low temperature.

The single rotor is clearly unable to account for the complexity of the observed spectrum. Coupled rotation of pairs of methyl groups with parallel axes suggested by the crystal structure was first represented with the Hamiltonian depending on the

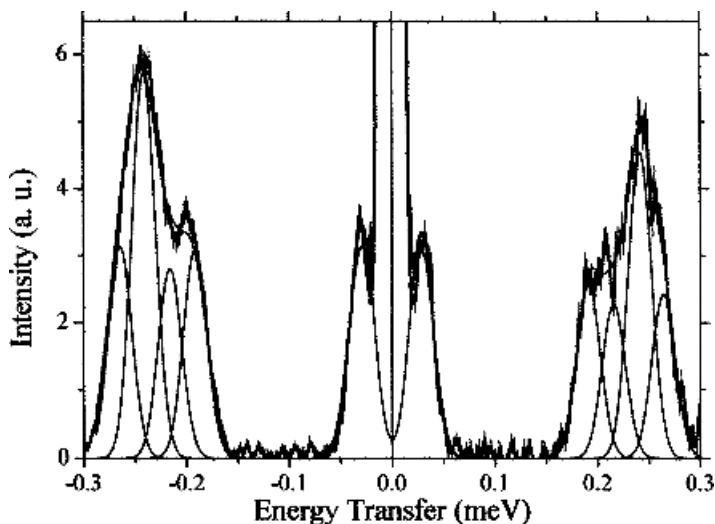


Figure 8.21 Left: the INS tunnelling spectrum of lithium acetate dihydrate at 1.5 K and band decomposition. Reproduced with permission from Chem. Phys. **290**, B. Nicolaï, A. Cousson and F. Fillaux, *The effect of methyl deuteration on the crystalline structure in Lithium acetate dihydrate*, 101, Copyright (2003) Elsevier.

angular coordinates θ_1 and θ_2 [84,85]:

$$H_2 = -B \left(\frac{\partial^2}{\partial \theta_1^2} + \frac{\partial^2}{\partial \theta_2^2} \right) + \frac{V_{03}}{2} \cos 3\theta_1 + \frac{V_{03}}{2} \cos 3\theta_2 + \frac{W_{12}}{2} \cos 3(\theta_1 - \theta_2) \quad (8.22)$$

Each top experiences the same on-site potential V_{03} and the coupling depends only on the phase difference of the two rotors. In contrast to the textbook case of coupled harmonic oscillators, this Hamiltonian cannot be diagonalized by simple transformation into normal coordinates [86]. On the other hand, numerical calculation of the eigenstates and eigenfunctions cannot be carried out with standard methods, for it requires very large basis sets with dimension $\sim 10^5$, and the analysis of the eigenfunctions would be cumbersome.

A more elegant analysis of the dynamics of coupled pairs is based on the crystal structure in which the face-to-face methyl groups are indistinguishable and form centrosymmetric pairs. Consequently, the dynamics are better represented with symmetry-adapted coordinates corresponding to in-phase $\theta_i = (\theta_1 + \theta_2)/2$ and anti-phase $\theta_a = (\theta_1 - \theta_2)/2$ rotation. In contrast, again, to the harmonic case, the choice of the symmetry-adapted coordinates is much more constrained. It is imposed by the periodicity of the rotors. The coordinates must retain the threefold and sixfold periodicity for in-phase and anti-phase rotation. The Hamiltonian can be thus rewritten as:

$$H_{2ia} = H_{2i}(\theta_i) + H_{2a}(\theta_a) \quad (8.23)$$

with

$$\begin{aligned}
 H_{2i}(\theta_i) &= -\frac{B}{2} \frac{d^2}{d\theta_i^2} + \frac{V_{3i}}{2} \cos 3\theta_i \\
 H_{2a}(\theta_a) &= -\frac{B}{2} \frac{d^2}{d\theta_a^2} + \frac{V_{3a}}{2} \cos 3\theta_a + \frac{W_{12a}}{2} \cos 6\theta_a
 \end{aligned}
 \tag{8.24}$$

An important consequence of the symmetry-adapted coordinates is that the rotational constant is divided by a factor 2 compared to the single rotor. The maximum frequency for free rotation is now in the range 325–350 μeV for a pair of CH_3 and 0.162–0.175 μeV for a pair of CD_3 . Therefore, transitions observed around 270 μeV may correspond to pairs rotating almost freely, in accordance with measurements of the spin–lattice relaxation [83].

INS experiments performed with partially deuterated samples ($\text{CH}_2\text{D}\text{COOLi}\cdot 2\text{H}_2\text{O}$) and binary isotope mixtures of CH_3 , CD_3 or CH_2D derivatives gave a more focused view of the rotational dynamics [84]. Finally, the estimated potential barrier $V_{3i} = (1.82 \pm 0.15)$ meV indicates nearly free rotation. In contrast to this, the effective potential barrier for anti-phase rotation is very high: $V_{3a} = 0.19$ and $W_{12a} = 31.64$, in meV units in Equation (8.24).

The phase transition is related to long-range ordering of the methyl groups in the honeycomb-like arrangement of acetate entities in the (a,b) plane (see Figure 8.19). Owing to the great stability of the positions of heavy atoms that remain virtually unchanged through the phase transition, the local potential arising from the mean crystal field is not changed. Therefore, the key parameter for the effective coupling between adjacent pairs of rotors is the angular mean amplitude depending on mass and temperature $\bar{\theta}(T) = \langle \theta^2(T) \rangle^{1/2}$ with:

$$\langle \theta^2(T) \rangle = \int_{-\pi/3}^{\pi/3} d\theta P(\theta, T) \theta^2
 \tag{8.25}$$

with the potential functions determined at low temperature for in-phase rotation, $\bar{\theta}_{\text{IH}} \approx 21^\circ$ for CH_3 pairs and $\bar{\theta}_{\text{ID}} \approx 11^\circ$ for CD_3 analogues.

Finally, there is clear evidence that the phase transition is a direct consequence of the quantum nature of methyl rotation. In the classical regime, methyl groups should become ordered at sufficiently low temperature. For CH_3 rotors, quantum effects are prevailing, the rotational wavefunction is largely delocalized and there is no ordering at any temperature. For the heavier CD_3 rotors, the wavefunction is more localized and long-range ordering can appear. One could say that the dynamics of deuterated methyl groups are ‘more’ classical than those of the hydrogenated analogue.

5 CONCLUSIONS

Vibrational spectroscopy with neutrons sheds new light on proton dynamics in solids. New representations of proton dynamics in hydrogen-bonded systems such as

$\text{KH}(\text{CF}_3\text{COO})_2$) or KHCO_3 are clearly characterized. Direct measurements of effective oscillator masses for proton modes are totally new information that could not be obtained with optical techniques.

Consequently, it is necessary to consider localized vibrations, instead of traditional normal modes. This is a dramatic breakthrough from the viewpoint of proton dynamics. Unfortunately, the spectacular potential of INS cannot be exploited for metal–organic or organometallic complexes containing complicated organic ligands. It is thus necessary to use simplified model molecules, but, so far, very little has been done along this line of research.

Tunnelling spectroscopy is unique to observing quantum nonlinear dynamics in crystals. Evidence for proton transfer along hydrogen bonds is another outstanding contribution of INS. It is another manifestation of the decoupling of proton dynamics from the crystal lattice. The quantum nature of proton transfer dynamics even at room temperature is quite unforeseen and contrasts with mechanisms based on semiclassical diffusion jumps.

The most significant contributions of tunnelling spectroscopy are rotational dynamics of dihydrogen ligands in Kubas complexes, free rotation of NH_3 ligands in Hofmann clathrates, or hindered rotation in cobalt hexamines. Similarly, tunnelling frequencies in metal acetate derivatives provide invaluable information on local crystal fields. Whenever single crystals can be studied, neutron diffraction techniques provide graphic views of the angular probability densities of quantum rotors. These maps are complementary to tunnelling spectroscopy. Temperature effects and selective deuteration are also necessary to fully determine rotational dynamics. Comparison of methyl rotation in various systems emphasizes the interplay of structures and dynamics. It is quite stimulating to realize that many details now accessible to experimental studies at an unprecedented level of accuracy are quite often beyond quantum chemistry calculations.

6 REFERENCES

1. K. Nakamoto, *Infrared Spectra of Inorganic and Coordination Compounds*, 2nd edn, John Wiley & Sons, Inc., New York, 1970.
2. G. Herzberg, *Molecular Spectra and Molecular Structure II, Infrared and Raman Spectra of Polyatomic Molecules*, Van Nostrand, Princeton, N.J., 1964.
3. E. B. Wilson, J. C. Decius, and P. C. Cross, *Molecular Vibrations*, McGraw Hill, New York, 1964.
4. S. Califano, V. Schettino, and N. Neto, *Lattice Dynamics of Molecular Crystals*, Springer, Berlin, 1981.
5. D. A. Long, *The Raman Effect, A Unified Treatment of the Theory of Raman Scattering by Molecules*, John Wiley & Sons, Inc., New York, 2002.
6. J. R. Ferraro, K. Nakamoto, and C. W. Brown, *Introductory Raman Spectroscopy*, 2nd edn, Academic Press, Amsterdam, 2003.
7. C. V. Raman and K. S. Krishnan, *Nature* **121**, 501 (1928).
8. S. W. Lovesey, *Nuclear Scattering*, vol. I of *Theory of Neutrons Scattered from Condensed Matter*, Clarendon Press, Oxford, 1984.
9. L. Landau and L. Lifchitz, *Mécanique Quantique*, vol. III of *Physique Théorique*, MIR, Moscow, 1966.

10. C. Cohen-Tannoudji, B. Diu, and F. Laloë, *Mécanique Quantique*, Hermann, Paris, 1977.
11. L. Golic and J. C. Speakman, *J. Chem. Soc.* 1745 (1965).
12. F. Fillaux and J. Tomkinson, *Chem. Phys.* **158**, 113 (1991).
13. A. J. Pertsin and A. I. Kitaigorodsky, *The Atom-Atom Potential Method*, Springer Series in Chemical Physics, Springer Berlin, 1987.
14. A. C. Zemach and R. J. Glauber, *Phys. Rev.* **101**, 118 (1956).
15. G. J. Kearley, *J. Chem. Soc. Faraday Trans. II* **82**, 41 (1986).
16. A. Griffin and H. Jobic, *J. Chem. Phys.* **75**, 5940 36 (1981).
17. J. O. Thomas, R. Tellegren, and I. Olovsson, *Acta Crystallogr. B* **30**, 1155 (1974).
18. J. O. Thomas, R. Tellegren, and I. Olovsson, *Acta Crystallogr. B* **30**, 2540 (1974).
19. F. Fillaux, A. Cousson, and D. Keen, *Phys. Rev.* **B 67**, 054301 (2003).
20. F. Fillaux, J. Tomkinson, and J. Penfold, *Chem. Phys.* **124**, 425 (1988).
21. K. Nakamoto, Y. A. Sarma, and K. Ogoshi, *J. Chem. Phys.* **43**, 1177 (1965).
22. F. Fillaux, J.-P. Fontaine, M.-H. Baron, G. J. Kearley, and J. Tomkinson, *Chem. Phys.* **176**, 249 (1993).
23. S. Kashida, S. Ikeda and Y. Nakai, *J. Phys. Soc. Jpn* **63**, 4643 (1994).
24. S. Ikeda and F. Fillaux, *Phys. Rev.* **B 59**, 4134 (1999).
25. S. Ikeda, S. Kashida, H. Sugimoto, Y. Yamada, S. M. Bennington, and F. Fillaux, *Phys. Rev.* **B 66**, 184302 (2002).
26. G. Pimentel, C. McClellan, and A. Lester, *The Hydrogen Bond*, W. H. Freeman, San Francisco, CA, 1960.
27. L. Pauling, *The Nature of the Chemical Bond*, Cornell University Press, Ithaca, N.Y., 1960.
28. S. N. Vinogradov and R. H. Linnell, *Hydrogen Bonding*, Van Nostrand-Reinhold, New York, 1971.
29. M. D. Joesten and L. J. Schaad, *Hydrogen Bonding*, Marcel Dekker, New York, 1974.
30. P. Schuster, G. Zundel, and C. Sandorfy, *The Hydrogen Bond. Recent Developments in Theory and Experiments*, vols. I, II and III, North-Holland, Amsterdam, 1976.
31. P. Schuster, *Hydrogen Bonds*, Springer, Berlin, 1984.
32. G. A. Jeffrey and W. Saenger, *Hydrogen Bonding in Biological Structures*, Springer, Berlin, 1991.
33. S. Scheiner, *Hydrogen Bonding: a Theoretical Perspective*, Oxford University Press, Oxford, 1997.
34. M. E. Tuckerman, D. Marx, M. L. Klein, and M. Parinello, *Science* **275**, 817 (1997).
35. C. L. Perrin and J. B. Nielson, *Annu. Rev. Phys. Chem.* **48**, 511 (1997).
36. V. Barone and C. Adamo, *J. Chem. Phys.* **105**, 11007 (1996).
37. W. Siebrand, Z. Smerdarchina, M. Z. Zgierski, and A. Fernandez-Ramos, *Int. Rev. Phys. Chem.* **18**, 5 (1999).
38. M. E. Tuckerman and D. Marx, *Phys. Rev. Lett.* **86**, 4946 (2001).
39. M. Ichikawa, *Chem. Phys. Lett.* **79**, 583 (1981).
40. P. Gilli, V. Bertolasi, V. Ferretti, and G. Gilli, *J. Am. Chem. Soc.* **116**, 909 (1994).
41. R. Graf, R. Meyer, T.-K. Ha, and R. R. Ernst, *J. Chem. Phys.* **75**, 2914 (1981).
42. J. L. Skinner and H. P. Trommsdorff, *J. Chem. Phys.* **89**, 897 (1988).
43. G. J. Kearley, F. Fillaux, M.-H. Baron, S. M. Bennington, and J. Tomkinson, *Science* **264**, 1285 (1994).
44. J. E. DelBene and M. J. T. Jordan, *Int. Rev. Phys. Chem.* **18**, 119 (1999).
45. A. Novak, P. Saumagne, and L. D. C. Bock, *J. Chim. Phys. Chim. Biol.* **60**, 1385 (1963).
46. G. Lucazeau and A. Novak, *J. Raman Spectrosc.* **1**, 573 (1973).
47. F. Fillaux, *Chem. Phys.* **74**, 395 (1983).
48. F. Fillaux, *Chem. Phys.* **74**, 405 (1983).
49. V. A. Benderskii, E. V. Vetoshkin, I. S. Ingibaeva, and H. P. Trommsdorff, *Chem. Phys.* **262**, 393 (2000).

50. F. Fillaux, M. H. Limage, and F. Romain, *Chem. Phys.* **276**, 181 (2002).
51. G. Herzberg, *Molecular Spectra and Molecular Structure*, Vol. 3, *Infrared and Raman Spectra of Polyatomic Molecules*, Van Nostrand, New York, 1964.
52. M. Prager and A. Heidemann, *Chem. Rev.* **97**, 2933 (1997).
53. M. Neumann and M. R. Johnson, *Chem. Phys.* **215**, 253 (1997).
54. P. Schiebel, G. J. Kearley, and M. R. Johnson, *J. Chem. Phys.* **108**, 2375 (1998).
55. G. J. Kubas, R. R. Ryan, B. I. Swanson, P. J. Vergamini, and H. J. Wasserman, *J. Am. Chem. Soc.* **106**, 451 (1984).
56. G. J. Kubas, *Metal Dihydrogen and σ -bond Complexes. Structure, Theory and Reactivity*, Kluwer Plenum, New York, (2001).
57. J. Eckert, *Spectrochim. Acta* **48A**, 363 (1992).
58. J. Eckert and G. J. Kubas, *J. Phys. Chem.* **97**, 2378 (1993).
59. J. D. Lewis, T. B. Malloy Jr, T. H. Chao, and J. Laane, *J. Mol. Structure* **12**, 472 (1972).
60. L. S. Van der Sluys, J. Eckert, O. Eisenstein, J. H. Hall, J. C. Huffman, S. A. Jackson, T. F. Koetde, G. J. Kubas, P. J. Vergamini, and K. G. Caulton, *J. Am. Chem. Soc.* **112**, 4831 (1990).
61. K. A. Hermann and F. Hochtlen, *Ber. Dtsch. Chem. Ges.* **36**, 1149 (1903).
62. H. G. Büttner, G. J. Kearley, C. J. Howard, and F. Fillaux, *Acta Crystallogr.* **B50**, 431 (1994).
63. J. H. Rayner and H. M. Powel, *J. Chem. Soc.* 319–328 (1952).
64. W. Wegener, C. Bostoen, and G. Goddens, *J. Phys.: Condens. Matter* **2**, 3177 (1990).
65. O. Rogalsky, P. Vorderwisch, A. Huller, and S. Hautecler, *J. Chem. Phys.* **116**, 1063 (2002).
66. M. Kolarschik and G. Voll, *Physica B* **222**, 1 (1996).
67. M. Havighorst and M. Prager, *Chem. Phys. Lett.* **250**, 232 (1996).
68. G. J. Kearley, H. G. Büttner, F. Fillaux, and M. F. Lautié, *Physica B* **226**, 199 (1996).
69. T. Miyoshi, T. Iwamoto, and Y. Sasaki, *Inorg. Chim. Acta* **1**, 120 (1967).
70. J. R. Durig, S. M. Craven and W. C. Harris, *Vibrational Spectra and Structure*, vol. 1, Marcel Dekker, New York, 1972, p. 73.
71. B. Nicolai, G. J. Kearley, A. Cousson, W. Paulus, F. Fillaux, F. Gentner, L. Schröder, and D. Watkin, *Acta Crystallogr.* **B 57**, 3644 (2001).
72. A. Heidemann, S. Clough, P. J. McDonald, A. J. Horsewill, and K. Neumaier, *Z. Phys.* **B 58**, 141 (1985).
73. J. N. van Niekerk and F. R. L. Schoening, *Acta Crystallogr.* **6**, 227 (1953).
74. G. M. Brown and R. Chidambaram, *Acta Crystallogr.* **B 29**, 2393 (1973).
75. E. F. Bertaut, D. T. Qui, P. Burlet, and J. M. Moreau, *Acta Crystallogr.* **B 30**, 2234 (1974).
76. H. van Kempen, T. Garofano, A. R. Miedema, and W. J. Huiskamp, *Physica* **31**, 1096 (1965).
77. W. Press, *Single Particle Rotation Motion in Molecular Crystals*, Springer Tracts Mod. Phys. **92** (1981).
78. G. J. Kearley, H. Blank, and J. K. Cockcroft, *J. Chem. Phys.* **86**, 5989 (1987).
79. W. Press and A. Kollmar, *Solid State Commun.* **17**, 405 (1975).
80. J. L. Galigné, M. Mouvet, and J. Falgueirettes, *Acta Crystallogr.* **B 26**, 368 (1970).
81. B. Nicolai, A. Cousson, and F. Fillaux, *Chem. Phys.* **290**, 101 (2003).
82. G. J. Kearley, B. Nicolai, P. G. Radaelli, and F. Fillaux, *Solid State Chem.* **126**, 184 (1996).
83. P. S. Allen and P. Branson, *J. Phys. C: Solid State Phys.* **11**, L121 (1978).
84. A. Heidemann, H. Eredrich, E. Gunther, and W. Hausler, *Z. Phys.* **B 76**, 335 (1989).
85. S. Clough, A. Heidemann, A. H. Horsewill, and M. N. J. Paley, *Z. Phys.* **B 55**, 1 (1984).
86. J. Dorignac and S. Flach, *Phys. Rev.* **B 65**, 214305 (2002).

Index

Note. *Italic* page numbers refer to figures, **bold** page numbers to tables

- acetaldehyde 81
 phenylhydrazone 118
acetaldoxime 98, 105
acetic acid 52
acetone 52, 79
 dimethylhydrazone, enehydrazine form 118
 ethylmethylhydrazone, enhydrazine form 119
 hydrazones 118
 methylhydrazone 118
 phenylhydrazone of 115
acetone-d₆ 147
acetonitrile 86, 96, 99, 108, 115
acetoxime 98, 99, **100**, 107
 free planar 101
N-acetyl-L-cysteine 184
N-acetyl-L-Met 184
acetylene 22
 π -complexes 119
activation parameters
 of [1, 3]-**B** shifts 42–6
 of rotation, oximate ligand **105**
acute promyelocytic leukemia 194
albumin 169, 190
 bovine serum 193
 gold-induced structural changes in 191
 human serum albumin (HSA) 182
 crystal structure of 191
 recombinant, interaction with cisplatin 183
 serum albumin 182, 188, 190
aluminium 41, 164, 197
AMD473 169, 174
amides, substituted 90–1
amido complexes, rotational isomerism of 86–98
 amido cyclopentadienyl complexes, dynamic behavior of 93–5
amines 110, 114, 132
 derivatives of 86
 orthometallated 136
 secondary 95, 115
amino acids 239
 interaction with platinum agents 182–4
 sulfur-containing 184, 187
ammonia 286, 291, 296–7, 302
 free rotation in Hofmann clathrates 290–1
Anderson–Kubo–Sack theory 85
AngioMARK **204**
aniline 290
antiferromagnetic coupling 225
antimony 193
 antiparasitic drugs 164, 193–7
 complexes 194
 medical uses of 163
 [Sb(GS)₃] 194
 Sb^{III}–trypanothione 195
 sodium stibogluconate 193
antiprisms
 square 25, 27
 4,4-bicapped 7
 bicapped **9**, 19
 capped 12, 208
 isomers 26
 twisted capped 12, 208
apo-transferrin 196
aquation
 kinetics and equilibria of 173–6
 processes of 174
argon 202
Arrhenius
 analysis 175

- Arrhenius (*cont.*)
 behavior 252, 258–9
 parameters 255, **263**
 plots 231, 254–5, 258
 process 255
 treatment 67
- arsenic 193
 trioxide 194
 clinical use of 163
- arthritis 188–93
- atom–atom interactions 278
- automorphism group 26
- axial state 237
- [1,3]-B shifts, activation parameters of
 42–6
- baby monster graph 24
- Bailar twists 17–18, 24
- balanced diameters 16–17
- barium, BaS₄ 202
- BBR3464 169, 174–5
- BDPP 140
- benzaldoxime 98, 105, 107
- benzene 290
 bishomobenzene 79, 81
 chromium tricarbonyl 252, 255
 muoniated 257
 rings 252, 254
- benzoic acid 285
- benzylamines, orthometallated 136
- Berry pseudorotation 9, 10, 16, 23–4
- biadduct 183
- bidisphenoid 7, 9, 25, 27
 isomers 26
- bimetallic complexes 150
- bipartite graph 22
- biphenyls 291
- bipyramids 4–5
 pentagonal 7, 9, 99, 115, 118, 122, 125
 complexes 114
 trigonal 4, 9, 15
- bipyridil 198
- bishomobenzene 79, 81
- bismuth 193, 195–7
 antiulcer drugs 164, 193–7
 [Bi(citrate)₂Bi]²⁻ 194
 [Bi(GS)₃] 194
- citrate 194
 complexes 196
 colloidal bismuth subcitrate (CBS)
 193–4
 complexes 194
 medical uses of 163
 nitrilotriacetate 196
 ranitidine bismuth citrate (RBC)
 193–4
 2D[¹H, ¹³C] HSQC NMR spectrum
 195
 subsalicylate (BSS) 193
- Bloch
 equations 167
 McConnell's modifications of 167
 theory 85
- Bloembergen, Purcell and Pound (BPP)
 expression 250
- Bohr
 frequency condition 269
 radii 245
- Boltzmann
 distribution 295
 factor 248
 weighted averages 232
- bonding, dihapto/monohapto 122
- borabararalanes 79, 81
- borabullvalene 81
- boranes 7, 9, 19–20, 46, 48, 50
 allylboranes 41, **43–5**, 52
 fluxional 42
 linear polyunsaturated 47–52
 bicyclic, chemical behavior of 78–9
 chloro(*di-n*-propyl)borane 47, 60
 cyclic allylboranes, dynamic behavior of
 53–77
 cyclic polyunsaturated organoboranes,
 chemoselectivity of 77–81
 cycloheptadienyl(*di-n*-propyl) borane,
 dynamic behavior of 60–1
 cycloheptatrienyl(*di-n*-propyl)borane
 borotropic migrations in 62–5
 dynamic processes in the
 irontricarbonyl complex 65–7
 equilibrium with 7-(*di-n*-
 propylboryl)norcaradiene
 61–5

- isomers 62
- ^{13}C NMR spectrum 62–3
- cyclononatetraenyl(di-*n*-propyl)borane
 - activation parameters of [1,3]-B shift in 73–4
 - borotropic migrations in 70–4
 - comparison with
 - cyclononatetraenyl(trimethyl)tin 70–5
 - NMR spectrum 67–8
 - ^{13}C – ^{13}C EXSY NMR spectrum 72
 - sigmatropic migrations in 70–5
 - synthesis 70–4
 - thermal isomerization of 74–5
 - thermal rearrangements in 70–5
- cyclooctatetraenyl(di-*n*-propyl)borane 67–70
- cyclopentadienylboranes, preparation of 58
- dialkylhaloborane 53
- five-vertex 9
- 2,4,6-heptatrienyl(di-*n*-propyl)borane 50–3
 - reaction with carbonyl compounds 52–3
 - synthesis and dynamic behavior 50–2
- 2-indenyl(diethyl)borane 60
- 1-indenyl(diethyl)borane
 - ^1H 2D EXSY NMR spectrum 59
 - synthesis and dynamic properties 58–60
- metallaboranes 18–20
 - polyhedra 1
- 2,4-pentadienyl(di-*n*-propyl)borane 47–9
- Z*-2,4-pentadienyl(di-*n*-propyl)borane 61
- 2,4-pentadienyl(di-*n*-propyl)borane
 - synthesis and dynamic behavior 47–8
 - temperature dependence in ^{13}C NMR spectrum 48
 - thermal cyclization 48–9
- pentamethylcyclopentadienylboranes 58
- phenalenyl(di-*n*-propyl)borane
 - borotropic migrations in 75–7
 - ^1H SST NMR spectrum 78
 - ^1H – ^1H EXSY spectrum 76
- polyhedral 1, 6
- reactions with carbonyl compounds 52–3
- seven-vertex 9
- spherical deltahedra in 8
- stable 18
- triallylborane 42
- tricyclic borane 78
- triorganoboranes 41, 57
 - allylic type, NMR studies of
 - intramolecular dynamics in 41–83
 - fluxional behavior of 46–52
 - vinyl boranes 50, 58
 - non-fluxional 52
 - reaction with carbonyl compounds 52–3
- 3-borinene 48–9
- borinic esters 52, 79, 81
- boron 18, 41, 46, 62, 70, 74
 - alkylboron dichlorides 79
 - 1-allylborolene, NMR spectra of 42
 - atomic configuration 46
 - boranes (hydrides), *see* boranes
 - cycloheptatrienyl derivatives of 72
 - cyclononatetraenyl derivatives of 72, 74
 - cyclopentadienyl derivatives of 58
 - di-*n*-propylboron chloride 61, 70, 74
 - diethylboron chloride 58
 - pentamethylcyclopentadienyl derivatives of 58
 - synthesis of cyclopentatrienyl derivatives 61–2
- borotropic migration 61
 - mechanisms of 62–5
- bovine serum albumin 193
- Bragg
 - diffraction 272
 - peaks 293
- Breit–Rabi diagram for muonium-like system 251
- Brillouin zones 273
- bromine 295–6
- Brownian diffusion 230
 - isotropic 229
- budotitane 186
- butadiene 46

- cadmium 41, 196, 290
 captopril 193
 carbon 115, 164, 277
 carbon–carbon bond 124, 245
 carbon–muon bond 245
 orthometallated C 136
 carbonyl compounds 79–81
 carbonyl groups 18
 carboplatin 169, 184
 carboranes 9, 19
 $C_2B_7H_9$ 11
 five-vertex 9
 isoelectric 7
 nine-vertex 9
 seven-vertex 9
 cerium 221
 chelate rings 107, 110, 147
 trends in 131
 chemical shifts 165
 temperature dependence of **112**
 chemoselectivity, of cyclic polyunsaturated
 organoboranes 77–81
 (R,R)-Chiraphos 138
 Chiraphos 137, 139
 patterns of NOE interactions 138
 (R,R)-Chiraphos, *R* and *S*
 orthopaladated, conformations
 of 139
 chlorine 93–4, 295–6
 chromatography 209
 chromium 253, 289
 benzene chromium tricarbonyl 252, 255
 diperoxocomplexes 120
 chrysotherapy 188, 193
 cinnamic acid 153
 cisplatin 163, 169, 170, 172–6, 185, 195
 half lives **180**
 interaction with DNA 183
 interaction with recombinant albumin
 183
 15N-cisplatin
 kinetic pathway for reaction with
 intrastrand –GG– 179
 $[^1H, ^{15}N]$ HSQC NMR spectrum 177
 ^{195}Pt -enriched cisplatin 177
 clathrates $(M(NH_3)_2M'(CN)_4 \cdot 2G)$ 290–1
 nickel–nickel 291
 cobalt 290
 Co(II) porphyrin complexes 238
 hexamine complex $(Co(NH_3)_6(PF_6)_2)$
 296
 rotational transitions **297**
 coface 15
 complexes
 monomeric/dimeric 186
 O-bonded (pentacoordinated) 155
 square-planar 137
 conformational mobility 131–61
 coordination compounds
 hydrazide(1–) ligands 110–14
 substituted hydrazines 110–14
 Cope rearrangement, 79
 copper 232, 291
 $Cu^{2+}(H_2O)_6$ complex 233
 $Cu^{II}-(2,2':6',6''\text{-terpyridine})_2(PF_6)_2$ 233
 isotopes 229
 planar complex, EPR spectrum 230
 square-planar complex 229
 as sterilizing agent 163
 bis(triphenylphosphine)-3,6,-di-*tert*-
 butyl-4,5-dimethoxy-*o*-
 semiquinone complex
 231
 coupling, spin-orbit 260
 cross-polytope 26
 cubes 3, 5, 6, 25, 27, 33
 isomers 26
 cyanide 193
 cyclobutadiene
 derivatives 29
 distortion 30
 cycloheptatriene–norcaradiene
 equilibrium 61–2
 cyclohexadiene ring 62
 cyclooctatetraenes 69–70
 cyclopentadienyl rings 95, 257–8, 262
 cyclopentadienylmetals 58
 cyclopentanone 52
 enol form 52
 9-cyclopentyl-9-borabarbaralane, diverse
 chemoselectivity of 79–81
 cyclophilin 188
 cyclopropane ring 62
 cyroprobe 209

- cysteine 182, 193, 195, 201
 L-cysteine 183, 187
 exchange between bound and free forms 196
 cystine 201
- DANTE 153
- de Broglie wavelength 270
- DE-Nol[®] 194
- Debye–Waller factor 278–9
- dehydroboration 49
- deltahedra 7
 dsd transformations in 18–20
 fluxionality/rigidity of **9**
 most spherical 6
 nine-vertex 4, 20
 six-vertex 18
- deoxyribonucleic acid *see* DNA
- DEPT experiments 171
- Desargues–Levy graph 23–4, 27
- deuterium 268, 273, 298
- deuterons 273
- 2-(di-*n*-butylboryl)-1-methylenecyclobutane 53
- 2-(di-*n*-butylboryl)-1-methylenecyclopropane 57
- 7-(di-*n*-propylboryl)norcaradiene 62
 equilibrium with cycloheptatrienyl(di-*n*-propyl)borane 61–5
- 1-(di-*n*-utylboryl)methyl-1-cyclobutene 53
- diabetes mellitus 197
- 1-(dialkylboryl)cyclobutenes
 dynamic equilibrium with
 2-(dialkylboryl)methylenecyclobutenes 53–7
¹³C NMR spectrum 55, 57
¹³C–¹³C EXSY spectrum 56
- 2-(dialkylboryl)methylenecyclobutenes
 dynamic equilibrium with
 1-(dialkylboryl)cyclobutenes 53–7
 phase sensitive ¹H–¹H EXSY spectrum 54
- diamagnetic systems 222
- diameters, balanced 16–17
- diamond–square–diamond (dsd)
 processes 1, 6–11, 17
 degenerate 8, 12
 double 12
 dsd situation 8
 dsd type 8
 forbidden 12
 single 12
 transformations, generation of
 metallaborane structures by
 18–20
- diastereoisomers, [EU(DOTAM)(H₂O)]³⁺ 207
- diastereomers 134, 136
- diazinane 192
- 1,1-dicarboxy-cyclobutane 169
- dichloromethane 226, 233
- diethylenetriamine 202
- 4,4'-diisothio-cyanantostilbene-2,2'-disulfonic acid (DIDS) 200
- dimerization 200
- dimers 156, 199–200
- dimetal systems 91
- dimethyldiazine 122
- N,N'*-dimethylphenylhydrazine 111
- S*-dimethyl(1-(α -naphthyl)-ethyl)amine 136
- dimethyl(1-(α -naphthyl)-ethyl)amine 138
 coordination 136
 possible isomers 137
- dimethylacetamide, ¹H NMR spectrum 91
- dimethylamide 89
- dimethylamine **100**
- dimethylalanine 86
- 1,2-dimethylethylhydrazine, isomers 123
- dimethylformamide, ¹H NMR spectrum 91
- 1,1-dimethylisopropylhydrazido complex 114
- 2,4-dinitrophenylhydrazine 111
- dinuclear complexes with M₂⁶⁺ core,
 restricted rotation 91–3
- diolefins 143, 147
- diphenylketimine **100**
- 2,2'-diphenylmethane 156
- 2,6-diphenylphenol 92

- 5,17-bis(diphenylphosphanyl)-
25,26,27,28-
tetrabenzylloxycalix[4]arene
156–7
- 1,4-bis(diphenylphosphanyl)butane 154
- exo*-8-((*o*-(diphenylphosphino)
benzyl)thio)borneol, structure 148
- (–)-(2*S*,4*S*)-2,4-
bis(diphenylphosphino)pentane
143
- diphoscalix 156–7
- diphosphane 91
chelating 156
- diphosphine complexes 153, 156
- dipolar interaction 224
- dipole moment 276
vector 270
- dipole–dipole couplings 220
- dithioethers 133
- diverse chemoselectivity 79
9-cyclopentyl-9-borabarbaralane
79–81
- DNA 169, 171–6, 182, 185–7
adducts **180**
monofunctional 178
interaction with cisplatin 183
platination 176–82, 184
- dodecahedra 3, 5, 36
 D_{2d} 7
pentagonal, double group 25
- Dotarem **204**
- drugs
anticancer 163
antiparasitic 193–7
antiulcer 193–7
neurotoxic 197
platinum, metabolism of 182
- DTPA-bis(amides), coordination
polyhedra 205
- dynamics, polyhedral 1–39
- dysprosium 221
salts 200
- EasySpin 230
- educts 231
- EHPG complex 186
- electron spin resonance (ESR) 246
- electron spins, interaction with
environment 223–6
- electrons
electron–electron spin 239
electron–muon interaction 251
properties of **245**
radical 259
- enantiomerization 207–8
- enantiomers 29–31, 123
of fluorocomplexes 118
of ketimines 97
of [Ln(DTPA)][–] complexes 202–4, 205
of metallocycles 132, 138
multiple 208
of oximes 105
paired 35
- epikernel principle 28
- erbium 221
- ergothionine 190, 192
- Erlich606 163
- erythrocytes 200
- ethanol 226, 233
- ethoxyacetylene 81
- ethyl groups 288
- ethyl methyl ketoxime 107
isomeric forms 107
- ethylene, coordinated 120
- ethylenediamine 204
bridges 204
complexes 133
- N,N*-ethylenebis(*o*-hydroxyphenylglycine)
186
- ethylmethylketone phenylhydrazone 118
isomers 118
- Euler's relationship 2
- europium 206
[Eu(DOTAM)(H₂O)]₃(, 2D EXSY
208
[Ln(DTPA)](202
- Eyring
equation 98, 112
plots 169
- Fermi
contact contribution 224–5
contact term 250
Golden Rule of 249

- interaction 246
- potential 272
- fermions 287
- ferromagnetic coupling 225
- five-vertex structures, B5H52(9
- fluorine 86, 91, 98–9, 107, 277
- fluoro oximate complexes 103
- force-field calculations 278–80
- Fourier
 - back-transformation 293
 - difference 293, 298
 - maps 294
 - expansion 288–9
 - terms 287
- free induction decay (FID) 228
- Gadobenate[®] 206
- gadolinium 202
 - complexes
 - 1,4,7,10-tetraazacyclododecane-1,4,7,10-tetraacetate (DOTA) 202
 - crystal structure 203
 - diethylenetriamine-*N,N,N',N'',N'''*-pentaacetate (DTPA) 202
 - crystal structure 203
 - water exchange 206
 - contrast agents **204**
 - [Gd(BOPTA)]²⁻ 206
 - [Gd(DO3A-butrol)] 207–8
 - [Gd(DO3A-HP)] 207
 - [Gd(DOTA)]⁻ 207
 - medical uses of 163
- Gadovist **204**
- Gale
 - diagrams 10, 11–18
 - allowed vertex motion of 16
 - standard 16
 - transformation 13–14
- gallium 197
- GARP method 172
- Gaussian profiles 284, 295
- germanium 58, 252
 - allylgermanes 41
 - GE(C₆H₅)₄ 253
- glutathione (GSH) 182, 184, 193–5, 200
- glycine 204
- gold
 - as antiarthritic agent 163
 - antiarthritic drugs 188–93
 - antiulcer drugs 164
 - auranofin 188, 190
 - tri-isopropylphosphine analogue of 192
 - aurocyanide 193
 - aurothioglucose 188
 - aurothiomalate 188, 193
 - dicyanoaurate(I) 193
 - medical uses of 163
- graphite 243
- guanine 182, 184
 - titanium, Cp₂TiCl₂ 187
- guanosine diphosphate 183
- guanosine triphosphate 183
- guanosine-5'-monophosphate (GMP) 177, 184
- halfspace, open 15
- halides, d transition 110
- Hamiltonian 246, 250, 274, 286–7, 291, 299–300
 - spin 223
- harmonic oscillator 275, 276
- Heisenberg exchange 225
- Helicobacter pylori* 193
- heme proteins 236
- hemoglobin 200, 236
- hepatocytes 206
- 1,3,6-heptatriene 50
- Z,Z*-1,3,5-heptatriene 52
- 1,3,6-heptatriene
 - changes in ¹³C NMR spectrum 51
 - isomers 50, 52
- Hermite polynomial 274
- heteroatoms 156
- hexagonal bipyramid 6, 25, 27
 - isomers 26
- hexagons, graph of 27
- hexamine complexes 295–7
- hexane 47, 58, 79
- histidine 237
 - imidazole 188
- L-HMet 184

- Hofmann clathrates 290–1
 nickel–nickel 290
 rotational transitions of NH₃ in
291
- HOMO 259, 262–3
 HOMO–LUMO 262
 crossing 9–10
 gap 262
- human serum albumin (HSA) 182
see also albumin
- Hund's rule 221
- hydrazines 85–6, 111, 114–15, 125
 substituted 110–14
- hydrazones 85–6
 isomerism with tungsten
 fluoro complexes 114–19
- hydroboration 49
- hydrogen 245–6, 268, 273
 bistrifluoroacetate complex 277
 hydrogen–hydrogen bond 287, 289
 muonium isotope **245–6**
 peroxide 85, 198
 sigmatropic migration 60
- hydrophobicity 209, 239
- hydroxylamine 85–6, 98
- hyperfine interaction 250
- hyperglycemia 197
- hyperinsulinemia 197
- hyperoctahedral graph 26
- hyperoctahedral restriction 26
- icosahedra 3, 5, 7, **9**, 36
 edge-coalesced 7, **9**
- icosahedral molecules 34–7
- imidazolidine-2-thione 192
- inelastic neutron scattering (INS) 268,
 270, 272–4, 276–9, 281–2, 284–92,
 297, 300–2
- INEPT experiments 171
- infrared spectra *see* spectroscopy, infrared
- INS *see* inelastic neutron scattering
- insulin 197
- intramolecular dynamics, NMR studies of
 41–83
- iodine 295–6
- iridium 20, 132
 compounds 149
- conformational mobility in chelated
 square-planar complexes 131–61
- [Ir(COD)(1,1'-
 bis(diisopropylphosphane)
 ferrocene)](PF₆) 151
¹H NMR spectrum 151
- [IrH₂L₂(P,S)]⁺ 148
- [IrTp^{5Me}(COD)] 149
- [M(diolefin)(diphosphane)]⁺ 151
- iron 197, 202, 221, 228, 236, 238–9, 290–1
 dicyclopentadienyl iron 256
 Fe(III)TPP(1-MeIm)₂ complexes 239
 ferrocene 256–61
 encapsulated in zeolite 261–3
 muoniated 258
 polycrystalline, muon spin relaxation
 257–8
- ferrocenyl derivatives 142
- iron tricarbonyl complex 65–7
 di-*n*-propylboryl group migrations 65
¹H–¹H EXSY spectrum 67
- irreducible representations (irreps) 28–31,
 34
- islands of intensity 280
- isomer count 21
- isomerism
 in oximate complexes 107–10
 rotational 96–8
 transition metal complexes with *n*,
n-two-center ligands 110–19
- isomerization 204
 degenerate 18
 fluoro complexes of groups 5 and 6, with
n-two-center ligands 98–110
 with fluoro complexes of groups 5 and 6,
 98–110
 free energy of activation 108
- isomers 32, 33, 34–5, 36, 37, 204
 endo 57
 permutational 21
- isopropyl groups 94, 288
- isotypes 289
- itaconate, hydrogenation 155
- Jahn–Teller
 active mode 233
 distortion 1, 232

- dynamics 219, 232–3
 - effect 1–39, 232, 233
 - problems **29**
 - theorem 28, 232
- Karplus equations 131, 133
- kernel symmetry 31
- ketimido complexes, rotational isomerism 86–98
- ketimines 95–7, 114–15
- Kramers
 - doublet 222
 - systems 221
- Kubas complexes 302
- tungsten complexes 289
- lanthanide 202, 206
- lanthanum 206
- Larmor frequency 249
- lead 252
 - Pb(C₆H₅)₄ 253–4
 - tetraphenyl 252
- Legendre polynomial 225
- leishmaniasis 193
- leukemia, acute promyelocytic 194
- leukocytes 193
- Lewis acids 41
- ligands
 - amido 86, 90, 93
 - rotation **94**, 95
 - amines 132
 - benzaldoximato 110
 - and biological activity of metallodrugs 163
 - bridging 152, 194
 - chelating 132, 152
 - chiral chelate L–L 131
 - dialkylamido 91–2
 - dihapto 108
 - dihydrogen, rotational dynamics of 286–90
 - EPPy_nPh_{3–n} 149
 - η²-bound, hindered rotation of 121–6
 - η²-coordinated hydrazido 112
 - ethylene 124–5
 - ferrocenyldiphosphanes 150
 - hindered rotation 97, 107, 112
 - H₂O, pK_a values **176**
 - hydrazide(1–) 110–14
 - hydrazido 122–3
 - hydrogen containing 288
 - identification by ¹⁵N NMR 171–2
 - imido 93
 - internal rotation 98
 - intracellular 190
 - ketimide 96
 - ketimido 86, 96
 - hindered rotation of 95–8
 - metal-containing 142
 - monohapto 108
 - monothiol 195
 - multidentate 202
 - n-donor two-center 98–126
 - nature of bonding 119–21
 - nitroso 236
 - N,N-two-center, bonding model 121
 - n,n-two-center
 - coupling constants of **112**
 - isomerism of transition metal complexes with 110–19
 - NO 237
 - octadentate 202
 - O,N-two-center 114
 - orthopalladated 136
 - PePy_n 146
 - phenolic 186
 - 1,1'-bis(phenylthiolate)ferrocene 152
 - (PhNN=CMe₂)⁻ 117
 - phosphine 132
 - P,N 152
 - P,N donor 134
 - chelating 144
 - PN₁ 145
 - activation free energy values for conformational inversion **146**
 - conformational change in square-planar complexes 146
 - PN₂ 146
 - PPh₃ 231
 - proton-containing 289
 - pyrazolato (Me²C³HN²) 123, 126
 - rotation of 123–4
 - soft 188
 - (S,S)-BDPP, structure 140

- ligands (*cont.*)
 (*S,S*)-Chiraphos, structure of 140
 (*S,S*)-diop, structure of 140
 substitution (exchange) 164
 thiomalate 193
 T^{Pmenth} and T^{P^Mmenth}, structure of 149
 transmaltol 200
 wrapping 165
- ligas, oxo 200
- lithium 58, 164
 acetate dihydrate (CH₃COOLi · 2H₂O)
 297
 crystal structure 298
 INS tunnelling spectrum 300
 methyl deuterated derivative
 (CD₃COOLi · 2H₂O) 298–9
 partially deuterated derivative
 (CH₂DCOOLi · 2H₂O) 301
 cycloheptadienide 60
 cyclononatetraenide 70, 74
 indenyllithium 58
 medical uses of 163
 pentadienyllithium 47
- Lorentzian function 250
- LUMO 259, 262–3
- lutetium 206
- macrophages 193
- magnesium 223
 allylmagnesium 41
- magnetic resonance imaging (MRI),
 contrast agents 164–5, 202–9
- Magnevist[®] 204, 206
- manganese 202, 221, 223, 291
 cyclopentadienyl manganese tricarbonyl
 255–6
 diacetate tetrahydrate (Mn(CH₃COO)₂ ·
 4H₂O) 292–3, 294, 296
 dioxolene complexes 231
- sp³d⁵ manifold, nine-orbital 5–6
- Marcus theory 225
- MARI spectrometer 280
- Mathieu's equation 287
- M(bidentate)₃ complexes 17, 24
- mercury 58
 allylmercury 41
 diallylmercury 41
- mesityl groups 143
- metallacycles 131
- eight-member 157
 boat 158
- five-member 139
 chiral puckered-ring (twist) 132–3
 conformational changes in 132–41
 conformational changes involving
 olefins 152–4
 main conformations 132
 meso symmetric envelope 132–3
 relationship between configuration
 and conformational stability 133
- higher
 boat 156
 conformational changes 156–8
- seven-member 139
 boat 154–5
 chair 154–5
 conformational changes 154–6
- six-member 139
 boat 142, 144–5, 150–1
 chair 142–3
 conformational changes in 142–52
 conformational changes involving
 olefins 152–4
 main conformations 132, 142
 skew (twist) 142–3, 150
- metalligand, [(C₆F₅)₃Pt(PPy_n)]⁻¹ 149
- metallo drugs, dynamics and kinetics of
 163–217
- metallothionein 182, 196
 renal synthesis 195
- metals
 metal environments (species) 165
 metal–carbon bonds 234
 metal–hydrogen bond 287
 metal–ligand bond 122
 metal–metal bond 91–2
 metal–muon adduct 260–1
 metal–nitrogen bond 93, 110
 metal–phenyl bond 264
 metal–sulfur bond 134
 quadrupolar nuclei, medical relevance
 of 164
 square-planar 131
- methanol 79, 81, 200, 226

- methionine 182
L-methionine 182, 184, 187
methyl rotor, single 291–5
methyl ethyl ketoxime 105
methyl groups 96, 286, 289, 293–5, 296, 297–301
2-methyl pyridine 174
methyl rotor, eigenstates and eigenfunctions 292
N-methyl-1,2-ethanediamine 133
N-methylanalide 90
N-methylalanine 86–7
NHMePh 87
methylaquocobaloxime 235
methylbispyrazolylmethane 150
methylenecyclobutane potassium 53
methylphenylformamide, ^1H NMR spectrum 91
microfilaments 169
microtubulins 184
migrations
 borotropic 62–5
 sigmatropic 70–5
 of dialkylboryl groups 70–4
Moebius transition state 74
molecular dynamics 251–2
molybdenum 85, 91–2, 98, 101, 110, 289
 enantiomers 101
 $[\text{Mo}(\eta^5\text{-C}_5\text{H}_5)(\text{NO})\text{I}(\text{NRNR}'\text{R}'')] 111$
 $[\text{Mo}(\eta^5\text{-C}_5\text{H}_5)(\text{NO})\text{I}_2(\text{NRNR}'\text{R}'')] 111$
 $[\text{MOF}_4\text{L}]^- 98$
 molybdenum–nitrogen bond 103
 $[\text{MoOF}_4(\text{anti-ON}=\text{CR}^1\text{R}^2)]^- 107\text{--}8$
 energy profile of isomerization 109
 $[\text{MoOF}_4(\text{ON}=\text{CMeEt})]^- 110$
 $[\text{MoOF}_4(\text{ON}=\text{CMe}_2)]^- 103$
 $[\text{MoOF}_4(\text{syn-ON}=\text{CR}^1\text{R}^2)]^- 107\text{--}8$
 energy profile of isomerization 109
 peroxofluorides 99
 reaction with oximes 98
monoadduct 183
monomers 156, 199–200
MRI *see* magnetic resonance imaging
MultiHance **204**
muonation 244
muonium 244–5, 258
 addition to ethene 245
 as isotope of hydrogen **245**
 muonium–metal bond 258
 vacuum-state 246
muons 243
 decay process 244
 in a longitudinal magnetic field 247–50
 in matter 244–6
 muon–electron (muonium like) system 250–1
 muon–electron spin 251
 muon–iron adduct 263
 neutrino 244
 positron 244
 properties of **245**
 spin polarization 247–8
 spin relaxation 249, 251, 254
 temperature dependences of rate 253
myocrisin 188
myoglobin 236
 MbNO 236–7

naphthyl ring 136
neodymium 221
neutrons 274, 288, 301
 diffraction 252, 297
nickel 147, 221, 232, 290
 complexes 154
 $\text{Ni}(\text{NH}_3)_6\text{X}_2 295$
nine-vertex structures, $\text{B}_9\text{H}_9^{2-} 9$
niobium 93, **94**, 95
nitric oxide 222, 236
nitrogen 90–1, 94, 99, 115, 164, 193
 nitrogen–carbon bond 117
nitrous oxide 222
nitroxyl 239
NMR *see* spectroscopy, nuclear magnetic resonance (NMR)
NOE *see* nuclear Overhauser effect
norane, nine-vertex 9
norcaradiene–cycloheptatriene equilibrium 61–2
nuclear magnetic resonance *see* spectroscopy, nuclear magnetic resonance (NMR)
nuclear Overhauser effect (NOE)
 experiments 138–40
 spectra 141

- nucleoside monophosphates 187
 nucleosides 188
 nucleotides 188
 platination of 176–82
 Nujol® 277
- octahedra 3, 5, 7, **9**, 15, 33, 99, 125
 bicapped 6
 capped **9**
 distortion of 32
 elongated 232
- octahedral molecules 31–4
- olefins 126
 bonding model 121
 complexes 148
 π -complexes 119–21
 coordinated 154
 conformational changes in
 metallacycles 152–4
 polymerization 95
- oligomers 199–200
- Omniscan **204**
- orbital crossing 10
- orbital symmetry 9
- organiodide 202
- organometallics, μ SR molecular dynamic
 studies on 243–65
- orthopalladated complex 140
- oscillating rearrangement 65
- oxalates 198, 201
- oxazolyphosphane 156
- oximate complexes
 dynamic behavior of 98–107
 mechanism of isomerism in 107–10
- oximate ligands, activation parameters of
 rotation **105**
- oximes 85–6, 98, 115
 configural isomers 105
- oxofluoroketimido complexes, of tungsten
 96–8
- oxygen 90–1, 99, 277
- palladium 132, 147, 290
 complexes 136, 150, 154, 156
 conformational mobility in chelated
 square-planar complexes 131–61
 [MX₂(Fe(C₅H₄SR)₂)] 152
- Pd(dioP)₂ 154
 [Pd(η^3 -allyl)(diphoscalix)](BF₄) 156–7,
 158
 PdIMe(L–L) 150–1
 PdMe₂(L–L) 150–1
 [PdMe₂(Pz₂CH–CH₃)] 150
 [PdXRf(FePy_n)] 146
- paramagnetic complex, [Fe(CN)₄(en)][–]
 133
- Pashen–Back regime 253
- Pauli principle 287–8
- pentamer 199–200
- pentamethylcyclopentadienyl groups
 94
- pentamethylcyclopentadienyls 58
- Pentostam® 193
- peptides, interaction with platinum agents
 182–4
- peroxo complexes 86
- Petersen graph 23–4
- phenanthroline 198
- phenomenological model 285
- phenyl groups 252, 288
- phenyl *o*-tolyl ketimine 97
- phenyl rings 115, 252
- 1-phenyl-1-(*N,N*-dimethylamino)ethane
 137
 patterns of NOE interactions 138
 R and *S* orthopalladated, conformations
 139
- 1-phenylbutane-1,3-dionato 185
- β -phenylhydroxylamine 98, **100**
- phonons 295
- phosphanylpyrazoles 152
- phosphines 132, 138, 142
 gold bound 190
 monodentate 139
- phosphinopyrazoles, structure 152
- phospholipids 169
- phosphorus 164, 193
 (*S,S*)-2,3-
 bis(diphenylphosphino)butane
 153
 iminophosphines, coordination
 147
- P(α -methyl-*N,N*-dimethylbenzylamine-
o)_nPh_{3–n} 146

- $P(CH_2CH_2(2\text{-pyridyl}))_nPh_{3-n}$ 146
 $P(o\text{-phosphino-}N,N\text{-dimethylbenzylamine})_nPh_{3-n}$ 144
 photochemotherapeutic agents 184
 photoirradiation 184
 π complexes 119–21
 picolinate 198
 pions 243–4
 pivot face 8
 Planck's constant. 269
 platinum 132, 147, 164, 290
 agents, interaction with amino acids, peptides and proteins 182–4
 η^3 -allylplatinum 148
 amine anticancer complexes, rate constants **166**
 am(m)ine complexes, variation in chemical shifts 172
 cis-[amminedichloro(2-methylpyridine)] 169
 anticancer drugs 164, 169–84, 170
 activation 173–6
 antitumor activity 164–5
 complexes 136, 150, 154, 156, 171–2
 bridged dinuclear 173–4
 dinuclear and trinuclear 174
 p*K_a* values for H₂O ligands **176**
 Pt–thiolate 184
 conformational mobility in chelated square-planar complexes 131–61
 [(C₆F₅)₃Pt(μ -PPy_{*n*})RhL₂] 150
 cis-DDP 169
 dichloro complex 157
 diiododiamine complex 184
 dinuclear anticancer agent reaction with 14-mer duplex 181
 ethylene complex 120
 medical uses of 163–4
 [MX₂(Fe(C₅H₄SR)₂)] 152
 π -complexes 122
 (PR₃)PtCl₂ 120
 [Pt(bipy)(men)]²⁺ 133
 cis-Pt(CBDCA)(NH₃)₂ 169
 PtCl(acac) 120
 [PtCl(dien)]⁺ 175
 cis-[PtCl(NH₃)₂(OH₂)]⁺ 173
 [(*trans*-PtCl(NH₃)₂)₂ μ -*trans*-Pt(NH₃)₂(NH₂(CH₂)_{*n*}NH₂)₂]⁴⁺ 169
 [PtCl(NH₃)₃]⁺ 175
 [{*trans*-PtCl(15NH₃)₂]₂(μ -¹⁵NH₂(CH₂)₆¹⁵NH₂)₂]²⁺ 178, 180
 [PtCl₂*meso*1,2-bis(2-hydroxyphenyl)ethylenediamine] 140–1
 [PtCl₂*S,S*(-)-1,2-bis(2-hydroxyphenyl)ethylenediamine] 141
 PtCl₂ 148
 PtCl₂(diop) 140
 [PtCl₂(diphoscalix)] 156–7, 158
 [PtCl₂(L–L)] 139
 cis-[PtCl₂(NH₃)(2-Py)] 174
 [PtCl₃(C₂H₄)]⁻ 120
 Pt(C₆F₅)₂ 152
 Pt(C₆F₅)X 152
 Pt(diop)₂ 154
 [PtI₂(*meso*-MeSCH(CF₃)CH(CF₃)SMe)] 134
 cis-[Pt(Met-N,S)₂]²⁺ 182
 cis-[Pt(NH₃)Cl(Met-N,S)]⁺ 182
 trans-[Pt(NH₃)Cl(Met-S)₂]⁺ 182
 cis-[Pt(NH₃)₂Cl(Met-S)]⁺ 182
 [Pt(NH₃)₂Cl(OH)] 183
 cis-[Pt(NH₃)₂Cl(OH)]⁺ 182
 cis-[Pt(NH₃)₂Cl(OH₂)]⁺ 175–7, 182
 cis-[Pt(NH₃)₂Cl₂] 163
 [*cis*-Pt(NH₃)₂Cl₂] 169
 cis-[Pt(NH₃)₂(H₂O)₂]²⁺ 183
 cis-[Pt(NH₃)₂(Met-N,S)] 182
 cis-[Pt(¹⁵NH₃)₂Cl(OH₂)]⁺ 173–4, 178
 cis-[Pt(¹⁵NH₃)₂(OH₂)₂]²⁺ 173–4, 178
 [Pt^{IV}(en)(N₃)₂(OH)₂] 184
 [Pt^{IV}(N₃)₂(OH)₂(NH₃)₂] 184
 [PtX(Me)(MeECH₂CH₂EMe)] 134
 conformations of 134–5
 polarization 234–6, 248
 polyaminocarboxylates 204
 polygons, planar 18
 polyhedra 11
 in boranes 1

- platinum (*cont.*)
 capping of 3–4
 chiral 21
 coface of 15
 coordination, $\text{Ln}^{\text{III}}[\text{DTPA-bis}(\text{amide})]$
 enantiomers 205
 dual pairs of 3, 5
 dualization of 4–5
 edges of 2, 5
 faces of 2, 5
 five-vertex 16
 forbidden 5–6
 Gale diagrams for 15
 metallaborane 1
 nine-vertex 19
 six-vertex 16–17
 ten-vertex 19
 isonido 20
 topology 2–6
 vertices of 2–3, 5
- polyhedral isomerizations
 degenerate 1, 7
 macroscopic models of 21–37
 microscopic models of 6–20
 planar 7–8
 topological representations of 21–7
- polytope 11
- porphyrin 237
 cobaltous 237
 ferrous protoporphyrin IX 238
- potassium
 hydrogen bistrifluoroacetate
 $(\text{KH}(\text{CF}_3\text{COO})_2^-)$ 276–9, 302
 hydrogen carbonate (KHCO_3) 269, 279,
 302
 crystalline structure 279
 INS spectrum 280, 284
 potential function and wave function
 283
 proton transfer in 283, 285
 $S(Q, \text{omega})$ 281
 oxalate 201
- Powell algorithm 103
- $\text{PPh}_2(o\text{-phosphino}N,N\text{-dimethylbenzylamine})$
 142
- praseodymium, $[\text{Ln}(\text{DTPA})]^-$ 202
- prisms
 dualization of 4–5
 trigonal 15
 bicapped 6
 capping of 4
 tricapped 9, 12, 204–5
 4,4,4-tricapped 4
- probability density 294, 296
- ProHance 204
- proline 190
- propylene 48
- 1-*n*-propyl-2-methyl-2-borolene 49
- proteins, interaction with platinum
 agents 182–4
- protium 245
- proton crystal model 280–2
- protons 244, 273, 288–9, 291, 293,
 301
 dynamics in solids 267–304
 vibrational 278–82
 properties of 245
- pseudoreflexion 11
- pseudorotation 11
- purine 178, 188
- PX_5 derivatives 9
- pyramids
 hexagonal 6
 pentagonal 15
 square 15, 200
- pyrazolyl 148
 borates 142, 149–50
 complexes 148
- 2-pyridinaldoxime 98
- 4-pyridinaldoxime 98
- pyridine 201
 ring 107
- pyridine-2-carbaldoxime 105, 107
- pyridine-4-carbaldoxime 105
- bis(2-pyridyl)methanol 150
- bis(6-substituted)-2-pyridylsilanes
 150
- pyrrole 290
- quadrupolar nuclei, medical relevance
 of 164
- quantum rotational dynamics for
 coupled rotors 297–301

- racemization 204, 205
- radicals
 metal adduct 260
 muon/hydrogen-agostic 258
 ring adduct 260
- Raman
 lines 271
 process 238
 scattering 271
 spectra *see* spectroscopy, Raman
- Ray/Dutt twists 17–18, 24
- Rayleigh scattering 271
- rearrangement, σ – π 122–3
- recoil line 275, 279–80, 281
- Redfield regime 227
- relaxation 226–7
 function 249
- rhenium 20
 [Re(R)(CO)₃(4,4'-Me₂-bpy)] 236
 [Re(R)(CO)₃(α -diimine)] 235
- rhodium 132, 147
 complexes 139, 143, 149
 square-planar and pentacoordinated isomers 156
 conformational mobility in chelated square-planar complexes 131–61
 [CpRh(C₂H₄)₂] 153
 [(C₆F₅)₃Pt(μ -PPy_{*n*})RhL₂] 150
 iminophosphane derivatives 147
 [M(diolefin)(diphosphane)]⁺ 151
 [Rh(COD)(PMes₂CH₂CH(OH)CH₂PR'₂)](PF₆) 143
 [Rh(COD)(PN₁)](BF₄) 142, 143
 [Rh(COD)(PN₃)](BF₄) 144
¹H EXSY spectrum 145
 [Rh(COD)(PR₂CH₂CH(OH)CH₂PR₂)](PF₆) 142
 [Rh(diolefin)(L–L)]⁺ 139
 [Rh(diolefin)(P*N_{*n*})]⁺ 147
 [Rh(diolefin)(PePy_{*n*})]⁺ 146
 [Rh(diolefin)(P,N)](BF₄) 147
 [Rh(diolefin)(PN₂)]BF₄ 146
 [Rh(diolefin)(PN₃)]BF₄ 144
 [Rh(diolefin)(COD)](PF₆) 154
³¹P variable temperature study 155
 [Rh(L–L)(COD)]⁺ 154–5
 [Rh(P,S)(COD)]⁺ 148
- [Rh(TFB)(P*N₁)](BF₄) 147
 [Rh(TFB)(PN₁)](BF₄) 147
 [Rh(TFB)(PN₂)](BF₄) 146
 [Rh(TFB)(PN₃)](BF₄) 145
 [RhTp^{3-Ph}(COD)] 149
 [RhTp^{3-Ph}(CO)₂] 149
 [RhTp^{3-Ph}(NBD)] 149
 [Tp^{iPr,4Br}Rh(CO)₂] 148
 [Tp^RRh(diolefin)] 148
 tris(pyrazolyl) complexes 148
- rhombic state 236–7
- rhombus 30–1
- ribonucleic acid (RNA) 169
- rotamers, anti/gauche 91–2
- rotation
 hindered 90, 288, 290
 of η^2 -bound ligands 121–6
 of ketimido ligands 95–8
 methyl 291–5
 methyl group 219
- rotational constants 286
- rotational transitions 289
- rotors, coupled, quantum rotational dynamics 297–301
- ruthenium
 anticancer agents/drugs 164 185–8
 complexes 187
 anticancer 164
 [(η^6 -arene)Ru(II)(en)X]ⁿ⁺ 187–8
 [(η^6 -Bip)Ru(en)Cl]⁺, time dependences of ¹H and ³¹P NMR spectra 189
 [(η^6 -Bip)Ru(II)(en)Cl] 187
trans-imidazolium(bisimidazole) tetrachloro-ruthenate(III) 187
trans-indazolium(bisindazole) tetrachloro-ruthenate(III) 187
trans-RuCl₄(Me₂SO)(Im)(ImH) 187
 [Ru^I(R)(CO)₂(α -diimine)] 235
 ruthenocene 252
- ruthenocene 252, 256
- salvarsan 163
- Schlenk equilibria 41
- Schneider–Freed programs 230
- Schottky anomalies 296
- selenium 134

- semiquinone radicals 222
- serum albumin 188, 190
- σ complex 122–4, 287
- sigmatropic migration
 di-*n*-propylboryl group 61, 64
 hydrogen 60
- silicon
 allylsilanes 41
 bispyridylsilanes, complexes 150
- Silver–Getz model 233
- single methyl rotor 291–5
- sodium 58
 stibogluconate 193
 thiopropanolsulfonate-S-Au(I) 190
- solganol 188
- solvents, aprotic 85
- spectrometry
 HPLC 187
 mass electrospray ionization (ESI-MS)
 195
- spectroscopy
 electron electron double resonance
 (ELDOR) 220
 electron nuclear double resonance
 (ENDOR) 220, 225, 228, 236–7,
 246
 electron paramagnetic resonance (EPR)
 219–42
 brief primer on 223–9
 combination of techniques, case
 example 236–9
 continuous wave (CW) 219–20, 225,
 227–8, 231, 235, 238
 detection of dynamic processes by
 229–36
 chemically induced dynamic
 electron polarization (CIDEP)
 234–6
 dynamic Jahn–Teller effect 232–3
 exchange processes 231–2
 slow tumbling 229–31
 measurement techniques 227–9
 pulse techniques 220
 scope of 221–3
 temperature-dependent 239
 time-domain experiments 234
 X-band 236
- electron spin echo envelope modulation
 (ESEEM) 220, 228–9, 236–7
 HYSCORE experiment 229
- infrared 269, 271, 273–4, 276, 278, 283,
 287
- microwave frequencies 220, 227–8
- muon spin relax-
 ation/rotation/resonance/research
 (μ SR)
 avoided level crossing (ALC- μ SR) 252
 studies of molecular dynamics of
 organometallics 243–65
 transverse field (TF- μ SR) 252
- nuclear magnetic resonance (NMR) 85,
 164, 190, 195, 197, 209, 246, 256,
 258–9, 262–3, 283–4
- computer programs 167
- dynamic 231–2
- exchange rate 165
- inverse 172–3
- magnetization transfer 167
- of metallodrugs 163–217
- methods of study by 164–9
- ^{195}Pt , ^{15}N and inverse [^1H , ^{15}N] 170–3
- saturation transfer experiments 192
- spectra, rate constants, lineshape
 simulation 167
- spin-echo 200
- studies of intramolecular dynamics
 41–83
- techniques
 COSY 165
 EXSY (exchange spectroscopy) 85,
 202
 1D 42, 168
 2D 167–8
 HMQC (heteronuclear multiple
 quantum coherence) 165, 196
 HSQC (heteronuclear single
 quantum coherence) 165,
 172–3, 175–6, 180, 182, 184,
 186, 194
 1D/2D 176
 HSQC-TOCSY 165, 184
 NOESY (nuclear Overhauser
 enhancement spectroscopy)
 165

- experiments 132, 134, 147, 152, 167
- phase sensitive 146
- ROESY (rotating frame overhauser enhancement spectroscopy) 165
- experiments 132, 138
- spectra 138
- TOCSY (total correlation spectroscopy) 165
- TROSY (transverse relaxation-optimized spectroscopy) 209
- quasielastic neutron scattering (QENS) 243, 254–5, 256, 258–9, 262–3, 283–4
- Raman 256, 268, 270–1, 273–4, 276, 278, 283, 287
- spin-echo 239
- of transition metal complexes groups 5 and 6, 85–129
- vibrational
 - neutron scattering techniques 271–6
 - coherent versus incoherent 272–3
 - contrast 273
 - nuclear cross-sections 272
 - penetration depth 273
 - scattering function 274–6
 - wavelength 273–4
 - with neutrons 267–304
 - techniques 269–78
- spin isomers 101
- spin labels 219, 222–3, 239
 - FE(III) tetraphenylporphyrin (TPP) 222
- spin probes 219, 222–3
 - 4-hydroxy-2,2,6,6-tetramethylpiperidinyl-1-oxyl (TEMPOL) 222
- spin-correlated radical pair (SCRIP) 234
- spin–lattice relaxation 168, 172, 238, 246, 252, 256, 299, 301
- spin–orbit coupling 224, 260–1, 262
- spin–spin coupling 165, 167
- spin–spin interaction 239, 272
- spin–spin relaxation 226–7
 - rates of 165–7
- splitting
 - hyperfine 229
 - spin–spin 239
 - zero-field 229
- $S(Q, \omega)$ maps 280–1
- square-planar complexes 131–61, 151, 154
 - copper 229
- square-planar molecules 29–31
- stereoselectivity, ligand coordination 131
- steric factor 108–9
- Stokes and anti-Stokes Raman lines 271
- sulfur 134, 147, 152
- switching edge 8
- symmetry group 26
- symmetry-allowed processes 10
- symmetry-forbidden processes 10
- syphilis, treatment of 163
- tantalum 85, 93, **94**, 95
 - fluorocomplexes 107, 126
 - fluoroximates 107, 126
 - pentafluoride 107
 - $[\text{Ta}(\eta^1\text{-pz})_2(\eta^2\text{-pz})_3]$, isomerism 123, 126
 - $[\text{Ta}(\text{ON}=\text{CMe}_2)\text{F}_5]^-$ 107
- tautomerization 284
- Taylor series 271
- technetium, medical uses of 163
- tellurium 134
- tetrahedra 3, 5, **9**, 36
 - bicapped 15
 - capping of 4
- tetrahydrofuran (THF) 47
- 1,4,7,10-tetrakis(carbamoylmethyl) 1,4,7-tetraazacyclodecane (DOTAM) 206
- tetramer 199–200
- N,N,N',N'-tetramethyl-2,3-butanediamine 136
 - possible isomers 137
- tetraphenyl metals 263
 - $(\text{M}(\text{C}_6\text{H}_5)_4)$ 252
- thallium 58
- thiocyanate 193
- thioethers 133, 184
 - derivatives 134
- thiol groups 223
- thiolates 190, 193
- thiols 184, 193
- thiones 192–3

- thiourea 192
- time scales 219–42
- tin 164, 252
- allylstannanes 41
 - cyclononatetraenyl(trimethyl)tin
 - comparison with dynamic properties of cyclononatetraenyl(di-*n*-propyl)borane 70–5
 - sigmatropic migrations in 74
 - cyclononatetraenyl derivatives of 72, 74
 - stannyl groups, sigmatropic migrations in 74
 - trimethylcycloheptatrienyltin 61
- titanium
- anticancer agents/drugs 164, 185–8
 - budotitane 185–6
 - complexes 185
 - biscyclopentadienyl 185
 - bis(β -diketonato) 185
 - [C_pTi(N=C'BuR)X₂] 95
 - ketimido complexes of 95–6
 - ketimido compounds 96
 - monocyclopentadienyl catalysts 95
 - [Ti(EHPG)(H₂O)] 186
 - titanium–nitrogen bond, rotation 96
 - titanocene dichloride 185–6
 - [Ti(HEHPG)(H₂O)₂O] 186
 - TMEDA complexes, diamagnetic 133
 - toluene 225
 - topological representations (top-reps) 1, 21–7, 29–31, 34–5, 36, 37
 - of polyhedral isomerizations 21–7
 - transferrin 186–7, 197
 - human 196
 - transition metals
 - acetylene compounds 120
 - complexes
 - dynamic behavior of groups 5 and 6, 85–129
 - isomerism with *n*, *n*-two-center ligands 110–19
 - d-block 5
 - d⁰ complexes
 - bonding of *n*-donor two center ligands in 119–21
 - dynamic behavior of 98–126
 - group 5 93–5
 - high-spin ions 202
 - olefin compounds 120
- transition state 107
- transitions
 - higher 289
 - ortho*–*para* 288
 - rotational 289
- trideuterioacetic acid 81
- trideuterioacetonitrile 81
- triethylamine 108, 111, 114, 118
- trifluoroacetate 276
- Trisenox[®] 163
- trypanothione 195
 - exchange between bound and free forms 196
- tubulin 169, 183–4
 - platination 183
- tungsten 85, 90–2, 98, 101, 110, 123–4, 289
 - complexes 125, 289
 - coupling constants with N,N-two-center ligands **112**
 - enantiomers 101
 - fluorides 110
 - fluoro complexes 107
 - isomerism with substituted hydrazones 114–19
 - halides 114
 - oxofluoramido complexes 91
 - oxofluoramido complexes, rotational isomerism in 86–91
 - oxofluoroketimido complexes, rotational isomerism 96–8
 - oxotetrafluoride 86, 96, 98, 118
 - oxyfluoride 86
 - peroxofluorides 99
 - π complex 124
 - reaction with oximes 98
 - tungsten–nitrogen bond 86, 96–7, 103, 111
 - hindered rotation 97
 - tungsten–oxygen bond 124
 - WF₆ 111
 - [W(O)Cl₂(C₂H₄)(PMePh₂)] 124–6
 - [WOF₄*MeCN] 86
 - WOF₄ 86–7, 90, 111, 115, 118, 122

- ^{19}F NMR spectrum 99
 $[\text{WOF}_4(\text{anti-ON}=\text{CHPh})]^-$, ^{19}F NMR spectra 106
 $[\text{WOF}_4(\text{anti-ON}=\text{CR}^1\text{R}^2)]^-$ 107–8
 energy profile of isomerization 109
 $[\text{WOF}_4\text{L}]^-$, ^{19}F NMR parameters **100**
 $[\text{WOF}_4(\text{MeNNMePh})]^-$, ^{19}F NMR spectrum 113
 $[\text{WOF}_4(\text{Me}_2\text{NN}^i\text{Pr})]^-$ 114
 $\text{WOF}_4(\text{MoOF}_4)$ 105
 $[\text{WOF}_4\text{N}=\text{C}(o\text{-CH}_3\text{C}_6\text{H}_4)\text{Ph}]^-$, ^{19}F NMR spectrum 97
 $[\text{WOF}_4(\text{N}=\text{CR}^1\text{R}^2)]^-$ 96
 $[\text{WOF}_4\text{NMePh}]^-$
 activation parameters **89**
 isomeric forms 91
 $[\text{WOF}_4(\text{NMePh})]^-$, isomerization 89–90
 $[\text{WOF}_4\text{NMePh}]^-$, ^1H NMR spectrum 87
 $[\text{WOF}_4(\text{NMePh})]^-$, $^1\text{H}^{13}\text{C}$ COSY spectrum 88
 $[\text{WOF}_4\text{NMe}_2]^-$
 activation parameters **89**
 ^1H NMR spectrum 87
 $[\text{WOF}_4(\text{ON}=\text{CMe}_2)]^-$ 101, 107
 ^{13}CH NMR spectrum 102
 ^{19}F NMR spectra 103–4
 $[\text{WOF}_4(\text{PHMeNN}^i\text{Pr})]^-$ 114
 $[\text{WOF}_4(\text{PhNN}=\text{CMe}_2)]^-$ 115–17
 isomers 116–17
 $[\text{WOF}_4(\text{R}^1\text{N}=\text{NR}^3\text{R}^4)]$ 114
 $[\text{WOF}_4(\text{syn-ON}=\text{CHPh})]^-$, ^{19}F NMR spectra 106
 $[\text{WOF}_4(\text{syn-ON}=\text{CR}^1\text{R}^2)]^-$ 107–8
 energy profile of isomerization 109
 $\text{W}_2\text{Me}_2(\text{NEt}_2)_4$, anti/gauche rearrangement 92
 tunnelling 282–301
 proton transfer 282–5
 rotational 285–301
 Tutton's salt 233
 tyrosine phosphatases 201
 ulcers 193
 van der Waals
 forces 289
 radii 297
 vanadium 164, 199
 antidiabetic drugs 164
 antidiabetic mimetics 197–201
 complexes 201
 chelated 198
 oxo diperoxo 201
 diperoxovanadates 198
 bis(ethylmaltolato)oxovanadium(IV) (BEOV) 199–200
 insulinomimetic ionic effect 197–8, 200
 bis(kojato)oxovanadium(IV) 201
 mono-peroxovanadates 198
 vanadates 197, 199–200
 2D EXSY NMR spectrum 199
 isomers 199
 ^{51}V NMR spectra 199
 $[\text{VO}(\text{O}_2)_2(\text{C}_2\text{O}_4)]^{3-}$ 201
 $[\text{VO}(\text{O}_2)_2\text{H}_2\text{O}]^-$ 201
 vanadyl 197–8, 200
 vibronic states 232–3
 wagging 204, 205
 Walsh orbital 62
 water–glycerol mixtures 226
 X-ray crystallography 136, 219, 232
 X-ray diffraction 123, 137, 143, 149, 155, 252, 292–3
 xenon 202
 ytterbium 206
 $[\text{Ln}(\text{DTPA})]^-$ 202
 $[\text{Yb}(\text{DOTA})]^-$ 206
 yttrium, $[\text{Y}(\text{DO3A-HP})]$, 2D ROESY spectra 208
 Zeeman
 energy 247–8, 250
 interaction 223–5, 229
 splitting 221, 249
 Zeise's salt 120–1
 zeolites 231, 261–3
 zinc 41, 195–6, 233, 291

With thanks to L. N. Derrick for compilation of this index.